Using Landscape Learning to Explore Diachronic Change:

A Quantitative Model and Western Stemmed Tradition Case Study

David B. Hunt

A dissertation

submitted in partial fulfillment of the

requirements for the degree of

Doctor of Philosophy

University of Washington

2022

Reading Committee:

Donald K. Grayson, Chair
Charlotte Beck
Darryl J. Holman
George T. Jones
Marcos Llobera

Program Authorized to Offer Degree:

Anthropology

University of Washington

Abstract

Using Landscape Learning to Explore Diachronic Change:

A Quantitative Model and Western Stemmed Tradition Case Study

David B. Hunt

Chair of the Supervisory Committee
Professor Emeritus Donald K. Grayson
Anthropology

In this research, I propose new methodologies for measuring landscape learning and gauging residence time on a landscape. I use a landscape learning model to set expectations and propose testable hypotheses utilizing these methods. The model and methodologies are then tested against data in the context of a Paleoindian colonizing event within the Old River Bed (ORB) delta in Utah.

I develop what I refer to as the Discoverability model to predict the order in which a random walker will discover patchy resources found on a neutral landscape, dependent only on distance and patch size. The simulation results for the model support my hypothesis that patch size affects encounter rate and that the model could be used to create a deterministic baseline for patch discovery against which to measure the accumulation of landscape knowledge.

I also present an original methodology to quantitatively determine toolstone patch sizes, or exposure extents, using hydrographic algorithms along with known primary source locations. These methods are tested on toolstone sources used by Paleoindians residing in the ORB delta.

The results demonstrate that, on average, the methodologies predicted 66% of the actual downslope flow of obsidian sediments and successfully returned an average scaled prediction of 89% of the area of the actual surveyed flow extents.

To test the Discoverability model, the ORB Paleoindian assemblages are divided into temporal groups. For each assemblage, the Discoverability values were calculated using the exposure and distance values for each toolstone source, and Discoverability lists (*Dlists)* of expected rank-order usage of toolstone sources are created. The corresponding Observed lists (*Olists*) were created using the observed toolstone proportions in each assemblage. The *Dlists* and *Olists* were then compared using Spearman's rank order correlation. From these results, the landscape learning variable (*%LL*) was calculated for each temporal group/assemblage.

The oldest temporal group's *Olist* returned a very strong correlation ($r_s = 0.777$) with its expected *Dlist*. This, in turn, returned the lowest level of landscape learning of any of the temporal groups (*%LL*=39.7%), as my model predicts. Importantly, the magnitude of difference in *%LL* (δ=35.1%) between the oldest and next oldest assemblage (~1096 cal years later) is significantly greater than any differences between any other subsequent temporal steps between the assemblages. These results indicate a significant step in landscape learning occurred between the earliest assemblage and the next temporally discrete assemblages. Overall, the results suggest that up to 48% of the variance in landscape learning over time at the ORB delta is explained by my Discoverability model. With limitations of scale and archaeological resolution, the model and resultant methods show promise as a means to quantify and rank the level of landscape learning within an assemblage.

University of Washington

Graduate School

This is to certify that I have examined this copy of a doctoral dissertation by

David B. Hunt

and have found that it is complete and satisfactory in all respects,
and that any and all revisions required by the final
examining committee have been made.

Chair of the Supervisory Committee:

_____

Donald K. Grayson

Reading Committee

_____

Donald K. Grayson

_____

Charlotte Beck

_____

Darryl J. Holman

_____

George T. Jones

_____

Marcos Llobera

Date: _____

TABLE OF CONTENTS

List of Figures

List of Tables

Acknowledgements

I am deeply grateful to my committee for their help and support: Don Grayson, Marcos Llobera, Charlotte Beck, Tom Jones, Darryl Holman, and Alan Gillespie. Don Grayson kindled my initial interest in the early colonization of the Americas, modelled the work of the scholar, and encouraged me throughout this process. This dissertation wouldn't have happened without his considerable guidance, support, and friendship. I am indebted to Marcos Llobera who taught me how to think about landscapes and convinced me, while waiting out a rainstorm during Mapping class, that "a returning student" could find a place in the UW graduate program. I would not have applied to the program without his encouragement. In a different way, Charlotte Beck and Tom Jones' "*Clovis and Western Stemmed: Population Migration and the Meeting of Two Technologies in the Intermountain West*" influenced me far more than I would realize when I read it in my tent during my first field school. It was a true honor to have them both on my committee.

Within the professional archaeology community, I found generous mentors and contributors. It is not an understatement to say that this project could not have been completed without the past work and present generosity of Craig Skinner. It is hard to imagine Great Basin archaeology without the decades of obsidian and fine-grained volcanic (FGV) research that he has amassed and freely shares with graduate students. Charlotte Beck was similarly generous in sharing all her Old River Bed (ORB) lithic data and images. Indeed, without access to the Old River Bed data provided by David Madsen, David Page, Daron Duke, Tom Jones, and Charlotte Beck, none of this work would be possible. Richard Holmer, Kathleen Hull, Richard Talbot, and Alex Nyers (NWROSL) also graciously provided datasets from their past work that is incorporated here.

Chapter 1: Introduction

1.1 Theoretical Framework: The Landscape Learning Model

While learning the lay of the land is critical to the success of any foraging group entering a novel landscape, the processes by which foragers familiarize themselves with, and adapt to, a new landscape are not well-understood (Anthony, 1997; Beaton, 1991; Kelly, 2003a; Kelly & Todd, 1988; Meltzer, 2002; Rockman & Steele, 2003). Understanding these processes is particularly challenging today because all historically known hunter-gatherers have long resided in their homelands (Meltzer, 2002, 2003). There are, however, four generalized expectations about what these initial colonization processes may have looked like:

1. It is generally accepted that environmental knowledge is acquired cumulatively, building a shared community knowledge base over time, but that environmental factors, such as unpredictable patchy resources or difficult terrain, may variably affect the speed and breadth of this knowledge accumulation (Golledge, 2003; Meltzer, 2002; Rockman, 2003, 2013; Roebroeks, 2003).

2. It is similarly accepted that colonizers would act to mitigate risk as they entered unknown lands. For example, it is expected that colonizers would carry with them critically needed material from known territories, until new, reliable sources were found. In contexts where trade is an unlikely factor, the presence of "exotic" material, such as non-local toolstone, in an archaeological assemblage is expected to signal the earliest forays into new land (Fitzhugh, 2004; Kelly & Todd, 1988; Rockman, 2003).

3. Over time, as a natural result of rising landscape knowledge, it is expected that archaeological assemblages would increasingly exhibit the use of local materials as environmental familiarization grows (Fitzhugh, 2004; Mandryk, 2003; Meltzer, 2002).

4. Finally, regional archaeological sites within the same temporal period are expected to exhibit the same level of landscape familiarization, reflecting the aggregation of individual knowledge, through social interaction, into the community knowledge base (Kelly, 2003b; Meltzer, 2003; Rockman, 2003, 2013; Tolan-Smith, 2003).

These expectations are codified into the Landscape Learning model, a model principally advanced by Rockman (Rockman, 2009, 2013; Rockman & Steele, 2003). Within this model, Rockman defines environmental knowledge in three basic forms: locational, limitational, and social. Locational knowledge involves understanding the topography of the land and the location of resources on that topography. Locational knowledge is considered the easiest and fastest form of landscape knowledge to acquire and is biased towards prominent landmarks and large, fixed, non-organic resources such as lithic sources (Kelly, 2003a; Rockman, 2003). However, not all resources are immediately evident to migrants, and it takes time and experience to accumulate detailed landscape knowledge at increasingly finer geographic scales (Meltzer, 2003). Limitational knowledge involves an understanding of the "usefulness and reliability" (Rockman, 2003, p. 5) of the resources at hand. These limitational parameters include issues of boundaries (both physical and social), seasonality and climate, and an overall economic familiarity (e.g., toolstone quality) with the landscape. Social knowledge involves the transmission of this knowledge, both horizontally (within the group and with external groups) and vertically (between generations), that allows the group as a whole to reduce risk and adapt to the new environment (Rockman, 2009). In this dissertation, I focus primarily on Rockman's locational knowledge as an indicator of landscape knowledge in general, and specifically as a potential gauge of the length of human residence on the landscape.

Landmark prominence is a key factor in the acquisition of locational knowledge. While Rockman does not define *prominence* directly, topographical prominence can be defined as an example of a "landscape affordance" (Llobera, 2001, p. 1007) or as the means by "which the environment lends or offers itself for action" (Kirchhoff, 2009, p. 5). Prominence affects the detection of a resource and, over time, changes in the detection and utilization of resources reflect processes of social change on that landscape (Llobera, 2001). This, in turn, allows us to link increasing affordance detection (i.e., increasing local resource knowledge and use) with increasing social knowledge, and thus gauge the overall socialization and landscape learning process occurring on the landscape. Importantly, the detection and utilization of these affordances by people is reflected in their material culture and the resultant archaeological record.

For the purposes of this research, prominence will be expressed as a function of the surface exposure of a lithic resource on the landscape (see Chapter 3 for a complete definition of "exposure"). During the locational phase of landscape learning, the model expects that the most prominent, or "most detectable", resources will be discovered in rank-order and utilized in corresponding proportions. For newcomers, who lack the benefits of time on the landscape and local social networks, it is expected that less prominent (i.e., less exposed and less discoverable) resources will be overlooked. As a result, we can expect that lithic assemblages produced by these earliest colonizers will reflect a high bias towards the most easily discovered lithic sources and correspondingly low spatial organization and efficiency (Kelly, 1995). This bias should decrease, and spatial optimization increase, as landscape learning increases, eventually peaking at "complete" landscape learning which, for the purposes of this study, is represented by the complete knowledge of the lithic source landscape.

Principles of the landscape learning model have found utility in evaluating the process of landscape familiarization or socialization by immigrants, specifically with regard to lithic sources (Fitzhugh 2004; Fitzhugh and Trusler 2009; Rockman 2009; Ford 2011; but see also Kitchel 2018). Fitzhugh (2004) focuses on a phase of the colonization process referred to as "regionalization" (after the colonization stages outlined in Spiess, Wilson, and Bradley (1998): pioneering, migration, regionalization), a period characterized by increasing local resource familiarization and decreasing dependence on resources from the migrants' home range (e.g., exotic toolstone). Even if the initial pioneering and migration forays into a region remain archaeologically invisible, the stages of regionalization occur across a broad continuum, from an early "settling in" (Fitzhugh, 2004, p. 14) period, where environmental knowledge is low and uncertainty high, to late stages marked by deep knowledge of the region, including its relevant resources and their specific qualities. Regionalization can then be expressed in terms of increasing certainty in, and knowledge of, the terrain and in the optimization and utilization of local resources over homeland resources. As settling in advances, migrants increasingly replace exotic, previously trusted resources with suitable, readily available, and efficiently acquired local substitutes.

My research specifically centers on developing methodologies to detect and quantify changes in locational knowledge over time, measured by the utilization of prominent resources. Following the landscape learning model, if assemblages were created within distinct temporal periods, we can expect to see lithic resource knowledge within those periods act as a "proxy measure of landscape knowledge" (Kitchel, 2018, p. 871), increasing over time in a predictable fashion. Successfully utilizing this model requires the methodologies to consistently measure lithic resource knowledge within a given archaeological assemblage and a method to then

compare these values between assemblages, methods which I propose and test here. This approach is dependent on a means to set a neutral "baseline" (Fitzhugh, 2004, p. 14) against which to compare regional landscape knowledge as it is acquired over time by settlements of the same population group. The methods to establishment this baseline, to measure lithic resource knowledge within a specific assemblage, and to then compare landscape learning levels over time, are the subject of Chapter 2.

There are, however, significant questions of scale, both temporal and spatial, that are not well addressed within the landscape learning model. The issue of scale is largely untested within this model and represents a significant and problematic variable. How quickly do people learn a landscape and how broadly? Ford (2011) attempted to use the landscape learning model within the context of the occupation of the Ivane Valley of New Guinea between 43,000 – 49,000 cal BP, but demonstrated what archaeologically appears as an almost instantaneous adaptation to local toolstone. In this case, it is likely the Ivane Valley is too small (<50 km^2) to detect landscape learning archaeologically within the large temporal span (~6000 years) examined. In contrast, Tolan-Smith (2003) suggests that, following a 7000-year abandonment during the last ice age, the landscape of England (~130,000 km^2, Kellner 2022) was re-learned and that landscape learning may be visible on scales of several millennia. England is roughly half the size of my study region (~284,000 km^2, described below) and Tolan-Smith's example may provide a useful guide to gauge spatial and temporal scale expectations.

If successful, applying these methods may yield otherwise inaccessible information about how people behave and adapt as they encounter unknown lands for the first time. They may specifically reveal information about the rate of landscape knowledge acquisition and provide a means to compare the levels of landscape learning between assemblages. Most importantly,

comparing the levels of landscape lithic resource knowledge across assemblages may provide a means to place otherwise undatable lithic assemblages into relative chronological order.

1.2 Methodology Testing

To determine if landscape learning can be detected and quantified across discrete temporal ranges, I used the results of archaeological research at the Old River Bed (ORB) delta in Utah as a testbed (Madsen, Schmitt, et al., 2015). At the ORB delta, numerous Western Stemmed Tradition (WST, described below) sites and artifacts are strongly associated with individual, chronologically-ordered distributaries within an extinct river delta complex. The ORB data affords the opportunity to detect landscape learning within known chronological time slices by analyzing lithic material sourcing, testing the utilization of prominent resources, and investigating what these patterns tell us about the accumulation of landscape knowledge and the colonization process.

1.2.1 Study Region

Lake Bonneville was the largest of the Great Basin pluvial lakes (Figure 1-1), with a depth (~1000 feet) and a surface area (50,500 km^2) rivaling the size of modern-day Lake Michigan (Atwood et al., 2016, p. 19; Currey et al., 1984). Lake Bonneville reached its highstand (~1552 m above sea level (ASL)) around 18,000 cal BP as it topped the lowest edge (the Zenda threshold) of its basin (C. G. Oviatt & Shroder, 2016; Shroder et al., 2016, p. 78). While people would eventually occupy the caves and rockshelters created by Lake Bonneville wave erosion (e.g., Bonneville Estates Rockshelter and Danger Cave), there is no evidence of human occupation coincident with the Bonneville shoreline at this level or time (Beck & Jones, 1997; Graf, 2007; Jennings, 1957; Rhode et al., 2005).
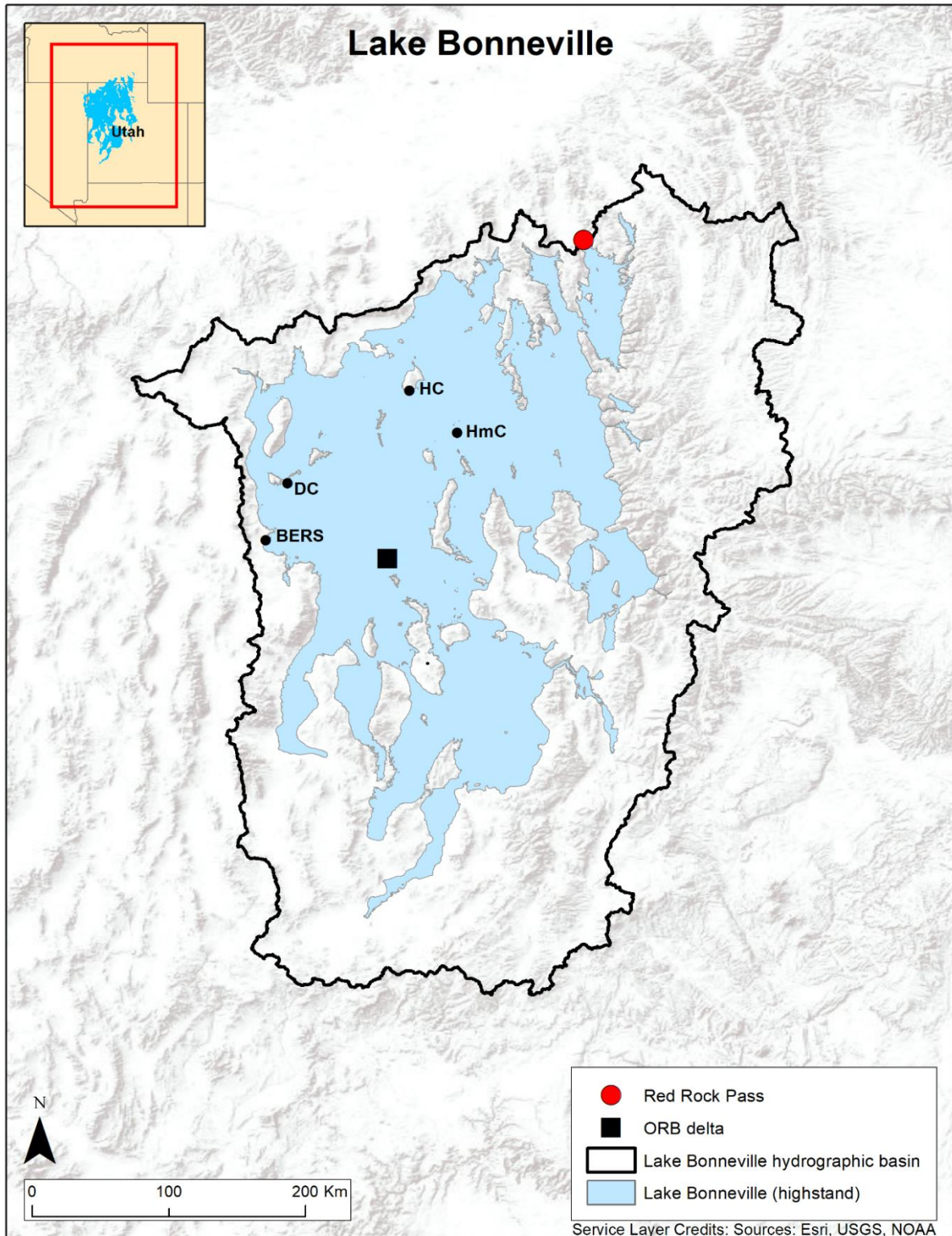
Figure 1-1: Lake Bonneville highstand (Chen & Maloof, 2017a) *in relation to the Bonneville hydrographic basin and WST-aged occupation sites -- BERS: Bonneville Estates Rock Shelter, DC: Danger Cave, HC: Hogup Cave, HmC: Homestead Cave.*

Around 18,000 cal BP, the edge of the Bonneville Basin near Red Rock Pass, Idaho collapsed, resulting in a cataclysmic flood outside the basin and a new shoreline within, the Provo shoreline, 125 m below the Bonneville shoreline (Hart et al., 2004; C. G. Oviatt & Shroder, 2016; Shroder et al., 2016). This shoreline fluctuated around 1450 m ASL for about 3000 years. Between 15,000 and 13,000 cal BP, evaporation outpaced lake input and the lake level fell an additional 200 m. During this regression and around 14,000 cal BP (~12,000 ^{14}C yr BP), as the lake dropped below ~1390 m ASL, the northern subbasin was cut off from the southern subbasin (Hart et al., 2004; C. G. Oviatt & Shroder, 2016). The last remaining connection between the northern and southern subbasins was a point of overflow at the Old River Bed threshold (Figure 1-2). Lake Bonneville continued its regression, arriving at elevations similar to modern-day Great Salt Lake levels (~1280 m ASL) around 13,000 cal BP (C. G. Oviatt & Shroder, 2016). This is coincident with the timing of the first signs of human occupation in the basin. At Bonneville Estates Rockshelter (Figure 1-1), the earliest unequivocal human occupation is dated to ~13,000 cal BP (11,010 ^{14}C yr BP), with a WST occupation evident from ~12,800 – 12,000 cal BP (10,800 – 10,300 ^{14}C yr BP) (Graf, 2007; Hockett, 2015; Rhode et al., 2005).

Following the separation of the northern and southern subbasins, a fan-like series of river distributaries formed, that meandered across the dried lake sediments of the northern subbasin (the Great Salt Lake basin) as the higher (~100 m) southern subbasin (the Sevier basin) drained to lower elevations (Madsen, 2016; Madsen, Schmitt, et al., 2015). The resultant delta, termed the ORB delta (Figure 1-2), created a new wetland environment coinciding with both the timing of the earliest inhabitations of the Great Basin and the appearance of the WST (described below). Over the course of about 3,600 cal years (~11,500 – 8,800 ^{14}C yr BP), various distributaries
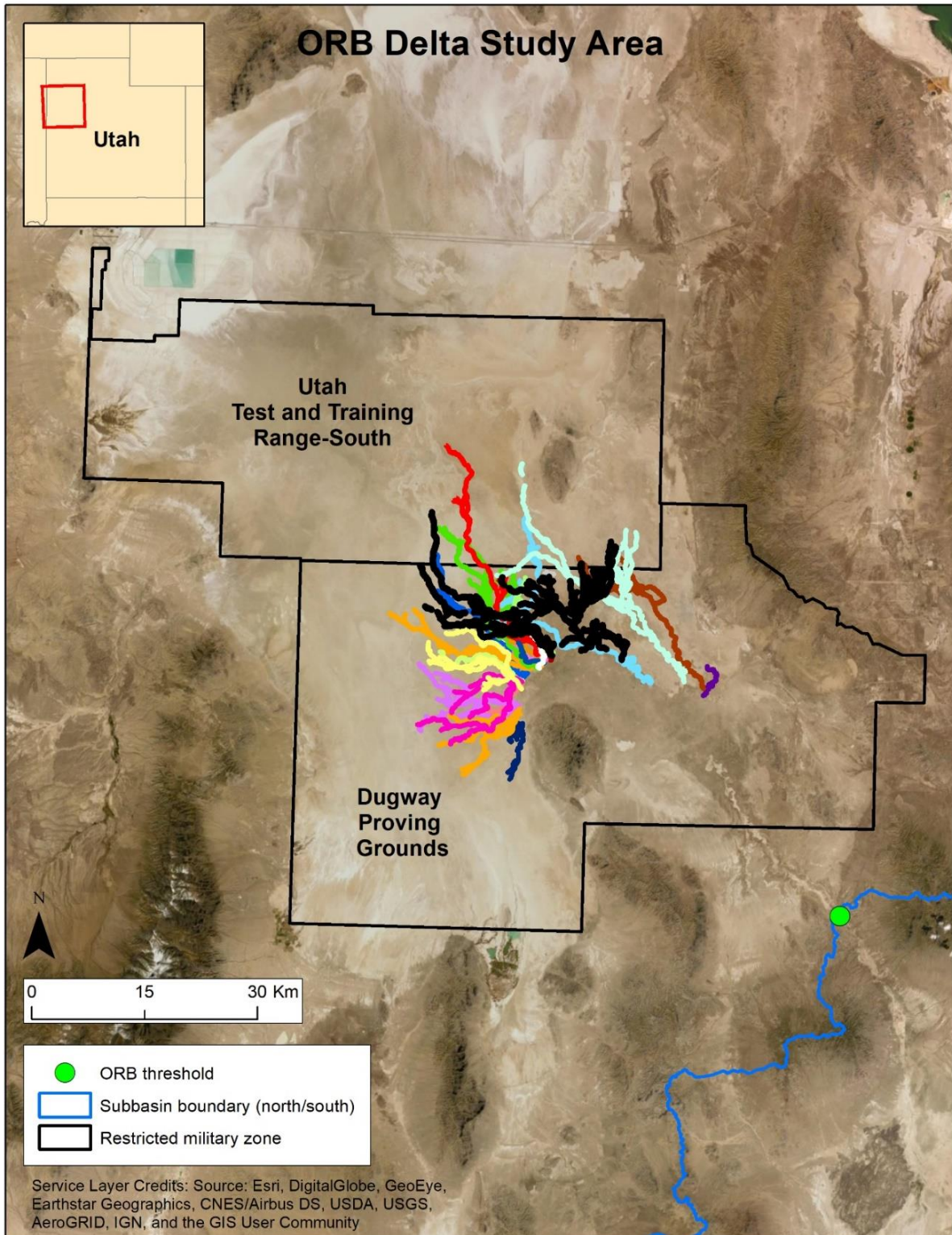
Figure 1-2: The Old River Bed (ORB) delta study region today - ORB channels shown according to assigned color name (after Madsen, Schmitt, et al., 2015). See also Appendix A, Tables A-1 and A-2. Channel data by David Page (personal comm., August 22, 2018).

formed and went extinct, creating a datable sequence of riverine habitats (Madsen, Schmitt, et al., 2015). Once the Sevier basin finally dried up, the drainage ceased, people moved away, and the region has remained dry until present, placing the extinct delta into a sort of stasis. This stasis was protected and aided in the mid-twentieth century when the region was incorporated into the U.S. Air Force's Dugway Proving Ground and the Utah Test and Training Range - South, restricted military zones for testing modern weapons that have effectively protected the delta's archaeological resources from development and illicit artifact collection.

1.2.2   Western Stemmed Tradition

The Western Stemmed Tradition is a lithic technology which consists of a varied collection of stemmed point types (Figure 1-3) that appear during the Paleoindian period and disappear around the onset of the Archaic period. (Beck & Jones, 2009; Bryan, 1980; Duke, 2011; Erlandson et al., 2011; Grayson, 2011; Haynes, 2007; Heizer & Hester, 1978; Kelly, 1978; Pendleton, 1979; Rosencrance, 2019; Smith et al., 2020; Swanson et al., 1964; Tuohy, 1974; Tuohy & Layton, 1977; Warren, 1967; Willig & Aikens, 1988). The Paleoindian period extends from the first occupations of the Americas and ends with the transition into the Archaic period, which occurs roughly around ~9500 cal BP (8500 ^{14}C yr BP) and is marked by the innovation of notched projectile point types and the intensive use of ground stones (Haynes, 2007; Madsen, 2007).
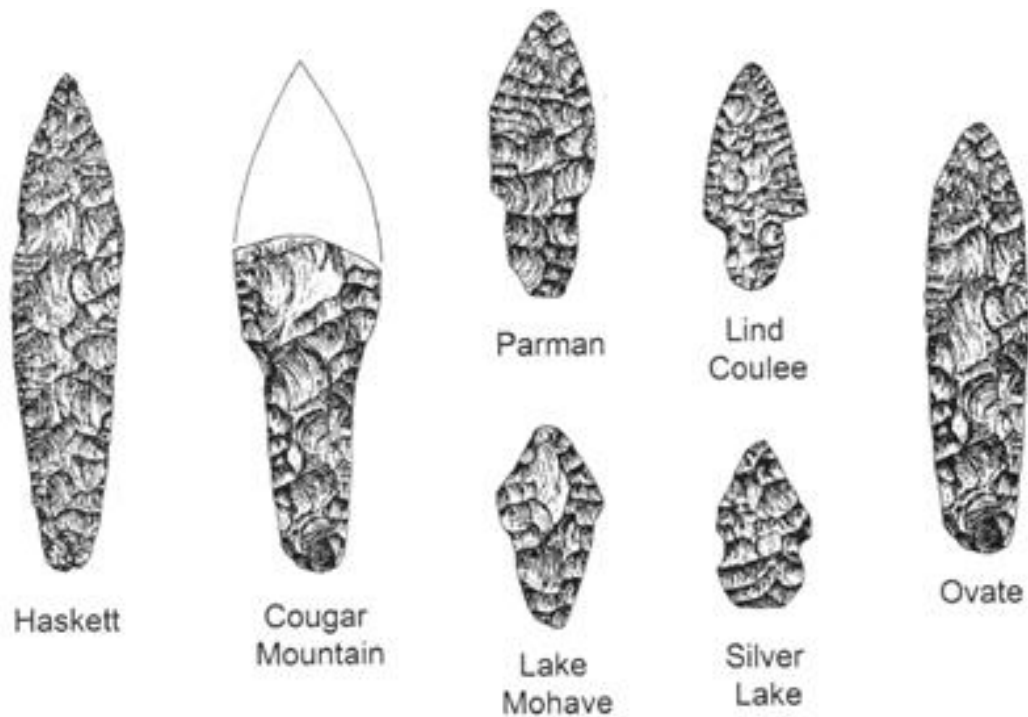
Figure 1-3: Notable Western Stemmed Tradition subtypes (used with permission, T. Jones). See also Duke (2011) and Rosencrance (2019) for Bonneville and Stubby subtypes

With a range that extends from the west coast to the Rocky Mountains (Figure 1-4), the

WST is most closely associated with the pluvial lakes of the Great Basin at the Terminal

Pleistocene/Early Holocene (TP/EH) boundary (Beck & Jones, 2009; Grayson, 2011). WST

points and sites are frequently found in valley bottoms and on valley edges, typically in what

would have been low-lying wetland areas, but which are now arid (Grayson, 1993, 2011;

Madsen, 2007; Smith & Barker, 2017).

The earliest WST date is recorded at the Cooper's Ferry site in Idaho, with a stemmed

point base discovered below bone dated to ~13,460 cal BP (11,630 ± 80 ^{14}C yr BP) (Davis et al.,

2019). Within the Great Basin, WST points make their earliest well-dated appearance at the

Paisley Caves, with a minimum age of ~13,000 cal BP (11,070 ± 25 ^{14}C yr BP) (Jenkins et al.,

2012, 2013; Waters & Stafford, 2007). At Paulina Lake, in Oregon, a stratum containing WST

points (subtype Windust) sets the latest date for the WST at ~7870 cal BP (7,080 ± 80 ^{14}C yr

Figure 1-4: Distribution of Western Stemmed Tradition (WST) diagnostic tool types (gray hatched region, after Madsen 2016), mentioned WST sites [CF: Cooper's Ferry, PC: The Paisley Caves), and the Old River Bed (ORB) delta study area. Light blue outline indicates the hydrographic Great Basin boundary (after Grayson, 2011).

BP), coincident with a period of significant population decrease in the Great Basin and the onset of the arid Middle Holocene (Beck & Jones, 1997; Connolly, 1999; Grayson, 2011; Louderback et al., 2011; Smith & Barker, 2017). As a result, we know that the WST spanned a great deal of time, ~5,590 cal BP years (~11,630 to 7,080 ^{14}C yr BP) in and around the Great Basin. Importantly, the first appearance of the WST and its temporal span coincide well with the emergence and lifespan of the ORB delta.

1.2.3 WST in the ORB

Madsen (2016) and other workers (Clark et al., 2016; Duke & Young, 2007; Madsen, Schmitt, et al., 2015; Charles G. Oviatt et al., 2003; Page, 2008, 2015a, 2015b; Page & Duke, 2015; Rhode et al., 2005; Schmitt et al., 2007; Skinner, 2021) have researched the ORB delta's geomorphological origins and have surveyed, collected, and analyzed the archaeological remains found along its individual distributaries. Madsen et al. (2015) documented 23 individual distributaries (color-coded in Figure 1-2, see Table A-1) and over 230 WST sites within the ORB delta. Ten of these distributaries have been reliably dated, by dating organic sediments, plant remains, or mollusk shells indicative of wetland environments, and are associated with Paleoindian sites (predominantly WST projectile point types, see Appendix A). A few Archaic era projectile point forms appear in the overall dataset, but these are generally considered to be intrusive objects that were deposited after the wetlands had dried (Beck & Jones, 2015). The extinction of the wetlands around ~9800 cal BP (8,800 ^{14}C yr BP) ensured the WST record along the distributary channels was not significantly overlain by later human groups (i.e., there are no palimpsests). As few charcoal or organic materials were recovered from the ORB delta archaeological sites, all site dates are relative estimates derived from the associated distributary

dates, beginning around ~13,000 cal BP (11,300 ^{14}C yr BP) (Madsen, Oviatt, et al., 2015).

Individual sites have been classified according to the distributary channel to which they belong, and according to whether they are on the channel margin or within the channel itself (Madsen et al., 2015). Sites on the margins are considered contemporaneous with the flow of the river, situated to exploit channel resources when it flowed, while sites within the channel are assumed to postdate the time the channel flowed. The majority of these artifacts (*n*=2288, but see Appendix A) fall within the broader WST typology and were classified to specific tool type (Beck & Jones, 2015; Charlotte Beck, personal comm., May 31, 2018).

The majority of the ORB delta artifacts are composed of obsidian or fine-grained volcanic (FGV) material which have been geochemically identified to regional lithic sources (Page, 2015a). Figure 1-5 presents the general locations of the 16 known lithic sources utilized during the WST occupation of the ORB delta (see Appendix A, Table A-42). Chapters 3 and 4 explore resource extents for these sources. As I noted above, the overall study area covers roughly 284,000 km^2 (using the lithic source points in Figure 1-5 to form a polygon), about twice the area that Tolan-Smith (2003) argues could have required one to two millennia to fully learn. The relationship between these artifacts and their lithic sources are well-defined and key to the potential success of my methodologies.

Importantly, the association of multiple sites with each of the ten dated channels provides the means to create pooled assemblages with significant temporal distinction. While the artifact counts for many sites are small (mean = 15.5), the expectation that sites within the same temporal period will exhibit the same level of landscape familiarization can be leveraged here. By pooling artifacts associated with each dated channel, statistically-valid sample groups can be created for comparison across discrete date ranges.
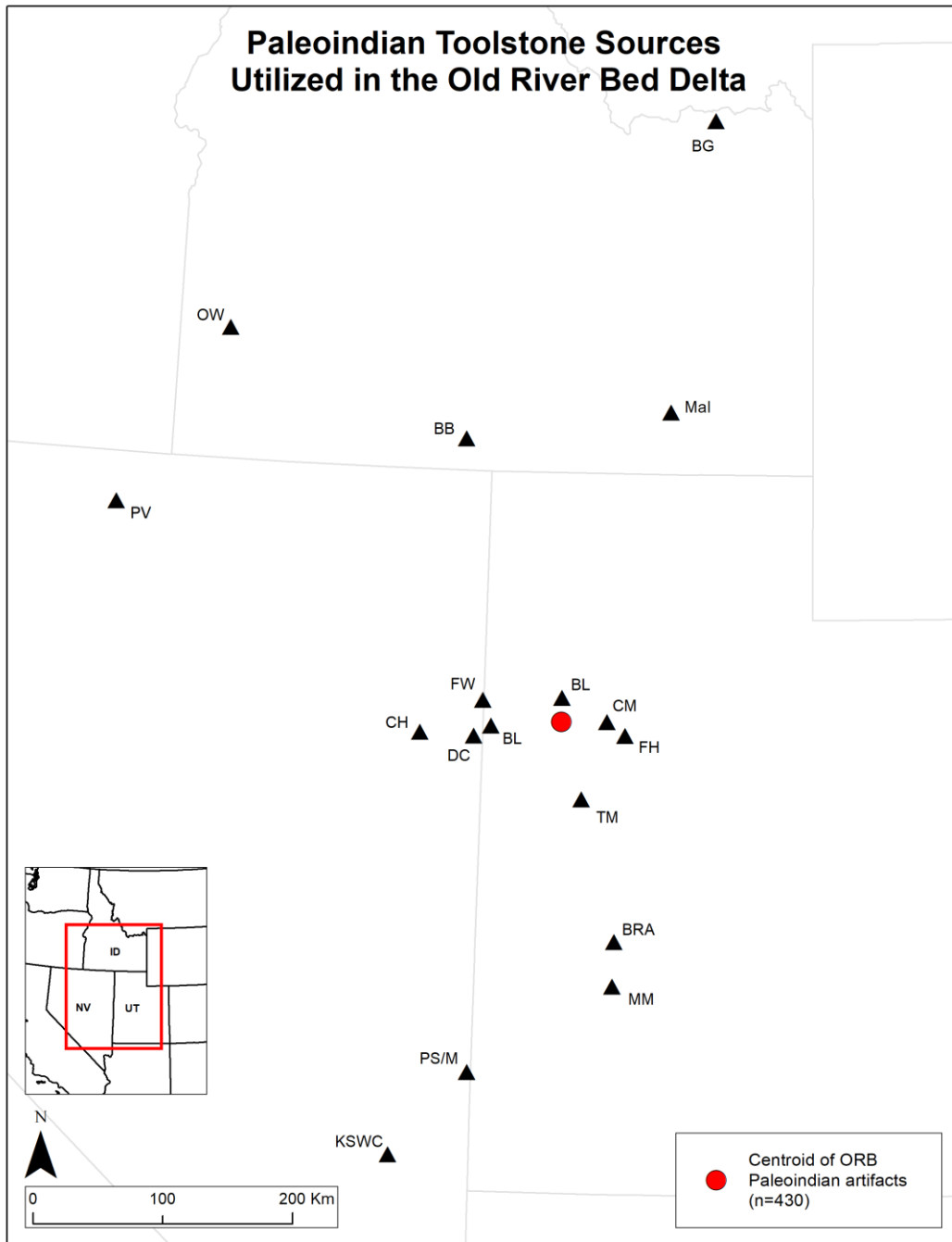
Figure 1-5: Rough locations of obsidian and fine-grained volcanic (FGV) toolstone sources utilized by Paleoindian people occupying the Old River Bed delta channels. Key: Badlands (BL), Brown's Bench (BB), Bear Gulch (BG), Black Rock Area (BRA), Currie Hills (CH), Cedar Mountain (CM), Deep Creek (DC), Ferguson Wash (FW), Flat Hills (FH), Kane Springs Wash Caldera (KSWC), Malad (Mal), Mineral Mountains (MM), Owyhee (OW), Panaca Summit/Modena (PS/M), Paradise Valley (PV), Topaz Mountain (TM) (Skinner, see Appendix D, Table D-2).

15

Finally, the WST archaeological data from the ORB delta allows us to test landscape learning in the context of a colonizing event as the delta essentially emerged as "new land" with the recession of Lake Bonneville and the formation of an extensive wetland in the ORB delta. The results in Madsen et al. (2015) support this view as two of the earliest channels (Mocha and Manga, undated but underlying Gold) have no known sites and the Gold channel, which first appeared around ~13200 cal BP (11,300 ^{14}C yr BP), presents only two WST sites. As younger channels emerge, the number of sites and their density increases, especially beginning with the large Black channel around ~12900 cal BP (spanning ~11,000-10,300 ^{14}C yr BP), and the archaeological record reflects continuous habitation throughout the remaining lifecycle of the delta (Madsen et al. 2015:43).

1.3 Dissertation Structure

This dissertation explores the landscape learning model and describes original methodologies designed to measure the accumulation of landscape knowledge.

I attempt to answer the following question:

Can landscape learning be detected in the archaeological record and used to place assemblages in relative chronological order?

In **Chapter 2**, I define the Discoverability equation, a measure of prominence, and argue that lithic resource discovery can be modeled using the Discoverability equation. This model expands on Brantingham's (2003, p. 487, 2006) "neutral model of stone raw material procurement", demonstrating that resource size on the landscape increases encounter rate. The methods in this chapter provide a theoretical means to quantify the likelihood of an encounter with a lithic resource patch in a neutral model, a value that can act as a baseline measure. I also

describe methods to then compare observed values against this expected baseline and to track change in landscape learning over time.

While most of the lithic resources utilized in the ORB delta are known, at least in general locational terms, we do not currently know how big they are. We do not know the actual exposure size of these resources which, because of alluvial and colluvial action, can manifest as extensive (hundreds of square kilometers) secondary extents. **Chapter 3** describes original methods for predicting these extents, demonstrates the predictions for five sources utilized at the ORB delta, reports on the actual extents observed during three seasons of survey, and calculates the effectiveness of these prediction methods.

Chapter 4 predicts the exposure values for the remaining ORB delta lithic resources, based on the success of Chapter 3. Combined, the surveyed and predicted extents from Chapters 3 and 4 provide the distance (*d*) and exposures (*E*) variables for calculating the Discoverability results in Chapter 5.

Chapter 5 examines the early archaeology of the ORB within the context of the landscape learning model developed here. The goal of this examination is to determine whether that model has the potential of placing undated lithic assemblages created by human foragers entering a novel landscape into relative chronological order.

Appendices: Appendix A explains the cleaning, merging, and filtering of several ORB data sources. The result of this work is a subset of Paleoindian artifacts for testing. Additional appendices represent supporting data tables and X-ray fluorescence (XRF) lab reports.

Note: Where radiocarbon dates are presented from the literature, the calendar dates shown in this chapter were calculated with OxCal 4.4.4 (Bronk Ramsey, 2021; Reimer et al., 2020).

Chapter 2: The Discoverability Model

"Building models from first principles is a critical step in any research

program aimed at understanding such complex spatio-temporal processes as

foraging movements." (Turchin, 2006, p. 453)

2.1 Introduction

Operationalizing the landscape learning theoretical framework requires the creation of two original methodologies. The first involves quantifying the prominence, or what I will call "discoverability", of patchy resources in terms of the locational attributes of surface exposure and distance. As will be shown, the Discoverability value represents the likelihood of a random walker, with no landscape knowledge, encountering a resource patch. These values will be used as a means for setting a "neutral" baseline against which to compare landscape learning over time. The second methodology provides a means to quantify levels of landscape learning for an assemblage in order to compare that assemblage, and other assemblages, to the baseline.

All examples shown or described in this chapter are available in the form of Python code/programs or Jupyter Notebooks located on my GitHub repository. See the "Repository and Software" section after the conclusion of this chapter for online access.

2.2 Defining Prominence / Discoverability

Brantingham (2003) created a "neutral model" computer simulation for modeling how an unbiased agent, moving via a simple (or Brownian) random walk on an unbiased landscape would accumulate lithic material in its toolkit, as a proxy for understanding assemblage formation. The goal of the model was to help understand what natural, probabilistic patterns of lithic acquisition could be expected when the agent "does not seek to optimize any specific currency" (2003, p. 492). In this way, the neutral model creates a baseline acquisition pattern,

devoid of human adaptive behaviors. With such a baseline, variation from that baseline can then be used to provide insight into human adaptations to the landscape.

Brantingham (2003; see also Tobler, 1970) demonstrated that as the distance of a lithic source from the starting point of a search (the central place or home site) increases, the proportion of that specific raw material observed in the final assemblage decreases exponentially, an example of the distance decay effect (*Equation* 2-1):

$$\frac{1}{d^2}$$ (Eq. 2-1)

This is a useful factor for calculating how patches at varying distances from a central point may be encountered in varying rates. Further, I propose that Brantingham's neutral model can be expanded by biasing, or modulating, an additional environmental variable, the size of the target (e.g., a lithic source/patch), without negatively affecting the overall neutral nature of Brantingham's original model.

Natural lithic sources vary greatly in size and are not uniformly distributed on the landscape. Obsidian sources in the Great Basin, for example, may be concentrated in dense flows or scattered as nodules in vast fields spread by explosive volcanic action. Defining a patch can be problematic because lithic sources may be spread out widely or the same flow may be exposed in multiple locations. Obsidian is also subject to colluvial and alluvial action, potentially creating enormous secondary distributions as erosion moves obsidian cobbles and pebbles downslope. Along the shores of Pleistocene Great Basin lakes, tertiary distribution may have further moved obsidian pebbles laterally as the secondary distributions were tumbled by wave action. The result of these natural forces is that, for many Great Basin obsidian sources, the full distribution extent may be spread across hundreds of square kilometers of exposure.

19

I propose that this *exposure* (*E*), the entire exposed surface distribution area of a lithic source, plays a key role in the discoverability of that source by mobile foragers. Even if the erosional distributions consist of pebbles too small to make tools, the presence of these distributions would have acted as a "signal" to alert hunter-gatherers that crucial toolstone resources were close at hand. Ethnographic studies report that hunter-gatherers are astute students of their environment, valuing environmental knowledge and attention to even the most subtle changes in the terrain and its appearance (Blurton Jones & Konner, 1976; Foster & Foster, 2000; Kelly, 1995). Hunter-gatherers would have quickly noticed the appearance of these distinctive sediments as they foraged and could easily follow them uphill to their sources (Meltzer, 2003). Original methods to predict the areal estimation of these exposures are detailed in Chapters 3 and 4.

The size of a source's exposure and its distance from a site will affect the probability of its detection – its *discoverability* – by a walker on an unlearned landscape. It follows that the sources that have been discovered will also affect the resultant compositions of hunter-gatherer lithic assemblages. The Discoverability (*D*) of a lithic source is then expressed in terms of exposure (*E*) and distance (*d*) relative to a site/assemblage. In its simplest terms, this can be expressed as shown in *Equation 2-2*:

$$D = E * \frac{1}{d^2} \qquad \text{(Eq. 2-2)}$$

I propose that for any given site (or assemblage) in an otherwise neutral landscape, if one knows: (*a*) all the lithic toolstone sources in the region (the lithic universe), (*b*) the distances between the site and those sources, and (*c*) the exposure areas of the sources, the site's *expected* lithic assemblage composition can be calculated. I refer to this site-specific baseline as the

Discoverability list (or *Dlist*). This baseline represents the resource proportions we would expect a random walker from a central place to encounter and accumulate on a wholly unlearned landscape, a "coming into the country" state of discoverability (Kelly & Todd, 1988).

The first step is calculating the Discoverability value (*Equation 2-2*) for each source using the distances relative to a specific site. Figure 2-1 illustrates the relationship of six sources (A - F) to a single site/assemblage. The sources vary in size (exposure) and distances from the site.

From these values, the site's Discoverability rank-order list (the *Dlist*) is created – the normalized, ranked list of lithic source proportions one would expect to find in a site assemblage in a neutral model. Table 2-1 demonstrates the calculation of the Discoverability values and normalized proportions for the site in Figure 2-1.
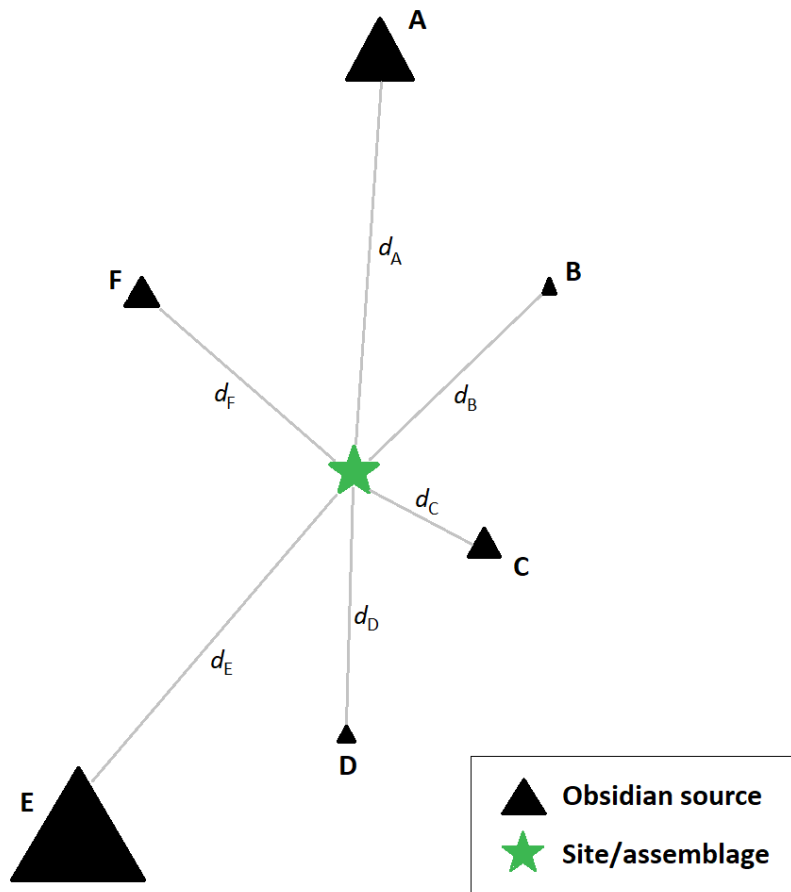
Figure 2-1: Illustration of the relationship between source exposures and distances relative to a given site/assemblage.

Table 2-1: Calculation of the Discoverability (D) values and normalized proportions

Lithic universe	d (*km*)	$\frac{1}{d^2}$	E (*km²*)	D	Normalized proportions (100*D/ΣD)
Source A	100	0.0001	14	0.0014	4.3%
Source B	50	0.0004	0.5	0.0002	0.6%
Source C	20	0.0025	7	0.0175	53.4%
Source D	75	0.00018	2	0.0004	1.1%
Source E	125	0.000064	100	0.0064	19.5%
Source F	60	0.00028	25	0.0069	21.2%
				0.0328	

Table 2-2 illustrates the expected lithic source proportions - a *Dlist* - based on the ranking of the normalized Discoverability values.

Table 2-2: The rank-order Discoverability list, or Dlist

Source	Expected proportions (*Dlist*) (100*D/ΣD)	Rank
Source C	53.4%	1
Source F	21.2%	2
Source E	19.5%	3
Source A	4.3%	4
Source D	1.1%	5
Source B	0.6%	6

The *Dlist* will, of course, vary from site to site, as the distances to sources will vary and affect the calculated discoverability value. Figure 2-2 illustrates how the distances vary for each of three sites operating within the same lithic universe of six sources.

Contrasting with this are the actual "observed" proportions of lithic material from a site. These proportions are known from the archaeological record, normalized to 100%, and make up the observed list (*Olist*). The expected distribution (*Dlist*) can then be compared statistically to the actual raw material rank-order (*Olist*) of an assemblage. The greater the correlation between
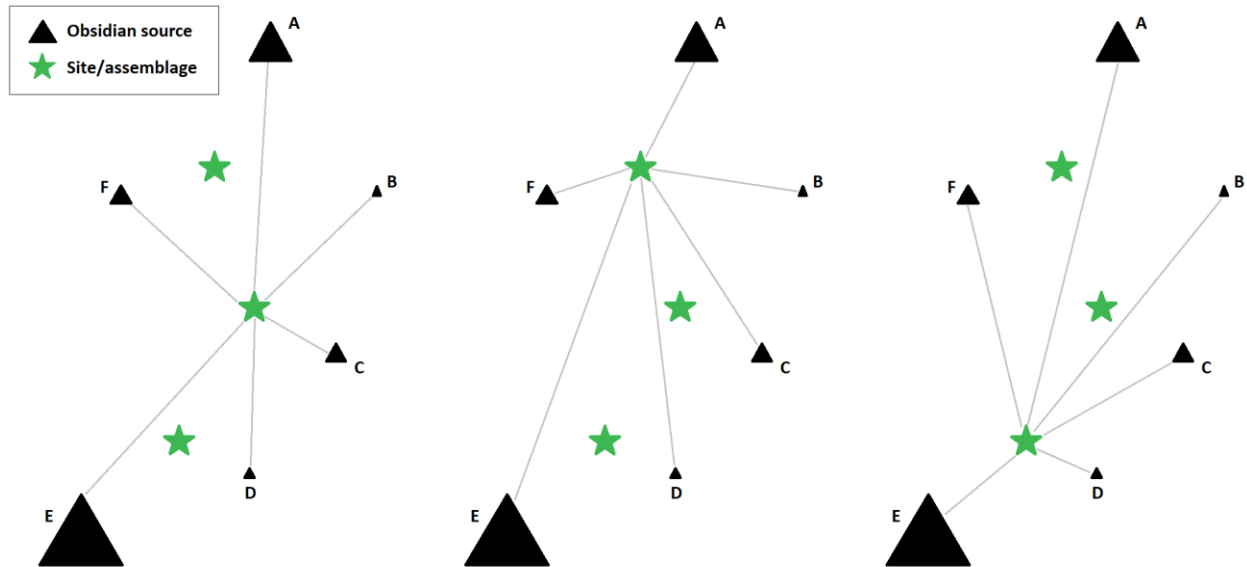
Figure 2-2: The Dlist for each site is dependent on the relative distances to all lithic sources. This illustration demonstrates the variable distances of regional sources from each of three sites.

the lists, the closer procurement/assemblage creation comes to a random walk on the landscape. Lack of significant correlation with the Discoverability rank order list (*Dlist*), then, is behavioral adaptation to the landscape; in this argument such variance represents landscape learning.

2.3 Estimating Relative Regionalization Levels

Under this model, I expect to observe a continuum of learning over time and propose that this continuum can be detected. Colonizers will initially utilize easily discoverable lithic resources while potentially retaining exotic (non-local) toolstone in their toolkit to reduce risk and uncertainty. During this early phase, their choices should most closely match the baseline, the *Dlist*. As "settling-in" progresses (Fitzhugh, 2004), less discoverable, but equally usable, patches will be discovered and incorporated into the universe of known lithic sources (this assumption is discussed below). With expanding knowledge, people will have the opportunity to make travel optimization choices when procuring lithic raw material (Beck et al., 2002). As efficiency decisions are made, I expect to observe more sources with lower discoverability values appearing in an assemblage. As regionalization is carried to completion, all available

23

sources will be discovered. As a result, late-stage regionalization should be characterized by assemblages that reflect maximum optimization of less discoverable sources and these "well settled" sites should exhibit the greatest variation from the baseline (the *Dlist*).

Two confounding issues must be addressed. First, when any two human groups meet on the landscape, issues of territoriality must be considered (Dyson-Hudson & Smith, 1978; Kelly, 1995; Speth et al., 2013). Where it is present in the Great Basin, obsidian is generally quite abundant (though see Ferguson Wash in Chapter 3 for a notable exception). Dyson-Hudson and Smith observe that if a resource is "so abundant" on the landscape that availability is assured, "then there is no benefit to be gained by its defense and territoriality is not expected to occur" (1978, p. 25). Similarly, in this study, lithic source quality is considered neutral. Beck and Jones (1990, 1997) find that obsidian and fine-grained volcanics (FGV), such as andesite and dacite, appear to have been used interchangeably and as acceptable alternatives when the need arises. This model will operate under these assumptions as regards these resources, but I recognize that it is highly unlikely that all known lithic resources were considered to be equal in terms of quality. This will become clear in subsequent chapters.

If these expectations and assumptions hold true, then I propose that the "extent" of landscape learning (*LL*) for an assemblage can be quantified on a scale from 0 to 100% (*%LL*). The higher the percentage, the greater the extent of landscape learning possessed by the people living there and the greater their residential time on the landscape. This will allow sites to be relatively ordered from lowest *%LL* to highest *%LL,* a ranking that should correspond to decreasing site age. This would then allow the evaluation of multiple sites to gauge the extent of landscape learning and place them in relative chronological order. For this project, the variance from the *Dlist* represents landscape learning, so *%LL* can be represented by *Equation* 2-3. Here

r_s^2 is the *coefficient of correlation* and the value $(1 - r_s^2)$ is also known as the *coefficient of nondetermination* (Zar, 2010, p. 364), appropriate for gauging the variance from a deterministically-derived baseline:

$$\%LL = (1 - r_s^2) * 100 \qquad \text{(Eq. 2-3)}$$

Table 2-3 presents a fictional example for the calculation of *%LL* for a single site.

Table 2-3: Calculation of %LL

Source	Expected proportions (*Dlist*)	Rank	Actual proportions (*Olist*)	Rank
Source C	53.4%	1	45%	1
Source F	21.2%	2	0%	5.5
Source E	19.5%	3	35%	2
Source A	4.3%	4	10%	4
Source D	1.1%	5	20%	3
Source B	0.6%	6	0%	5.5

Spearman's rank-order correlation (*Dlist*/*Olist*), r_s:	0.493
Coefficient of correlation (r_s^2):	0.243
%LL = $(1-r_s^2) * 100\%$:	75.7%

2.4 Hypotheses and Expectations

The Discoverability model allows for several straightforward hypotheses and anticipates the following results:

If colonizing groups entered a new land with little regional experience:

1. For the oldest sites/assemblages, the *Olist* will conform/correlate most closely with its *Dlist*, indicating a more deterministic utilization of the landscape, exhibiting greater exploitation of highly discoverable resources, and less-optimized spatial efficiency.

2. For increasingly younger sites/assemblages, there will be decreasing conformity/correlation between their *Olists* and *Dlists* as landscape learning increases and as factors other than discoverability (e.g., travel optimization) affect toolstone selection.

3. The youngest sites/assemblages will exhibit the lowest conformity/correlation between its *Olists* and *Dlists* and source discoverability will not factor highly into source selection.

4. Exotic or unknown material (or remote outliers) within the oldest sites/assemblages may occur, consistent with an early regionalization stage.

Similarly, if a study region does not reflect a colonizing event, I expect the following evidence as the result of pre-existing shared knowledge and expansive landscape learning:

1. Oldest and youngest sites/assemblages will display a similar lack of correlation between the *Olists* and *Dlists*, indicating that people were familiar with the landscape prior to the occupation of the region. In the opposite way, if all assemblages, across temporal periods, indicate similar correlations between their *Olists* and *Dlists*, landscape learning may take much longer than previously understood.

2. Little or no exotic or unknown material will be present in the oldest, or any, assemblages.

There is, of course, the possibility that the model described herein is simply flawed and too simplistic to adequately model the confounding behavior of people on a landscape. If this occurs, I will re-examine the model and its assumptions. Specifically, if all assemblages show high

correlation between the *Dlist* and *Olist*, the model may simply not properly detect landscape learning.

2.5 Random Walks and Exposure

The first step in building a methodology of Discoverability is verifying the assumptions of my Discoverability formulation – essentially, that, on an unbiased landscape, patches of different sizes and distances will be discovered at different rates, presumably with larger patches encountered at higher overall rates than smaller patches. Confirming this assumption provides the empirical warrant required to then build the baseline against which landscape learning will be measured (R. Chapman & Wylie, 2016). To test this hypothesis, I used a model based on a random walk simulator. While there are numerous permutations of random walk simulators within the broader field of movement ecology, three variations have been used extensively in biological modeling: simple random walks, correlated random walks, and Lévy walks (Codling et al., 2008; Viswanathan et al., 2011).

The most basic of the random walk models is the simple random walk (SRW). In an SRW, step movement is both uncorrelated and unbiased. The walk is uncorrelated in that the direction of each step is independent of the previous step (Codling et al., 2008; Viswanathan et al., 2011). This walk is also unbiased in the sense that there is "no preferred direction" (Codling et al., 2008, p. 813): the walker will just as likely reverse course as continue forward. In two-dimensions, when modeled on a grid, the walker has nine possible moves of equal probability ($p = 1/9$) at each step – to move any of the eight surrounding (nearest neighbor) cells or to just stay in place. The result from a series of such steps is a path across the walking plane that resembles Brownian motion and Fickian diffusion (Bartumeus et al., 2005), as shown in Figure 2-3. This figure also demonstrates the cumulative nature of compounded, independent walks, in this case 100 walks

of 10,000 steps, each beginning at the grid center. From this example, we can see that the areas closest to the center are visited more often and with more complete coverage, creating a "gradient of learning" that emanates from the center – those cells closest to the center are far more commonly encountered than those near the outer edge of the learned landscape.
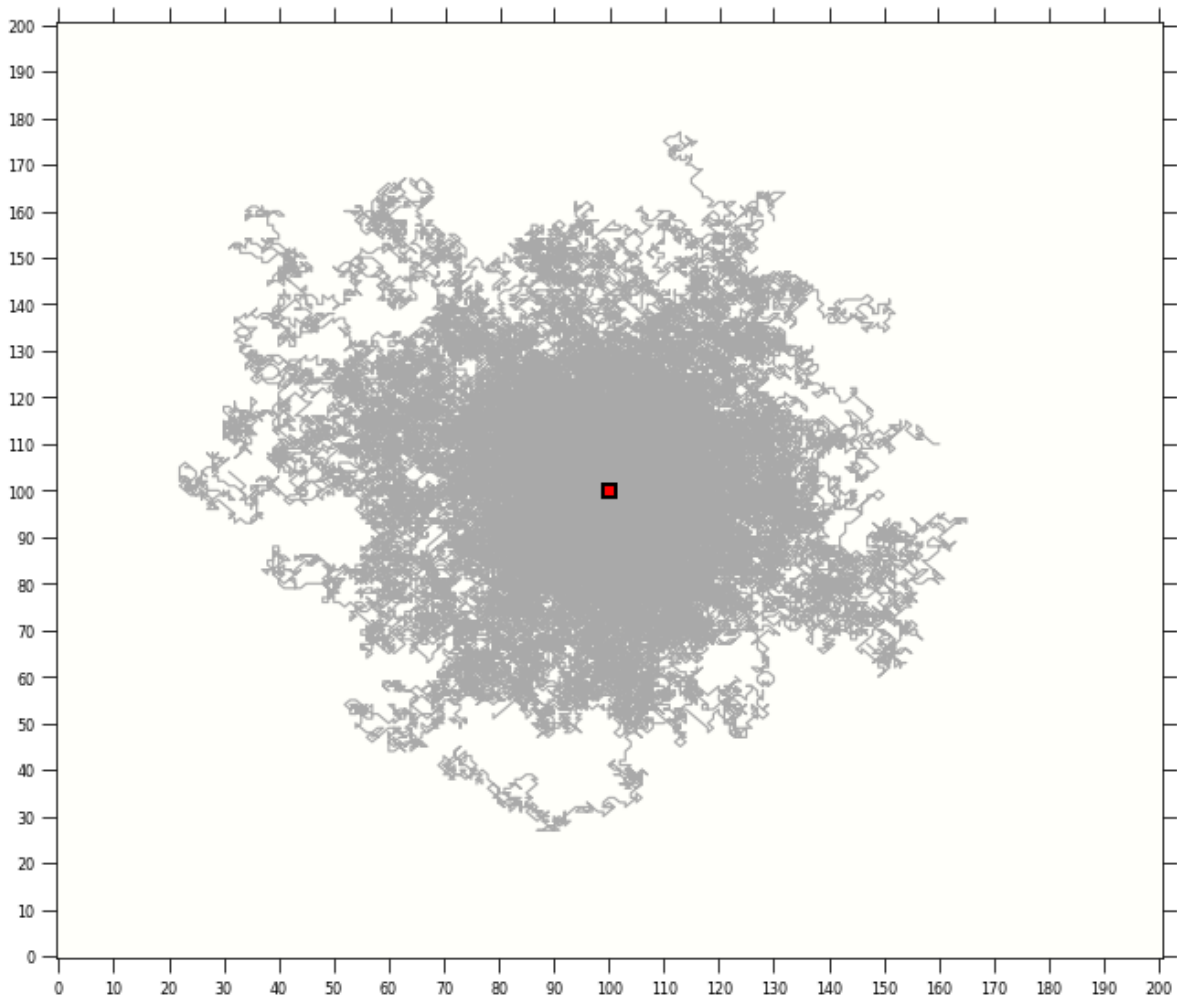
Figure 2-3: A random walk (100 walks of 1,000 steps each), illustrating Brownian motion and Fickian diffusion, with all walks beginning at a central place, marked by the red square. Here, a correlated random walk (discussed below) with a concentration parameter = 0 is used to mimic a simple random walk.

SRWs have been successfully used as first-order approximations of long-term motion and to model the nature of large-scale animal population diffusion (Bartumeus et al., 2005;

Benhamou, 2007; Bovet & Benhamou, 1988; Turchin, 2006; Viswanathan et al., 2011).

However, they have also been criticized for being "brainless" and failing to model animal motion at lower scales where the animal may be interacting with a stochastic environment, whether it be with the terrain itself or in encounters with mates or prey. SRWs also result in repeat encounters with the same target because of the high tortuosity inherent in their fractal nature (Viswanathan et al., 2011). However, one of the most important critiques, by Patlak (1953), argued that SRWs failed to model directional persistence – "the tendency of animals to continue moving in the same direction" (Bartumeus et al., 2005, p. 3078; Viswanathan et al., 2011).

Correlated random walk models (CRWs) were developed in response to these critiques. Animals tend to move forward more than backwards, what Bovet & Benhamou refer to as "cephalo-caudal polarization" (1988, p. 419), and with bilateral symmetry, turning equally left or right. To mimic this behavior, CRWs use a symmetrical, unimodal, probabilistic distribution centered on angle zero (representing forward direction). CRWs specifically address the issue of directional persistence by biasing directional selection, utilizing a degree of correlation in the probabilistic selection of successive-step turning angles (Codling et al., 2008; Viswanathan et al., 2011). With these attributes, the turning angle of zero (i.e., no turn) is most heavily biased at the local level, inducing more straight-line sequences of steps (Bartumeus et al., 2005; Benhamou, 2006; Bovet & Benhamou, 1988; Codling et al., 2008; Viswanathan et al., 2011). As a result, a CRW "behaves like linear movement at very small scales … and like Brownian motion at very large scales" (Turchin, 1996, p. 2088). The severity of the walk bias is adjusted by modulating the concentration of the probability density around the mode.

To accomplish this, CRWs make use of "wrapped" distributions – a probabilistic distribution on a line that is wrapped around a unit circle, following Mardia & Jupp (2000, p. 47,

Equation 3.5.54). In a wrapped distribution, the variable x on the linear distribution is transformed to x_ω lying on the circle, using *Equation* 2-4:

$$x_{\omega} = x \,(\mathrm{mod}\, 2\pi) \qquad\qquad\text{(Eq. 2-4)}$$

While a normal or von Mises distribution can be used, the Cauchy distribution is often employed (Figure 2-4) and resembles the Student *t* distribution with one degree of freedom (Abuzaid et al., 2015; Codling et al., 2008; Fisher, 1993; Lehoczky, 2015; Mardia & Jupp, 2000; Siegrist, 2020). The Cauchy distribution is favored for its "fat tails", which provide more robust handling of outliers. It has also been found to represent animal movement better than Gaussian models (Abuzaid et al., 2015; Bartumeus et al., 2005; Ben-Israel, 2013; Codling et al., 2008; Crist & Haefner, 1994; Jander, 1957; Kareiva & Shigesada, 1983; Siniff, 1967; Viswanathan et al., 2011).
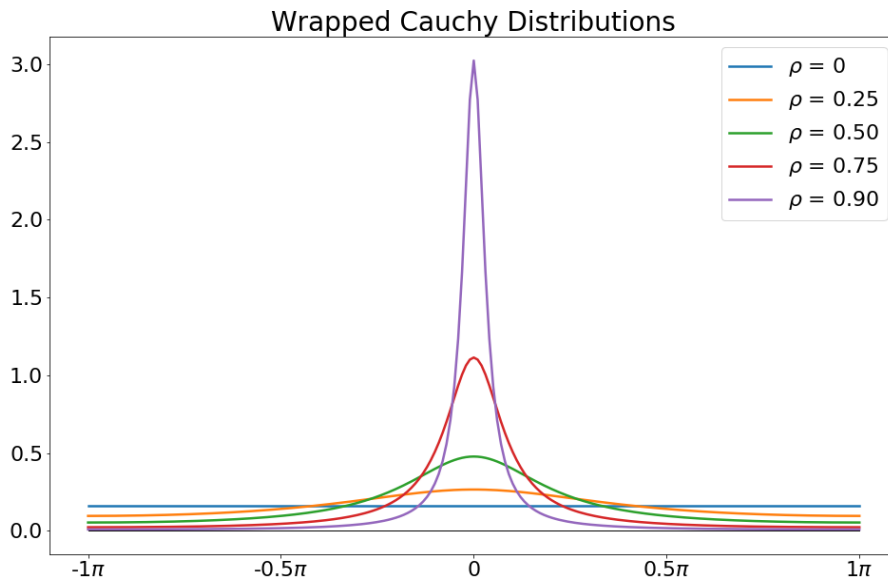
Figure 2-4: Linear representation of continuous circular Cauchy distributions at varying concentration levels (ρ)

To create a directional distribution, the Cauchy distribution is wrapped around a unit circle using the probability density function shown in *Equation* 2-5 below (Mardia & Jupp, 2000, p. 51, Eq. 3.5.69):

$$c(\theta\,;\,\mu,\rho) = \frac{1}{2\pi}\,\frac{1-\rho^2}{1+\rho^2-2\rho\cos(\theta-\mu)},\ -\pi \leq \theta < \pi,\ \mu < 2\pi,\ 0 \leq \rho < 1 \qquad \text{(Eq. 2-5)}$$

Here, two parameters control the distribution: the location parameter (μ), and the concentration parameter or mean resultant length (ρ, *where* $\rho = e^{-\sigma}$) (Abuzaid et al., 2015; Batschelet, 1981; Codling et al., 2008; Jammalamadaka & SenGupta, 1996; Kent & Tyler, 1988; Mardia & Jupp, 2000). In the analyses presented here, μ will be zero radians (centered on 0°), representing forward motion. The ρ value modulates the concentration around μ with a range between 0 and 1; the larger the ρ value, the greater the concentration of the distribution moves toward μ, increasing directional persistence. When $\rho = 0$, the distribution around the circle will be uniform, with equal probability of any angle being selected. When $\rho = 1$, the concentration of the distribution is entirely centered at μ, inducing straight-line walks (Abuzaid et al., 2015; Bartumeus et al., 2005; Fisher, 1993; Jammalamadaka & SenGupta, 1996; Kato & Jones, 2013). Figure 2-5 illustrates wrapped Cauchy distributions with varying ρ values.
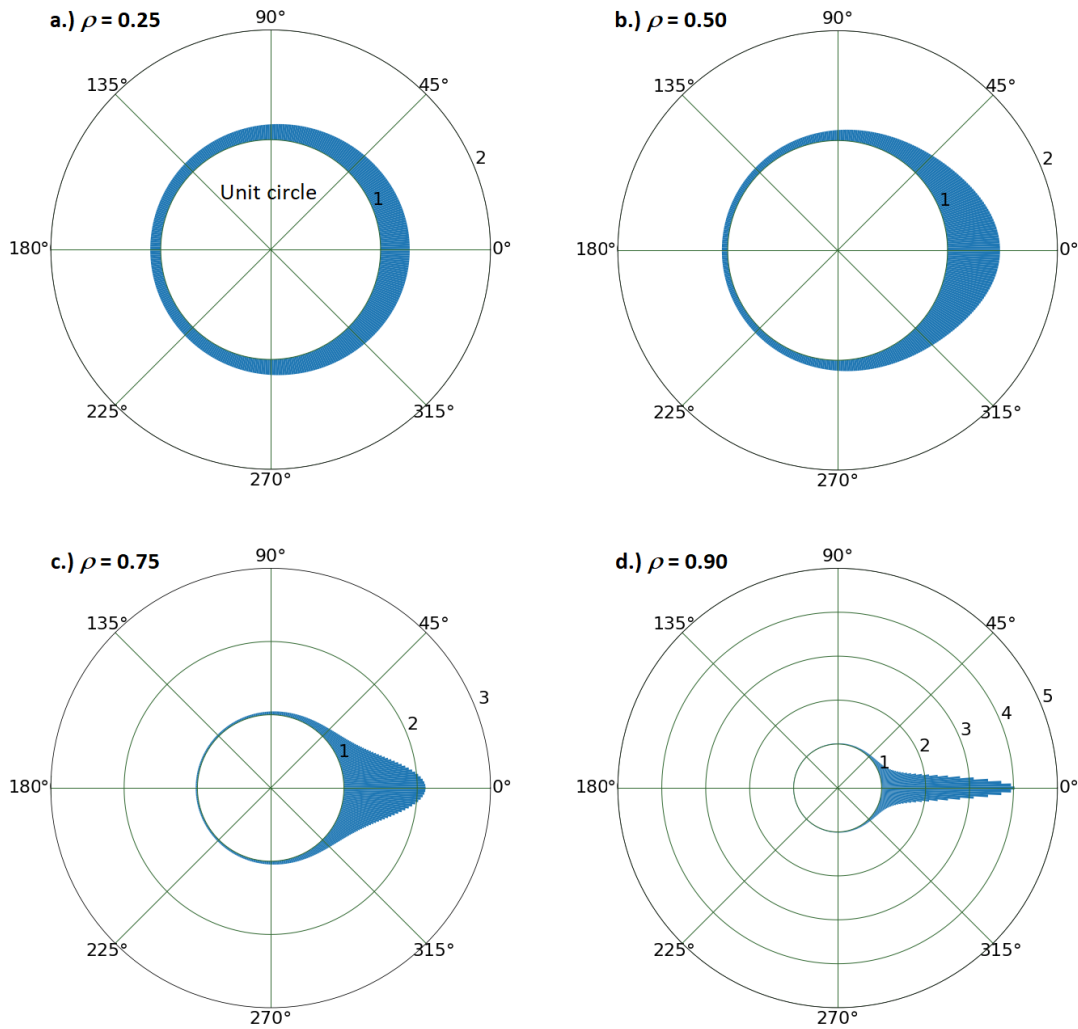
Figure 2-5: Polar representations of the wrapped Cauchy distribution with μ = 0 and four different concentration parameters ρ, illustrating the increasing probability concentration centering around μ as ρ increases from 0 to 1 (after Batschelet, 1965, p. 10, Figure 7.3)

To implement the wrapped Cauchy distribution in my correlated random walk, the circumference of the wrapped circle is divided into octants, representing each of the eight nearest neighbor cells surrounding a cell in a grid (Figure 2-6). The first octant (labelled A) is centered on the mode of the distribution and represents straight-forward motion. The cumulative probabilities represented by these octants are then applied to the selection of successive steps, depending on the concentration parameter chosen for a particular set of test walks. While this

strategy necessarily transforms a continuous probability distribution into discrete segments, it

will provide the variation needed for this model's approach.
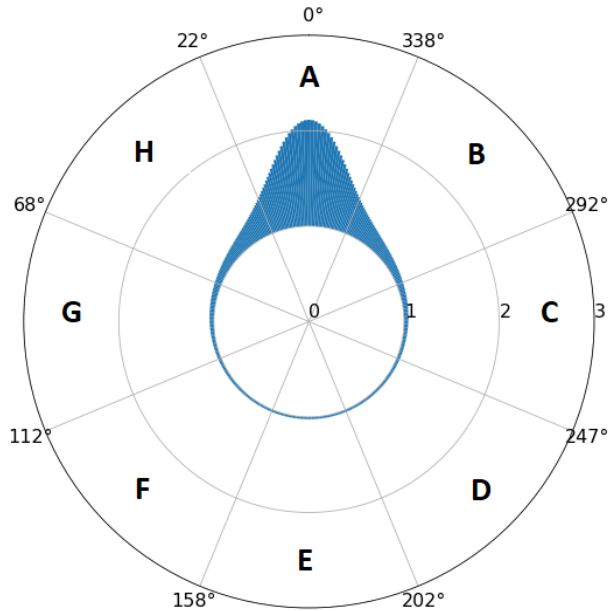
*Figure 2-6: A wrapped Cauchy distribution ($\rho = 0.75$) divided into 8 "nearest neighbor" octants
A - H, with A representing forward motion and E representing reverse direction.*

Table 2-4 shows show the cumulative probability increases in the A octant (forward

motion) as the concentration parameter ρ increases from 0 to 1 ("near 0" and "near 1" shown

here since absolute 0 and 1 result in "divide by zero" and "infinity" results, respectively).

*Table 2-4: Probabilities for the eight possible grid step directions, dependent on the
concentration parameter ρ*

ρ	$\pm s$	A	B	C	D	E	F	G	H	Sum
0.01	4.61	12.5%	12.5%	12.5%	12.5%	12.5%	12.5%	12.5%	12.5%	100%
0.10	2.30	15.2%	14.2%	12.3%	10.8%	10.3%	10.8%	12.3%	14.2%	100%
0.25	1.39	20.4%	16.5%	11.2%	8.4%	7.6%	8.4%	11.2%	16.5%	100%
0.50	0.69	34.3%	18.1%	7.8%	4.9%	4.2%	4.9%	7.8%	18.1%	100%
0.75	0.29	60.3%	13.1%	3.7%	2.1%	1.8%	2.1%	3.7%	13.1%	100%
0.90	0.11	83.5%	5.7%	1.4%	0.8%	0.7%	0.8%	1.4%	5.7%	100%
0.99	0.01	98.4%	0.6%	0.1%	0.1%	0.1%	0.1%	0.1%	0.6%	100%

Figure 2-7 demonstrates how the concentration parameter affects the random walk, creating a correlated random walk (CRW). The red path ($\rho = 0$) represents a simple random walk (SRW) where there is equal likelihood of selecting any of the eight possible directions from step to step. The resultant path is quite tortuous, resulting in high resampling of cells along the way. As ρ increases, tortuosity decreases, and we see increasing stretches of "straight-forward" travel as directional persistence increases. While not shown, a path where $\rho = 1$ would simply result in a path that begins at the grid center and moves directly away in a straight line. The range of behavior shown here ($0 \leq \rho < 1$) allows me to use a single CRW model to test discovery in various modes, as will be seen below.
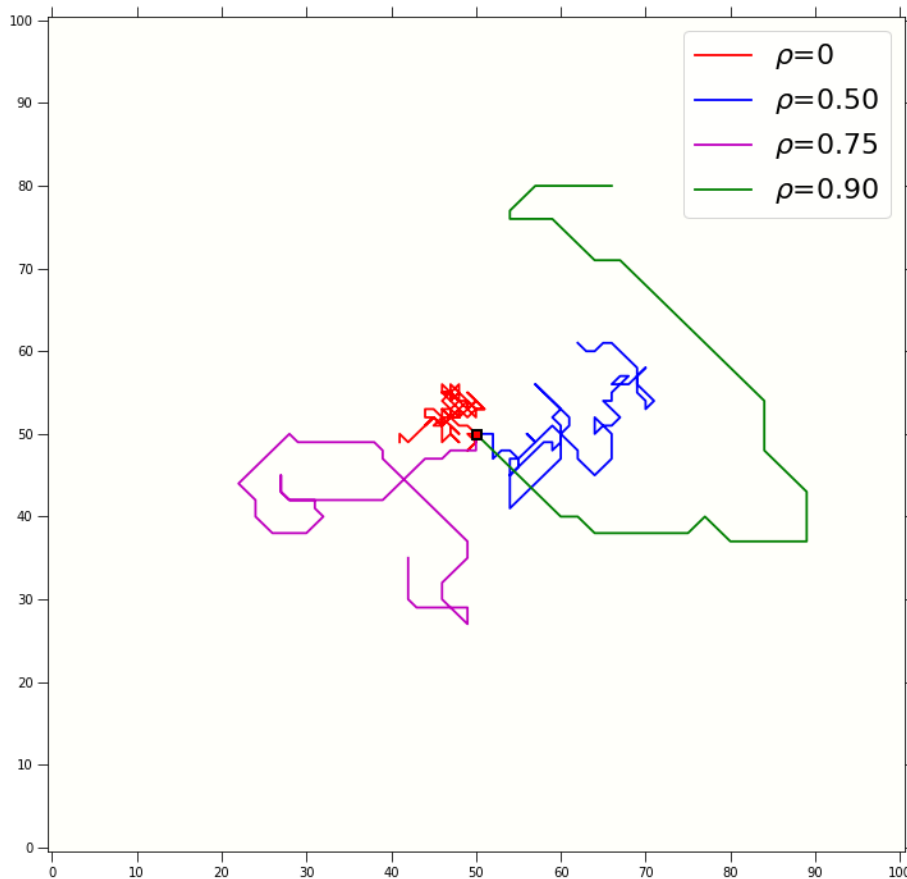
Figure 2-7: Four correlated random walks (CRW) of 250 steps, each using different concentration parameters, illustrating increasing directional persistence and diminishing tortuosity as ρ increases.

34

For completeness, I mention a third simulation method recently used in movement ecology: Lévy walks or flights. These are a form of random walk where both the turning angle and the step length at each step event are variable. A Lévy walk and a flight differ from each other in that walks encounter any targets between the starting and ending points while flights jump directly to the ending point before continuing foraging (Viswanathan et al., 2011). Flights may be more useful for some models, but since "a Lévy walk allows detection of foraging targets both at the end points of Lévy paths and at intermediate steps between them" (Brantingham, 2006, p. 438), a walk is more useful in a model where the goal is the discoverability of an unknown resource as a byproduct of other foraging activity (encounters vs. embedded procurement, *sensu* Binford, 1979).

Lévy walks have found usefulness in modeling foraging mobility in various species, including humans, but are not without issues (Benhamou, 2007; Codling et al., 2008; Pontzer et al., 2014; Viswanathan et al., 2002). Like CRWs, Lévy walks are modulated primarily by a single parameter (μ in this case) that typically ranges between 1 and 3, with values near 1 resulting in extremely long straight paths and values near 3 returning a stepping behavior similar to that of a SRW (Viswanathan et al., 2011). The power law that determines step length also has an extremely long tail, which can result in unrealistically long steps, requiring artificial truncation within the model (Brantingham, 2006).

Fortunately, CRWs appear to mimic Lévy flights and animal paths as ρ approaches 1 (Auger-Méthé et al., 2015; Bartumeus et al., 2005; Benhamou, 2007; Reynolds, 2010). As a result, a single CRW model can be used to replicate foraging mobility patterns from simple random walks using Brownian motion ($\rho = 0$) to patterns reflecting long, straight journeys (ρ *near 1*). More importantly, since I am most interested in verifying that patch size impacts

encounter rates, and not in the specific form of the path taken by people to achieve the encounter, this can be accomplished using a single CRW model while testing across the full range of $0 \leq \rho < 1$. I describe the implementation of such a model below.

2.6 CRW Tests

To test the relationship of exposure, or patch size, to discoverability in a neutral model, I created a two-dimensional CRW simulator using Jupyter Notebook and the Python programming language (*Project Jupyter*, 2021). The simulated landscape is represented by a two-dimensional grid of 200 x 200 cells. Following Brantingham (2003), the landscape is considered neutral (absent of topography) and uniformly productive (all cells are equally likely to contain target resources), and thus all cells are equally likely destinations during a forager walk. For this experiment, each walk begins at the center of the grid, a central place (Bell, 1990; Bettinger & Eerkens, 2004; Kelly, 1995), referred to here as "Home". For this experiment, walks were run in sets of 100 walks of 10,000 steps each. The direction of the first step in each walk is chosen randomly ($p = 1/8$) and all subsequent steps are chosen based on the probability weightings, as described in Table 2-4, according to the concentration parameter for this set of walks. This first random step initially introduces a local directional bias, at a very small scale, which progressively vanishes (Benhamou, 2006; Codling et al., 2008). The walk continues for up to 10,000 steps unless it encounters the test patch or the grid boundary.

The patch is represented by non-zero values in a 200 x 200 cell array that runs parallel to the grid/step array. As each grid cell is entered, the patch array is tested for the presence of a patch. Walks are terminated when the agent encounters the patch or when the agent encounters the grid boundary (known as an absorbing or non-rebounding border). For walks that encounter a patch, the encounter is tallied, along with the distance of the patch from Home. While I am not

concerned in this experiment with traditional questions of central place foraging, such as round-trip energy costs or in-field processing, the experiment does look at the accumulation of resource encounters as walks are repeated from the central place.

To test how patch-size may affect Discoverability, I devised a simple test scenario within this program. Single patches of various sizes (1x1 cells, 2x2, 3x3 … 9x9), as described in Table 2-5, were placed at increasing increments away from Home as shown in Figure 2-8. Only one patch is placed per set of walks.

Table 2-5: Patch absolute and relative sizes

Patch size	Patch area	Step size increase
1x1	1	--
2x2	4	400%
3x3	9	225%
4x4	16	178%
5x5	25	156%
6x6	36	144%
7x7	49	136%
8x8	64	131%
9x9	81	127%
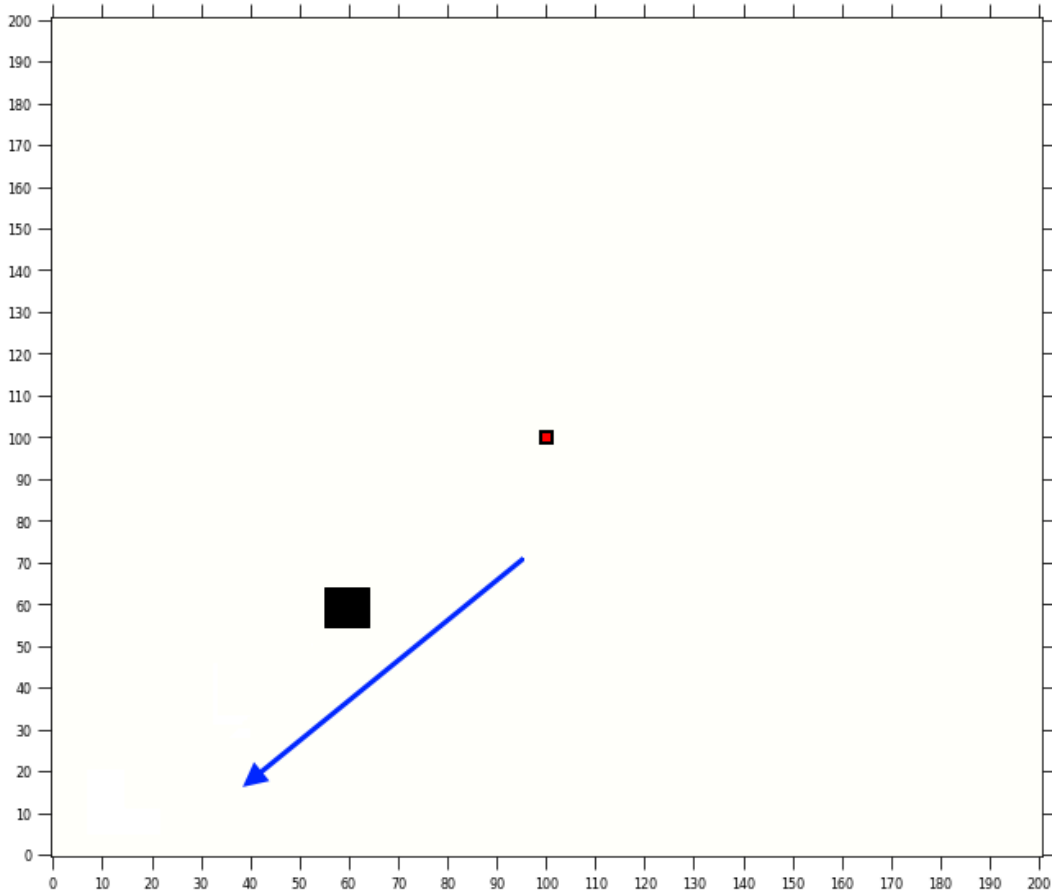
Figure 2-8: Demonstrating the placement positions of a single patch size (8x8), at increasing distances from Home. In these tests, only one patch is present in the grid at a time.

For each patch size, a single target patch is initially positioned one cell away from Home and 100 walks of 10,000 steps are run. During the 100 walks, each encounter with the target patch is tallied. If a walk encounters the patch, the walk is terminated. This prevents revisits to an already "discovered" patch during a single walk. Similarly, if a walker hits the grid border, the walk is terminated. Following each set of 100 walks, the patch is moved one cell in both the negative *x* and negative *y* directions, moving further away from Home. A new set of 100 walks is run on the new patch position, and this is repeated until the patch reaches the lower left grid corner.

Figure 2-9 illustrates one set of 100 walks with an 8x8 patch. During the set of 100 walks, the 8x8 cell patch was encountered, at the displayed distance, 19 times. In total, 230,841 steps were taken. Many walks were truncated before reaching 10,000 steps as a result of either encountering the patch or the grid boundary.
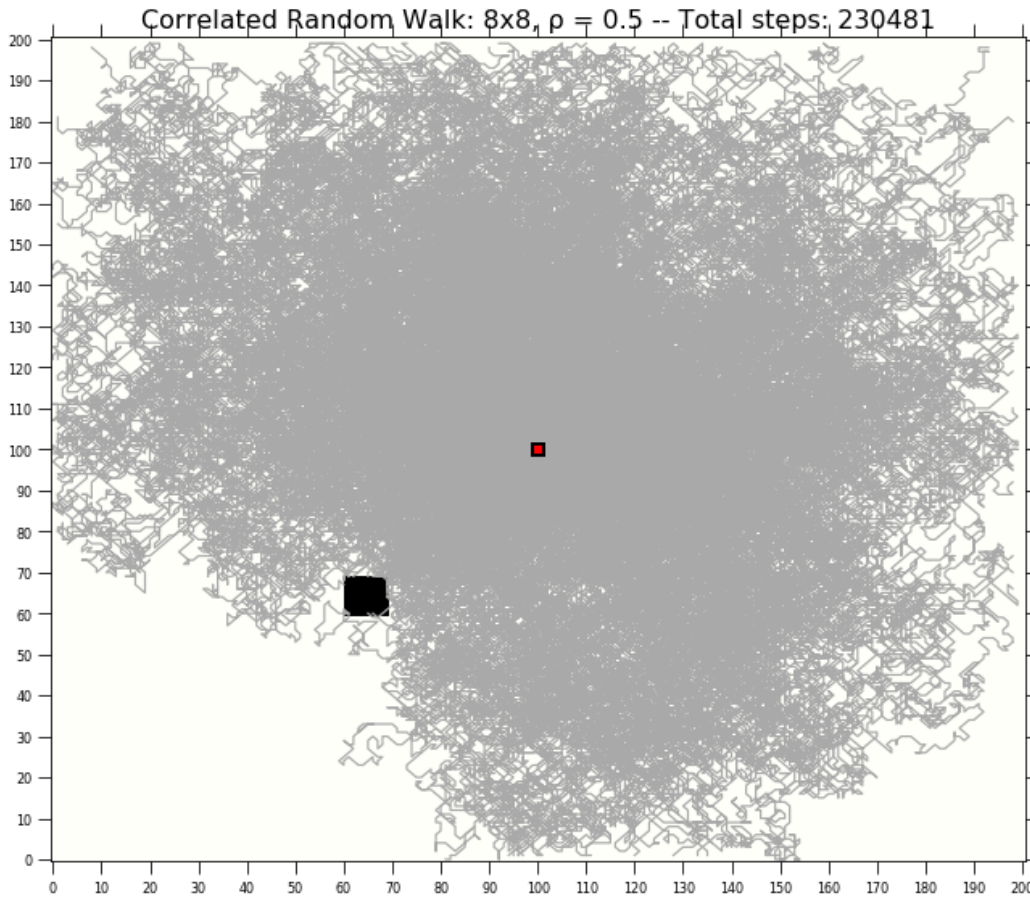
Figure 2-9: Full set of 100 walks searching for one 8x8 patch (ρ = 0.5)

Following the procedure described above, the discoverability of variably sized patches (sized 1x1 … 9x9) was tested using each of the following wrapped Cauchy distribution concentration levels (ρ): 0, 0.25, 0.50, 0.75, 0.90, and 0.95. For programming reasons, 0 was tested using the value 0.0000000001.

2.7 Results

Once these experiments were run, the data specific to each concentration parameter were analyzed and graphed. Then, for each patch size, the encounter tally and distance data were segregated for graphing. An example tally set for 100 walks of 10,000 steps using $\rho = 0.25$ is shown in Table 2-6.

Table 2-6: Encounters (walks with a patch encounter)
for each patch size ($\rho = 0.25$)

Patch size	*n*
1x1	855
2x2	1287
3x3	1490
4x4	1562
5x5	1705
6x6	1751
7x7	1880
8x8	1910
9x9	1932

For each concentration level and for each patch size, the numbers of encounters were plotted against the distance of the patch from Home and the data points were fitted to a line using the scipy.optimize.curve_fit function within the SciPy 1.6.1 library (Virtanen et al., 2020). Across all concentration levels tested, encounters vs. distance uniformly illustrate an exponential decay in the number of encounters as distance increases. Encounters vs. the natural log of distance produce linear results for all patch sizes. Figure 2-10 and Figure 2-11 illustrate this exponential decay for the lowest and highest concentration parameters tested against 5x5 patches. Similarly, Figure 2-12 and Figure 2-13 display the linear relationship exhibited in the semi-log graphs of the same data.
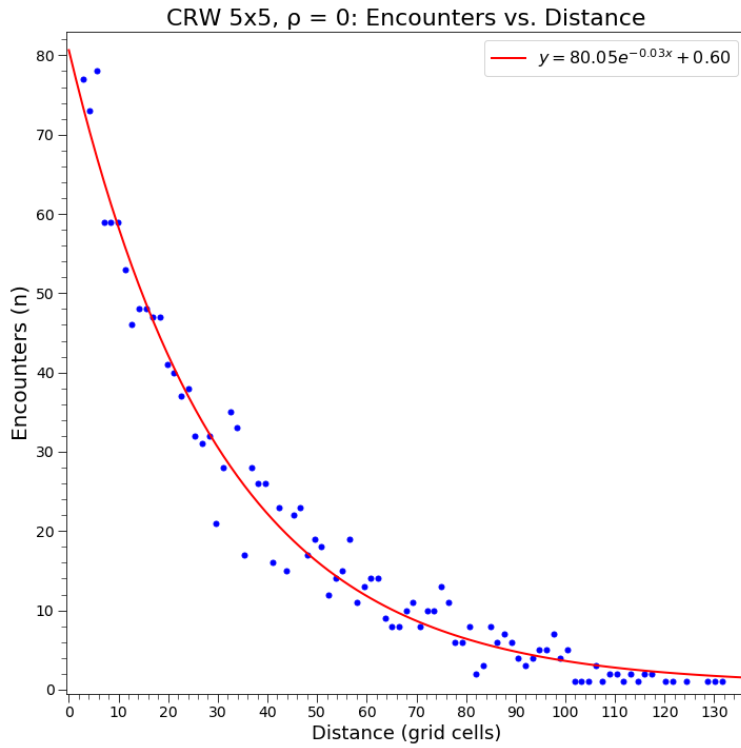
Figure 2-10: Encounters vs. distance, ρ = 0, 5x5 patches
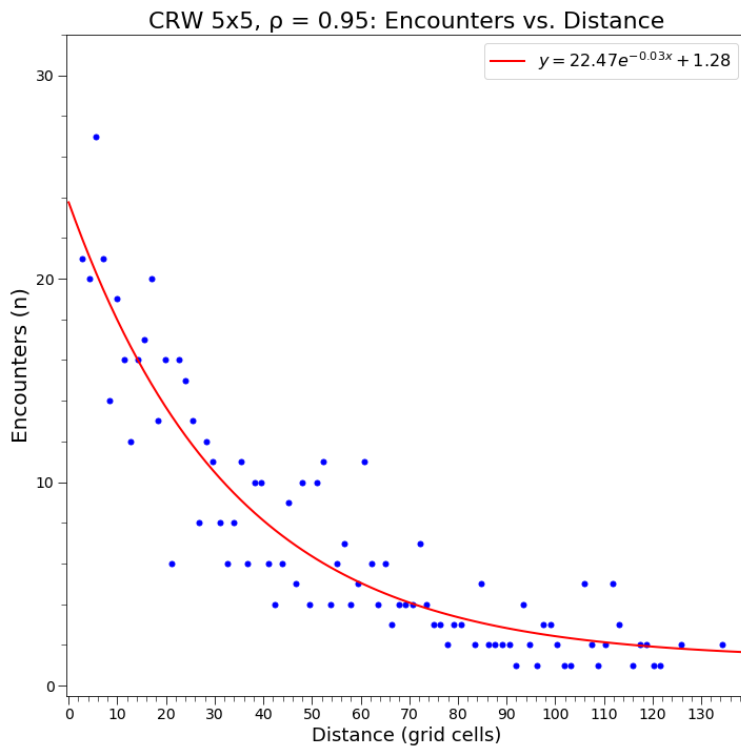
Figure 2-11: Encounters vs. distance, ρ = 0.95, 5x5 patches
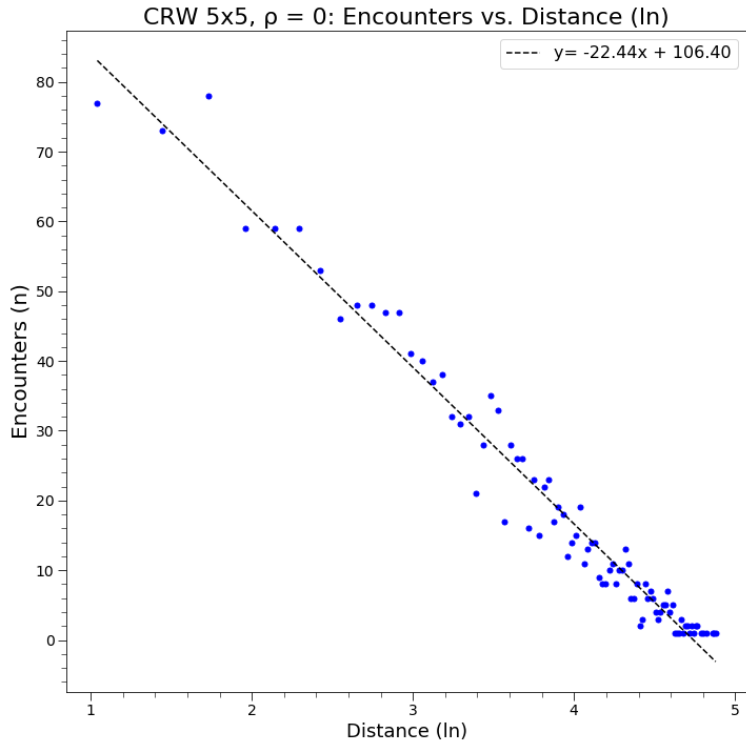
Figure 2-12: Encounters vs. distance (ln), ρ = 0, 5x5 patches
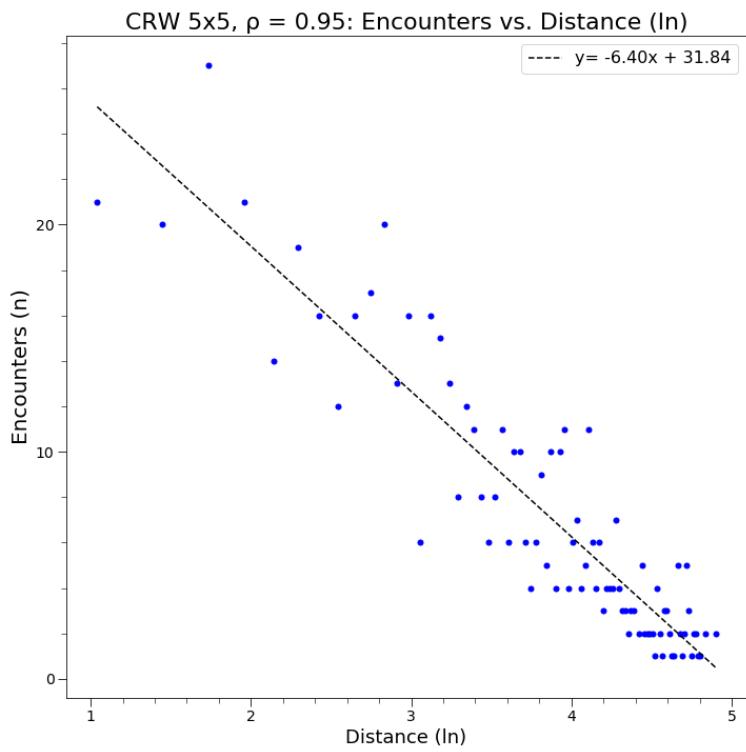
Figure 2-13: Encounters vs. distance (ln), ρ = 0.95, 5x5 patches

When the exponential decay lines for each concentration level are graphed together, the curves present consistently increasing slopes as patch size increases, as shown in Figure 2-14 and Figure 2-15, which represent the $\rho = 0$ and $\rho = 0.95$ walk results respectively. Figure 2-16 and Figure 2-17 show these results in semi-log form.

All graphs for all patch sizes at each concentration level as well as the grouped concentration level graphs are available in the GitHub repository (see section 2.10).

2.8 Testing the Slopes and Intercepts

For each concentration level, each of the nine semi-log regression lines was tested against the others for significant differences in slope ($\alpha = 0.05$) to ensure they were not estimates of the same population slope, β, using the procedure spelled out in Zar (2010, p. 387). If the null hypothesis (H_0: $\beta_1 = \beta_2$) is rejected, two different regression populations are represented by the regression lines. If the null hypothesis is not rejected, the lines were further tested to determine if their elevations were significantly different, following the procedure for comparing two elevations in Zar (2010, p. 391). The results of the tests follow in Figure 2-18 and Figure 2-19.

In almost all cases, the regression line comparisons reject the null hypothesis (Table 2-7). It is notable that the comparisons increasingly fail as directional persistence (ρ) increases.

Table 2-7: Linear regression line comparisons

ρ	H_0 rejected (n)	H_0 not rejected (n)	% rejected
0.01	31	5	86%
0.25	32	4	89%
0.50	32	4	89%
0.75	33	3	92%
0.90	35	1	97%
0.95	35	1	97%
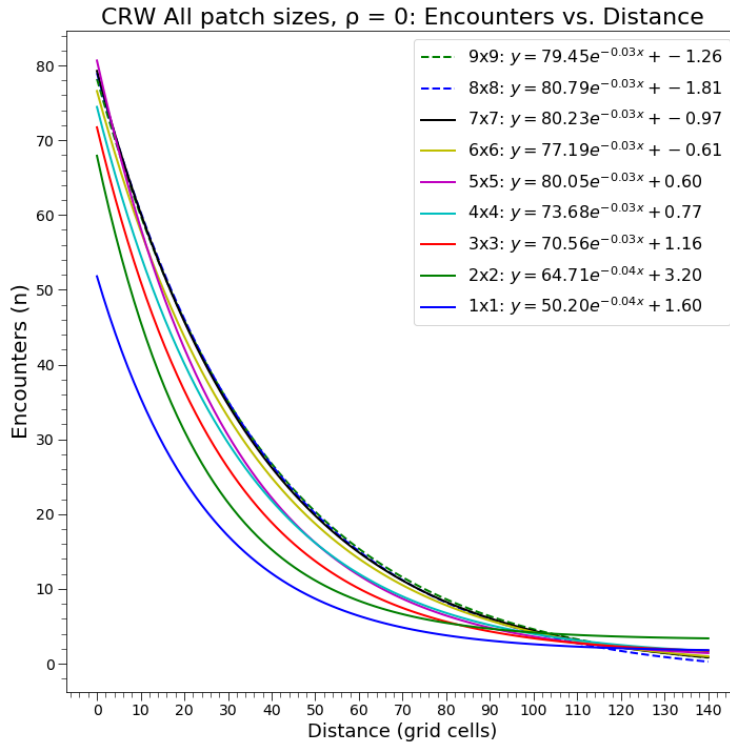
Figure 2-14: All patch size decay curves ($\rho = 0$)
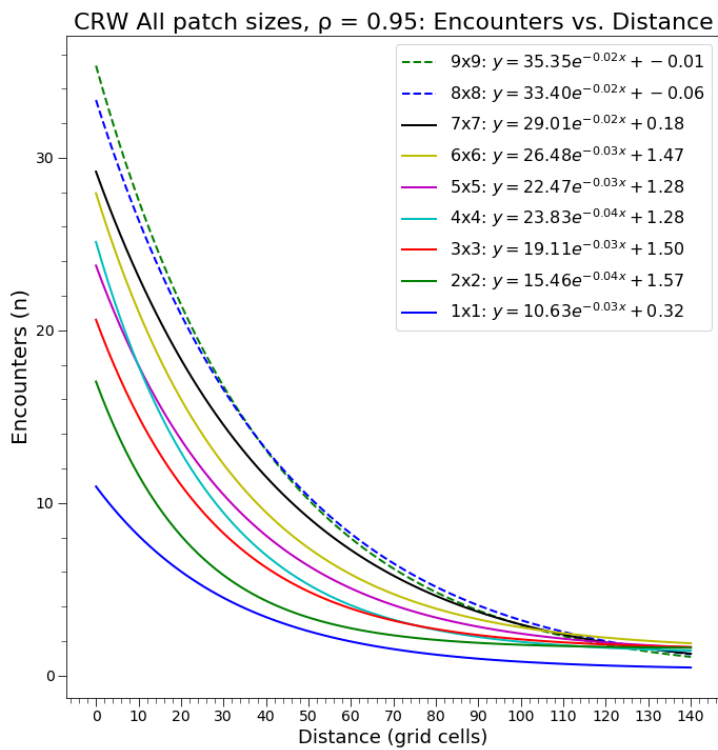
Figure 2-15: All patch size decay curves ($\rho = 0.95$)
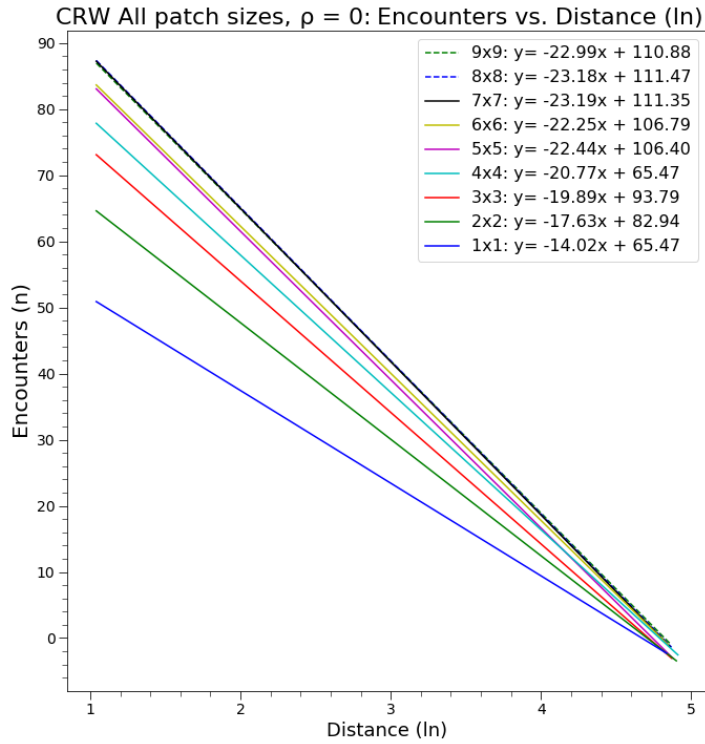
Figure 2-16: All patch sizes semi-log lines ($\rho = 0$)
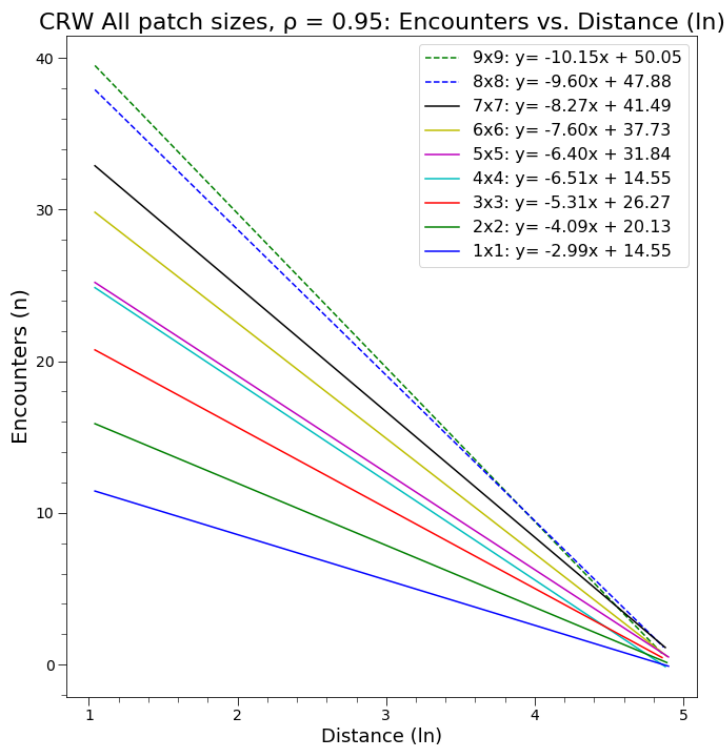
Figure 2-17: All patch sizes semi-log lines ($\rho = 0.95$)

$\rho = 0$

	1x1	2x2	3x3	4x4	5x5	6x6	7x7	8x8	9x9
1x1		●	●	●	●	●	●	●	●
2x2			●	●	●	●	●	●	●
3x3				○	●	●	●	●	●
4x4					●	●	●	●	●
5x5						○	○	○	○
6x6							✗	✗	○
7x7								✗	✗
8x8									✗

$\rho = 0.25$

	1x1	2x2	3x3	4x4	5x5	6x6	7x7	8x8	9x9
1x1		●	●	●	●	●	●	●	●
2x2			●	●	●	●	●	●	●
3x3				✗	○	●	●	●	●
4x4					○	●	●	●	●
5x5						✗	●	●	●
6x6							○	●	●
7x7								●	✗
8x8									✗

$\rho = 0.50$

	1x1	2x2	3x3	4x4	5x5	6x6	7x7	8x8	9x9
1x1		●	●	●	●	●	●	●	●
2x2			●	●	●	●	●	●	●
3x3				●	●	●	●	●	●
4x4					✗	●	●	●	●
5x5						✗	●	●	●
6x6							✗	●	●
7x7								○	●
8x8									✗

●   Ho is rejected, slopes are not the same

○   Ho is not rejected for slope, but is rejected for intercept/elevation

✗   Ho is not rejected (for either test)

Figure 2-18: Results of linear regression comparisons for a) $\rho = 0$, b) $\rho = 0.25$, and c) $\rho = 0.50$

$\rho = 0.75$

	1x1	2x2	3x3	4x4	5x5	6x6	7x7	8x8	9x9
1x1		●	●	●	●	●	●	●	●
2x2			●	●	●	●	●	●	●
3x3				●	●	●	●	●	●
4x4					●	●	●	●	●
5x5						●	●	●	●
6x6							○	○	●
7x7								✗	✗
8x8									✗

$\rho = 0.90$

	1x1	2x2	3x3	4x4	5x5	6x6	7x7	8x8	9x9
1x1		●	●	●	●	●	●	●	●
2x2			○	●	●	●	●	●	●
3x3				●	●	●	●	●	●
4x4					●	●	●	●	●
5x5						○	○	●	●
6x6							✗	●	●
7x7								●	●
8x8									○

$\rho = 0.95$

	1x1	2x2	3x3	4x4	5x5	6x6	7x7	8x8	9x9
1x1		●	●	●	●	●	●	●	●
2x2			●	●	●	●	●	●	●
3x3				●	●	●	●	●	●
4x4					○	●	●	●	●
5x5						●	●	●	●
6x6							○	●	●
7x7								●	●
8x8									✗

●   Ho is rejected, slopes are not the same

○   Ho is not rejected for slope, but is rejected for intercept/elevation

✗   Ho is not rejected (for either test)

Figure 2-19: Results of linear regression comparisons for a) $\rho = 0.75$, b) $\rho = 0.90$, and c) $\rho = 0.95$

2.9 Conclusion

In this chapter, I developed a model to predict the order in which patchy resources would be found on a neutral landscape dependent only on patch size and distance. This work drew from Brantingham's (2003) neutral model of raw material procurement and expanded it by varying patch size. The results of this model should predict the rank-order discoverability of resource patches on an unlearned landscape.

To test this model, I built a CRW simulator specific to this purpose. The simulator allows me to systematically test how encounter rates change as patch size and distance vary. The simulator tracked encounters of correlated random walkers and their encounter rates with patches varying in size from 1x1 cells to 9x9 cells on a 200x200 cell grid. CRWs with concentration parameters from $0 \leq \rho < 1$ were tested and consistently returned size-dependent linear regression results.

Nearly all the resultant regression lines differ significantly from one another in terms of slope and/or elevation, and thus represent different sample populations. For a few cases at the higher patch sizes where the relative size change between patches is not as great (for example, 8x8 patches vs. 9x9 patches), the results did not differ significantly. That outcome is to be expected in a random walk process in which patch sizes approach one another closely. A remarkable observation from the results is that as directional persistence (ρ) increases, the cases where the null hypothesis could not be rejected diminish considerably.

The results overwhelming support the hypothesis that patch size affects discoverability. With this empirical warrant in hand, I can now rank sources by relative Discoverability and set the baseline of an "unknown landscape" against which to measure Landscape Learning over time (see Chapter 5).

2.10 Repository and Software

The following software tools were used to create the programs described in this chapter:

Anaconda Navigator, v. 1.9.12 ("Anaconda Software Distribution," 2021). The versions of all installs and libraries encapsulated in this aggregation are listed in the environment.yml file in the repository referenced below.

Jupyter Notebook, v. 6.0.3 (*Project Jupyter*, 2021). Three notebooks were created to run the CRW simulation, graph and analyze the resultant data, and to replicate various figures that appear in this chapter.

Python v. 3.7.6 (64-bit) (Python Software Foundation, 2021). The CRWutils.py file was written using this Python version.

GitHub repository (*GitHub*, 2021). All notebooks, code, data (.csv files), and graphical output are available in this GitHub repository assigned DOI: 10.5281/zenodo.6544114. Also available directly at GitHub: https://github.com/davehunt00/dhunt00_dissertation

Chapter 3: A Method for Predicting the Discoverability of Obsidian Sources

3.1 Introduction

Testing the Discoverability model, as outlined in Chapter 2, requires a means to quantify the areal extent, or discoverable signal, of obsidian sources on the landscape. In this chapter, I test a method for predicting this signal starting with known primary source exposures, using these as upslope catchments, and then applying hydrographic computational algorithms to predict the downslope distribution of obsidian sediments. Five obsidian toolstone sources, used by people occupying the Old River Bed (ORB) delta (see Appendix A, Table A-42), were predicted at varying levels of digital elevation model (DEM) smoothing, field tested, and evaluated for precision. The results provide a gauge of the level of smoothing required to operationalize this method of predicting the secondary distribution of sediments and the scale factor of that extent.

3.2 Regional Geology

The Great Basin resides within the Basin and Range Province, a region of north-south oriented, horst and graben mountain ranges and valleys, within the western United States (R. L. Christiansen & Lipman, 1972; Grayson, 2011; Hunt, 1967). The province emerged around 60 million years ago (Ma) as the result of tectonic events in the early Cenozoic and, over time, resulted in a "rugged erosional topography with towering pinnacles rising above narrow usually dry valleys" (Lipman et al., 1978, p. 134). In the late Cenozoic (beginning ~20 Ma), this region entered an age of rhyolitic volcanism that extended to at least the middle Pleistocene (as recently as 0.5 Ma) and remains seismically active today (E. H. Christiansen et al., 1986; Crecraft et al., 1981; Lipman et al., 1978). It was during this geologically recent period of volcanism that the

primary sources of obsidian (a glassy form of rhyolite) in this region were formed, mostly along

existing fault lines (Crecraft et al., 1981; Rowley et al., 2002).

Obsidian forms as the result of various eruptive mechanisms (Hughes & Smith, 1993). In

the Great Basin and the surrounding region, including the Snake River Plain to the north, the two

most common mechanisms are rhyolitic lava flows and pyroclastic ash-flow tuffs (Armstrong,

1970; E. H. Christiansen et al., 1984; Crecraft et al., 1981; Lindsey, 1979; Lipman et al., 1978;

Rowley et al., 2002; Williams et al., 1997). In the first case, obsidian deposits form when highly

viscous silicic-rich magma is extruded during an eruption and the basal members of these flows

cool quickly against the surrounding environment, forming bands, or veins, of glass. These

deposits comprise the most chemically homogenous glass. Obsidian may also be formed during

pyroclastic eruptions of ash-flow sheets, or tuff, resulting in obsidian nodules forming *in situ*

(Ellis et al., 2012; Hughes & Smith, 1993; Monnereau et al., 2021). The Great Basin, and

particularly the nearby Snake River Plain, were subjected to massive ash-flow eruptions covering

hundreds of square kilometres. These flows are variously welded, dependent on temperature, and

may produce obsidian nodules large enough for tools.

The following five regional sources were used to test the methodology described in this

chapter (Table 3-1):

Table 3-1: Ages (millions of years) of obsidian sources being investigated

Obsidian source	Age	Reference
Black Rock Area	2.2 – 2.6 Ma	Crecraft et al., 1981; Hintze et al., 2003
Ferguson Wash	Unknown, poorly studied	Armstrong, 1970; Jackson et al., 2009
Mineral Mountains	0.79 Ma	Evans & Nash, 1978; Lipman et al., 1978
Panaca Summit/Modena	11 – 13 Ma	Rowley et al., 2002; Williams et al., 1997
Topaz Mountain	6 – 7 Ma	E. H. Christiansen et al., 1984; Lindsey, 1979, 1982

In the time since their formations, alluvial and colluvial forces have transported obsidian sediments – their secondary distribution – from uphill locations to the valley bottoms (Lipman et al., 1978; Miller & Juilleret, 2020; Rowley et al., 2002). This form of erosion, described by Hunt (1967, p. 340), repeats itself throughout the Great Basin:

> A typical basin in the Basin and Range Province consists of two kinds of ground. At the center is a playa or alluvial flat of clayey or silty ground, with or without a crust of salts, and surrounding this are gravel fans that rise from the flats to the foot of the bordering mountains. Many of the fans are several miles long and more than a thousand feet high. They consist of coarse debris, mostly gravel and sand deposited at the mouths of canyons by streams flowing from the mountains.

That the first people known to have moved into and lived in the Great Basin discovered and made extensive use of these primary obsidian sources for tools is clear (Beck & Jones, 1990; Grayson, 2011; Jenkins et al., 2012; Jones, Beck, Jones, et al., 2003; Madsen, Schmitt, et al., 2015). Further, due to the unique geochemical signature of each obsidian flow, the primary locations of almost all obsidian sources utilized by early peoples are known today, at least in the general sense of tens of square kilometers (Jackson et al., 2009; Madsen, Schmitt, et al., 2015; see also Skinner, Appendix D, Table D-2). What is less well-known, and which forms a central aspect of my thesis, is how the secondary distributions, the downslope alluvial and colluvial flows of obsidian sediments, may have created a massive "signal" on the valley bottoms where early inhabitants of the Great Basin made their living (Grayson, 2011). These signals, up to several orders of magnitude larger than the primary sources themselves, consist of obsidian granules and pebbles (2 – 64 mm, per the Wentworth scale) within the greater alluvial package

and would effectively inform alert hunter-gatherers that tool-grade lithic sources were close at hand (Wentworth, 1922).

3.3 The Discoverability Model Overview

The goal for this portion of the project was to develop and test a method for reliably estimating the size or surface area exposure of these secondary signals. Modern geographical information systems (GIS) provide numerous tools and algorithms to analyze drainage networks and downslope flow patterns as a means for understanding hydrographic processes and to simulate sediment erosion (Fairfield & Leymarie, 1991; Freeman, 1991; O'Callaghan & Mark, 1984; Quinn et al., 1991; Tarboton, 1997). Alluvial flows in particular have been the subject of recent research using these tools (Argialas & Tzotsos, 2006; Miliaresis & Argialas, 2000; Nangia, 2010; Norini et al., 2016). Each methodology shares similar processes for calculating the downslope flow of material (water or sediments):

1. Determine the location of the primary source exposure.

2. Acquire a suitable regional digital elevation model (DEM) raster.

3. Condition the DEM for hydrographic analysis.

    a. Fill artificial sinks.

    b. Smooth the raster to eliminate dams and flat spots which might hinder a flow calculation.

4. Establish a catchment region. This can be the upslope area from an alluvial fan apex or an artificial "starting point" for downslope analysis. In my model, I describe the use of a weighted raster representing the obsidian primary sources that simulate the starting points for downslope erosional flow, as well as the use of "proxy sources" when primary sources are poorly defined.

5. Perform the downslope analysis or simulation that disperses hydrographic and erosional action to lower elevations within the regional raster. Various algorithms are available to define downslope drainage networks and disperse flows downslope. In my model, I use the Multiple Flow Direction method (described below).

While there are inherent limitations in any attempt to model what is ultimately an infinitely dynamic process, recent hydrographic algorithms provide quite accurate models. Specific limitations will be discussed *in situ* as the general steps are described.

3.3.1 Determine primary source location

In this method, the primary source location acts as the seed for downslope flow calculations. For these test cases, I used obsidian sources with primary exposures that are well described in the literature (Hull 1994; Jackson et al. 2009; Talbot et al. 2015). In section 3.6.4 and in Chapter 4, I offer strategies for creating a polygon when only sample points are available for a primary source.

3.3.2 Acquire Suitable Regional DEMs

For each study region, I acquired U. S. Geological Survey (USGS) 1/3 arc-second DEMs using *The National Map Viewer* tools (Archuleta et al., 2017; U.S. Geological Survey, 2020c). The 1/3 arc-second DEMs provide resolution of approximately 10 m per cell (U.S. Geological Survey, 2020a). Due to remote locations of the obsidian sources that I am researching, which have both low human population densities and generally low economic use, there are no higher resolution DEMs (such as LiDAR) available.

I also acquired GIS shapefiles for regional Watershed Boundary Datasets (WBD) (U.S. Geological Survey, 2020b). The WBD datasets describe the surface drainage for a region, at various scales. These provide useful limiting boundaries and a means to reduce the overall

computational load, by clipping large DEMs down to regions within hydrographic subbasins that capture any downslope flow of water and sediment.

For each obsidian source (Black Rock Area, Ferguson Wash, Mineral Mountains, Panaca Summit/Modena, and Topaz Mountain), I created a seamless, clipped DEM encompassing the source's local subbasin or subbasins using the ArcMap GIS program (Esri, 2021a). Figure 3-1 is an example from the Mineral Mountains region. The primary obsidian source locations for the Mineral Mountains are well-researched and shown as black polygons (Jackson et al., 2009). They are positioned at high altitude, but below the range crest or eastern hydrographic boundary, and downslope flow will likely run west into the lower subbasin floors.
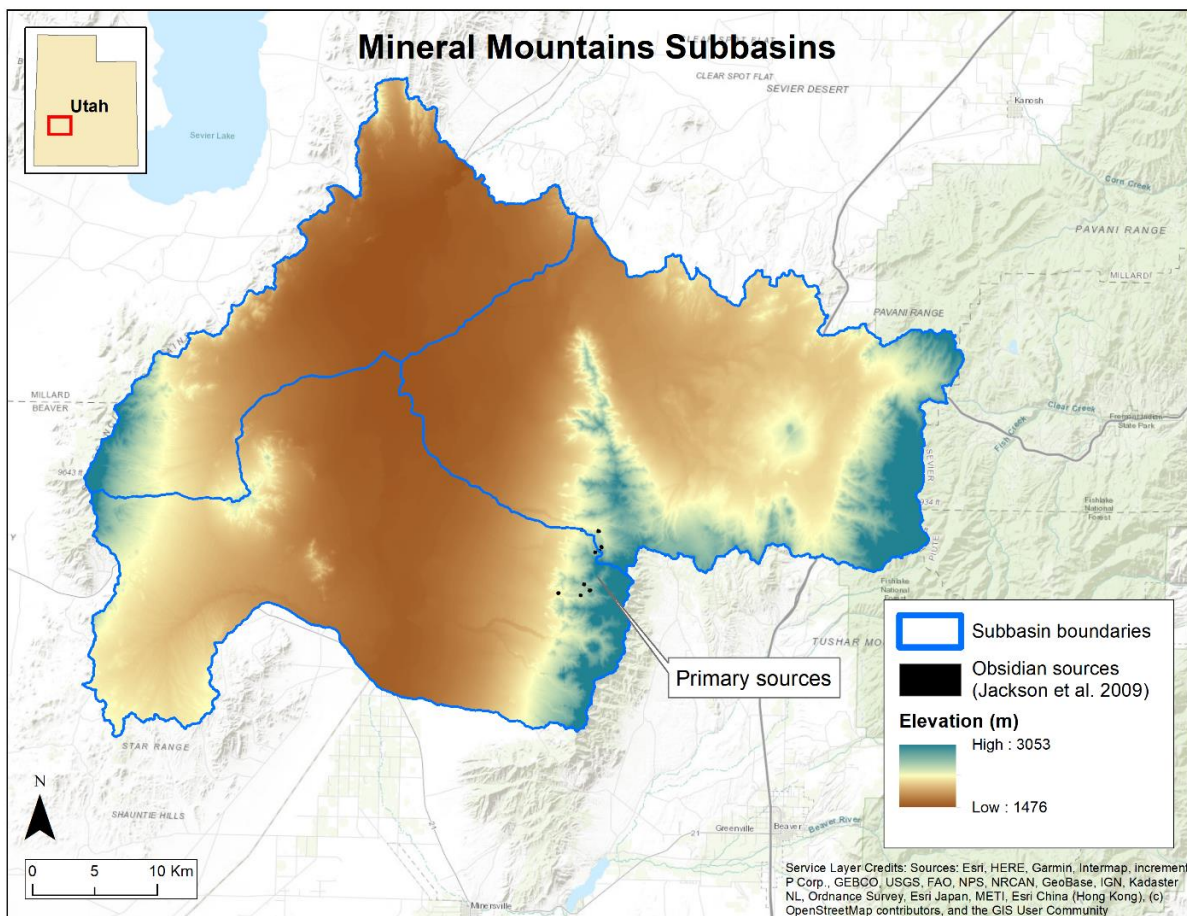
Figure 3-1: Example of a digital elevation model (DEM) showing the subbasins in the vicinity of the Mineral Mountains primary obsidian sources.

3.3.3 Condition the DEM

A DEM is a discrete, gridded representation of a continuous topology. As such, it needs to be prepared, or "conditioned" (Jenson & Domingue, 1988), so that hydrographic flow can be simulated over the topology it represents.

a) **Fill artificial sinks:** DEMs are subject to errors, called pits or sinks, where a cell (or cells) contain(s) an elevation value lower than its eight nearest neighbors (Figure 3-2a). Sinks greater than 10 m wide are extremely rare in the natural environment but common in DEMs (Mark, 1988). Sinks in DEMs are typically the result of errors in surface interpolation (continuous to discrete), rounding errors (real numbers rounded to integer values), or satellite photographic classification errors, for example confusing treetops with the ground surface (Costa-Cabral & Burges, 1994; Esri, 2020d; Jenson & Domingue, 1988; Mark, 1988). These artificial pits need to be removed as they cause hydrographic flow algorithms to terminate unnaturally at these low spots.
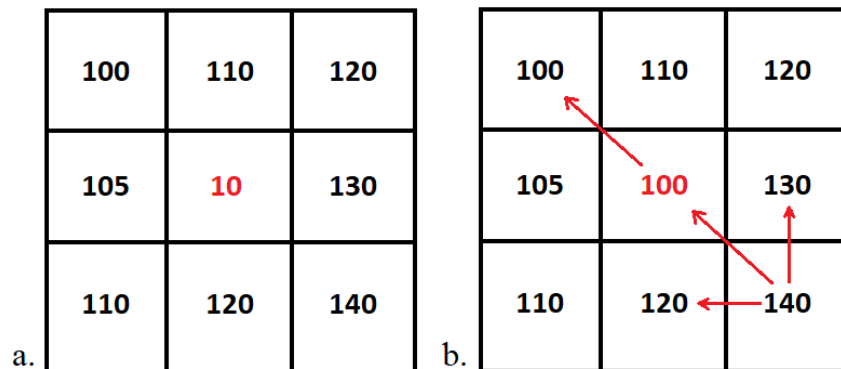
Figure 3-2: A sink in a digital elevation model (DEM), before (a) and after (b) Fill function, arrows indicate possible new flow paths.

The process for sink removal is straightforward. The ArcMap 10.0 *Fill* function (Esri, 2021b) is an iterative tool that locates each sink, evaluates the eight neighboring cells, and assigns the sink cell to the same value as the neighboring "pour point" value

(the neighboring cell with the lowest elevation). The end result is a depressionless DEM where every cell will "be part of at least one monotonically decreasing path of cells leading to an edge of the data set" (Jenson & Domingue, 1988, p. 1594), allowing continuous flow through the erroneous cell (Figure 3-2b).

b) **Smooth the raster:** Along with sinks, raised ridges or "dams", both natural and artificial, and flat areas can stymie hydrographic flow algorithms. Like sinks, dams can be the result of interpolation or rounding errors, except in a "positive" direction, creating a ridge through which flow algorithms cannot pass (Fairfield & Leymarie, 1991; O'Callaghan & Mark, 1984; Quinn et al., 1991). There are also recent anthropogenic barriers on the landscape such as raised railway beds, highways, and pipelines that appear in DEMs which will block computed flow patterns. In very flat areas, such as basin bottoms, these linear structures can be particularly problematic, rising several meters above and transecting natural valley bottoms or very gently sloping areas (see the Panaca Summit/Modena discussion in section 3.6.4 for a particularly vexing issue and workaround). Finally, in a DEM represented by integer elevation values, large "flat" blocks of cells containing the same value, resulting either from rounding in the interpolation of very gentle natural slopes, or from the computational filling in of large sinks as described above, can also create artificial flow termination points or pools.

To predict millennia of hydrographic flow and erosion at a regional scale, it is necessary to eliminate such obstructions by smoothing the DEM. The amount of smoothing to apply to the model during this predictive stage is somewhat subjective and the product of trial and error which must be evaluated against results from the field. However, in this study, it is not entirely subjective as there are known observation and/or

collection data points from previous workers (Hull, 1994; Jackson et al., 2009; Talbot et al., 2015; also Skinner, Appendix D, Table D-2) and my own field work (Appendix B, Table B-6). One can expect that the flow must extend at least to these points (see the source-specific results below).

The ArcMap 10.0 *Focal Statistics* function (Esri, 2021c) takes a filled DEM and creates a new raster that sets each cell value to a statistical value based on the values of the neighboring cells. In this case, I used the Mean value with neighborhoods of increasing sizes (3x3, 5x5, 7x7, 11x11, and 21x21 cells) which create increasingly smoothed surfaces as the averages are spread out. This is especially useful when "smoothing" large flat areas as the fractional averages will give the flat area a gentle slope. The smoothed DEMs, now grids of averaged real numbers or floating-point values, provide a continuously sloped gradient for water and sediment to "flow" across (Figure 3-3).

100	110	120
105	100	130
110	120	140

3x3 Neighborhood Mean →

	116.875	
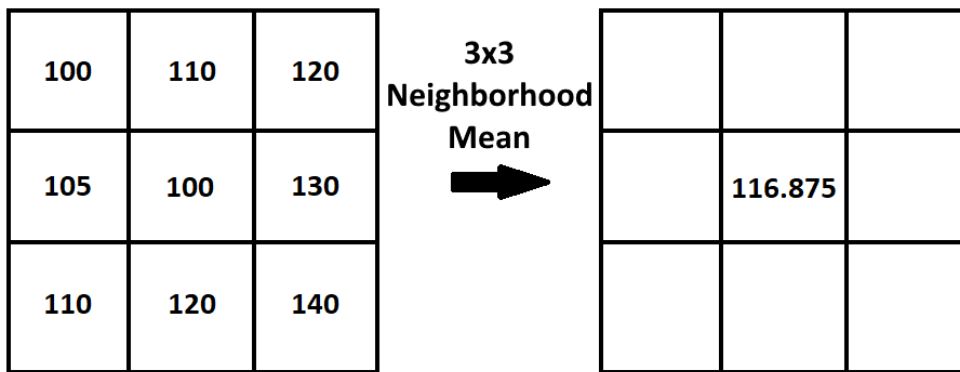
Figure 3-3: The 3x3 neighborhood mean for a single cell produced by the Focal Statistics function

3.3.4 Establish a Catchment Region

In hydrology, the catchment area is the uphill region that feeds into drainage channels (Freeman, 1991; O'Callaghan & Mark, 1984; Tarboton, 1997). While the size of the catchment region is important when calculating aspects like the volume of water in a channel, for this project I only need to know how material will flow downhill from specific points or areas – a "top down" approach. As my interest is in the flow of obsidian sediment from its primary exposure to its extended and diffuse secondary distribution, I need to know the exact topographical locations of each primary source or sources. For this project, these primary sources will act as the catchment region.

For the five study areas (see Table 3-1), the primary source locations are illustrated in maps from previous work (Jackson et al., 2009; Talbot et al., 2015). From these, I created polygons and weighted rasters which were used in the flow direction and accumulation calculations. Figure 3-4 demonstrates the weighted raster for the Mineral Mountains. In this raster, the raster cells representing the primary sources are set to 1 and the cells representing the remainder of the region are set to zero.
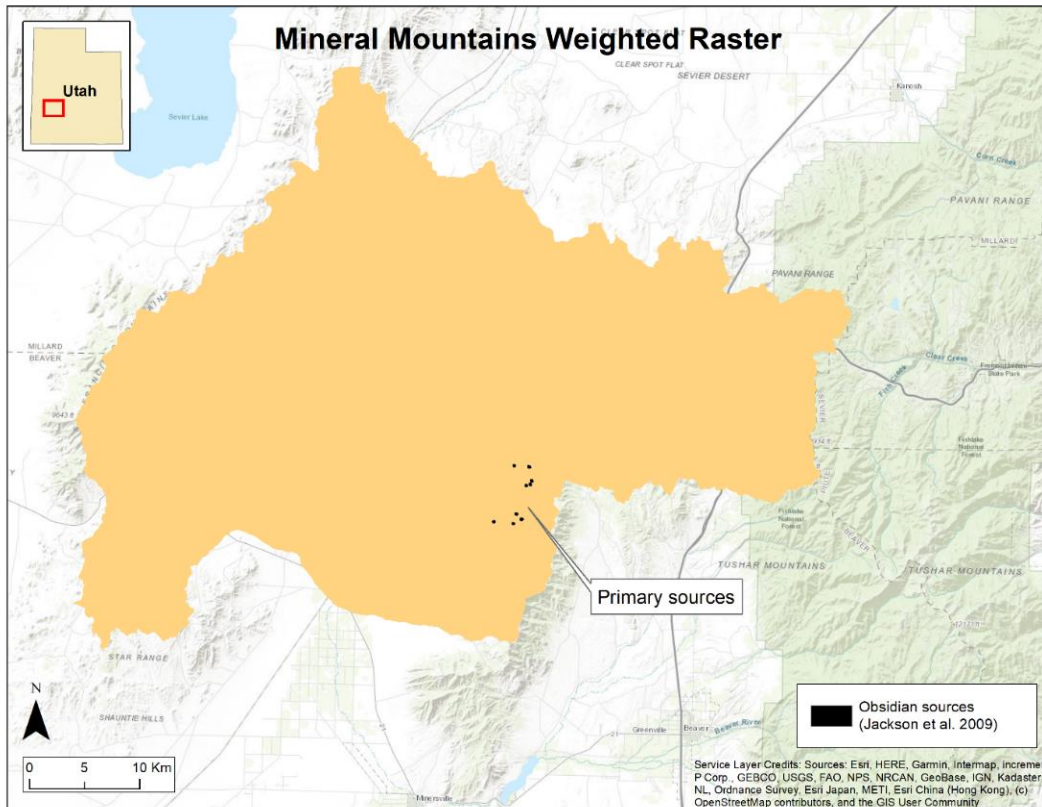
Figure 3-4: The primary source weighted raster for the Mineral Mountains subbasins.

3.3.5 Perform the Downslope Analysis/Simulation

The final step of predicting downslope flow using a DEM is calculating the direction and accumulation of the flow as it moves from one cell to the next in a grid. This problem has been addressed by multiple researchers and algorithms (Costa-Cabral & Burges, 1994; Fairfield & Leymarie, 1991; Freeman, 1991; O'Callaghan & Mark, 1984; Qin et al., 2011; Quinn et al., 1991; Seibert & McGlynn, 2007; Tarboton, 1997; Tarboton et al., 1991). As my goal here is to predict the extent of flows, not drainage channels or volumes, I have chosen the Multiple Flow Direction (MFD) method (Freeman, 1991; Quinn et al., 1991). Freeman's algorithm has weaknesses in flat regions and sinks, but both issues are addressed by earlier steps in my process and the MFD algorithm works well with the sort of divergent alluvial flows being explored here (O'Callaghan & Mark, 1984).

The MFD method assumes that outflow from any given cell will be divergently dispersed to all its lower neighboring cells. The flow is fractionally allocated based on the slopes between the sending cell and the receiving cells (see *Equation 3-1,* after Freeman, 1991, p. 415, where best results were achieved using the constant *p* = 1.1):

$$f_i = \frac{Max(0, Slope_i^p)}{\sum_{j=1}^8 (Max(0, Slope_j^p))} \tag{Eq. 3-1}$$

Figure 3-5 provides a simple example of a single cell (center) and the allocation of flow to three downslope cells. In execution, the MFD algorithm is recursive, as many cells will have multiple cells flowing into them. The recursive nature of the algorithm captures the full accumulation of flow into each downslope cell.
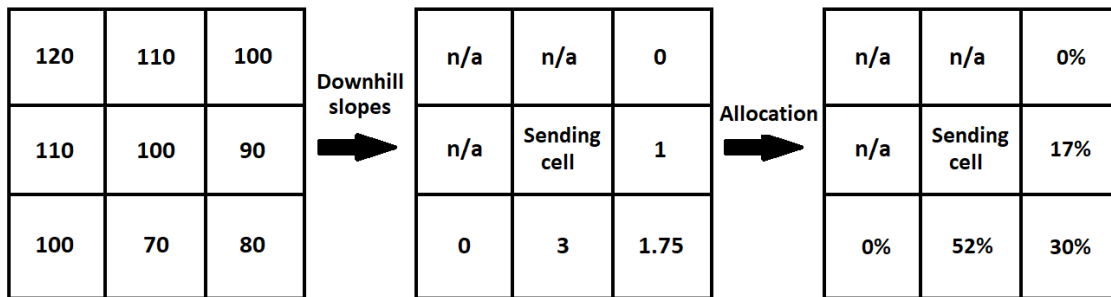
Figure 3-5: Multiple Flow Direction (MFD) allocation of flow based on downhill slopes (elevations in meters, 10 meter cell size).

The System for Automated Geoscientific Analyses (SAGA) is a specialized, open-source GIS system tailored to geoscientific methods (Conrad et al., 2015). I used SAGA v. 7.5.0 and its *Flow Accumulation (Top Down)* functionality (based on the *ta_hydrology* module) to model downslope flow. This function accepts an elevation model and a weighted DEM representing the catchment region; in this case, the filled and smoothed regional DEM and the weighted DEM of the primary source locations, respectively. The function allows the user to select one of several

61

different accumulation algorithms (cited above), including Freeman's (1991) MFD algorithm. Figure 3-6 shows the calculated flow raster for the 11x11 smoothed DEM in the Mineral Mountains:
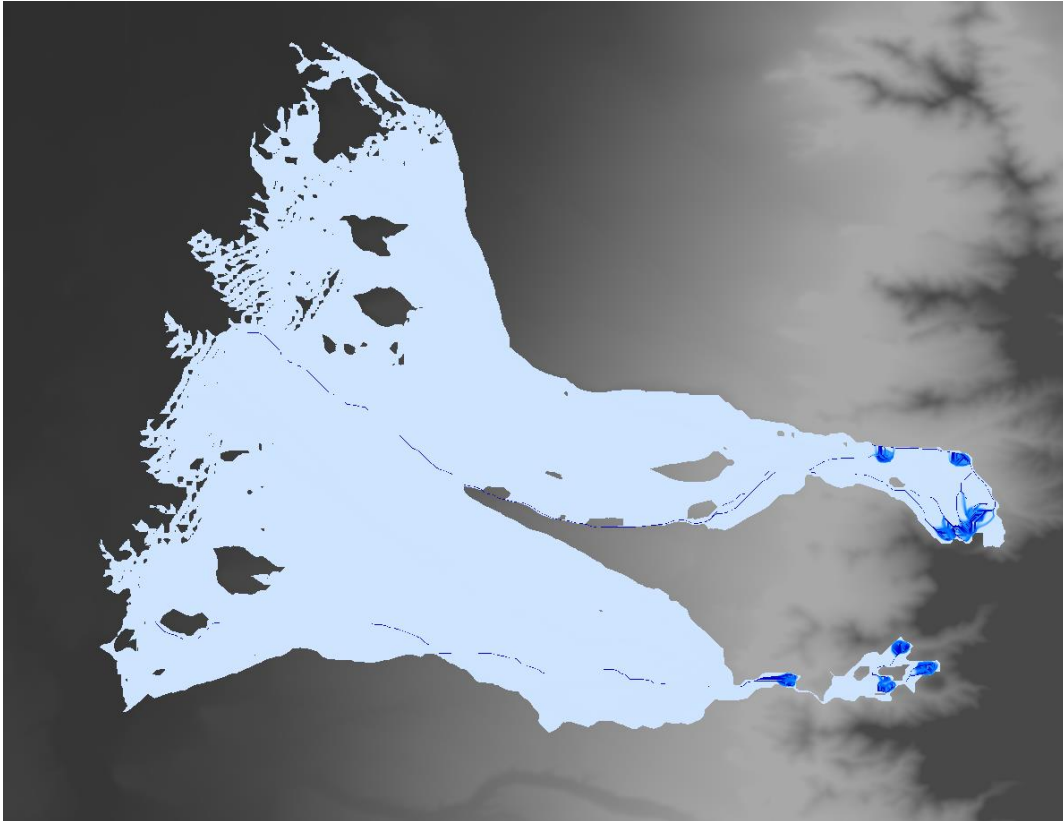
Figure 3-6: A flow accumulation (blue, moving east to west) calculated using the Multiple Flow Direction (MFD) algorithm on an 11x11 smoothed digital elevation model (DEM).

I created flow accumulation rasters for each of the smoothed DEMS (3x3, 5x5, 7x7, 11x11, and 21x21 nearest neighbors) using SAGA. These DEMs were then imported into ArcMap and various ArcMap functions were used to convert the flow accumulation rasters into polygons and outlines that could be used to create maps and inform fieldwork. The 11x11 flow accumulation in context of the Mineral Mountains hydrographic subbasin is shown in Figure 3-7.
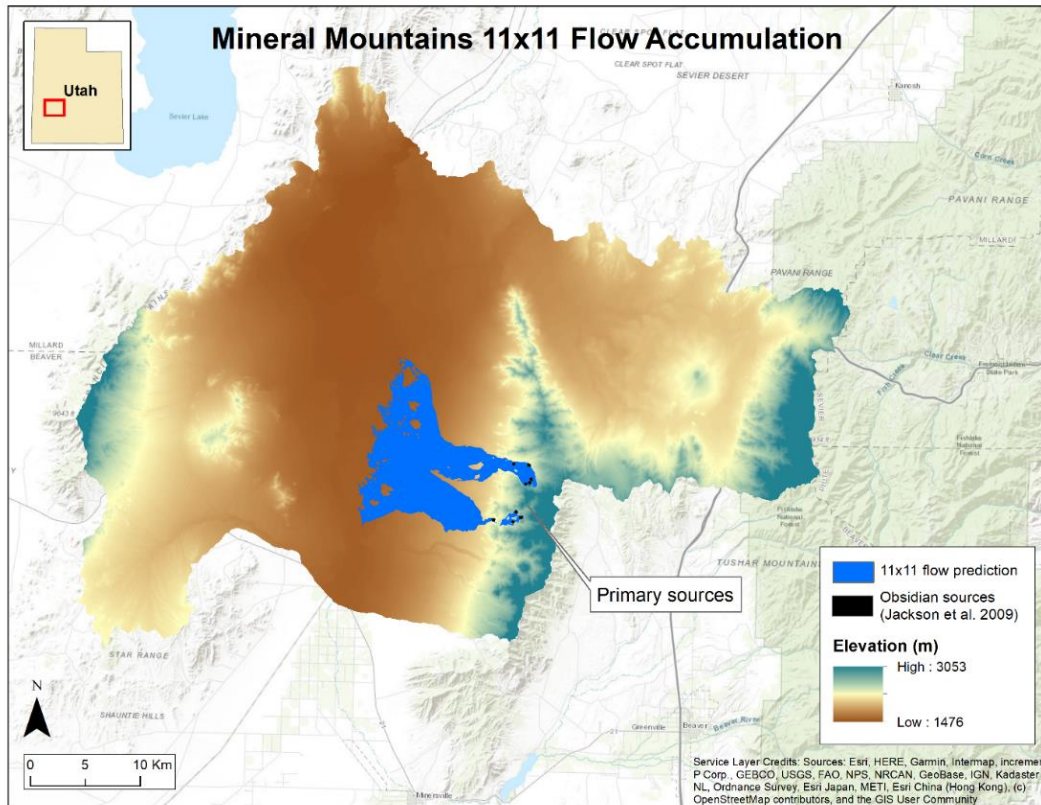
Figure 3-7: Mineral Mountains 11x11 flow accumulation.

All five flow accumulations (3x3 to 21x21 nearest neighbors) can be "stacked" to show the areas with the highest likelihood to contain secondary obsidian deposits downslope from the primary sources (Figure 3-8).
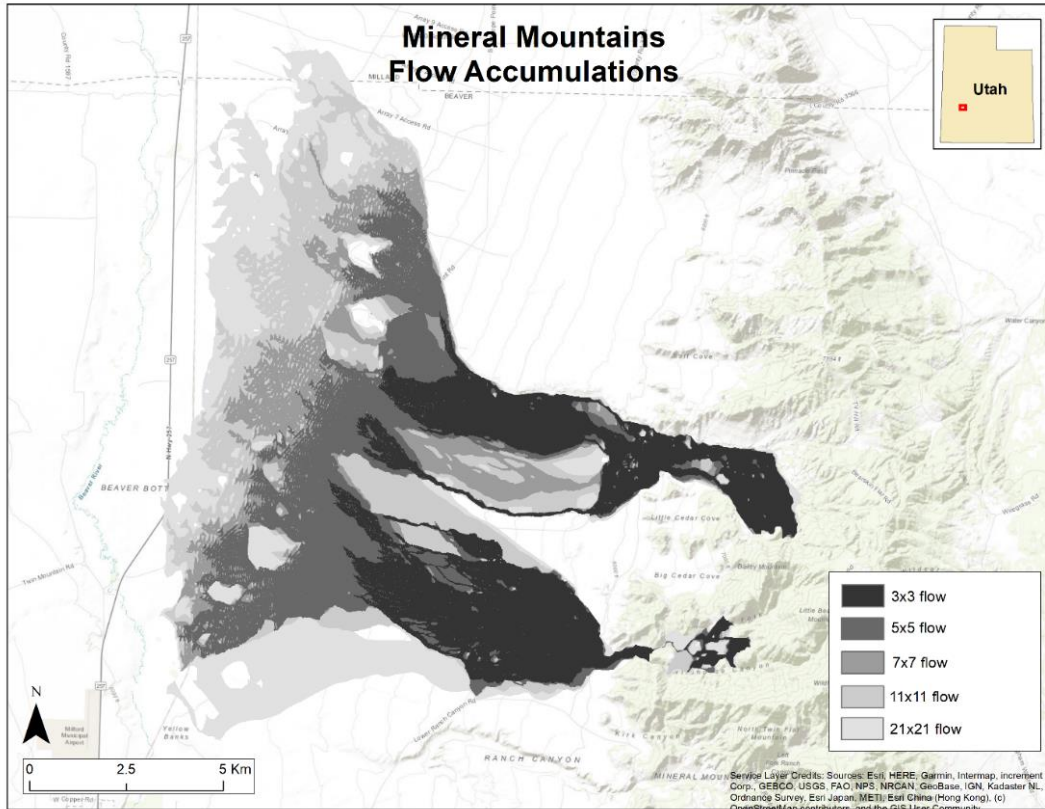
*Figure 3-8: Stacked flow accumulation digital elevation models for varying levels of elevation
smoothing (darkest is lowest nearest neighbor smoothing starting at 3x3,
lightest is highest smoothing, at 21x21).*

3.3.6 Preparing for Survey Field Work

The final step of analysis is creating the maps that were used for fieldwork. Using ArcMap, I created outline perimeters for each flow. As can be seen in Figure 3-8, most of the flow variation occurs at the distal ends (the left north-south running edge in this diagram), the lowest energy extents of the flows. The "sides" of the flow (in this case the east-west running edges) are quite uniform regardless of the level of smoothing. The 'islands' or voids that can be seen in Figure 3-8 within the flows are of no concern here as they are interior to the general flow; a hunter-gatherer would encounter the flow signal regardless of the interior void. Rather, the outline of the flow – the interface between the secondary deposit and a person walking across the landscape is most important. Figure 3-9 shows this outline along with transects placed at 1

kilometer spacing. From this map, I generated the UTM coordinates for the intersections

between the outline and the transects and the angle of the transect to use during the fieldwork

that tested the accuracy of the models.
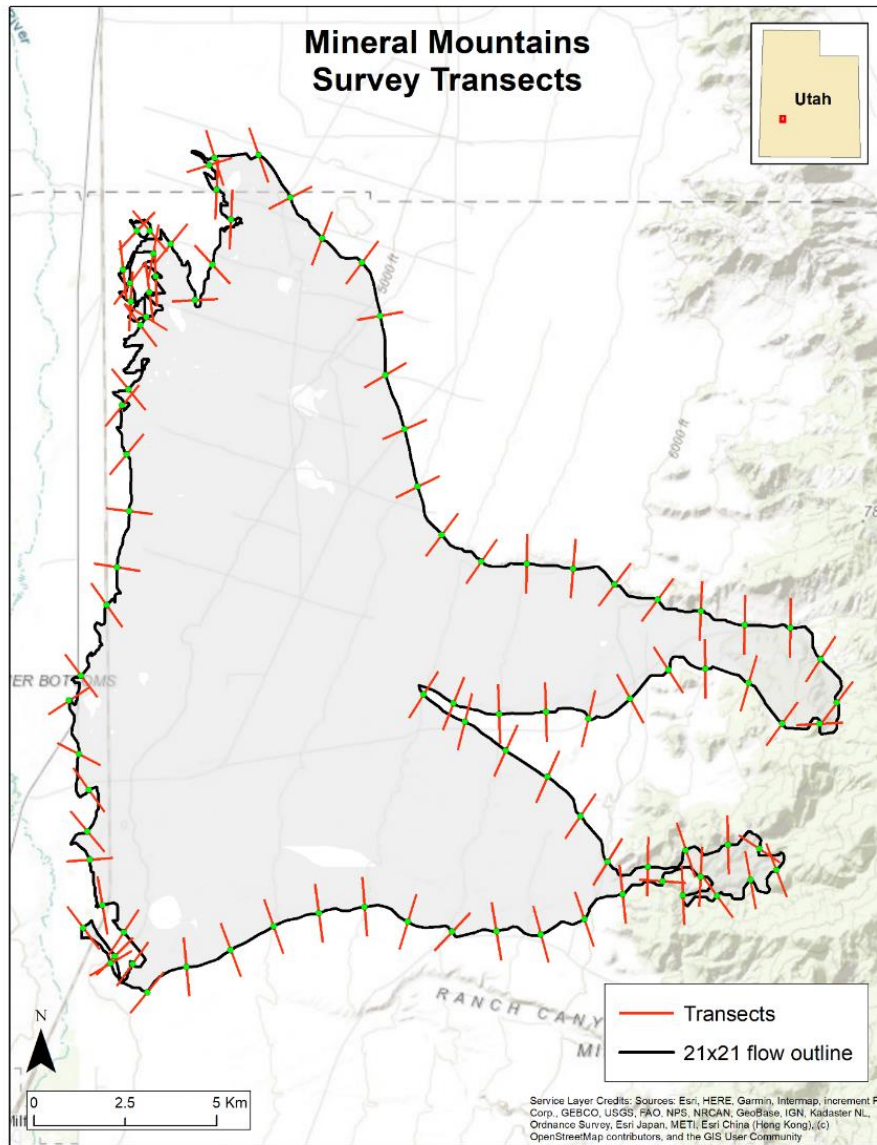
Figure 3-9: Outline of the 21x21 flow and survey transects

3.4 Survey Methodology

Survey field work was carried out, by myself and an assistant, during the summers of 2020 and 2021.

For each of the five survey areas, I used the regional flow prediction that best fit the known samples or previous observation points and prepared survey transect maps and lists of survey starting points, as described above. The process of running the transects involved locating the starting point and observing whether obsidian was present in the sediment around that predicted flow edge. If obsidian sediment was present, the surveyor moved "outward" from the flow, on the transect bearing, looking for the most exterior edge of the flow. This edge was considered "found" when there was no further presence of obsidian sediment observed after 100 m from the last observation point. If no obsidian was observed near the starting point, then the bearing was reversed, and the surveyor moved "inward" until the flow edge was found. A natural (non-artifactual) obsidian sample was taken at the most external edge of the flow.

The survey transects generated by these processes (as in Figure 3-9) are idealized in that not all transects can or need to be run. Various restrictions occur in the field, such as impassable terrain, private property, livestock, and other access limitations. Also, in some cases, the survey flow prediction was incorrect (extended too far or not far enough), requiring abandonment of some transects or the ad hoc creation of new transects in the field. In these cases, I worked "from the known to the unknown", using the last known observation points and knowledge of the hydrographic basin to close the sides of the flow polygon.

In addition, the size of obsidian sediment varies significantly over the course of a secondary flow. Close to the primary source, large tool-sized nodules may appear, but these nodules naturally diminish in size the farther the secondary distribution expands outward. At the

most distal ends of an alluvial flow, flow energy is dissipating, and the sediment package transitions to extremely fine-grained sediments and silt. Obsidian pebbles similarly diminish in size, making the distal edge of the secondary flow the hardest to define as obsidian grains move below 2 mm in size. These grains can still be recognized at this low end, and I suggest that hunter-gatherers did make this connection, but below 2 mm there are visual limitations. Similarly, as will be discussed below, the flow predictions are most unreliable at the distal ends where this transition occurs due to limitations in the accuracy of DEM elevations and the extremely gentle slopes typical of most basin bottoms. Together, these factors compound the level of imprecision at the distal ends of these surveyed extents.

3.5 Analyzing Survey Results

The overarching goal of this process is to determine if this methodology can be used to accurately predict the extent and scale of the secondary distribution of obsidian when only the primary source location is known. Five known primary sources were used to predict secondary flows and then surveyed to determine the actual flows. Following survey data collection, these observed secondary extents were mapped as polygons. These were then compared against the original predicted flows using a modified Confusion Matrix (Bruce & Bruce, 2017; Kulkarni et al., 2020; Marcos Llobera, personal comm., April 2, 2021).

A Confusion Matrix is a tool used to test the predictive performance of a classification model. In this case, the Confusion Matrix was used to test how well my model classified, or predicted, the area that would contain secondary flows versus what was observed during the survey.

This binary classification test can be illustrated by a simple 2x2 matrix and the following definitions:

Predicted flow		
	Negative	**Positive**
Negative	TN	FP
Positive	FN	TP

Observed flow (label at left of table)

- True Positive (TP) is the area that was correctly classified, or predicted, to contain secondary flow.

- False Positive (FP) is the area predicted to contain flow but did not (was classified as positive when it was negative).

- False Negative (FN) is the observed flow area that is outside the prediction (area classified as negative when it should be positive).

- True Negative (TN) is area accurately classified as containing no flow. In this case, it is the area that is outside both the predicted and the observed flow.

This is further illustrated in Figure 3-10:
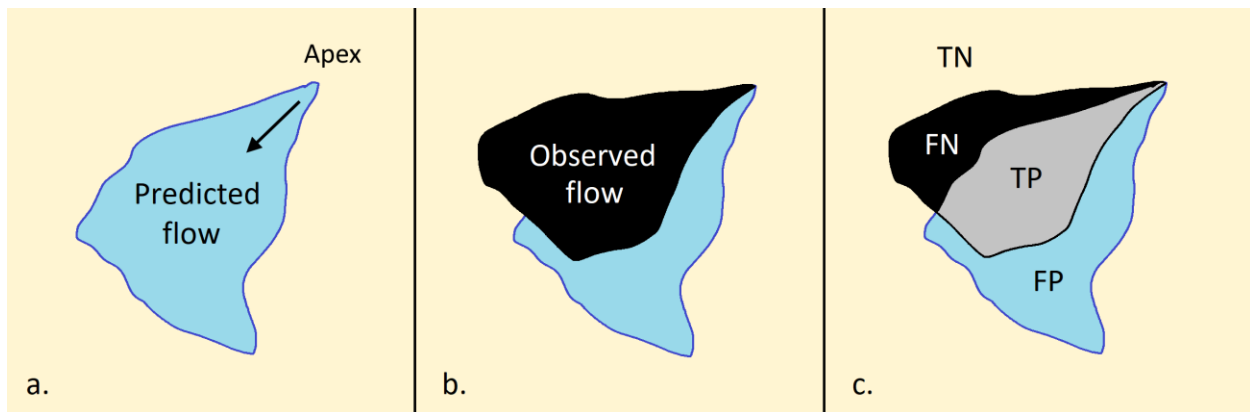
Figure 3-10: Mapping flow predictions to actuals using a modified Confusion Matrix; a) the flow predicted by one smoothing level of the model, b) the observed surveyed flow, c) the overlapping and non-overlapping regions mapped to Confusion Matrix nomenclature.

Confusion Matrices are typically used to determine the accuracy and precision of a model using the following formulas (Kulkarni et al., 2020):

$$\text{Accuracy} = \frac{TN+TP}{TN+FP+FN+TP} \tag{Eq. 3-2}$$

$$\text{Precision} = \frac{TP}{TP+FP} \tag{Eq. 3-3}$$

In the case of predicting secondary flows, two factors require modification to the typical Confusion Matrix application. First, my model involves progressively smoothing the flow prediction, for example, starting with a 3x3 nearest neighbor average and progressing to a 21x21 nearest neighbor average. If taken to extremes, increasing the nearest neighbor value would eventually smooth the entire DEM to a single regional average, or a flat surface. This would not provide a useful predictive model. Second, in my model, True Negative (TN) is essentially equal to infinity, as it represents all of the world where the flow is not. This eliminates the usefulness of the standard Confusion Matrix Accuracy calculation.

In my modified use, I want to find the smoothing level that provides a balance between correct classification and excessive smoothing. Therefore, to find the best fit, I use the ratio of the correctly predicted flow (TP) to the observed flow and then penalize that value using the ratio of the incorrectly predicted flow (FP) to the observed flow:

$$\text{Best Fit} = \frac{TP}{Observed} - \frac{FP}{Observed} = \frac{TP-FP}{Observed} \tag{Eq. 3-4}$$

Table 3-2 illustrates these calculations using the Black Rock Area (BRA) data, using increasing smoothing levels (3x3 to 21x21 in increments of 2). As can be clearly seen, as Smoothing increases, the "% survey predicted" increases, and will increase eventually to 100% with sufficient smoothing. At the same time, the predictions inside and outside the actual surveyed flow (353 km^2 at BRA) are at odds with each other. As smoothing increases, the "%

prediction inside observed" decreases while "% prediction outside observed" increases. To find

the optimal smoothing level, the highest TP offset by the least FP, I balance these values, using

the "% prediction inside observed" and penalize it with the "% prediction outside observed"

(after *Equation* 3-4). This value is seen in the "(TP/FP)/observed" column, revealing that the

13x13 smoothing level provides the "best fit" and optimal predictive value for the BRA. This

method was repeated for each of the five survey areas to determine if there is an average

smoothing level that is best for predicting secondary obsidian flows from known primary sources

(more below).

3.6 Regional Site Considerations and Obsidian Flow Predictions

3.6.1 Black Rock Area

Location: Millard County, Utah

Alternative names: None

Hull (1994) sample points: *n*=7 (Appendix D, Table D-1)

Skinner sample points: *n*=10 (Appendix D, Table D-2)

Hunt 2019 observation points: *n*=17 (Appendix B, Table B-6)

ORB Paleoindian artifacts: *n*=10 (Appendix A, Table A-37)

The Black Rock Area (BRA) is an expansive region with multiple primary obsidian source exposures (Figure 3-11) in Millard County, Utah, east of the Cricket Range and north of the Mineral Mountains (Figure 3-12). Hull (1994, p. 10) suggested that the area is one of the largest primary sources of obsidian in Utah, measuring in at 50 km^2. However, based on just the primary outcrops documented in Jackson et al. (2009), an outline of the area covers at least three times the area estimated by Hull. This knowledge set my own early expectations that the secondary obsidian distributions emanating from the BRA would likely cover several hundred square kilometers.

BRA Geology

While the region experienced volcanism beginning about 20 Ma and continuing to about 0.97 Ma, Crecraft, Nash, & Evans (1981) state that silicic volcanism occurred in a tight range between 2.6 to 2.2 Ma in the BRA. It was during this time that regional primary obsidian sources were formed from quickly-cooling rhyolitic flows containing at least 76% silica

Figure 3-11: Black Rock Area: typical primary source exposure in the Coyote Hills

(Crecraft et al., 1981). Hintze et al. (2003) mapped and named the local rhyolite flow the

"Cudahy Mine rhyolite" (*Tcr*) (Figure 3-13). This area produces a black obsidian as well as a

"snowflake" obsidian which contains phenocrysts (embedded crystals) that do not knap well

(Jackson et al., 2009). The largest Cudahy Mine rhyolite flow manifests as the Coyote Hills,

where Jackson et al. (2009) report over 37 separate obsidian exposures, although several smaller

rhyolite exposures also occur to the east (see Figure 3-13).

More recently, about 18,000 cal ya, much of the region, including some BRA primary

sources, was inundated by Pleistocene Lake Bonneville at its height (Chen & Maloof, 2017b; C.

G. Oviatt & Jewell, 2016; Utah Geospatial Reference Center, 2017), reaching about 1552 m

above sea level at this location (Figure 3-14). After Lake Bonneville receded, the areas below the

remnant shoreline were covered in lacustrine fine silt, sandy loam, and pebble fields, which

remain today.

The Coyote Hills, as well as the South Twin Peaks, Black Point, and Dee's Ridge to the east, are topographically moderate hills, with almost all areas rising less than 300 m above the basin floor.

BRA Archaeology

The archaeological significance of the BRA is well appreciated in Utah state prehistory and the region has been subject to numerous archaeological surveys (Hull, 1994; Jackson et al., 2009; Mullins et al., 2009). There are over 2000 sites, both prehistoric and historic, reported within the local subbasins (Utah Division of State History, 2020). Most of the prehistoric sites are obsidian lithic scatters of varying sizes although Jackson et al. (2009) report at least five prehistoric quarries, three in the Coyote Hills (42MD1089, 42MD1090, and 42MD1091) and two at Black Point (42MD871 and 42MD872). However, the detection of prehistoric quarrying is confounded by historic and contemporary obsidian and pumice mining. Many of the large obsidian exposures in the Coyote Hills show deep pitting that is likely the result of mechanized excavation. On the west side of the Coyote Hills, the Cudahy Mine destroyed a significant portion of the hillside in the process of mining pumice for household cleansers in the early 20th century (Everts, 1991). On the south end of the Coyote Hills, modern surface mining for jewelry-grade obsidian continues today.

BRA Past Work

Our understanding of the scope and extent of the BRA primary and secondary obsidian extents has changed significantly in the last 25 years and is illustrated in Figure 3-15. The earliest X-ray fluorescence (XRF) testing at this locality by Nelson & Holmes (1979) and Nelson (1984) provide insufficient locational data to be helpful here (only detailed to township-range sections or quarter sections). Hull (1994) provides a useful early dataset of XRF tests on seven

73

samples from the region. These samples appear to be centered on primary sources, though the township and range quarter-quarter-quarter descriptions can still be several hundred meters off when compared to modern GPS coordinates. Skinner (Table D-2) has aggregated an extensive dataset of Intermountain West XRF test results, including 10 XRF samples from the BRA, and these capture the southeast extent of BRA obsidian. In 2019, I conducted a pilot survey and observed obsidian (Table B-6, *n*=17) at various points around the BRA. While these are not XRF test points, they provide a useful indication that obsidian is distributed on the southwest slope of the Coyote Hills. The work by Jackson et al. (2009), however, provides the best resource of primary obsidian sources throughout the region and suggests a secondary distribution as well.

All this information was used in selecting the best flow prediction for the BRA obsidian.

BRA Flow Prediction

Using the process described in section 3.3, five flow distributions were created.

The starting requirement for all flow prediction is the location of the primary sources, illustrated for BRA in Figure 3-13. Using these primary source starting points (Jackson et al., 2009), the downslope flows were predicted for 3x3, 5x5, 7x7, 11x11, and 21x21 nearest neighbor smoothed DEMs. These are presented in "stacked" form in Figure 3-16, with the 3x3 nearest neighborhood flow represented by the darkest shade and the 21x21 flow represented by the lightest shade.

A comparison to the known sample points by Hull (1994), Skinner (Table D-2), and my own pilot project (Table B-6) revealed some anomalies (Figure 3-17). Hull (1994) targeted primary sources and her samples find good concordance with the flow predictions. However, three of Skinner's sample points, particularly SO-65-1352 and SO-65-1353, appear to be well out of range of the predictions. Finally, a cluster of my own observation points in the southwest,

near the active quarry, are problematic. These points appear to be on the other side of the highest Coyote Hills ridge and the subbasin boundary. In this case, I suspect that Jackson et al. (2009) chose not to consider the active quarry as a prehistoric exposure simply because the natural exposure has been completely destroyed.

In preparation for fieldwork, I created a polygon shapefile to represent the location of the active quarry as a primary source. I then replicated the flow generation steps to recreate the five flows while including this primary source on the south slope of Coyote Hills. The result was a large dispersal prediction, which is shown in context of the original northern flows in Figure 3-18. This ensured that I was prepared to run the appropriate survey transects if it appeared that a secondary distribution was occurring south of the ridge. There were still problematic sample points, particularly BRA07 and SO-65-1352, but the flow prediction covered more of these anomalous points. The final 21x21 prediction outline and transects for both north and south flows are shown in Figure 3-19.

BRA Survey Results

The Black Rock Area secondary distribution of obsidian was surveyed during the summer of 2020 and the observed extent is illustrated in Figure 3-20. As suspected, the BRA secondary distribution is expansive, covering more than 353 km^2 with a perimeter of ~193 km. During the survey, 233 observation points were recorded, and 164 natural obsidian samples were collected (Table B-1). Of these collected samples, 32 were submitted to Northwest Research Obsidian Studies Laboratory (NWROSL) for X-ray Fluorescence (XRF) testing (Table C-1 and Appendix E) and were confirmed as "Black Rock Area" obsidian (green triangles in Figure 3-20).

The surveyed flow encompasses almost all previous sample points recorded by Hull (1994), Skinner (Table D-2), and myself (Table B-6), with minor exceptions (no previously

recorded points are more than 150 m outside the surveyed extent). However, there are large areas of secondary (or tertiary) distribution that the predictions did not account for, to the west and south of the Coyote Hills (annotated as A and B in Figure 3-21). Given the impact on the area by the rise and fall of Lake Bonneville, I suspect that obsidian was transported into these areas as the result of longshore movement and thousands of years of wave action on the west side of the obsidian-bearing hills. The Beaver River also flows south along the west side of these hills and may have entrained some sediments south, particularly in the area parallel to the Antelope Mountains, towards the town of Milford. There is also intermingling of the Black Rock Area obsidian sediments with those of the Mineral Mountains to the south, which is discussed below. There may also be undiscovered, or now fully eroded, obsidian sources that occupied the west side of the hills that account for the extensive secondary distribution in regions A and B.

Aside from these anomalies, the predicted flows provided a generally accurate guide for the secondary distribution extents. Following the modified Confusion Matrix methodology described in section 3.5, the optimal smoothing level for the BRA occurs at the 13x13 nearest neighbor average (Table 3-2). At this level, 64% of the actual survey region was predicted by the 13x13 model.

Table 3-2: Confusion Matrix results for the Black Rock Area.

Smoothing	Predicted flow area (km²)	TP	FP	% survey predicted	% prediction inside observed	% prediction outside observed	TP/ observed	FP/ observed	(TP-FP)/ observed
3x3	116.2	110.5	5.7	31%	95%	5%	31%	2%	29.7%
5x5	144.3	130.8	13.5	37%	91%	9%	37%	4%	33.3%
7x7	194.3	168.6	25.7	48%	87%	13%	48%	7%	40.5%
9x9	225.1	187.7	37.4	53%	83%	17%	53%	11%	42.6%
11x11	259.0	212.1	46.9	60%	82%	18%	60%	13%	46.8%
13x13	**287.9**	**226.9**	**61.1**	**64%**	**79%**	**21%**	**64%**	**17%**	**47.0%**
15x15	302.6	233.5	69.1	66%	77%	23%	66%	20%	46.6%
17x17	312.8	237.9	75.0	67%	76%	24%	67%	21%	46.2%
19x19	324.5	241.6	82.9	68%	74%	26%	68%	24%	45.0%
21x21	330.6	242.0	88.6	69%	73%	27%	69%	25%	43.5%
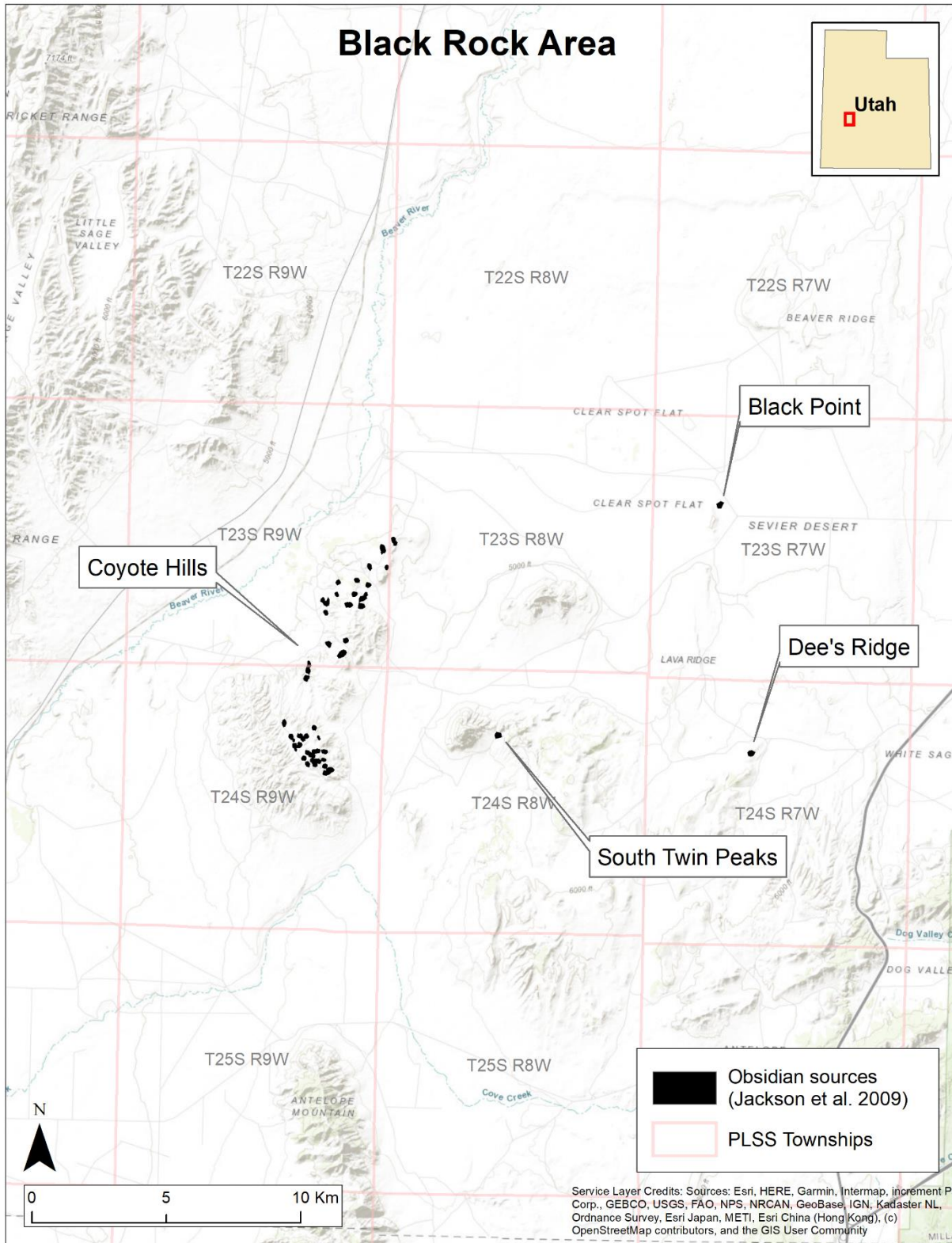
Figure 3-12: Black Rock Area regional view.
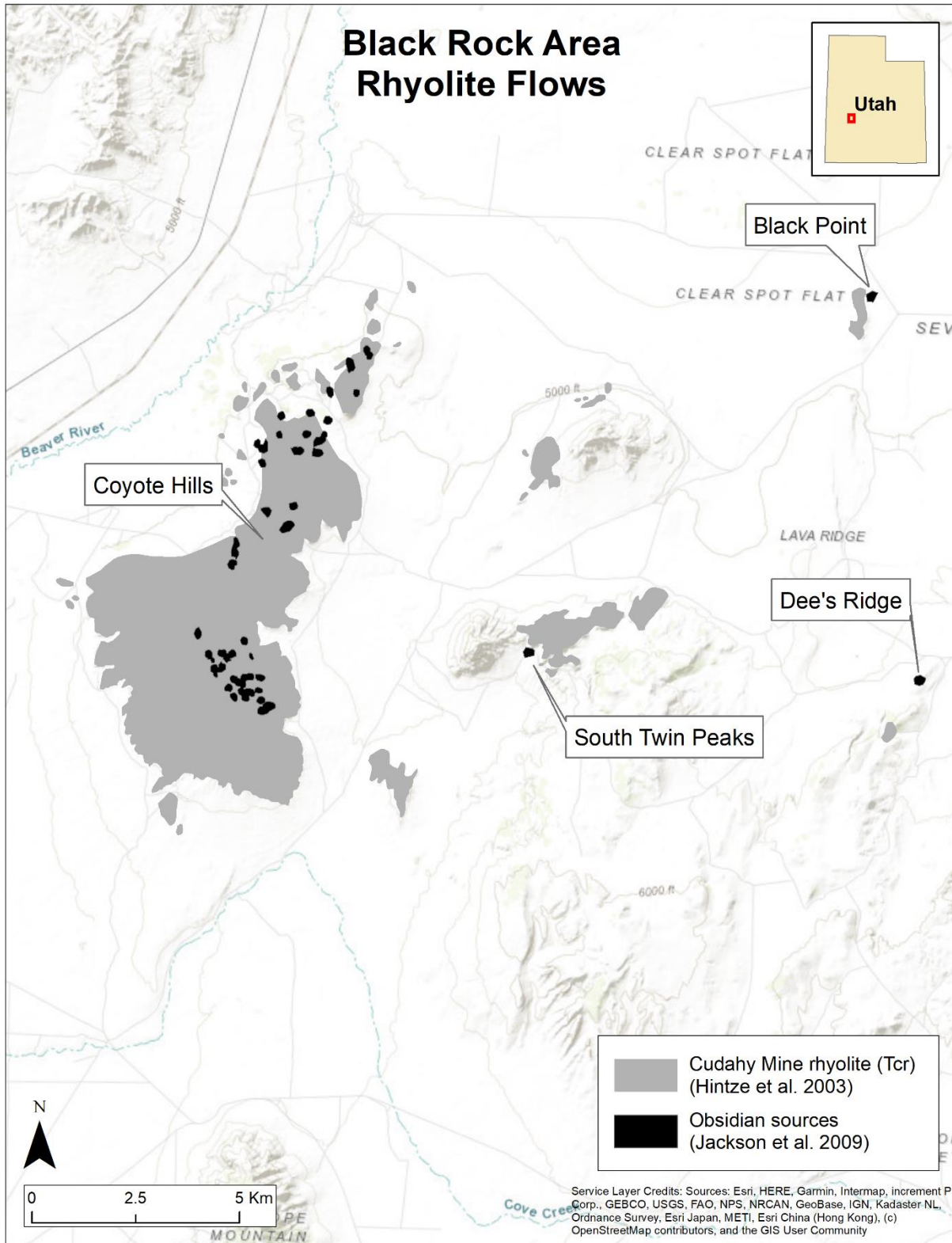
Figure 3-13: Black Rock Area rhyolite and obsidian.
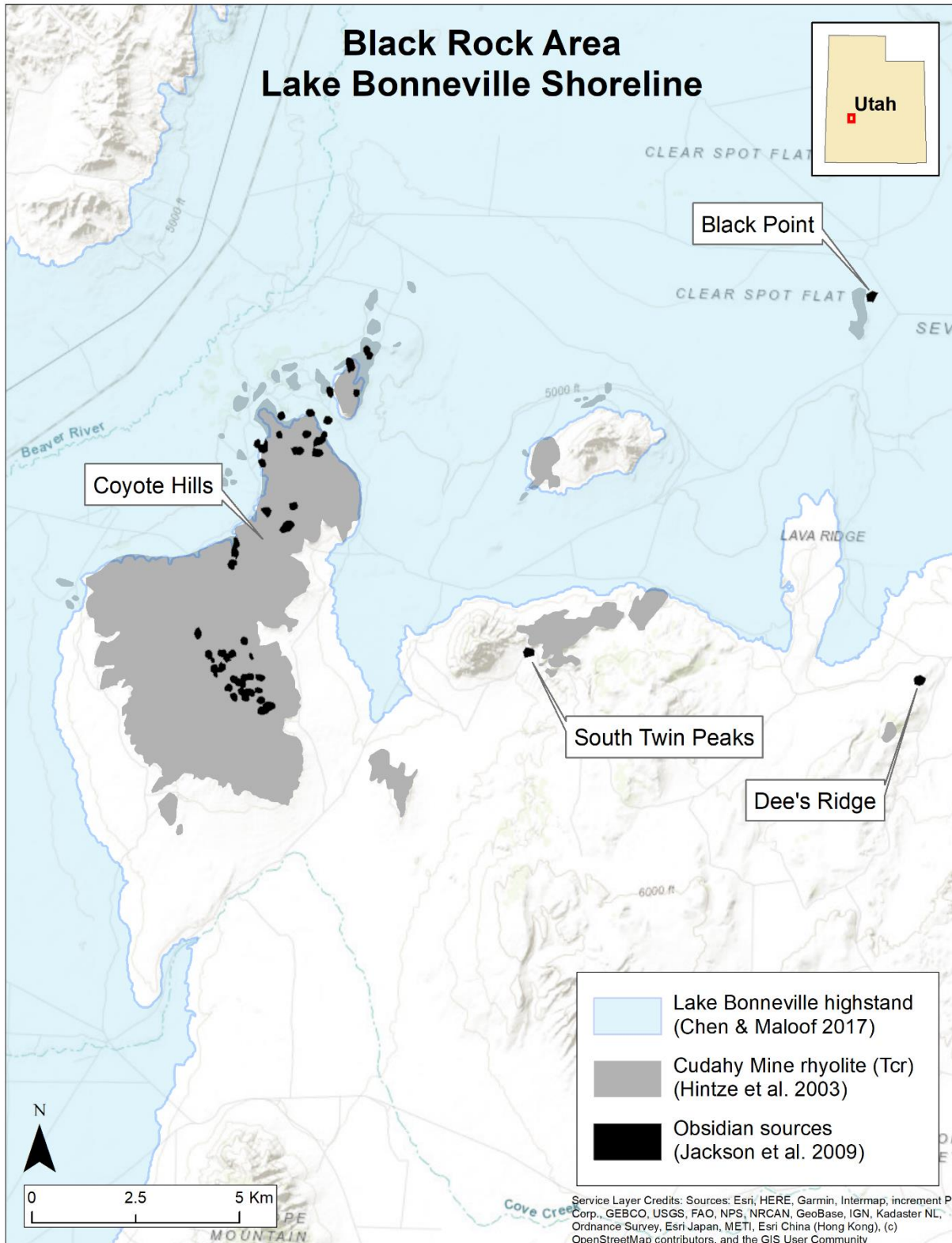
Figure 3-14: Black Rock Area primary sources in relation to the Lake Bonneville highstand.
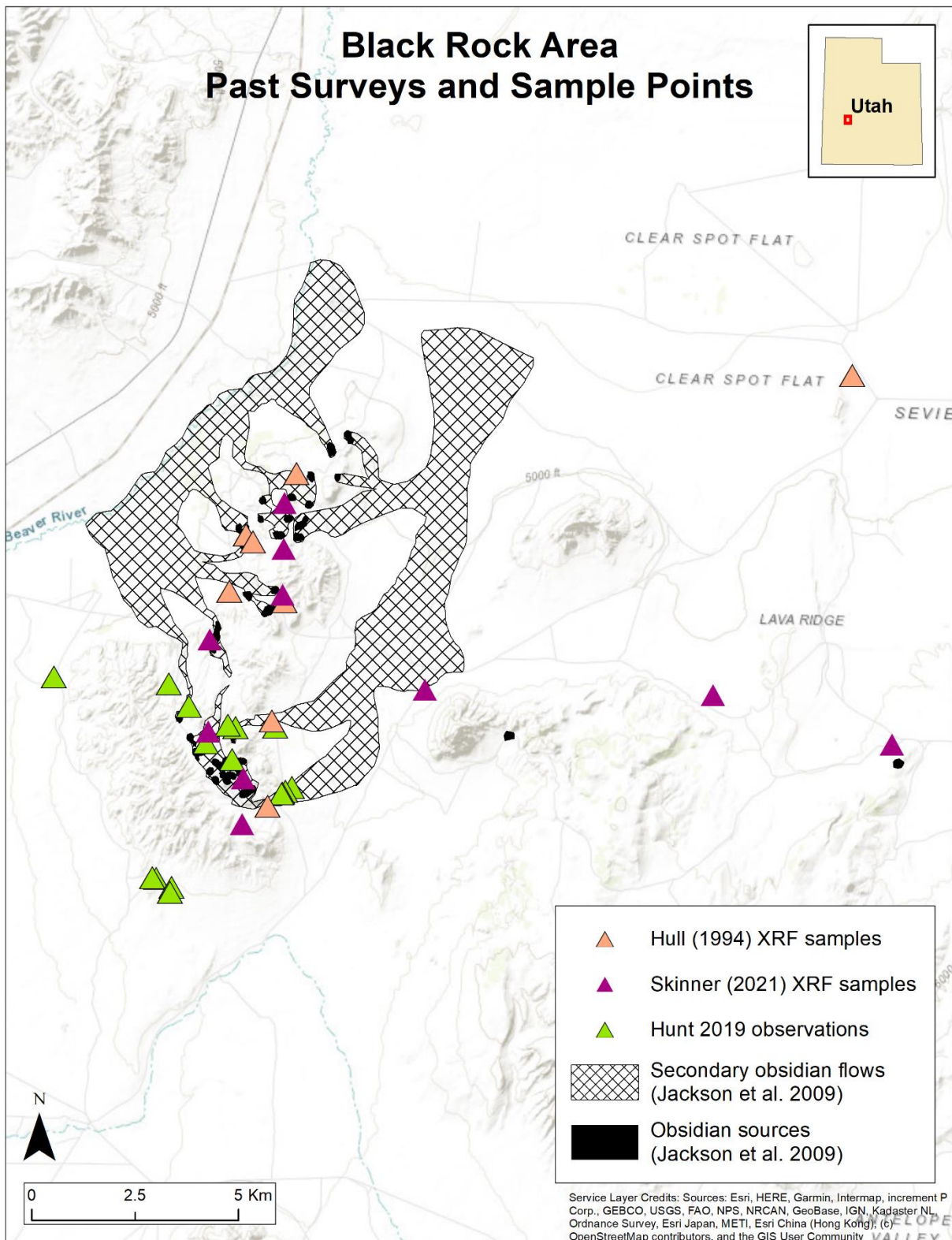
Figure 3-15: Black Rock Area past surveys and sample points.
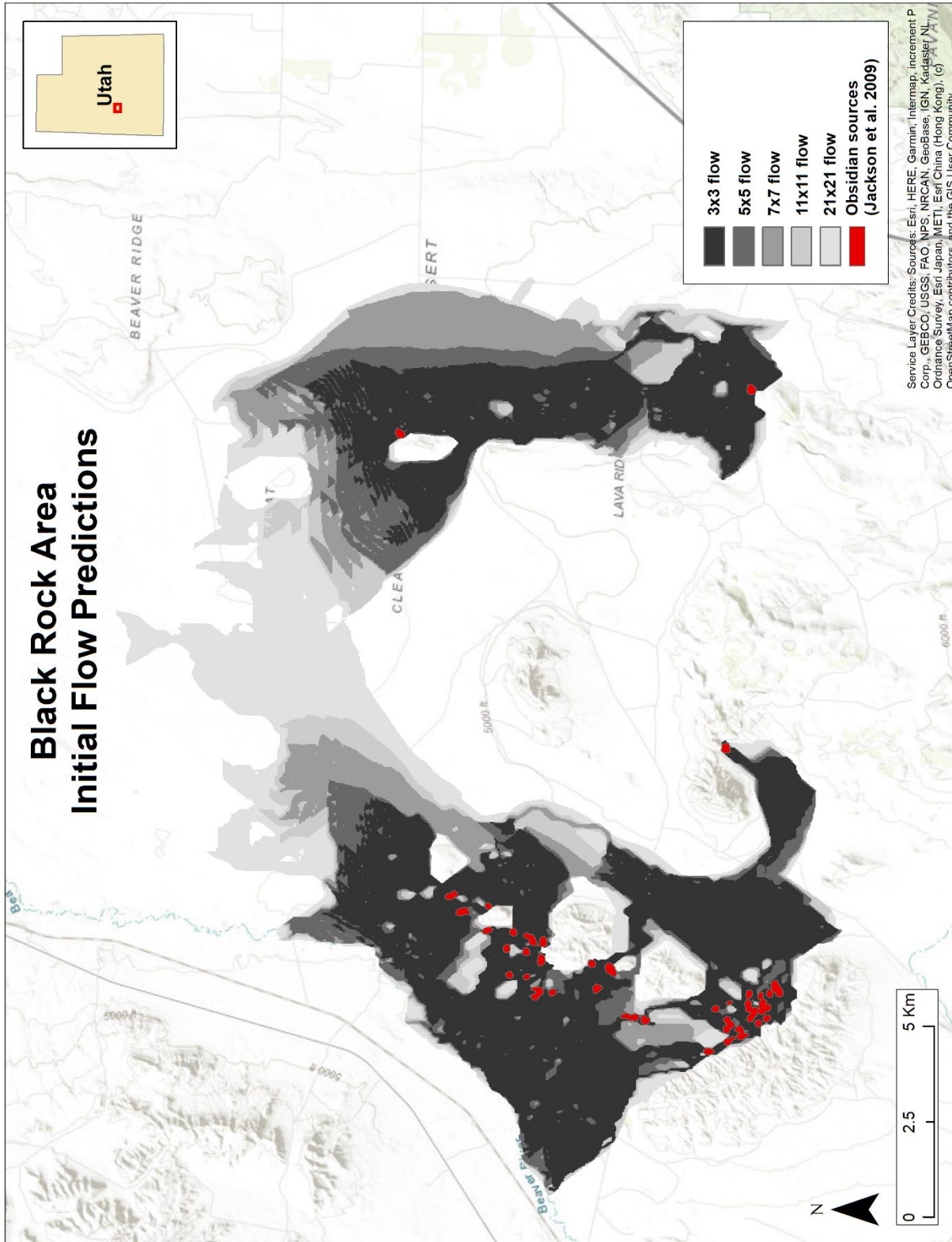
Figure 3-16: Black Rock Area initial flow predictions.
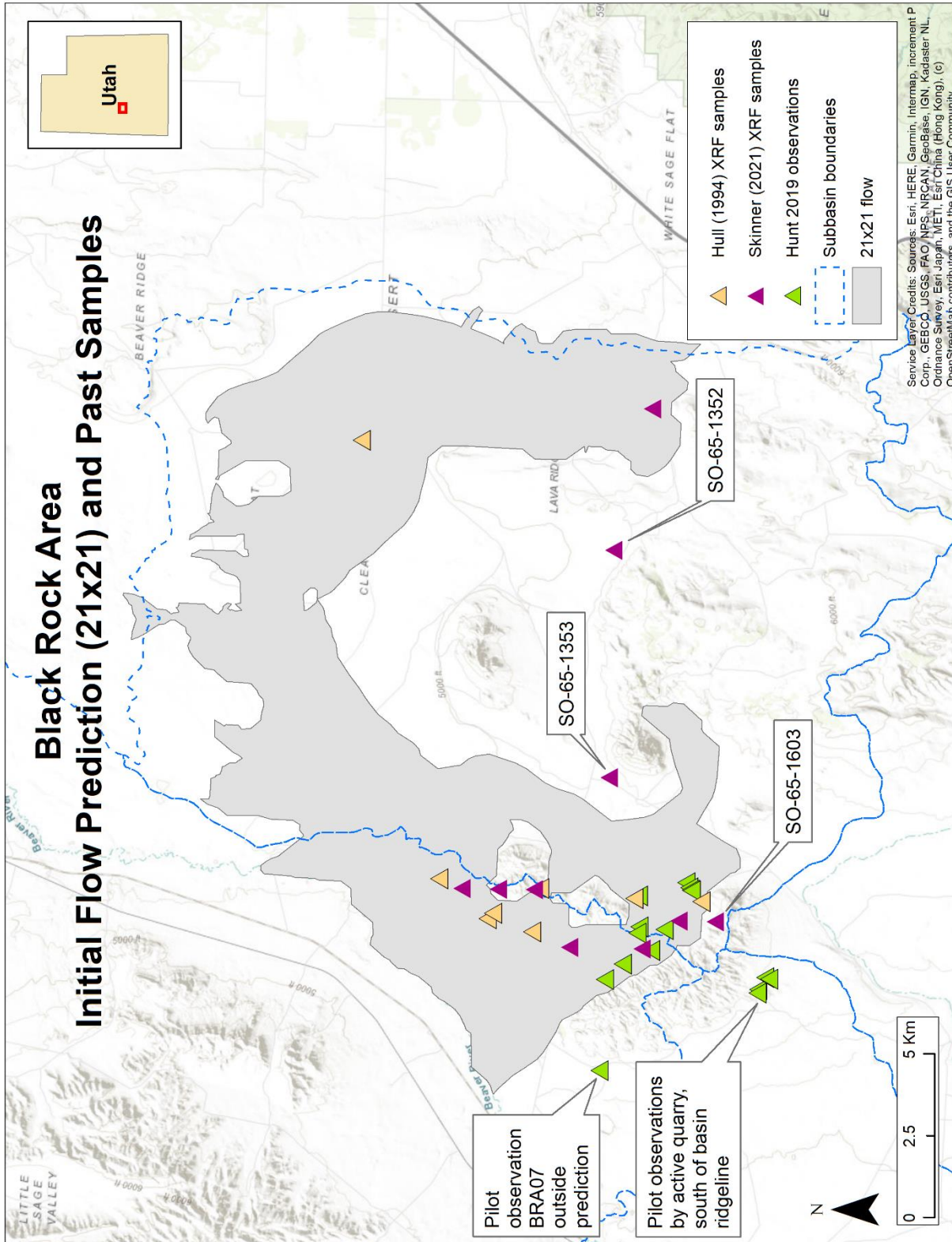
Figure 3-17: Black Rock Area initial 21x21 flow prediction in comparison with past sampling.
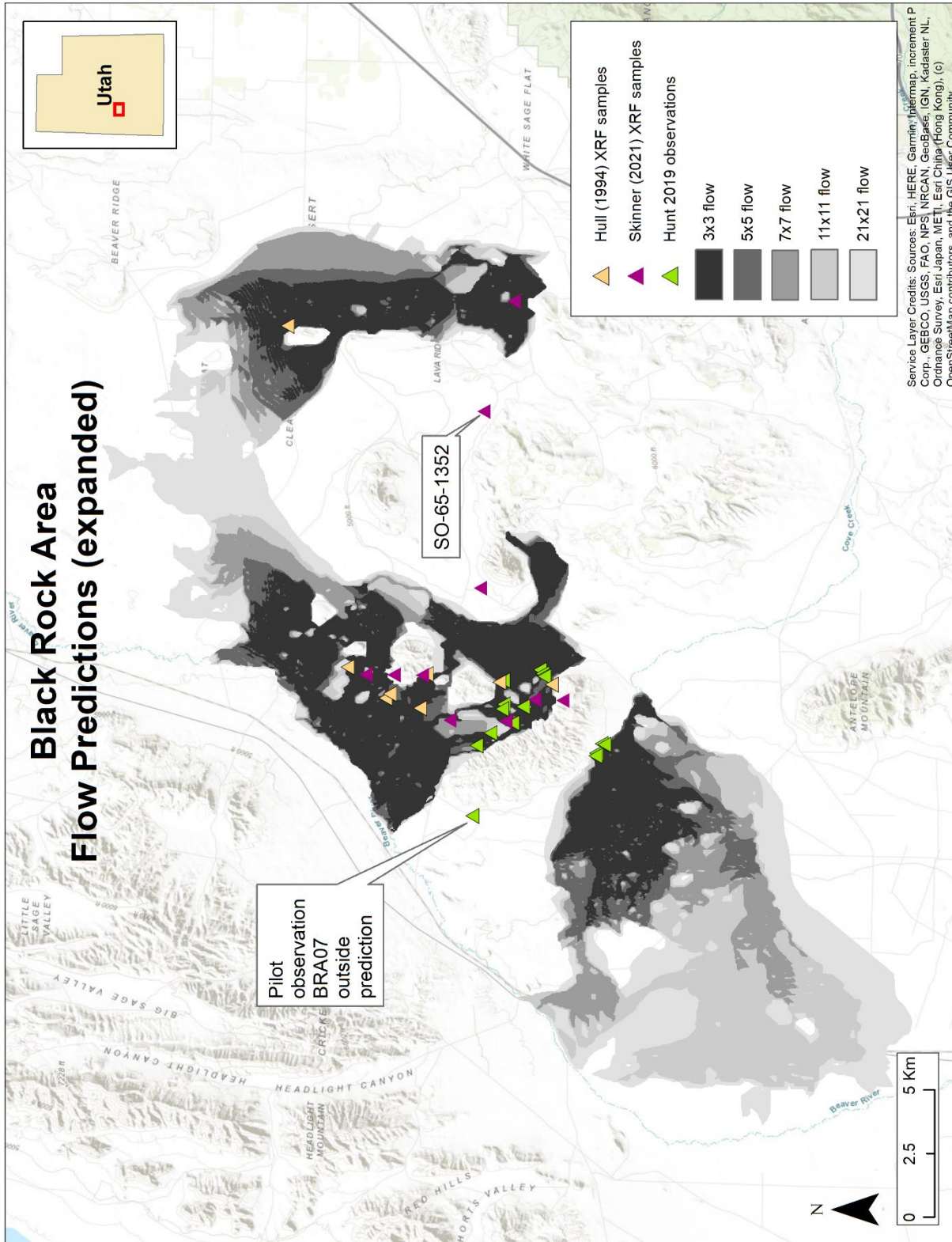
Figure 3-18: Black Rock Area flow predictions including expanded southern region.
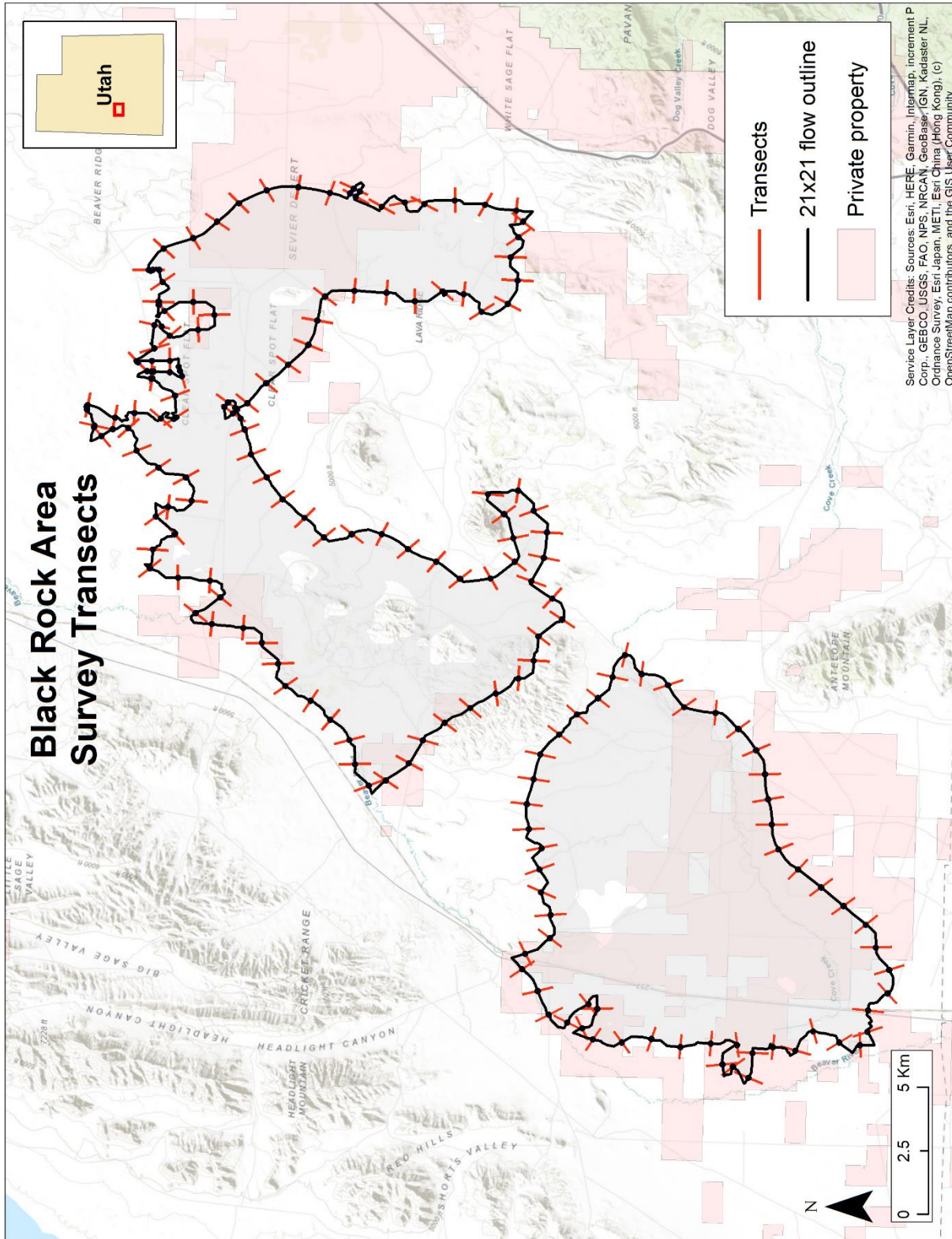
Figure 3-19: Black Rock Area 21x21 survey outline and transects.
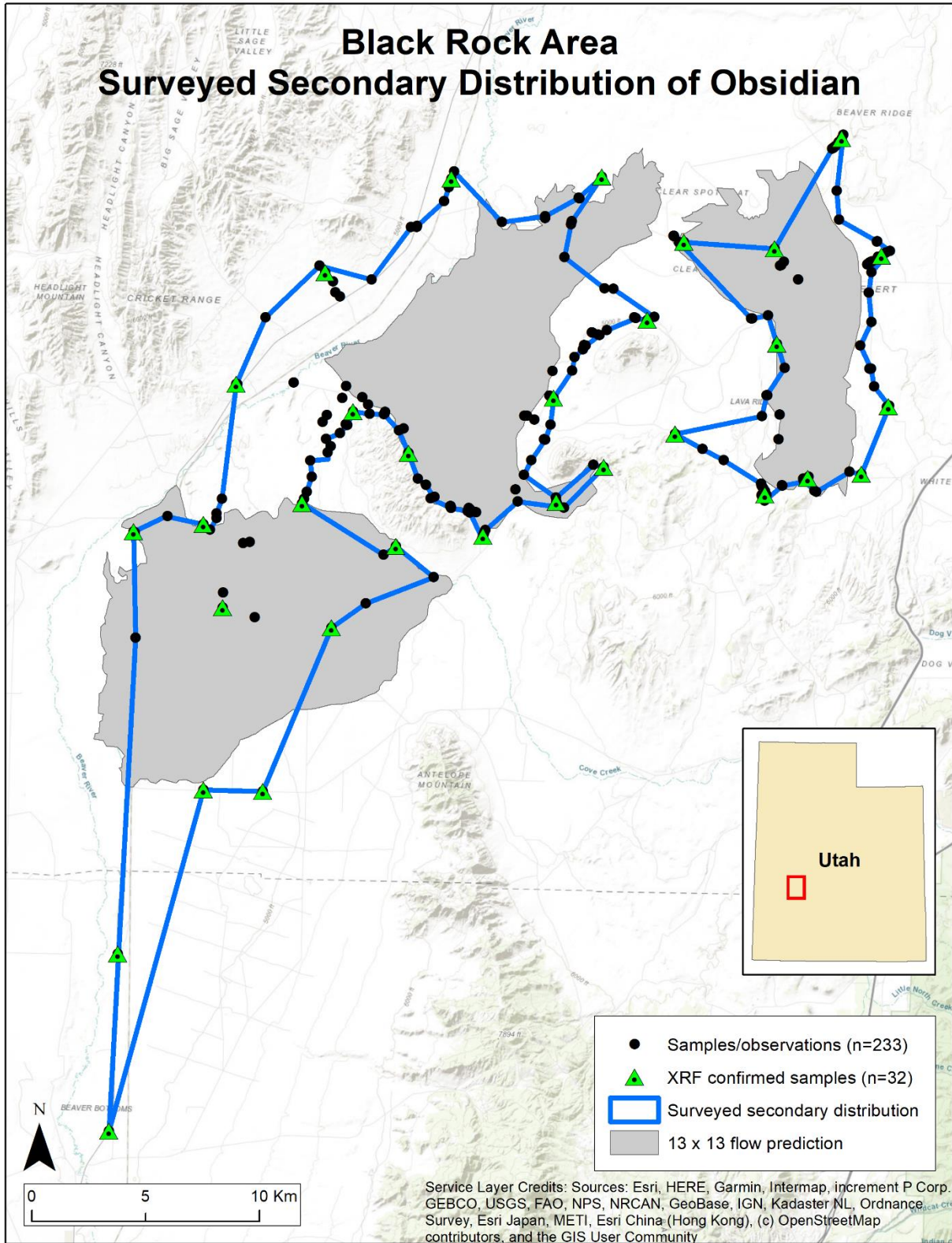
*Figure 3-20: Black Rock Area surveyed secondary distribution of obsidian
in comparison to 13x13 flow prediction.*
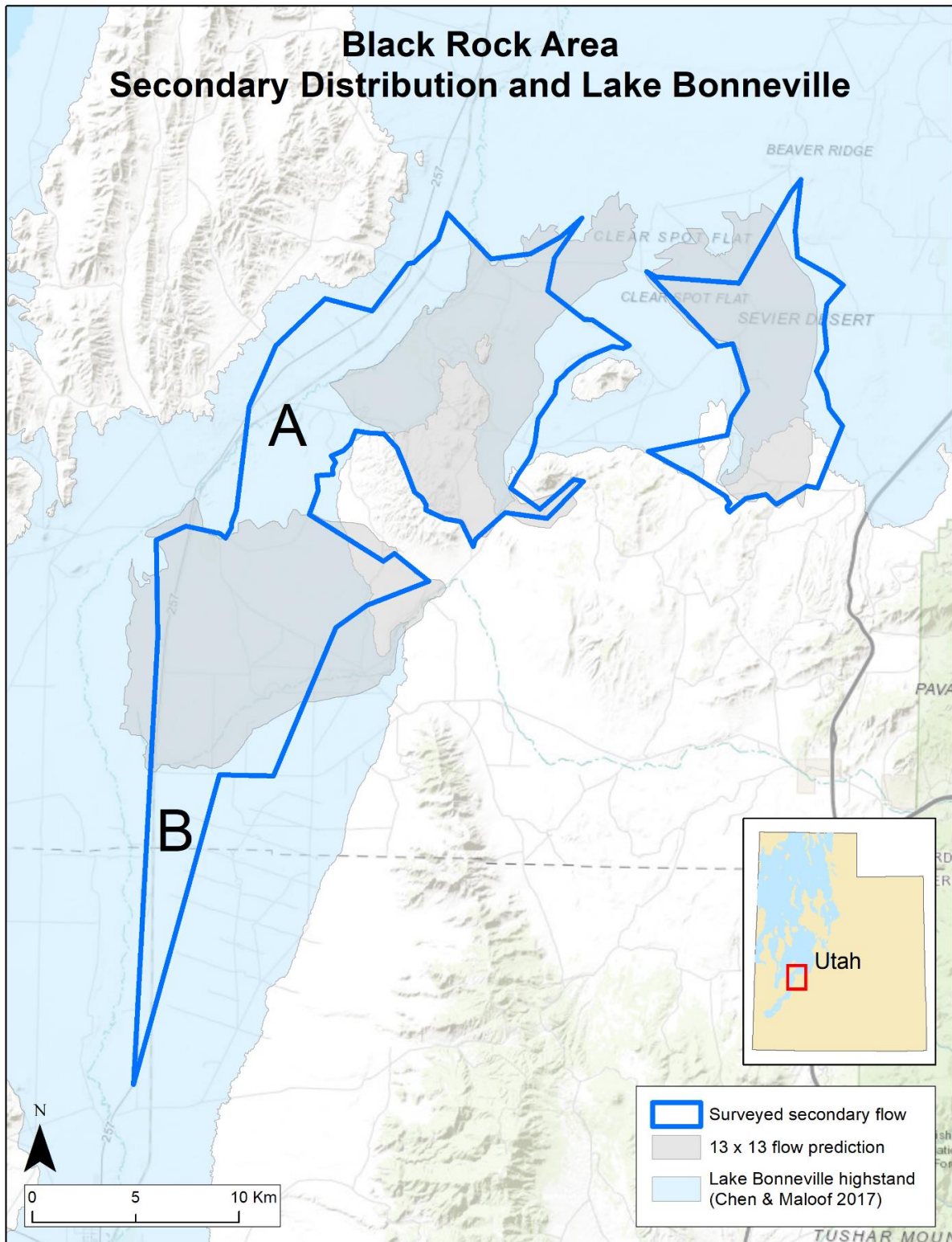
Figure 3-21: Black Rock Area surveyed secondary distribution in relation to the Lake Bonneville shore. Obsidian observed in areas A and B, extending well beyond the regions predicted by hydrographic movement, suggest sediment movement by Lake Bonneville wave action.

3.6.2 Ferguson Wash

Location: Elko County, Nevada and Tooele County, Utah

Alternative names: Dead Cedar Wash, Ferguson Flat

Skinner sample points: *n*=4 (Table D-2)

Hunt 2019 observation points: *n*=36 (Table B-6)

ORB Paleoindian artifacts: *n*=1 (Table A-37)

Ferguson Wash (FW) is a small primary obsidian source originating in Elko County, Nevada, with a secondary alluvial flow (Figure 3-22) into Tooele County, Utah (Jackson et al., 2009). The source is located near the state border, about 35 km south of Wendover, on unnamed phenorhyolitic hills south of the Lead Mine Hills, east of the Goshute Mountains (and the smaller Ferguson Mountain), and west of the expansive mud flats that make up the western edge of the Great Salt Lake Desert. The source is less than 3 km south from the restricted Utah Test and Training Range South military zone.

Figure 3-22: Ferguson Wash flowing south from the primary source area [near 11S 750183 4476826]

Ainsworth (2001) and Hockett (2001b) make the case that the name "Ferguson Wash" is a misnomer, in that there is no actual place named "Ferguson Wash", rather that the nearest geographical features are Dead Cedar Wash, to which some secondary deposits are near, and Ferguson Flat, which is more to the west. Regardless, the name has stuck, though the source may appear as "Dead Cedar Wash" or "Ferguson Flat" in some reports.

FW Geology

The age of Elko County volcanism is not well researched, but several studies (Coats, 1987; Crafford, 2007; Regnier, 1960; Smith Jr. & Ketner, 1976) describe similar phenorhyolitic flows and domes across Nevada. A K-Ar date of 15.0 ± 1.0 Ma is offered by Armstrong for the Palisade rhyolite in Eureka County, who notes the "consistent regional pattern" (1970, pp. 212–213) of volcanic activity shifting from the west/central area of the Great Basin bringing volcanic activity to the eastern edge around the Miocene (~23 Ma). This is consistent with the broad range of regional volcanism suggested by Crecraft, Nash & Evans (1981), beginning about 20 Ma (discussed in section 3.2, above).

Phenorhyolitic flows and domes were mapped by Crafford (2007) on the Nevada side of the state border (as *Tr3*) and by Hintze et al. (2000) on the Utah side (as *Tmr*). The FW primary source, as mapped by Jackson et al. (2009) is shown in context of these geological structures in Figure 3-26.

At present, there appears to be only one primary area of exposure, about 300 m long at this location (Freund et al., 2021; Hockett, 2001a; Jackson et al., 2009). Hockett (2001b) describes this location as a "massive exposure of several beds of welded tuff, capped by rhyolite" with two distinctly-colored beds. One is a "pinkish-orange tuff" bed (Figure 3-23), loosely welded, and the other a "greyish tuff" bed, more tightly welded (Figure 3-24). Phenorhyolitic flows differ from

rhyolitic flows in that obsidian forms not as a layer but directly within the tuffs as nodules (as in

Figure 3-24). These nodules then erode from the beds directly as pebbles, rarely exceeding 4 cm

in diameter at this locality. Hockett (2001b) questions whether the full extent of the exposure has

been discovered based on similar nodules found 4 miles to the north.

Figure 3-23: Ferguson Wash "pinkish-orange" welded tuff [11T 750346 4477032]

Figure 3-24: Ferguson Wash "greyish tuff" with in situ obsidian nodules [11T 750266 4477077]

The Ferguson Wash area was completely inundated by Pleistocene Lake Bonneville at its height, around 18,000 cal BP, as illustrated in Figure 3-27 (Chen & Maloof, 2017b; O'Connor, 2016; C. G. Oviatt & Jewell, 2016; C. G. Oviatt & Shroder, 2016; Utah Geospatial Reference Center, 2017). As noted earlier, Lake Bonneville reached its highstand at approximately 1552 masl. A catastrophic failure of the north basin wall and subsequent regional warming reduced the lake to the Provo shoreline level at roughly 1450 masl, around 14,500 cal years ago. The lake continued receding, arriving at the Gilbert shoreline level (1290 masl) around 13,000 cal year ago before settling into its current levels as the Great Salt Lake (~1275 masl) (C. G. Oviatt & Shroder, 2016). What is clear from this prehistory and Figure 3-27, is that the Ferguson Wash area was subjected to wave action for millennia, even before its subsequent exposure to erosion and alluvial forces. It is possible Lake Bonneville longshore currents are responsible for the far-flung northward distribution of cobbles noted by Hockett (2001b).

After Lake Bonneville receded, the area was covered in lacustrine fine silt, sandy loam, and pebble fields, which remain today.

FW Archaeology

Several dozen prehistoric sites are recorded surrounding the Ferguson Wash area (Utah Department of Heritage and Arts, 2020; Utah Division of State History, 2020; Wallace, 2017, 2018). These are almost exclusively lithic scatters, occasionally with diagnostic artifacts present. The sites range in classification from "Paleoindian" to Fremont, representing activity in the region over a great deal of time. Also present are recent historical sites as the hillside was used as a target site for World War II munitions practice.

Use of FW obsidian is known from multiple archaeological sites, predominantly during the Archaic. Madsen and Schmitt (2005) associated a Rosegate corner-notched point found at the

Buzz-cut Dune site with FW obsidian. Similarly, Page and Skinner (2008) sourced 21 Danger

Cave artifacts back to FW (Jackson et al., 2009). At the Bonneville Estates rockshelter, less than

10 km to the north, Goebel et al. (2018) report that a majority (52%) of the Archaic and none of

the Paleoindian artifacts at that site were manufactured using FW obsidian. However, from the

Old River Bed XRF data (see Appendix A), there are only eight FW-sourced artifacts, spanning

types from Silver Lake (*n*=4) to Rosegate (Page, 2015a). Of these, only one is included in the

final, cleaned Paleoindian dataset (Table A-37) associated with a dated ORB delta channel. So,

while the available material size may have limited the use of FW obsidian for larger Paleoindian

points, it does appear that it was utilized during the Paleoindian period.

FW Past Work

Our understanding of the FW primary, secondary, and tertiary obsidian extents relies on

relatively recent work, in comparison to other sources explored here, and is illustrated in Figure

3-28. Ainsworth (2001) provides the earliest description of the primary source location and the

flow of secondary alluvium into the lake flats. Ainsworth also describes a tertiary extent,

reworked by the neighboring Dead Cedar Wash alluvial fan. Jackson et al. (2009) provide a more

extensive description of the primary source and secondary flow, extending it quite a bit farther

east. Skinner (Table D-2) provides three unique XRF sample locations, which include samples

by Hockett (2001a). In 2019, I conducted a pilot survey and observed the primary sources

(photos above) and the secondary distributions of obsidian at various points around the primary

source (Table B-6, *n*=36). While these are not XRF-tested samples, these observations provided

a useful indicator of how obsidian is flowing out of the FW source into the flats in preparation

for field work.

FW Flow Prediction

Using the process described in the beginning of this chapter, five flow distributions were created.

The starting requirement for all flow prediction is the location of the primary source and this is illustrated for FW in Figure 3-26. I used the outline provided by Jackson et al. (2009) versus Ainsworth (2001) as it was larger and fit more closely with my own 2019 observations of the source. Using this primary source as the starting point, the downslope flows were predicted for 3x3, 5x5, 7x7, 11x11, and 21x21 nearest neighbor smoothed DEMs. These are presented in "stacked" form in Figure 3-29, with the 3x3 nearest neighborhood flow represented by the darkest shade and the 21x21 flow represented by the lightest shade.

During preparation for field work, the comparison to the known sample points by Skinner (Table D-2), and my own pilot project observations (Table B-6) showed good concordance with the 21x21 flow prediction, with one exception, sample SO-65-896 (Figure 3-30). It seemed likely this was the result of rounding in a conversion "round-trip" as the original location was reported in UTM, converted to decimal degrees (with only one decimal point of precision), and then back to UTM. I added in a point to the figure based on the original UTM value report by Hockett (2001b). This moved the point from ~530 m away from the 21x21 flow to ~390 m away. This area was investigated during fieldwork to verify the location and ensure there is no obsidian flowing down Dead Cedar Wash or alternative unknown primary sources (see below).

The final 21x21 prediction outline and transects are shown in Figure 3-31. An important consideration here was that the distal ends of most of the FW flow predictions (3x3 is the only exception) appear to extend into the restricted military zone to the north. This boundary is at the UTM northing of 4479648 m and is preceded by a dirt road about 100 feet south of the

93

boundary. Knowing that during field work we would need to stay well below the southern boundary of the installation, I included a survey track that cut across the predicted flows that could help assess if the flows really extended that far north and east before working near the military zone. The extent of the secondary flow mapped by Jackson et al. (2009) suggested it would not flow that far.

FW Survey Results

The Ferguson Wash secondary distribution was surveyed during the summer of 2020 and the observed extent is illustrated in Figure 3-32. FW is the smallest of the secondary distributions surveyed, with an area of only ~4 km^2 and a perimeter of ~14 km. During the survey, 118 observation points were recorded, and 37 natural obsidian samples were collected (Table B-2). Of these collected samples, 13 were submitted to NWROSL for XRF testing (Table C-2) and were confirmed as "Ferguson Wash" obsidian (green triangles in Figure 3-32).

As an aside, I note that the original XRF lab report, Appendix E, classified these samples as "Ferguson Wash, Type B", "a newly identified subtype of Ferguson Wash obsidian, distinguished by elevated strontium (Sr) and yttrium (Y) levels relative to the well-characterized Ferguson Wash source" (Alex Nyers, personal comm., November 12, 2021). I questioned these results, the samples were retested on new spectrometers, and confirmed to be "Ferguson Wash" samples, as shown in Appendix F. The error was attributed to equipment issues and all survey samples are confirmed as secondary outflow from the FW primary source.

Skinner (Table D-2) reports three FW samples taken by Hockett (2001a). Two of these points (Figure 3-28) are within 300 m of the observed flow and it is reasonable that conditions on the ground have changed in the last 20 years. However, sample SO-65-896 was clearly out of scope, positioned more than 800 m from the observed flow edge and at an elevated position. I

surveyed this sample location and observed only large basaltic boulders, no obsidian, and geology out of character with the primary and secondary source areas. I also surveyed the mouth of Dead Cedar Wash, just before it empties into the flat, and no obsidian is evident in this wash. It appears this sample point may have a recordation error. Aside from this point, the surveyed flow encompasses almost all previous sample/observation points recorded by Skinner (Table D-2) and me, with minor exceptions.

As the secondary distribution flows south and east into the lake flat, the survey found good concordance with the secondary distribution illustrated in Jackson et al. (2009, Figure 10-2). However, the observed eastern flow is truncated even compared the 5x5 predicted flow (Figure 3-33). As can be seen in Table 3-3, even very low smoothing levels (5x5 and 7x7) result in a "blow out" or "flooding" of the region with regard to flow prediction and the Confusion Matrix results provide no meaningful information.

Table 3-3: Confusion Matrix results for Ferguson Wash

Smoothing	Predicted flow area (km²)	TP	FP	% survey predicted	% prediction inside observed	% prediction outside observed	TP/ observed	FP/ observed	(TP-FP)/ observed
3x3	0.1	0.0	0.1	0%	21%	79%	0.5%	1.8%	-1.3%
5x5	16.4	3.9	12.5	99%	24%	76%	99.1%	313%	-214%
7x7	20.0	3.9	16.1	99%	20%	80%	99.1%	404%	-305%

I attribute the failure of the model in this case to two factors. First, Ferguson Wash is unusual in that the primary and secondary source areas were entirely submerged during the Lake Bonneville highstand (Chen & Maloof, 2017b; O'Connor, 2016; C. G. Oviatt & Jewell, 2016; C. G. Oviatt & Shroder, 2016). During this period, longshore transport may account for the movement of obsidian to the north of the primary source area, but the receding shorelines may have also covered the eastward movement of this FW obsidian with lacustrine sediments. Similar

results have been observed in other survey regions as flows move into the very flat basin bottoms affected by Lake Bonneville (see the discussion of the Fish Springs Flat in the Topaz Mountain section). In these cases, I believe the discernable grains of obsidian (< 2mm) have been sorted into lacustrine silts and out of sight.

Second, FW is unique in that the primary source and the proximal end of the secondary flow are at very low elevations when compared to the distal end in the basin bottom. In this case, the primary source is only about 25 m above the point where it erodes into a wash. The apex of that wash, at about 1400 masl, is only about 100 m above the distal end of the 5x5 flow prediction (at about 1300 masl), which is more than 5.5 km away. In these low slope regions, my model treats the sediment like water, allowing the flow to disperse without regard to particle size.

The effect of this dynamic shoreline environment on the primary source and its past erosional history, as well as the very low-slope basin bottom, appear to have resulted in an excessive flow prediction with the model used here. As a result of these issues, the predictions at FW are considered to have failed.
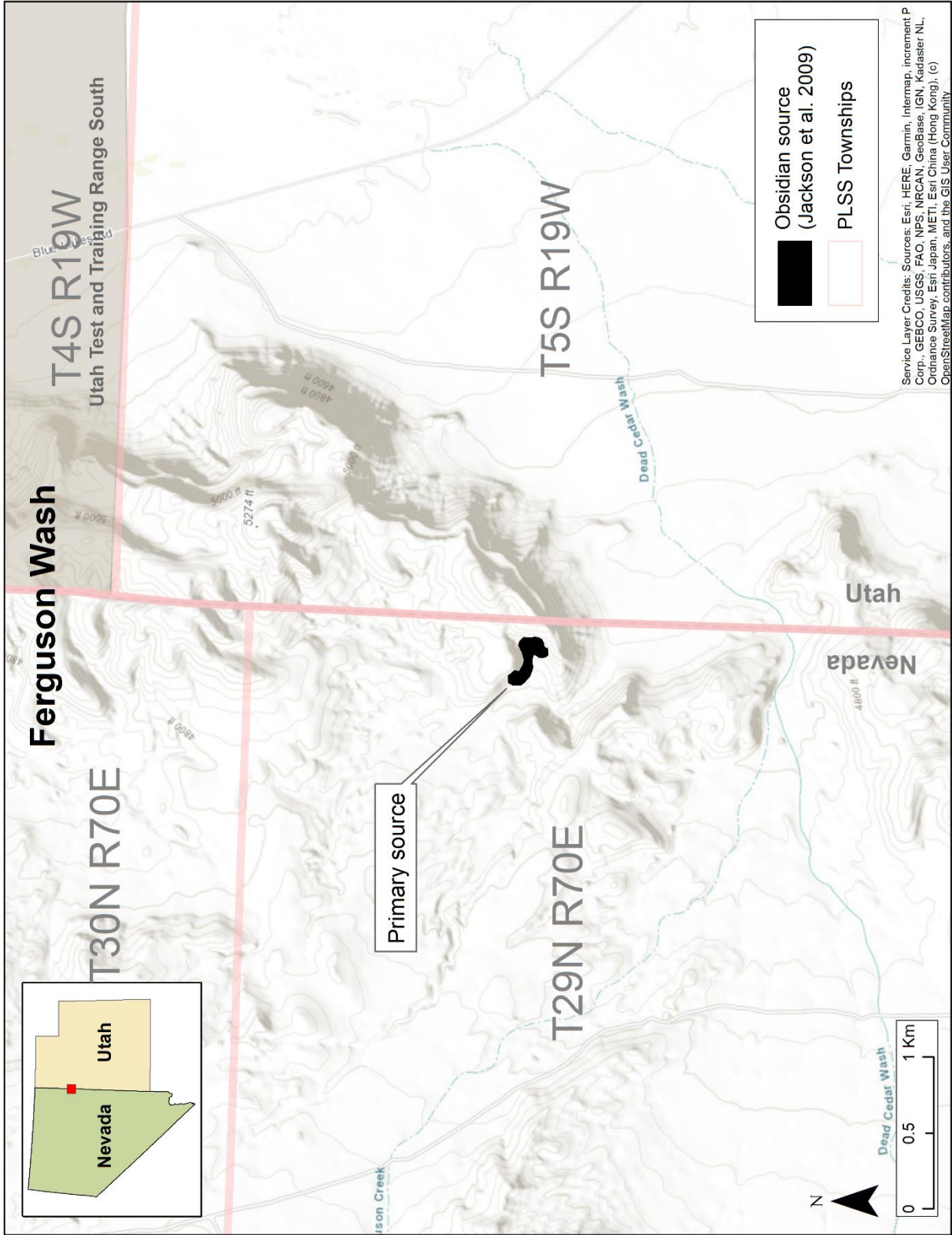
Figure 3-25: Ferguson Wash regional view.
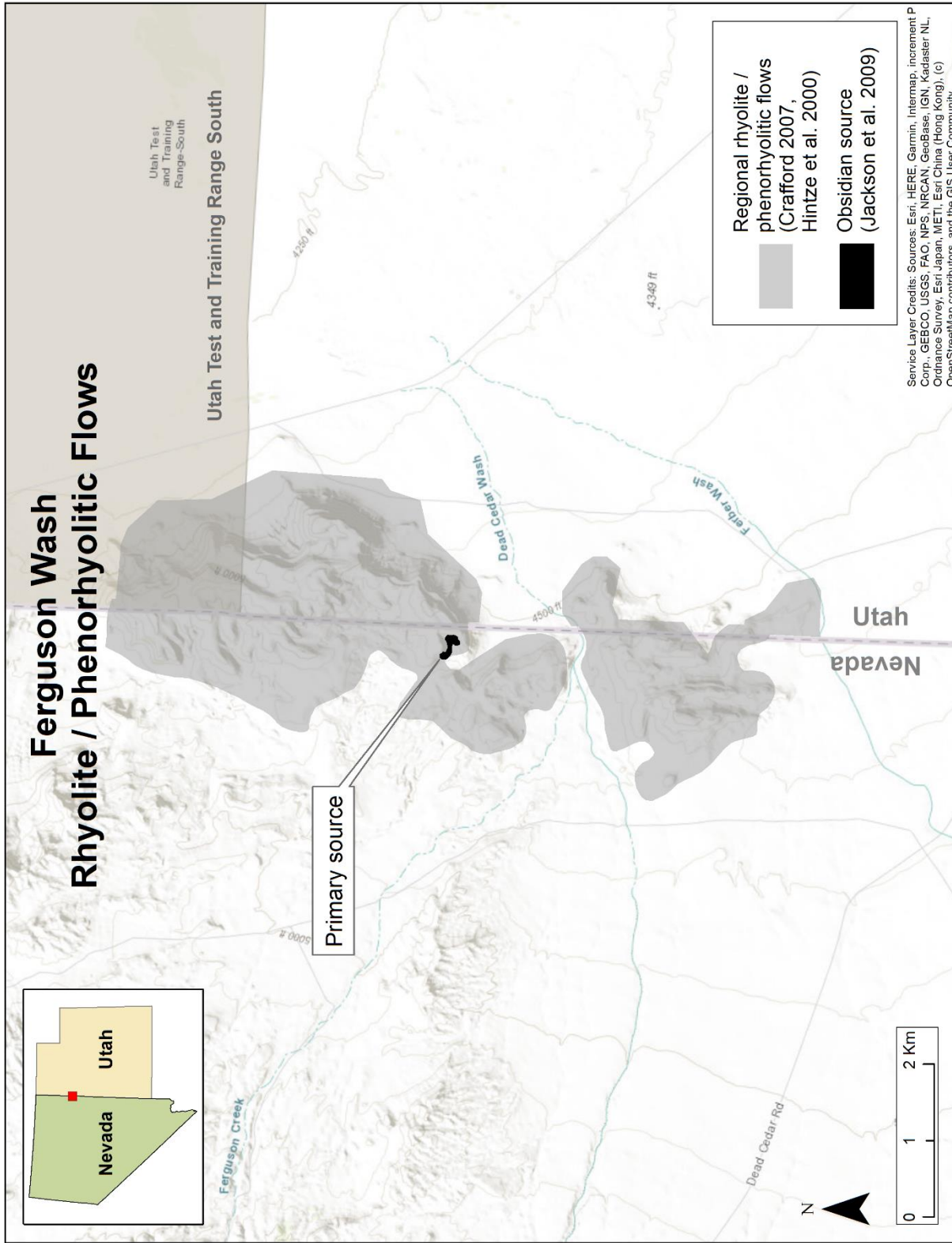
Figure 3-26: Ferguson Wash rhyolite and obsidian.
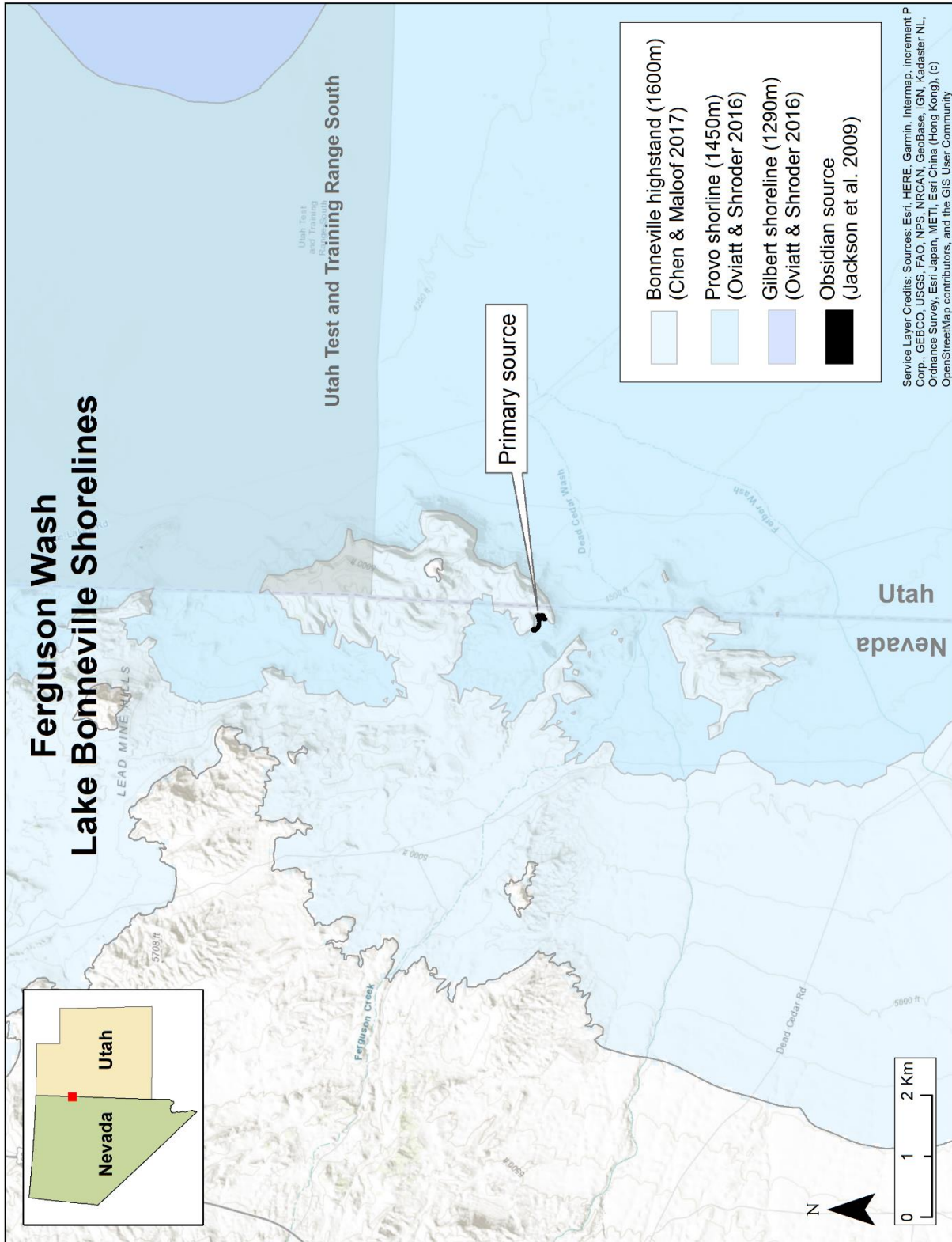
Figure 3-27: Ferguson Wash primary sources in relation to the Lake Bonneville highstand and subsequent receding shorelines.
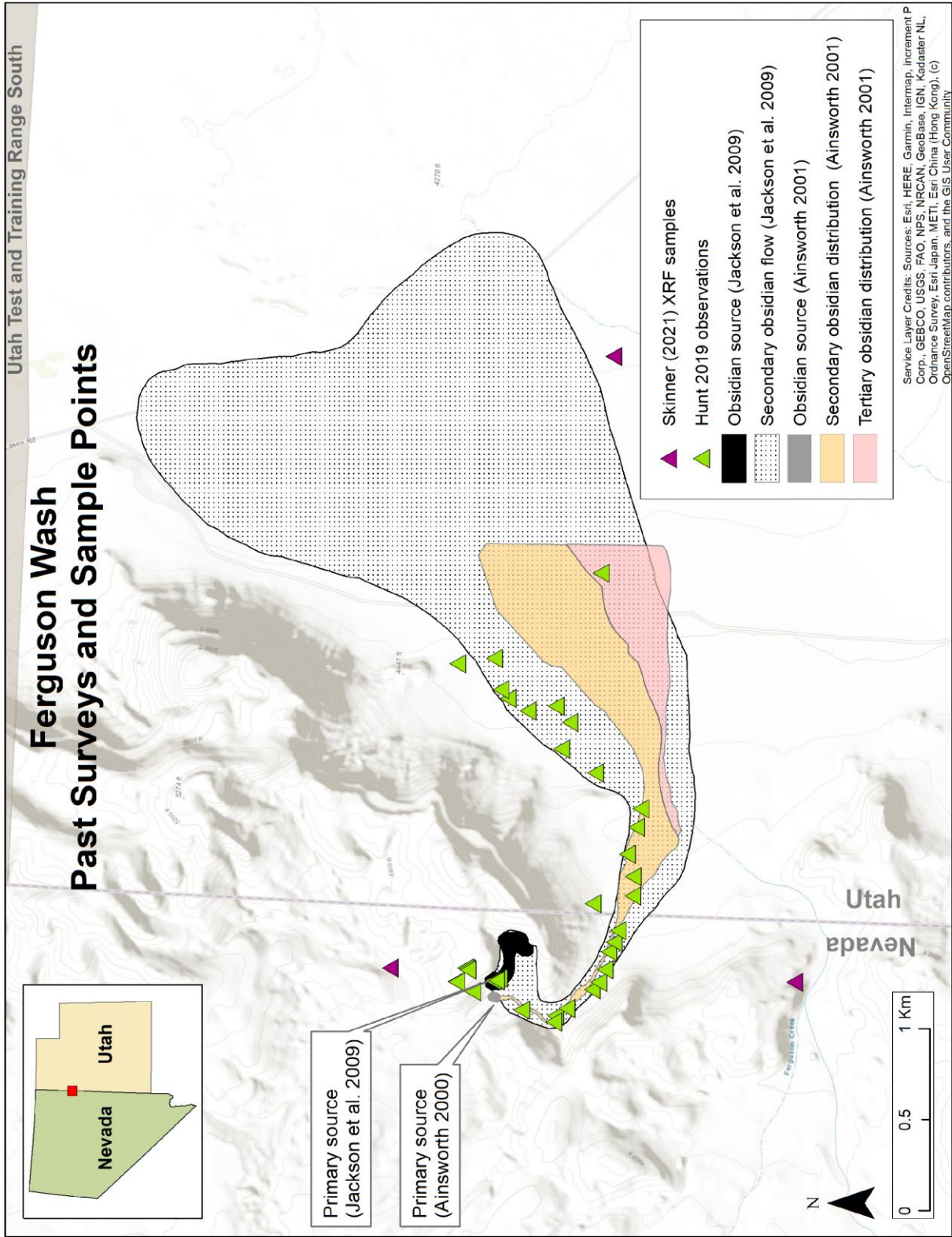
Figure 3-28: Ferguson Wash past surveys and sample points.
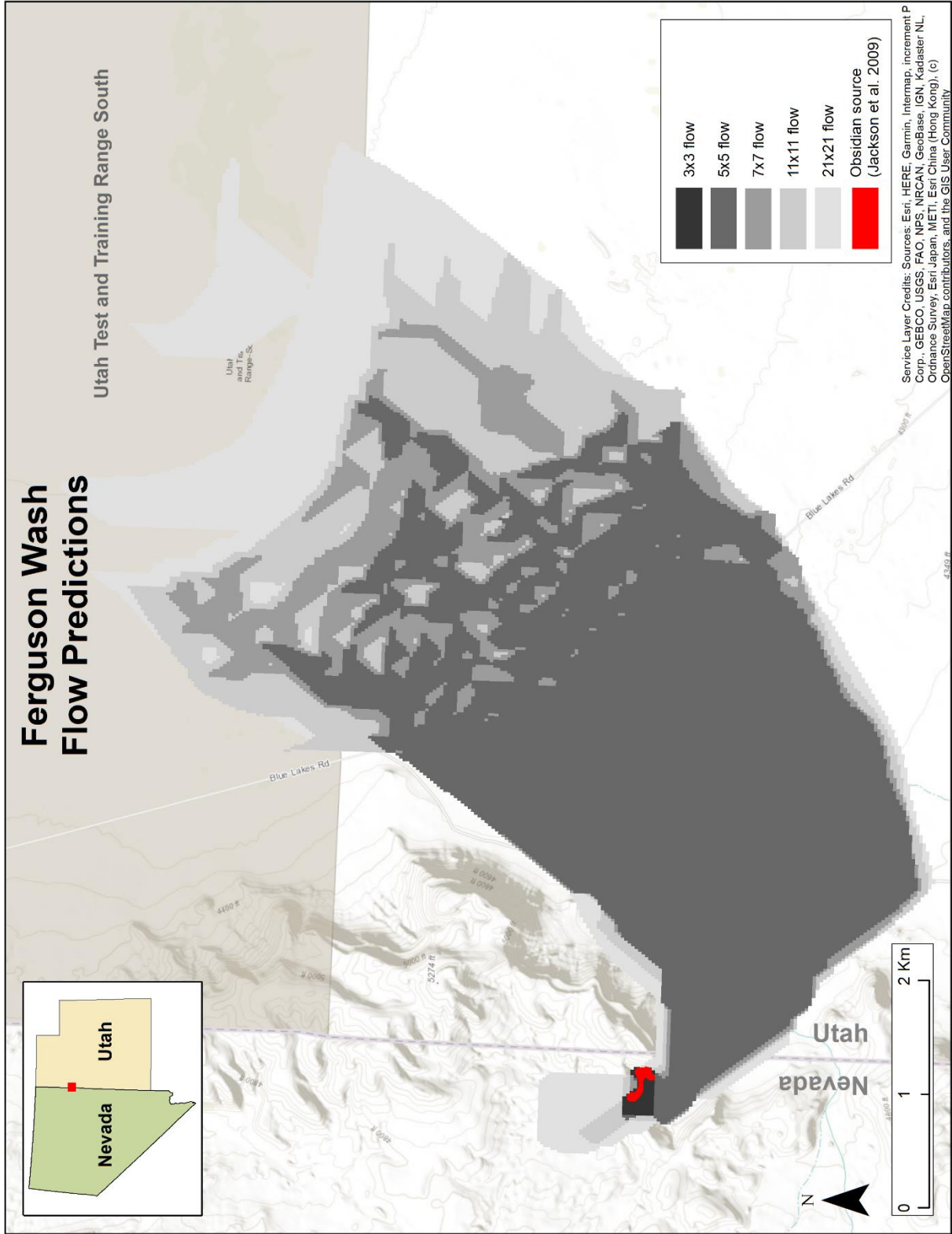
Figure 3-29: Ferguson Wash flow predictions.
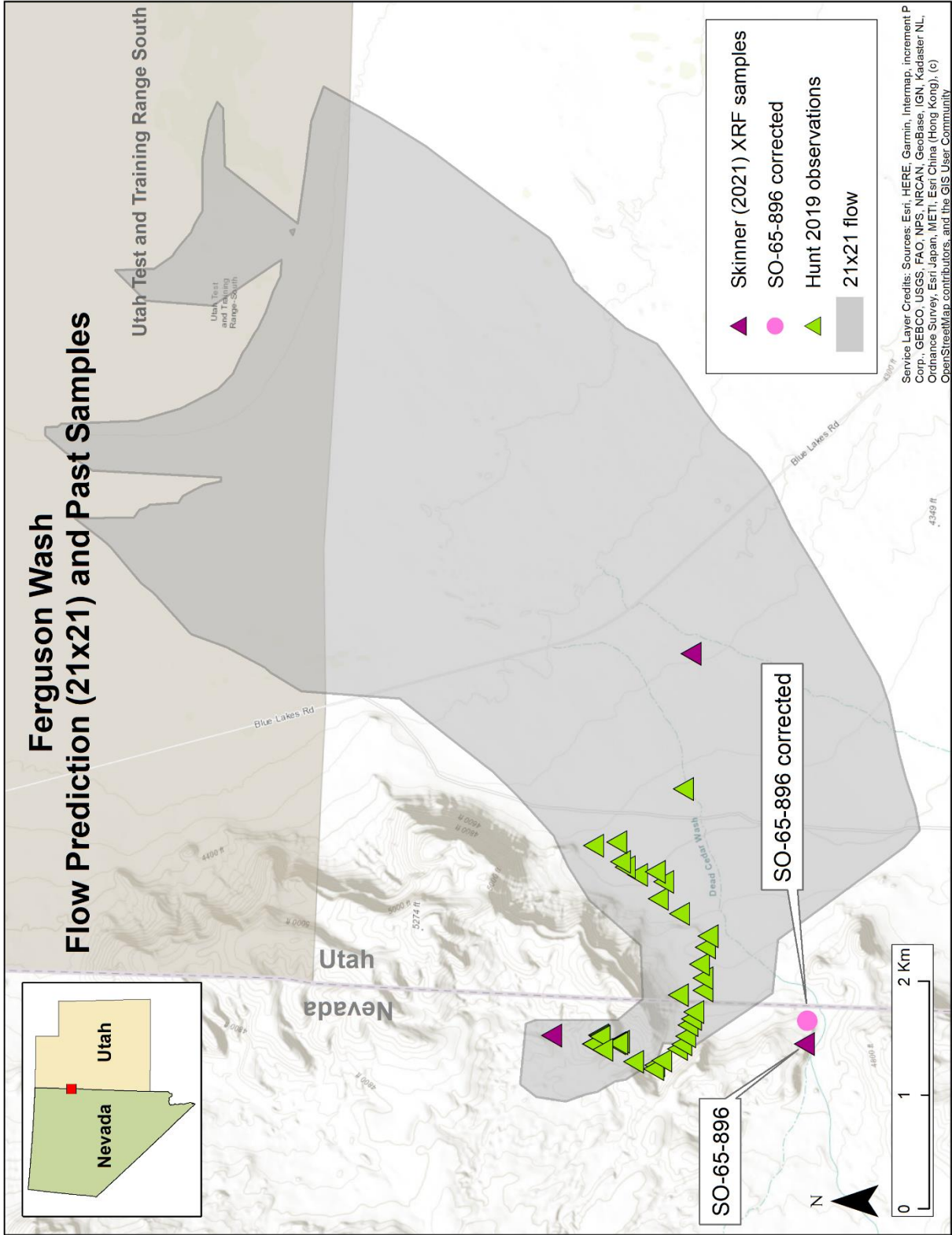
Figure 3-30: Ferguson Wash 21x21 flow prediction in comparison with past sampling.
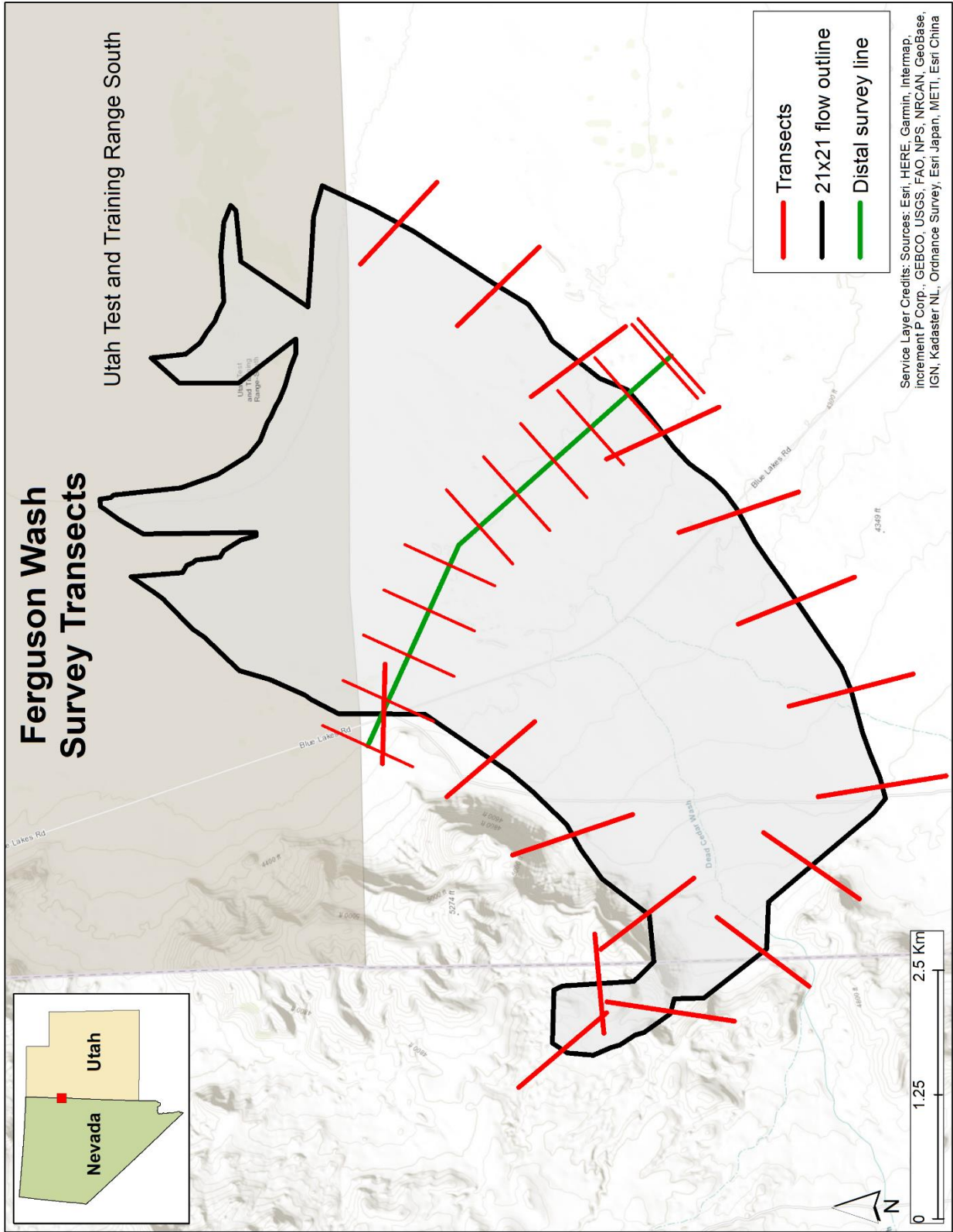
Figure 3-31: Ferguson Wash 21x21 survey outline and transects.
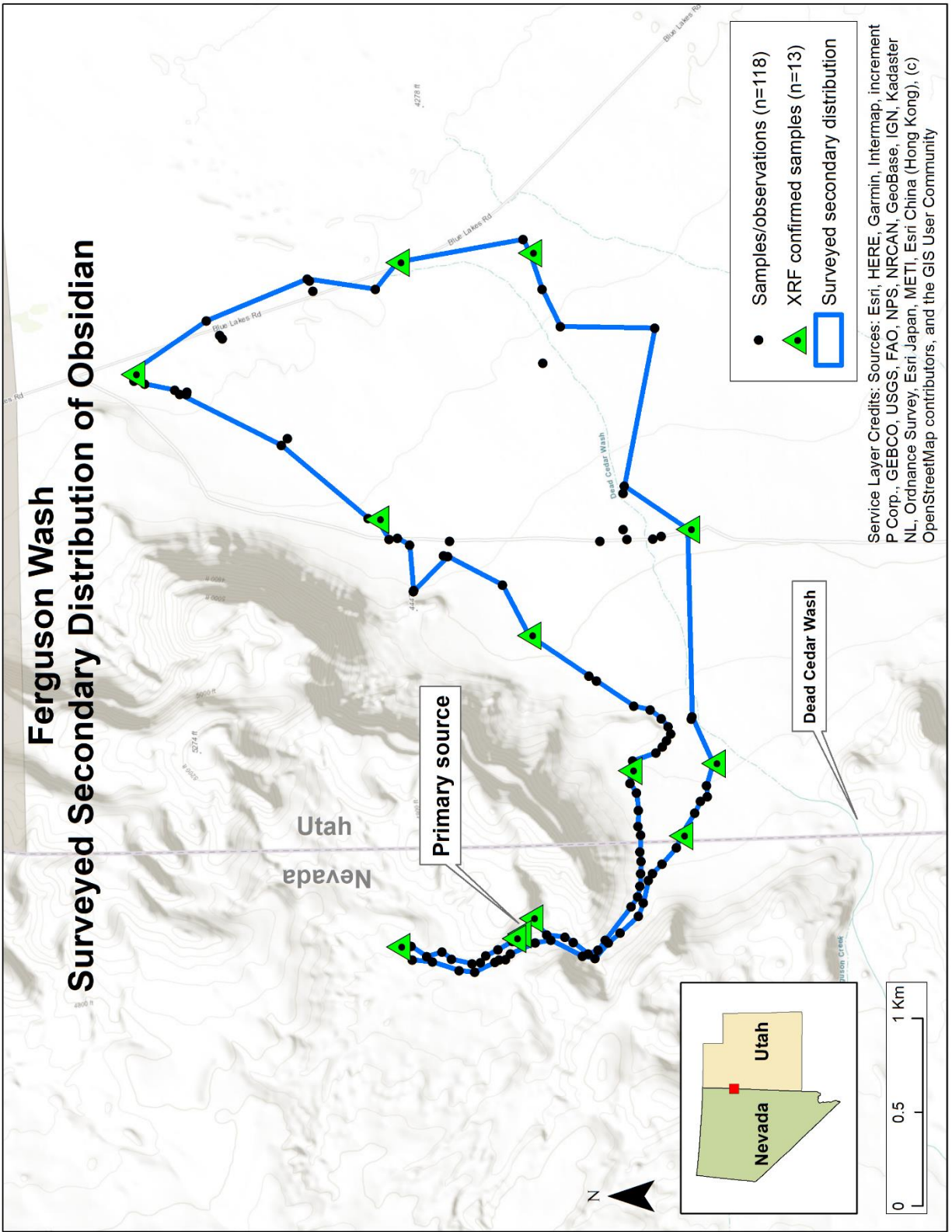
Figure 3-32: Ferguson Wash surveyed secondary distribution of obsidian.
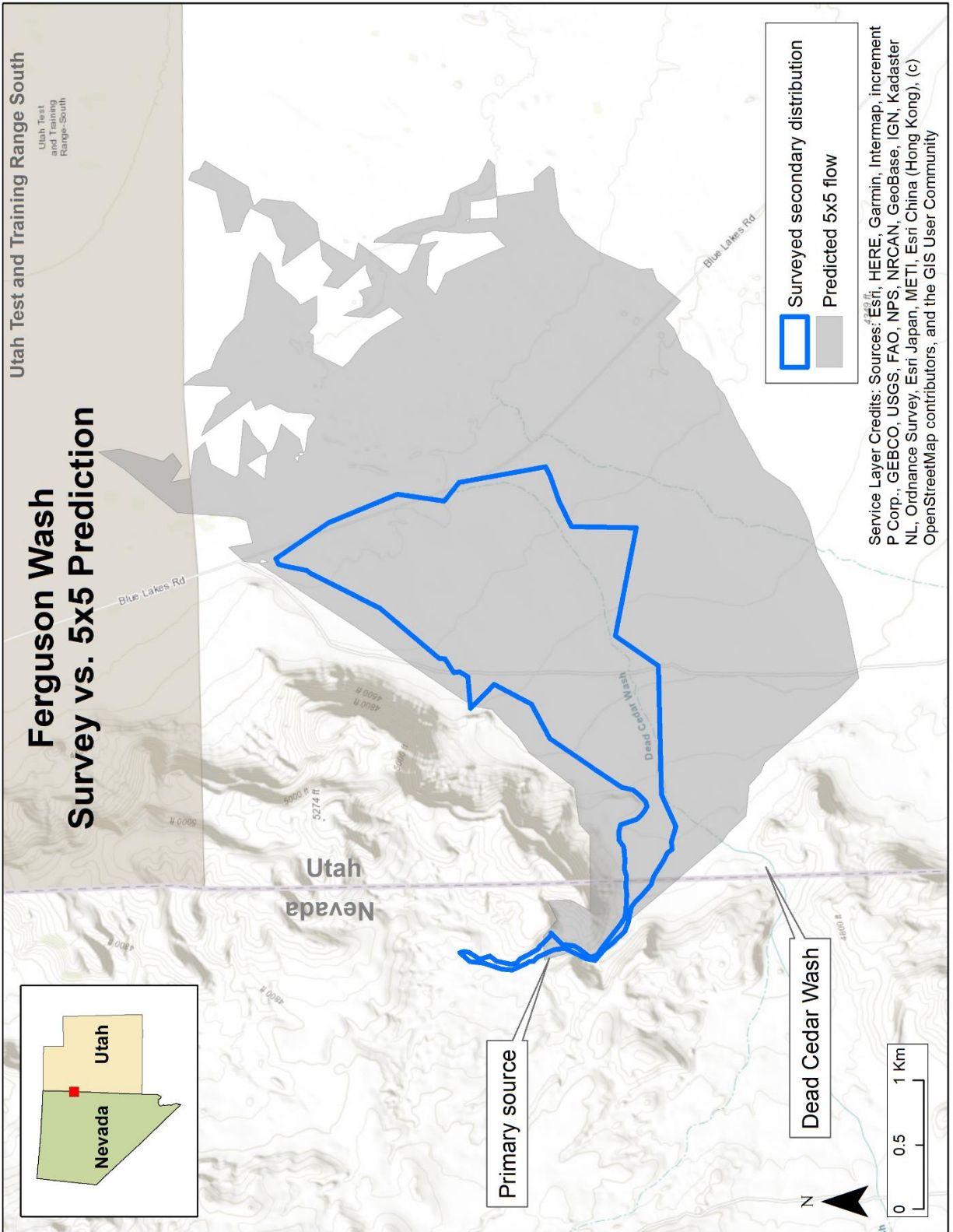
Figure 3-33: Ferguson Wash surveyed secondary distribution in relation to the 5x5 flow prediction.

3.6.3 Mineral Mountains

Location: Beaver County, Utah

Alternative names: Wildhorse Canyon, Wild Horse Canyon, Bailey Ridge, Negro Mag Wash

Hull (1994) sample points: *n*=22 (Table D-1)

Skinner sample points: *n*=8 (Table D-2)

Hunt 2019 observation points: *n*=20 (Table B-6)

ORB Paleoindian artifacts: *n*=9 (Table A-37)

The Mineral Mountains (MM) is a horst and graben range in Beaver County, Utah, about 15 km east of the town of Milford and directly south of the Black Rock Area previously described (Figure 3-36). The rhyolitic flows in the MM are geologically relatively recent and the area is still geothermally active. A commercial geothermal plant operates only a few kilometers from the two main primary obsidian source locations (Figure 3-37): the Wildhorse Canyon and Bailey Ridge sources (Lipman et al., 1978). The Pumice Hole Mine source is also found near these sources and is discussed in Chapter 4. Two additional obsidian sources, the Kirk Canyon and Pumice Hole Mine B sources, are known a few kilometers south in the range and are likely the result of later eruptions. These latter sources contain abundant phenocrysts, making them unsuitable for knapping (Hull, 1994; Jackson et al., 2009). This project focused on mapping the secondary distributions of the Wildhorse Canyon and Bailey Ridge obsidian (Figure 3-34).

MM Geology

The Mineral Mountains were formed from a granitic batholith approximately $9 - 15$ Ma and rise about a kilometer above the basin floor (Evans, Jr. et al., 1978). Around 0.79 ± 0.08 Ma, two highly-fluid, silicic rhyolitic flows erupted (Evans, Jr. et al., 1978; Lipman et al., 1978).

Figure 3-34: Obsidian exposure at the mouth of Wildhorse Canyon.

These flows, up to 100 m thick, emerged in the north end of the range at Bailey Ridge, including flow into Negro Mag Wash, and in the central region at Wildhorse Canyon, as illustrated in Figure 3-37 (Rowley et al., 2005). The flows are highly silicic (76.5% SiO_2) and nonporphyritic with "less than 0.5 percent total phenocrysts" (Lipman et al., 1978, p. 137), resulting in an obsidian that knaps exceptionally well (Hull, 1994). The two flows are also highly laminar, indicating flows of low viscosity, and are geochemically similar, to the point of being indistinguishable from each other by XRF testing (Evans, Jr. et al., 1978; Hull, 1994; Lipman et al., 1978). In the literature, the source is known predominantly as Wildhorse Canyon (or Wild Horse Canyon) obsidian.

Figure 3-38 illustrates the relationship of the MM to the Lake Bonneville highstand shoreline (Chen & Maloof, 2017b; C. G. Oviatt & Jewell, 2016; Utah Geospatial Reference Center, 2017). The MM are located on the southernmost arm of Lake Bonneville. While the

primary sources were not affected by the highstand, the secondary distribution likely was as it flowed westward (as will be shown below). This southern arm of the lake was completely drained as the lake receded to the Provo shoreline. After Lake Bonneville receded, the areas below the remnant shoreline were covered in lacustrine fine silt, sandy loam, and pebble fields, which remain today.

Most recently, the Milford Flat Fire of 2007 stripped the mouth of Wildhorse Canyon of vegetation, which has not returned. This was followed by a flash flood in 2008, significantly impacting the canyon and downslope area, covering up to 40% of the alluvial fan (Jackson et al., 2009). This may have impacted survey results.

MM Archaeology

The archaeological sites at Wildhorse Canyon and Bailey Ridge have been extensively studied and surveyed in recent decades. The Wildhorse Canyon site (42BE52) was first recorded in 1964 when it was recognized as an extensive quarry site (Weide, 1964). Similarly, the Bailey Ridge site was first recorded as an undisturbed quarry and "chipping" site in 1974 (Fike, 1974). Since then, numerous surveys of the downslope secondary distributions and local lithic scatters, consisting of thousands of artifacts and millions of flakes, have been merged under the 42BE52 trinomial. The full extent of the combined sites exceeds 54 km^2 (Jackson et al., 2009; Utah Department of Heritage and Arts, 2020). The alluvial flows are so rich with material that at least three quarries (42BE236, 42BE248, and 42BE270) have been recorded within the fans themselves, each extending more than 1000 m across (Jackson et al., 2009; Utah Department of Heritage and Arts, 2020). Hundreds of smaller sites, primarily lithic scatters, surround the Mineral Mountains primary obsidian sources.

Bailey Ridge and Wildhorse Canyon have been subjected to contemporary disturbances. Both sites were mined in the 1950s for perlite, a form of hydrated volcanic glass with industrial uses, such as thermal and acoustic insulation (Tripp, 2000). The remnants of this activity are evident today in the form of abandoned equipment and trenches from mechanical excavation (Figure 3-35). Wildhorse Canyon is still frequented by obsidian collectors and knappers; during my pilot project I witnessed a family fill the back of their minivan with obsidian from Wildhorse Canyon to use for knapping.

Figure 3-35: Abandoned bulldozer at Wildhorse Canyon.

MM Past Work

Our understanding of the scope and extent of the MM primary and secondary obsidian extents is illustrated in Figure 3-39. Hull (1994) provides an early dataset of XRF testing on 22 samples from Bailey Ridge (labelled as Negro Mag Wash in her report) and Wildhorse Canyon (Table D-1). These samples appear to be centered on primary sources, though the township and

range descriptions can be several hundred meters off when compared to modern GPS coordinates. Skinner (Table D-2) provides an additional eight sample locations (Table D-2). In 2019, I conducted a pilot survey and observed obsidian at various points around the MM primary sources (Table B-6, *n*=20). The work by Jackson et al. (2009), however, provides the best resource of primary obsidian sources at the MM, as well as an excellent secondary distribution survey, illustrating the alluvial fan emanating from the two primary sources.

All this information was used in selecting the best flow prediction for the MM obsidian.

MM Flow Prediction

Using the process described in the beginning of this chapter, five flow distributions were created.

The starting requirement for all flow prediction is the location of the primary sources and is illustrated for MM in Figure 3-37, which were derived from Jackson et al. (2009). Using these primary sources as the starting points, the downslope flows were predicted for 3x3, 5x5, 7x7, 11x11, and 21x21 nearest neighbor smoothed DEMs. These are presented in "stacked" form, in Figure 3-40, with the 3x3 nearest neighborhood flow represented by the darkest shade and the 21x21 flow represented by the lightest shade.

A comparison to the known sample points by Hull (1994), Skinner (Table D-2), and my own pilot project shows good concordance with, at least, the top of the predicted flows (Figure 3-41), though there are a few samples around the apex of the fans that fall outside the projected flows. These suggest the primary source extents may be greater than known, allowing some alluvial flow into smaller neighboring canyons and Big Cedar Cove that lies between Bailey Ridge and Wildhorse Canyon. A comparison of the secondary flow recorded by Jackson et al.

(2009), as seen in Figure 3-39, with the 21x21 flow illustrated in Figure 3-41 show a remarkable similarity and suggests a positive correlation with the predicted flow.

The final 21x21 prediction outline and transects are shown in Figure 3-42.

MM Survey Results

The Mineral Mountains secondary distribution was surveyed during the summer of 2020 and the observed extent is illustrated in Figure 3-43. The MM extent covers an area of ~160 km^2 with a perimeter of ~77 km. During the survey, 70 observation points were recorded, and 54 natural obsidian samples were collected (Table B-3). Of these collected samples, 22 were submitted to NWROSL for XRF testing (Table C-3) and were confirmed as "Wildhorse Canyon" obsidian (green triangles in Figure 3-43).

The surveyed flow encompasses almost all previous sample points recorded by Hull (1994), Skinner (Table D-2), and myself, with minor exceptions. In the primary source regions, a few previously recorded points are up to ~700 m outside the surveyed extent. This is an extremely rugged and overgrown region and it would be easy to miss specimens; however, the placement of these points would not significantly affect the predicted secondary distributions.

Survey access in the predicted secondary flow areas was significantly restricted by private property (Figure 3-42). The valley is used extensively by the wind, solar, and geothermal energy industries as well as for hog farming. Almost 50% of the land within the final survey outline is private property. The bottom of the flow also spills into a heavily modified basin bottom where a railway and a highway skirt the basin bottom and parallel the distal end of the predicted flows.

Despite these limitations, the predicted flows provided an exceptionally accurate guide for the secondary distribution extents. Following the modified Confusion Matrix methodology described in section 3.5, the optimal smoothing level for the MM occurs at the 23x23 nearest

neighbor average (Table 3-4). At this level, 82% of the observed secondary extent was predicted by the model.

Table 3-4: Confusion Matrix results for the Mineral Mountains.

Smoothing	Predicted flow area (km²)	TP	FP	% survey predicted	% prediction inside observed	% prediction outside observed	TP/ observed	FP/ observed	(TP-FP)/ observed
3x3	35.1	32.1	3.0	20%	91%	9%	20%	2%	18.1%
5x5	70.0	66.3	3.7	41%	95%	5%	41%	2%	39.1%
7x7	82.1	78.5	3.6	49%	96%	4%	49%	2%	46.8%
9x9	98.1	94.1	4.0	59%	96%	4%	59%	3%	56.2%
11x11	106.5	102.3	4.3	64%	96%	4%	64%	3%	61.2%
13x13	122.4	116.4	6.0	73%	95%	5%	73%	4%	68.9%
15x15	127.6	121.0	6.6	75%	95%	5%	75%	4%	71.3%
17x17	119.5	114.9	4.6	72%	96%	4%	72%	3%	68.9%
19x19	131.8	125.2	6.6	78%	95%	5%	78%	4%	74.1%
21x21	134.6	126.5	8.0	79%	94%	6%	79%	5%	73.9%
23x23	**142.0**	**131.0**	**11.0**	**82%**	**92%**	**8%**	**82%**	**7%**	**74.9%**
25x25	144.7	132.1	12.5	82%	91%	9%	82%	8%	74.6%
27x27	146.9	133.4	13.5	83%	91%	9%	83%	8%	74.8%
29x29	149.9	134.8	15.0	84%	90%	10%	84%	9%	74.8%
31x31	152.6	136.0	16.6	85%	89%	11%	85%	10%	74.5%

In addition, the MM results provide an excellent example of the impact of Lake Bonneville on the secondary distribution beyond the hydrographic flow predictions. Figure 3-44 illustrates the relationship between the 13x13 and 23x23 flow predictions and the Lake Bonneville highstand shoreline (Chen & Maloof, 2017b). Above the shoreline (to the east), we can see tight conformance between both flow predictions, even though the difference in smoothing levels is quite large. East of the shoreline, the 13x13 and 23x23 predictions provide almost identical fits. Below the shoreline, which is still 5 to 8 km upslope from the basin bottom, the observed secondary distribution is more spread out than predicted. The north shoreline (annotated by "A") appears to show the sharp impact of longshore transport to the north. This eventually results in

spreading out the distribution, leading to a broader base by the time the flow hits the basin

bottom. This additional impact will be discussed further when deciding on a "universal" nearest

neighbor averaging scheme for other obsidian sources (see below).
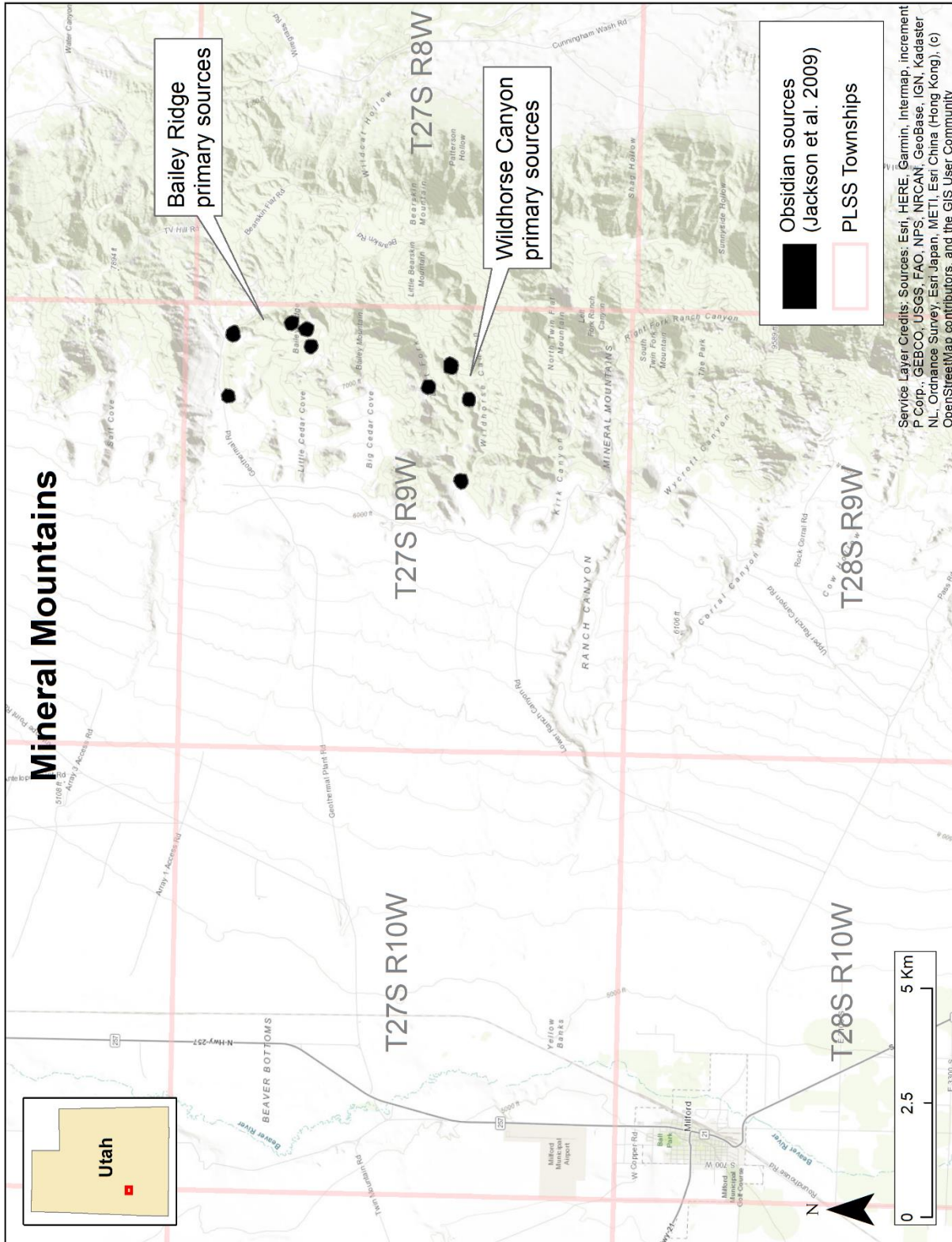
Figure 3-36: Mineral Mountains regional view.
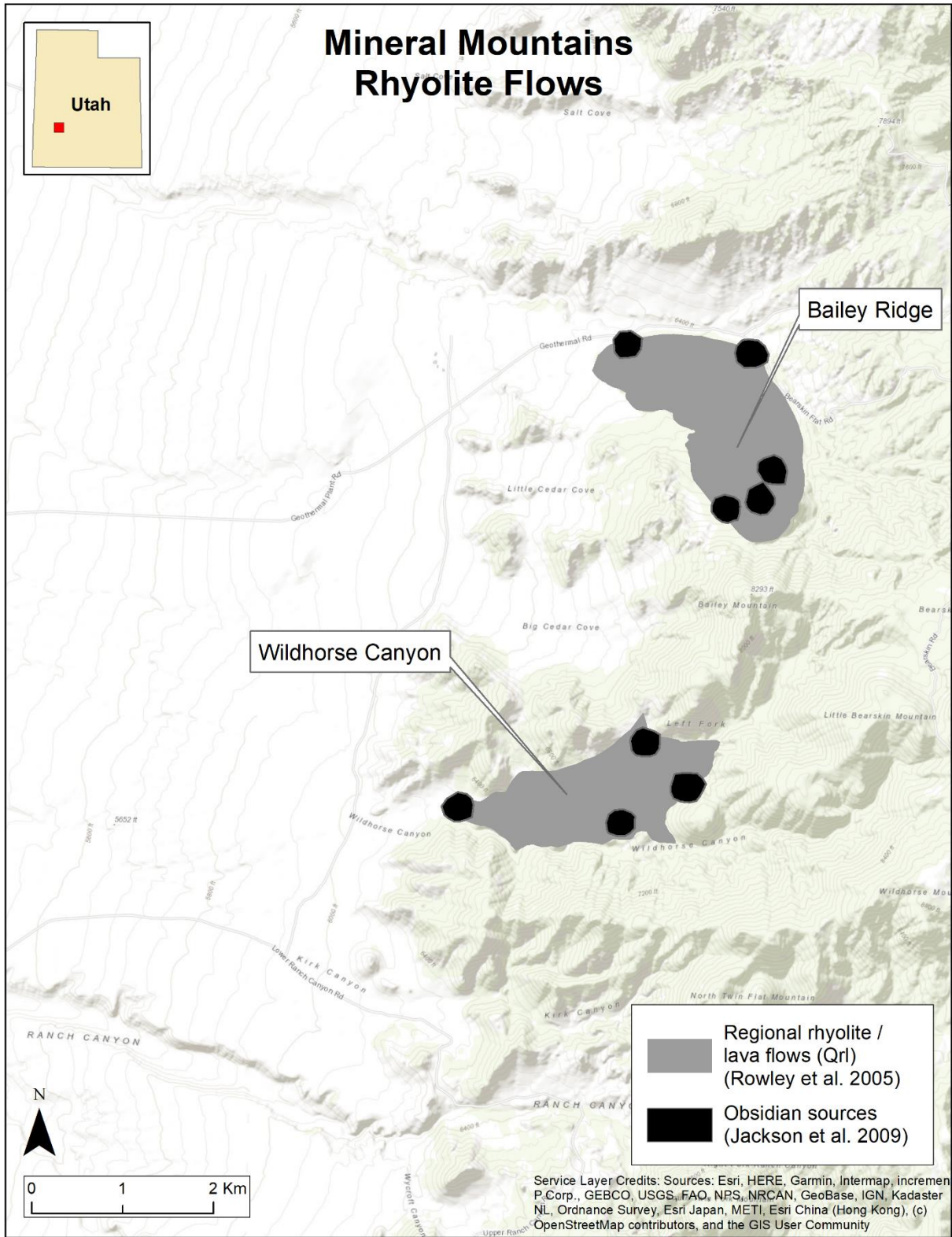
Figure 3-37: Mineral Mountains rhyolite and obsidian.
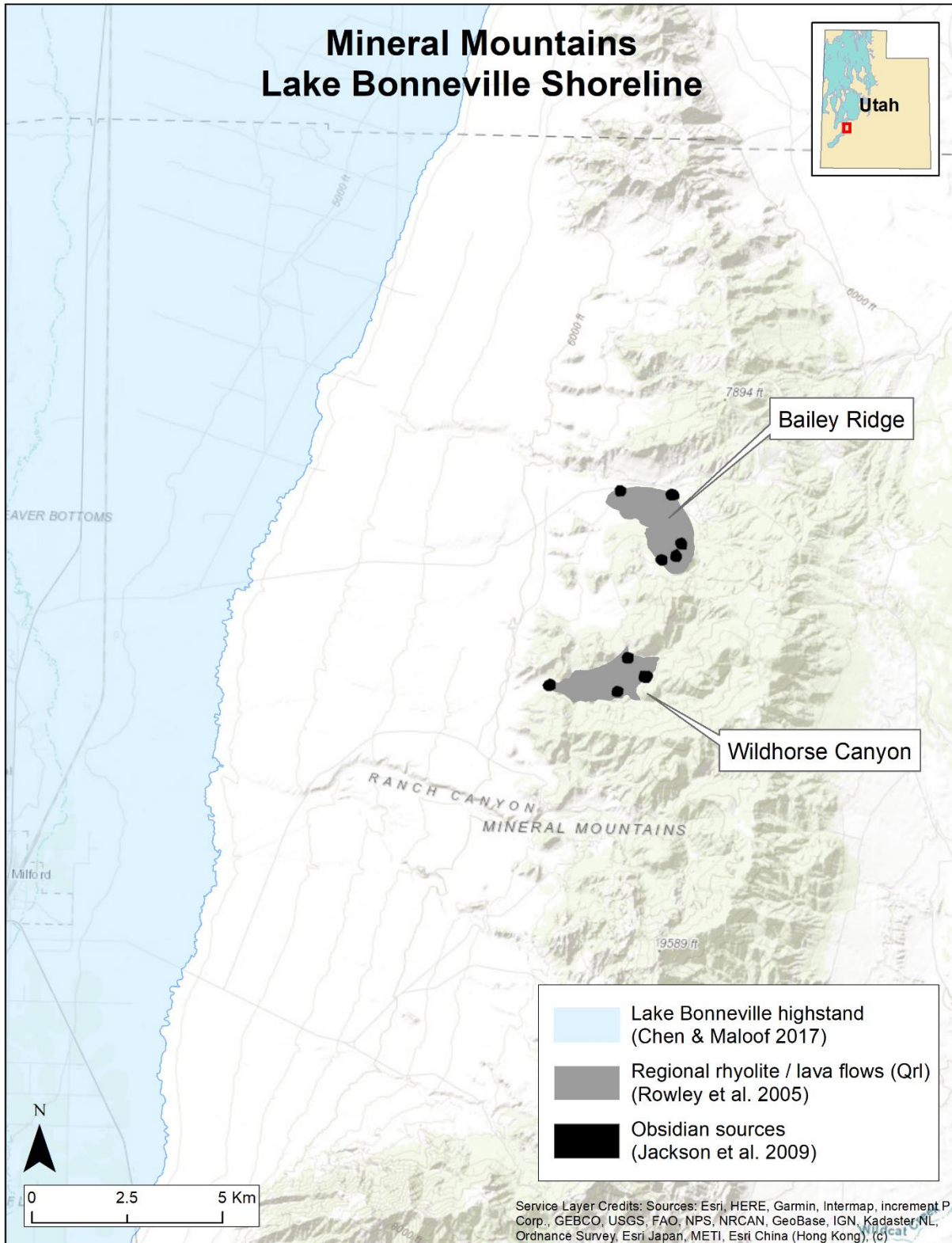
Figure 3-38: Mineral Mountains primary sources in relation to the Lake Bonneville highstand.
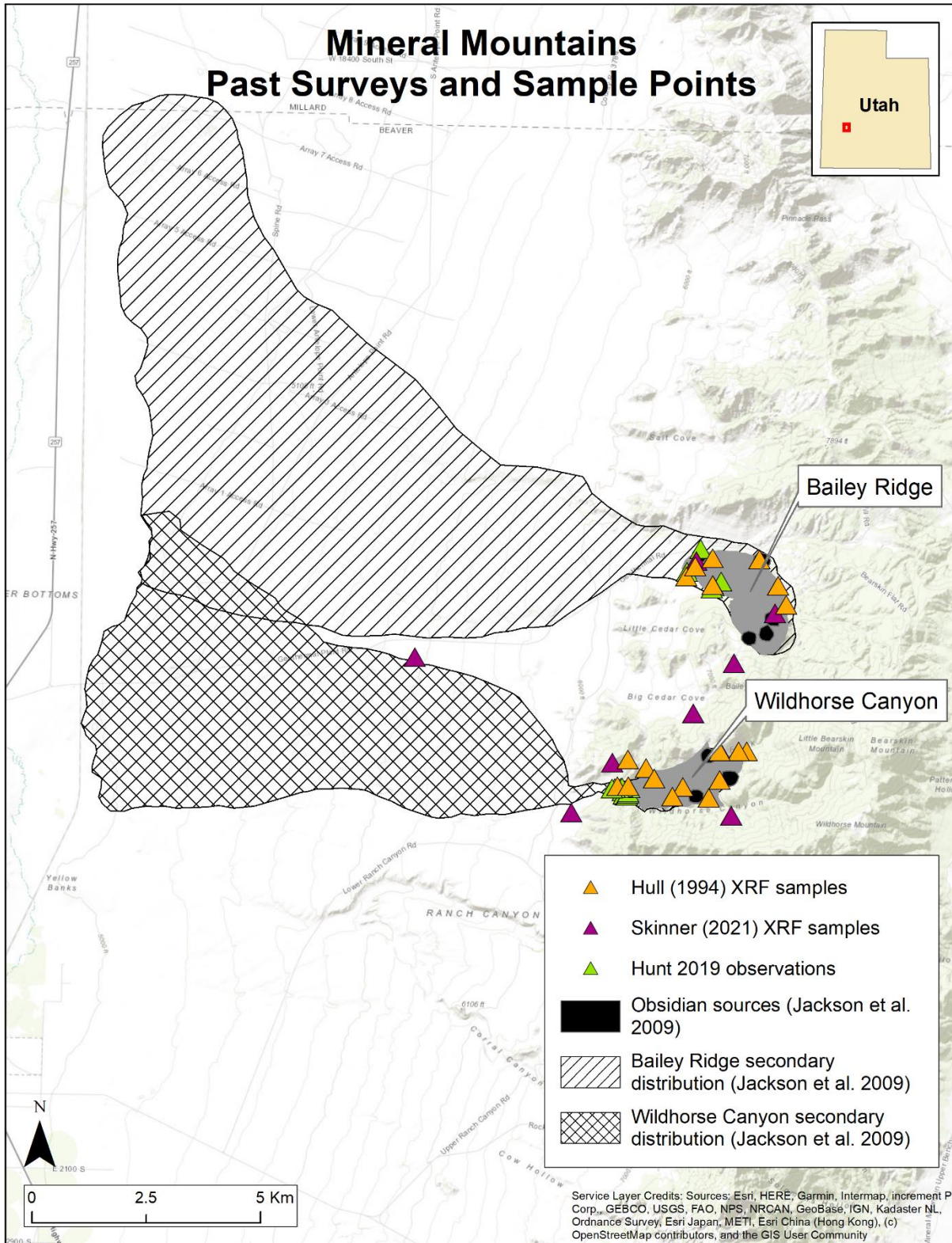
Figure 3-39: Mineral Mountains past surveys and sample points.
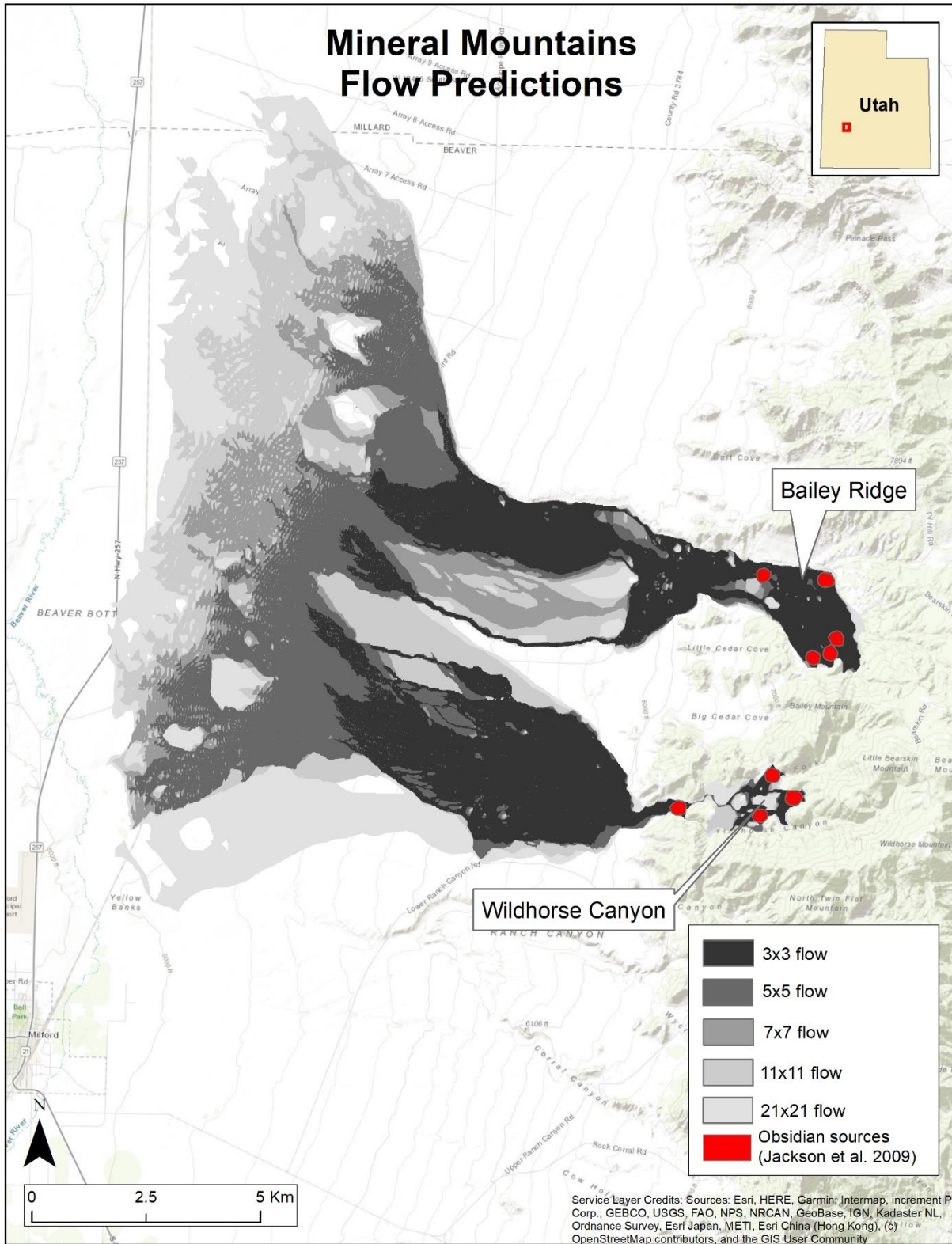
Figure 3-40: Mineral Mountains flow predictions.
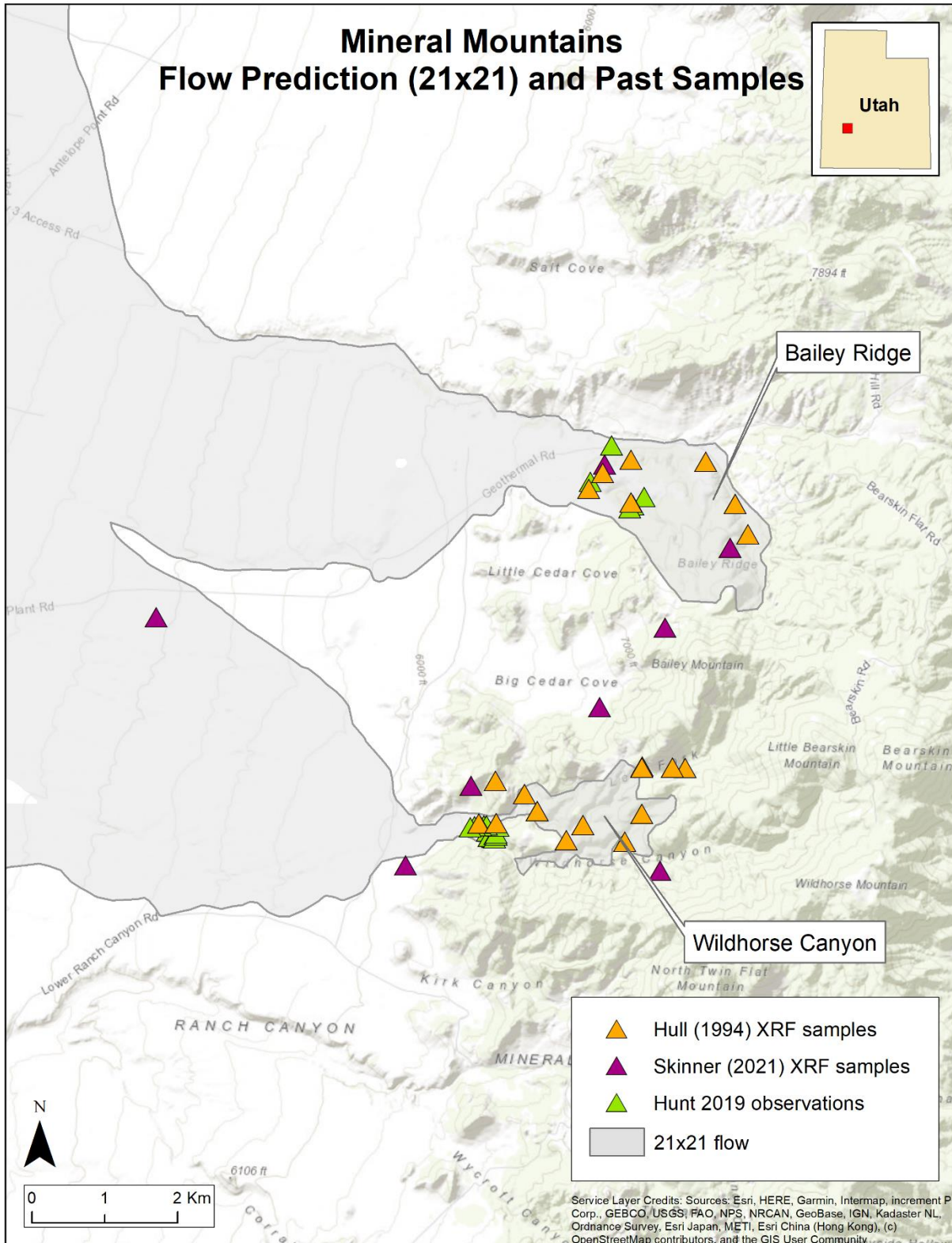
Figure 3-41: Mineral Mountains 21x21 flow prediction in comparison with past sampling.
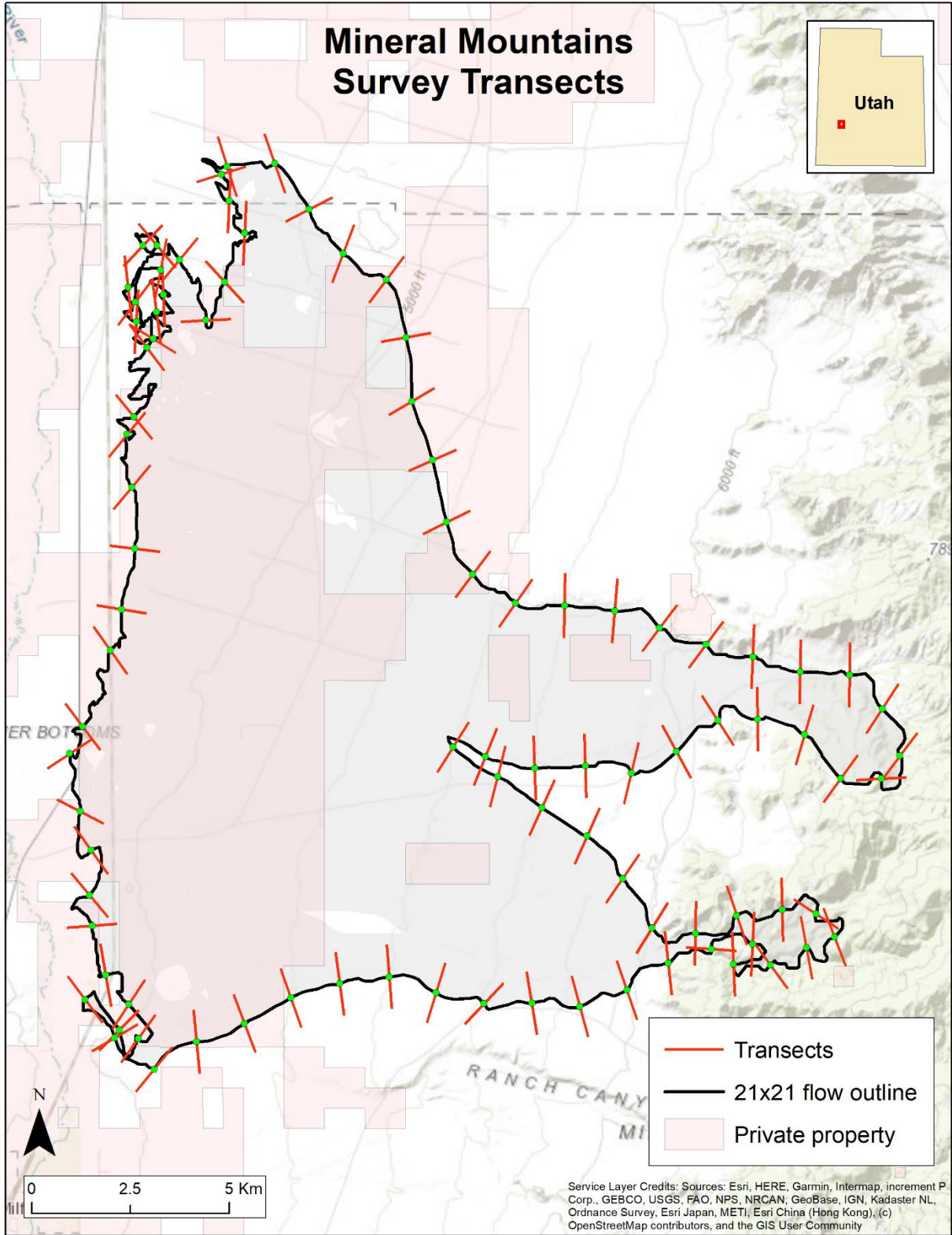
Figure 3-42: Mineral Mountains 21x21 survey outline and transects.
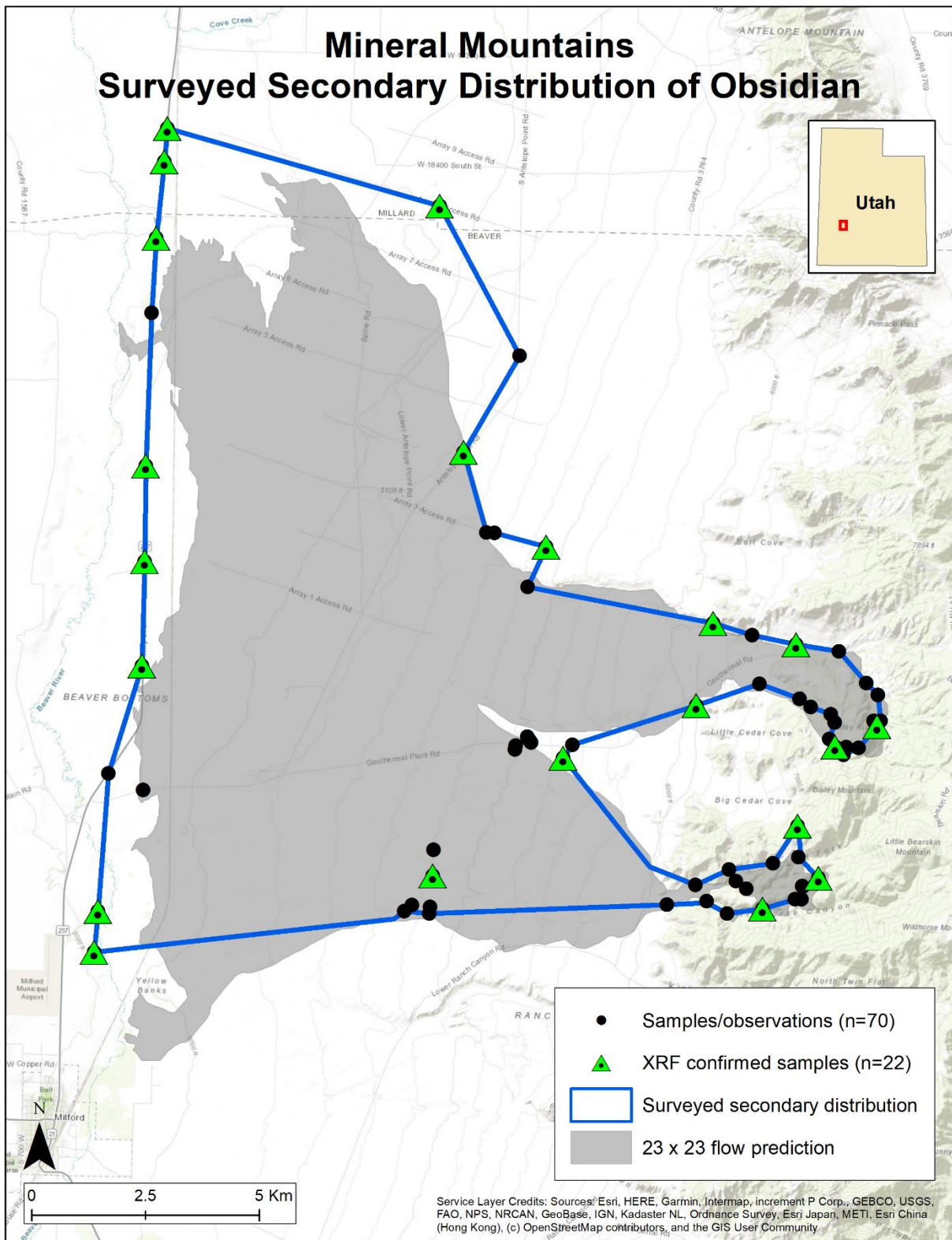
Figure 3-43: Mineral Mountains surveyed secondary distribution of obsidian.
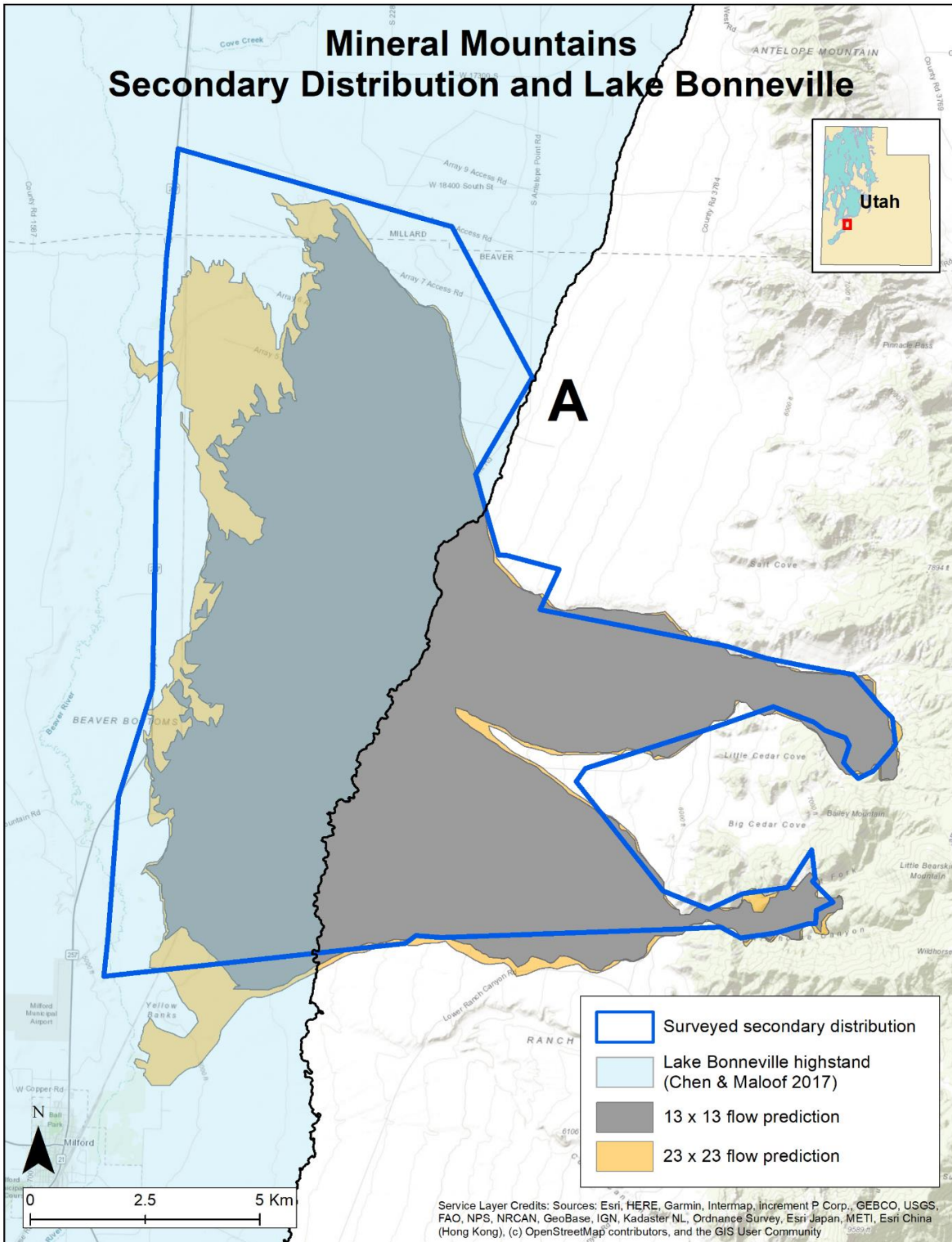
Figure 3-44: Mineral Mountains surveyed secondary distribution in relation to Lake Bonneville. The survey profile at label "A" suggests influence on the secondary distribution by the highstand shoreline.

3.6.4 Panaca Summit/Modena

Location: Lincoln County, Nevada and Iron County, Utah

Alternative names: Modena, Panaca Summit, Panaca Summit/Modena area (PS/MA) (Hull 1994)

Hull (1994) sample points: n=10 (Table D-1)

Skinner sample points: n=8 (Table D-2)

Talbot (2015) sample points: n=65 (Table D-3)

Hunt 2019 observation points: n=14 (Table B-6)

ORB Paleoindian artifacts: n=1 (Table A-37)

The Panaca Summit/Modena (PS/M) obsidian originates in the hills of eastern Lincoln County, Nevada. The primary source erodes both eastward and westward from this hilltop area. To the east it flows more than 35 km, across Prohibition Flat and down Gold Springs Wash (Figure 3-45) into and around the town of Modena in Iron County, Utah as well as into the nearby basin bottom and playa on the western edge of the Escalante Desert (Figure 3-52). To the west, it flows through Gleason Canyon Wash and Flatnose Wash and then more than 20 km further out to Dry Valley, near Echo Canyon State Park.

The source appears in the literature as "Panaca Summit" or "Modena" obsidian; however, both are misnomers. Panaca Summit lies more than 13 km to the southwest and has no association with either the primary or secondary sources while the town of Modena is 15 km to the east and is simply the downslope recipient of secondary distribution nodules. The combination name "Panaca Summit/Modena" is the current best-practice appellation in the literature, though Talbot et al. (2015) suggest Prohibition Spring or Prohibition Flat better describes the source geographically. The misnaming is the result of XRF testing in the 1970s and

1980s on samples from the surrounding area before the actual primary source location was recorded in 1998 (Jackson et al., 2009; Nelson, 1984; Rowley et al., 2002; Talbot et al., 2015; Umshler, 1975)

Figure 3-45: Looking east across Gold Springs Wash [near 11S 762137 4187156].

PS/M Geology

The PS/M primary obsidian source area lies between the Indian Peak and Caliente calderas (Figure 3-46), which formed in the middle Cenozoic Era (Best et al., 2013). Their formation about 36 Ma and subsequent activity between 25 – 18 Ma shaped the PS/M locale.
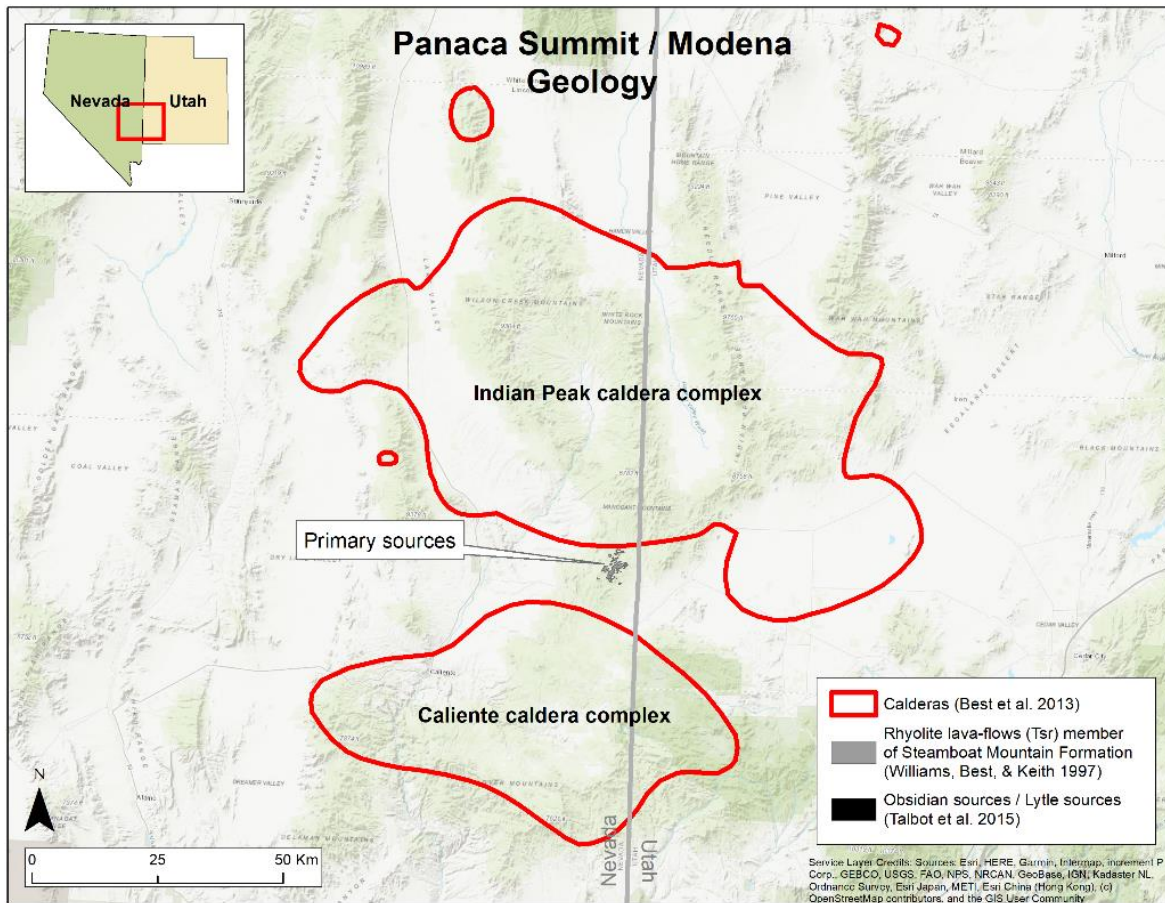
Figure 3-46: Panaca Summit/Modena location, relative to the Indian Peak and Caliente calderas.

Between 13 and 11 Ma, rhyolitic lava-flows (75% SiO_2) of the Steamboat Mountain Formation erupted, forming a dome and lava flows up to 250 m thick in areas around Prohibition Spring (Rowley et al., 2002; Williams et al., 1997). In some instances, the basal members of the flows cooled so rapidly upon contacting the ground that it formed discontinuous lenses of glass: the obsidian now present at in the Prohibition Spring area (Rowley et al., 2002). Figure 3-47 illustrates the resultant phenomenon well: lenses of glassy obsidian forming at the bottoms of a series of overlapping rhyolitic flows emanating from a central dome area (Talbot et al., 2015). At the surface, these lenses of obsidian manifest as veins or ledges of solid obsidian, up to a meter thick, with a low incidence of small phenocrysts (Rowley et al., 2002; Williams et al., 1997).
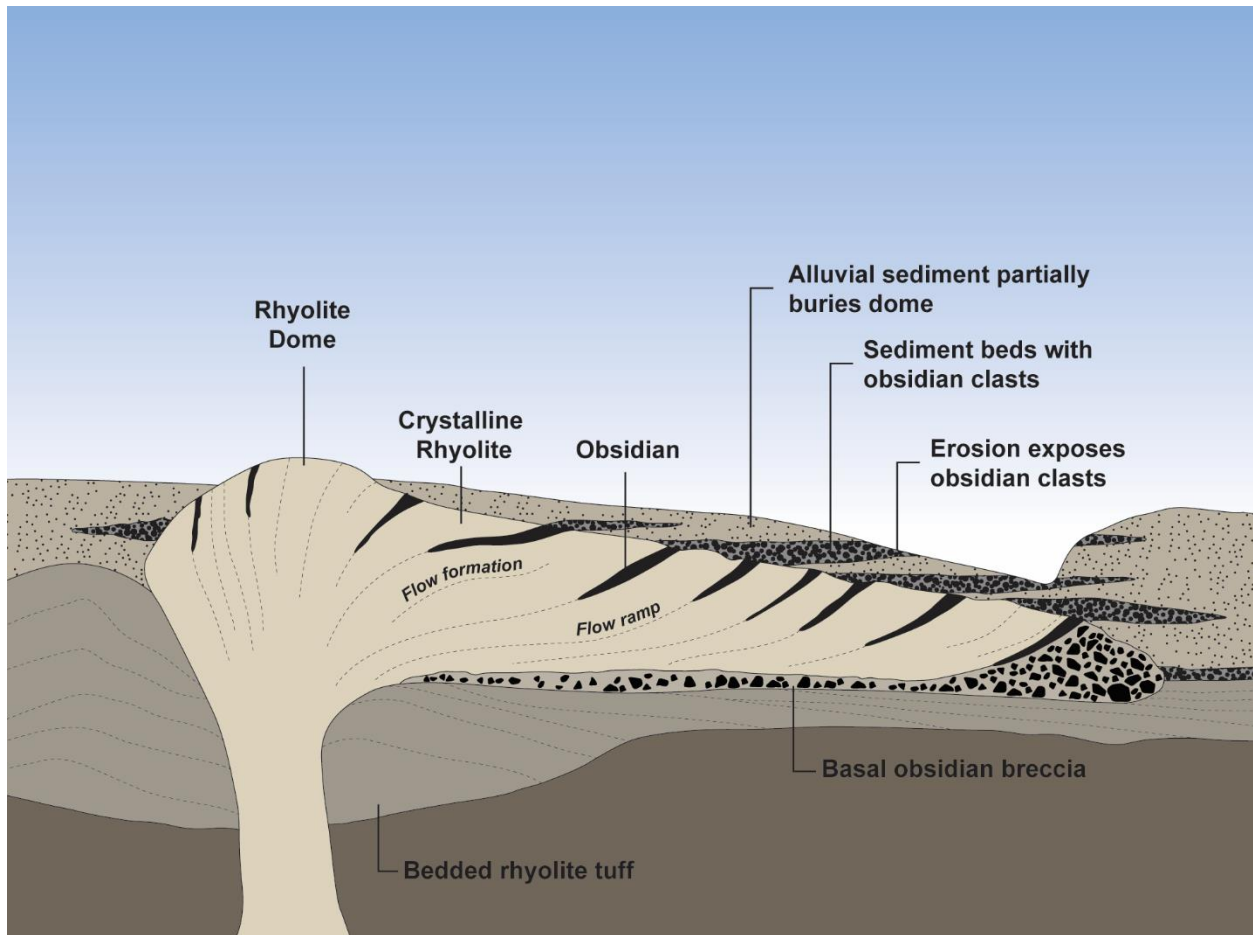
Figure 3-47: Illustration of discontinuous obsidian lens formations at Panaca Summit/Modena. Courtesy of the Museum of Peoples and Cultures, Brigham Young University.

During the Pleistocene, PS/M obsidian nodules, some as large as boulders (> 25 cm per the Wentworth scale), eroded off the lenses and washed downhill to the east, consolidating with other material into massive sediment beds, up to 5 m thick (Rowley et al., 2002; Talbot et al., 2015; Wentworth, 1922; Williams et al., 1997). These sediments traveled tens of kilometers to the east, well past the town of Modena. As will be discussed below, the flow development is less clear on the western side of the hills, where nodules are much smaller, rarely exceeding 4 cm.

PS/M Archaeology

The PS/M geochemical signature was first identified by Umshler (1975), using samples from the secondary distribution near the town of Modena, Utah. Nelson (1984) similarly

published an XRF sample taken near Modena. However, it was not until 1998 that avocational archaeologists Manetta and Farrel Lytle identified six primary sources, now referred to as the "Lytle sources", upslope in Nevada, more than 15 km west of the previously published sample locations and namesake (Rowley et al., 2002; Talbot et al., 2015). According to Rowley (2002), all that remains of the original obsidian veins are the dense talus fields (Figure 3-48) of natural and cultural flakes recorded by the Lytles, the result of millennia of prehistoric mining activity, natural cracking, and erosion. While Rowley claims the obsidian ledges are "mined out" (2002, p. 2), Talbot et al. counter that while extensive mining did occur, it is "certainly not mined out" (Talbot et al., 2015, p. 39), as large nodules are abundant in the area, and no one has yet excavated the talus areas to confirm or deny the existence of remaining vein exposures. We also know that the PS/M sources were exploited from Paleoindian to at least Fremont times and that artifacts fashioned from PS/M obsidian have been identified at sites throughout Nevada, Utah, and as far west as Death Valley (Estes, 2009; Haarklau et al., 2005; Jones, Beck, Jones, et al., 2003; Madsen, Schmitt, et al., 2015; Nelson, 1984; Talbot et al., 2015; Umshler, 1975).

Around the Lytle sources are dozens of small archaeological sites and perhaps hundreds of unrecorded lithic scatters. The natural corridor through the mountain pass at the southern end of the region, now occupied by Highway 319 and a railroad, has been the most thoroughly studied. Over 50 sites are recorded, and the corridor is considered a meeting point for the Virgin Anasazi and Fremont people (Talbot et al., 2015).

*Figure 3-48: The Lytle #1 primary source location, now just a massive field
of natural and cultural flakes.*

PS/M Past Work

The earliest XRF testing at this locality by Umshler (1975), Nelson & Holmes (1979), and

Nelson (1984) provide insufficient locational data to be helpful here (only detailed to township-

range sections or quarter sections). Hull (1994) provides an early dataset of XRF testing on 10

samples (Table D-1) from the region (converted from township and range descriptions to GPS

centroids which introduces several hundred meters of potential error). Jackson et al. (2009)

provides some insight on the secondary flow but was focused on Utah, not Nevada. Skinner

(Table D-2) provides eight XRF samples from PS/M. In 2019, I conducted a pilot survey and

observed obsidian at various points around PS/M (Table B-6, *n*=14). While these are not XRF

test points, they provide a useful indicator of how obsidian is distributed on the hillside.

Talbot et al. (2015) provides the most comprehensive survey to date of the PS/M primary source region itself, the result of three seasons of field school surveys and these are used extensively here for the flow analysis. Along with mapping the Lytle sources, they surveyed cobble density surrounding the talus fields, which is used in the flow prediction below. They also XRF tested 65 nodules (Table D-3), primarily from the eastern hillside region, which are mapped in Figure 3-54.

All this information was used in selecting the best flow prediction to use for the PS/M obsidian.

PS/M Flow Prediction

Using the process described in the beginning of this chapter, five flow distributions were created. During this process, however, natural and anthropomorphic challenges emerged.

First, as there are no known remaining obsidian ledges or veins, what is or is not "primary" is now subjective at this site. Talbot et al. (2015) describe the obsidian cobble field that surrounds the Lytle source areas and it is quite robust, producing nodules that fall into Wentworth's boulder classification. As such, I used this distribution field as the primary source (Figure 3-54). From the flow predictions that follow, this is simply an interpretative issue of where primary flows end and secondary flows begin and likely has little impact on the final flow extent.

Second, the hillside where the PS/M primary resources originate drains eastward to a narrow channel, or bottleneck, at the bottom of Gold Springs Wash, between the foothills of Mt. Elenore to the north and an unnamed ridge and hill to the south (see callout at the Natural Bottleneck noted in Figure 3-52). This narrow passage is the conflux of the natural flow of Gold Springs Wash into the flats by the town of Modena and the routes of a Union Pacific railroad, on

raised beds, and that of a state highway (Hwy 319) which includes an overpass over the railway (Figure 3-49). All three converge into a narrow natural passage that is only about 500 m wide and channels movement for more than 2 km as it travels east. The anthropogenic structures significantly stand above the natural topography and pre-date modern DEM imagery. As such, their impact is incorporated into that imagery. When applying the flow prediction process described above, these obstacles form a dam that hinders accurate predictions for natural sediment flows.

Figure 3-49: Anthropogenic dams at the Panaca Summit/Modena bottleneck; raised railroad bed and highway overpass.

I investigated several methods to overcome this impediment. The first was to increase the smoothing aspect of the DEM to "average out" the dams. This had the negative impact of "blowing out", or over-smoothing, the naturally very flat terrain to the east of the channel, resulting in any flow that got past the dam to unrealistically and completely fill the basin to the east. Another method, provided by D'Avello, Brennan and Loomis (2016), acts like a "cookie cutter", removing the offending portion of a DEM and replacing it with a patch that is the average of the surrounding edges. This approach did not work in this instance and seemed to only create a similar, more dense, linear dam.

As my intention is to model the flow of sediment from this natural channel eastward into the flats, I chose to modify the weighted raster to include an artificial source, or "proxy", that originates at the dam itself. Since the original flow predictions make it clear that sediment moving off the Prohibition Flat hillside and travelling down Gold Springs Wash is channeled strictly through this passage, "leap-frogging" the dam should not have significantly impacted the eastward flow prediction. Figure 3-50 illustrates this solution with an artificial source 1000 m wide, spanning the bottleneck region. This approach is similar to the "donut" approach but bypasses the averaging step.
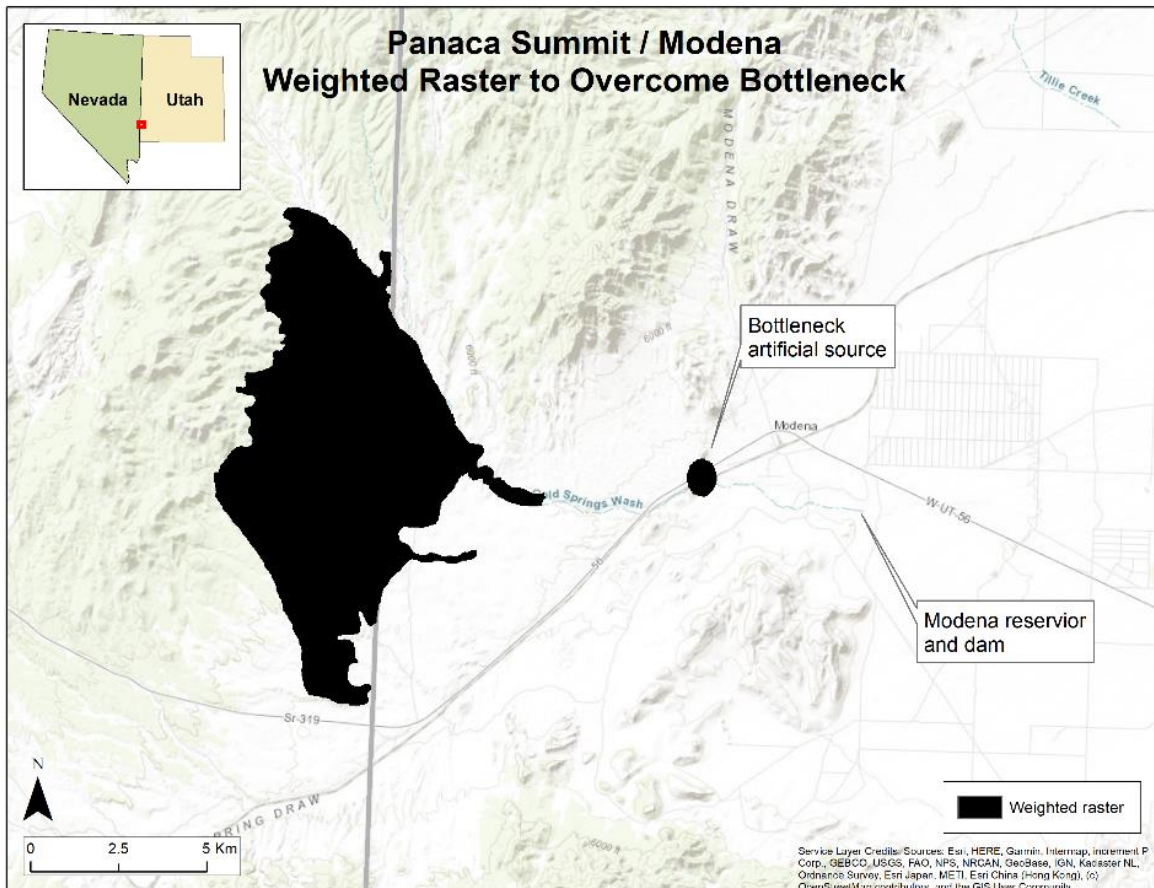
Figure 3-50: Weighted raster used to predict Panaca Summit/Modena flow showing artificial source used to overcome channel bottleneck.

Another dilemma presented itself to the west. Skinner's sample SO-65-1738 appeared to be well out of range of the predicted flow (Figure 3-54). SO-65-1738 is more than 18 km to the northwest of the known primary sources and, more importantly, on the opposite side of the hydrographic basin ridgeline. This suggested that there is, or was at one time, a primary source exposure west of the ridgeline. During the 2020 field season, I performed a survey near SO-65-1738 and discovered a second sample of PS/M obsidian in a road cut in Flatnose Wash (sample #103 in Table B-4, confirmed by XRF test), clearly indicating that a western flow needed to be considered in the overall flow predictions.

To this end, I used a method like that in the bottleneck procedure above to create a proxy primary source. Three of Hull's samples are the western-most samples on the ridge (M-04, M-06, and M-10). I created a polygon using these three samples and then used this polygon to create a weighted raster. Figure 3-51 illustrates the proxy primary source and the resultant 21x21 flow prediction generated using just this proxy source. The prediction flows westward along Gleason Canyon Wash, connecting with Flatnose Wash, and then captures sample SO-65-1738. Note that the eastern flow from the proxy source mimics the earlier predictions but is similarly restricted by the bottleneck region.

This proxy primary source was incorporated into the weighted DEM and used to generate 3x3, 5x5, 7x7, 11x11, and 21x21 flow predictions using the method described above. These are presented in "stacked" form in Figure 3-55, with the 3x3 nearest neighborhood flow represented by the darkest shade and the 21x21 flow represented by the lightest shade.

In the east, the 21x21 flow abruptly terminates just as it escapes from the bottleneck and passes south of the town of Modena. It is here that the eastern 21x21 flow hits a real dam, the Modena reservoir. While the eastern 11x11 smoothing appears to allow the flow to move around
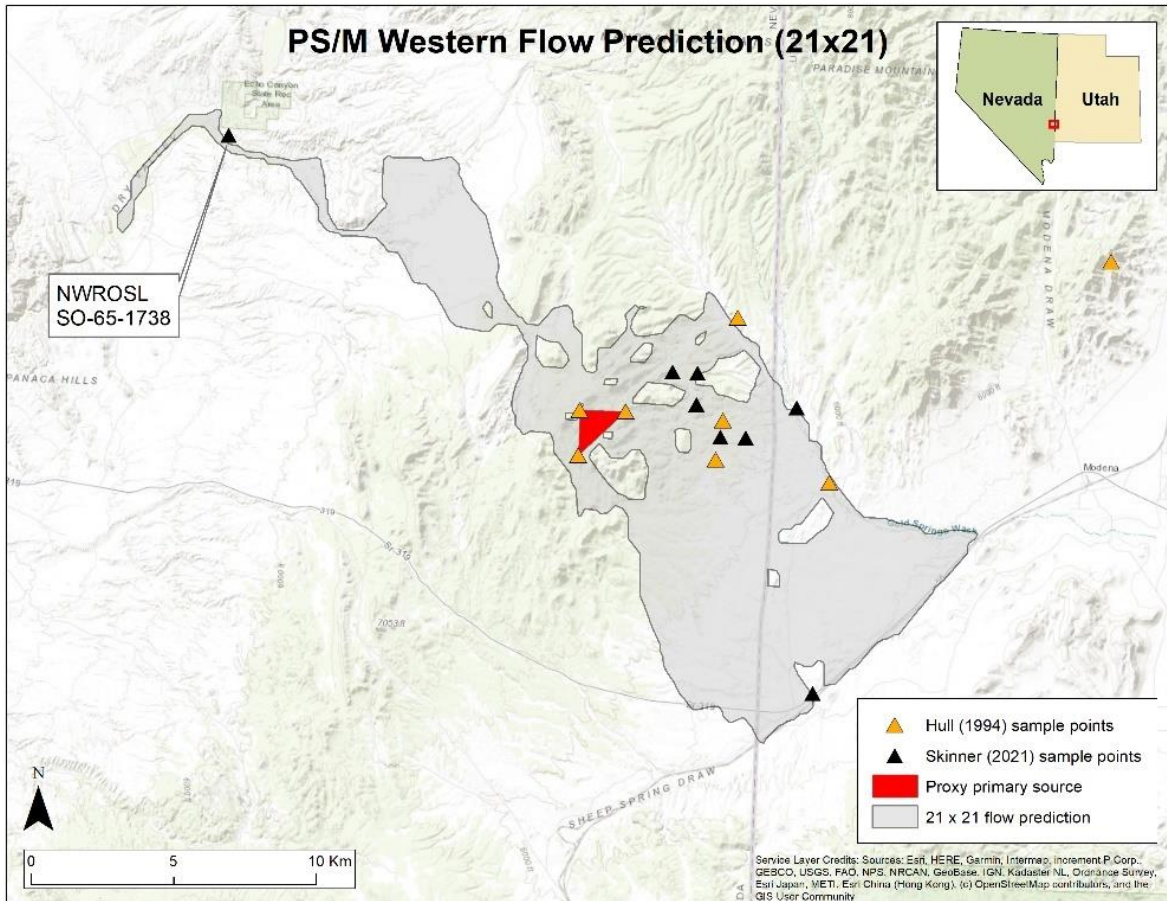
Figure 3-51: Panaca Summit/Modena western flow prediction (21x21) derived from proxy primary source.

the dam, the 21x21 smoothing is too much, creating a wide raised area that stops this flow from continuing. A comparison to the known sample points by Hull (1994), Talbot et al. (2015), Skinner (Table D-2), and my own pilot project (Table B-6) shows good concordance with this 11x11 flow to the east of the PS/M ridge (Figure 3-56). For this reason, field work in the east was based on this flow prediction and the final flow outlines and transects for the 11x11 flow are shown in Figure 3-57.

To the west, the 21x21 flow appeared to provide the best prediction, based primarily on the placement of sample SO-65-1738 (Figure 3-58). The final flow outlines and transects for the 21x21 flow are shown in Figure 3-59.

Survey Results

The Panaca Summit/Modena secondary distribution was surveyed during the summers of 2020 and 2021. The observed extent is illustrated in Figure 3-60. The PS/M extent covers an area of ~330 km^2 with a perimeter of ~165 km. During the survey, 126 observation points were recorded, and 104 natural obsidian samples were collected (Table B-4). Of these collected samples, 28 were submitted to NWROSL for XRF testing (Table C-4) and were confirmed as "Modena" obsidian (green triangles in Figure 3-60).

The surveyed flow encompasses almost all previous sample points recorded by Hull (1994), Talbot et al. (2015), Skinner (Table D-2), and myself (Table B-6), with mostly minor exceptions. On the eastern slope, a single previously recorded point is ~570 m outside the surveyed extent and two are less than 300 m outside the extent. The placement of these points would not materially affect the predicted secondary distributions. The only significant anomaly is to the northeast, where Hull's (1994) M-01 appears to be more than 240 m above the Escalante Valley (Figure 3-56). While this point is interpolated from a township and range location, the range of error still places it considerably above the valley bottom. During the 2020 survey season, I surveyed the drainage below the elevation point and saw no evidence of obsidian flowing downhill. This appears to be a recording error.

Following the modified Confusion Matrix methodology described in section 3.5, the optimal smoothing level for PS/M occurs at the 13x13 nearest neighbor average (Table 3-5). At this level, 54% of the actual survey region was predicted by the model.

Smoothing	Predicted flow area (km²)	TP	FP	% survey predicted	% prediction inside observed	% prediction outside observed	TP/ observed	FP/ observed	(TP-FP)/ observed
3x3	93.3	90.5	2.9	27%	97%	3%	27%	1%	26.6%
5x5	106.1	102.2	4.0	31%	96%	4%	31%	1%	29.8%
7x7	112.4	107.7	4.7	33%	96%	4%	33%	1%	31.2%
9x9	143.6	132.7	10.9	40%	92%	8%	40%	3%	36.9%
11x11	177.3	152.9	24.4	46%	86%	14%	46%	7%	39.0%
13x13	**222.9**	**176.8**	**46.1**	**54%**	**79%**	**21%**	**54%**	**14%**	**39.6%**
15x15	233.7	173.7	60.1	53%	74%	26%	53%	18%	34.5%
17x17	221.9	169.0	52.9	51%	76%	24%	51%	16%	35.2%
19x19	154.1	136.5	17.6	41%	89%	11%	41%	5%	36.0%
21x21	156.9	136.9	20.0	42%	87%	13%	42%	6%	35.5%
23x23	162.5	138.7	23.7	42%	85%	15%	42%	7%	34.9%
25x25	165.6	139.5	26.0	42%	84%	16%	42%	8%	34.4%

The model performed adequately for initiating surveys but suffered in two key areas. In the east, we see that the observed flow extends much further south and east past the bottleneck area (annotated as "A" in Figure 3-60) than the prediction allows. At the same time, the eastern side likely would benefit from a higher smoothing than 11x11, but anthropogenic modifications impacted these predictions. This area is an enormous basin bottom and the unpredicted flow in this area demonstrates the difficulty the model has with these extremely low slope / low energy environments, in this case, not filling the basin accurately. This area is also comprised of large areas of private property and agricultural land, complicating accurate survey.

To the west, the area annotated as "B" has a high occurrence of small obsidian pebbles, typically less than 2 cm in diameter. These occupy the hills to the south of the Gleason Canyon Wash and suggest additional, unknown primary obsidian sources in that region, perhaps a pyroclastic tuff or ancient obsidian source that has degraded to marekanites (Apache tears). As

discussed earlier, model accuracy is incumbent on known primary sources, some of which may

still be unknown at PS/M.
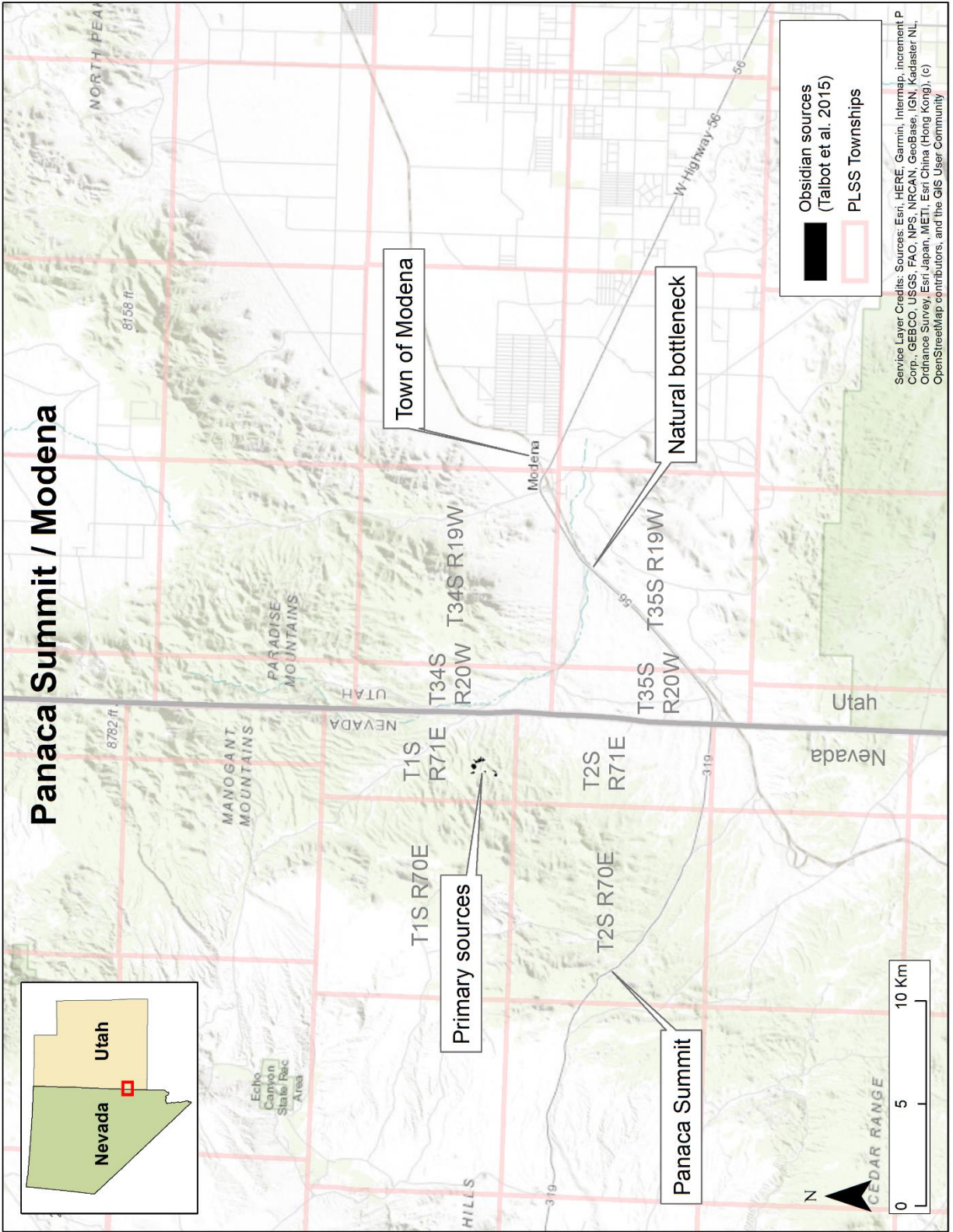
Figure 3-52: Panaca Summit/Modena regional view.
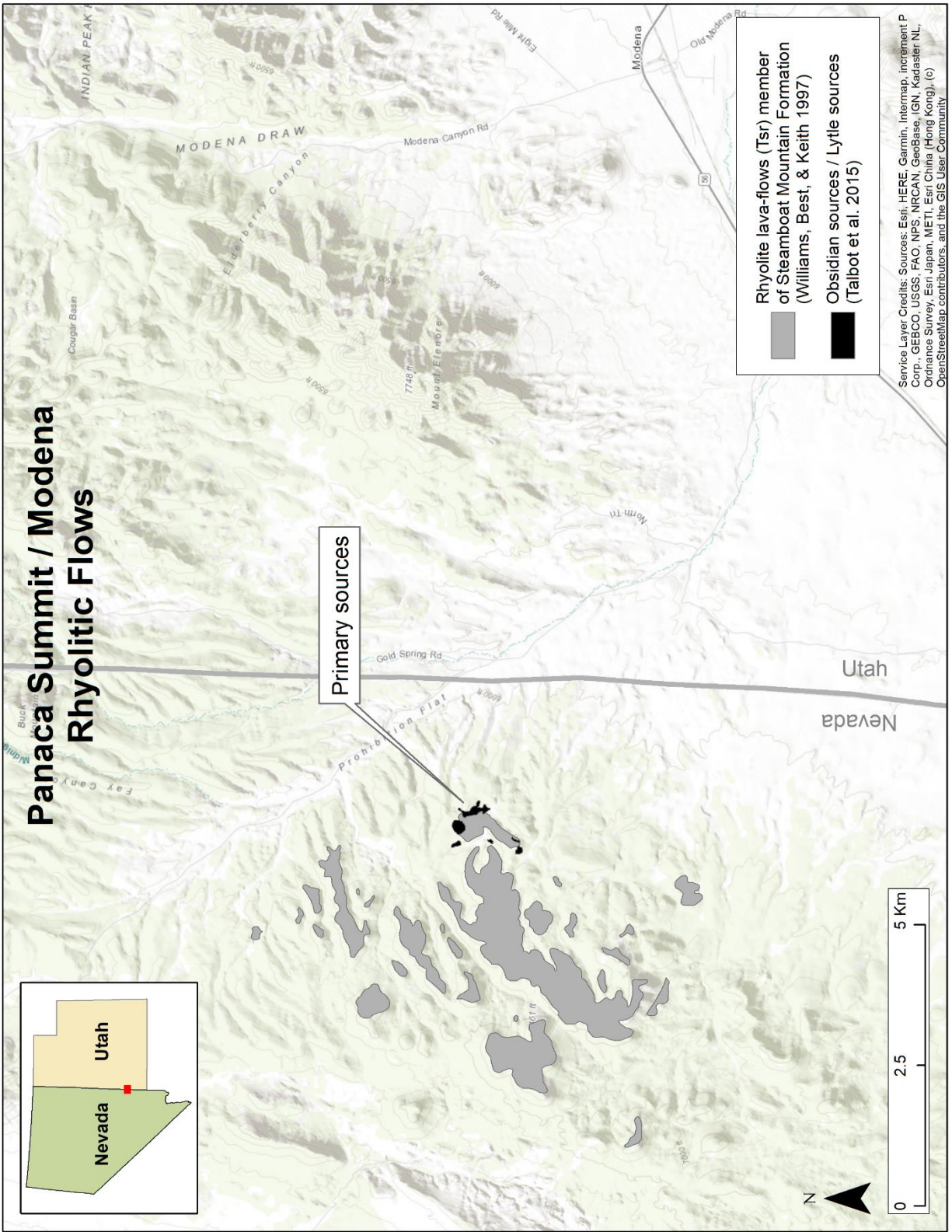
Figure 3-53: Panaca Summit/Modena rhyolite and obsidian.
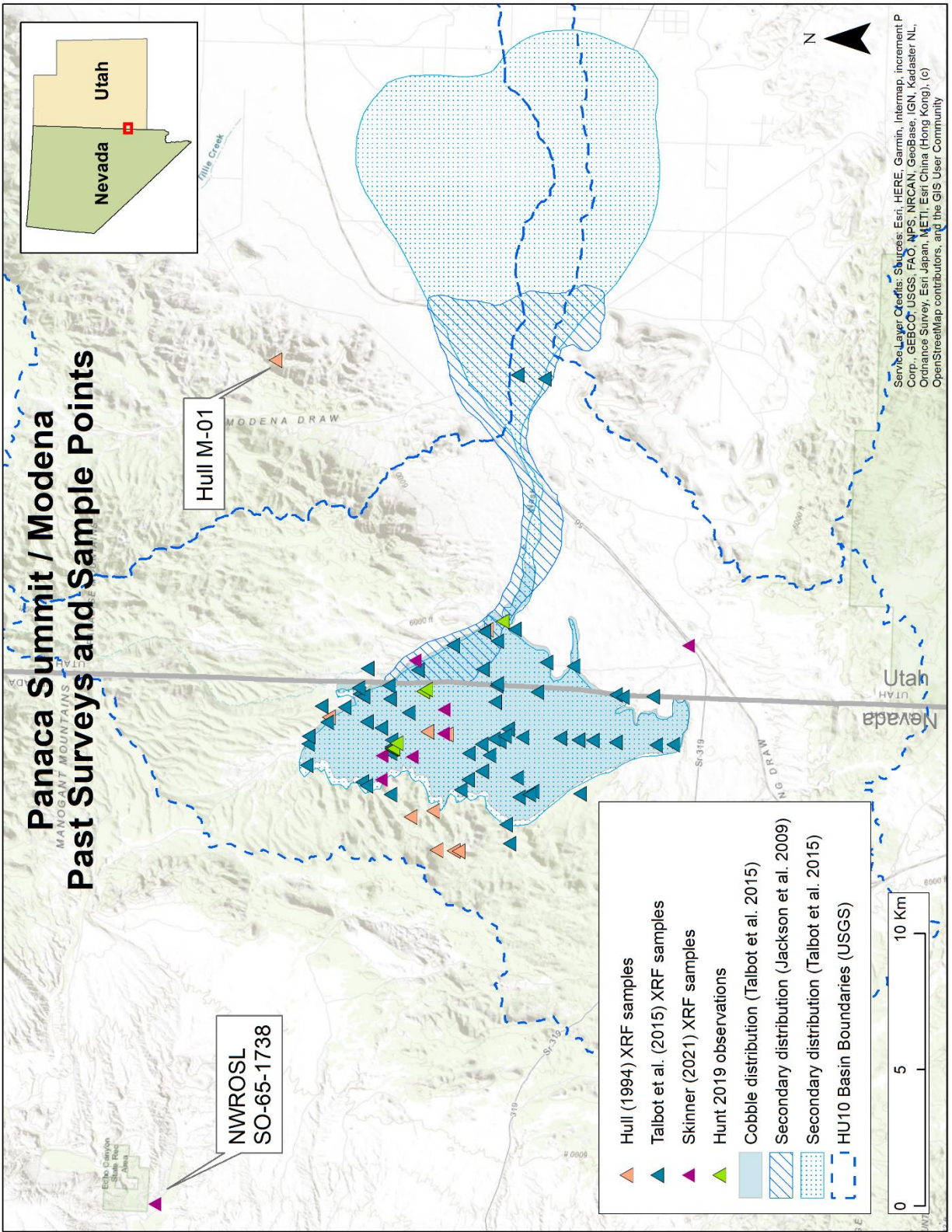
Figure 3-54: Panaca Summit/Modena past surveys and sample points.
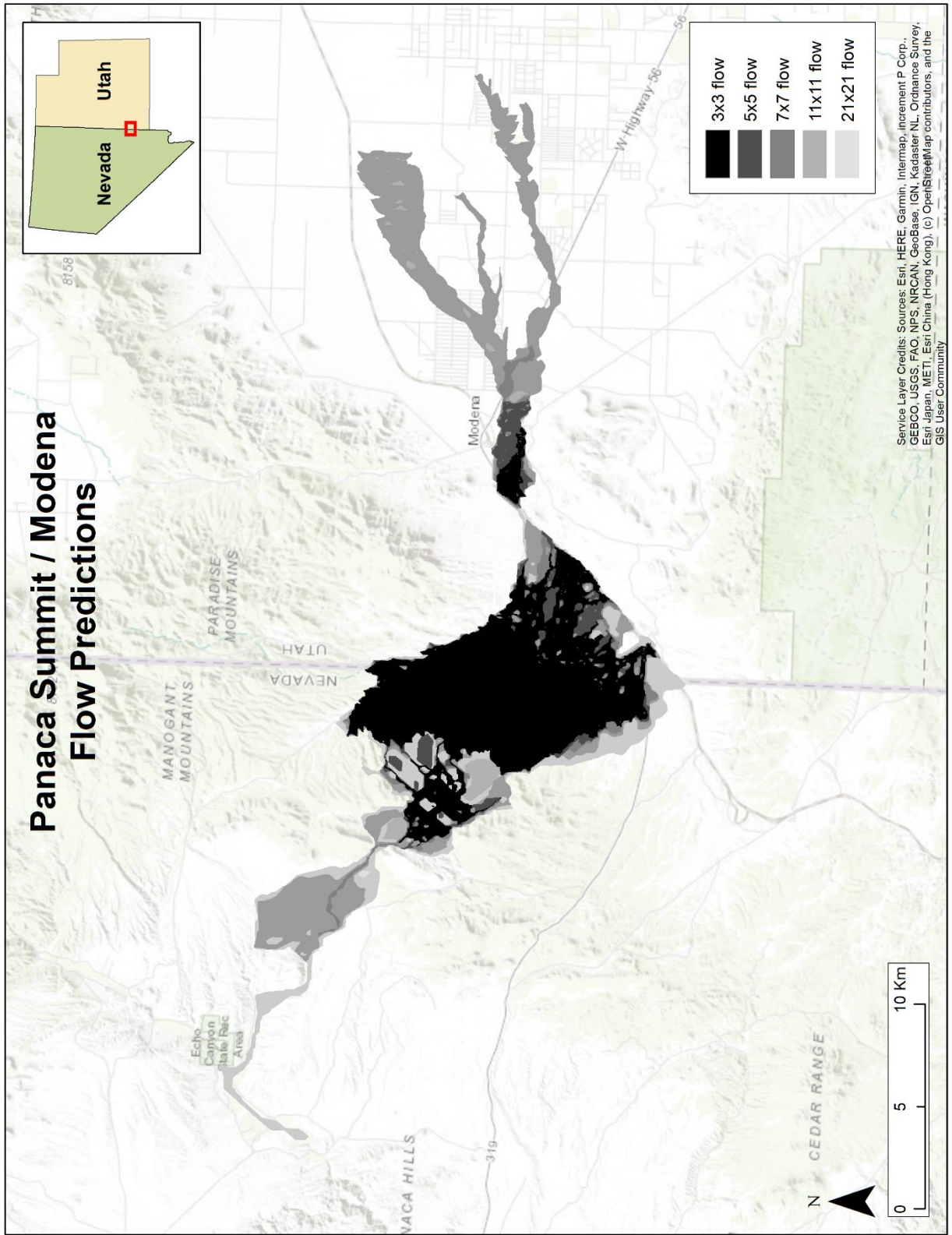
Figure 3-55: Panaca Summit/Modena flow predictions.
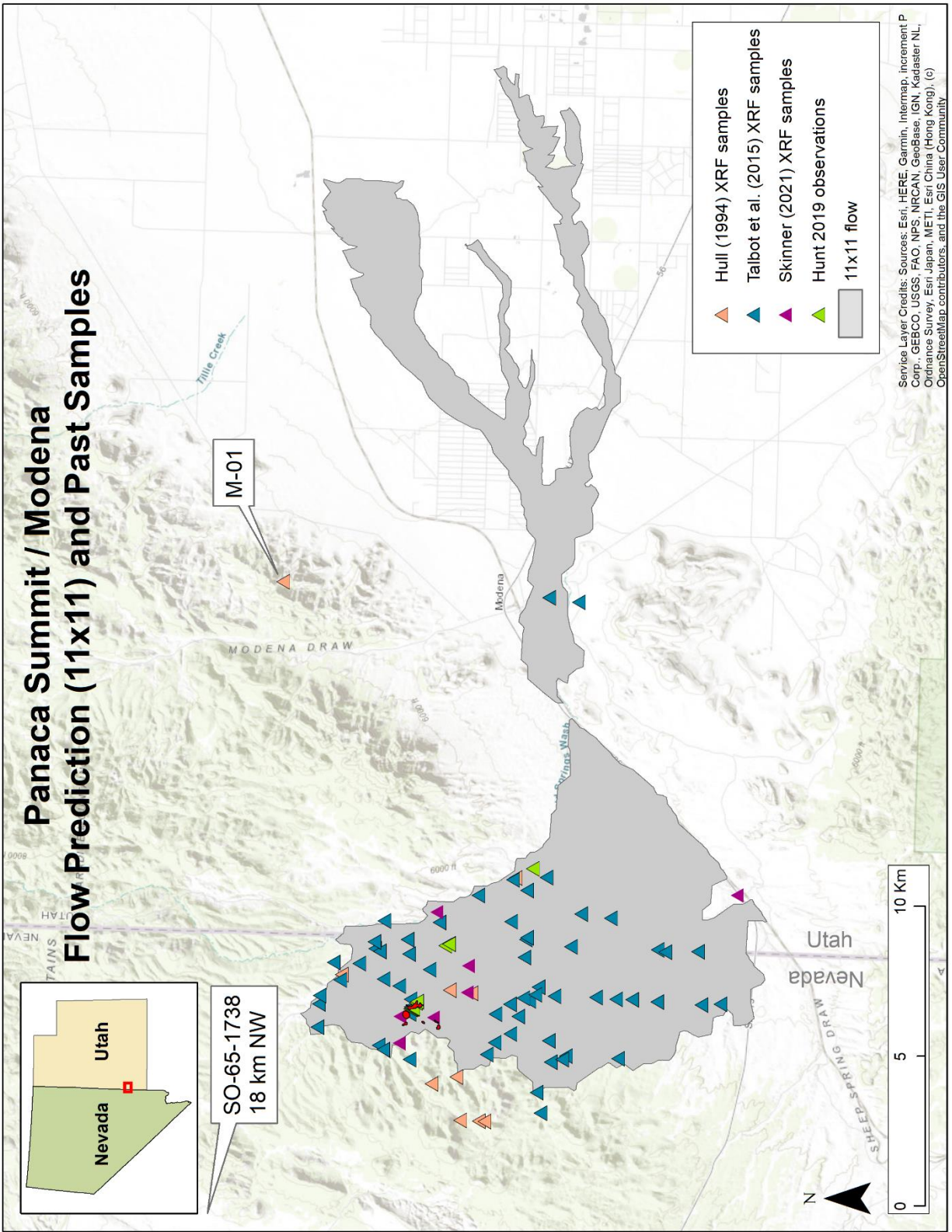
Figure 3-56: Panaca Summit/Modena 11x11 flow prediction in comparison with past sampling.
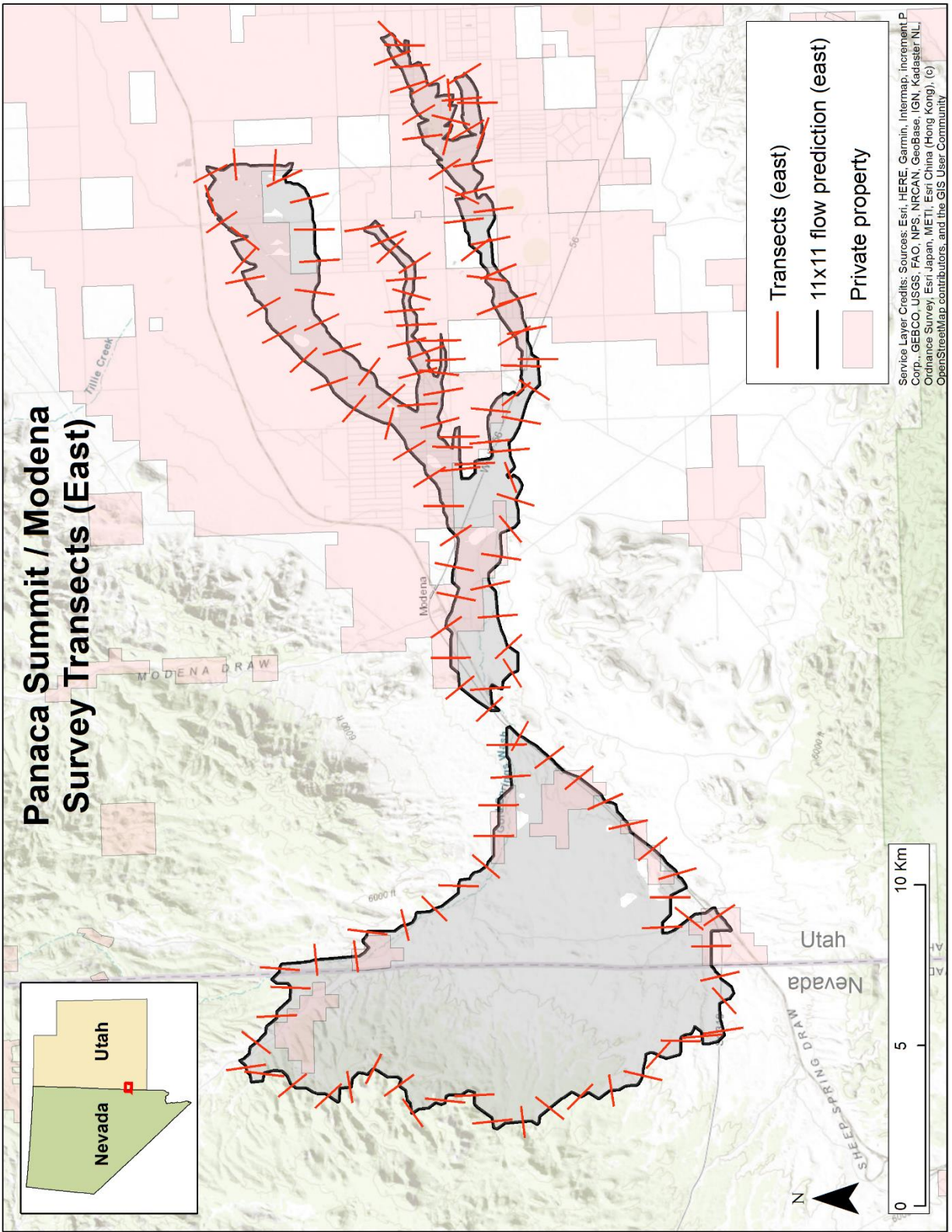
Figure 3-57: Panaca Summit/Modena 11x11 survey outline and transects (east).
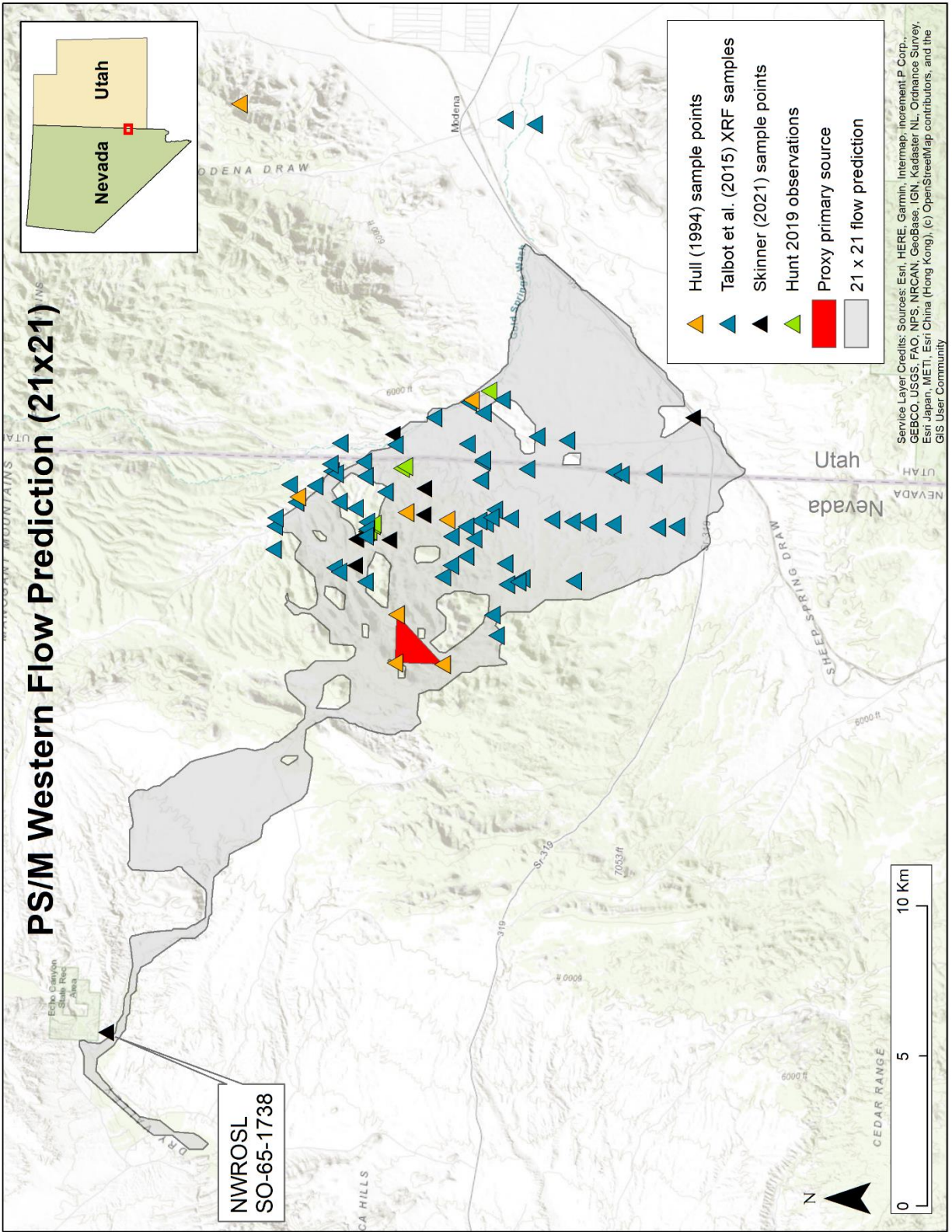
Figure 3-58: Panaca Summit/Modena western flow prediction using a proxy primary source.
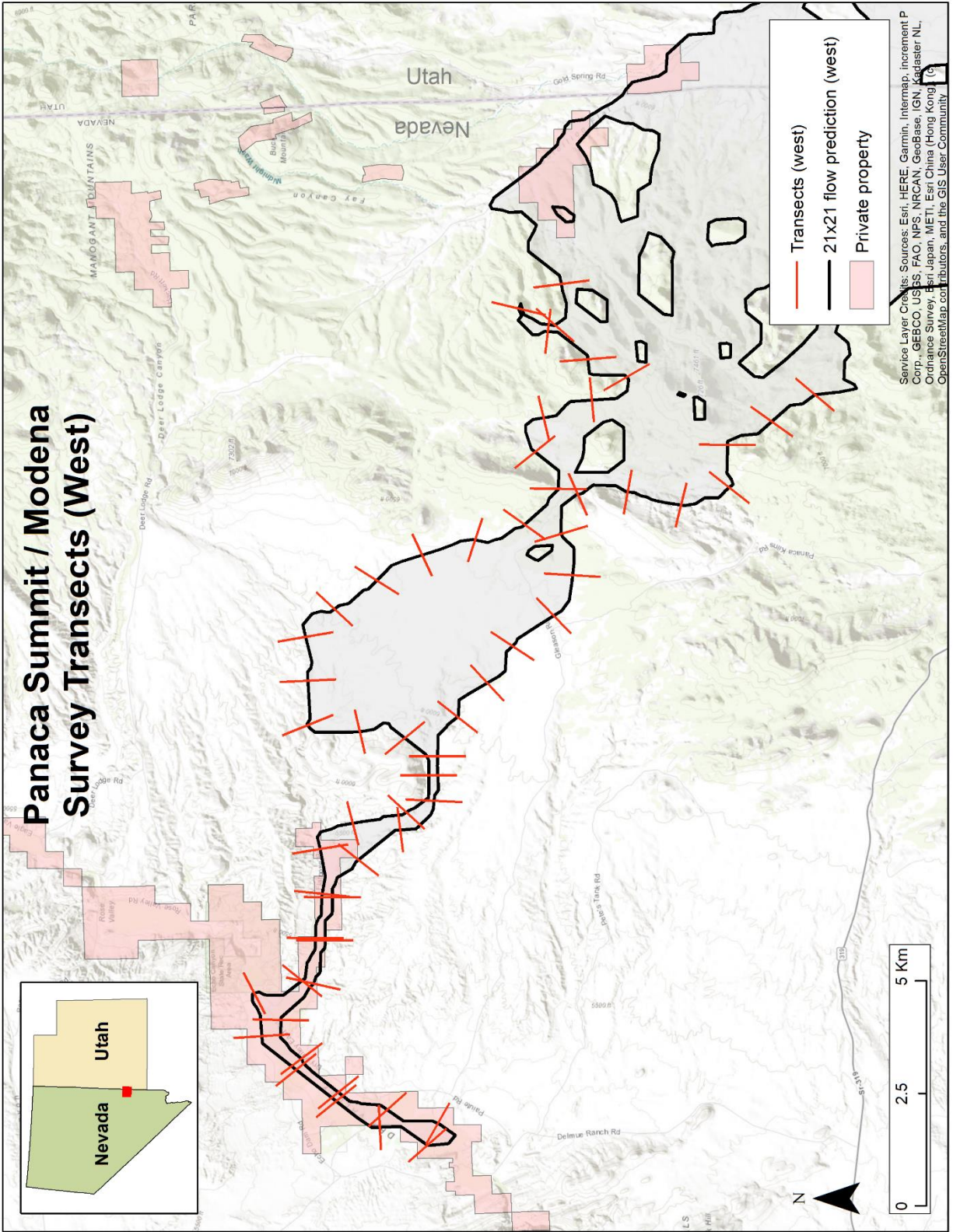
Figure 3-59: Panaca Summit/Modena 21x21 survey outline and transects (west).
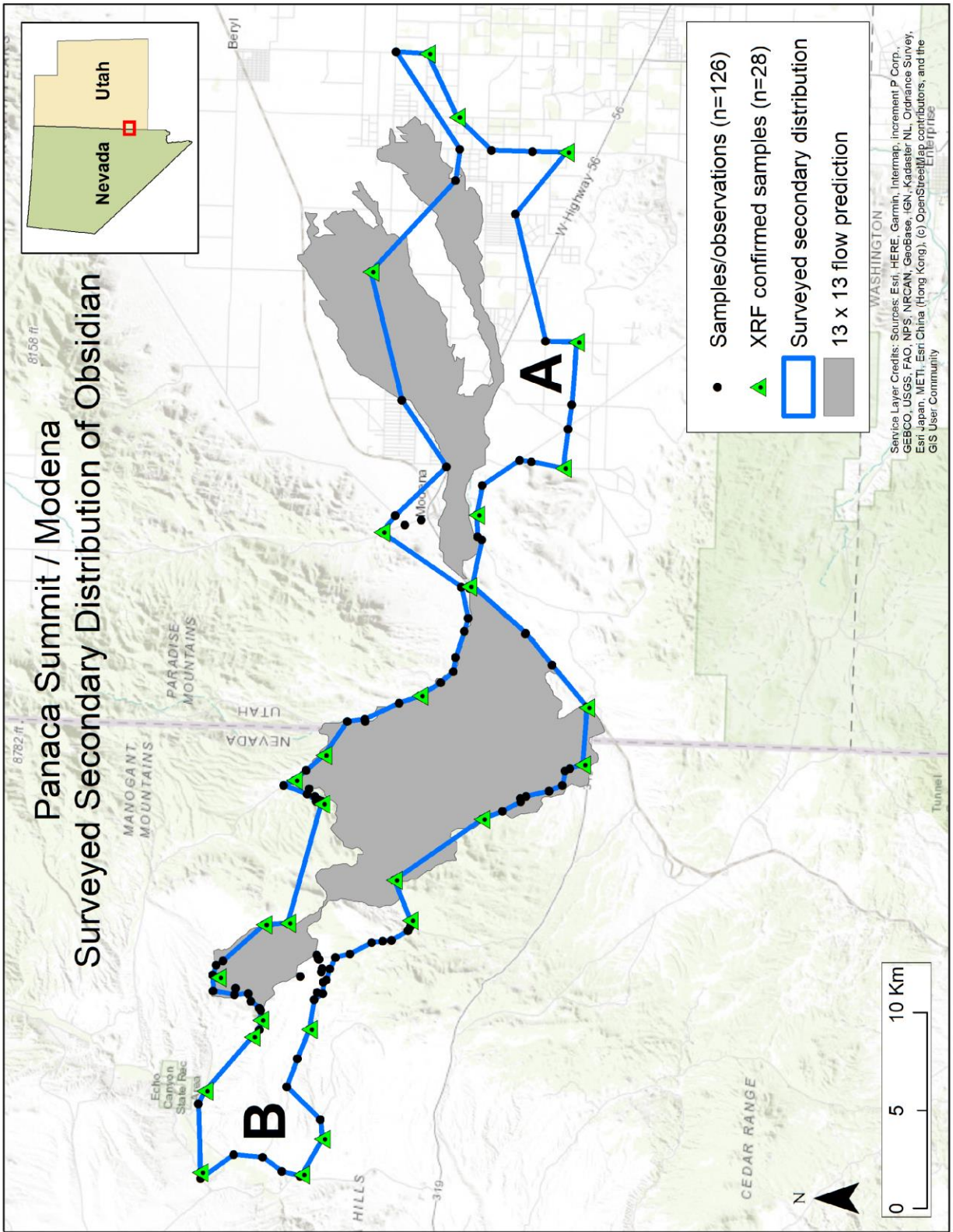
Figure 3-60: Panaca Summit/Modena surveyed secondary distribution of obsidian.

3.6.5 Topaz Mountain

Location: Juab County, Utah

Alternative names: None

Hull (1994) sample points: *n*=10 (Table D-1)

Skinner sample points: *n*=11 (Table D-2)

Hunt 2019 observation points: *n*=10 (Table B-6)

ORB Paleoindian artifacts: *n*=130 (Table A-37)

The Topaz Mountain (TM) obsidian originates in the Thomas Mountain range in Juab County, Utah (Figure 3-63). Four separate TM primary sources are situated along ridges of the Thomas Range to the north of Topaz Mountain and one newly recorded source resides close to the basin bottom in the north end of the range. These sources erode in multiple directions: eastward into Pismire Wash and the basin bottom between the Thomas Range and Keg Mountain (Figure 3-61), westward into the valley named The Dell between the Thomas Range and Spor Mountain, southwest into Fish Springs Flat, and north along the east side of the Black Rock Hills.

TM Geology

The Thomas Range is a remnant structure of the western edge of the Thomas caldera, which formed about 42 Ma and then collapsed around 38 Ma (Lindsey, 1982). The mountain range was further modified during the basin-and-range faulting period, circa 21 Ma. This also signaled the beginning of an extensive period of alkali-rhyolitic eruptions in the region. Spor Mountain, just two or three kilometers to the west of Topaz Mountain, experienced rhyolitic eruptions around 21 Ma, while the Thomas Range rhyolitic eruptions occurred much later,

Figure 3-61: Looking to the east from the Thomas Range, into the expansive Pismire Wash area [near 12T 319783 4401463].

between 6.3 ± 0.4 and 6.8 ± 0.3 Ma (Lindsey, 1979, 1982). These most recent rhyolitic eruptions, from at least 12 separate vents across the range, with thicknesses up to 700 m and a total volume of up to 50 km^3, have been named the Thomas Range Rhyolite (Figure 3-64).

The Thomas Mountain Rhyolite is a high-silica, fluorine-rich (up to 1.5 % wt.) rhyolite known for producing topaz, a widely collected gemstone (E. H. Christiansen et al., 1984, 1986). The obsidian members of the Thomas Mountain Rhyolite were created as the result of rapid cooling of the magma and appear as discontinuous, "steeply dipping" lenses (Lindsey, 1982, p. 27; Staatz & Carr, 1964) and were identified at four locations (Figure 3-64) within the Thomas Range (Jackson et al., 2009). The obsidian contains low percentages of phenocrysts (typically less than 4 – 5%) and some is porphyritic (Staatz & Carr, 1964, p. 95).

More recently, around 18,000 cal BP, the Thomas Range was surrounded by Pleistocene Lake Bonneville at its height (Chen & Maloof, 2017b; C. G. Oviatt & Jewell, 2016; Utah Geospatial Reference Center, 2017), as illustrated in Figure 3-65. After Lake Bonneville receded, the valley bottoms, which include the flats below Pismire Wash, Fish Springs Flat, and the flats around the Black Rock Hills, were covered in lacustrine fine silt, sandy loam, and pebble fields, which remain today.

The Spor Mountain/Thomas Range region is rich in commercially-useful elements and minerals, such as uranium and beryllium, and mines are abundant in the area, including the large Brush Wellman beryllium mine at the south end of Spor Mountain (Lindsey, 1998). There is also an active commercial rockhounding and topaz-collecting operation operating at the base of Topaz Mountain.

TM Archaeology

Three Topaz Mountain primary obsidian sources were recorded in 1981 (42JB275, 42JB276, and 42JB277) and are notable in their high altitude (~2130 m) exposures and difficulty to access, on the steep ridges along the imposing western crests of the Thomas Range (Cartwright, 1981; Raymond, 1981a, 1981b). The authors of the original site reports note that quarrying activity is evident and that the exposures saddle multiple drainages, allowing for extensive colluvial and alluvial action to both the east and west. To the west, sites 42JB296, 42JB440, and 42JB450 are noted lithic scatters with potential surface quarrying activity of the colluvial cobbles (Montgomery, 1981; Nielsen, 1990; Nielson, 1990). To the east, 42JB278 is a primary obsidian exposure but composed only of small nodules (Jackson et al., 2009). The regional survey by Jackson et al. (2009) provides the most comprehensive examination of an area with surprisingly little previous archaeological focus.

TM Past Work

The earliest XRF testing at this locality by Nelson & Holmes (1979) and Nelson (1984) provide insufficient locational data to be helpful here (only detailed to township-range sections or quarter sections). Hull (1994) provides an early dataset of XRF testing on 10 samples (Table D-1) from the region (converted from township and range descriptions to GPS centroids which introduces several hundred meters of potential error). Skinner (Table D-2) provides 11 XRF samples from TM. In 2019, I conducted a pilot survey and observed obsidian at various points around the TM (Table B-6, n=10). While these are not XRF test points, they provide a useful indicator of how obsidian is distributed in the washes to the east and southwest. Jackson et al. (2009) provides some insight on the secondary flow but this seems limited when compared to the other point observations above (Figure 3-66).

It is clear from the point scatter that several surveyors have observed obsidian flowing to the west, into the valley between the Thomas Range and Spor Mountain, known as The Dell. Similarly, my own observations far to the east and southeast in Pismire Wash indicate that the secondary distribution extends much further into the valley than suggested by Jackson et al. (2009). Finally, Skinner (Table D-2) records a sample (SO-65-1434) far to the northwest of the all the other samples -- this area was investigated during my survey fieldwork and resulted in recording a new primary source area (discussed below).

All this information was used in selecting the best flow prediction to use for the TM obsidian.

TM Flow Prediction

Using the process described in the beginning of this chapter, five flow distributions were created.

The starting requirement for all flow prediction is the location of the primary sources. Prior to the 2020 field season, the primary source outlines were derived solely from Jackson et al. (2009), as seen in Figure 3-64. Using these primary sources as the starting points, the downslope flows were predicted for 3x3, 5x5, 7x7, 11x11, and 21x21 nearest neighbor smoothed DEMs. These are presented in "stacked" form in Figure 3-67, with the 3x3 nearest neighborhood flow represented by the darkest shade and the 21x21 flow represented by the lightest shade.

A comparison to the known sample points by Hull (1994), Skinner (Table D-2), and my own pilot project showed good concordance with the predicted flows (

Figure 3-68), especially the 21x21 flow, though the predicted flows extended significantly beyond past sampling. The flow into Fish Springs Flat and north into the Dugway Valley suggested an expansive secondary distribution of several hundred square kilometers. The transect map used during the 2020 field season is illustrated in Figure 3-69.

However, like the situation in western PS/M, Skinner's SO-65-1434 at the north end of the Thomas Range, appeared well out of range of the flow prediction based on the four previously recorded primary sources. This suggested that there was an unrecorded primary source in that area. I investigated this at the end the 2020 field season, discovering an additional primary source (described below) eroding from an exposed tuff. Using this information, I expanded the flow prediction (Figure 3-70) and created a localized transect map (Figure 3-71) for the 2021 field season.

Survey Results

The Topaz Mountain secondary distribution was surveyed during the summers of 2020 and 2021. The observed extent is illustrated in Figure 3-72. The full TM extent covers an area of ~309 km^2 with a perimeter of ~157 km. During the survey, 150 observation points were

150

recorded, and 107 natural obsidian samples were collected (Table B-5). Of these collected samples, 22 were submitted to NWROSL for XRF testing (Table C-5) and were confirmed as "Topaz Mountain" obsidian (green triangles in Figure 3-72).

The surveyed flow encompasses almost all previous sample points recorded by Hull (1994), Skinner (Table D-2), and myself, with mostly minor exceptions (two points are less than 210 m outside the survey outline). However, Hull's sample, T-4, which appeared appropriately positioned in the 21x21 flow prediction (Figure 3-68), is outside the observed survey outline by ~2 km (Figure 3-72). The most likely explanation, even allowing for error inherent in the conversion of the original township and range coordinates to centroid UTM coordinates, is that the flow does, or did, extend into that area but was not observed during my survey. This area is difficult to access, but further survey in that area is warranted in the future.

Skinner's sample (SO-65-1434) triggered further investigation and survey to the north of the Thomas Range, leading to the addition of a new Topaz Mountain obsidian source location. This source manifests as an ash-flow tuff (Figure 3-62) with embedded obsidian nodules. These rarely exceed 4 cm in diameter and are predominantly < 1cm in size. While this source may have produced little in the way of raw materials for tools, it cast a significant signal north for hunter-gatherers to encounter.

Figure 3-62: Northern primary source in tuff. Left, the pink tuff topped by gray conglomerate. Right, close-up of pink tuff and embedded obsidian pebbles [near 12S 311935 4409623].

Following the modified Confusion Matrix methodology described in section 3.5, the optimal smoothing level for TM occurs at the 11x11 nearest neighbor average (Table 3-6). At this level, 63% of the actual survey region was predicted by the model.

Table 3-6: Confusion Matrix results for Topaz Mountain.

Smoothing	Predicted flow area (km²)	TP	FP	% survey predicted	% prediction inside observed	% prediction outside observed	TP/ observed	FP/ observed	(TP-FP)/ observed
3x3	183.9	83.4	100.5	27%	45%	55%	27%	33%	-5.6%
5x5	129.0	73.3	56.2	24%	57%	44%	24%	18%	5.5%
7x7	243.6	118.3	125.6	38%	49%	52%	38%	41%	-2.4%
9x9	256.3	168.2	88.1	54%	66%	34%	54%	29%	25.9%
11x11	**268.6**	**194.7**	**73.9**	**63%**	**72%**	**28%**	**63%**	**24%**	**39.1%**
13x13	280.8	198.3	82.4	64%	71%	29%	64%	27%	37.5%
15x15	363.6	230.6	133.1	75%	63%	37%	75%	43%	31.5%
17x17	380.9	233.7	147.2	76%	61%	39%	76%	48%	28.0%
19x19	422.5	258.7	163.8	84%	61%	39%	84%	53%	30.7%
21x21	457.6	268.9	188.7	87%	59%	41%	87%	61%	26.0%
23x23	472.9	267.3	205.6	87%	57%	43%	87%	67%	20.0%
25x25	476.5	267.1	209.5	86%	56%	44%	86%	68%	18.7%

As has been seen in other source regions, the model's predictions suffer in the large flat basin bottoms. At Topaz Mountain, to the west in the Fish Springs Flat, the prediction is both too

extensive (traveling north to the Fish Spring Wildlife Refuge) and not expansive enough (failing

to capture flow to the extreme southwest as the basin abuts the eastern edge of the Fish Springs

Range. Similarly, in the flow predicted from the new northern source, even the 11x11 prediction

expands well into the Dugway Proving Grounds, but the observed flow vanishes much earlier,

reminiscent of the Ferguson Wash flow. As in that case, these areas were impacted by the Lake

Bonneville highstand (Figure 3-73) and that may be confounding model accuracy.
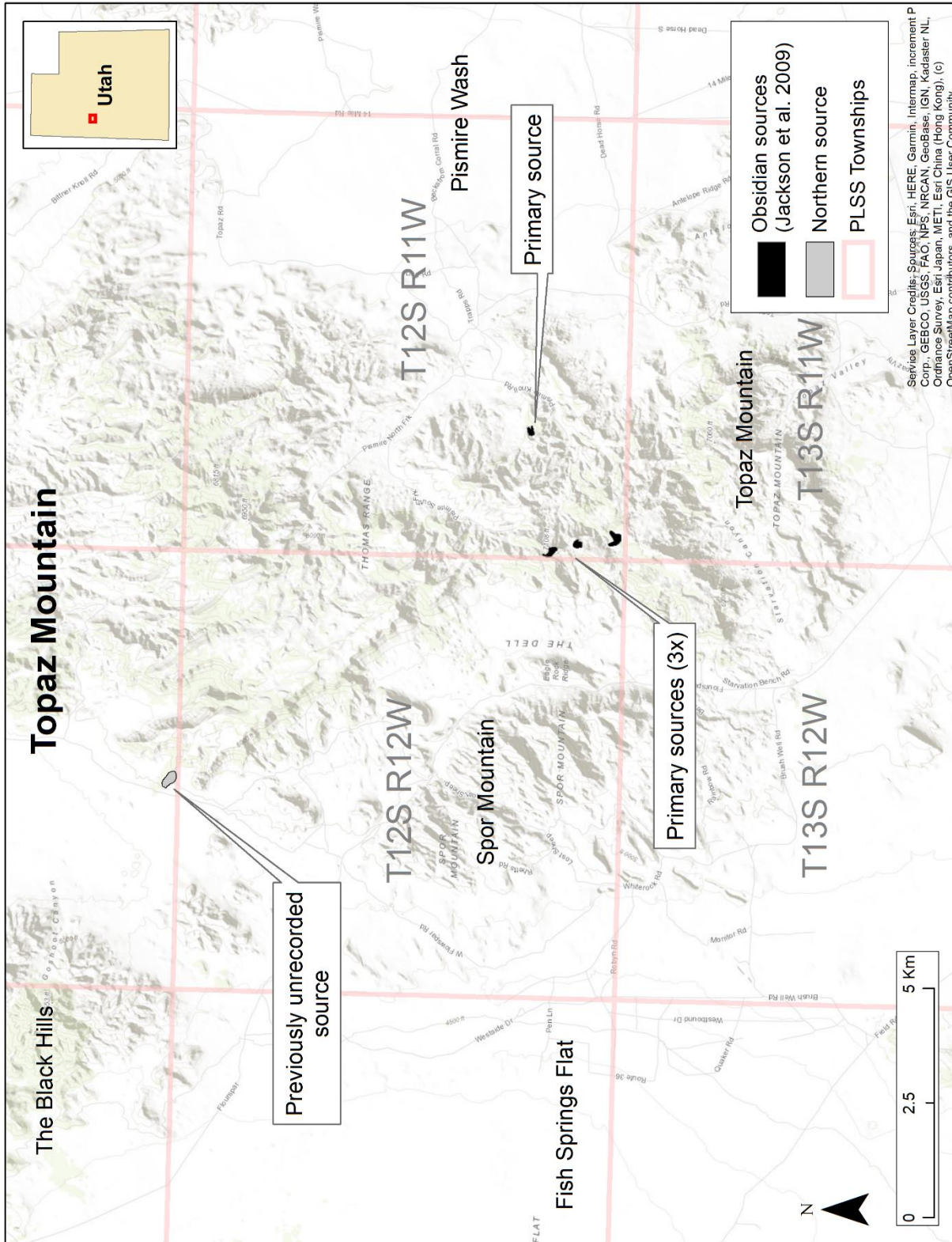
Figure 3-63: Topaz Mountain regional view.
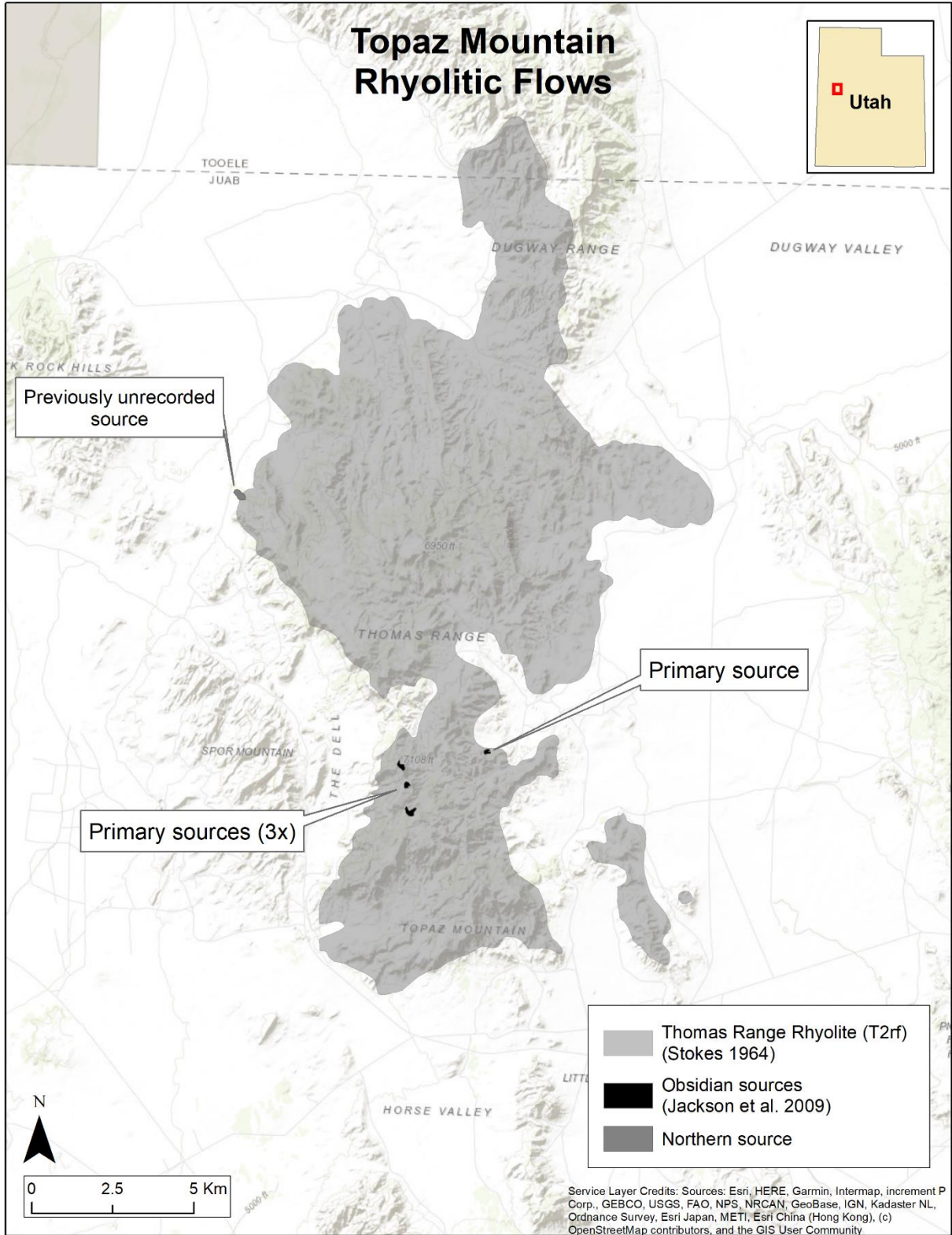
Figure 3-64: Topaz Mountain/Thomas Range Rhyolite and obsidian.
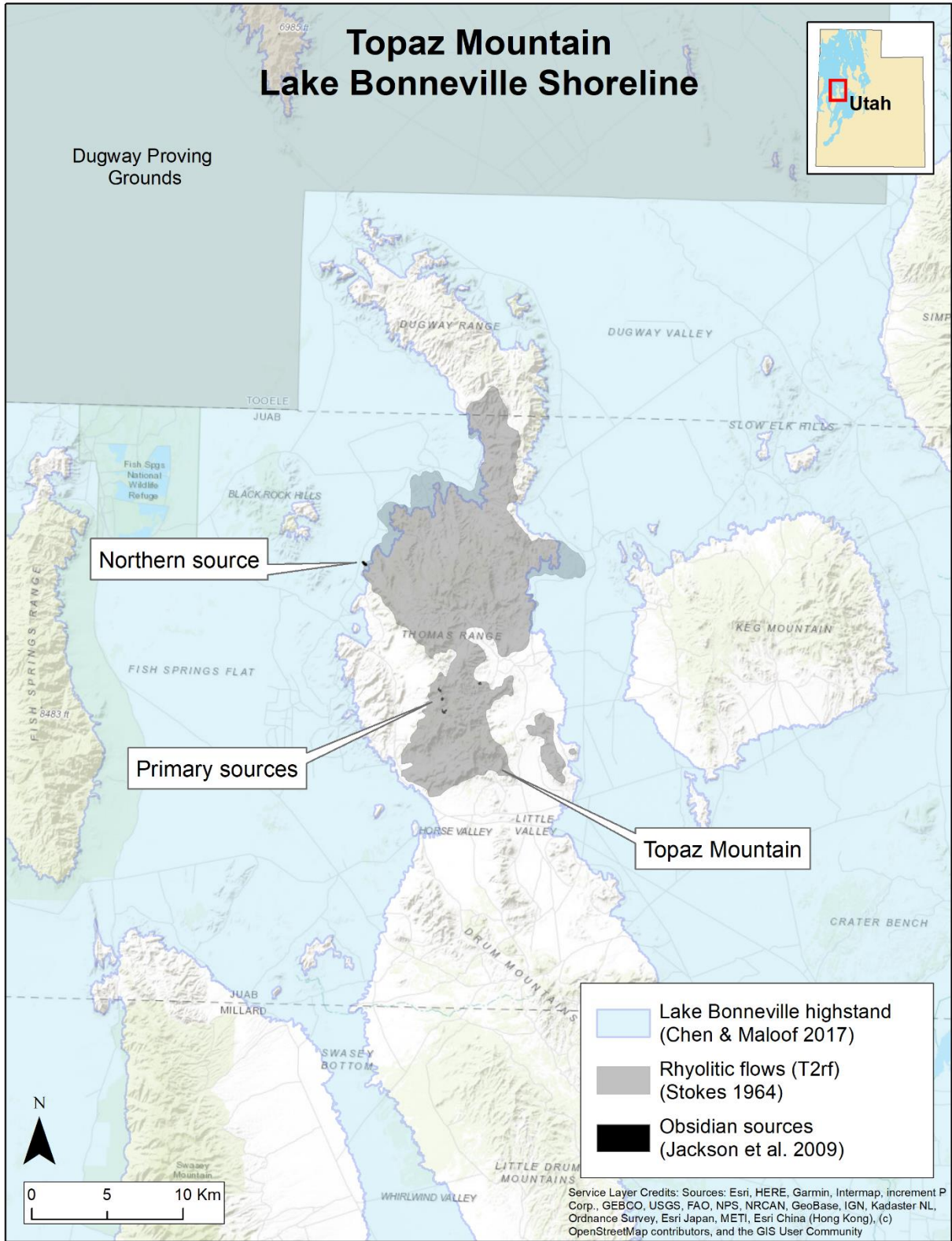
Figure 3-65:Topaz Mountain/Thomas Range primary sources in relation to the Lake Bonneville highstand.
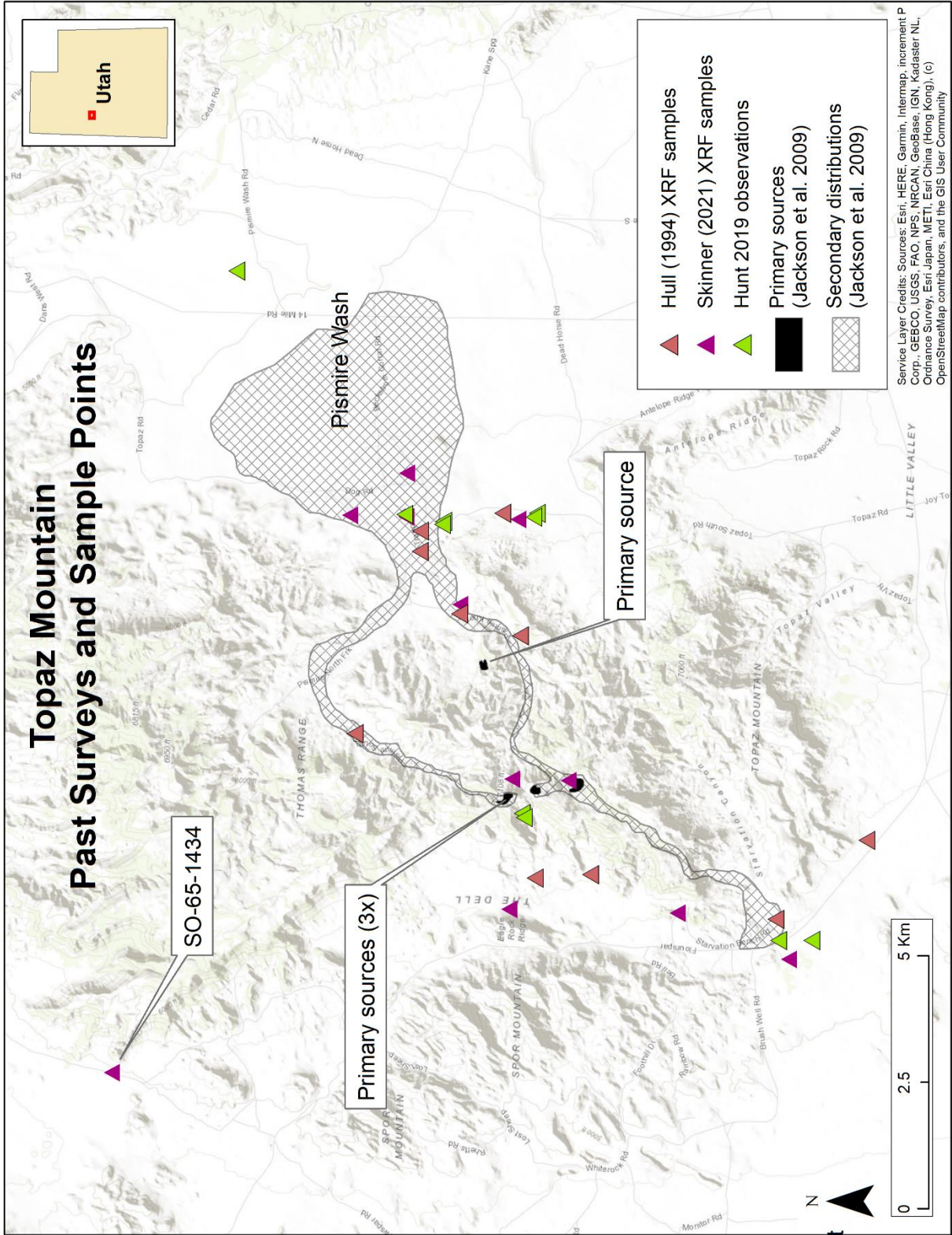
Figure 3-66: Topaz Mountain past surveys and sample points.
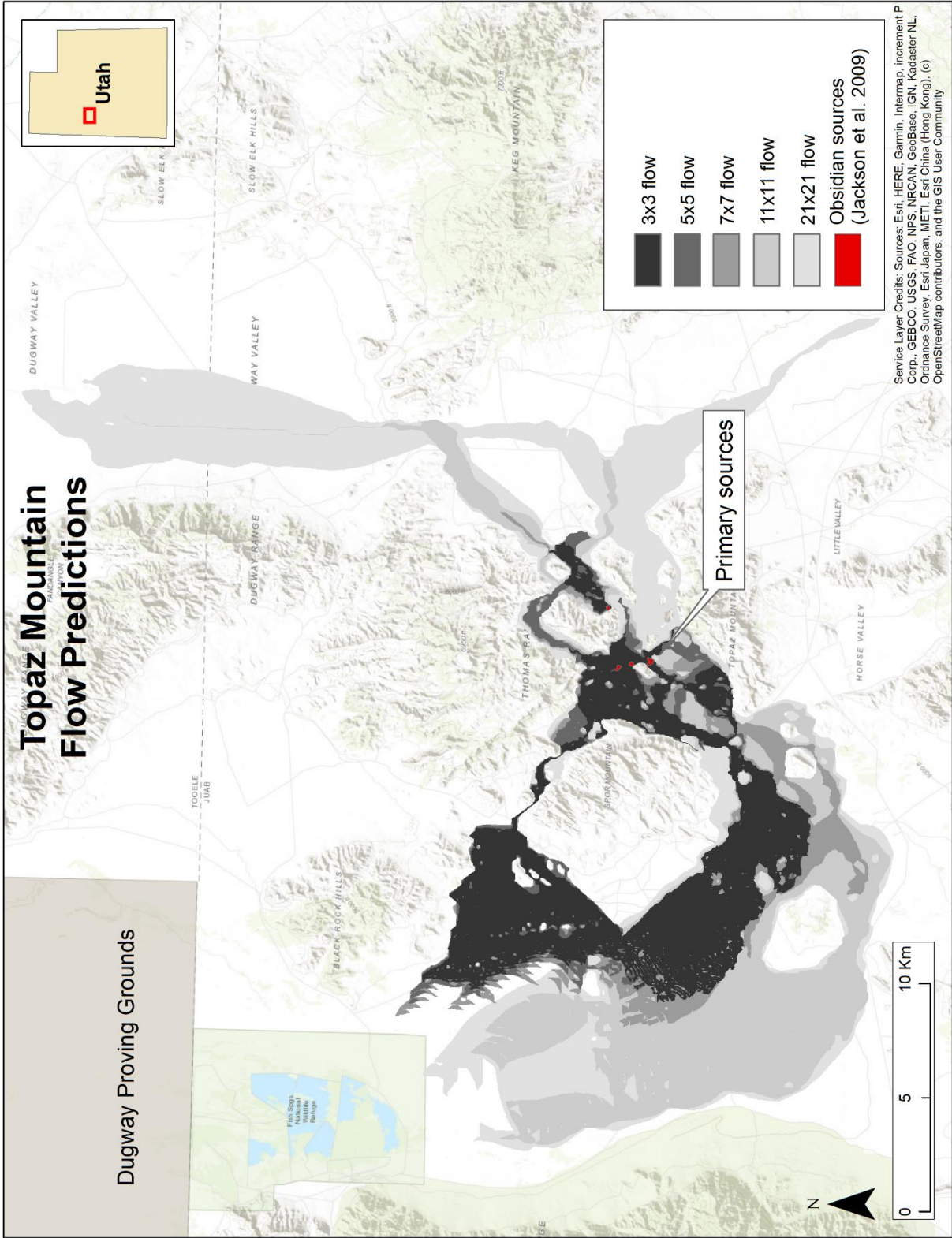
Figure 3-67: Topaz Mountain flow predictions.
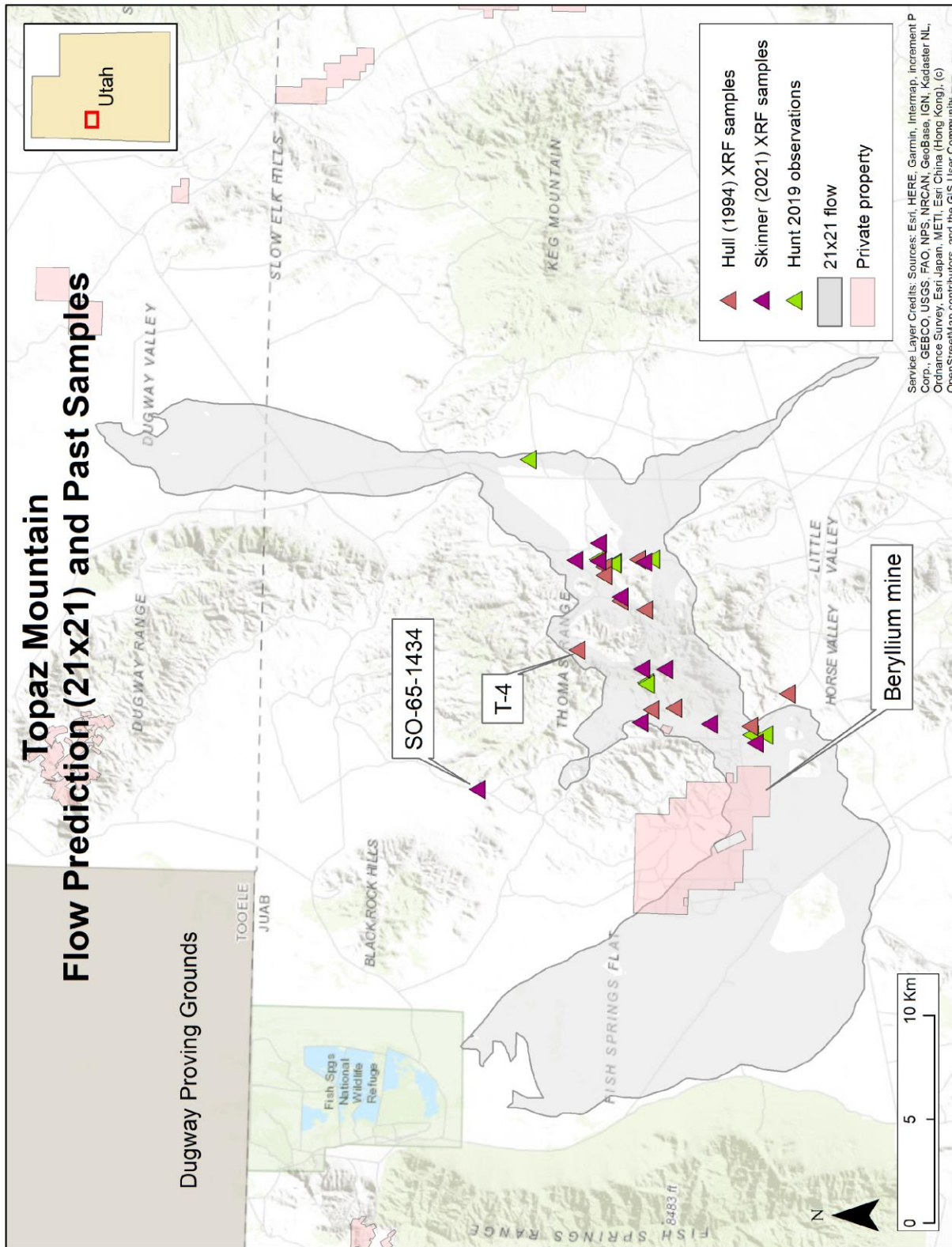
Figure 3-68: Topaz Mountain 21x21 flow prediction in comparison with past sampling.
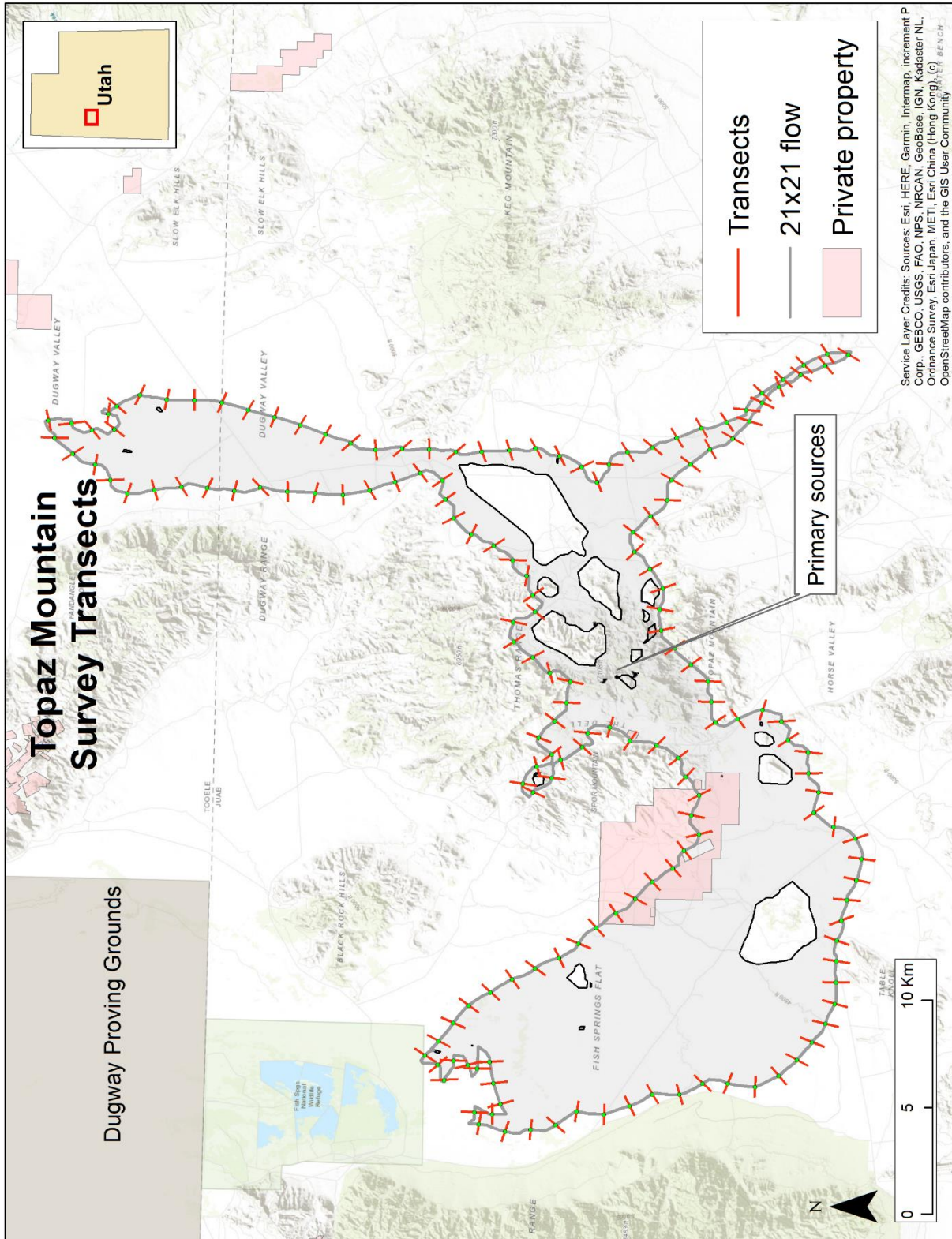
Figure 3-69: Topaz Mountain 21x21 survey outline and transects.
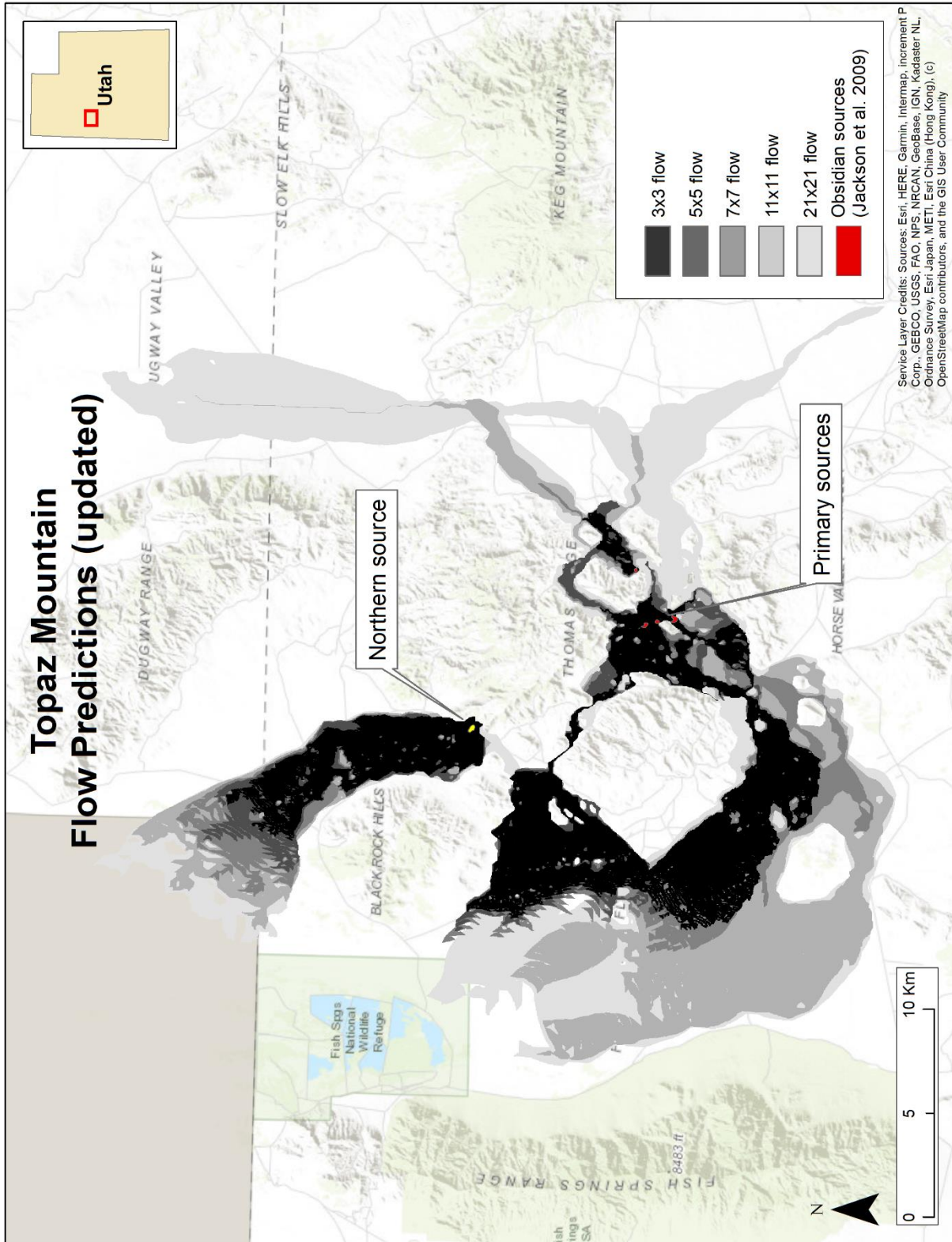
Figure 3-70: Topaz Mountain expanded flow predictions.
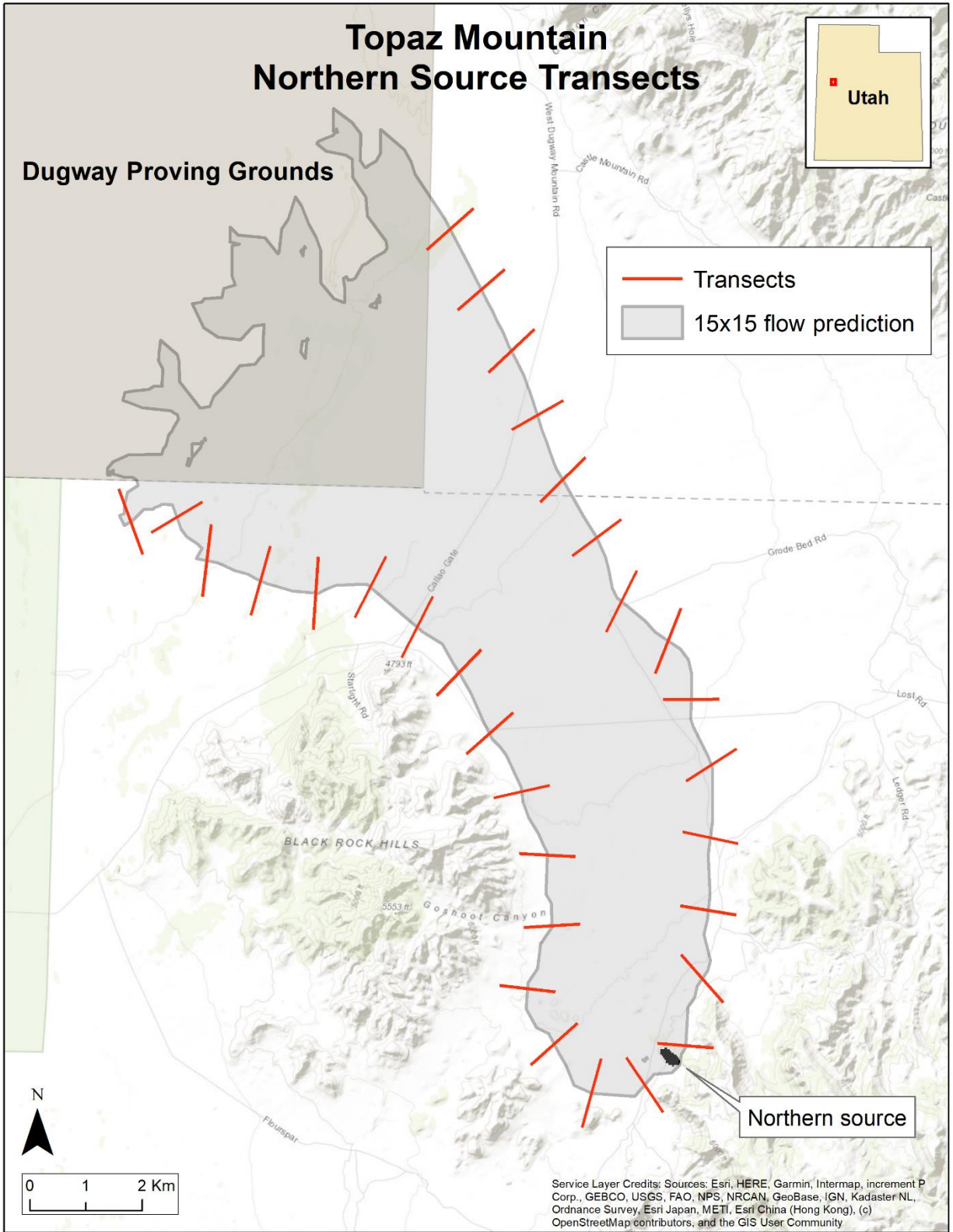
Figure 3-71: Topaz Mountain northern source 15x15 survey outline and transects.
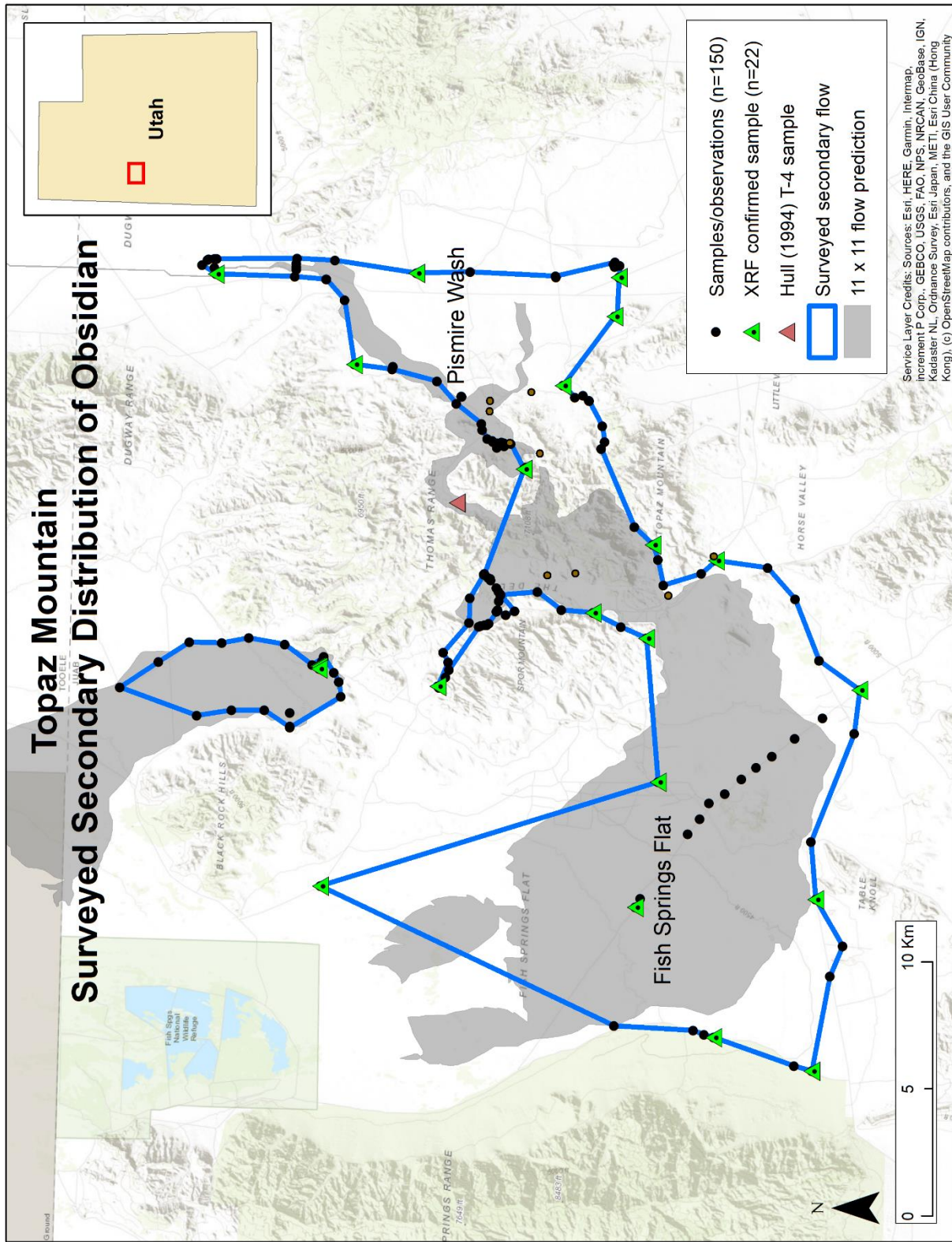
Figure 3-72: Topaz Mountain survey results.
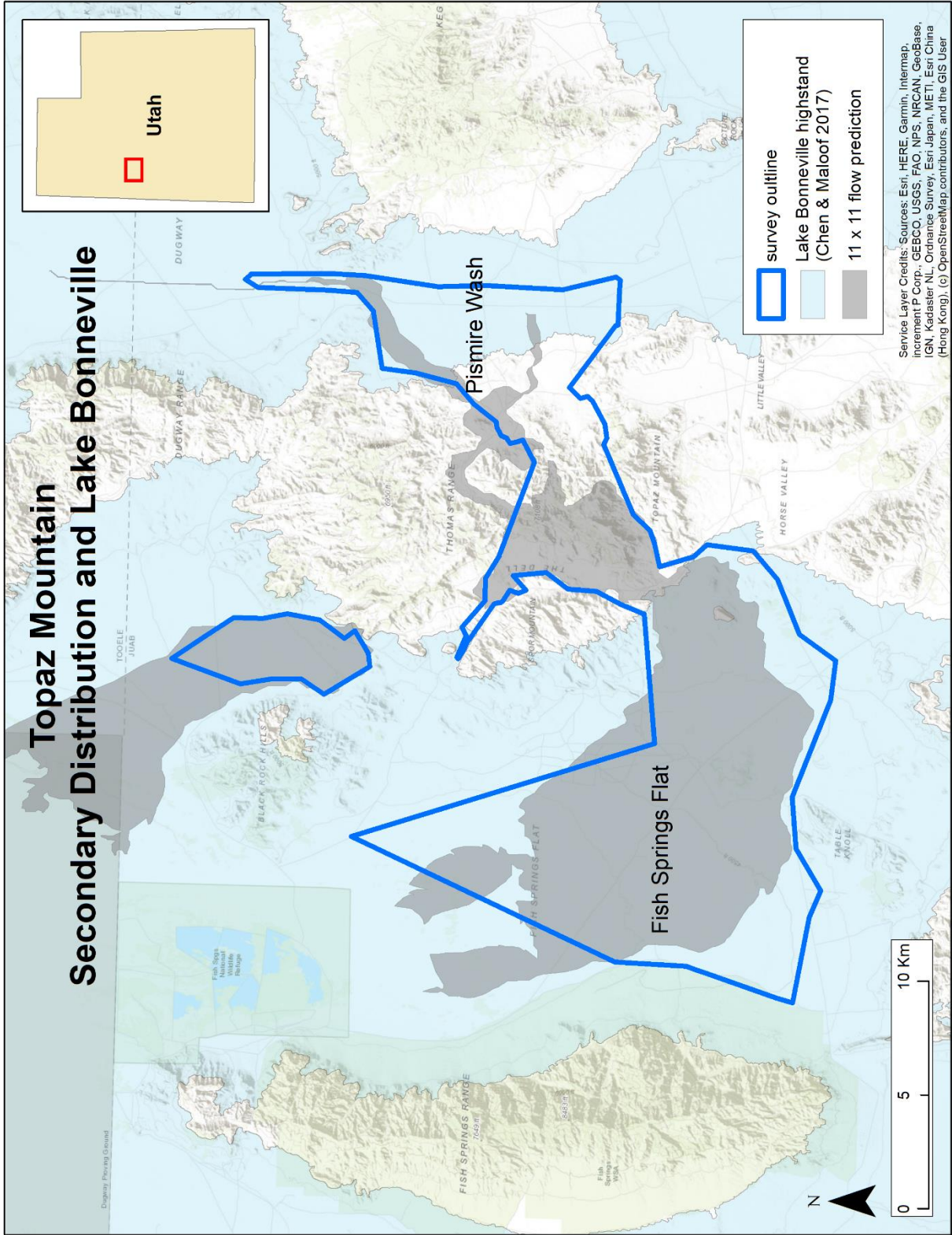
Figure 3-73: Topaz Mountain secondary distribution in relation to Lake Bonneville.

3.7 Conclusion

The goal of this chapter is to determine if a universal methodology, using known primary obsidian source data, can be applied to determine the extent and scale of a source's secondary distribution. This distribution represents the exposure component of the Discoverability signal (*Equation* 2-2) that this source would have presented on the landscape to hunter-gatherers seeking toolstone. While the accuracy and precision of matching the exact flow would be optimal, in terms of Discoverability the ultimate goal is one of exposure scale (*E*) and the scale factor of that signal in comparison to other sources.

$$D = E * \frac{1}{d^2}$$ (Eq. 2-2)

Using the Best Fit equation (*Equation* 3-4 above), the optimal DEM smoothing was determined for each of the five test sources. These are summarized in Table 3-7. As noted in section 3.6.2, the conditions at Ferguson Wash produced results far out of the norm and this was attributed to the full immersion of the site by Lake Bonneville. For this reason, those results are excluded here.

Table 3-7: Best Fit smoothing summary.

Source	Observed extent (km²)	Predicted extend (km²)	Best Fit smoothing	Best Fit extent (km²)	% survey predicted	Scale factor (prediction / observed)
BRA	353	288	13x13	227	64%	82%
MM	160	142	23x23	142	82%	89%
PS/M	330	223	13x13	223	54%	68%
TM	309	269	11x11	269	63%	87%
Average	**288**	**230**	**15x15**	**215**	**66%**	**81% ± 10**

From these results, limited as they are, we see that the average correctly predicted flow (TP/observed) is 66%. However, just in terms of scale factor of the flow, when comparing the size of the predicted flow (regardless of precision) to the size of the observed extent, this value improves dramatically to 81%. This alone suggests that the scale factor is consistent when comparing prediction results.

If the average Best Fit smoothing (15x15) is applied to all four sources, we see further improvement in these results (Table 3-8):

Table 3-8: Scale factor results with 15x15 smoothing.

Source	Observed extent (km²)	15x15 extent (km²)	% survey predicted	Scale factor
BRA	353	303	66%	86%
MM	160	128	75%	80%
PS/M	330	234	49%	71%
TM	309	364	75%	118%
Average	**288**	**257**	**66%**	**89% ± 20**

This level of smoothing (15x15), which I am naming the Smoothing Index, will now be applied in Chapter 4, as E is calculated for each of the obsidian and fine-grained volcanic sources that were utilized in the final cleaned Paleoindian dataset from the ORB delta (Appendix A).

Chapter 4: Flow Predictions for Toolstone Sources Used by the Paleoindian Occupants of the Old River Bed delta

4.1 Introduction

The purpose of this chapter is to quantify the discoverability of the obsidian and fine-grained volcanic (FGV) toolstone sources used within the Old River Bed (ORB) assemblage (Madsen, Schmitt, et al., 2015). The previous chapter provides a guide for the level of digital elevation model (DEM) smoothing needed to predict the secondary distributions of these sources and then extract a discoverability value from the extent of the sources.

Accomplishing this goal requires a dataset of geolocated Paleoindian artifacts associated with dated channels within the ORB delta/wetlands. The steps taken to generate this dataset, and the dataset itself, are provided in Appendix A. The process described in that appendix provided a total of 442 Paleoindian artifacts in association with a dated ORB channel and with an assigned geochemical (source) type (Table 4-1). Each of these sources will be described briefly in the following sections and an exposure (E) value, as described in Chapter 3, will be calculated for each. Those samples returning an "unknown" geochemical signature (n=12) will be dropped from further analysis.

4.2 Methodology

A distinction needs to be made between the sources surveyed in Chapter 3 and those representing the full complement of toolstone sources used in the ORB (Table 4-1). The sources surveyed in Chapter 3 served as test examples for the flow prediction methodology. Part of the selection process for those test areas included the requirement of an adequate existing description of the primary source. This allowed initial predictions that were tested by field work and, in some cases, led to the discovery of additional primary sources. The data available for

characterizing the primary source areas for each of the remaining sources in Table 4-1 varies

significantly. Some sources (e.g., Brown's Bench) are widely studied with many sample points

by multiple authors, while other sources (e.g., Paradise Valley) are represented by only a few

Table 4-1: Old River Bed delta Paleoindian toolstone sources.
Bolded sources are documented in Chapter 3.

Sources	Totals
Badlands	18
Bear Gulch	1
Black Rock Area	10
Browns Bench	41
Browns Bench Area	5
Cedar Mountain	8
Currie Hills	3
Deep Creek	10
Ferguson Wash	1
Flat Hills	182
Kane Springs Wash Caldera	1
Malad	4
Mineral Mountains	9
Panaca Summit/Modena	1
Owyhee	2
Paradise Valley	3
Pumice Hole Mine	1
Topaz Mountain	130
Unknown 1	1
Unknown FGV	6
Unknown OBS	5
Total	**442**

sample points or by sample points that are generalized to township-range sections with much

lower spatial precision. I have also relied primarily on samples recorded using a GPS device,

though even some of those are limited in precision. In cases where overlap in sample sets occurs

between two authors, I have chosen the data points with the greatest available precision.

In cases where only sporadic samples on the landscape are available (e.g., Currie Hills) or appear isolated to a single topographical flow path (e.g., Cedar Mountain), I use GIS tools to apply a 20-meter buffer around these points. These buffers are then used to create the weighted rasters (section 3.3.4) by capturing several raster cells to act as seeds, or proxy sources, for calculating flow accumulations. Where extended cobble fields are known from the literature (e.g., Panaca Summit/Modena and Bear Gulch) or can be inferred by high sample density (e.g., Browns Bench and Owyhee), I aggregate points to form a polygon or polygons that effectively represent a cobble field and use these to create the weighted raster.

It should also be noted that for many samples, it is unknown whether the sample was originally collected from a primary or secondary context. This exposes one weakness of the prediction model in that it assumes the most elevated, or upslope, seed is a primary source and that there is no distribution above it in elevation. This is a problem that only more fieldwork at each source location can eliminate. For now, the scale of a source's discoverability is represented by the flow prediction from known sample points. There is much more work to be done here.

4.3   Fine-grained Volcanics

Chapter 3 discusses the physical characteristics and formation processes of obsidian; however, within the Great Basin, non-glassy volcanic rock has long been recognized as a key raw material in lithic assemblages (Arkush & Pitblado, 2000; Beck & Jones, 1990; Jones & Beck, 1990). Over the years, a number of appellations have been applied to this material, from the most commonly used, "basalt" (Graf, 1995; Jones & Beck, 1990; Rice, 1972; Sargeant, 1973; Tuohy, 1968), to "glassy basalt" (Arkush & Pitblado, 2000, p. 12), "fine-grained eruptives" (Rogers, 1939, p. 16), and perhaps even "dull obsidian" (Amsden, 1937, p. 78). Over time, it was recognized that these artifacts were usually not fashioned from actual "basalt" but rather from

fine-grained volcanic rock within a range of silica-alkali compositions (Figure 4-1), primarily

composed of andesite, dacite, trachyandesite, or trachydacite (Duke, 2011, 2013; Jones et al.,

1997; Le Bas, 1986; Page, 2008). Within archaeological literature, the attribution "fine-grained

volcanic(s)", or FGV(s), is now the standard term for this family of toolstone raw material.

While obsidian provenance analysis via X-ray fluorescence (XRF) has been in practice for

more than half a century (Cann & Renfrew, 1964; Jack & Heizer, 1968), XRF testing on non-

glassy volcanic material is a relatively recent endeavor (M. S. Shackley, 2010). In the 1990s,

pioneering efforts by workers like Latham et al. (1992), Weisler and Woodhead (1995) and Jones

et al. (1997) demonstrated that XRF could, in fact, be used to geochemically identify FGVs.

Unlike obsidian, which is formed from "supercooled liquid silica melt" (Hughes, 1986, p. 21)

and is therefore compositionally homogenous, FGVs represent the same melt differentially

cooled and crystalized, raising concerns of geochemical heterogeneity, which could lead to

inaccurate and irreproducible XRF readings. These concerns have been alleviated and with

appropriate sample selection, XRF is now considered a standard means of identifying FGV

geochemical types (Jones et al., 1997; Craig Skinner, personal comm., May 31, 2021).

The geographical sourcing of FGV types within the Great Basin has been led by workers

such as Jones et al. (1997), Page (2008), Skinner (Page & Skinner, 2008; see also Appendix D,

Table D-2), and Duke (2011, 2013). The work by Page (2008) is of particular importance to this

project as he identifies the sources of five FGV types/subtypes (Badlands A, Cedar Mountain B,

Currie Hills, Deep Creek A, and Flat Hills A, C, D, and E) that appear in the ORB dataset. The

total alkali-silica range of these samples is illustrated by the hatched area in Figure 4-1

Understanding the geographical location of these FGV sources allows their inclusion in my final

Discoverability analysis and increases the overall size of the artifact dataset (n=442).
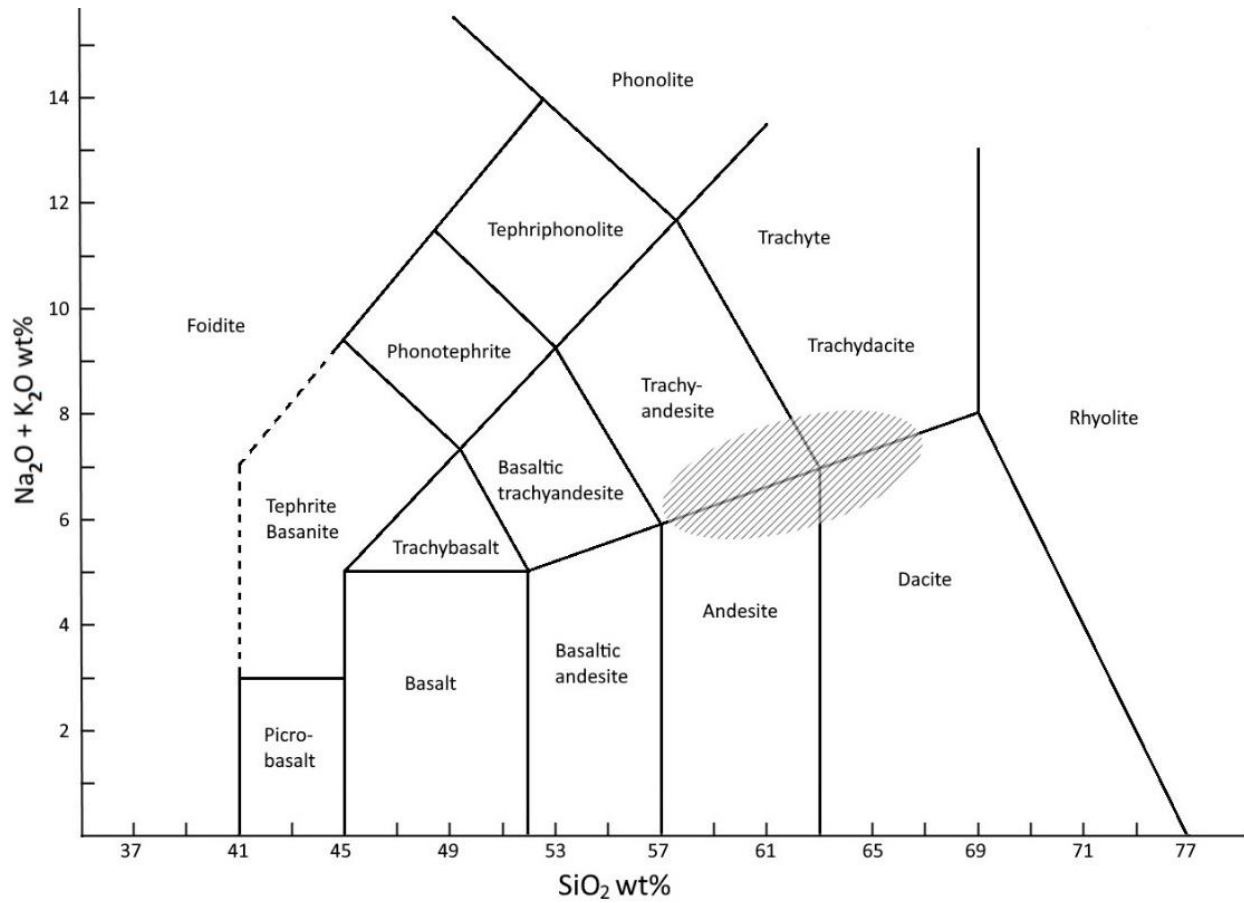
Figure 4-1: Total Alkali Silica (TAS) diagram showing the general range (hatched region) of alkali-silica profiles from several known fine-grained volcanic (FGV) sources identified in Old River Bed delta artifacts (after Le Bas, 1986; Le Bas & Streckeisen, 1991; Page, 2008).

4.4 ORB Sources

4.4.1 Badlands

Source type: Fine-grained volcanic; trachyandesite (Page, 2008)

Location: Western Tooele County, Utah and eastern Elko and White Pine Counties, Nevada. The Badlands A subtype is present ~60 km east at Wildcat Mountain, Tooele County, Utah.

Alternative names: None, but two subtypes (A and B) and its distribution geographically overlaps with the Deep Creek FGV distribution.

Page (2008) sample points: *n*=14 (see Appendix D, Table D-5)

Skinner sample points: *n*=27 (see Appendix D, Table D-2)

ORB Paleoindian artifacts: *n*=18 (Table 4-1)

The distributions of Badlands and Deep Creek FGV types are found largely overlapping to the northwest of the Deep Creek Range in western Tooele County, Utah and southeast of White Horse Mountain in Elko County, Nevada. For my purposes here, it would make sense methodologically to combine the Badlands and Deep Creek types into a single Discoverability signal, save for an exposure of Badlands A FGV present at Wildcat Mountain (see inset in Figure 4-2). This exposure, roughly 70 km northeast of the Old River Bed sites, and deep within the Utah Test and Training Range-South military zone, is significantly closer to the ORB than the western exposure. For this reason, the Badlands and Deep Creek FGV types are presented separately, though they share many of the same landscape attributes.

Compared to our understanding of many of the other areas I discuss here, the geology of this region has not been examined in detail. Crafford (2007) defines the region's low-lying, unnamed ridges as andesite or dacite flows from 30 to 45 Ma (*Ta1* in Figure 4-2). Aside from these volcanic flows, the area is largely comprised of more recent sedimentary deposits and

alluvium. To the east, at Wildcat Mountain, Moore and Sorensen (1979) suggest a late Permian or early Pennsylvanian origin (roughly 300 Ma) for the mountain, with a Tertiary (5.3 – 56 Ma) basalt on the west side, but go no further. Clark et al. (2016) document the latitic/trachyandesite intrusions on the west side of Wildcat Mountain (*Tlw* in the Figure 4-2 inset) and suggest a possible Eocene age (roughly 34 – 56 Ma; they specifically note that the geology was not dated), in line with the timing of regional volcanism (see section 3.2).

Archaeologically, most of our understanding of this area and of the Badlands FGV geochemical type comes from the work by Page (2008), who classifies the source as a trachyandesite and other unknown FGV types. Duke (2013) makes the point that there is no distinct primary source location for the Badlands type, so all samples are in a context of secondary distribution.

Two sets of sample points were used for the flow prediction. Page (2008) provides 14 FGV samples in secondary context for the western distribution region. Skinner (Table D-2), who provided the XRF analysis for Page, provided 28 sample points, of which 14 were unique from Page (2008). Three of these samples are located at Wildcat Mountain and characterize the Badlands A signature for that exposure. One of the Skinner samples is located more than 100 km to the west in Mahoney Canyon on the east side of Big Bald Mountain, Nevada. This single, distant sample was excluded from the flow calculations as it will have no impact on the overall ORB discoverability calculations for the majority exposure extent for the Badlands FGV, which is quite close to the ORB delta.

The points were combined (*n*=28), buffered to 20 m, and the 15x15 flow is predicted in Figure 4-2.

The Badlands FGV source has an exposure (*E*) value of 72 km^2.
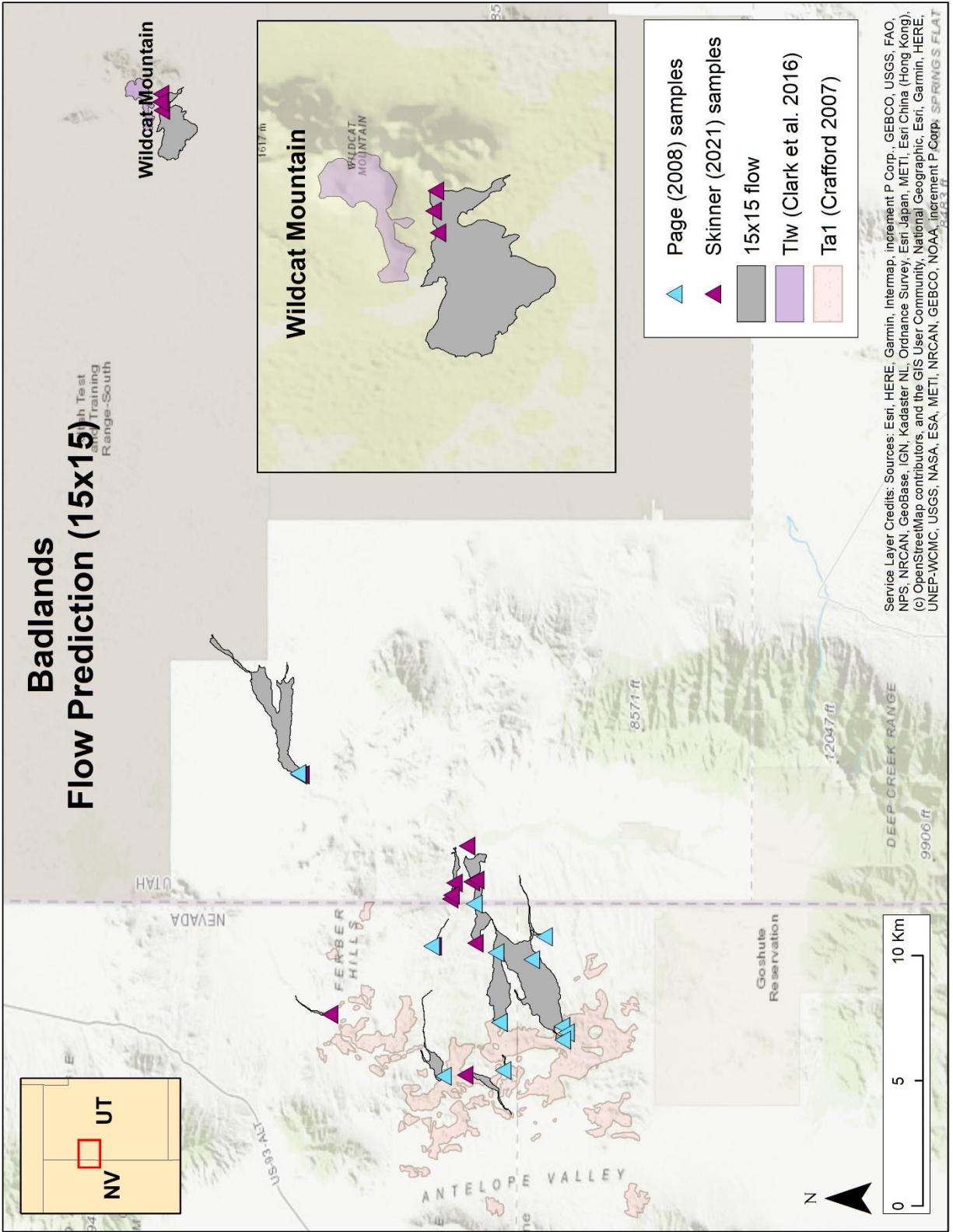
Figure 4-2: Badlands fine-grained volcanics (FGV) 15x15 flow prediction.

4.4.2   Bear Gulch

Source Type: Obsidian

Location: Clark County, Idaho

Alternative names: Big Table Mountain (Willingham, 1995), Camas/Dry Creek (Michels 1983, cited in Bailey, 1992; Wright et al., 1990), Centennial (Sappington, 1981), F.M.Y. 90 Group (Griffin et al., 1969), Spring Creek (Gallagher, 1979), Reas Creek (Fowler, 2014), Warm Creek Spring (Kimball 1976, cited in Holmer, 1997), West Camas Creek (Gallagher, 1979)

Skinner sample points: *n*=7 (Table D-2, two samples share identical locations with two others)

Richard Holmer (personal comm., July 24, 2019): *n*=4 (Table D-4)

ORB Paleoindian artifacts: *n*=1 (Table 4-1)

The Snake River Plain experienced a series of explosive eruptions of high-silica rhyolites over the last 16 Ma. These occurred as the North American continental plate moved in a southwest direction over a mantle hot spot (Figure 4-3) which now, after effectively cutting across the northern Basin and Range Province, resides beneath the Yellowstone caldera (Morgan & McIntosh, 2005). These pyroclastic eruptions produced massive ash-flow sheets, the basal units of which, in some instances, cooled quickly enough to form artifact-grade obsidian (Hughes & Smith, 1993; Morgan & McIntosh, 2005).
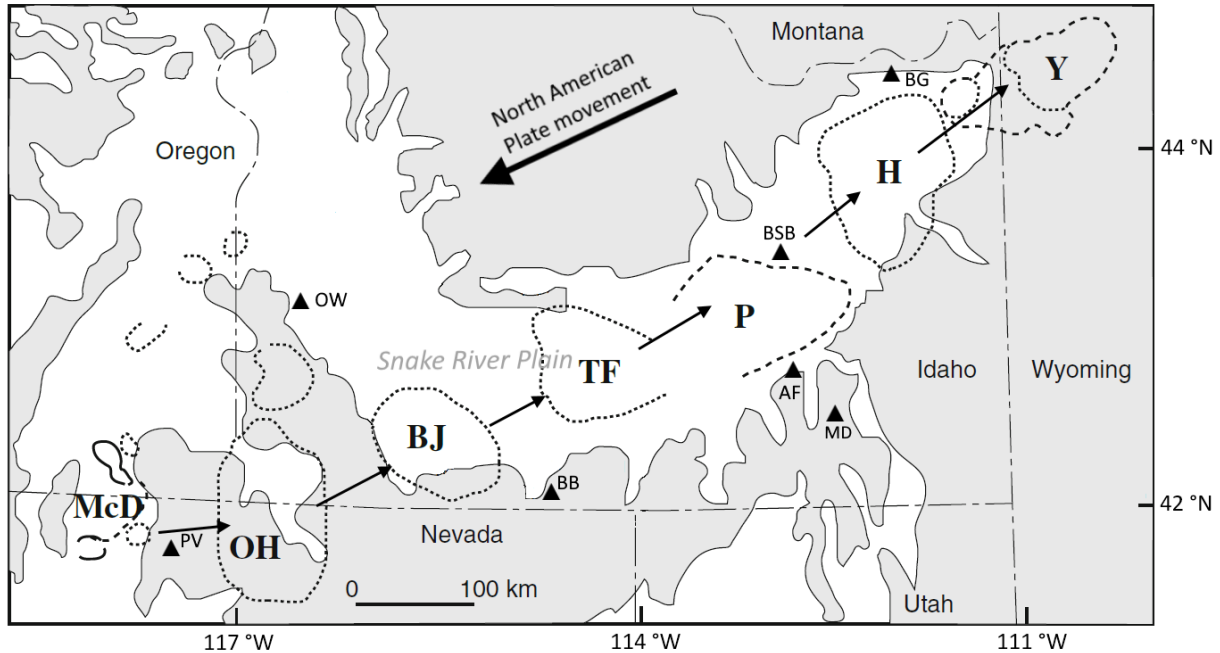
Figure 4-3: Progression of the Yellowstone hot spot and resultant eruptive centers across the Snake River Plain; large abbreviations: McD, McDermitt (~16.1 Ma), OH, Owyhee Humboldt (~14 Ma), BJ, Bruneau-Jarbridge (~12.7 Ma), TF, Twin Falls (~10.8 Ma), P, Picabo (~10.2 Ma), H, Heise (~6.6 Ma), and Y, Yellowstone (~2.05 Ma). Black triangles are common obsidian source locations: AF, American Falls, BB, Brown's Bench, BG, Bear Gulch, BSB, Big Southern Butte, MD, Malad, OW, Owyhee, PV, Paradise Valley. After Ellis et al. (2012). Eruptive center dates are from Ellis et al. (2012).

The origins of the obsidian found in the Bear Gulch area, south of Big Table Mountain and within the Centennial Mountains of Idaho, are geologically poorly understood. First identified as geochemically distinct by Griffin et al. (1969), Sappington (1981) reported that its origins were variously attributed to either an obsidian welded tuff or an ignimbrite, but suggests it is best characterized as a vitrophyre. Willingham (1995) argues that the obsidian boulders and cobbles are the product of obsidian outcrops exposed during Pliocene (5.33 – 2.58 Ma) uplift of the mountains around Big Table Mountain and the subsequent erosion of the same. Homing in on the primary source location was equally difficult, made more challenging by the host of names attached to the obsidian (see list above), including that of a nearby obsidian with a similar name

(Centennial Valley) but a distinctly different geochemical signature. Hughes and Nelson (1987) established the central source area around Bear Gulch and attached the current appellation.

The detection of Bear Gulch obsidian in numerous archaeological sites, over a widespread geographical area, was a key motivator in the search for the Bear Gulch source location. First recognized in samples found in Yellowstone National Park (described then as "Field Museum Yellowstone 90", or "FMY 90"), Bear Gulch obsidian is found in archaeological sites throughout states to the east (Minnesota, Ohio, Illinois, Indiana), to the south in Iowa and along the Mississippi Valley, and north into Montana and Alberta (Hughes, 2007b; Hughes & Nelson, 1987; Scheiber & Finley, 2011; Willingham, 1995). The resource has been exploited by Native Americans for millennia, appearing in assemblages ranging from Paleoindian to Hopewell (Hughes, 2007b; Willingham, 1995). Willingham reports multiple large quarries at Big Table Mountain, many with "debitage backfill over one meter thick" (1995, p. 3).

Willingham (1995) provides the best and most current regional outline of the source (Figure 4-4), encompassing almost 63 km^2, but includes no specific details of primary source outcrops. The known boundaries of this source includes the southern side of Big Table Mountain, Castle Peak, and Bear Gulch, and extends southeast along a ridge, almost to Button Peak. In this case, I methodologically treated this extent in the same manner as the cobble field on the east slope of Panaca Summit/Modena and converted the outline of this extent to a polygon that was used to calculate the flow prediction. It is notable that the prediction captures all of the sample points provided by Holmer (Table D-4) and 5 of the 7 samples provided by Skinner (Table D-2), with the only two exceptions (two samples that share the same location) occurring about 500 m from the predicted flow edge.

The Bear Gulch obsidian source has an exposure (*E*) value of 129 km^2.
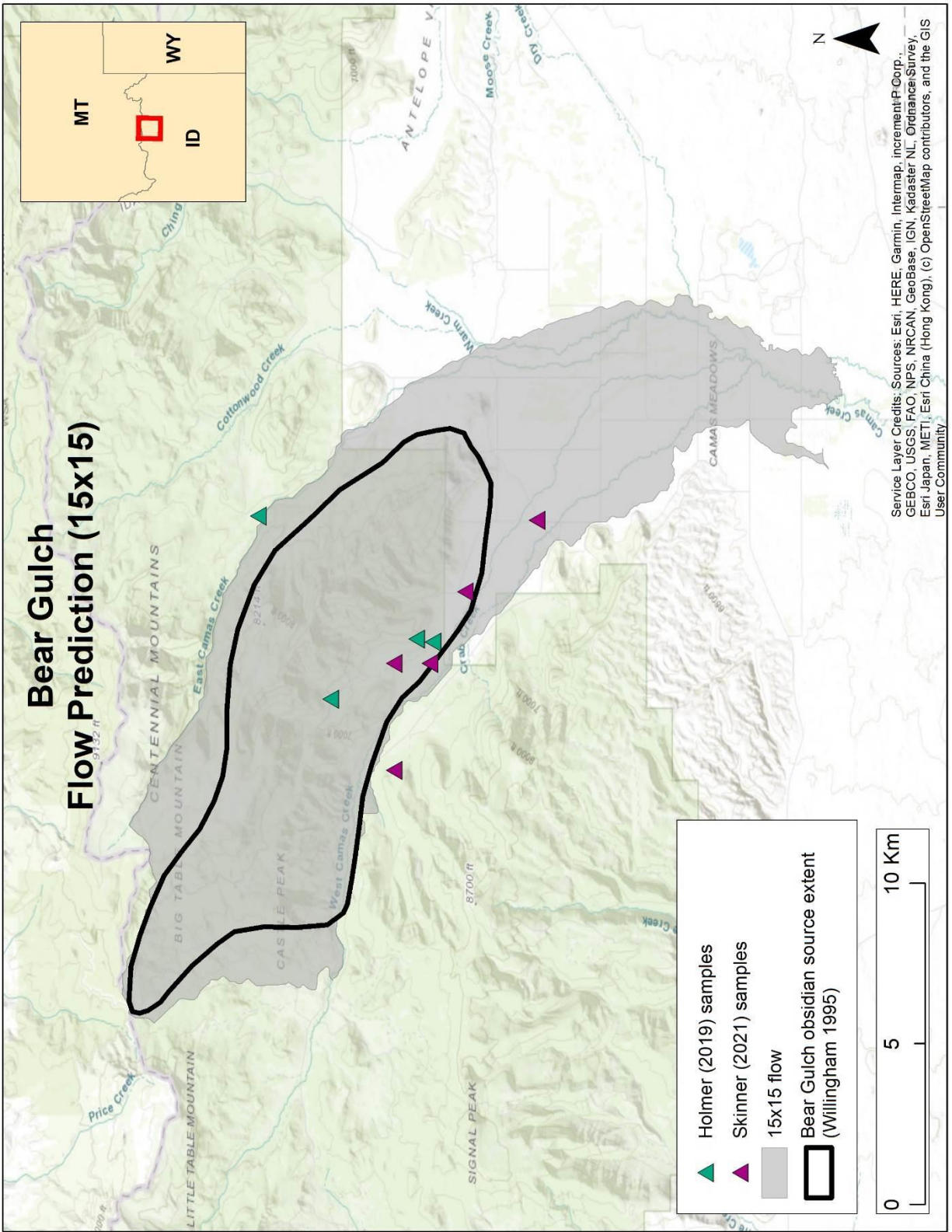
Figure 4-4: Bear Gulch obsidian 15x15 flow prediction.

4.4.3 Brown's Bench, Brown's Bench Area, and Butte Valley Group A

Source Type: Obsidian

Location: Twin Falls and Cassia Counties, Idaho

Alternative names or localities: Browns Bench (Bowers & Savage, 1962), Brown's Bench Ranch (Hughes, 1990), Cedar Creek (Bailey, 1992), Coal Bank Creek (Jones, Beck, Jones, et al., 2003), Coal Bank Spring (Page & Bacon, 2016), Cottonwood Ranch (Hughes, 1990), Goose Creek, Hudson Ridge, Jackpot (Skinner, 2021), Little House Creek (Bailey, 1992), Murphy Springs (Page & Bacon, 2016), Rock Creek (Gallagher, 1979), Mahogany Butte (Fowler, 2014), Three Creeks (Gallagher, 1979), Three Creek Landfill, Three Creek 2 (Bailey, 1992), and Twin Meadows (Hughes, 1990)

Page and Bacon (2016) sample points: Brown's Bench type (*n=58*), Brown's Bench Area type (*n=12*), Butte Valley Group A type (*n=28*) (Table D-6)

Richard Holmer (personal comm., July 24, 2019): *n=18* (Table D-4)

Skinner sample points: Brown's Bench type (*n=45*), Brown's Bench Area type (*n=4*), Butte Valley Group A type (*n=7*) (Table D-2)

ORB artifacts: Brown's Bench type (*n=41*), Brown's Bench Areas type (*n=5*), Butte Valley Group A (*n=0*) (Table 4-1)

In the central Snake River Plain, the Bruneau-Jarbridge (BJ) and Twin Falls (TF) eruptive centers (Figure 4-3) produced a succession of massive rhyolitic ignimbrites, beginning around 13 Ma (Ellis et al., 2012). The Bruneau-Jarbridge center produced at least nine of these intensely-welded ignimbrites between 12.8 and 10.5 Ma, creating accumulations over 500 m thick which are characterized as the Cougar Point Tuff (Bonnichsen et al., 1988, 2008; Cathey & Nash, 2004; Ellis et al., 2012). These ignimbrite eruptions were expansive and are considered to have been

regionally devasting, with one such eruption, Cougar Point Tuff XIII, ejecting more than 1,000

km^3 of material across the Plain (Ellis et al., 2012). The region was also subjected to numerous

large-volume rhyolitic lava flows following individual ignimbrites (Bonnichsen et al., 2008). The

end result was a cumulative volume of tens of thousands of cubic-kilometers of rhyolitic magma

spread across southern Idaho, northern Nevada, and northwestern Utah (Bailey, 1992;

Bonnichsen et al., 2008; Reid et al., 2015).

The Brown's Bench fault in southern Idaho (BB in Figure 4-3) exposes at least 13 such

ignimbrites, most of which likely correlate with the Cougar Point Tuff succession, but about

which little more is known (Ellis et al., 2012). The ignimbrites produced vitrophyre sources as

they cooled, creating a widespread obsidian source in the Brown's Bench region with cobbles up

to 30 cm in diameter (Bailey, 1992; Reid, 2014; Sappington, 1981).

That Brown's Bench obsidians have been exploited as toolstone sources since the

Pleistocene/Holocene transition is widely accepted. Brown's Bench obsidian is present in

numerous archaeological contexts within the Snake River Plain region and appears in many other

sites outside of Idaho, some up to 250 km away (Arkush & Pitblado, 2000; Bailey, 1992; Beck &

Jones, 1990, 1994; Bowers & Savage, 1962; Fowler, 2014; Hildebrandt et al., 2016; Hockett,

1995; Hughes, 1990, 2013; Hughes & Smith, 1993; Jones, Beck, Jones, et al., 2003; King, 2016;

Madsen, Schmitt, et al., 2015; Page & Skinner, 2008; Reid, 2014; Scheiber & Finley, 2011).

However, understanding the primary sources and regional extents of the Brown's Bench

obsidians is complicated by several factors, including the multiple volcanic eruptions and modes

(ignimbrite vs. lava) noted above, the massive scale of these eruptions both in volumetric and

areal extents, the patchwork of past geological and archaeological studies using variable naming

conventions (see alternative names list above), and even the persistence of placeholder names for

initially unknown sources (e.g., the Butte Valley Group A). Butte Valley is more than 200 km away from the region, but this major Brown's Bench geochemical subtype carries this name as a result of its first characterization as an unknown "Group A" in the analysis of artifacts at the Butte Valley site in Nevada by Jones & Beck (1990). These authors were also the first to recognize the unknown Group A obsidian as a member of the Brown's Bench family (Jones, Beck, Jones, et al., 2003), yet the name persists in the literature. As a result of this work, it is clear that at least three geochemical types are present within the greater Brown's Bench region. These are now largely standardized on the names Brown's Bench, Brown's Bench Area, and Butte Valley Group A (though see Page & Bacon, 2016 for suggested name updates: Browns Bench Variety 1 - 3).

Page and Bacon (2016) document an extensive survey and sampling of the Brown's Bench region with the dual goals of refining the spatial extents and the geochemical characterizations of the Brown's Bench obsidians. The authors explored whether the three geochemical signatures represent three geographically distinct source areas. Their survey's areal extent results are illustrated in Figure 4-5. What becomes clear from their survey is that the three Brown's Bench geochemical types are spatially overlapping, leaving no clearly distinct source areas. In terms of determining how "discoverable" or how large a signal the Brown's Bench obsidians presented on the landscape, these three types are combined into a single type, simply referred to as "Brown's Bench" going forward. When analyzing the Old River Bed delta data (see Chapter 5), artifacts from these geochemical types will be similarly grouped.
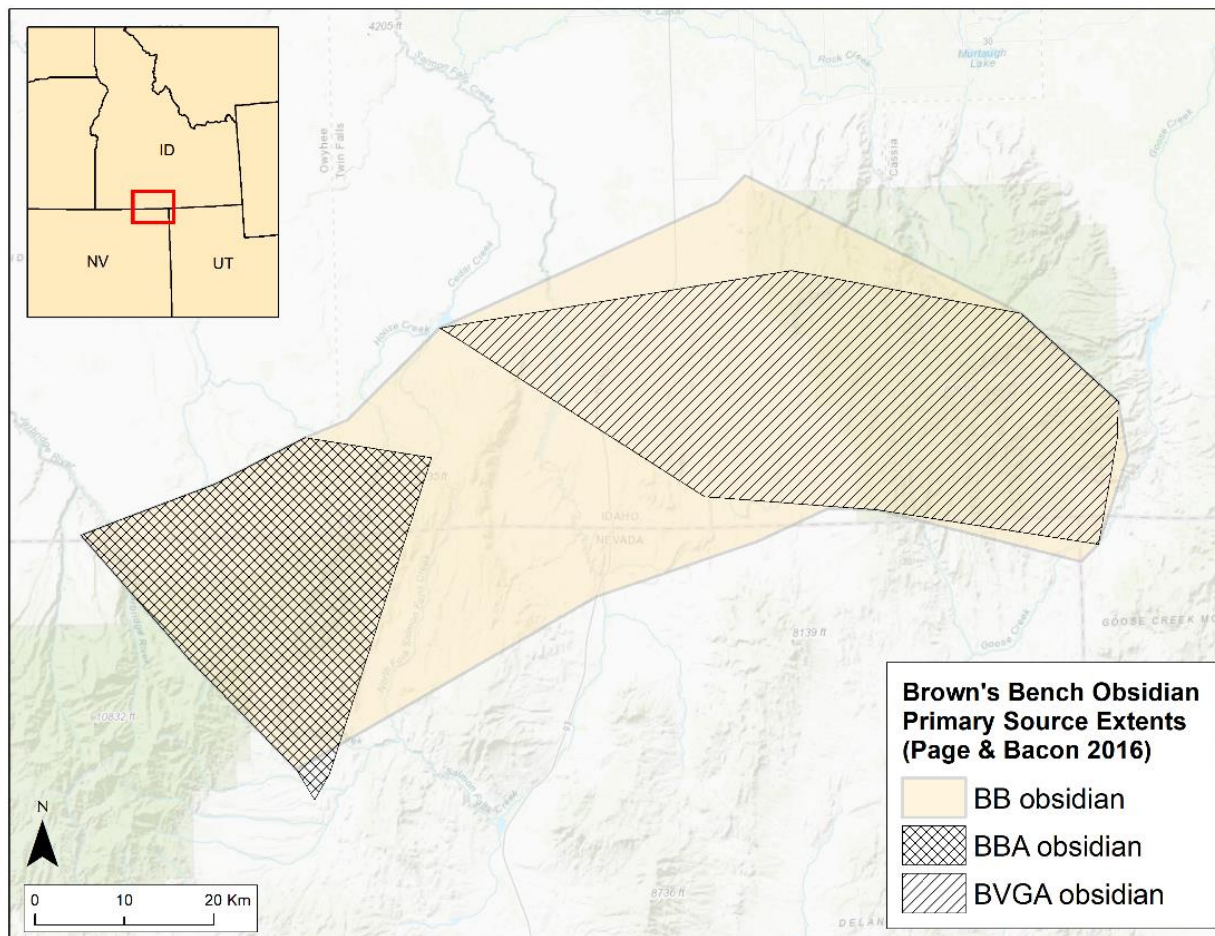
Figure 4-5: The primary source extents of the three main obsidian geochemical types associated with Brown's Bench: Brown's Bench (BB), Brown's Bench Area (BBA), and Butte Valley Group A (BVGA), after data and description in Page and Bacon 2016.

As surveyed by Page and Bacon (2016), the BB areal extent is approximately 3580 km^2, BBA is ~800 km^2, and BVGA is ~1445 km^2. Both BBA and BVGA are almost completely subsumed within the larger BB extent.

The Brown's Bench region presents the most complicated distribution of a geochemical type (or group of types) that was used as toolstone in the ORB. Figure 4-6 illustrates the combined distribution of sample points from Page & Bacon (2016) and Skinner (Table D-2). The contexts of Skinner's northern sample points, whether in primary source locations (some do

appear at elevation) or secondary (particularly those along the rivers), are unknown. The northern points are, in general, also at considerable distance from the southern point cluster.

With this consideration in mind, the BB, BBA, and BVGA datasets from both Page and Bacon (2016), Holmer (Table D-4), and Skinner (Table D-2) were combined and flow predictions generated using two methods. I treated the region surveyed by Page and Bacon as a single cobble field (as on the eastern slope of the Panaca Summit/Modena source) and generated 20 m buffers around the remaining points. Together, these areas were used as the proxy sources for a 15x15 flow prediction.

The combined Brown's Bench obsidian source has an exposure (E) value of 5173 km^2.
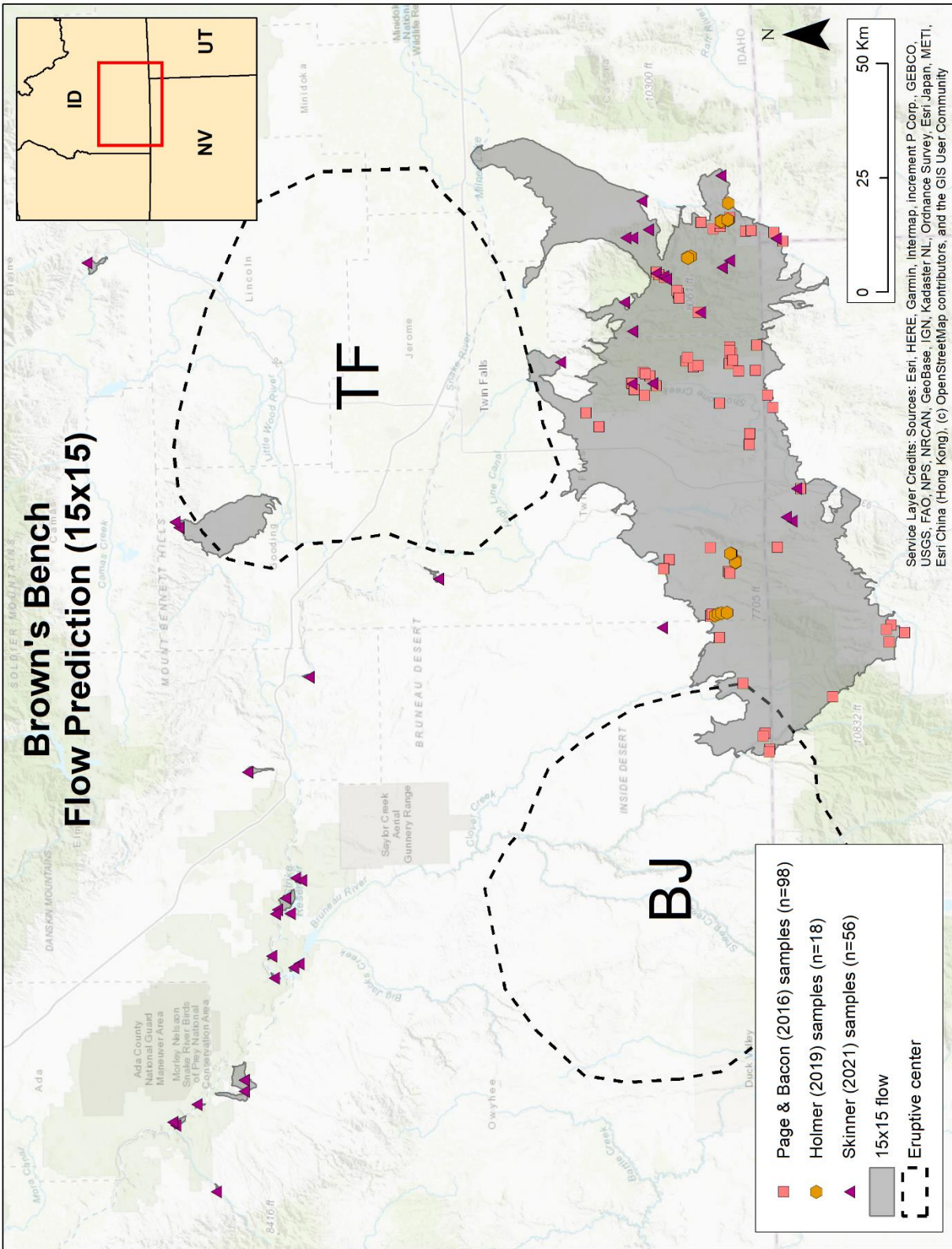
Figure 4-6: Brown's Bench obsidian 15x15 flow prediction and Brown's Bench, Brown's Bench Area, and Butte Valley Group A sample point distributions (Page & Bacon, 2016; Holmer, 2019; Skinner, 2021) in relationship to the putative Bruneau-Jarbridge and Twin Falls eruptive centers (Ellis et al., 2012).

4.4.4   Cedar Mountain

Source Type: Fine-grained volcanic; andesite and other unknown igneous types (Page, 2008)

Location: Tooele County, Utah

Alternative names: None, but nine subtypes (A - I)

Page (2008) sample points: $n=28$ (samples comprised of a mix of subtypes A - I) (Table D-5)

Skinner sample points: $n=1$ (Table D-2, subtype B)

ORB artifacts: $n=8$ (Table 4-1)

The Cedar Mountain Range lies about 100 km southwest of Salt Lake City, Utah, and its ridge forms a portion of the eastern border of the Dugway Proving Grounds military installation. The range is Paleozoic in origin (composed of various sedimentary formations) and capped with basaltic andesite and rhyolite from early Tertiary volcanic activity, approximately 40 Ma (Clark et al., 2016; Hintze, 1988; Maurer, 1970; Page, 2008). At its height, Lake Bonneville surrounded the range (Chen & Maloof, 2017a) and Maurer (1970) notes that large areas of the Tertiary volcanic rock are now overlain by recent sand dunes.

The Cedar Mountain FGV source was extensively documented by Page (2008), who provides the most complete dataset of andesite samples. Page classifies the Cedar Mountain FGV into nine subtypes (A - I) but geographically these are widely distributed within the local area. For the purposes of determining a Discoverability signal, 20 m buffers of the complete set of Cedar Mountain subtypes were used to generate the flow predictions (Figure 4-7). Page (2008) notes that large cobbles are readily available and that these have been distributed by alluvial transport within an area of about 5 km in diameter and up to 10 km southeast of the source, well in line with the scale of the flow prediction here. Archaeologically, Duke (2011, p. 110) notes

that the abundance of phenocrysts in the Cedar Mountain FGV is approaching a level that may limit its knapping utility.

The Cedar Mountain prediction (Figure 4-7) presents a Discoverability exposure (E) signal of 37 km^2.
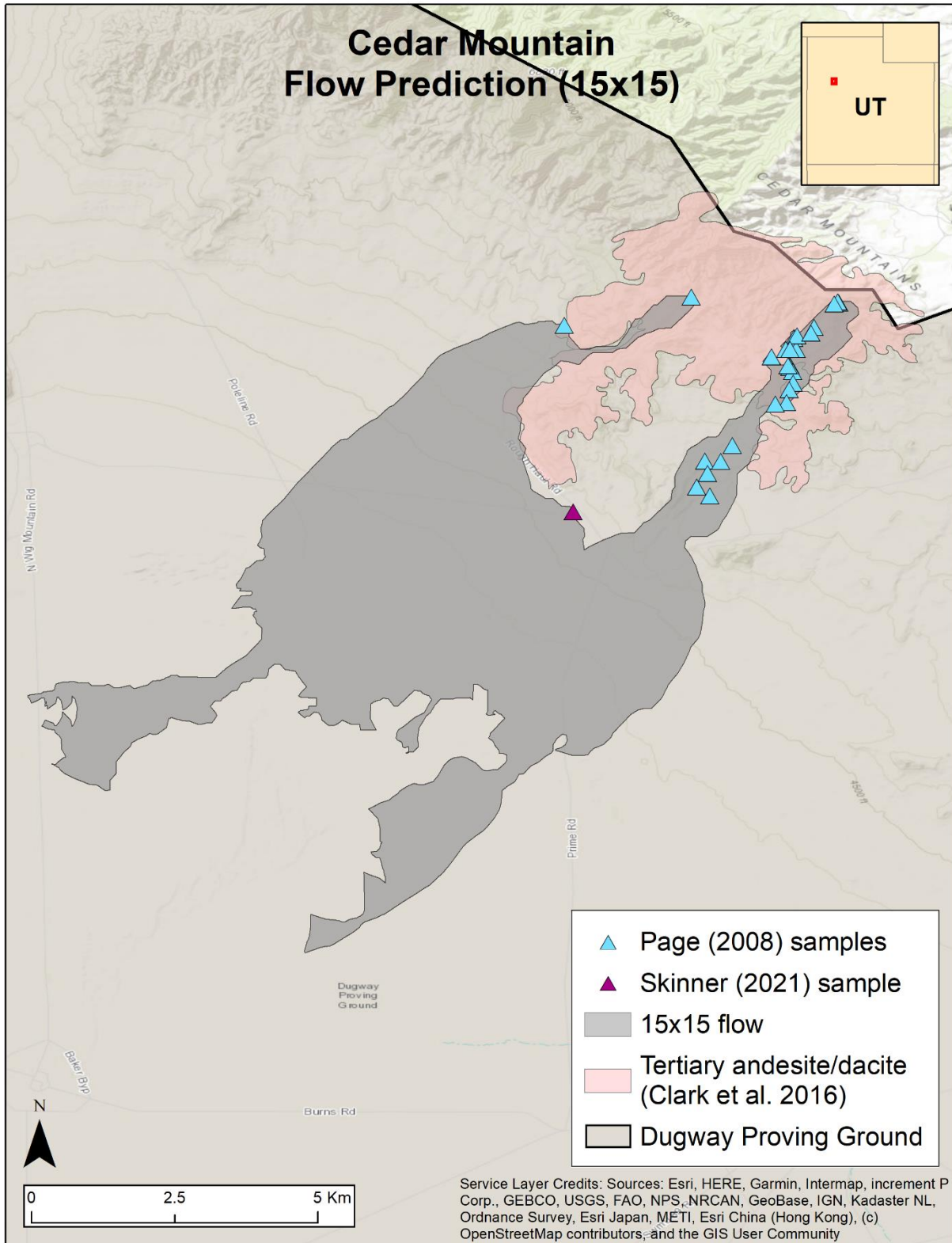
Figure 4-7: Cedar Mountain fine-grained volcanics (FGV) 15x15 flow prediction.

4.4.5   Currie Hills

Source Type: Fine-grained volcanic; dacite, trachydacite, trachyandesite, and other igneous types (Page, 2008)

Location: Elko County, Nevada

Alternative names: None

Jones (personal comm., July 10, 2021) sample points: $n=1$

Skinner sample points: $n=1$ (Table D-2)

Hunt 2021 observation points: $n=3$ (Table B-7)

ORB artifacts: $n=3$ (Table 4-1)

The Currie Hills FGV is found in Elko Country, Nevada, 30 km directly west of the Badlands and Deep Creek FGV locations. As discussed above, the geology of this area is poorly documented, but Crafford (2007) defines the region's low-lying, unnamed ridges as andesite or dacite flows from 30 to 45 Ma (*Ta1* in Figure 4-2). Aside from these volcanic flows, this area is also largely comprised of more recent sedimentary deposits and alluvium.

The first recording of the Currie Hills FGV extent appears in DeChambre (1979, p. 1) which reports a lithic scatter of "fine grained, black basalt" with "nodules of source material" in the southern Currie Hills (26Ek1976). This was followed by Murphy (1981, p. 1) which records "a large basalt quarry which covers at least ¼ mile by 1 mile" (26Ek3870), approximately 2 km west of 26Ek1976. In Murphy (1981, p. 1), part of the site "is a series of hills where the nodules of basalt are weathering out". An additional lithic scatter (26Ek7320) was recorded by Zerga (1988) just over 19 km to the north with natural cobbles to 8 inches.

To predict the flow extent, I used shapefiles provided by Daron Duke (personal comm., July 11, 2021) for sites 26Ek1976 and 26Ek7320. The site report for 26Ek3870 provided a

detailed map that was georeferenced, and a shapefile was generated from that image, which corresponds with a similar, but smaller, polygon from Duke. Tom Jones (personal comm., July 10, 2021) provided two sample locations, one within 100 m of 26Ek7320 and the other along state highway 93A. The latter was excluded here as it was unclear if its context was affected by road construction. There is one XRF sample reported by Skinner (Table D-2). Finally, during a site visit in 2021, I recorded three FGV observations (Table B-7). It is clear from the sampling distribution that this source is still largely unknown and there is likely a large expanse that will be exposed by further field work. A weighted raster was generated using the known quarry site polygons and 20 m buffers around individual sample points.

With the information we have now, the Currie Hills prediction (Figure 4-8) presents a Discoverability exposure (E) signal of 26 km^2.
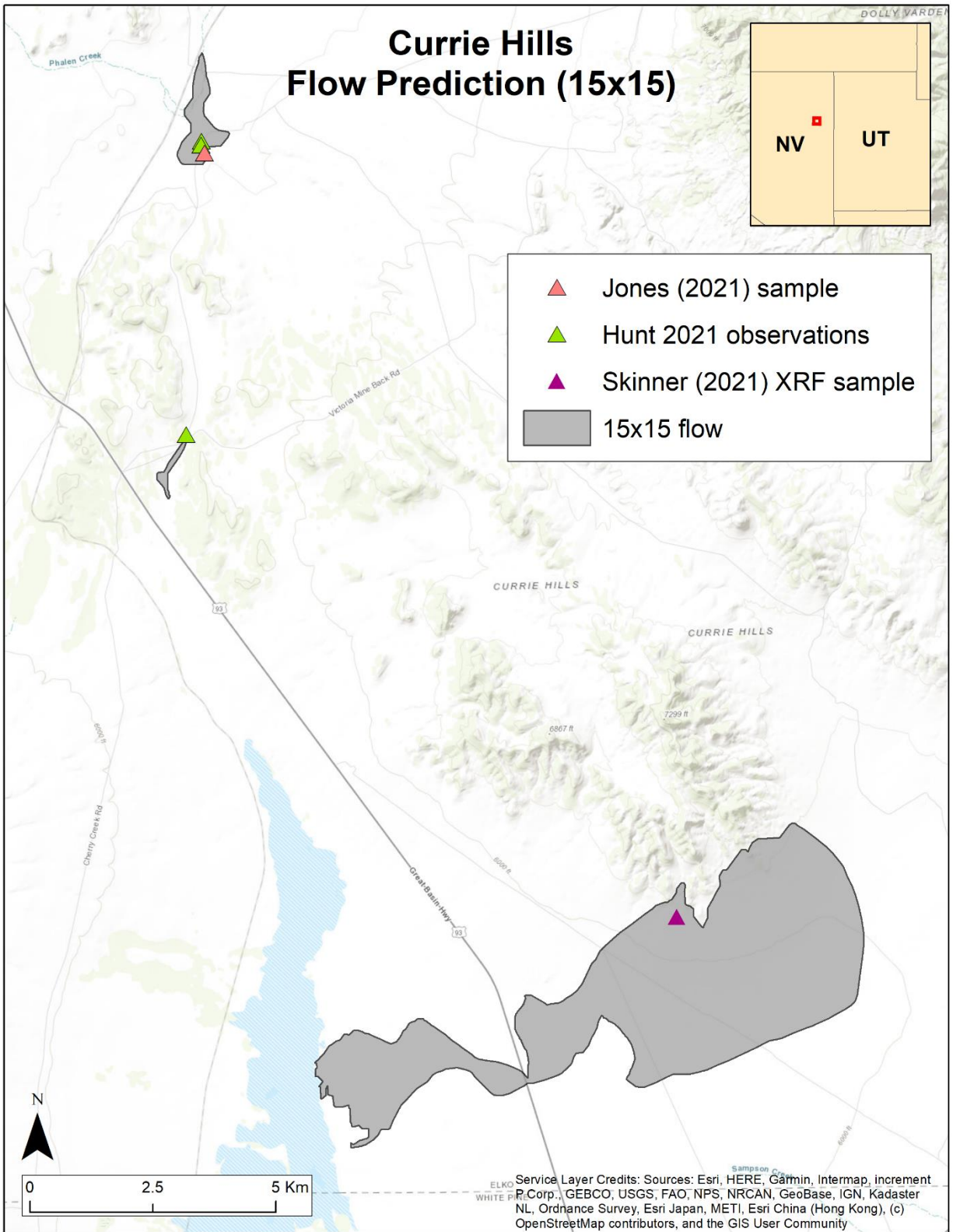
Figure 4-8: Currie Hills fine-grained volcanics (FGV) 15x15 flow prediction.

4.4.6 Deep Creek

Source Type: Fine-grained volcanic; andesite and trachyandesite (Page, 2008)

Location: Western Tooele County, Utah and eastern Elko and White Pine Counties, Nevada.

Alternative names: None, but four subtypes (A - D) and geographically overlaps with the Badlands FGV

Page (2008) sample points: $n=18$ (samples comprised of a mix of subtypes, Table D-5)

Skinner sample points: $n=15$ (all subtype A, Table D-2)

ORB artifacts: $n=10$ (Table 4-1)

As discussed above, the Deep Creek and Badlands FGV types are found largely overlapping to the northwest of the Deep Creek Range in western Tooele County, Utah and southeast of White Horse Mountain in Elko County, Nevada. Crafford (2007) defines the region's low-lying, unnamed ridges as andesite or dacite flows from 30 to 45 Ma (*Ta1* in Figure 4-9). Aside from these volcanic flows, the area is largely comprised of more recent sedimentary deposits and alluvium.

Archaeologically and geologically, most of our understanding of this area and of the Deep Creek FGV geochemical type comes from the work by Page (2008) who classifies it as andesite and trachyandesite.

Two sets of sample points were available. Page (2008) provides 18 FGV samples in secondary context. Skinner (Table D-2), who provided the XRF analysis for Page, provided 15 sample points, of which three (SO-65-1058, -1393, and -1397) were not provided by Page (2008). These points were combined ($n=21$), buffered to 20 m, and the 15x15 flow is predicted in Figure 4-9.

The Deep Creek prediction (Figure 4-9) presents a Discoverability exposure (E) signal of 108 km^2.
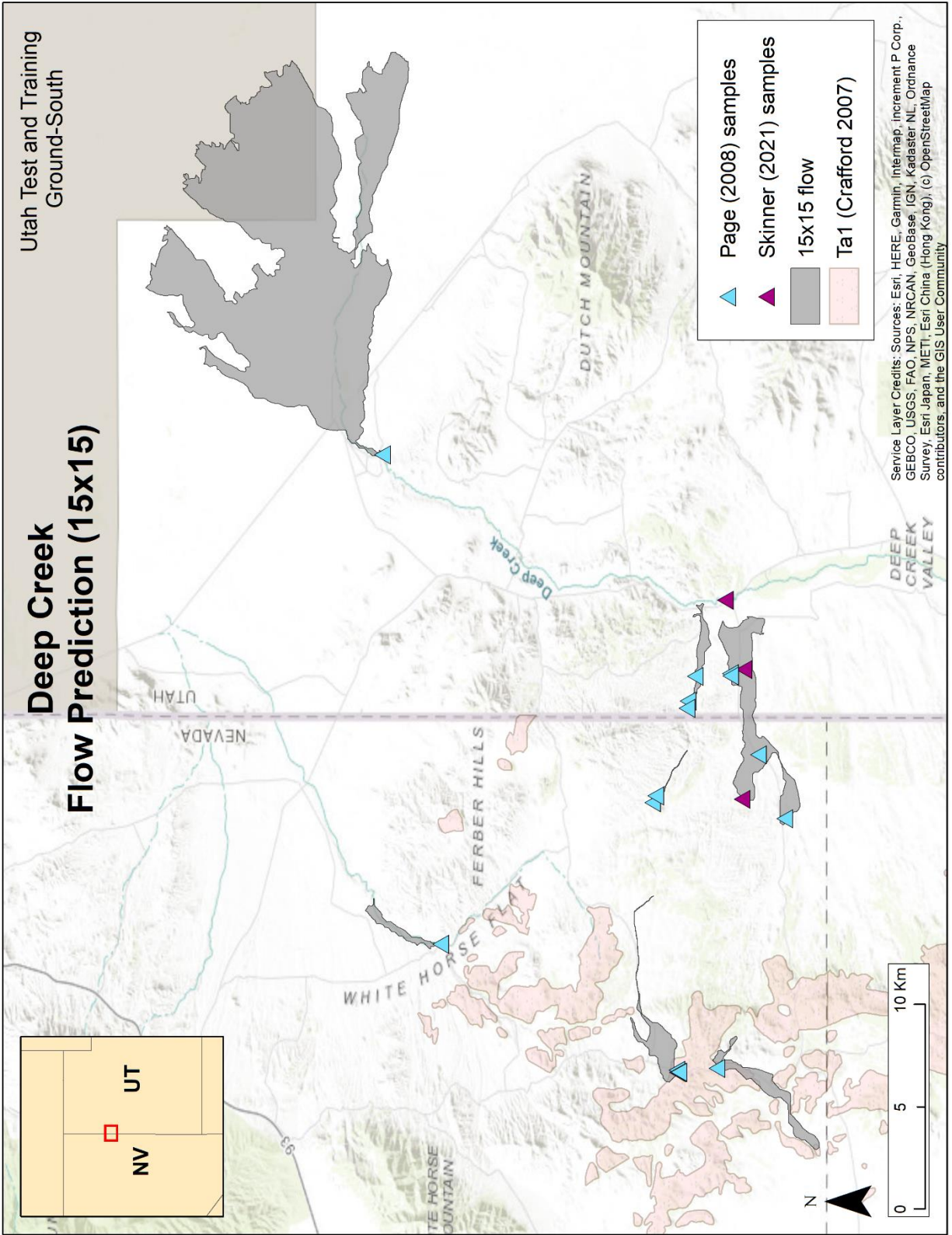
Figure 4-9: Deep Creek fine-grained volcanics (FGV) 15x15 flow prediction.

4.4.7 Flat Hills

Source Type: Fine-grained volcanic; andesite, dacite and trachydacite (Page, 2008)

Location: Tooele County, Utah

Alternative names: None, but five subtypes (A, B, C, D, and E)

Page (2008) sample points: $n=26$ (samples comprised of a mix of subtypes) (Table D-5)

ORB artifacts: $n=182$ (Table 4-1)

The Flat Hills lie about 2 km south of the town of Dugway, Utah, at the southern end of the Cedar Mountain Range, within Tooele County.

The Flat Hills FGV source was extensively documented by Page (2008), who provides the most complete dataset of FGV samples. Page classifies the Flat Hills FGV into five subtypes (A, B, C, D, and E) but these cluster within the area. Types A, B, D, and E all fall in a northern cluster, while all the C types appear in a cluster about 3 km farther south.

At its height, Lake Bonneville inundated almost the entire area (Chen & Maloof, 2017a). As there are no FGV primary sources in the Flat Hills, which are sedimentary in origin, Page (2008) suggests the material in this area is the result of a tombolo, or sandbar, joining the Flat Hills with the Cedar Mountains during the Provo recession. FGV secondary material was then deposited on this tombolo as Lake Bonneville wave action entrained FGV nodules.

Archaeologically, as can be seen from Table 4-1, the Flat Hills were significantly exploited for toolstone by the people living in the Old River Bed delta across multiple temporal periods.

For the purposes of determining a Discoverability signal, 20 m buffers of the complete set of Flat Hills subtypes were used to generate the flow predictions. While these samples do not appear to represent a primary source, the deposits should be eroding by alluvial/colluvial action to the east into the lower elevations of Skull Valley.

The Flat Hills prediction (Figure 4-10) presents a Discoverability exposure (E) signal of 21 km^2.
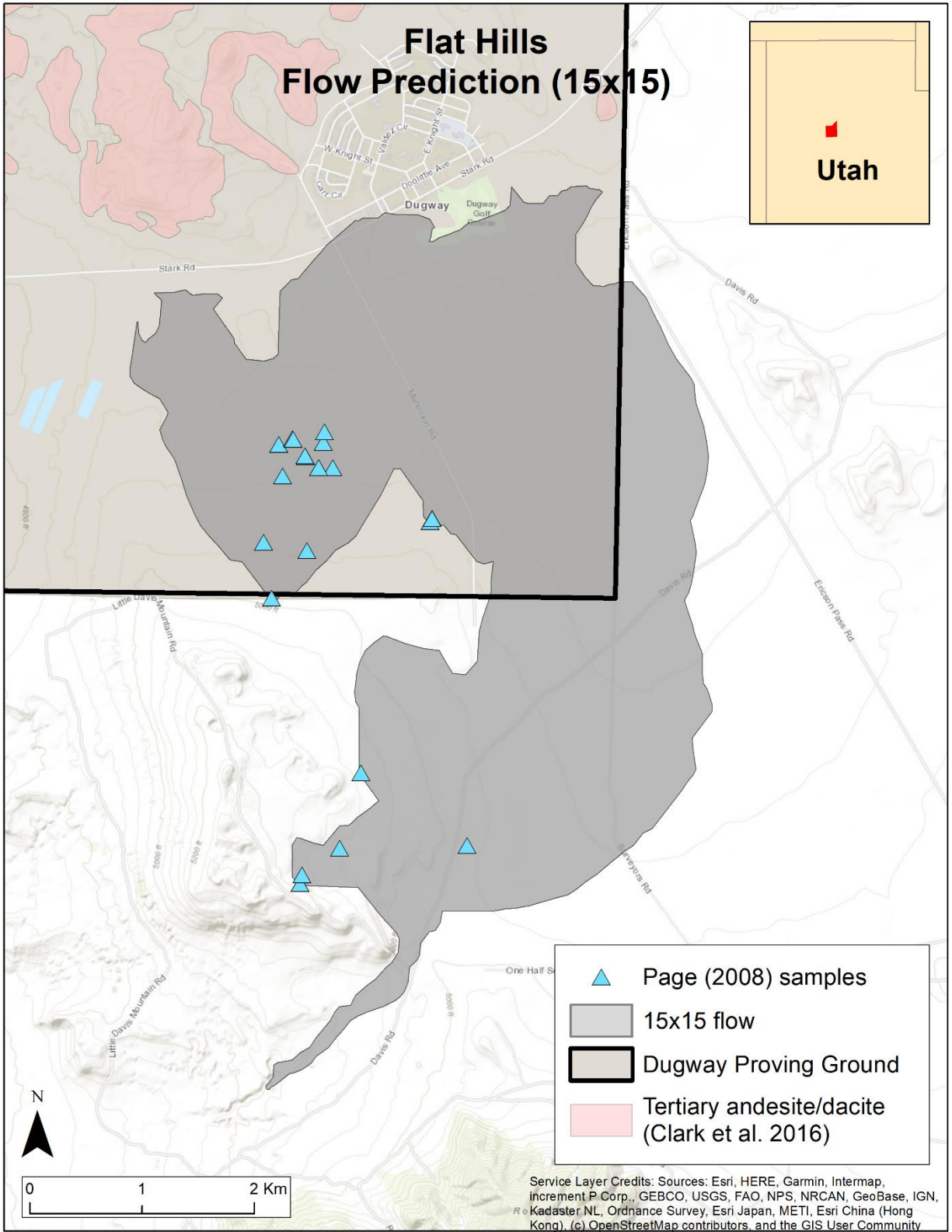
Figure 4-10: Flat Hills fine-grained volcanics (FGV) 15x15 flow prediction.

4.4.8   Kane Springs Wash Caldera

Source type: Obsidian; two subtypes (Variety 1 and Variety 2)

Location: Lincoln County, Nevada

Alternative names: Kane Spring Wash (Nelson & Holmes, 1979; Sappington, 1981)

Variety 1: Delamar Mountains (Skinner, 2021), Kane Springs C (Johnson & Wagner, 2005);

Variety 2: Kane Spring, Kane Springs, Kane Springs A (Johnson & Wagner, 2005)

Skinner sample points: *n*=25 (Table D-2)

ORB Paleoindian artifacts: *n*=1 (Table 4-1)

The Kane Springs Wash Caldera (KSWC) obsidian is found in southeastern Nevada, in Lincoln County, and about 110 km north of Las Vegas. The source material appears in the Delamar and Meadow Valley Mountains, in and around the remnants of a collapsed Miocene-aged (23.3 to 5.3 Ma) volcanic caldera.

The caldera formed about 14.1 Ma ago with the eruption and collapse of a rhyolitic dome (Novak, 1984, 1985; Novak & Mahood, 1986). Two subsequent highly silicic, rhyolitic magma flows were then constrained within the rim of this caldera (Figure 4-11), forming obsidian as they were quenched. These intracaldera units are referred to as the "early moat rhyolite" (sometime between 14.1 and 13.3 Ma) and the "late moat rhyolite" (around 13.3 Ma). Obsidian from the early moat rhyolite now bears the label "KSWC Variety 1" and, due to its older age, largely manifests as marekanites (Apache tears) (Johnson & Wagner, 2005; S. M. Shackley, 2021). Primary sources for Variety 1 occurred in both the Delamar and Meadow Valley mountains at one time, but these sources are unknown or are now eroded and depleted. Obsidian from the late moat rhyolite is labelled "KSWC Variety 2" and primary exposures, yielding cobbles to 15 cm, are still present on the western rim of the caldera, with secondary distributions

within the Delamar Mountains, downslope into Kane Springs Wash, and as far southwest as Coyote Spring Valley.

The Kane Springs Wash Caldera obsidians (Varieties 1 and 2) are now geochemically well-characterized (Johnson & Wagner, 2005; Skinner & Thatcher, 2005). "Kane Spring Wash" obsidian was first analyzed and characterized by Nelson & Holmes (1979, as source #15), and corresponds with Variety 2. The township-range location for this sample places it near the southwestern-most sample in Figure 4-11, at the southern mouth of Kane Spring Canyon. Johnson & Wagner (2005; see also Skinner, Appendix D, Table D-2) provides a large sample set (*n*=25) that was used to distinguish the geochemical signatures and rough distributions of Varieties 1 and 2.

Prehistorically, the KSWC obsidian was widely used in the region (Hull, 2010) and there is some evidence of exploitation during the Paleoindian period, with Jensen (2004, 2005) reporting both a fluted point and stemmed points at a local site matched to KSWC obsidian.

To predict the secondary flow extent, the early and late moat rhyolites reported by Novak & Mahood (1986, Figure 1) provide the best description of the parental units for KSWC obsidian and are in good concordance with the known sample points. The outline of this extent was converted to polygons that served as the proxy primary sources to calculate the flow prediction. In addition, it is clear from the survey by Johnson & Wagner (2005) that primary sources, particularly those of Variety 1, occurred outside of these areas, most notably in the Meadow Valley Mountains. For this reason, I also applied 20 m buffers to the known sample points and merged the rhyolite polygons and the 20 m buffers to serve as the proxy primary sources when creating the weighted raster used for the flow prediction.

The Kane Springs Wash Caldera obsidian source has an exposure (*E*) value of 207 km^2.
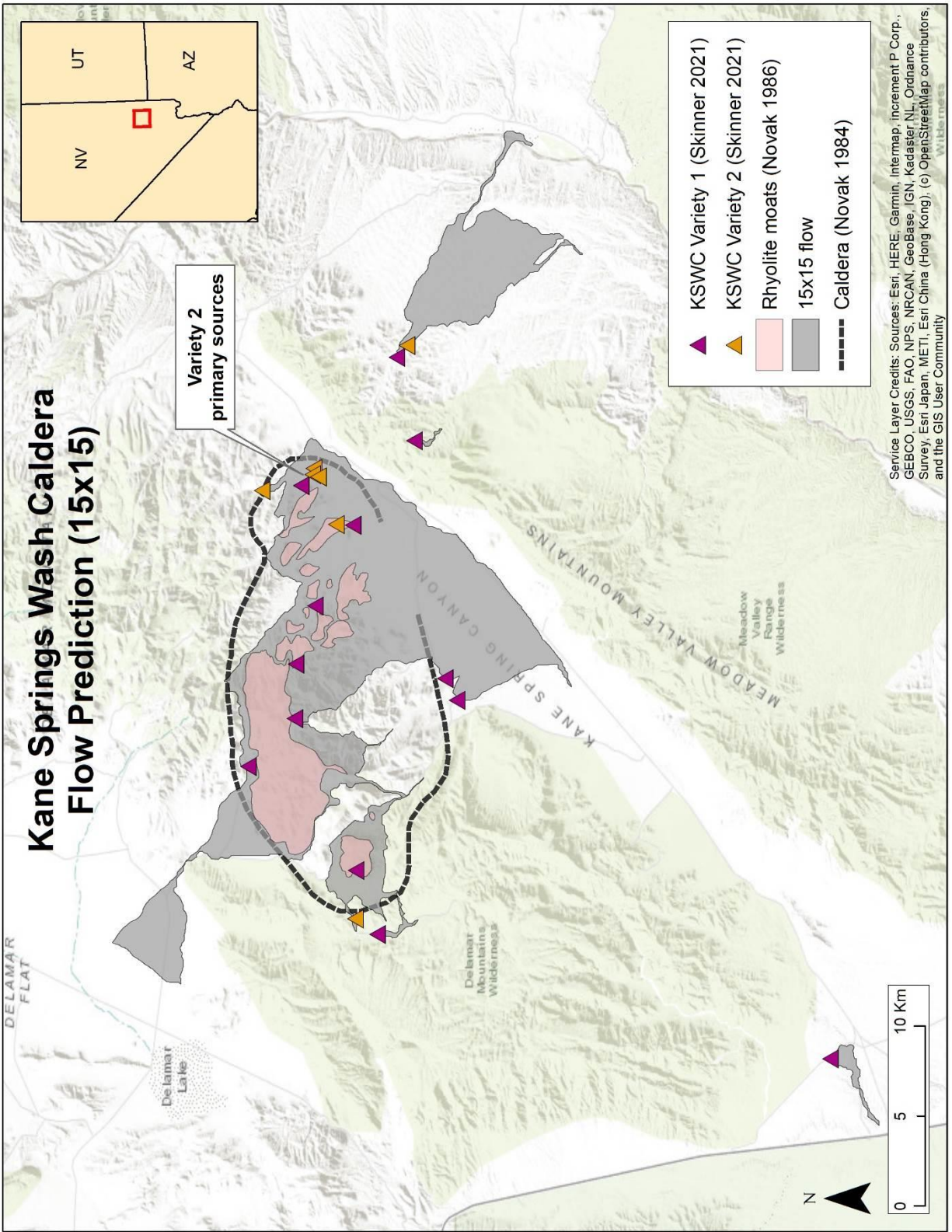
Figure 4-11: Kane Springs Wash Caldera obsidian 15x15 flow prediction.

4.4.9 Malad

Source type: Obsidian

Location: Oneida and Bannock Counties, Idaho

Alternative names: Dairy Creek, Garden Creek Gap, Hawkins, Oneida, Wright Creek (Fowler, 2014; Gallagher, 1979; Holmer, 1997; Sappington, 1981)

Richard Holmer (personal comm., July 24, 2019): n=1 (Table D-4)

Skinner sample points: n=5 (Table D-2)

ORB Paleoindian artifacts: n=4 (Table 4-1)

The Malad obsidian is found in Oneida and Bannock Counties, Idaho, primarily in the fork between the confluence of the Dairy and Wright Creeks, 8 km northwest of Elkhorn Mountain. This region is just south of the Picabo eruptive center (Figure 4-3) described earlier; obsidian in the area manifests as high-quality cobbles, up to 25 cm, within a pyroclastic tuff (Ellis et al., 2012; J. Moore, 2009; Whitman, 2013). This tuff is currently commercially mined in the Wright Creek area for pumice used to manufacture high-grade industrial abrasives.

Malad obsidian was first analyzed and characterized by Nelson & Holmes (1979, see also Gallagher, 1979; Nelson, 1984). Since that time it has become recognized as one of the most commonly exploited obsidian sources in Idaho (Fowler, 2014; Holmer, 1997; Reid, 2014; Whitman, 2013; Willson, 2007). Malad obsidian is also found in archaeological contexts at considerable distance (>1200 km), recorded at sites in Arkansas, Colorado, Iowa, Kansas, Nebraska, Nevada, North Dakota, Oklahoma, Texas, Utah, and Wyoming (Fowler, 2014; Holmer, 1997; Hughes, 2007a; Logan et al., 2001).

Our understanding of the extent of the Malad obsidian is limited, with only a few sample points using GPS coordinates reported by Holmer (Table D-4) and Skinner (Table D-2). There

are no known primary source exposures, aside from the broad distribution of cobbles within the tuff. These appear to be emanating from Miocene-aged (23.3 to 5.3 Ma) volcanic deposits (*Tpf* in Figure 4-12), which overlay an older Oligocene (39.9 – 23.3 Ma) volcanic deposit (*Tov* in Figure 4-12).

The Miocene volcanic deposit recorded by Link (2002) provides the best description of this cobble-rich extent and finds good concordance with the known sample points. The outline of this extent was converted to polygons that served as the proxy primary sources to calculate the flow prediction. The prediction captures 3 of the 5 samples provided by Skinner (Table D-2), and the two exceptions are less than 600 m outside the prediction.

It should be noted that Bailey (1992) reports the presence of Malad obsidian within the Hess Pumice Mine tailings. Marshall (1961) argues that, globally, obsidian is rarely older than the Miocene due to the instability of glass and the natural hydration, or devitrification, process that breaks down obsidian into marekanites and, eventually, perlite. Since the known samples fall within the same geochemical signature, it seems most likely the mines (indicated on Figure 4-12) are encroaching on the *Tpf* deposit as they work the Oligocene-aged *Tov* deposit.

The Malad obsidian source has an exposure (*E*) value of 24 km^2.
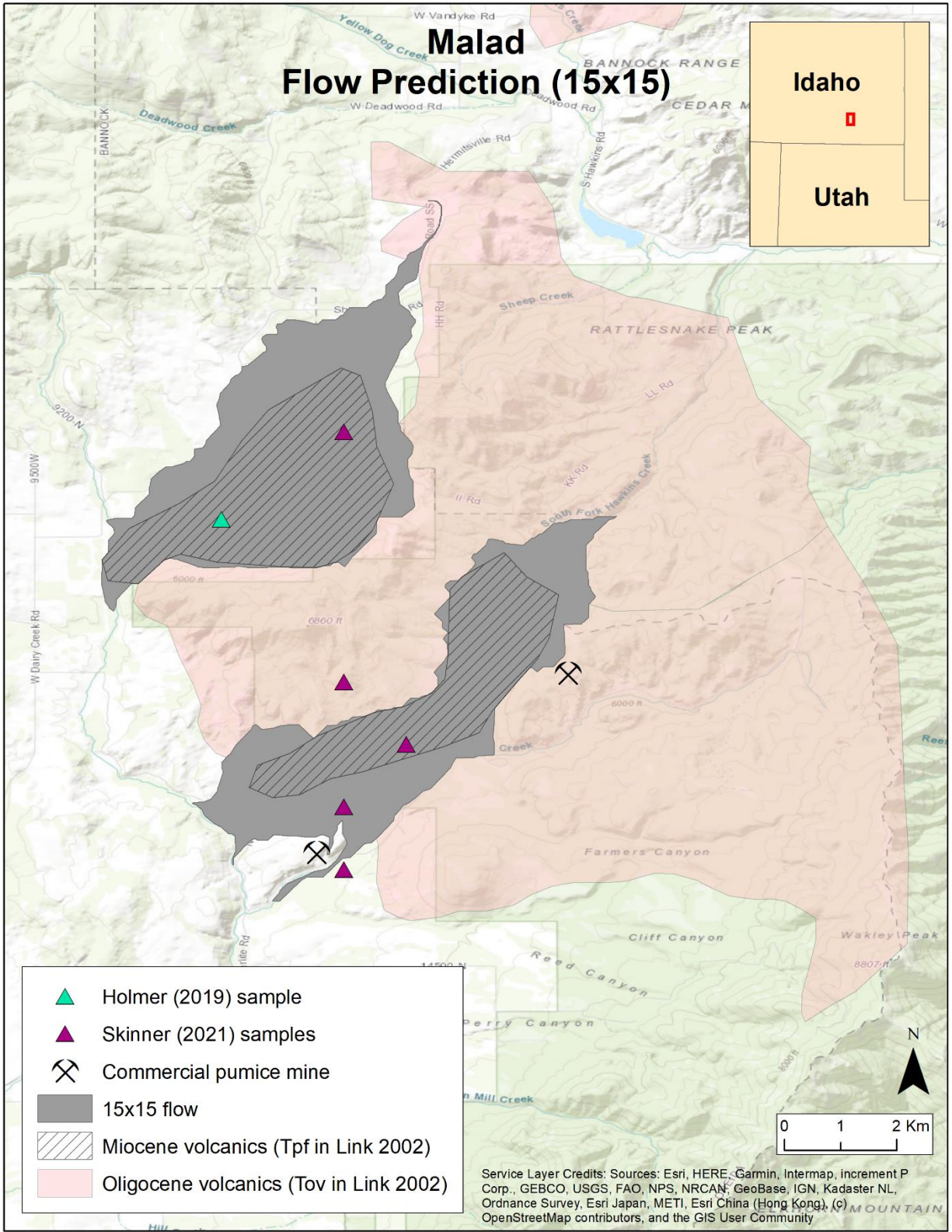
Figure 4-12: Malad obsidian 15x15 flow prediction.

4.4.10 Owyhee

Source type: Obsidian

Location: Owyhee County, Idaho and Malheur County, Oregon

Alternative names: Browns Castle, Oreana, Toy Pass (Holmer, 1997)

Richard Holmer (personal comm., July 24, 2019): n=4 (Table D-4)

Skinner sample points: n=53 (Table D-2)

ORB artifacts: n=2 (Table 4-1)

The Owyhee obsidian manifests as massive cobble distributions found in northern Owyhee County, Idaho, and into Malheur County, Oregon. Sappington (1981), one of the earliest obsidian researchers in the region, suggested the distribution extends more than 1600 km^2. In Idaho, obsidian nodules are primarily clustered on the east slope of the Owyhee Mountains, though other samples are scattered northwest of this cluster. Over 100 km to the northwest, in Oregon, another smaller cluster appears near Grassy Mountain (Figure 4-14).

Both clusters are located north of the Owyhee eruptive centers (Figure 4-3) and in regions described by Bennett as "rhyolitic pyroclastic and lava flows" (1976, p. 7; see also Lewis et al., 2012; Walker & MacLeod, 1991). These appear to be emanating from Miocene-aged (23.3 to 5.3 Ma) volcanic deposits (*Tmr* and *Trh* in Figure 4-14) that erupted approximately 14 Ma ago (Bennett, 1976; Ellis et al., 2012; Lewis et al., 2012; Walker & MacLeod, 1991).

The Owyhee obsidian geochemical signature was first analyzed and characterized by Nelson (1984). Like Malad, Owyhee has become recognized as one of the most commonly exploited sources of toolstone in Idaho (Fowler, 2014; Holmer, 1997; Reid, 2014; Whitman, 2013; Willson, 2005, 2007). The distribution region is well-researched and has been extensively sampled (Bailey, 1992; Holmer, 1997; Nelson & Holmes, 1979; Sappington, 1981; Skinner,

2021); however, there are no known primary source outcrops, aside from the broad distributions of high-quality cobbles, up to 20 cm, within the tuff (Bailey, 1992; Ellis et al., 2012; J. Moore, 2009).

The Owyhee cobble fields are reminiscent of those on the east slope of the Panaca Summit/Modena source area (section 3.6.4). For this reason, I used a similar strategy to create the proxy source. I created polygons that aggregated known sample points (n=57) from Holmer (1997) and Skinner (Table D-2) (Figure 4-13) to represent the localized cobble fields. An aggregation of points within 15 km of each other seemed to provide the fewest, tight clusters and these were then used as the proxy sources for flow prediction (Figure 4-14).

The Owyhee obsidian source has an exposure (E) value of 829 km^2.
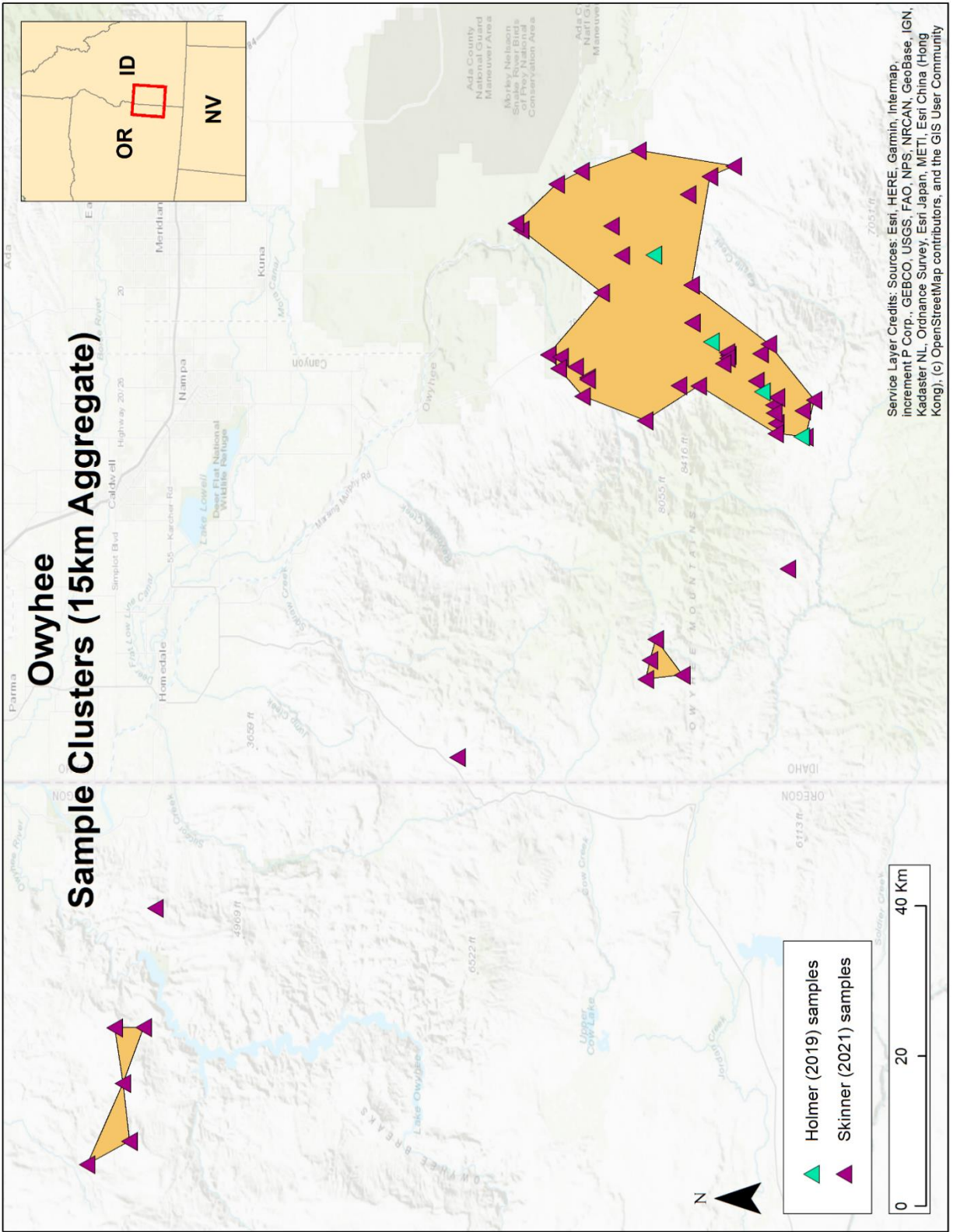
Figure 4-13: Proxy sources generated from sample clustering.
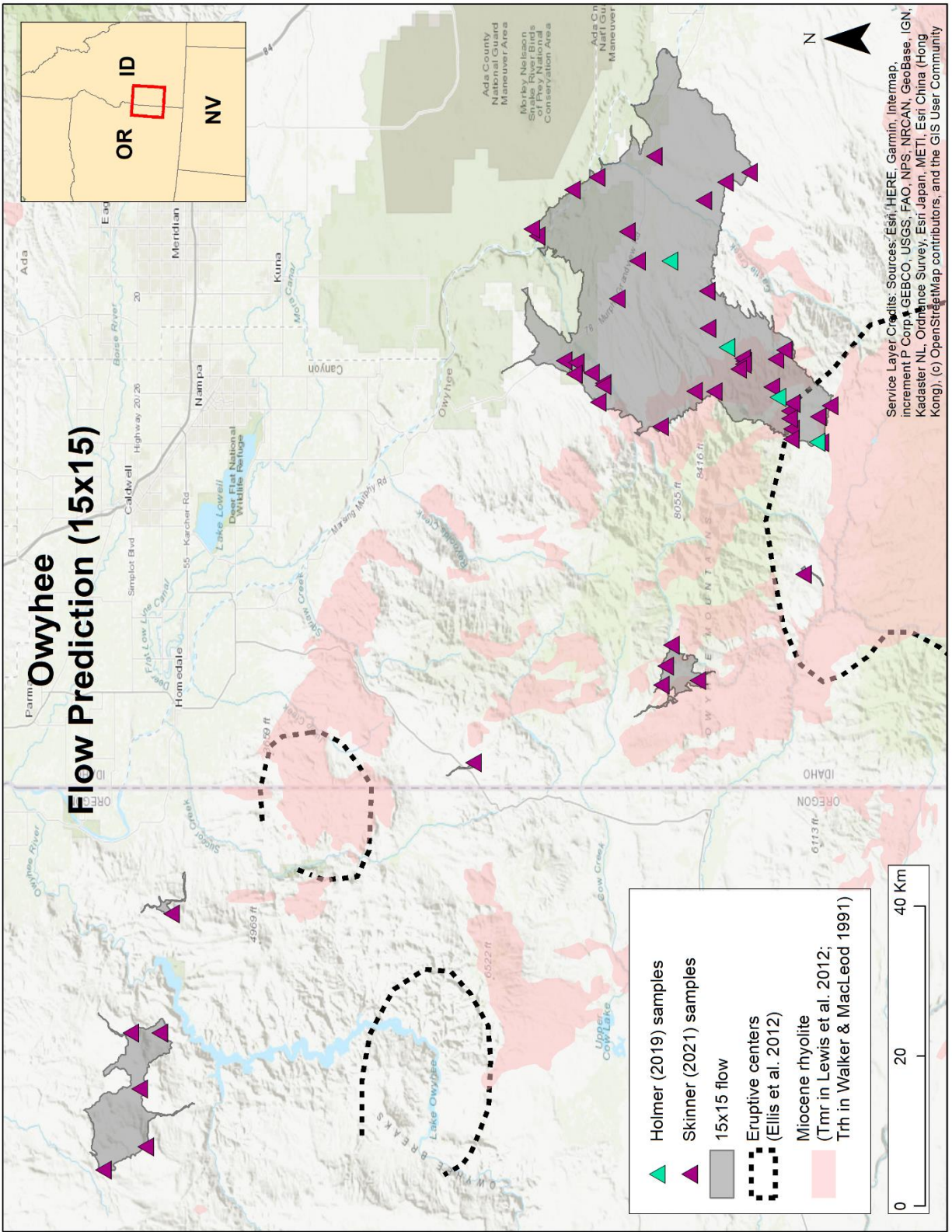
Figure 4-14: Owyhee obsidian 15x15 flow prediction.

4.4.11 Paradise Valley

Source Type: Obsidian

Location: Humboldt County, Nevada

Alternative names: Santa Rosa Mountain (Moore, 2009)

Skinner sample points: *n*=3 (Table D-2)

ORB artifacts: *n*=3 (Table 4-1)

The Paradise Valley obsidian is found in the Santa Rosa Mountains in Humboldt County, Nevada (Figure 4-15). This region is less than 30 km southwest of the Owyhee eruptive center (Figure 4-3) described earlier. This region was subjected to silicic volcanism beginning around 16.6 Ma, continuing to about 12 Ma. As a result, middle- to late-Miocene rhyolitic flows dominate the western edge of the eruptive center (Brueseke & Hart, 2008; Ellis et al., 2012; *Geologic Map of Nevada - Data series 249*, 2021).

Archaeologically, the Paradise Valley obsidian is a prominent regional toolstone (Beck & Jones, 2011; Elston & Budy, 1990; Hughes, 1990; Hutchins & Simons, 2000; Jones, Beck, Jones, et al., 2003; LaValley, 2013; Newlander, 2012; Stephenson & Wilkinson, 1969), but the source itself is poorly described. Sappington (1981) states that it is geochemically well-characterized, but provided no references to support this claim. Nelson (1984, Figure 1) appears to illustrate and enumerate the location for this source, as well as several other eastern Nevada sources, but these sources are then absent from his results (1984, Table 6). Skinner (Table D-2) provides the current best characterization of this source.

Similarly, our understanding of the source extent is limited. Skinner (Table D-2) reports three XRF sample points with GPS coordinates. Sappington (1981) reports a single sample observation at T41N R43E, section 3, approximately 42 km southeast of the Santa Rosa

Mountains, in the Little Humboldt River Valley, and close to the Chimney Dam. Moore (2009) reports this same location, and seven other locations, without attribution: six in sections within T43N R39E (sections 2, 11, 14, 15, 22, 23), and one in T42N R38E, section 17, all in the Santa Rosa Mountains (Figure 4-15). However, our precise understanding of the source location is limited to the three data points provided by Skinner.

To predict the Paradise Valley extent, I used the method described in section 3.6.4 and formed a proxy source polygon using the three points from Skinner. While this produces a significant flow into the southern Paradise Valley, it does not capture the source regions suggested by Sappington or Moore. The secondary extent is probably considerably larger than this prediction, but without more definitive data the methodology must rely on these confirmed sample locations. Our understanding of Paradise Valley would benefit significantly from targeted field work in this area.

The Paradise Valley obsidian source has an exposure (E) value of 134 km^2.
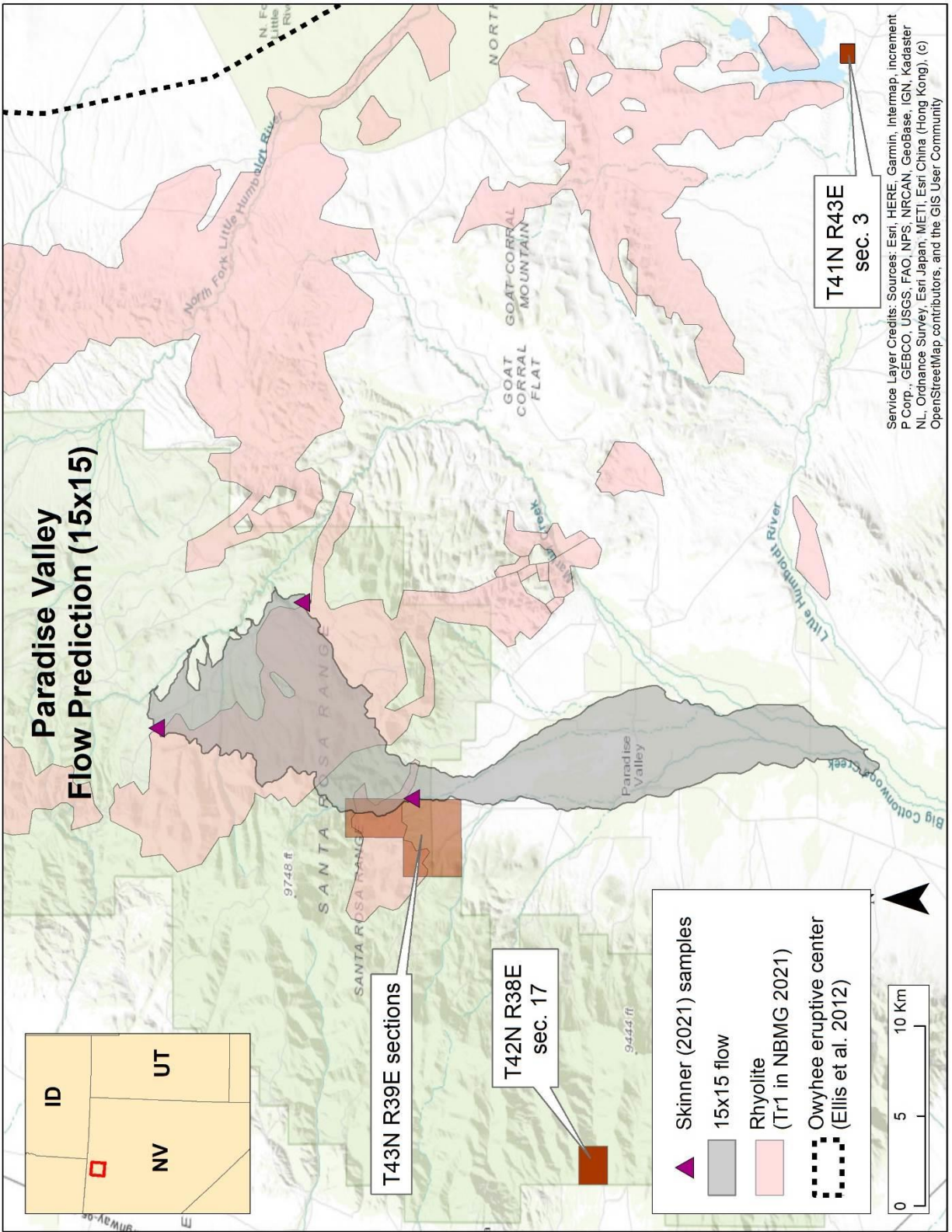
Figure 4-15: Paradise Valley obsidian 15x15 flow prediction.

4.4.12 Pumice Hole Mine

Location: Beaver County, Utah

Alternative names: n/a

Skinner sample points: *n*=3 (Table D-2)

ORB Paleoindian artifacts: *n*=1 (Table 4-1)

The Pumice Hole Mine (PHM) obsidian type presents an enduring enigma in Great Basin obsidian research.

The PHM type was originally recorded by Nelson and Holmes (1979, Table III, Source 3), using a single sample received from a second party (Hull, 1994). This party stated the sample was collected within T28S R9W sec 2, NE1/4 (Figure 4-16) - south of Wildhorse Canyon, near South Twin Fork Mountain, and close to Ranch Canyon. This information was repeated, with minor XRF data variations, in Nelson (1984, Table 4, Source #4).

During the Kern River Pipeline survey, Hull (1994, pp. 7–13) noted that obsidian found in the Ranch Canyon alluvium contained "abundant phenocrysts" and knapped poorly, even crumbling when this was attempted. Within the report, Hull's personal communications with Nelson and others note the visual differences between the previously tested obsidian by Nelson and Holmes (1979) and the samples collected by Hull in Ranch Canyon. These differences suggested that the original sample may have come from another, unknown, location.

This suggestion gained support as a result of a regional survey by Jackson et al. (2009), who also surveyed the Wildhorse Canyon and Bailey Ridge areas to the north of Ranch Canyon. All 10 samples collected by the authors were XRF tested and classified as "Pumice Hole Mine Type B", which originates from pyroclastic deposits above Ranch Canyon. This led Jackson et

al. (2009, p. 115) to assert that the "Pumice Hole Mine obsidian by Nelson and Holmes actually originated from a source outside the Mineral Mountains".

However, around 2006, UC Davis graduate student Clint Cole collected three samples that XRF-tested in the range of the original PHM type (Craig Skinner, personal comm., October 28, 2021). Two of the samples were located between Bailey Ridge and Wildhorse Canyon, above Big Cedar Cove, and one appears at the mouth of Wildhorse Canyon. As such, the secondary distribution from these points flows into the flows emanating from Bailey Ridge and Wildhorse Canyon. To a hunter-gatherer discovering these sources for the first time, these would appear as a single signal on the landscape.

For this reason, I am combining the Mineral Mountains (Bailey Ridge and Wildhorse Canyon) and PHM flows into a single Discoverability signal. The PHM flow was predicted by creating 20 m buffers around the three points by Cole. When this flow (Figure 4-16) is considered in relation to the actual flow results from the Mineral Mountains survey, it adds 10.1 km^2 of flow extent (gray hatched areas) to the overall actual MM survey (originally 160 km^2).

The updated and combined Mineral Mountains (now including PHM) obsidian source has an exposure (E) value of 170 km^2.
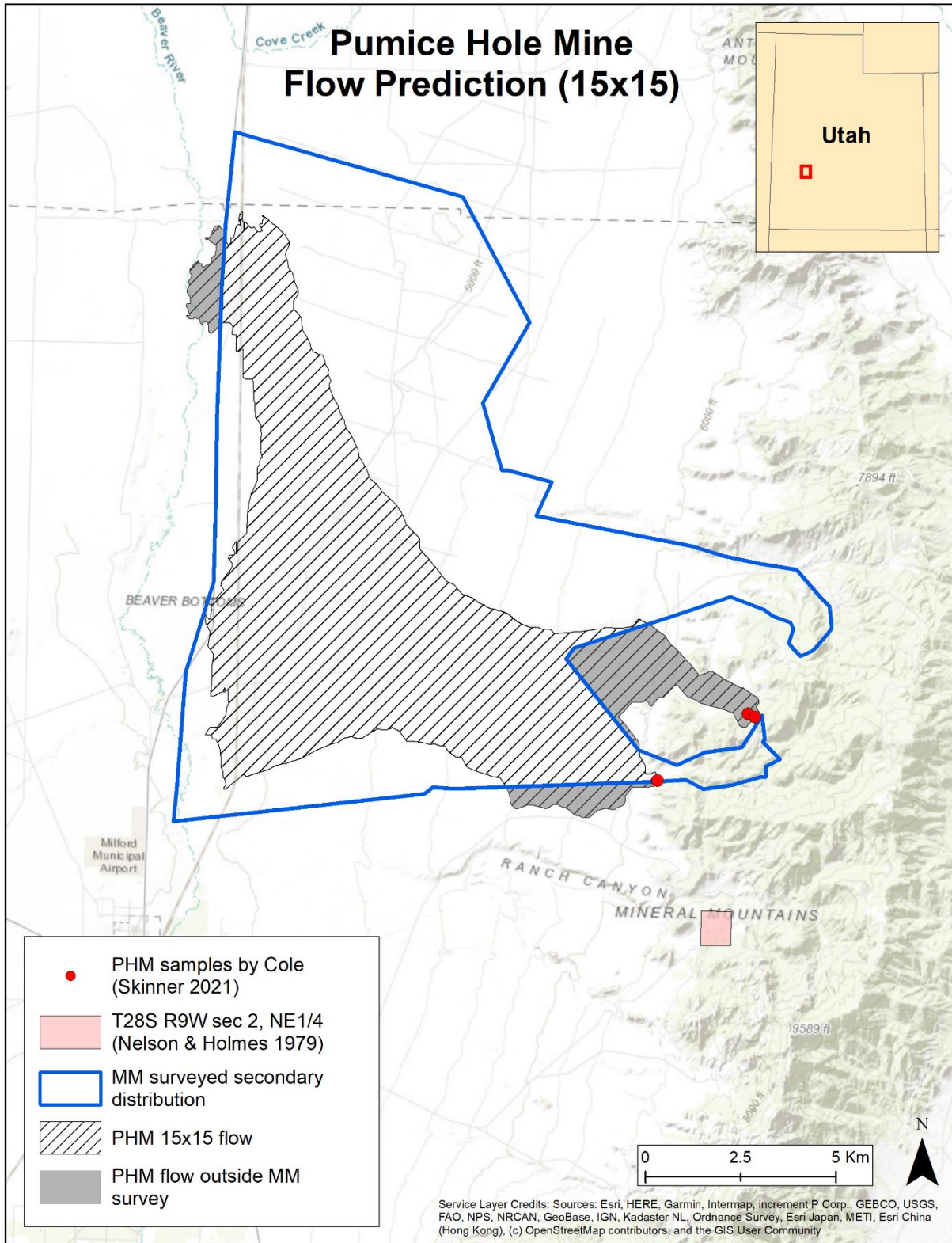
Figure 4-16: Pumice Hole Mine obsidian 15x15 flow in relation to the actual survey outline for Mineral Mountains sources.

4.5   Summary

In this chapter, the secondary distribution extents (E) were predicted for 14 obsidian and FGV types used by people living in the Old River Bed delta. The Brown's Bench (BB), Brown's Bench Area (BBA) and the Butte Valley Group A (BVGA) types were combined into a single Discoverability signal, as the extents of these distinct types overlap significantly. Similarly, the Pumice Hole Mine (PHM) type was merged into the Mineral Mountains extent. The final E values for all ORB types are summarized in Table 4-2 and these will be used in Chapter 5 as the Discoverability hypothesis is tested.

Table 4-2: Old River Bed delta toolstone sources and their resultant exposure (E) values.
Bolded sources were surveyed and discussed in Chapter 3.

Sources	ORB artifacts	E (km²)
Badlands	18	66
Bear Gulch	1	129
Black Rock Area	10	**353**
Browns Bench + Browns Bench Area + Butte Valley Group A	46	5173
Cedar Mountain	8	37
Currie Hills	3	26
Deep Creek	10	108
Ferguson Wash	1	**4**
Flat Hills	182	21
Kane Springs Wash Caldera	1	207
Malad	4	24
Mineral Mountains + Pumice Hole Mine	10	**170**
Panaca Summit/Modena	1	**358**
Owyhee	2	829
Paradise Valley	3	134
Topaz Mountain	130	**309**
Totals	**430**	

Chapter 5: Testing the Discoverability Model

5.1 Introduction

In this chapter, I test the Discoverability model described in Chapter 2. This is accomplished using the toolstone source exposure (E) values surveyed and predicted in Chapters 3 and 4 in conjunction with temporal groupings of Paleoindian artifacts from the Old River Bed (ORB) delta in Utah (described in Appendix A). The expected toolstone proportions, ranked according to their Discoverability values, will be compared to their observed proportions using Spearman's rank-order correlation and other statistical tests. Finally, the landscape learning variable (*%LL*) will be calculated from the coefficient of determination for various temporal groups and plotted over the time of the Paleoindian occupation of the ORB delta. The goal of these tests is to determine if, in fact, changes in landscape learning can be detected at the ORB delta using the proposed Discoverability methodology.

5.2 Establishing Temporal Groups of Paleoindian Artifacts

Small sample sizes routinely pose difficulties in the statistical analysis of Paleoindian assemblages. To counter this issue, rather than group ORB Paleoindian artifacts by site (mean = 15.5 artifacts/site), I grouped artifacts into larger temporal clusters or assemblages, with the goal of creating the largest number of temporally distinct clusters with the highest counts of artifacts. The cleaned ORB Paleoindian database (Appendix A) with known toolstone sources (via X-ray fluorescence) are associated with the dated ORB channels listed in Table 5-1. For each channel, a midpoint age is determined, using the midpoint of the channel age ranges reported by Madsen et al. (2015).

Table 5-1: Paleoindian artifacts associated with dated Old River Bed delta channels.

Channel Association	Paleoindian Artifacts w/XRF *	Channel Age (^{14}C yr BP) †	Midpoint Age (^{14}C yr BP)
Black	229	~11,000-10,300	10,650
Limestone	4	~10,500-10,000	10,250
Yellow	2	~10,300-10,100	10,200
Green	69	~10,300-9,800	10,050
Red	4	~ 9,860-9,740	9,800
Blue B	24	~10,000-9,500	9,750
Light Blue	78	~9,800-8,800	9,300
Lavender	20	~9,100-9,000	9,050
Total:	**430**		

* See Appendix A
† Madsen et al., 2015

These data will be examined in two ways. First, I will pool artifacts within non-overlapping date ranges, resulting in three discrete age groups, designated A1 – A3 (Table 5-2). This will create the largest possible sample groups. Second, I will test artifacts directly associated with the individually dated channels. This offers the greatest available number of distinct temporal periods for comparison. In this latter case, only channels with a sample count of 20 or more sourced artifacts will be used. Five such groups emerged from this process, designated C1 – C5 (Table 5-3). In each case, the groups were placed in order of midpoint channel age.

Table 5-2: Grouping artifacts by discrete, non-overlapping channel age spans.

Group	Channel Associations	Paleoindian Artifacts w/XRF*	Age Span (^{14}C yr BP) †	Midpoint Age (^{14}C yr BP/ cal BP) ‡
A1	Black	229	~11,000-10,300	10,650/12,674
A2	Green & Yellow	71	~10,300-9,800	10,050/11,578
A3	Light Blue & Lavender	98	~9,800-8,800	9,300/10,444
	Total:	**398**		

Table 5-3: Grouping artifacts by individual channels.

Group	Channel Association	Paleoindian Artifacts w/XRF*	Channel Age (^{14}C yr BP) †	Midpoint Age (^{14}C yr BP/ cal BP) ‡
C1	Black	229	~11,000-10,300	10,650/12,674
C2	Green	69	~10,300-9,800	10,050/11,578
C3	Blue B	24	~10,000-9,500	9,750/11,167
C4	Light Blue	78	~9,800-8,800	9,300/10,444
C5	Lavender	20	~9,100-9,000	9,050/10,221
	Total:	**420**		

* See Appendix A

† Madsen et al. 2015

‡ Calendar dates calculated with OxCal 4.4.4 (Bronk Ramsey, 2021; Reimer et al., 2020), using the Midpoint Age radiocarbon date ± 50 years

These data are further broken out by toolstone source within each group. Table 5-4 and Table 5-5 present the actual artifact counts (*n*) per toolstone source.

Table 5-4: A groups actual artifact counts (n).

Source	A1 n	A2 n	A3 n	Totals
Badlands	14	0	1	**15**
Bear Gulch	0	0	1	**1**
Black Rock Area	5	2	2	**9**
Brown's Bench	23	11	11	**45**
Cedar Mountain	6	0	2	**8**
Currie Hills	2	1	0	**3**
Deep Creek	7	1	1	**9**
Ferguson Wash	0	0	0	**0**
Flat Hills	117	20	38	**175**
Kane Springs Wash Caldera	0	0	0	**0**
Malad	3	0	0	**3**
Mineral Mountains	3	2	3	**8**
Owyhee	1	1	0	**2**
Panaca Summit/Modena	0	0	1	**1**
Paradise Valley	0	1	1	**2**
Topaz Mtn	48	32	37	**117**
Totals:	**229**	**71**	**98**	**398**

Table 5-5: C groups actual artifact counts (n).

Source	C1 n	C2 n	C3 n	C4 n	C5 n	Totals
Badlands	14	0	2	1	0	**17**
Bear Gulch	0	0	0	1	0	**1**
Black Rock Area	5	2	1	2	0	**10**
Brown's Bench	23	11	1	8	3	**46**
Cedar Mountain	6	0	0	2	0	**8**
Currie Hills	2	1	0	0	0	**3**
Deep Creek	7	1	1	1	0	**10**
Ferguson Wash	0	0	1	0	0	**1**
Flat Hills	117	20	5	38	0	**180**
Kane Springs Wash Caldera	0	0	1	0	0	**1**
Malad	3	0	0	0	0	**3**
Mineral Mountains	3	2	1	2	1	**9**
Owyhee	1	1	0	0	0	**2**
Panaca Summit/Modena	0	0	0	1	0	**2**
Paradise Valley	0	1	0	1	0	**1**
Topaz Mtn	48	30	11	21	16	**126**
Totals:	**229**	**69**	**24**	**78**	**20**	**420**

5.3 Establishing the Distances (*d*)

Figure 5-1 (full regional scale) and Figure 5-2 (smaller scale) illustrate the distribution of

utilized toolstone source exposures (*n*=16) in relation to the overall centroid of the ORB

Paleoindian artifacts (*n*=430).
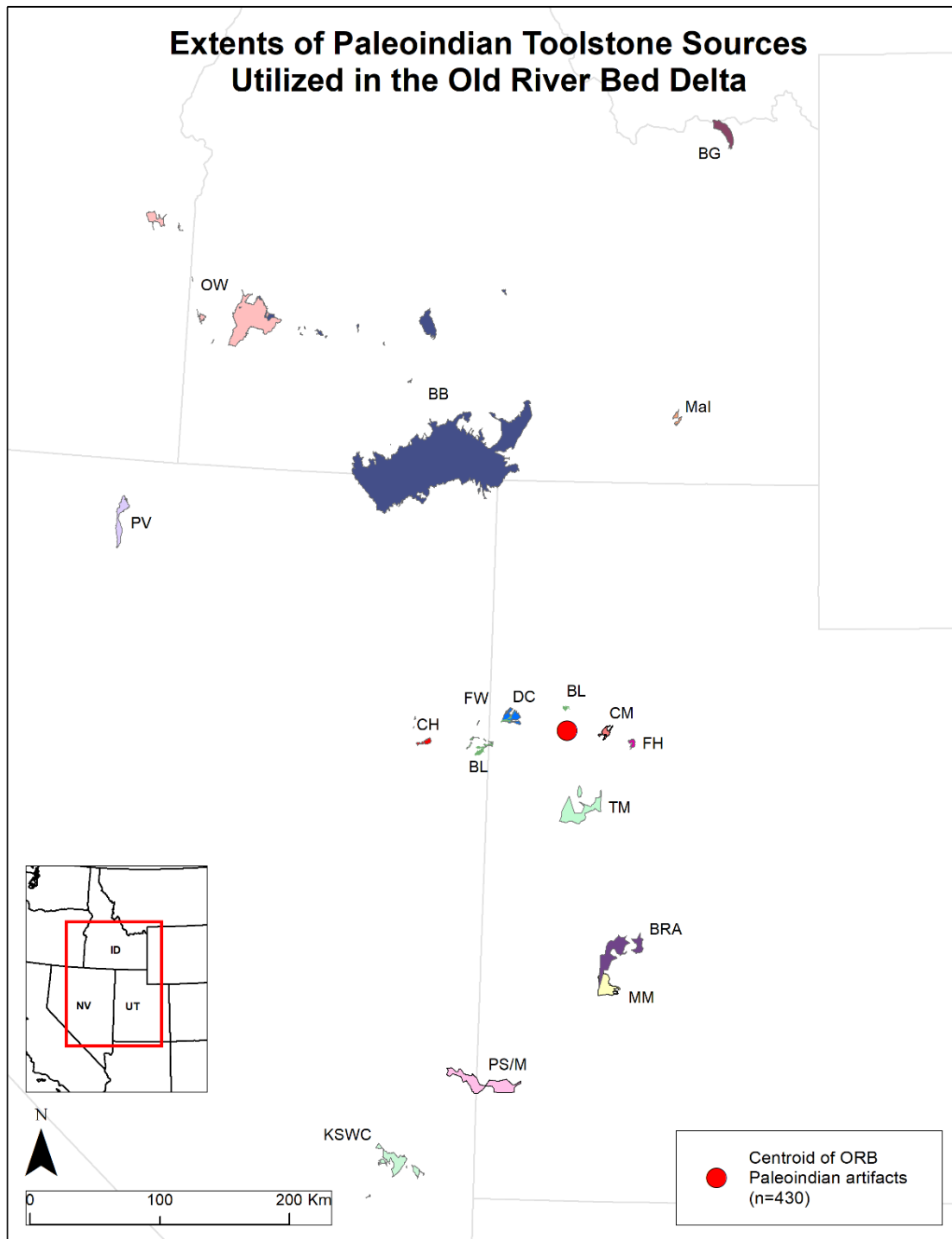
Figure 5-1: Extents of obsidian and fine-grained volcanic (FGV) toolstone sources utilized by Paleoindian people occupying the Old River Bed delta channels. Key: Badlands (BL), Brown's Bench (BB), Bear Gulch (BG), Black Rock Area (BRA), Currie Hills (CH), Cedar Mountain (CM), Deep Creek (DC), Ferguson Wash (FW), Flat Hills (FH), Kane Springs Wash Caldera (KSWC), Malad (Mal), Mineral Mountains (MM), Owyhee (OW), Panaca Summit/Modena (PS/M), Paradise Valley (PV), Topaz Mountain (TM). See Chapters 3 & 4 for individual source details.
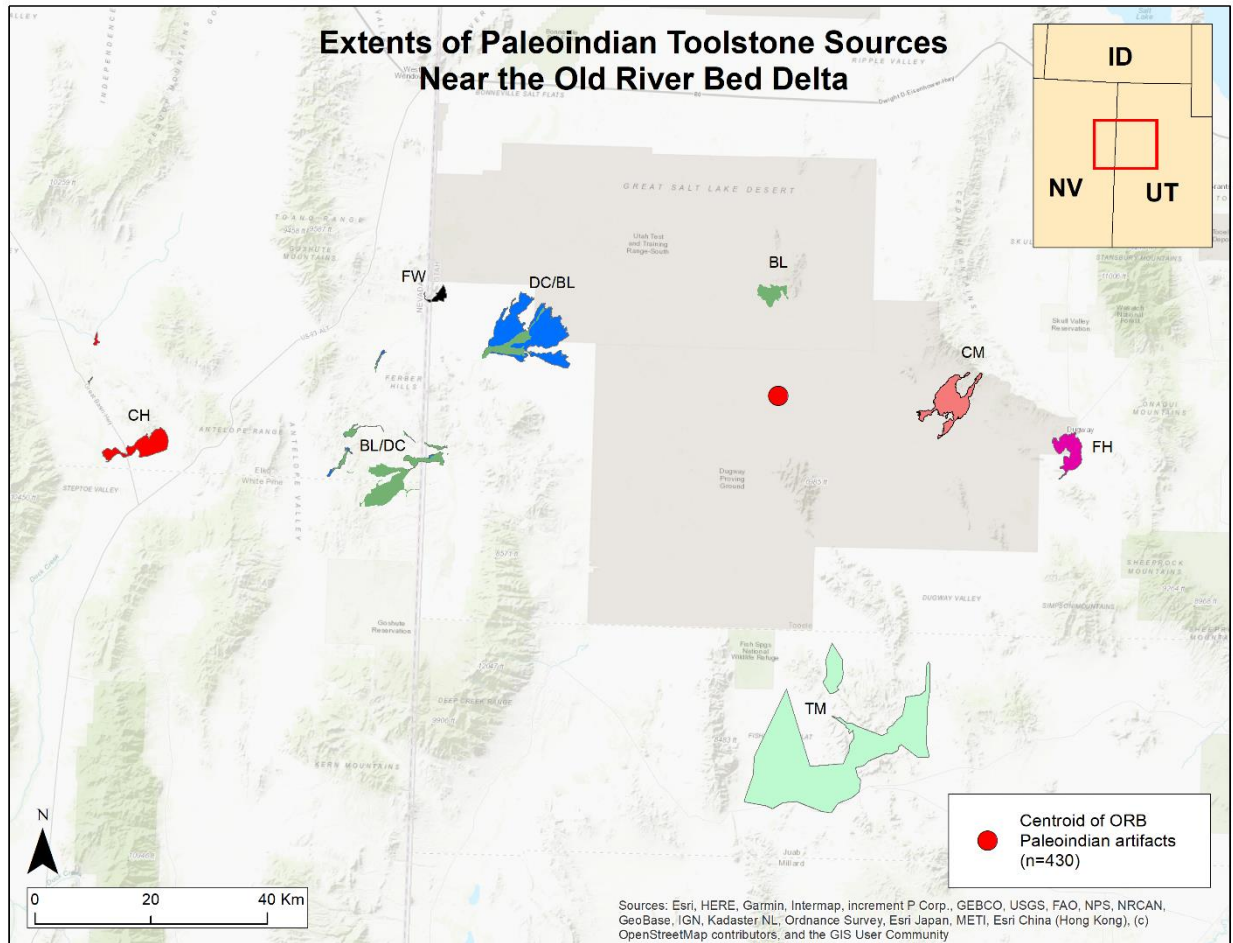
Figure 5-2: Extents of obsidian and fine-grained volcanics (FGV) toolstone sources utilized by Paleoindian people occupying the Old River Bed delta channels (smaller scale). Key: Badlands (BL), Currie Hills (CH), Cedar Mountain (CM), Deep Creek (DC), Ferguson Wash (FW), Flat Hills (FH), and Topaz Mountain (TM). See Chapters 3 & 4 for individual source details.

To determine the Discoverability of each toolstone source in relation to the artifact pools listed in Tables 5-2 and 5-3, the distance (*d*) of the artifacts from the originating source extents (*E*) must be determined. For each group of artifacts, a centroid was calculated using an average of the pooled artifact UTM coordinates (Tables 5-6 and 5-7).

Table 5-6: A groups centroids.

Group Name	Channel Associations	Easting (UTM 12)	Northing
A1	Black	300899	4462256
A2	Green & Yellow	300546	4455275
A3	Light Blue & Lavender	306576	4457929

Table 5-7: C groups centroids.

Group Name	Channel Associations	Easting (UTM 12)	Northing
C1	Black	300899	4462256
C2	Green	300588	4455346
C3	Blue B	297658	4457739
C4	Light Blue	297903	4449522
C5	Lavender	308800	4460085

Using these centroids and the extents surveyed and predicted in Chapters 3 and 4, the least-cost path (LCP) distances from the centroid to the closest discoverable edge of each source extent were calculated. To calculate the LCP, an anisotropic (directionally-dependent) accumulated cost surface (ACS) is derived from a cost, or friction, surface using a cumulative cost algorithm. This was accomplished by applying the ArcMap *Path Distance* (Esri 2022a) function to a regional digital elevation model (DEM), which acts as the friction surface, and using Tobler's (1993) hiking function to calculate travel time (provided in CSV file form by Tripcevich 2009). Tobler's hiking function calculates hiking velocity as it relates to slope; speed increases at slightly negative slopes and decreases when slope increases. The least cumulative cost distance is then generated from this anisotropic cost surface by using the ArcMap *Cost Distance* function (Esri 2022b). Finally, the resultant raster is converted to polylines which represent the most cost-effective travel path between each centroid and the edges of the flow extents. Figure 5-3 illustrates the LCP distances for the A1 groups. The least-cost path distances calculated for each source, dependent on group centroids, are shown in Table 5-8 and Table 5-9. These distances are used in the subsequent Discoverability calculations.

Table 5-8: Least-cost distances (d) of the A groups centroids to the nearest source extent edge.

Source	A1 (km)	A2 (km)	A3 (km)	Mean
Badlands	13.4	20.4	19.6	17.8
Bear Gulch	493.9	500.9	496.7	497.2
Black Rock Area	176.2	168.8	169.9	171.6
Brown's Bench	201.0	208.0	207.3	205.4
Cedar Mountain	26.3	26.4	19.4	24.0
Currie Hills	111.0	109.3	115.0	111.8
Deep Creek	35.4	38.1	42.7	38.7
Ferguson Wash	61.1	63.9	68.6	64.5
Flat Hills	51.1	48.6	43.8	47.8
Kane Springs Wash Caldera	375.8	368.8	374.3	373.0
Malad	265.5	273.8	269.6	269.6
Mineral Mountains	200.7	193.7	194.7	196.3
Owyhee	397.1	402.8	403.9	401.3
Panaca Summit/Modena	284.6	277.7	283.0	281.8
Paradise Valley	402.6	405.7	410.2	406.2
Topaz Mountain	48.9	41.9	42.5	44.4

Table 5-9: Least-cost distances (d) of the C groups centroids to the nearest source extent edge.

Source	C1 (km)	C2 (km)	C3 (km)	C4 (km)	C5 (km)	Mean
Badlands	13.4	19.9	18.5	26.6	18.4	19.4
Bear Gulch	493.9	503.3	552.1	510.1	495.6	511.0
Black Rock Area	176.2	168.2	171.1	162.8	169.3	169.5
Brown's Bench	201.0	207.4	203.9	212.2	206.1	206.1
Cedar Mountain	26.3	25.8	28.2	30.6	17.9	25.8
Currie Hills	111.0	109.8	106.0	106.1	116.2	109.8
Deep Creek	35.4	38.5	34.7	38.3	44.8	38.3
Ferguson Wash	61.1	64.3	60.4	64.0	70.5	64.1
Flat Hills	51.1	49.5	53.3	51.9	43.0	49.8
Kane Springs Wash Caldera	375.8	369.1	370.3	362.3	377.4	371.0
Malad	265.5	275.1	273.9	281.9	267.5	272.8
Mineral Mountains	200.7	193.4	196.6	188.4	196.1	195.0
Owyhee	397.1	407.2	403.5	411.4	407.5	405.3
Panaca Summit/Modena	284.6	280.6	281.9	273.9	290.2	282.2
Paradise Valley	402.6	406.4	452.7	407.3	411.9	416.2
Topaz Mountain	48.9	46.7	50.1	41.8	43.9	46.3
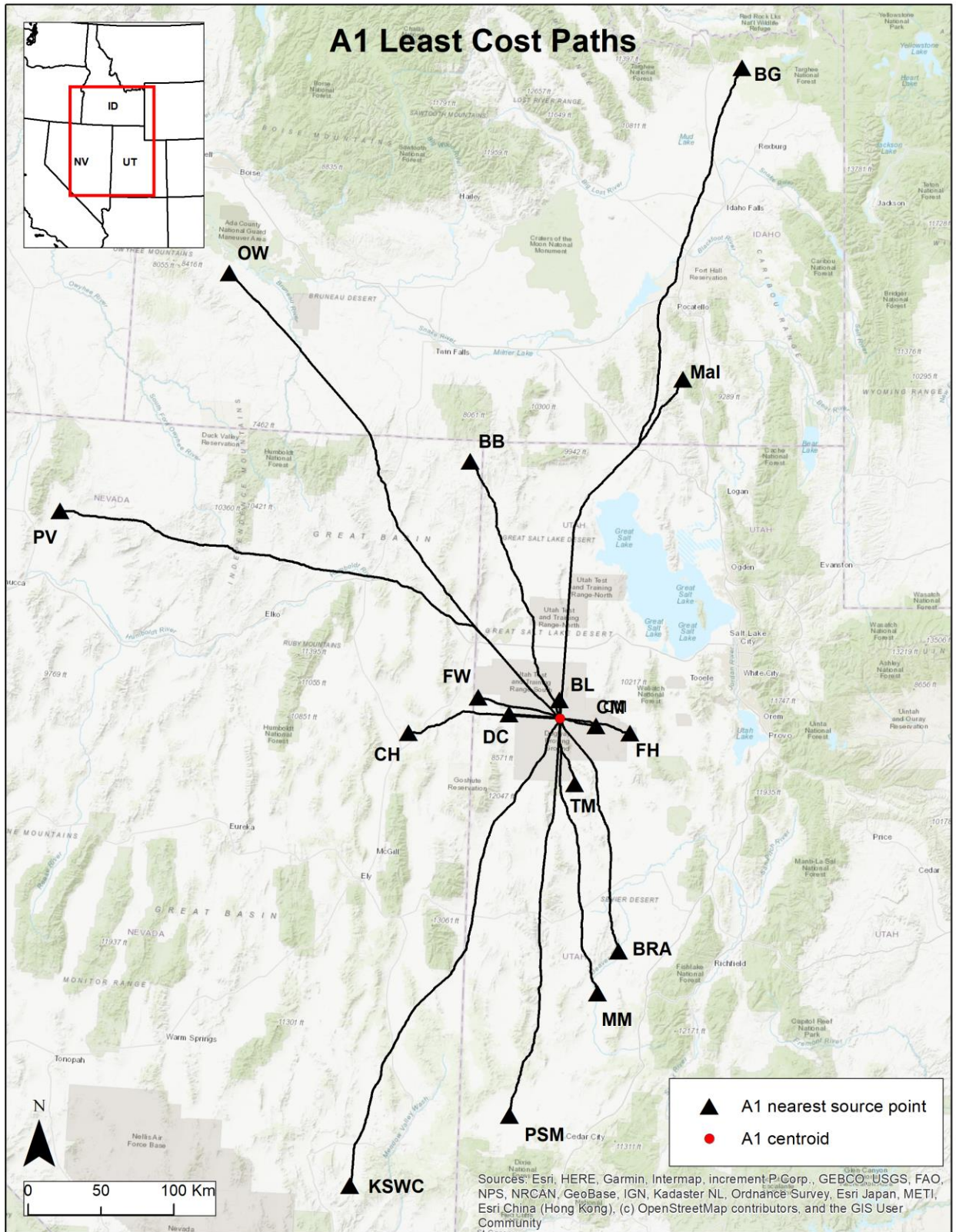
Figure 5-3: Least-cost paths from the A1 centroid to nearest source extents

5.4 Creating the Group *Dlists* and *Olists*

Using the distance (*d*) and exposure (*E*) values for each toolstone source, the Discoverability value (*D*) was calculated for each source using *Equation* 2-2:

$$D = E * \frac{1}{d^2}$$

(Eq. 2-2)

Within each group, the *D* values were normalized to a percentage that represents the "expected" proportion of source use within that pooled group. These percentages were then ranked, with any tied ranks receiving an average of the tied scores. This ranked list is the group's Discoverability list, or *Dlist*, the expected ranked order of toolstone source use in an unknown/unlearned landscape. Similarly, the Observed list, or *Olist*, is calculated by determining the proportion of the actual number of artifacts belonging to each known source. These proportions are then ranked, creating the *Olist*.

Table 5-10 presents the calculations of the *Dlist* and the *Olist* for the A1 group. The Group A and Group C *Dlists* and *Olists* are shown in Table 5-11 and Table 5-12, respectively. The large number of ties shown in these tables reflects the unfortunately small samples of sourced ORB Paleoindian artifacts available for the analyses presented here. Those small samples, and resultant large number of tied ranks (most notable for group C5 in Table 5-12), decrease the potential accuracy and precision of statistical analyses applied to them. I return to this issue in the summary.

Table 5-10: Calculation of Discoverability (D) values, the Dlist ranks, and the Olist ranks for the A1 pool.

Source	d (km)	E (km²)	D	Expected proportions (100×D/ΣD)	Dlist rank	Artifact counts (N=229)	Observed proportions (100×n/N)	Olist rank
Badlands	13.4	66	0.369566	45.86%	1	14	6.1%	4
Bear Gulch	493.9	128.8	0.000528	0.07%	15	0	0.0%	14
Black Rock Area	176.2	353	0.011370	1.41%	6	5	2.2%	7
Brown's Bench	201.0	5173	0.128041	15.89%	2	23	10.0%	3
Cedar Mountain	26.3	37	0.053356	6.62%	5	6	2.6%	6
Currie Hills	111.0	26.1	0.002117	0.26%	11	2	0.9%	10
Deep Creek	35.4	107.6	0.086040	10.68%	4	7	3.1%	5
Ferguson Wash	61.1	4	0.001072	0.13%	13	0	0.0%	14
Flat Hills	51.1	21	0.008049	1.00%	7	117	51.1%	1
Kane Springs Wash Caldera	375.8	207	0.001466	0.18%	12	0	0.0%	14
Malad	265.5	23.8	0.000338	0.04%	16	3	1.3%	8.5
Mineral Mountains	200.7	170	0.004221	0.52%	10	3	1.3%	8.5
Owyhee	397.1	829.4	0.005260	0.65%	8	1	0.4%	11
Panaca Summit/Modena	284.6	358	0.004419	0.55%	9	0	0.0%	14
Paradise Valley	402.6	134.2	0.000828	0.10%	14	0	0.0%	14
Topaz Mountain	48.9	309	0.129164	16.03%	3	48	21.0%	2

Table 5-11: Dlist and Olist ranked list pairs for the A groups.

Source	A1 Dlist	A1 Olist	A2 Dlist	A2 Olist	A3 Dlist	A3 Olist
Badlands	1	4	2	13	1	9
Bear Gulch	15	14	15	13	15	9
Black Rock Area	6	7	6	4.5	6	5.5
Brown's Bench	2	3	3	3	3	3
Cedar Mountain	5	6	5	13	4	5.5
Currie Hills	11	10	11	7.5	11	14
Deep Creek	4	5	4	7.5	5	9
Ferguson Wash	13	14	13	13	13	14
Flat Hills	7	1	7	2	7	1
Kane Springs Wash Caldera	12	14	12	13	12	14
Malad	16	8.5	16	13	16	14
Mineral Mountains	10	8.5	9	4.5	10	4
Owyhee	8	11	8	7.5	8	14
Panaca Summit/Modena	9	14	10	13	9	9
Paradise Valley	14	14	14	7.5	14	9
Topaz Mountain	3	2	1	1	2	2

Table 5-12: Dlist and Olist ranked list pairs for the C groups.

Source	C1 Dlist	C1 Olist	C2 Dlist	C2 Olist	C3 Dlist	C3 Olist	C4 Dlist	C4 Olist	C5 Dlist	C5 Olist
Badlands	1	4	2	13	1	3	3	9	3	10
Bear Gulch	15	14	15	13	15	13	15	9	15	10
Black Rock Area	6	7	6	4.5	6	6.5	6	5	6	10
Brown's Bench	2	3	3	3	3	6.5	2	3	2	2
Cedar Mountain	5	6	5	13	5	13	5	5	5	10
Currie Hills	11	10	11	7.5	11	13	11	14	11	10
Deep Creek	4	5	4	7.5	4	6.5	4	9	4	10
Ferguson Wash	13	14	13	13	13	6.5	13	14	13	10
Flat Hills	7	1	7	2	7	2	7	1	7	10
Kane Springs Wash Caldera	12	14	12	13	12	6.5	12	14	12	10
Malad	16	8.5	16	13	16	13	16	14	16	10
Mineral Mountains	10	8.5	9	4.5	10	6.5	9	5	9	3
Owyhee	8	11	8	7.5	8	13	8	14	8	10
Panaca Summit/Modena	9	14	10	13	9	13	10	9	10	10
Paradise Valley	14	14	14	7.5	14	13	14	9	14	10
Topaz Mountain	3	2	1	1	2	1	1	2	1	1

5.5 A Groups Analysis

The A groups represent the largest available sample clusters of ORB Paleoindian artifacts within non-overlapping temporal ranges (see Table 5-2).

If the utilization of toolstone is deterministic, driven only by its Discoverability variables, I expect to see a strongly positive monotonic relationship between the *Dlist* and *Olist* for each group; that is, a significant positive correlation between the two sets. The *Dlist* and *Olist* ranked lists are, by definition, ordinal data and Spearman's (1904) rank-order correlation test is a non-parametric monotonicity test appropriate for such a comparison. For 100% positive monotonic results, Spearman's should return an r_s of +1, (*Dlist* = *Olist*) and decrease toward zero (increasingly non-monotonic) as landscape learning affects the *Olist*.

5.5.1 A Groups Correlation Statistics

For each A group, the Spearman's rank order correlation coefficient for the relationship between the *Dlist* and *Olist* was calculated (Table 5-13) and the *p* values for all A groups are significant ($\alpha = 0.05$). For the A groups, the correlation coefficients indicate an initially high correlation, falling off to moderately correlated data.

Table 5-13: A groups Spearman's r_s results.

Group	Spearman's r_s	*p* value
A1	0.777	0.0004
A2	0.502	0.048
A3	0.592	0.016

5.5.2 A Groups Descriptive Statistics

Among the A groups, outliers may be subjectively assessed by calculating the absolute difference between the expected rank for a given source versus the actual observed rank (Table 5-14) and by review of scatter plots presenting the bivariate relationships between the A group *Dlists* and *Olists* (Figures 5-3 – 5-5).

For the A1 group, Malad and Flat Hills have the most extreme rank differences and are potential outliers (see also Figure 5-4). For Malad, this is simply a case of a source with a very low Discoverability rank (16th) which is elevated by 3 artifacts appearing in the assemblage. However, the case with Flat Hills is remarkable. As shown in Table 5-4, the artifact counts for Flat Hills are extremely high relative to all other source counts. This raises Flat Hills to the 1st rank of the A1 *Olist*, and a marked difference from its expected *Dlist* rank (7th). In fact, it is evident from Table 5-4 that Flat Hills is a highly utilized source across all the A groups (discussed further below).

The Cedar Mountain source is quite close to the ORB but is absent from the pooled A2 assemblage. As a result, the expected (5th) and the observed (13th) ranks for this source differ substantially.

The Badlands source appears exceptionally underutilized in the A2 and A3 groups, where it is expected to command the 2nd and 1st ranks, respectively. This is anomalous to its utilization in A1, where its expected rank was 1st and it appears in the 4th rank. The Badlands source is, on average, only about 18 km (Table 5-8) from the A groups clusters, while the highly utilized Flat Hills source is about 48 km away. That Page (2008) classifies Badlands as a high-quality fine-grained volcanic (FGV) suggests that adaptive factors other than distance, exposure, and quality might be at play here. Those factors might also explain the virtual abandonment of this source in later temporal periods. This becomes even more evident when evaluating the C groups (below).

Table 5-14: A groups rank differences with potential outliers highlighted.

Source	A1 diffs	A2 diffs	A3 diffs
Badlands	3	**11**	**8**
Bear Gulch	1	2	6
Black Rock Area	1	1.5	0.5
Brown's Bench	1	0	0
Cedar Mountain	1	**8**	1.5
Currie Hills	1	3.5	3
Deep Creek	1	3.5	4
Ferguson Wash	1	0	1
Flat Hills	**6**	5	6
Kane Springs Wash Caldera	2	1	2
Malad	**7.5**	3	2
Mineral Mountains	1.5	4.5	6
Owyhee	3	0.5	6
Panaca Summit/Modena	5	3	0
Paradise Valley	0	6.5	5
Topaz Mountain	1	0	0

Figures 5-4, 5-5, and 5-6 illustrate the scatter plots for the A groups, with possible outliers labeled.
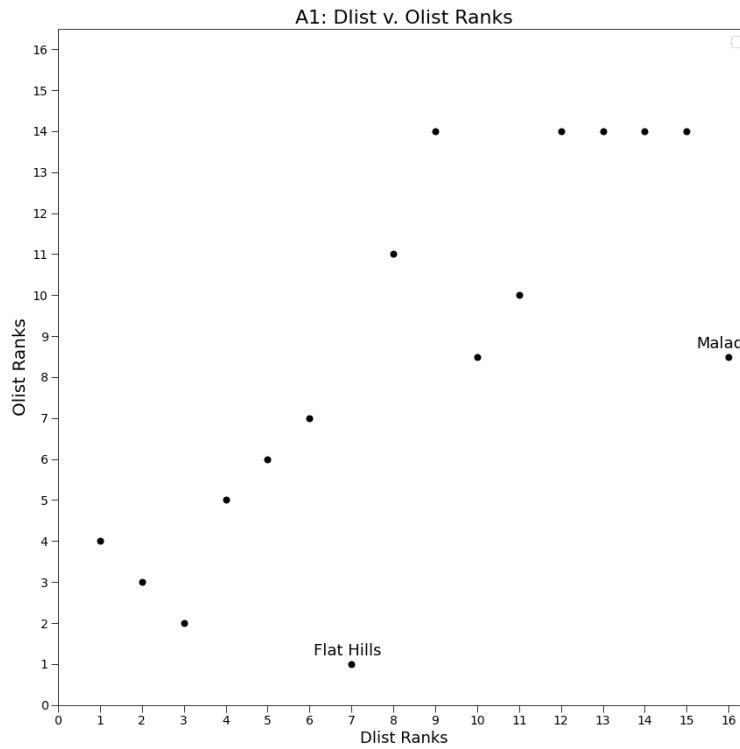
Figure 5-4: A1 scatter plot with Flat Hills and Malad outliers noted.
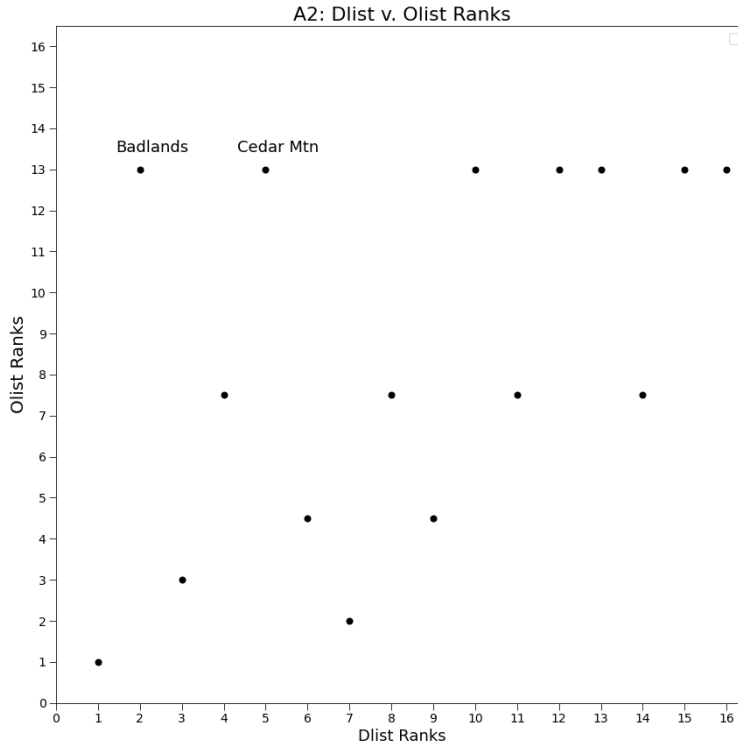
Figure 5-5: A2 scatter plot with Badlands and Cedar Mountain outliers noted.
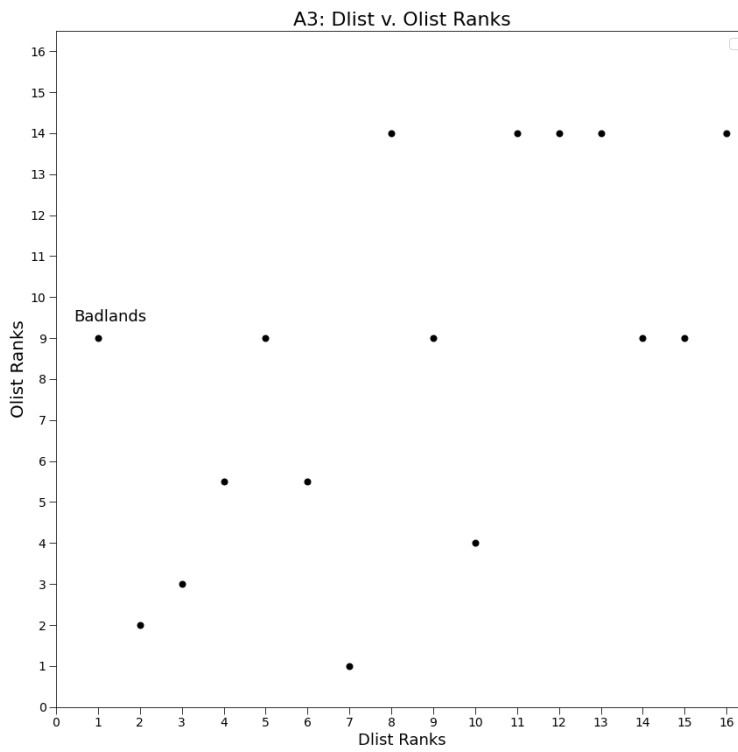
Figure 5-6: A3 scatter plot with Badlands outlier noted.

230

5.5.3 A Groups Landscape Learning

The level of landscape learning for each A group was calculated using *Equation* 2-3:

$$\%LL = (1 - r_s{}^2) * 100 \qquad\qquad \text{(Eq. 2-3)}$$

Table 5-15: A groups %LL calculation.

Group	Spearman's r_s	$r_s{}^2$	%LL
A1	0.777	0.603	39.7%
A2	0.502	0.252	74.8%
A3	0.592	0.350	65.0%

The A groups *%LL* and midpoint ages are presented in Table 5-16 and plotted in Figure

5-7 (using calibrated years BP).

Table 5-16: A groups %LL and mean ages.

Group	%LL	Midpoint Age (^{14}C yr BP/cal BP)
A1	39.6	10,650/12,674
A2	74.8	10,050/11,578
A3	65.0	9,300/10,444
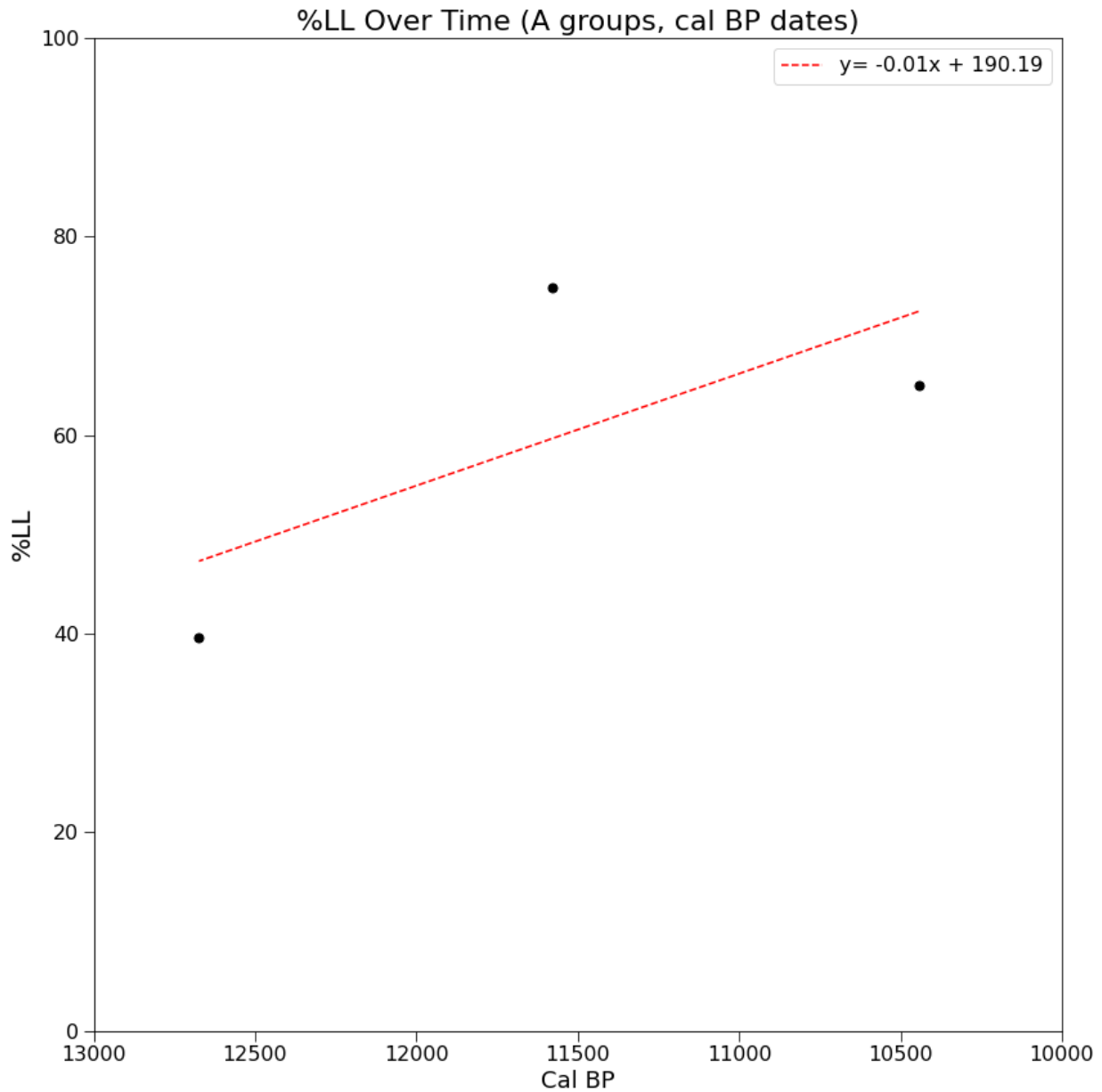
Figure 5-7: Regression of %LL across A groups using calibrated years BP.

The fitted line returns a Pearson's *r* of 0.692 (*p* = 0.514) and a coefficient of determination (R^2) of 0.479, suggesting that ~48% of the variance of *%LL* over time is explained by my model. While *%LL* appears to present an upward trend over time, there is not much more that can be concluded with statistical rigor from only these three sample points. Using radiocarbon rather than calibrated dates in this analysis produces slightly lower results (R^2 = 0.425).

5.5.4 A Groups Outliers Discussion

The descriptive statistics reveal a few instances of possible outliers, which are highlighted in Table 5-14. In the Flat Hills case, there are many more samples than expected (n=117 or 51% of the entire A1 group sample set). As noted in section 5.5.2, Flat Hills presents more samples than expected in all three A groups.

Flat Hills FGV may also stand out as a geological and logistical outlier when considering all the toolstone sources utilized in the ORB. Flat Hills FGV manifests as cobbles of high quality and large enough for tools, mixed within a sandbar (tombolo) on the basin bottom, remnants of material transported and deposited by receding Lake Bonneville (Page, 2008; see also Chapter 4). This exposure differs significantly from the alluvial fan patterns seen in basin bottoms during my survey work, described in Chapter 3, where only pebbles, usually too small for tools, reach the basin bottom. These small pebbles may present a Discoverability signal but rarely present a quarrying opportunity. The geologic phenomenon of Flat Hills FGV, its high quality, and easy accessibility at low elevation, may have resulted in a greater attractiveness upon discovery, fueling higher utilization early in the occupation of the ORB. It is possible that this explains why Flat Hills is consistently very highly ranked across all groups, when its discoverability index suggests it should rank much lower. This source was clearly "learned" at the earliest dated periods at the ORB occupation, and well-utilized across all occupation periods, exceeding the predictions derived from the model presented here. On the other hand, given that I have used a significance level of $\alpha = 0.05$, one outlier is not unexpected by chance within a set of 16 samples, and it is possible, though unlikely, that this has occurred by chance.

5.6 C Groups Analysis

The C groups divide the ORB Paleoindian artifacts into the largest number of distinct

temporal groups while maintaining statistically meaningful assemblage sizes.

5.6.1 C Groups Correlation Statistics

For each C group, the Spearman's rank order correlation coefficient was calculated and the

p values for all C groups are significant ($\alpha = 0.05$). For the C groups, the correlation coefficients

indicate an initially high correlation, falling off to moderately correlated data.

Table 5-17: C groups Spearman's r_s results.

Group	Spearman's r_s	p value
C1 (Black channel)	0.777	0.0004
C2 (Green)	0.570	0.021
C3 (Blue B)	0.597	0.015
C4 (Light Blue)	0.648	0.007
C5 (Lavender)	0.500	0.048

5.6.2 C Groups Descriptive Statistics

As with the A groups, among the C groups, outliers may be detected by calculating the

absolute difference between the expected rank for a given source versus the actual observed rank

(Table 5-18) and by review of scatter plots presenting the bivariate relationships between the C

group *Dlists* and *Olists* (Figures 5-8 – 5-12).

The C1 group (the Black channel) is the same as the A1 group (see above) with the same

potential outliers; Malad and Flat Hills have the most extreme rank differences (see also Figure

5-8).

As in the A2 group, the Cedar Mountain source is absent from the C2 pooled assemblage

(the Green channel). As a result, the expected (5th) and the observed (13th) ranks for this source

differ substantially.

The C3 group comprises a smaller set of artifacts (*n*=24) from the Blue B channel. Cedar Mountain is absent from this assemblage, resulting in the largest rank difference. A single sample from Ferguson Wash creates the second largest rank difference.

As in the A groups, the Badlands source appears remarkably underutilized in the C2 – C5 groups, where it is expected to occupy one of the top 3 ranks in each group. This is anomalous to its utilization in A1/C1, where its expected rank was 1st and it appears in the 4th rank, resulting in an unremarkable difference. As noted above, the Badlands FGV appears to be almost abandoned in later temporal groups, superseded by Flat Hills FGV as the dominant toolstone.

In the C5 group, it is important to note that this group has the lowest sample size (*n*=20) and exhibits the lowest toolstone source richness (*n*=3) of all the groups. This results in thirteen tied ranks where source samples are absent, a prime example of the sample size problem I noted above and to which I return in the summary.

Table 5-18: C groups rank differences with potential outliers highlighted

Source	C1 diff	C2 diff	C3 diff	C4 diff	C5 diff
Badlands	3	**11**	2	**6**	**7**
Bear Gulch	1	2	2	**6**	5
Black Rock Area	1	1.5	0.5	1	4
Brown's Bench	1	0	3.5	1	0
Cedar Mountain	1	**8**	**8**	0	5
Currie Hills	1	3.5	2	3	1
Deep Creek	1	3.5	2.5	5	6
Ferguson Wash	1	0	**6.5**	1	3
Flat Hills	**6**	5	5	**6**	3
Kane Springs Wash Caldera	2	1	5.5	2	2
Malad	**7.5**	3	3	2	6
Mineral Mountains	1.5	4.5	3.5	4	6
Owyhee	3	0.5	5	**6**	2
Panaca Summit/Modena	5	3	4	1	0
Paradise Valley	0	6.5	1	5	4
Topaz Mtn	1	0	1	1	0

Figures 5-8 through 5-12 present the plots for the C groups, with possible outliers labeled.
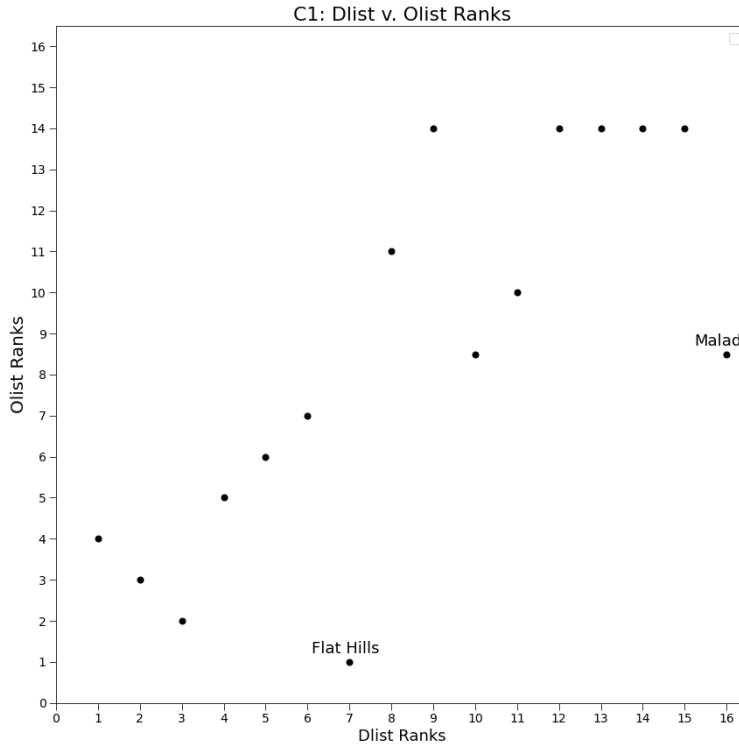
*Figure 5-8: C1 scatter plot with Flat Hills and Malad outliers indicated.
Note: the C1 group is identical to the A1 group.*
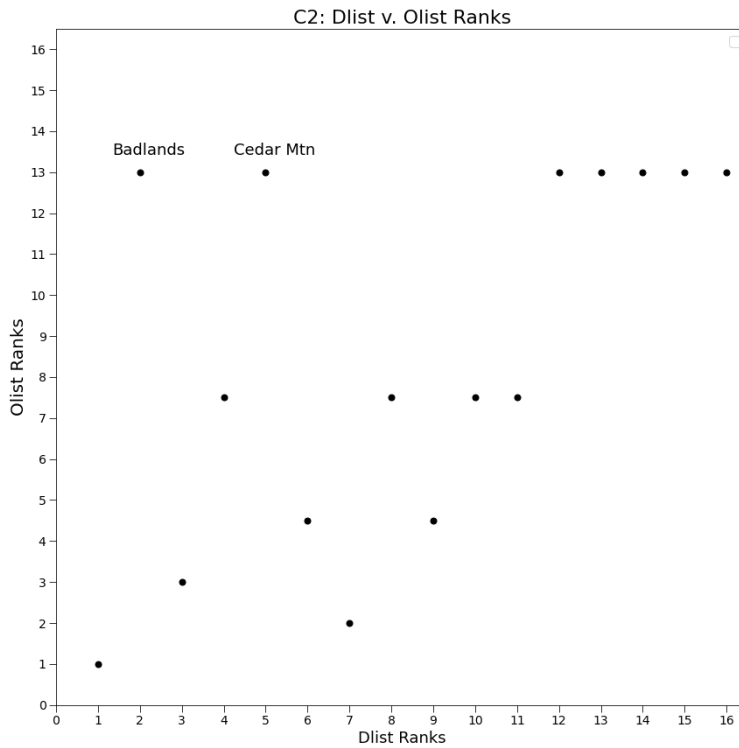
Figure 5-9: C2 scatter plot with Badlands and Cedar Mountain outliers indicated.

236
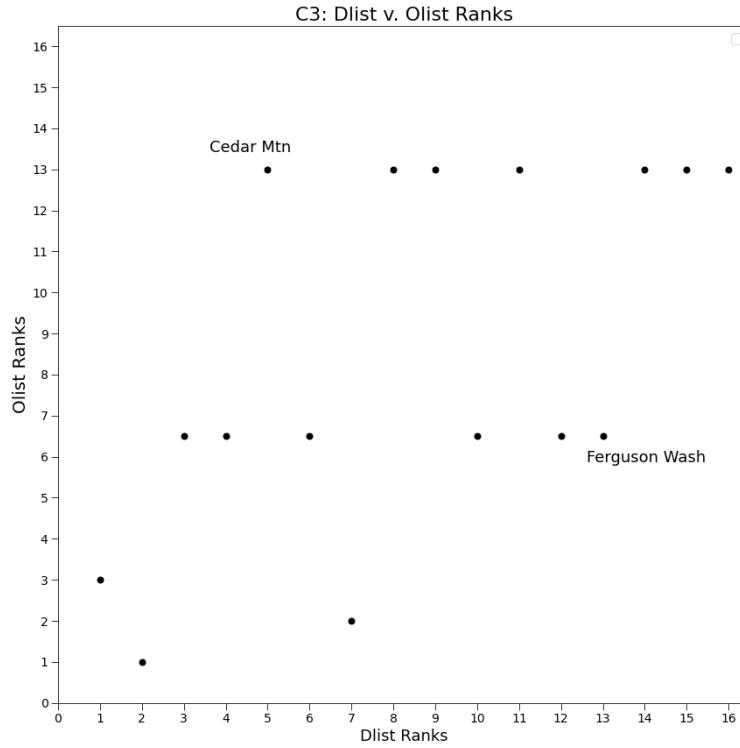
Figure 5-10: C3 scatter plot with Cedar Mountain and Ferguson Wash outliers indicated.
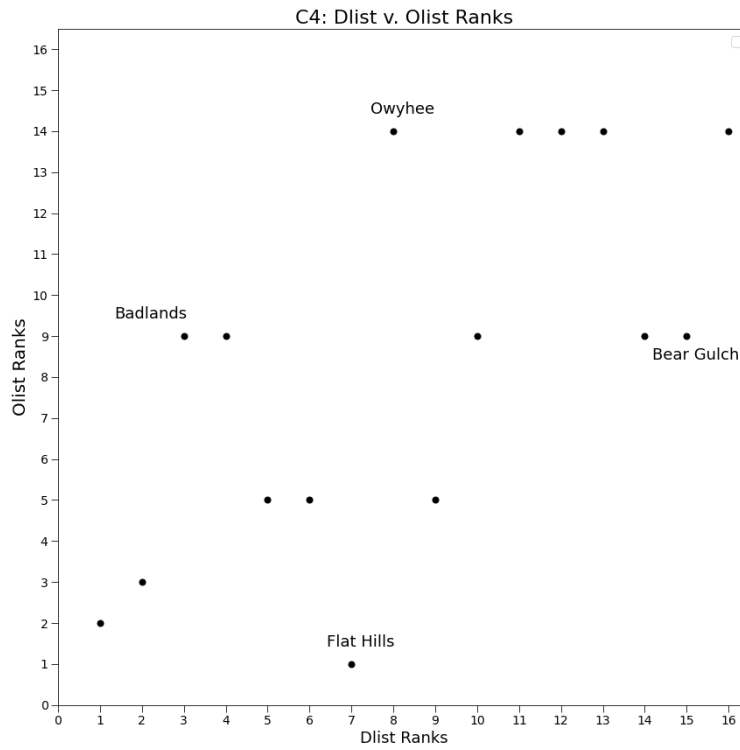
Figure 5-11: C4 scatter plot with outliers indicated.

237
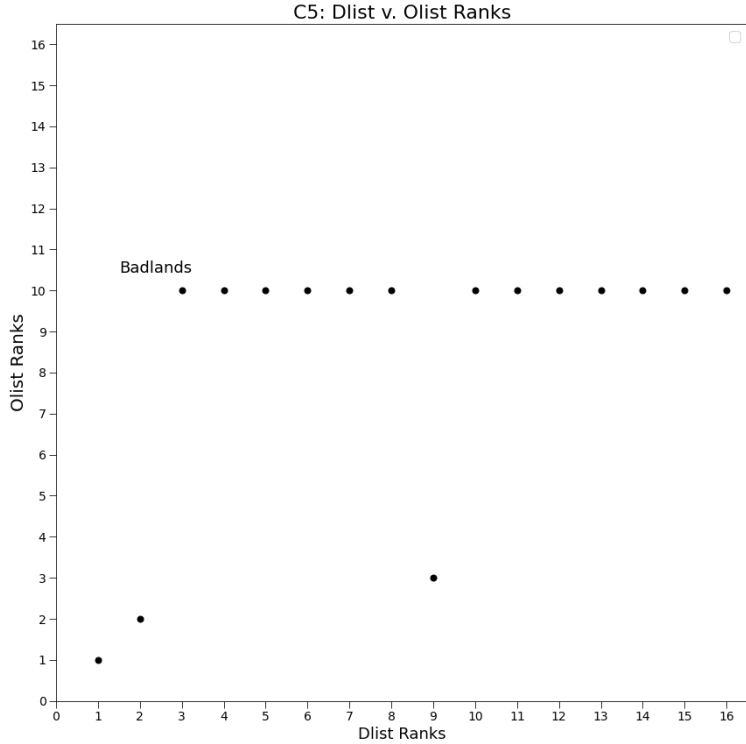
Figure 5-12: C5 scatter plot with Badlands outlier indicated.

5.6.3 C Groups Landscape Learning

The level of landscape learning for each C group was calculated using *Equation* 2-3:

$$\%LL = (1 - r_s^2) * 100 \qquad\qquad \text{(Eq. 2-3)}$$

Table 5-19: C groups %LL results.

Group	Spearman's *r*	r_s^2	*%LL*
C1	0.777	0.603	39.7%
C2	0.570	0.325	67.5%
C3	0.597	0.357	64.3%
C4	0.648	0.420	58.0%
C5	0.500	0.250	75.0%

The C groups *%LL* and midpoint ages are presented in Table 5-20 and plotted in Figure

5-13 (using calibrated years BP).

238

Table 5-20: C groups %LL and mean ages.

Group	*%LL*	**Midpoint Age** (^{14}C yr BP/cal BP)
C1	39.7	10,650/12,674
C2	67.5	10,050/11,578
C3	64.3	9,750/11,167
C4	58.0	9,300/10,444
C5	75.0	9,050/10,221
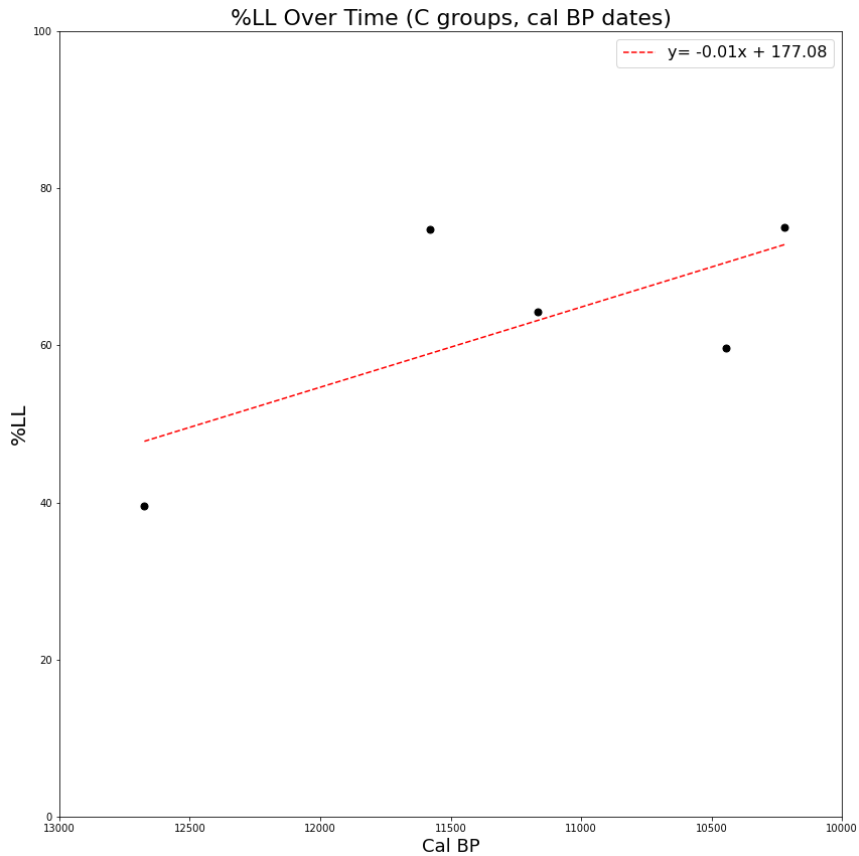
Figure 5-13: Regression of %LL across A groups using calibrated years BP.

Using calibrated year dates, the fitted line returns a Pearson's *r* of 0.689 ($p = 0.20$) and a coefficient of determination (R^2) of 0.474, suggesting that ~47% of the variance of *%LL* over time is explained by my model. Using radiocarbon dates in this analysis produces slightly lower results ($R^2 = 0.442$).

5.7 Summary

In this chapter, I tested the Discoverability model, which hypothesizes that landscape learning can be detected over time by analyzing the utilization of known toolstone resources and the relation of those resources to a given assemblage in terms of exposure size (*E*) and distance (*d*).

Using the Paleoindian artifact data recorded at the ORB delta (Appendix A), artifacts were divided into non-overlapping, discrete temporal ranges. The A groups (*n*=3) emphasized grouping the largest available sample sizes per temporal group while the C groups (*n*=5) emphasized creating the largest number of distinct temporal groups. These groupings provided the best possibilities for analyzing landscape learning despite the small sample sizes available. I then applied my Discoverability equation (Eq. 2-2) and the *%LL* equation (Eq. 2-3) to each of these discrete assemblages in conjunction with the source extents surveyed and predicted in Chapters 3 and 4.

For both the A and C groups, the oldest assemblages (A1 and C1 were identical) presented very strong correlations (r_s = 0.777) with their expected, and deterministic, *Dlists*. This, in turn, returned the lowest level of landscape learning of any of the temporal groups (*%LL*=39.7%), as the model predicts. Importantly, the magnitude of difference in *%LL* (δ=35.1% and 27.8%) between the oldest and next oldest assemblages (A1:A2 and C1:C2) is significantly greater than any differences between any other subsequent temporal steps for either the A or C groups. Even the differences between the A1/C1 values and the next lowest *%LL* values in each group were 25.3% (A1:A3) and 18.3% (C1:C4), greater than any differences between any subsequent time periods (the next greatest difference is C4:C5 at 17%). These results seem to indicate a

significant step in landscape learning between the earliest assemblages and the next temporally discrete assemblages.

There are multiple reasons why we may not see greater discrimination between the later temporal assemblages. The most obvious is the limitations of the available sample sizes, particularly in the C groups (C3 and C5 are especially small, see Table 5-5). The small sample sizes are further affected by the large number of available obsidian/FGV sources (n=16) which dilute the rank values within the *Dlists* and increases the number of ties for those groups.

It is also likely that by the time of the "next oldest" temporal group, the landscape has largely been learned. The age step between A1:A2 and C1:C2 is ~1096 cal years (see Tables 5-2 and 5-3). While we see a significant *%LL* step, we do not see any significant change in toolstone source richness (Table 5-21) between the earliest and later temporal assemblages. In fact, A1/C1 have the highest level of source richness (n=11) of the temporal groups. This seems to imply that the ORB delta lithic universe was "learned" within that first temporal step. The variation in *%LL* we see beyond this first step then may be random variations or variations dependent on other human behaviors this model does not quantify.

Table 5-21: Toolstone source richness by temporal group.

Temporal group	Toolstone richness n
A1	11
A2	9
A3	11
C1	11
C2	9
C3	9
C4	11
C5	3

Finally, both the A and C groups provide similar R^2 values, 0.479 and 0.474, respectively, suggesting that up to 48% of the variance in landscape learning over time is explained by my Discoverability model.

5.8 Repository and Software

GitHub repository (*GitHub*, 2021). All Jupyter notebooks, spreadsheets, and source extent shapefiles used for the calculations in this chapter are available in GitHub repository DOI: 10.5281/zenodo.6544114. These are also available directly at GitHub:

https://github.com/davehunt00/dhunt00_dissertation

The following software tools were used to create the programs described in this chapter:

Anaconda Navigator, v. 1.9.12 ("Anaconda Software Distribution," 2021). The versions of all installs and libraries encapsulated in this aggregation are listed in the environment.yml file in the repository referenced below.

Jupyter Notebook, v. 6.0.3 (*Project Jupyter*, 2021). Jupyter notebooks were created to run the regression analysis, graph and analyze the resultant data, and to replicate various figures that appear in this chapter.

Python v. 3.7.6 (64-bit) (Python Software Foundation, 2021). The Jupyter notebooks utilize this Python version.

ArcGIS Desktop 10.8.1 (Esri, 2021a). The toolstone source extent shapefiles were created using this software and are available in the GitHub repository.

Chapter 6:   Conclusions

In this dissertation, I proposed new methodologies for measuring landscape learning and gauging residence time on a landscape. I used the landscape learning model to set expectations and proposed testable hypotheses utilizing these methods. The model and methodologies were then tested against data in the context of a Paleoindian colonizing event within the Old River Bed (ORB) delta in Utah.

At the conclusion of Chapter 1, I asked:

> *Can landscape learning be detected in the archaeological record and used to*
>
> *place assemblages in relative chronological order?*

In Chapter 2, I developed and demonstrated my Discoverability model, a model to predict the order in which a random walker will discover patchy resources found on a neutral landscape, dependent only on distance and patch size. The simulation results for the model positively supported my hypothesis that patch size affects encounter rate and that the model could be used to create a deterministic baseline for patch discovery on an otherwise "unknown landscape"; in other words, a baseline against which to measure the accumulation of landscape knowledge over time.

The Discoverability model requires knowing the size of the resource patches on the landscape. In the Great Basin, most prehistorically utilized lithic sources are geographically known as point samples and in general locational terms. However, the size of the secondary distributions, the flow of obsidian or fine-grained volcanic (FGV) sediments by alluvial or colluvial action, are unknown. This is important because I argue that these secondary distributions likely acted as signals to hunter-gatherers as they foraged, directing them to primary sources.

In Chapter 3 I presented an original methodology to quantitatively determine these toolstone patch sizes, or exposure extents (E). My methodology uses hydrographic algorithms along with known primary source locations or, in their absence, proxy sources as algorithm seeds, to predict the primary and secondary distribution signals on the landscape.

Testing this methodology involved extensive field work at five of the 16 toolstone sources used by Paleoindians residing in the ORB delta. The results (Tables 3-7 and 3-8) demonstrate that, on average, the methodologies predicted 66% of the actual downslope flow of obsidian sediments. From these tests, the optimal digital elevation model (DEM) smoothing (the Smoothing Index) was determined, and when this level of smoothing was applied to the hydrographic models for all sources (less Ferguson Wash, excluded by exception), the methodology successfully returned an average scaled prediction of 89% of the area of the actual surveyed flow extents. The success of these tests validates my method to then predict patch size of many sources at a consistent scale without the need for extensive field work. There is, however, room for improvement in these methodologies. They are reliant on some knowledge of upslope toolstone sources, though I demonstrate how a few point samples can provide a proxy for the primary source. Also, while the flow predictions conformed well in steeper areas, they suffered in the very flat basin bottoms typical of the Great Basin. Increased resolution of digital elevation data, such as that of LiDAR datasets, may help increase the predictive performance of these methods in the future.

In Chapter 4, the optimal Smoothing Index was used to predict the secondary distributions of the remaining 11 toolstone sources that were not surveyed. Together with the five surveyed sources these provided the exposure (E) variable inputs for the Discoverability model.

In Chapter 5, I tested my Discoverability model using the exposure (E) values derived from the ORB toolstone sources in Chapters 3 and 4. The ORB Paleoindian assemblages were divided into temporal groups and centroids for each assemblage were determined. Using these centroids and the nearest exposure edge of the 16 toolstone sources, the distances (d) were calculated. For each assemblage, the Discoverability values (D) were calculated using the E and d values (Eq. 2-2) for each toolstone source and the *Dlists* of expected rank-order usage of toolstone sources were created. The corresponding *Olists* were created using the observed toolstone proportions in each assemblage. The *Dlists* and *Olists* were then compared using Spearman's rank order correlation. From these results, the landscape learning variable (*%LL*) was calculated (Eq. 2-3) for each temporal group/assemblage.

The oldest temporal group's *Olist* returned a very strong correlation ($r_s = 0.777$) with its expected *Dlist*. This, in turn, returned the lowest level of landscape learning of any of the temporal groups (*%LL*=39.7%), as my model predicts. Importantly, the magnitude of difference in *%LL* (δ=35.2%) between the oldest and next oldest assemblage (~1096 cal years later) is significantly greater than the differences between any other subsequent temporal steps between the assemblages. These results indicate a significant step in landscape learning between the earliest assemblage and the next temporally discrete assemblages.

While there are multiple reasons why we may not see greater discrimination in *%LL* between the later temporal groups, in this case study the most obvious is the limitation of available sample sizes. The small sample sizes are further affected by the large number of regionally utilized toolstone sources (*n*=16) which dilute the rank values and negatively affect the strength of the rank correlation tests. It is also likely that the landscape had been fully learned between the first temporal assemblage and the next, a span of ~1096 cal years. This is not out of

line with expectations set in Chapter 1, though it seems to occur more quickly than Tolan-Smith (2003) predicts (one to two millennia) at this regional scale, albeit in a very different geographic setting. At the ORB delta, it appears that landscape learning occurred quickly relative to the resolution of the archaeological record, perhaps culminating within ~1100 years. Variation in landscape learning (*%LL*) between later assemblages is likely the result of small sample sizes and human behavioral variations not quantified by this model. Overall, the results suggest that up to 48% of the variance in landscape learning over time at the ORB delta is explained by my Discoverability model.

The answer, then, to my opening question is "Yes, with limitations". It does appear that the methods introduced here effectively measure the accumulation of landscape knowledge and therefore, act as a proxy for residence on the landscape. With this information, the methods show promise as a means to place assemblages in relative order, based on increasing landscape knowledge. However, there appear to be two primary limitations. Given the speed at which landscape learning appears to occur, even at this large regional scale, the archaeological record under examination must provide sufficient temporal resolution in proportion to the regional scale. Second, the methods are limited by adequate sample sizes, a common problem with Paleoindian data, which themselves are subject to further dilution depending on the number of resource patches that exist within the resource universe. If these two conditions can be overcome, the model and resultant methods show promise as a means to quantify and rank the level of landscape learning in a set of assemblages and, therefore, place them in relative chronological order.

Prior to this study, there have been no methods offered to effectively capture and measure this important aspect of human adaptation to new, unknown landscapes. Within the scope of this

dissertation, I have proposed and tested original methods to set a baseline against which to measure landscape learning, methods to quantify landscape learning based on resource usage, methods to predict lithic resource patch size inclusive of secondary distributions and signals on the landscape, and methods to compare these predictions with surveyed results. These methods have shown success, despite limitations in the available test data, in gauging this important aspect of human adaption.

Investigations continue at the ORB delta, and I hope to see more extensive X-ray fluorescence (XRF) analyses released in the future. These will provide an even better dataset for further investigations of this model and these methodologies. Further research avenues include improvements, as noted in Chapters 3 and 4, in flow predictions, perhaps with the addition of algorithms that factor in particle size. Other primary sources, such as clay or temper sources in ceramic studies, may similarly benefit from these means to quantify landscape learning.

References Cited

Abuzaid, A. H., El-hanjouri, M. M., & Kulab, M. M. (2015). On discordance tests for the wrapped Cauchy distribution. *Open Journal of Statistics*, *5*, 245–253. https://doi.org/10.4236/ojs.2015.54026

Ainsworth, P. (2001). *Utah Obsidian, Email to Craig E. Skinner, Peter Ainsworth, Ted Goebel, November 1, 2001*.

Amsden, C. A. (1937). The Lake Mohave artifacts. In Campbell, E. W. C, Campbell, W. H., Antevs, E., Amsden, C. A., Barbieri, J. A., and Bode, F. D. (Eds.), *The Archaeology of Pleistocene Lake Mohave (pp. 51-97).* Southwest Museum Papers 11.

Anaconda Software Distribution. (2021). In *Anaconda Documentation: Vol. Vers. 1.9.* Anaconda, Inc. https://docs.anaconda.com

Anthony, D. W. (1997). Prehistoric migration as social pattern. In J. Chapman & H. Hamerow (Eds.), *Migrations and Invasions in Archaeological Explanation* (pp. 21–32). Archaeopress.

Archuleta, C.-A. M., Constance, E. W., Arundel, S. T., Lowe, A. J., Mantey, K. S., & Phillips, L. A. (2017). The National Map seamless digital elevation model specifications. *U.S. Geological Survey*, *Techniques and Methods 11-B9*, 39. https://doi.org/10.3133/tm11B9

Argialas, D., & Tzotsos, A. (2006). Automatic extraction of physiographic features and alluvial fans in Nevada, USA from digital elevation models and satellite imagery through multiresolution segmentation and object oriented classification. *American Society for Photogrammetry and Remote Sensing - Annual Conference of the American Society for Photogrammetry and Remote Sensing 2006: Prospecting for Geospatial Information Integration*, *1*, 68–77.

Arkush, B. S., & Pitblado, B. L. (2000). Paleoarchaic surface assemblages in the Great Salt Lake Desert, northwestern Utah. *Journal of California and Great Basin Anthropology*, *22*, 12–42.

Armstrong, R. L. (1970). Geochronology of Tertiary igneous rocks, eastern Basin and Range Province, western Utah, eastern Nevada, and vicinity, U.S.A. *Geochimica et Cosmochimica Acta*, *34*, 203–232. https://doi.org/10.1016/0016-7037(70)90007-4

Atwood, G., Wambeam, T. J., & Anderson, N. J. (2016). The present as a key to the past: Paleoshoreline correlation insights from Great Salt Lake. In *Developments in Earth Surface Processes* (1st ed., Vol. 20). Elsevier B.V. https://doi.org/10.1016/B978-0-444-63590-7.00001-9

Auger-Méthé, M., Derocher, A. E., Plank, M. J., Codling, E. A., & Lewis, M. A. (2015). Differentiating the Lévy walk from a composite correlated random walk. *Methods in Ecology and Evolution*, *6*, 1179–1189. https://doi.org/10.1111/2041-210X.12412

Bailey, J. (1992). *X-ray fluorescence characterization of volcanic glass artifacts from Wilson Butte Cave, Idaho*. [Master's thesis, University of Alberta]. (Accession Order No. AAT MM77363). Available from ProQuest Dissertations & Theses Global. (304019237).

Bartumeus, F., Da Luz, M. G. E., Viswanathan, G. M., & Catalan, J. (2005). Animal search strategies: A quantitative random-walk analysis. *Ecology*, *86*, 3078–3087.

Batschelet, E. (1965). *Statistical methods for the analysis of problems in animal orientation and certain biological rhythms (AIBS monograph)*. American Institute of Biological Sciences.

Batschelet, E. (1981). *Circular statistics in biology*. Academic Press, Inc.

Beaton, J. M. (1991). Colonizing continents: Some problems from Australia and the Americas. In T. D. Dillehay & D. J. Meltzer (Eds.), *The First Americans: Search and Research* (pp. 209–230). CRC Press.

Beck, C., & Jones, G. T. (1990). Toolstone selection and lithic technology in early Great Basin prehistory. *Journal of Field Archaeology*, *17*, 283–299. https://doi.org/10.2307/530023

Beck, C., & Jones, G. T. (1994). Dating surface asssemblages using obsidian hydration. In C. Beck (Ed.), *Dating in Exposed and Surface Contexts* (pp. 47–76). University of New Mexico Press.

Beck, C., & Jones, G. T. (1997). The Terminal Pleistocene / Early Holocene archaeology of the Great Basin. *Journal of World Prehistory*, *11*, 161–236. http://link.springer.com/article/10.1007/BF02221204

Beck, C., & Jones, G. T. (2009). *The Archaeology of the Eastern Nevada Paleolithic, Part 1: The Sunshine Locality*. University of Utah Press.

Beck, C., & Jones, G. T. (2011). The Role of Mobility and Exchange in the Conveyance of Toolstone During the Great Basin Paleoarchaic. In R.E. Hughes (Ed.), *Perspectives on Prehistoric Trade and Exchange in California and the Great Basin* (pp. 55-82). University of Utah Press.

Beck, C., & Jones, G. T. (2015). Lithic analysis. In D. B. Madsen, D. N. Schmitt, & D. Page (Eds.), *The Paleoarchaic Occupation of the Old River Bed Delta* (pp. 97–208). University of Utah Press.

Beck, C., Taylor, A. K., Jones, G. T., Fadem, C. M., Cook, C. R., & Millward, S. A. (2002). Rocks are heavy: Transport costs and Paleoarchaic quarry behavior in the Great Basin. *Journal of Anthropological Archaeology*, *21*, 481–507. https://doi.org/10.1016/S0278-4165(02)00007-7

Bell, W. J. (1990). *Searching Behavior, Chapman and Hall Animal Behavior Series*. Springer Netherlands. http://link.springer.com/10.1007/978-94-011-3098-1_12

Ben-Israel, A. (2013). A concentrated Cauchy distribution with finite moments. *Annals of Operations Research*, *208*, 147–153. https://doi.org/10.1007/s10479-011-0995-z

Benhamou, S. (2006). Detecting an orientation component in animal paths when the preferred direction is individual-dependent. *Ecology*, *87*, 518–528.

Benhamou, S. (2007). How many animals really do the Lévy walk? *Ecology*, *88*, 1962–1969.

Bennett, E. H. (1976). *Reconnaissance geology and geochemistry of the South Mountain - Juniper Mountain region, Owyhee County, Idaho, Pamphlet No. 166*. Idaho Bureau of Mines and Geology.

Best, M. G., Christiansen, E. H., Deino, A. L., Gromme, S., Hart, G. L., & Tingey, D. G. (2013). The 36-18 Ma Indian Peak-Caliente ignimbrite field and calderas, southeastern Great Basin, USA: Multicyclic super-eruptions. *Geosphere*, *9*, 864–950. https://doi.org/10.1130/GES00902.1

Bettinger, R. L., & Eerkens, J. (2004). Evolutionary implications of metrical variation in Great Basin projectile points. *Archeological Papers of the American Anthropological Association*, *7*, 177–191. https://doi.org/10.1525/ap3a.1997.7.1.177

Binford, L. (1979). Organization and formation processes: Looking at curated technologies. *Journal of Anthropological Research*, *35*, 255–273.

Blurton Jones, N., & Konner, M. J. (1976). !Kung knowledge of animal behavior (or: The proper study of mankind is animals). In R. B. Lee & I. DeVore (Eds.), *Kalahari Hunter-Gatherers: Studies of the !Kung San and Their Neighbors* (pp. 325–348). Harvard University Press.

Bonnichsen, B., Leeman, W. P., Honjo, N., McIntosh, W. C., & Godchaux, M. M. (2008). Miocene silicic volcanism in southwestern Idaho: Geochronology, geochemistry, and evolution of the central Snake River Plain. *Bulletin of Volcanology*, *70*, 315–342. https://doi.org/10.1007/s00445-007-0141-6

Bonnichsen, B., Leeman, W. P., Jenks, M. D., & Honjo, N. (1988). Geologic field trip guide to the Central and Western Snake River Plain, Idaho, emphasizing the silicic volcanic rocks. In Paul Karl Link & W. Hackett (Eds.), *Guidebook to the Geology of Central and Southern Idaho* (pp. 247–282). Idaho Geological Survey.

Bovet, P., & Benhamou, S. (1988). Spatial analysis of animals' movements using a correlated random walk model. *Journal of Theoretical Biology*, *131*, 419–433. https://doi.org/10.1016/S0022-5193(88)80038-9

Bowers, A. W., & Savage, C. N. (1962). *Primitive man on Browns Bench*. Idaho Bureau of Mines and Geology.

Brantingham, P. J. (2003). A neutral model of stone raw material procurement. *American Antiquity*, *68*, 487–509.

Brantingham, P. J. (2006). Measuring forager mobility. *Current Anthropology*, *47*, 435–459. https://doi.org/10.1086/503062

Bronk Ramsey, C. (2021). *OxCal 4.4*. https://c14.arch.ox.ac.uk/oxcal.html

Bruce, P., & Bruce, A. (2017). *Practical statistics for data scientists: 50 essential concepts*. O'Reilly Media, Incorporated.

Brueseke, M. E., & Hart, W. K. (2008). Geology and Petrology of the Mid-Miocene Santa Rosa-Calico Volcanic Field, Northern Nevada. *Nevada Bureau of Mines and Geology Bulletin*, *March*.

Bryan, A. (1980). The Stemmed Point Tradition: An Early Technological Tradition in Western North America. In L. B. Harten, C. N. Warren, & D. R. Tuohy (Eds.), *Anthropological Papers in Memory of Earl H. Swanson Jr.* (pp. 77–107). Idaho State Museum of Natural History.

Cann, J. R., & Renfrew, C. (1964). The characterization of obsidian and its application to the Mediterranean region. *Proceedings of the Prehistoric Society*, *30*, 111–133. https://doi.org/10.1017/S0079497X00015097

Cartwright, C. (1981). *Utah Antiquities Site Form: 42JB275*. Utah Department of Heritage and Arts.

Cathey, H. E., & Nash, B. P. (2004). The Cougar Point Tuff: Implications for thermochemical zonation and longevity of high-temperature, large-volume silicic magmas of the Miocene Yellowstone hotspot. *Journal of Petrology*, *45*, 27–58. https://doi.org/10.1093/petrology/egg081

Chapman, R., & Wylie, A. (2016). *Evidential Reasoning in Archaeology*. Bloomsbury Academic Publishing.

Chen, C. Y., & Maloof, A. C. (2017a). Dataset: Revisiting the deformed high shoreline of Lake Bonneville: Datasets and Supplementary Materials. *Quaternary Science Reviews*. https://doi.org/http://dx.doi.org/10.17632/fhvsfjx7j6.1#file-5ebe6271-3670-4e38-817c-1dd719f6348b

Chen, C. Y., & Maloof, A. C. (2017b). Revisiting the deformed high shoreline of Lake Bonneville. *Quaternary Science Reviews*, *159*, 169–189. https://doi.org/10.1016/j.quascirev.2016.12.019

Christiansen, E. H., Bikun, J. V., Sheridan, M. F., & Burt, D. M. (1984). Geochemical evolution of topaz rhyolites from the Thomas Range and Spor Mountain, Utah. *American Mineralogist*, *69*, 223–236.

Christiansen, E. H., Burt, D. M., & Sheridan, M. F. (1986). The geology and geochemistry of Cenozoic topaz rhyolites from the western United States. *Geological Society of America Special Paper 205*.

Christiansen, R. L., & Lipman, P. W. (1972). Cenozoic volcanism and plate-tectonic evolution of the western United States. II. Late Cenozoic. *Philosophical Transactions of the Royal Society of London*, *271*, 249–284.

Clark, D. L., Oviatt, C. G., & Page, D. (2016). *Geologic map of Dugway Proving Ground and adjacent areas, Tooele County, Utah*. Utah Geologic Survey.

Clewlow, C. W. J. (1968). Surface Archaeology of the Black Rock Desert, Nevada. *Reports of the University of California Archaeological Survey No.73*, 1–93.

Coats, R. R. (1987). Geology of Elko County, Nevada. In *Nevada Bureau of Mines and Geology Bulletin* (Vol. 101). Nevada Bureau of Mines and Geology.

Codling, E. A., Plank, M. J., & Benhamou, S. (2008). Random walk models in biology. *Interface: Journal of the Royal Society*, *5*, 813–834. https://doi.org/10.1098/rsif.2008.0014

Connolly, T. J. (1999). *Newberry Crater: A Ten-thousand-year Record of Human Occupation and Environmental Change in the Basin-Plateau Borderlands*. University of Utah Anthropological Paper 121.

Conrad, O., Bechtel, B., Bock, M., Dietrich, H., Fischer, E., Gerlitz, L., Wehberg, J., Wichmann, V., & Boehner, J. (2015). System for Automated Geoscientific Analyses (SAGA) v. 7.4.0. *Geoscientific Model Development*, *8*. https://doi.org/doi:10.5194/gmd-8-1991-2015

Costa-Cabral, M. C., & Burges, S. J. (1994). Digital Elevation Model Networks (DEMON): A model of flow over hillslopes for computation of contributing and dispersal areas. *Water Resources Research*, *30*, 1681–1692. https://doi.org/10.1029/93WR03512

Crafford, A. E. J. (2007). *Geologic Map of Nevada: U.S. Geological Survey Data Series 249* (pp. 1–46). U.S. Geological Survey.

Crecraft, H. R., Nash, W. P., & Evans, Jr., S. H. (1981). Late Cenozoic volcanism at Twin Peaks, Utah: Geology and petrology. *Journal of Geophysical Research*, *86*, 10303–10320.

Crist, T. O., & Haefner, J. W. (1994). Spatial model of movement and foraging in harvester ants (Pogonomyrmex) (II): The roles of environment and seed dispersion. In *Journal of Theoretical Biology, 166*, 315–323. https://doi.org/10.1006/jtbi.1994.1028

Currey, D. R., Atwood, G., & Mabey, D. R. (1984). *Major Levels of Great Salt Lake and Lake Bonneville*. Utah Geological and Mineral Survey Map 73.

D'Avello, T., Brennan, J., & Loomis, L. (2016). *Modifying Digital Elevation Models to Develop More Realistic Wetness Index Layers for Soil Survey Applications*. https://www.nrcs.usda.gov/wps/PA_NRCSConsumption/download?cid=nrcseprd1257808&ext=pdf

Davis, L. G., Madsen, D. B., Becerra-Valdivia, L., Higham, T., Sisson, D. A., Skinner, S. M., Stueber, D., Nyers, A. J., Keen-Zebert, A., Neudorf, C., Cheyney, M., Izuho, M., Iizuka, F., Burns, S. R., Epps, C. W., Willis, S. C., & Buvit, I. (2019). Late Upper Paleolithic occupation at Cooper's Ferry, Idaho, USA, ~16,000 years ago. *Science*, *365*, 891–897. https://doi.org/10.1126/science.aax9830

DeChambre, D. J. (1979). *Site survey form: 26EK1976*. Bureau of Land Management, Elko District.

Duke, D. G. (2011). *If the desert blooms: A technological perspective on Paleoindian ecology in the Great Basin from the Old River Bed, Utah* [Doctoral dissertation, University of Nevada, Reno]. (Accession Order No. AAT 3472837). Available from ProQuest Dissertations & Theses Global; Publicly Available Content Database. (894264178).

Duke, D. G. (2013). The exploded fine-grained volcanic sources of the desert west and the primacy of tool function in material selection. *North American Archaeologist*, *34*, 323–354. https://doi.org/10.2190/NA.34.4.c

Duke, D. G., & Young, D. C. (2007). Episodic permanance in Paleoarchaic basin selection and settlement. In K. E. Graf & D. N. Schmitt (Eds.), *Paleoindian or Paleoarchaic? Great Basin Human Ecology at the Pleistocene/Holocene Transition* (pp. 123–138). University of Utah Press.

Dyson-Hudson, R., & Smith, E. A. (1978). Human territoriality: An ecological reassessment. *American Anthropologist*, *80*, 21–41.

Ellis, B. S., Branney, M. J., Barry, T. L., Barfod, D., Bindeman, I., Wolff, J. A., & Bonnichsen, B. (2012). Geochemical correlation of three large-volume ignimbrites from the Yellowstone hotspot track, Idaho, USA. *Bulletin of Volcanology*, *74*, 261–277. https://doi.org/10.1007/s00445-011-0510-z

Elston, R. G., & Budy, E. E. (Eds.). (1990). *The Archaeology of James Creek Shelter.* University of Utah Anthropological Papers 115.

Erlandson, J. M., Rick, T. C., Braje, T. J., Casperson, M., Culleton, B., Fulfrost, B., Garcia, T., Guthrie, D. A., Jew, N., Kennett, D. J., Moss, M. L., Reeder, L., Skinner, C., Watts, J., & Willis, L. (2011). Paleoindian seafaring, maritime technologies, and coastal foraging on California's Channel Islands. *Science*, *331*, 1181–1185. https://doi.org/10.1126/science.1201477

Esri. (2021a). *ArcGIS Desktop*. Release 10.8. Redlands, CA: Environmental Systems Research Institute.

Esri. (2021b). *Fill.* Retrieved on November 1, 2021, from https://desktop.arcgis.com/en/arcmap/latest/tools/spatial-analyst-toolbox/fill.htm

Esri. (2021c). *How Focal Statistics works*. Retrieved on November 1, 2021, from https://desktop.arcgis.com/en/arcmap/latest/tools/spatial-analyst-toolbox/how-focal-statistics-works.htm

Esri. (2021d). *How Sink works*. Retrieved on November 1, 2021, from https://desktop.arcgis.com/en/arcmap/latest/tools/spatial-analyst-toolbox/how-sink-works.htm

Esri. (2021e). *Mean Center*. Retrieved on November 1, 2021, from https://desktop.arcgis.com/en/arcmap/latest/tools/spatial-statistics-toolbox/mean-center.htm

Esri. (2022a). *Path Distance*. Retrieved on May 2, 2022, from https://pro.arcgis.com/en/pro-app/2.8/tool-reference/spatial-analyst/path-distance.htm

Esri. (2022b). *Cost Distance*. Retrieved on May 2, 2022, from https://pro.arcgis.com/en/pro-app/2.8/tool-reference/spatial-analyst/cost-distance.htm

Estes, M. B. (2009). *Paleoindian occupations in the Great Basin: A comparative study of lithic technological organization , mobility, and landscape use from Jakes Valley, Nevada*. [Master's thesis, University of Nevada, Reno]. (Accession Order No. AAT 1464433). Available from ProQuest Dissertations & Theses Global. (304943187).

Evans, Jr., S. H., Nash, W. P., & University of Utah, Department of Geology and Geography. (1978). *Quaternary rhyolite from the Mineral Mountains, Utah, USA*. All U.S. Government Documents (Utah Regional Depository).

Everts, M. L. (1991). *Cudahy Mine*. Mineral Resources Data System (MRDS), U.S. Geological Survey. https://mrdata.usgs.gov/mrds/show.php?labno=10101543

Fairfield, J., & Leymarie, P. (1991). Drainage networks from grid digital elevation models. *Water Resources Research*, *27*, 709–717. https://doi.org/10.1029/90WR02658

Fike, R. E. (1974). *Antiquities site inventory: 42BE88*. Bureau of Land Management.

Fisher, N. I. (1993). *Statistical Analysis of Circular Data*. Cambridge University Press.

Fitzhugh, B. (2004). Colonizing the Kodiak Archipelago: Trends in raw material use and lithic technologies at the Tanginak Spring site. *Arctic Anthropology*, *41*, 14–40. https://doi.org/10.1353/arc.2011.0076

Fitzhugh, B., & Trusler, A. K. (2009). Experimentation and Innovation in the Archaeological Record. A Case Study in Technological Evolution from Kodiak, Alaska. *Pattern and Process in Cultural Evolution*, 203–220.

Ford, A. (2011). Learning the lithic landscape: using raw material sources to investigate Pleistocene colonisation in the Ivane Valley, Papua New Guinea. *Archaeology in Oceania*, *46*, 42–53.

Foster, C., & Foster, D. (2000). *The Great Dance: A Hunter's Story*. Aardvark Pictures / Earthrise. https://www.cultureunplugged.com/documentary/watch-online/filmedia/play/2419/The-Great-Dance

Fowler, B. L. (2014). *Obsidian toolstone conveyance: Southern Idaho forager mobility*. [Master's thesis, Utah State University]. (Accession Order No. AAT 1584407). Available from ProQuest Dissertations & Theses Global. (1659783206).

Freeman, T. G. (1991). Calculating catchment area with divergent flow based on a regular grid. *Computers and Geosciences*, *17*, 413–422. https://doi.org/10.1016/0098-3004(91)90048-I

Freund, K. P., Johnson, L. R. M., & Duke, D. (April 30-May 2, 2021). *The character and use of Ferguson Wash obsidian in Eastern Great Basin prehistory* [Poster presentation]. International Obsidian Conference 2021, http://arf.berkeley.edu/files/attachments/pages/IOC_Posters2021.pdf

Frison, G. C., & Todd, L. C. (Eds.). (1987). *The Horner Site: The Type Site of the Cody Cultural Complex*. Academic Press, Inc.

Gallagher, J. G. (1979). *The Archaeology of the Sheepeater Battleground and Redfish Overhang sites*. U.S.D.A Forest Service, Intermountain Region.

Geologic Map of Nevada - Data series 249. (2021). Nevada Bureau of Mines and Geology Open Data, University of Nevada. https://data-nbmg.opendata.arcgis.com/

Gibbon, G., & Ames, K. M. (Eds.). (1998). *Archaeology of Prehistoric Native America: An Encyclopedia*. Garland Reference Library of the Humanities, Vol. 1537, Garland Press.

GitHub. (2021). GitHub, Inc., https://github.com/about

Goebel, T., Holmes, A., Keene, J. L., & Coe, M. M. (2018). Technological Change from the Terminal Pleistocene Through Early Holocene in the Eastern Great Basin, USA: The Record from Bonneville Estates Rockshelter. In E. Robinson, & F. Sellet (Eds.), *Lithic Technological Organization and Paleoenvironmental Changes. Global and Diachronic Perspectives, Studies in Human Ecology and Adaptation 9* (pp. 235–261). Springer International Publishing AG. https://doi.org/10.1007/978-3-319-64407-3_11

Golledge, R. G. (2003). Human wayfinding and cognitive maps. In M. Rockman & J. Steele (Eds.), *Colonization of Unfamiliar Landscapes: The Archaeology of Adaptation* (pp. 25–43). Routledge.

Google Earth Pro. (2020). Google LLC. https://www.google.com/earth/

Graf, K. E. (1995). *Paleoindian technological provisioning in the northwestern Great Basin* [Master's thesis, University of Nevada, Reno]. (Accession Order No. AAT 1406398). Available from ProQuest Dissertations & Theses Global. (205436522).

Graf, K. E. (2007). Stratigraphy and chronology of the Pleistocene to Holocene transition at Bonneville Estates Rockshelter, eastern Great Basin. In K. E. Graf & D. N. Schmitt (Eds.), *Paleoindian or Paleoarchaic? Great Basin Human Ecology at the Pleistocene/Holocene Transition* (pp. 82–104). University of Utah Press.

Grayson, D. K. (1993). *The Desert's Past: A Natural Prehistory of the Great Basin*. Smithsonian Institution Press.

Grayson, D. K. (2011). *The Great Basin: A Natural Prehistory*. University of California Press.

Griffin, J. B., Gordus, A. A., & Wright, G. A. (1969). Identification of the sources of Hopewellian obsidian in the Middle West. *American Antiquity*, *34*, 1–14.

Haarklau, L., Johnson, L., & Wagner, D. L. (2005). *Fingerprints in the Great Basin: The Nellis Air Force Base Regional Obsidian Sourcing Study*. Prewitt and Associates, Inc., Austin. Submitted to Nellis Air Force Base, Nevada.

Hamilton, T. A. (2012). *A case for Paleoindian use of Pinto projectile points in the Great Basin: Morphological analysis from the Old River Bed, Utah* [University of Nevada, Reno]. (Accession Order No. AAT 1518994). Available from ProQuest Dissertations & Theses Global. (1073449514).

Hart, W. S., Quade, J., Madsen, D. B., Kaufman, D. S., & Oviatt, C. G. (2004). The ^{87}Sr/^{86}Sr ratios of lacustrine carbonates and lake-level history of the Bonneville paleolake system. *Bulletin of the Geological Society of America*, *116*, 1107–1119. https://doi.org/10.1130/B25330.1

Haynes, G. (2007). Paleoindian or Paleoarchaic? In K. E. Graf & D. N. Schmitt (Eds.), *Paleoindian or Paleoarchaic? Great Basin Human Ecology at the Pleistocene/Holocene Transition* (pp. 251–258). University of Utah Press.

Heizer, R. F., & Hester, T. R. (1978). *Great Basin Projectile Points: Forms and Chronology*. Ballena Press Publications in Archaeology, Ethnology and History, No. 10.

Hildebrandt, W. R., Colligan, K., & Bloomer, W. (2016). Flaked Stone Production Patterns. *Prehistory of Nevada's Northern Tier: Archaeological Investigations along the Ruby Pipeline*, 237–260.

Hintze, L. F. (1988). *Geologic history of Utah* Brigham Young University Geology Studies Special Publication 7.

Hintze, L. F., Davis, F. D., Rowley, P. D., Cunningham, C. G., Steven, T. A., Willis, G. C., Hintze, L. F., Davis, F. D., Rowley, P. D., Cunningham, C. G., Steven, T. A., & Willis, G. C. (2003). *Geologic map of the Richfield 30' x 60' quadrangle, southeast Millard County and parts of Beaver, Piute, and Sevier Counties*. Utah Geological Survey Map 195. https://doi.org/10.34191/m-195dm

Hintze, L. F., Willis, G. C., Laes, D. Y. M., Sprinkel, D. A., & Brown, K. D. (2000). *Digital geologic map of Utah*. Utah Geological Survey. https://geology.utah.gov/apps/intgeomap/

Hockett, B. S. (1995). Chronology of Elko Series and Split Stemmed Points from Northeastern Nevada. *Journal of California and Great Basin Anthropology*, *17*, 41–53.

Hockett, B. S. (2001a). *Dead Cedar/Ferguson Wash Obsidian, Email to Craig E. Skinner, Peter Ainsworth, Ted Goebel, November 1, 2001*.

Hockett, B. S. (2001b). *Re: Dead Cedar/Ferguson Wash Obsidian, Email to Craig E. Skinner, Peter Ainsworth, Ted Goebel, November 3, 2001*.

Hockett, B. S. (2015). The zooarchaeology of Bonneville Estates Rockshelter: 13,000 years of Great Basin hunting strategies. *Journal of Archaeological Science: Reports*, *2*, 291–301. https://doi.org/10.1016/j.jasrep.2015.02.011

Holmer, R. N. (1997). Volcanic glass utilization in Eastern Idaho. *Tebiwa*, *26*, 186–204.

Hughes, R. E. (1986). *Diachronic variability in obsidian procurement patterns in Northeastern California and Southcentral Oregon*. University of California Press.

Hughes, R. E. (1990). Obsidian sources at James Creek Shelter, and trace element geochemistry of some northeastern Nevada volcanic glass. In R. G. Elston & E. E. Budy (Eds.), *The Archaeology of James Creek Shelter* (pp. 297–305). University of Utah Anthropological Papers 115.

Hughes, R. E. (2007a). Provenance analysis of obsidian. In G. C. Frison, D. N. Walker, & D. R. Bach (Eds.), *Medicine Lodge Creek: Holocene Archaeology of the Eastern Big Horn Basin, Wyoming, Volume I*. Clovis Press.

Hughes, R. E. (2007b). The geologic sources for obsidian artifacts from Minnesota archaeological sites. *The Minnesota Archaeologist*, *66*, 53–68.

Hughes, R. E. (2013). Long-term continuity and change in obsidian conveyance at Danger Cave, Utah. In N. J. Parezo & J. C. Janetski (Eds.), *Archaeology in the Great Basin and Southwest: Papers in Honor of Don D. Fowler* (pp. 210–225). University of Utah Press.

Hughes, R. E., & Nelson, F. W. (1987). New findings on obsidian source utilization in Iowa. *Plains Anthropologist*, *32*, 313–316.

Hughes, R. E., & Smith, R. L. (1993). Archaeology, geology, and geochemistry in obsidian provenance studies. *Special Paper of the Geological Society of America*, *283*, 79–91. https://doi.org/10.1130/SPE283-p79

Hull, K. L. (1994). Obsidian studies. In *Kern River Pipeline Cultural Resources Data Recovery Report: Utah, Volume I, Research Context and Data Analysis* (pp. 7-1–7-63). Dames & Moore, Report Submitted to the Federal Regulatory Commission, Washington, D.C.

Hull, K. L. (2010). *Research design for obsidian hydration chronology-building in Lincoln County, Nevada*. USDI Bureau of Land Management.

Hunt, C. B. (1967). *Physiography of the United States*. W. H. Freeman.

Hutchins, J., & Simons, D. D. (2000). Obsidian Studies in the Truckee Meadows, Nevada. *Journal of California and Great Basin Anthropology*, *22*, 151–163.

Jack, R. N., & Heizer, R. F. (1968). "Finger-printing" of some Mesoamerican obsidian artifacts. *Contributions of the University of California Archaeological Research Facility*, *5*, 81–100.

Jackson, R., Spidell, J., Kennelly-Spidell, D., & Kovak, A. (2009). *A Historic Context for Native American Procurement of Obsidian in the State of Utah*. Pacific Legacy, Inc., Cameron Park, California. Submitted to Logan Simpson Design, Inc., Salt Lake City.

Jammalamadaka, S. R., & SenGupta, A. (1996). *Topics in Circular Statistics*. World Scientific Publishing Company.

Jander, R. (1957). Die optische Richtungsorientierung der roten Waldameise (Formica rufa L.). *Zeitschrift Fur Vergleichende Physiologie*, *40*, 162–238.

Janetski, J. C., Bodily, M. L., Newbold, B. A., & Yoder, D. T. (2012). The Paleoarchaic to Early Archaic transition on the Colorado Plateau: The archaeology of North Creek Shelter. *American Antiquity*, *77*, 125–159.

Jenkins, D. L., Davis, L. G., Stafford, T. W., Campos, P. F., Connolly, T. J., Cummings, L. S., Hofreiter, M., Hockett, B. S., Mcdonough, K., Luthe, I., Grady, P. W. O., Swisher, M. E., White, F., Yates, B., Ii, R. M. Y., Yost, C., & Willerslev, E. (2013). Geochronology, Archaeological Context, and DNA at the Paisley Caves. In K. E. Graf, C. V. Ketron, & M. R. Waters (Eds.), *Paleoamerican Odyssey* (pp. 485–510). Texas A & M University Press.

Jenkins, D. L., Davis, L. G., Stafford, T. W., Campos, P. F., Hockett, B. S., Jones, G. T., Cummings, L. S., Yost, C., Connolly, T. J., Yohe, R. M., Gibbons, S. C., Raghavan, M., Rasmussen, M., Paijmans, J. L. a, Hofreiter, M., Kemp, B. M., Barta, J. L., Monroe, C., Gilbert, M. T. P., & Willerslev, E. (2012). Clovis age Western Stemmed projectile points and human coprolites at the Paisley Caves. *Science*, *337*, 223–228. https://doi.org/10.1126/science.1218443

Jennings, J. D. (1957). *Danger Cave.* University of Utah Anthropological Papers 27.

Jensen, E. (2004). Kane Springs Fluted Point and a Short Literary Digression. *In Situ: Newsletter of the Nevada Archaeological Association*, *8*(4), 12–16.

Jensen, E. (2005). Flutes and glyphs and life lessons. *In Situ: Newsletter of the Nevada Archaeological Association*, *9*(2), 10–13.

Jenson, S. K., & Domingue, J. O. (1988). Extracting topographic structure from digital elevation data for geographic information system analysis. *Photogrammetric Engineering and Remote Sensing*, *54*, 1593–1600.

Johnson, L., & Wagner, D. L. (2005). Obsidian source characterization study. In L. Haarklau, L. Johnson, & D. L. Wagner (Eds.), *Fingerprints in the Great Basin: The Nellis Air Force Base Regional Obsidian Sourcing Study* (pp. 25–50). U.S. Army Corps of Engineers, Fort Worth District.

Jones, G. T., Bailey, D. G., & Beck, C. (1997). Source provenance of andesite artefacts using non-destructive XRF analysis. *Journal of Archaeological Science*, *24*, 929–943. https://doi.org/10.1006/jasc.1996.0172

Jones, G. T., & Beck, C. (1990). An obsidian hydration chronology of Late Pleistocene-Early Holocene surface assemblages from Butte Valley, Nevada. *Journal of California and Great Basin Anthropology*, *12*, 84–100.

Jones, G. T., Beck, C., Jones, E. E., & Hughes, R. E. (2003). Lithic source use and Paleoarchaic foraging territories in the Great Basin. *American Antiquity*, *68*, 5–38. https://doi.org/10.2307/3557031

Kareiva, P. M., & Shigesada, N. (1983). Analyzing insect movement as a correlated random walk. *Oecologia*, *56*(2), 234–238.

Kato, S., & Jones, M. C. (2013). An extended family of circular distributions related to wrapped Cauchy distributions via Brownian motion. *Bernoulli*, *19*, 154–171. https://doi.org/10.3150/11-BEJ397

Kellner, P. (2022). *England*. Britannica. https://www.britannica.com/place/England

Kelly, R. L. (1978). *Paleo-Indian Settlement Patterns at Pleistocene Lake Tonopah, Nevada*. [Unpublished Bachelor of Arts thesis]. Cornell University.

Kelly, R. L. (1995). *The Foraging Spectrum: Diversity in Hunter-Gatherer Lifeways*. Smithsonian Institution Press.

Kelly, R. L. (2003a). Colonization of new land by hunter-gatherers: Expectations and implications based on ethnographic data. In M. Rockman & J. Steele (Eds.), *Colonization of Unfamiliar Landscapes: The Archaeology of Adaptation* (pp. 44–58). Routledge.

Kelly, R. L. (2003b). Maybe we do know when people first came to North America; and what does it mean if we do? *Quaternary International*, *109*, 133–145. https://doi.org/10.1016/S1040-6182(02)00209-4

Kelly, R. L., & Todd, L. C. (1988). Coming into the country: Early Paleoindian hunting and mobility. *American Antiquity*, *53*, 231–244.

Kent, J. T., & Tyler, D. E. (1988). Maximum likelihood estimation for the wrapped Cauchy distribution. *Journal of Applied Statistics*, *15*, 247–254.

King, J. (2016). Obsidian conveyance patterns. In W. Hildebrant, K. McGuire, J. King, A. Ruby, & D. C. Young (Eds.), *Prehistory of Nevada's Northern Tier: Archaeological investigations Along the Ruby Pipeline* (pp. 303–327). American Museum of Natural History Anthropological Papers No. 101.

Kirchhoff, M. D. (2009). Material Agency: A Theoretical Framework for Ascribing Agency to Material Culture. *Techne: Research in Philosophy & Technology*, *13*, 206–220.

Kitchel, N. R. (2018). Questioning the visibility of the landscape learning process during the Paleoindian colonization of northeastern North America. *Journal of Archaeological Science: Reports, 17*, 871-878. https://doi.org/10.1016/j.jasrep.2016.10.009

Kulkarni, A., Chong, D., & Batarseh, F. A. (2020). Foundations of data imbalance and solutions for a data democracy. *Data Democracy: At the Nexus of Artificial Intelligence, Software Development, and Knowledge Engineering*, 83–106. https://doi.org/10.1016/B978-0-12-818366-3.00005-8

Latham, T. S., Sutton, P. A., & Verosub, K. L. (1992). Non-destructive XRF characterization of basaltic artifacts from Truckee, California. *Geoarchaeology*, *7*, 81–101. https://doi.org/10.1002/gea.3340070202

LaValley, S. J. (2013). *Late Holocene Toolstone Procurement and Land-Use Strategies in the Black Rock Desert and High Rock Country of Northwest Nevada*. [Master's thesis, University of Nevada, Reno]. (Accession Order No. AAT 1540192). Available from ProQuest Dissertations & Theses Global. (1416355237).

Layton, T. N. (1970). *High Rock archaeology: An interpretation of the prehistory of the northweste*rn Great Basin. [Unpublished doctoral dissertation]. Harvard University.

Le Bas, M. J. (1986). A chemical classification of volcanic rocks based on the total alkali-silica diagram. *Journal of Petrology*, *27*, 745–750.

Le Bas, M. J., & Streckeisen, A. L. (1991). The IUGS systematics of igneous rocks. *Journal of the Geological Society*, *148*, 825–833. https://doi.org/10.1144/gsjgs.148.5.0825

Lehoczky, J. P. (2015). Distributions, Statistical: Special and Continuous. In *International Encyclopedia of the Social & Behavioral Sciences: Second Edition* (Vol. 6). Elsevier. https://doi.org/10.1016/B978-0-08-097086-8.42115-X

Lewis, R. S., Link, P. K., Stanford, L. R., & Long, S. P. (2012). *Geologic map of Idaho*. Idaho Geological Survey. https://www.idahogeology.org/Product/M-9

Lindsey, D. A. (1979). *Geologic map and cross-section of Tertiary rocks in the Thomas Range and northern Drum Mountains, Juab Country, Utah. U.S. Geological Survey Miscellaneous Investigation Map I-1176, scale 1:62,500*. U.S. Geological Survey.

Lindsey, D. A. (1982). Tertiary volcanic rocks and uranium in the Thomas Range and northern Drum Mountains, Juab County, Utah. *U.S. Geological Survey Professional Papers*, *1221*. https://doi.org/10.3133/pp1221

Lindsey, D. A. (1998). *Slides of the fluorspar, beryllium, and uranium deposits at Spor Mountain, Utah*. U.S. Geological Survey. https://pubs.usgs.gov/of/1998/ofr-98-0524/HOME.HTM

Link, Paul K. (2002). *Geology of Oneida County, Idaho*. Idaho State University, Geosciences Dept. https://digitalatlas.cose.isu.edu/counties/geomaps/geomap.htm

Lipman, P. W., Rowley, P. D., Mehnert, H. H., Evans, Jr., S. H., Nash, W. P., Brown, F. H., Izett, G. A., Naeser, C. W., & Friedman, I. (1978). Pleistocene rhyolite of the Mineral Mountains, Utah - Geothermal and archaeological significance. *Journal of Research of the U.S. Geological Society*, *6*(1), 133–147.

Llobera, M. (2001). Building Past Landscape Perception With GIS: Understanding Topographic Prominence. *Journal of Archaeological Science*, *28*, 1005–1014. https://doi.org/10.1006/jasc.2001.0720

Logan, B., Hughes, R. E., & Henning, D. R. (2001). Western Oneota Obsidian: Sources and implications. *Plains Anthropologist*, *46*, 55–64. https://doi.org/10.1080/2052546.2001.11932057

Louderback, L. A. (2014). *The ecology of human diets during the Holocene at North Creek Shelter , Utah*. [Doctoral dissertation, University of Washington]. (Accession Order No. AAT 3641783). Available from Dissertations & Theses @ University of Washington WCLP; ProQuest Dissertations & Theses Global. (1623001406).

Louderback, L. A., Grayson, D. K., & Llobera, M. (2010). Middle-Holocene climates and human population densities in the Great Basin, western USA. *The Holocene*, *21*, 366–373. https://doi.org/10.1177/0959683610374888

Madsen, D. B. (2007). The Paleoarchaic to Archaic Transition in the Great Basin. In K. E. Graf & D. N. Schmitt (Eds.), *Paleoindian or Paleoarchaic? Great Basin Human Ecology at the Pleistocene/Holocene Transition* (pp. 3–20). University of Utah Press.

Madsen, D. B. (2016). The early human occupation of the Bonneville Basin. In Charles G. Oviatt & J. F. Shroder (Eds.), *Developments in Earth Surface Processes, Lake Bonneville: A Scientific Update*, *20*, 504–525. Elsevier B.V. https://doi.org/10.1016/B978-0-444-63590-7.00018-4

Madsen, D. B., Oviatt, C. G., & Young, D. C. (2015). Old River Bed Delta Geomorphology and Chronology. In D. B. Madsen, D. N. Schmitt, & D. Page (Eds.), *The Paleoarchaic Occupation of the Old River Bed Delta* (pp. 30–60). University of Utah Press.

Madsen, D. B., & Schmitt, D. N. (2005). *Buzz-cut Dune and Fremont Foraging at the Margin of Horticulture*. University of Utah Press.

Madsen, D. B., Schmitt, D. N., & Page, D. (Eds.). (2015). *The Paleoarchaic Occupation of the Old River Bed Delta*. University of Utah Press.

Mandryk, C. A. S. (2003). Forward. In M. Rockman & J. Steele (Eds.), *Colonization of Unfamiliar Landscapes: The Archaeology of Adaptation* (pp. xiii–xv). Routledge.

Mardia, K. V., & Jupp, P. E. (2000). *Directional Statistics*. Wiley.

Mark, D. M. (1988). *Modelling in Geomorphological Systems*. John Wiley.

Marshall, R. R. (1961). Devitrification of natural glass. *Geological Society of America Bulletin*, *72*, 1493–1520.

Maurer, R. E. (1970). *Geology of the Cedar Mountains, Tooele County, Utah*. [Doctoral dissertation, University of Utah]. (Accession Order No. AAT 7019993). Available from ProQuest Dissertations & Theses Global. (288081513).

Meltzer, D. J. (2002). What do you do when no one's been there before? Thoughts on the exploration and colonization of new lands. In N. G. Jablonski (Ed.), *The First Americans: the Pleistocene Colonization of the New World* (pp. 27–58). Memiors of the California Academy of Sciences No. 27.

Meltzer, D. J. (2003). Lessons in landscape learning. In M. Rockman & J. Steele (Eds.), *Colonization of Unfamiliar Landscapes: The Archaeology of Adaptation* (pp. 222–239). Routledge.

Miliaresis, G. C., & Argialas, D. P. (2000). Extraction and delineation of alluvial fans from digital elevation models and Landsat Thematic Mapper images. *Photogrammetric Engineering and Remote Sensing*, *66*, 1093–1101.

Miller, B. A., & Juilleret, J. (2020). The colluvium and alluvium problem: Historical review and current state of definitions. *Earth-Science Reviews*, *209*, 103316. https://doi.org/10.1016/j.earscirev.2020.103316

Monnereau, L. R., Ellis, B. S., Szymanowski, D., Bachmann, O., & Guillong, M. (2021). Obsidian pyroclasts in the Yellowstone-Snake River Plain ignimbrites are dominantly juvenile in origin. *Bulletin of Volcanology*, *83*(4), 1–13. https://doi.org/10.1007/s00445-021-01448-1

Montgomery, J. (1981). *Utah Antiquities Site Form: 42JB296*. Utah Department of Heritage and Arts.

Moore, J. (2009). *Great Basin Tool-Stone Sources*. NDOT Obsidian and Tool-Stone Sourcing Project: 2002 Progress Report. Report on file, Nevada Department of Transportation, Environmental Services Division, Cultural Resources Section, Carson City.

Moore, W. J., & Sorensen, M. L. (1979). *Geologic map of the Tooele 1° x 2° quadrangle, Utah*. U.S. Geological Survey Miscellaneous Investigations Series Map I-1132, scale 1:250,000.

Morgan, L. A., & McIntosh, W. C. (2005). Timing and development of the Heise volcanic field, Snake River Plain, Idaho, western USA. *Bulletin of the Geological Society of America*, *117*, 288–306. https://doi.org/10.1130/B25519.1

Mullins, D., Karpinski, M., Adams, J., Karpinski, E., & Grimes, A. (2009). *A cultural resources survey of 6,202 acres within the Black Rock Obsidian Source Area of the Milford Flat ESR Project, Millard County, Utah*. Logan Simpson Design, Inc., Salt Lake City, On file with Utah Division of State History, State Project No. U-07-Ll-1266b,i,s.

Murphy, T. (1981). *Cultural Resources Inventory Record: Site 26EK3870*. U.S. Department of the Interior, Bureau of Land Management.

Nangia, V. (2010). Evaluation of a GIS-based watershed modeling approach for sediment transport. *International Journal of Agricultural and Biological Engineering*, *3*, 43-53. https://doi.org/10.3965/j.issn.1934-6344.2010.03.043-053

Nelson, F. W. (1984). X-ray fluorescence analysis of some western North American obsidians. In R. E. Hughes (Ed.), *Obsidian Studies in the Great Basin* (pp. 27–62). Archaeological Research Center, University of California, Berkeley.

Nelson, F. W., & Holmes, R. D. (1979). *Trace element analysis of obsidian sources and artifacts from western Utah*. Antiquities Section, Division of State History.

Newlander, K. (2012). *Exchange, embedded procurement, and hunter-gatherer mobility: A case study from the North American Great Basin*. [Doctoral dissertation, University of Michigan]. (Accession Order No. AAT 3519661). Available from ProQuest Dissertations & Theses Global. (1026968975).

Nielsen, G. (1990). *Intermountain Antiquities Computer System: 42JB440*. Utah Department of Heritage and Arts.

Nielson, A. (1990). *Intermountain Antiquities Computer System: 42JB450*. Utah Department of Heritage and Arts.

Norini, G., Clara, M., Jill, I., Aquino, D. T., Mahar, A., & Lagmay, F. (2016). Delineation of alluvial fans from Digital Elevation Models with a GIS algorithm for the geomorphological mapping of the Earth and Mars. *Geomorphology*, *273*, 134–149. https://doi.org/10.1016/j.geomorph.2016.08.010

Novak, S. W. (1984). Eruptive history of the rhyolitic Kane Springs Wash volcanic center, Nevada. *Journal of Geophysical Research*, *89*, 8603–8615. https://doi.org/10.1029/JB089iB10p08603

Novak, S. W. (1985). *Geology and geochemical evolution of the Kane Springs Wash volcanic center, Lincoln County, Nevada*. [Doctoral dissertation, Stanford University]. (Accession Order No. AAT8602520). Available from ProQuest Dissertations & Theses Global. (303400246).

Novak, S. W., & Mahood, G. A. (1986). Rise and fall of a basalt-trachyte-rhyolite magma system at the Kane Springs Wash Caldera, Nevada. *Contribution to Mineralogy and Petrology*, *94*, 352–373.

O'Callaghan, J. F., & Mark, D. M. (1984). The extraction of ordered vector drainage networks from elevation data. *Computer Vision, Graphics, and Image Processing*, *28*, 323–344.

O'Connor, J. (2016). The Bonneville Flood—A veritable débâcle. In Charles G. Oviatt & J. F. Shroder (Eds.), *Developments in Earth Surface Processes, Lake Bonneville: A Scientific Update*, *20*, 105–126. Elsevier B.V. https://doi.org/10.1016/B978-0-444-63590-7.00006-8

Oviatt, C. G., & Jewell, P. W. (2016). The Bonneville shoreline: Reconsidering Gilbert's interpretation. In Charles G. Oviatt & J. F. Shroder (Eds.), *Developments in Earth Surface Processes, Lake Bonneville: A Scientific Update, 20*, 88–104. Elsevier B.V. https://doi.org/10.1016/B978-0-444-63590-7.00005-6

Oviatt, C. G., & Shroder, J. F. (2016). Introduction. In Charles G. Oviatt & J. F. Shroder (Eds.), *Developments in Earth Surface Processes, Lake Bonneville: A Scientific Update*, 20, xxv–xxxvi. Elsevier B.V. https://doi.org/10.1016/B978-0-444-63590-7.09993-5

Oviatt, Charles G., Madsen, D. B., & Schmitt, D. N. (2003). Late Pleistocene and early Holocene rivers and wetlands in the Bonneville basin of western North America. *Quaternary Research*, *60*, 200–210. https://doi.org/10.1016/S0033-5894(03)00084-X

Page, D. (2008). *Fine-grained volcanic toolstone sources and early use in the Bonneville Basin of Western Utah and Eastern Nevada*. [Doctoral dissertation, University of Nevada, Reno]. (Accession Order No. AAT 1455650). Available from ProQuest Dissertations & Theses Global. (304536340).

Page, D. (2015a). Results of XRF and pXRF analysis, supplemental digital material. In D. B. Madsen, D. N. Schmitt, & D. Page (Eds.), *The Paleoarchaic Occupation of the Old River Bed Delta*. University of Utah Press. https://uofupress.lib.utah.edu/wp-content/uploads/sites/21/2018/01/Chapter-6-SDM-Results-of-XRF-and-PXRF-Analysis.pdf

Page, D. (2015b). Source assignment tables, supplemental digital material. In D. B. Madsen, D. N. Schmitt, & D. Page (Eds.), *The Paleoarchaic Occupation of the Old River Bed Delta*. University of Utah Press. https://uofupress.lib.utah.edu/wp-content/uploads/sites/21/2018/01/Chapter-6-SDM-Source-Assignment-Tables.pdf

Page, D., & Bacon, S. (2016). *Browns Bench predictive modeling, resampling, and geochemical characterization across portions of Idaho, Nevada, and Utah*. Desert Research Institute, Reno, Nevada.

Page, D., & Duke, D. G. (2015). Toolstone Sourcing, Lithic Resource Use, and Paleoarchaic Mobility in the Western Bonneville Basin. In D. B. Madsen, D. N. Schmitt, & D. Page (Eds.), *The Paleoarchaic Occupation of the Old River Bed Delta* (pp. 209–236). University of Utah Press.

Page, D., & Skinner, C. E. (October 8-11, 2008). *Obsidian source use at Danger Cave* [Poster presentation]. The 31st Biennial Great Basin Anthropological Conference, Portland, Oregon.

Patlak, C. S. (1953). Random walk with persistence and external bias. *The Bulletin of Mathematical Biophysics*, *15*, 311–338. https://doi.org/10.1007/BF02476407

Pendleton, L. S. (1979). *Lithic technology in early Nevada assemblages*. [Master's thesis, California State University, Long Beach]. (Accession Order No. AAT 1314424). Available from ProQuest Dissertations & Theses Global. (303019230)

Pontzer, H., Raichlen, D. A., Mabulla, A. Z. P., Wood, B. M., Gordon, A. D., & Marlowe, F. W. (2014). Evidence of Lévy walk foraging patterns in human hunter-gatherers. *Proceedings of the National Academy of Sciences*, *111*, 728–733. https://doi.org/10.1073/pnas.1318616111

Project Jupyter. (2021). https://jupyter.org/

Python Software Foundation. (2021). *Python computer language*. v. 3.7.6. https://www.python.org/

Qin, C. Z., Zhu, A. X., Pei, T., Li, B. L., Scholten, T., Behrens, T., & Zhou, C. H. (2011). An approach to computing topographic wetness index based on maximum downslope gradient. *Precision Agriculture*, *12*, 32–43. https://doi.org/10.1007/s11119-009-9152-y

Quinn, P., Beven, K., Chevallier, P., & Planchon, O. (1991). The prediction of hillslope flow paths for distributed hydrological modelling using digital terrain models. *Hydrological Processes*, *5*, 59–79.

Raymond, A. W. (1981a). *Utah Antiquities Site Form: 42JB276*. Utah Department of Heritage and Arts.

Raymond, A. W. (1981b). *Utah Antiquities Site Form: 42JB277*. Utah Department of Heritage and Arts.

Regnier, J. (1960). Cenozoic geology in the vicinity of Carlin, Nevada. *Bulletin of the Geological Society of America*, *71*, 1180–1210.

Reid, K. C. (2014). Through the glass, darkly: Patterns of obsidian and fine grained volcanic toolstone acquisition on the Southern Plateau. In D. H. MacDonald, W. Andrefsky Jr., & P.-L. Yu (Eds.), *Lithics in the West:Using Lithic Analysis to Solve Archaeological Problems in Western North America* (pp. 97–119). The University of Montana.

Reid, K. C., Hughes, R. E., Root, M. J., & Rondeau, M. F. (2015). Clovis in Idaho: An update on its distribution, technology, and chronology. In A. M. Smallwood & T. A. Jennings (Eds.), *Clovis: On the Edge of a New Understanding* (pp. 53–81). Texas A&M University Press.

Reimer, P. J., Austin, W. E. N., Bard, E., Bayliss, A., Blackwell, P. G., Bronk Ramsey, C., Butzin, M., Cheng, H., Edwards, R. L., Friedrich, M., Grootes, P. M., Guilderson, T. P., Hajdas, I., Heaton, T. J., Hogg, A. G., Hughen, K. A., Kromer, B., Manning, S. W., Muscheler, R., … Talamo, S. (2020). The IntCal20 Northern Hemisphere Radiocarbon Age Calibration Curve (0-55 cal kBP). *Radiocarbon*, *62*, 725–757. https://doi.org/10.1017/RDC.2020.41

Reynolds, A. M. (2010). Bridging the gulf between correlated random walks and Lévy walks: Autocorrelation as a source of Lévy walk movement patterns. *Interface: Journal of the Royal Society*, *7*, 1753–1758. https://doi.org/10.1098/rsif.2010.0292

Rhode, D., Goebel, T., Graf, K. E., Hockett, B. S., Jones, K. T., Madsen, D. B., Oviatt, C. G., & Schmitt, D. N. (2005). Latest Pleistocene-early Holocene human occupation and paleoenvironmental change in the Bonneville Basin, Utah-Nevada. In J. L. Pederson & C. M. Dehler (Eds.), *Field Guide 6: Interior Western United States* (pp. 211–230). The Geological Society of America.

Rhode, D., & Louderback, L. A. (2007). Dietary plant use in the Bonneville Basin during the terminal Pleistocene/early Holocene transition. In K. E. Graf & D. N. Schmitt (Eds.), *Paleoindian or Paleoarchaic? Great Basin Human Ecology at the Pleistocene/Holocene Transition* (pp. 231–247). University of Utah Press.

Rhode, D., & Louderback, L. A. (2015). Bonneville Basin Environments during the Pleistocene-Holocene Transition. In D. B. Madsen, D. N. Schmitt, & D. Page (Eds.), *The Paleoarchaic Occupation of the Old River Bed Delta* (pp. 22–29). University of Utah Press.

Rice, D. G. (1972). *The Windust phase in lower Snake River region prehistory*. [Doctoral dissertation, Washington State University]. (Accession Order No. AAT 7306173). Available from ProQuest Dissertations & Theses Global. (302641955).

Rockman, M. (2003). Knowledge and learning in the archaeology of colonization. In M. Rockman & J. Steele (Eds.), *Colonization of Unfamiliar Landscapes: The Archaeology of Adaptation* (pp. 3–24). Routledge.

Rockman, M. (2009). Landscape learning in relation to evolutionary theory. In A. M. Prentiss, I. Kuijt, & J. C. Chatters (Eds.), *Macroevolution in Human Prehistory: Evolutionary Theory and Processual Archaeology* (pp. 51–71). Springer. https://doi.org/10.1007/978-1-4419-0682-3

Rockman, M. (2013). Apprentice to the environment: Hunter-gatherers and landscape learning. In W. Wendrich (Ed.), *Archaeology and apprenticeship: Body knowledge, identity, and communities of practice* (pp. 99–118). University of Arizona Press.

Rockman, M., & Steele, J. (Eds.). (2003). *Colonization of Unfamiliar Landscapes: The Archaeology of Adaptation*. Routledge.

Roebroeks, W. (2003). Landscape learning and the earliest peopling of Europe. In M. Rockman & J. Steele (Eds.), *Colonization of Unfamiliar Landscapes: The Archaeology of Adaptation* (pp. 99–115). Routledge.

Rogers, M. J. (1939). Early lithic industries of the Lower Basin of the Colorado River and adjacent desert areas. In *San Diego Museum Papers* (Vol. 3). https://doi.org/10.1525/aa.1941.43.3.02a00160

Rosencrance, R. L. (2019). *Assessing the chronological variation within Western Stemmed Tradition projectile points*. [Master's thesis, University of Nevada, Reno]. (Accession Order No. AAT 13884064). Available from ProQuest Dissertations & Theses Global. (2280627007).

Rowley, P. D., Lytle, F. W., Lytle, M. B., & Stever, K. R. (2002). *Geology of the Modena obsidian source, Prohibition Flat area, Lincoln County, Nevada*. Report on file at Bureau of Land Management, Ely Field Office.

Rowley, P. D., Vice, G. S., McDonald, R. E., Anderson, J. J., Machette, M. N., Maxwell, D. J., Ekren, E. B., Cunningham, C. G., Steven, T. A., & Wardlaw, B. R. (2005). *Interim geologic map of the Beaver 30' x 60' quadrangle, Beaver, Piute, Iron, and Garfield counties, Utah*. Utah Geologic Society. https://ugspub.nr.utah.gov/publications/open_file_reports/ofr-454.pdf

Sappington, R. L. (1981). A progress report on the obsidian and vitrophyre sourcing project. *Idaho Archaeologist*, *4*, 4–17.

Sargeant, K. E. (1973). *The Haskett tradition: A view from Redfish Overhang*. [Unpublished Master's thesis]. Idaho State University.

Scheiber, L. L., & Finley, J. B. (2011). Obsidian source use in the Greater Yellowstone area, Wyoming Basin, and Central Rocky Mountains. *American Antiquity*, *76*(2), 372–394.

Schmitt, D. N., Madsen, D. B., Oviatt, C. G., & Quist, R. (2007). Late Pleistocene/early Holocene geomorphology and human occupation of the Old River Bed Delta, western Utah. In K. E. Graf & D. N. Schmitt (Eds.), *Paleoindian or Paleoarchaic? Great Basin Human Ecology at the Pleistocene/Holocene Transition* (pp. 105–119). University of Utah Press.

Schroth, A. B. (1994). *The Pinto point controversy in the western United States*. [Doctoral dissertation, University of California, Riverside]. (Accession Order No. AAT 9522233). Available from ProQuest Dissertations & Theses Global. (304094884).

Seibert, J., & McGlynn, B. L. (2007). A new triangular multiple flow direction algorithm for computing upslope areas from gridded digital elevation models. *Water Resources Research*, *43*(4), 1–8. https://doi.org/10.1029/2006WR005128

Shackley, M. S. (Ed.). (2010). *X-ray fluorescence spectrometry (XRF) in geoarchaeology*. Springer.

Shackley, S. M. (2021). *Source provenance of obsidian artifacts from five sites in southwest Utah*. Geoarchaeological XRF Laboratory. https://cloudfront.escholarship.org/dist/prd/content/qt9312n4wj/qt9312n4wj.pdf

Shroder, J. F., Cornwell, K., Oviatt, C. G., & Lowndes, T. C. (2016). Landslides, Alluvial Fans, and Dam Failure at Red Rock Pass: The Outlet of Lake Bonneville. In *Developments in Earth Surface Processes* (1st ed., Vol. 20). Elsevier B.V. https://doi.org/10.1016/B978-0-444-63590-7.00004-4

Siegrist, K. (2020). *The Cauchy Distribution*. LibreTexts: Statistics. https://stats.libretexts.org/@go/page/10372

Siniff, D. B. (1967). *A simulation model of animal movement behaviors*. [Unpublished doctoral thesis]. University of Minnesota.

Skinner, C. E. (2021). *Northwest Research Obsidian Source Reference Database*. Northwest Research Obsidian Studies Laboratory. http://www.obsidianlab.com/universe.html

Skinner, C. E., & Thatcher, J. J. (2005). X-ray fluorescence trace element provenance analysis of geologic sources of obsidian from the Nevada Test and Training Range and surrounding regoin, Nevada and California. In L. Haarklau, L. Johnson, & D. L. Wagner (Eds.), *Fingerprints in the Great Basin: The Nellis Air Force Base Regional Obsidian Sourcing Study*. U.S. Army Corps of Engineers, Fort Worth District.

Smith, G. M., & Barker, P. (2017). The Terminal Pleistocene/Early Holocene Record in the Northwestern Great Basin: What We Know, What We Don't Know, and How We May Be Wrong. *PaleoAmerica*, *3*(1), 13–47. https://doi.org/10.1080/20555563.2016.1272395

Smith, G. M., Duke, D., Jenkins, D. L., Goebel, T., Davis, L. G., O'Grady, P., Stueber, D., Pratt, J. E., & Smith, H. L. (2020). The Western Stemmed Tradition: Problems and prospects in Paleoindian archaeology in the Intermountain West. *PaleoAmerica*, *6*, 23–42. https://doi.org/10.1080/20555563.2019.1653153

Smith Jr., J. F., & Ketner, K. B. (1976). Stratigraphy of post-Paleozoic rocks and summary of resources in the Carlin-Pinon Range Area, Nevada. *United States Geological Survey, Professional Paper*, *867-B*, 1–48. https://doi.org/10.3133/pp867B

Spearman, C. (1904). The proof and measurement of association between two things. *The American Journal of Psychology*, *15*, 72–101. https://doi.org/10.1093/ije/dyq191

Speth, J. D., Newlander, K., White, A. A., Lemke, A. K., & Anderson, L. E. (2013). Early Paleoindian big-game hunting in North America: Provisioning or politics? *Quaternary International*, *285*, 111–139. https://doi.org/10.1016/j.quaint.2010.10.027

Spiess, A., Wilson, D., & Bradley, J. W. (1998). Paleoindian Occupation in the New England Maritime Region: Beyond Cultural Ecology. *Archaeology of Eastern North America*, *26*, 201–264.

Staatz, M., & Carr, W. (1964). Geology and mineral deposits of the Thomas and Dugway Ranges, Juab and Tooele Counties, Utah. *Professional Papers of the U.S. Geological Survey*, *415*, 188.

Stephenson, R. L., & Wilkinson, K. (1969). *Nevada Archaeological Survey, Research Papers No. 1: Archaeological Reconnaissance of the Winnemucca-Battle Mountain area of Nevada*. University of Nevada, Reno.

Swanson, E. H., Powers, R., & Bryan, A. L. (1964). The material culture of the 1959 southwestern Idaho survey. *Tebiwa*, *7*(2), 1–27.

Talbot, R. K., Richens, L. D., Searcy, M. T., Christiansen, E. H., & Ure, S. M. (2015). *Obsidian Crossroads: An Archaeological Investigation of the Panaca Summit/Modena Obsidian Source in Lincoln County, Nevada*. Brigham Young University.

Tarboton, D. G. (1997). A new method for the determination of flow directions and upslope areas in grid digital elevation models. *Water Resources Research*, *33*, 309–319.

Tarboton, D. G., Bras, R. L., & Rodriguez-Iturbe, I. (1991). On the extraction of channel networks from digital elevation data. *Hydrological Processes*, *5*, 81–100. https://doi.org/10.1002/hyp.3360050107

Thomas, D. (1981). How to classify the projectile points from Monitor Valley, Nevada. *Journal of California and Great Basin Anthropology*, *3*, 7–43.

Tobler, W. R. (1970). A computer movie simulating urban growth in the Detroit region. *Economic Geography*, *46*, 234–240.

Tobler, W. R. (1973). Three presentations on geographical analysis and modeling: Non-isotropic geographic modeling speculations on the geometry of geography global spatial analysis. *Technical Report 93-1*. National Center for Geographic Information and Analysis, University of California, Santa Barbara.

Tolan-Smith, C. (2003). The social context of landscape learning and the Lateglacial: Early Postglacial recolonization of the British Isles. In M. Rockman & J. Steele (Eds.), *Colonization of Unfamiliar Landscapes: The Archaeology of Adaptation* (pp. 116–129). Routledge.

Tripcevich, N. (2009). *Cost-distance Analysis*. Retrieved from http://mapaspects.org/node/3744/ on May 2, 2022.

Tripp, B. T. (2000). The Basin Perlite Company Mine and Mill, Beaver County, Southwest Utah. *Utah Geological Survey Notes*, *32*(3), 6–7.

Tuohy, D. R. (1974). *A comparative study of late Paleo-Indian manifestations of the western Great Basin*. In R. Elston (Ed.), *Collected Papers on Great Basin Archaeology* (pp. 91-116), Nevada Archaeological Survey Research Paper 5, University of Nevada, Reno.

Tuohy, D. R. (1968). Some early lithic sites in Western Nevada. In C. Irwin-Williams (Ed.), *Early Man in Western North America, Symposium of the Soutwestern Anthropological Association* (Vol. 1, Issue 4, pp. 27–38). Eastern New Mexico University Paleo-Indian Institute.

Tuohy, D. R., & Layton, T. N. (1977). Towards the Establishment of a New Series of Great Basin Projectile Points. *Nevada Archaeological Survey Reporter*, *10*(6), 1–5.

Turchin, P. (1996). Fractal analyses of animal movement: A critique. *Ecology*, *77*, 2086–2090.

Turchin, P. (2006). Comment. In "Measuring forager mobility" by Jeffrey P. Brantingham. *Current Anthropology*, *47*, 453–454.

U.S. Geological Survey. (2020a). *3D Elevation Program (3DEP)*. https://www.usgs.gov/core-science-systems/ngp/3dep/about-3dep-products-services

U.S. Geological Survey. (2020b). *NHD 20200615 for Utah State or Territory FileGDB 10.1 Model Version 2.2.1*. ScienceBase-Catalog. https://www.sciencebase.gov/catalog/item/4f5545cce4b018de15819ca9

U.S. Geological Survey. (2020c). *The National Map Viewer*. Department of the Interior, U.S. Geological Survey. https://viewer.nationalmap.gov/advanced-viewer/

Umshler, D. B. (1975). *Source of the Evan's Mound obsidian*. New Mexico Institute of Mining and Technology, Socorro.

Utah Department of Heritage and Arts. (2020). *Archaeology Report Records*. J. Willard Marriott Digital Library, The University of Utah.

Utah Division of State History. (2020). *SEGO*.

Utah Geospatial Reference Center. (2017). *Historic Lake Bonneville*. https://gis.utah.gov/data/water/historic-lake-bonneville/

Virtanen, P., Gommers, R., Oliphant, T. E., Haberland, M., Reddy, T., Cournapeau, D., Burovski, E., Peterson, P., Weckesser, W., Bright, J., van der Walt, S. J., Brett, M., Wilson, J., Millman, K. J., Mayorov, N., Nelson, A. R. J., Jones, E., Kern, R., Larson, E., … Vázquez-Baeza, Y. (2020). SciPy 1.0: fundamental algorithms for scientific computing in Python. *Nature Methods*, *17*(3), 261–272. https://doi.org/10.1038/s41592-019-0686-2

Viswanathan, G. M., Bartumeus, F., Buldyrev, S. V., Catalan, J., Fulco, U. L., Havlin, S., Da Luz, M. G. E., Lyra, M. L., Raposo, E. P., & Stanley, H. E. (2002). Lévy flight random searches in biological phenomena. *Physica A: Statistical Mechanics and Its Applications*, *314*, 208–213. https://doi.org/10.1016/S0378-4371(02)01157-3

Viswanathan, G. M., Da Luz, M. G. E., Raposo, E. P., & Stanley, H. E. (2011). *The Physics of Foraging: An Introduction to Random Searches and Biological Encounters*. Cambridge University Press.

Walker, G. W., & MacLeod, N. S. (1991). *Geologic map of Oregon*. U.S. Geological Survey. https://ngmdb.usgs.gov/Prodesc/proddesc_16259.htm

Wallace, B. N. (2017). *MU505, TG506, OD508 munitions response sites, Tooele County, Utah: Results of a cultural resources inventory, Final report, Volume 1*. On file with Utah Division of State History, State Project No. U-15-UI-0799b.

Wallace, B. N. (2018). *Remedial investigations for MU505 and TG506 munitions response sites, Tooele County, Utah: Cultural resource monitoring results, Final report, Volume 2*. On file with Utah Division of State History, State Project No. U-18-OM-0118.

Warren, C. N. (1967). The San Dieguito complex: A review and hypothesis. *American Antiquity*, *32*, 168–185. http://www.jstor.org/stable/277902

Warren, C. N. (1980). Pinto points and problems in Mojave Desert archaeology. In L. B. Harten, C. N. Warren, & D. R. Tuohy (Eds.), *Anthropological Papers in Memory of Earl H. Swanson, Jr.* (pp. 67–76). Idaho Museum of Natural History.

Waters, M. R., & Stafford, T. W. (2007). Redefining the age of Clovis: implications for the peopling of the Americas. *Science*, *315*(5815), 1122–1126. https://doi.org/10.1126/science.1137166

Weide, D. L. (1964). *Site survey sheet: 42BE52*. University of Utah, Dept. of Anthropology.

Weisler, M. I., & Woodhead, J. D. (1995). Basalt Pb isotope analysis and the prehistoric settlement of Polynesia. *Proceedings of the National Academy of Sciences of the United States of America*, *92*(6), 1881–1885. https://doi.org/10.1073/pnas.92.6.1881

Wentworth, C. K. (1922). A scale of grade and class terms for clastic sediments. *The Journal of Geology*, *30*, 377–392. https://doi.org/10.1086/622910

Whitman, S. J. (2013). *Near or far: An analysis of prehistoric obsidian procurement behavior in the greater Yellowstone area*. [Master's thesis, Northern Arizona University]. (Accession Order No. AAT 1537817). Available from ProQuest Dissertations & Theses Global. (1368239131).

Williams, V. S., Best, M. G., & Keith, J. D. (1997). *Geologic map of the Ursine-Panaca Summit - Deer Lodge area, Lincoln County, Nevada, and Iron County, Utah*. U.S. Geological Survey.

Willig, J. A., & Aikens, C. M. (1988). The Clovis-Archaic Interface in Far Western North America. In J. A. Willig, C. M. Aikens, & J. L. Fagan (Eds.), *Eary Human Occupation in Far Western North America: The Clovis-Archaic Interface* (pp. 1–40). Nevada State Museum Anthropological Papers 21.

Willingham, C. (1995). Big Table Mountain: An obsidian source in the Centennial Mountains of Eastern Idaho. *Idaho Archaeologist*, *18*, 3–7.

Willson, C. A. (2005). *X-ray fluorescence analysis of obsidian associated with Late Archaic sites in Southwestern Idaho and Southeastern Oregon: Issues in addressing mobility*. University of Idaho. [Unpublished master's thesis]. University of Idaho.

Willson, C. A. (2007). A re-evaluation of X-ray fluorescence data from Idaho and southeastern Oregon. *Idaho Archaeologist*, *30*, 17–26.

Wright, G. A., Chaya, H., & McDonald, J. (1990). The location of the Field Museum Yellowstone (F.M.Y., 90) Group obsidian source. *Plains Anthropologist*, *35*, 71–74. https://doi.org/10.1080/2052546.1990.11909556

Zar, J. H. (2010). *Biostatistical Analysis* (5th ed.). Prentice Hall.

Zerga, D. (1988). *Intermountain Antiquities Computer System: Site 26EK7320*. Bureau of Land Management.

Appendix A: Data Cleaning and Dataset Development

A.1 Introduction

This appendix describes the steps in the preparation, cleaning, and union of several disparate datasets from previous research in the Old River Bed (ORB) region into a single dataset of geolocated Paleoindian artifacts associated with dated channels within the ORB delta/wetlands. This dataset will be used to test my hypotheses about the Discoverability of ORB-utilized lithic sources over time. It will also be used to generate the full list of obsidian and fine-grained volcanic (FGV) sources exploited within this curated, temporal dataset.

Note: The location data for the archaeological sites and artifacts referenced in this appendix have been removed from the public copy of this work, for legal site protection reasons. For access to the unredacted edition of this appendix, please contact the Utah State Historic Preservation Office, Salt Lake City, Utah.

A.2 Data Sources

I acquired this data from the following sources:

1. The monograph "*The Paleoarchaic Occupation of the Old River Bed Delta*" by Madsen, Schmitt, and Page (2015). Hereafter referred to simply as "the monograph".

2. "*ORB Final General File.xls*", created by Charlotte Beck and provided by her on May 31, 2018. This file lists 2288 artifacts classified to type, and includes coordinates, metrics, and site assignments for most of the ORB artifacts described in the monograph (see Beck & Jones, 2015)

3. Beck similarly provided individual spreadsheets for each major artifact type (for example, "*Final ORB Projectile Points.xls*") which expand on artifact metrics.

4. Beck also provided a spreadsheet named "*site_channel_list.xls*" that lists all the ORB delta sites and each site's associated channel.

5. David Page provided ArcMap/GIS shapefiles for the ORB delta channels (personal comm., August 22, 2018).

6. The X-ray fluorescence (XRF) data was published as an online supplement to the monograph, authored by David Page, and available as a spreadsheet named "*Dugway Table 7_XRF_pXRF trace element concentration estimates for 2007 obsidian and FGV artifacts from DPG and UTTR.xls*" (Page, 2015b). Hereafter referred to simply as "the XRF spreadsheet".

Using these resources, I created an artifact database in Microsoft Access 365 (v. 16.0, 64-bit) to clean, filter, and unify these disparate datasets.

Throughout this appendix, site identifiers (e.g., 42TO1234) may be referred to by the last four digits of the site's Smithsonian trinomial identifier (e.g., 1234).

A.3 Database Tables

Testing my model in the context of the ORB requires that we recognize that many of the chronological positions of the channels and sites are relative, and that the geology is complex (Madsen, Schmitt, et al., 2015). As a result, it is perhaps unreasonable to expect high chronological precision from the data. My goal in appendix is to verify and group as many sites and artifacts as possible with dated ORB channels, in the process creating the largest possible sample groups, or pools, for known date ranges. Using this approach, I hope to detect diachronic change across multiple temporal bands spanning the ~3,500-year lifecycle of the active delta. Using the methods described in Chapter 2 for the determination of each site's *Dlist* and *Olist*, the results from each group will be pooled for comparison across time. These macro-scale pools will

then be evaluated to determine if a landscape learning continuum can be detected among the earliest groups entering the landscape and long-term residential groups.

A.3.1 Channels

The monograph provides both relative and absolute dating for various ORB channels.

The channel table (Table A-1) and the relative chronological order of the channels are derived from the monograph (Madsen, Schmitt, et al., 2015; Table 3.1). Relative dating was inferred by the monograph authors from channel intersections and overlaps. Table 4.10 in the monograph divides the Blue channel sites into two dated ranges. For this reason, I split the Blue channel in two, Blue A (the older,) and Blue B.

This data is stored within the Channel table in the database. Each channel is identified by ChannelID.

Table A-1: Old River Bed delta channels, roughly in relative order.

ChannelID	Channel Name
1	Mango *
2	Mocha *
3	Gold
4	Black
5	Limestone
6	Yellow
7	Fuchsia
8	Green
9	Red
10	Blue A
25	Blue B
11	Lime
12	Royal Blue
13	Lavender
14	Navy
15	Coral
16	Orange
17	Pink
18	Buff
19	White
20	Brown
21	Light Blue
22	Seafoam
23	Rust
24	Light Green **

* The Mango and Mocha channels are considered by Madsen et al. (2015, p. 54) to

be as old or older than the Gold channel; however, these channels have not been

dated and there are no sites associated with them.

** An additional channel, Light Green, was provided in the Page ArcMap/GIS

shapefiles (data source 5 in section A.2). This channel is not mentioned in the

monograph. It appears to overlie the Light Blue channel at one point and underlie the

Brown channel, so it is likely a younger channel. It is undated.

Table A-2 presents the dated ORB channels. Artifacts associated with these channels will

make up the temporal groups that will be compared against one another.

Table A-2: Dated Old River Bed delta channels.

Channel Association	Channel Age (^{14}C yr BP)
Gold	~11,300 - 10,500
Black	~11,000 - 10,300
Yellow	~10,300 - 10,100
Limestone	~10,500 - 10,000
Green	~10,300 - 9,800
Blue A	~10,000 - 9,500
Blue B	~10,000 - 9,500
Red	~9,860 - 9,740
Lime	~9,800 - >9,200
Lavender	~9,100 - 9,000
Light Blue	~9,800 - 8,800

Derived from Madsen et al. 2015, Tables 4.2 – 4.10.

A.3.2 SitesChannels

The SitesChannels table is an associative (or junction) table that links sites and, therefore, artifacts to channels and was created by importing the "*site_channel_list.xls*" spreadsheet into Access. This list was then modified using the following update command to associate the channel color from the spreadsheet with ChannelID in the Channel table.

UPDATE SitesChannels sc

left outer join Channel ch

on (sc.ChannelColor = ch.ChannelName)

set sc.ChannelId = ch.ChannelId

This table indicates which sites are found in association with which colored channel (Table A-3 provides a truncated example).

Table A-3: Example of the SitesChannels structure.

ChannelID	SiteID
…	…
21	42TO1671
4	42TO1672
4	42TO1673
…	…

I made one modification to the ChannelColor column provided in the spreadsheet. Site 42TO3140 was originally assigned to "Buff/Royal?". This was changed to "Buff" for naming integrity but, in the end, this channel assignment is irrelevant as neither channel has been dated as of this writing and, therefore, will not fall into one of the dated groups.

There are inconsistencies between the original "*site_channel_list.xls*" spreadsheet and the monograph, enumerated below:

1. In the spreadsheet, 41 sites are assigned to the Black channel, in contrast to Table 4.2 in the monograph, which has 36. The additional sites are 42TO1384 (Archaic types only), 1671 (changed to Light Blue, see item 7.a below), 1683 (contains WST types), 1891 (non-descript), and 1921 (changed to Limestone, see item 3 below). It is not clear why these sites were omitted from Table 4.2 in the monograph.

2. In the spreadsheet, the Yellow channel was missing site 42TO3521, but listed in Table 4.4 in the monograph. While this site likely only contains Archaic artifacts, it is included for completeness. The monograph (p. 74) claims it is a debitage scatter post-dating the flow of the Yellow channel.

3. The Limestone channel is missing entirely from the spreadsheet. In the spreadsheet, site 42TO1921 is assigned to the Black channel and 1922 is assigned to "N/A", but the monograph's Figure 4.4 shows them both on the Limestone channel. At this stage in the cleaning, these sites were switched to Limestone in accordance with the monograph's Tables 4.9 and 5.37; however, both were eventually reassigned back to Black after the visual review stage in section A.5.3, below.

4. The Blue channel lists 10 sites; however, they are split across two date ranges which, for this study, are split into Blue A and Blue B (see section A.3.1, above). Sites

42TO3227 and 3232 were assigned to Blue A (ChannelID = 25) and the remainder (*n=8*) to Blue B (ChannelID = 10).

5. The Lime channel is missing entirely from the spreadsheet. Sites 42TO3520 and 3522 were added manually to the SitesChannels table (per the monograph, Tables 4.6 and 5.37).

6. The Lavender channel has two sites that are inconsistently recorded. Site 42TO2955 has a Great Basin Concave Base point associated with it but does not appear in the monograph's Table 4.7 or Table 5.37. Site 42TO3239 has a crescent associated with it and appears in the monograph's Table 4.7, but not in Table 5.37. These sites were left in the SitesChannels table.

7. The Light Blue channel dataset is problematic. Table 4.8 in the monograph shows 26 sites. Table 5.37 in the monograph lists 18. The *site_channel_list.xls* spreadsheet lists 35 sites.

   a) In the spreadsheet, site 42TO1671 is listed on the Black channel. In the monograph's Table 5.37 and in Figure 4.6 it is clearly on the Light Blue channel. The channel assignment for site 1671 was changed to Light Blue.

   b) The following sites (Table A-4) appear in the spreadsheet but are missing from the monograph's Table 4.8. These were compared against the "*ORB Final General File.xls*" spreadsheet to determine if any artifacts were recorded for the sites. Eight of the sites had no recorded artifacts.

Table A-4: Missing sites analysis.

SiteID	Notes
42TO1154	No artifacts
42TO1158	No artifacts
42TO1168	No artifacts, does not appear in Figure 4.20 in the monograph
42TO1173	Archaic artifacts only
42TO1174	No artifacts
42TO1183	No artifacts
42TO1184	No artifacts
42TO1185	No artifacts
42TO1382	No artifacts
42TO1676	Archaic artifacts only

These sites were added to table SiteChannels for completeness but will have no bearing on my study, since there are no associated artifacts or only Archaic artifacts.

8. The Red channel is not discussed in Chapter 4 of the monograph. It only has one date (Madsen et al., 2015). Table 5.37 in the monograph lists two sites (4DM02 and 4DM03) on the Red channel, which include WST artifacts. The "*site_channels_list.xls"* also includes sites 04DM01 and 04DM05, which I have left assigned to the Red channel.

A.3.3 Artifact and Isolate Tables

The data for the Artifact and Isolate tables originates from the Excel spreadsheet "*ORB Final General File.xls*". This is a listing of 2288 artifacts catalogued at the ORB delta and the surrounding area and then classified by Beck & Jones (2015) to lithic types (CLASS$, TYPE$, and TECH$). For each artifact, I created a field called "SampleID" which is the combination of the SITE$ (site trinomial) and FS$ (field sample number) values (e.g., SITE$ of 42TO1163 and FS$ of 5 combine to create 42TO1163.5). Of these 2288 artifacts, 315 are isolates not assigned to a site. These artifacts have SITE$ values with values of either "DPGIF" or "ISO".

These 2288 artifacts were divided into two groups in the Access database: artifacts assigned to a site (hereafter referred to as site-artifacts) remained in the Artifact table (*n=*1973) and isolated finds were moved to the Isolate table (*n=*315).

The Artifact and Isolate tables both use the following structure (Table A-5):

Table A-5: Artifact and Isolate tables data structure and definitions.

Field Name	Data type	Definition
SampleID	Text	Combination of SITE$ and FS$
SiteID	Text	SITE$, site trinomial from the spreadsheet
FS$	Text	Field sample number
UTME	Number	UTM easting, within 12 N
UTMN	Number	UTM northing, within 12 N
PMAT$	Text	Physical material (i.e., obsidian, FGV)
WEIGHT	Number	Artifact weight
ABRASION$	Text	Artifact surface wear
TECH$	Text	Lithic classification (high level)
TYPE$	Text	Lithic type
CLASS$	Text	Class within lithic type
UsesCentroid	Text	Indicates (Y/N) use of site centroid coordinates in cases where artifact coordinates are incomplete
DBH Notes	Text	Any notes created by me

A.4 ORB Site-Artifacts

This section describes the data cleaning and review of the site-associated samples in the Artifact table (beginning with *n=*1973).

A.4.1 Initial Cleaning of Site-Artifact Data

The first step in cleaning the site-artifact data was eliminating duplicates, of which there were several (with the same site ID, Site$, and field sample ID, FS$) in the spreadsheet. These were discovered using Excel's Conditional Formatting / Highlight Cells Rules / Duplicate Values function. The following artifacts with duplicate SITE$ and FS$ numbers are listed here (debitage/indeterminate flakes which share a field sample number are excluded). The SampleID

(Site$ + FS$) in bold indicates the artifact that was retained following review of each duplicate

pair (Table A-6). The resolutions are described below the table.

Table A-6: Duplicate Site-Artifacts from "ORB Final General File.xls" spreadsheet

SITE$	FS$	UTME	UTMN	PMAT$	WT (g)	ABRASION$	CLASS$	TYPE$	TECH$
42TO1163	**5**	■	■	OBS	0.98	HEAVY	ABLADE	ABLADE	PP
42TO1163	5	■	■	OBS	0.98	HEAVY	IND BLADE	UNCL PP	PP
42TO1371	97	■	■	FGV	5.37	HEAVY	BF BEAK A	SCRAPER	BIFACE
42TO1371	**97**	■	■	FGV	5.37	EXTREME	STUBBY 4	STUBBY	PP
42TO1668	1	■	■	FGV	4.26	MEDIUM	INT FLAKE	INT FLAKE	FLAKE
42TO1668	**1**	■	■	FGV	3.02	EXTREME	IND BLADE	UNCL PP	PP
42TO1677	**15A**	■	■	OBS	2.83	EXTREME	IND BIFACE	IND BIFACE	BIFACE
42TO1677	**15B**	■	■	FGV	16.66	MEDIUM	AM UNIFACE	AM UNIFACE	UNIFACE
42TO1686	52	■	■	OBS	2.35	EXTREME	STUBBY 1	STUBBY	PP
42TO1686	**52**	■	■	OBS	2.35	EXTREME	STUBBY 2	STUBBY	PP
42TO1688	**56A**	■	■	OBS	3.83	MEDIUM	AM BIFACE	AM BIFACE	BIFACE
42TO1688	**56B**	■	■	FGV	1.95	MEDIUM	STUBBY 5	STUBBY	PP
42TO1859	**3**	■	■	FGV	2.26	EXTREME	PINTO	PINTO	PP
42TO1859	3	■	■	OBS	2.26	EXTREME	PINTO	PINTO	PP
42TO1920	**36**	■	■	FGV	7.68	HEAVY	AM BIFACE	AM BIFACE	BIFACE
42TO1920	3	■	■	FGV	12.9	MEDIUM	UF END SCRPR	SCRAPER	UNIFACE
42TO2553	**3**	■	■	FGV	17.58	HEAVY	CM/H STEM	CM/H STEM	PP
42TO2553	**3B**	■	■	OBS	5.57	MEDIUM	WST BLADE	WST BLADE	PP
42TO3140	13A	■	■	OBS	8.83	MINIMAL	AM UNIFACE	AM UNIFACE	UNIFACE
42TO3140	**13B**	■	■	OBS	8.83	MEDIUM	UF BEAK B	SCRAPER	UNIFACE
42TO3230	**5A**	■	■	FGV	4.51	HEAVY	S LAKE STEM	SILVER LAKE	PP
42TO3230	**5B**	■	■	FGV	3.68	HEAVY	WST STEM	WST STEM	PP

Duplicate resolutions:

42TO1163.5: This is a clear duplicate; the samples have the same UTM as well as the same

weight and general description. It is also a duplicated in the *"Final ORB Projectile Points.xls"*

spreadsheet. This artifact was not XRF tested. I deleted the second duplicate (IND BLADE).

42TO1371.97: This is a clear duplicate; the samples have the same UTM when the

typographical error is corrected (see below), as well as the same weight and general description.

It is not duplicated in the *"Final ORB Projectile Points.xls"* spreadsheet where it is classified as

a Stubby. This artifact was XRF tested but described in the XRF spreadsheet as a scraper. I

deleted the duplicate (Type$ = Scraper) and retained the Stubby record. I also updated the

UTME (from ■ to ■) as the original is 303 km east of the ORB and clearly a typographical error.

42TO1668.1: This a clear misnumbering of the sample; the samples have differing coordinates, material, weight, and classification. The artifact with UTME = ■ is a duplicate of ■ (identical UTME, UTMN, weight, and general description). The record was deleted. Sample 42TO1668.1 was not XRF tested.

42TO1677.15: This is a clear misnumbering; the samples have the same coordinates but differing material, weights, and descriptions. I cannot make a duplication determination with the data I have. I have modified the field sample numbers to include an "A" and "B" suffix. Neither sample was XRF tested.

42TO1686.52: This is a clear duplicate; the samples have the same UTM as well as the same weight and general description. It is not duplicated in the "*Final ORB Projectile Points.xls*" spreadsheet where it is classified as a Stubby2. I deleted the Stubby1 record. Sample 42TO1686.52 was not XRF tested.

42TO1688.56: This appears to be a misnumbering; the samples have the same UTM coordinates but differing material, weight, and classification. It is not duplicated in the "*Final ORB Projectile Points.xls*" spreadsheet where it is classified as a Stubby. Sample 42TO1688.56 also appears in the *"ORB Bifaces Final 2011.xls"* with the same weight. I cannot make a duplication determination with the data I have. I have modified the field sample numbers to include an "A" and "B" suffix. Neither sample was XRF tested.

42TO1859.3: This appears to be a duplicate; the samples have the same weight and general descriptions, but the UTM coordinates are more than 2 kilometers apart. It is not duplicated in

the "*Final ORB Projectile Points.xls*" spreadsheet where it is similarly classified but where there is a typographical error (a missing digit) in the UTMN. The UTME in "*Final ORB Projectile Points.xls*" matches the first instance in Table A-6, above. This sample was XRF tested, but as obsidian, not FGV, like the second instance in Table A-6. In the Site-by-Site review (A.5, below), it is clear that the second instance (UTMN = ■) is the duplicate as it does not cluster with the rest of the artifacts from site 42TO1859. This sample was deleted.

42TO1920.36: This duplication is the result of a typographical error in the second instance's field sample number. In the "*ORB Scrapers Final 2011.xls*", sample 42TO1920.3 is a scraper at the same UTM coordinates and the same weight. I corrected the field sample number for the scraper, from 36 to 3. Neither sample was XRF tested.

42TO2553.3: This appears to be a misnumbering; the samples have the same coordinates, but differing material, weight, and classifications. Importantly for this study, both are WST artifacts. Both appear in "*Final ORB Projectile Points.xls*". The sample classified as CM (Cougar Mountain) was XRF tested, so I left that as the official artifact for this sample number. However, the other WST BLADE is significant. I changed that field sample number to 3B; this sample was not XRF tested.

42TO3140.13: This appears to be a misnumbering; the samples have the differing coordinates, but the same weight and material. Neither appears in the "*Final ORB Projectile Points.xls*" spreadsheet, but the scraper is in the "*ORB Scrapers Final 2011.xls*" spreadsheet. I cannot make a duplication determination with the data I have. I changed the field sample numbers for the scraper to 13A and the uniface to 13B. Neither sample was XRF tested.

42TO3230.5: This appears to be a misnumbering; the samples have the same coordinates but differing weight and classifications. Both records are duplicated in the *"Final ORB Projectile*

Points.xls" spreadsheet, repeating the same metrics, so there are clearly two artifacts here. I have modified the field sample numbers to include an "A" and "B" suffix. Neither sample was XRF tested.

There were 1973 artifacts at the beginning of this cleaning stage. Five duplicates were deleted, leaving 1968**.** The duplicates were not preserved in the database (other than in the original spreadsheet) as they serve no useful purpose.

A.5 Site-by-Site Review for Data Fidelity

As just noted, there are 1968 remaining artifacts assigned to an identified ORB site (a site with a trinomial ID associated with an ORB channel) and associated with a specific ORB channel. Both the channel and the site are significant contextual identifiers for each artifact, so the remaining 1968 artifacts were cleaned and inspected for each channel, on a site-by-site basis.

There are several artifacts missing UTM coordinates (with placeholders, entered as 99, 99) but assigned to sites. Often these are collections of flakes/debitage, but a few are assigned to more specific artifact types. For these site-assigned artifacts, I used the ArcMap (Esri, 2021e) *Mean Center* function to generate centroid coordinates from the site's artifact points and then substituted that value for each incomplete artifact. In these cases, the UsesCentroid field in the Artifact table is set to "Y" for the artifact to clearly indicate that this method was applied.

The sites were reviewed according to assigned channel, roughly in order from oldest to more recent.

A.5.1 Gold Channel (2 sites, 45 artifacts)

The Gold channel is the oldest dated channel. The following site was geolocated and visually reviewed using ArcMap, and all artifact data appear correct and have the appropriate channel association (Table A-7):

Table A-7: Gold channel sites without changes.

Site	Channel	# of Artifacts
42TO3141	Gold	6
Total		**6**

The following Gold channel site required corrections or warranted further comment:

42TO3142 [Gold, 39 artifacts]

- This site is situated within a complex area of smaller channels that seem to overlie the Gold channel. The monograph (p. 91) suggests it may be a palimpsest but still associates the site with the Gold channel. The site may in fact be associated with an unknown channel that overlies the Gold channel (Figure A-1). While there is not enough evidence in the aerial images to change the monograph's channel association, it is possible this is a younger site or would be better associated with meanderings of the Blue channel.
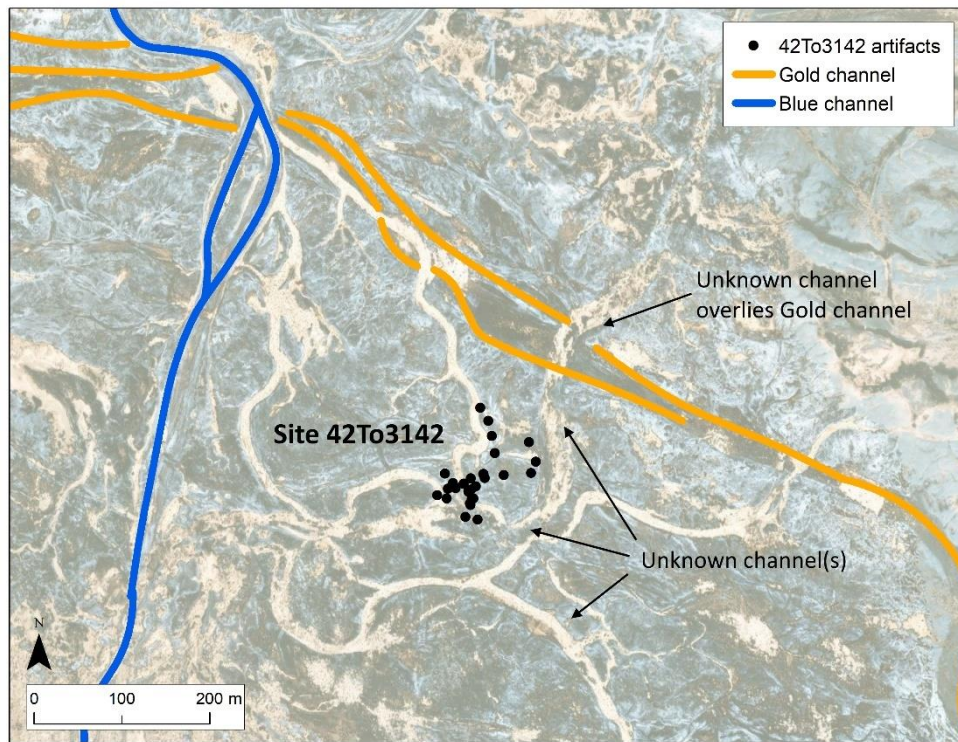
Figure A-1: Site 42TO3142 in context to Gold and Blue channels

A.5.2 Black Channel (39 sites, 697 artifacts)

The following Black channel sites were geolocated and visually reviewed using ArcMap, and all artifact data appear correct and have the appropriate channel association (Table A-8):

Table A-8: Black channel sites without changes.

Site	Channel	# of Artifacts
42TO1356	Black	1
42TO1385	Black	1
42TO1666	Black	15
42TO1667	Black	1
42TO1669	Black	5
42TO1670	Black	3
42TO1672	Black	8
42to1673	Black	2
42TO1682	Black	7
42TO1685	Black	39
42TO1687	Black	10
42TO1861	Black	19
42TO1876	Black	13
42TO1920	Black	26
42TO1923	Black	6
42TO1924	Black	46
Total		**202**

There is some discord between the monograph's Table 4.2 (which lists Black channel sites) and the "*ORB Final General File.xls*" artifact spreadsheet. Three sites (1384, 1683, and 1891) appear in the spreadsheet but not the table. These sites are included here as part of the working dataset.

The following Black channel sites required corrections or warranted further comment:

42TO1368 [Black, 11 artifacts]

- Artifacts 42TO1368.1A and 1B appear in the "*ORB Final General File.xls*" artifact

  spreadsheet. 1B is correctly positioned within the site cluster, while 1A is about 3700 m

  south, suggesting an error. There are no obvious corrections (typographical errors, transposed

digits, or other sites to which it might belong) but also not enough reason to discard this sample. It is probably best to treat 42TO1368.1A as an isolate (still closely associated with the Black channel) rather than as part of the 42TO1368 assemblage.

42TO1369 [Black, 47 artifacts]

- There are 47 artifacts associated with this site, but thirty-three (33) are missing coordinates (Table A-9). Most of these appear to be flakes from a lithic scatter, but two unclassified projectile points and a biface are also missing coordinates. These 33 artifacts were set to the site's Mean Center UTM coordinates (■, ■) and UsesCentroid was set to "Y".

Table A-9: 42TO1369 artifacts missing coordinates.

SampleID	TYPE$	TECH$	UTME	UTMN
42TO1369.15	IND BIFACE	BIFACE	99	99
42TO1369.15	CORT FLAKE	FLAKE	99	99
42TO1369.15	INT FLAKE	FLAKE	99	99
42TO1369.15	INT FLAKE	FLAKE	99	99
42TO1369.15	INT FLAKE	FLAKE	99	99
42TO1369.15	INT FLAKE	FLAKE	99	99
42TO1369.15	INT FLAKE	FLAKE	99	99
42TO1369.15	INT FLAKE	FLAKE	99	99
42TO1369.15	INT FLAKE	FLAKE	99	99
42TO1369.15	INT FLAKE	FLAKE	99	99
42TO1369.15	INT FLAKE	FLAKE	99	99
42TO1369.15	INT FLAKE	FLAKE	99	99
42TO1369.15	INT FLAKE	FLAKE	99	99
42TO1369.15	INT FLAKE	FLAKE	99	99
42TO1369.15	INT FLAKE	FLAKE	99	99
42TO1369.15	INT FLAKE	FLAKE	99	99
42TO1369.15	INT FLAKE	FLAKE	99	99
42TO1369.15	INT FLAKE	FLAKE	99	99
42TO1369.15	INT FLAKE	FLAKE	99	99
42TO1369.15	INT FLAKE	FLAKE	99	99
42TO1369.15	INT FLAKE	FLAKE	99	99
42TO1369.15	INT FLAKE	FLAKE	99	99
42TO1369.15	INT FLAKE	FLAKE	99	99
42TO1369.15	INT FLAKE	FLAKE	99	99
42TO1369.15	INT FLAKE	FLAKE	99	99
42TO1369.15	INT FLAKE	FLAKE	99	99
42TO1369.15	INT FLAKE	FLAKE	99	99
42TO1369.15	INT FLAKE	FLAKE	99	99
42TO1369.15	INT FLAKE	FLAKE	99	99
42TO1369.15	INT FLAKE	FLAKE	99	99
42TO1369.15	INT FLAKE	FLAKE	99	99
42TO1369.16	UNCL PP	PP	99	99
42TO1369.17	UNCL PP	PP	99	99

42TO1370 [Black, 11 artifacts]

- Artifact 42TO1370.5 has an incorrect UTMN; it places the artifact exactly 6km north of the site cluster. The UTMN was changed from ■ to ■, in accordance with other site artifacts.

42TO1371 [Black, 45 artifacts]

- Artifact 42TO1371.47 is missing the UTMN coordinate. Adding a UTMN at ■ places the artifact in the cluster approximately between the previous and next sequential artifacts (60 m difference). This artifact was XRF tested, so it important to place it appropriately.

42TO1384 [Black, 2 artifacts]:

- All artifact data appear correct, but this site does not appear in the monograph's Table 4.2 (listing Black channel sites). It is found in the general artifact spreadsheet and is clearly situated on the Black channel (Figure A-2).
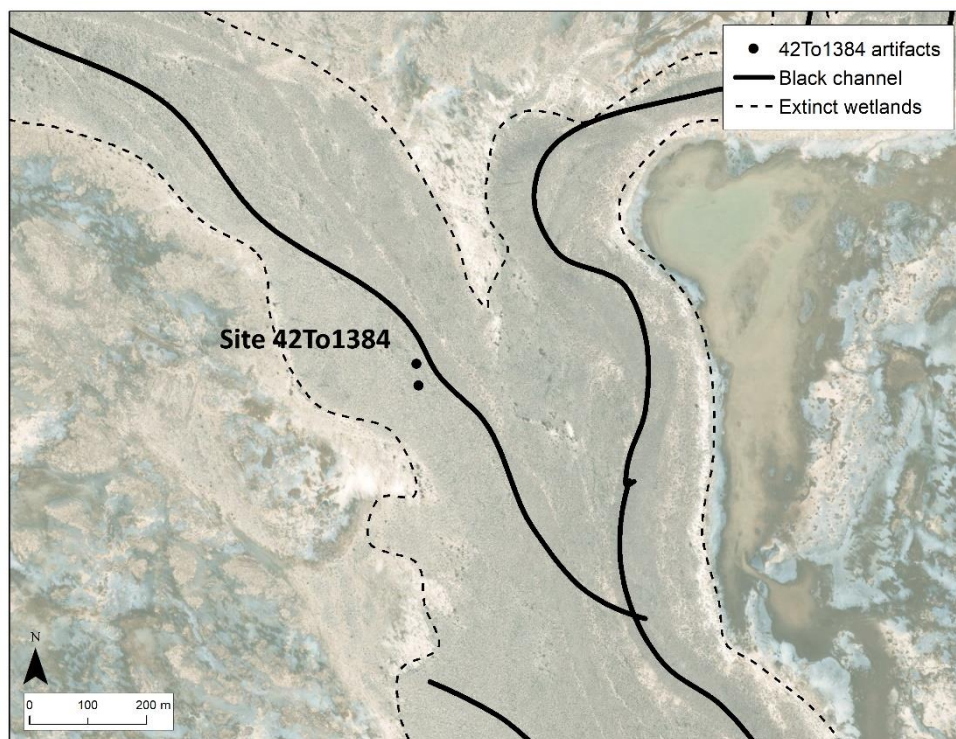
Figure A-2: Site 42TO1384 in context with the Black channel

42TO1668 [Black, 10 artifacts]

- Two samples within this site group have coordinates that place them within the site 42TO1686 cluster. The FS$ number for one sample (42TO1668.66) is also well outside the sample count total for site 1668. This is most likely a case of transposed site numbers. These two samples (11 and 66) were reassigned to site 42TO1686.

- This, in turn, introduces two duplicates into 42TO1686. This is likely due to the original error as the UTM coordinates are in accord with the artifacts in the cluster. The artifacts moved from 1668 have been designated with a "B" (11B and 66B) and the artifacts originally assigned to 1686 as 11A and 66A. It is possible 1686.66B is a duplicate, as the weight and classifications are similar, but there is not enough evidence to delete this record.

42TO1680 [Black, 5 artifacts]

- Artifact 42TO1680.1 has an incorrect UTME; it is missing a digit. The UTME was changed from ■ to ■, in accord with the other site samples.

42TO1681 [Black / Light Blue, 6 artifacts]

- Two of the six samples from this site are problematic (Table A-10). Samples 1 and 3 have a UTME that places them more than 4 km to the east, well away from the Black channel (close to Light Blue). There are no obvious culprits here – no typographical errors or missing or transposed digits. The field sample numbers are sequential and non-replicative. Both errant samples are significant artifacts for this study and Sample 3 was XRF tested.

Table A-10: 42TO1681 artifacts.

SampleID	WEIGHT	TYPE$	TECH$	UTME	UTMN
42TO1681.1	5.79	WST BLADE	PP	■	■
42TO1681.2		UNCL PP	PP	■	■
42TO1681.3	1.11	PINTO	PP	■	■
42TO1681.4		SQ STEM	PP	■	■
42TO1681.5		IND BIFACE	BIFACE	■	■
42TO1681.6		IND BIFACE	BIFACE	■	■

Once all artifact points were projected on a map, it was easy to see that artifacts 42TO1681.1 and 3 were using the same coordinates as 42TO1679.1 and 3, down to the final decimal. However, the artifact classifications and attributes (specifically, Weight) suggest these are not duplicate artifacts, just incorrectly entered UTM coordinates for the two 42TO1681 artifacts (compare with Table A-11).

Table A-11: Comparison with 42TO1679 artifacts.

SampleID	WEIGHT	TYPE$	TECH$	UTME	UTMN
42TO1679.1	2.28	STUBBY	PP	■	■
42TO1679.3	2.59	IND STEM	PP	■	■

- The Mean Center was calculated for the 42TO1681 artifact cluster (not including the two artifacts in contention). The mean values (■, ■) were used to update the coordinates for 42TO1681.1 and 3 and UsesCentroid was set to "Y".

42TO1683 [Black, 14 artifacts]

- This site does not appear in the monograph's Table 4.2 (listing Black channel sites) but the site's artifacts are found in the "*ORB Final General File.xls*" spreadsheet. The site is situated between two branches of the Black channel; however, the Light Green and Brown channels also run closely by (Figure A-3). Here, I have associated it with the Black channel.
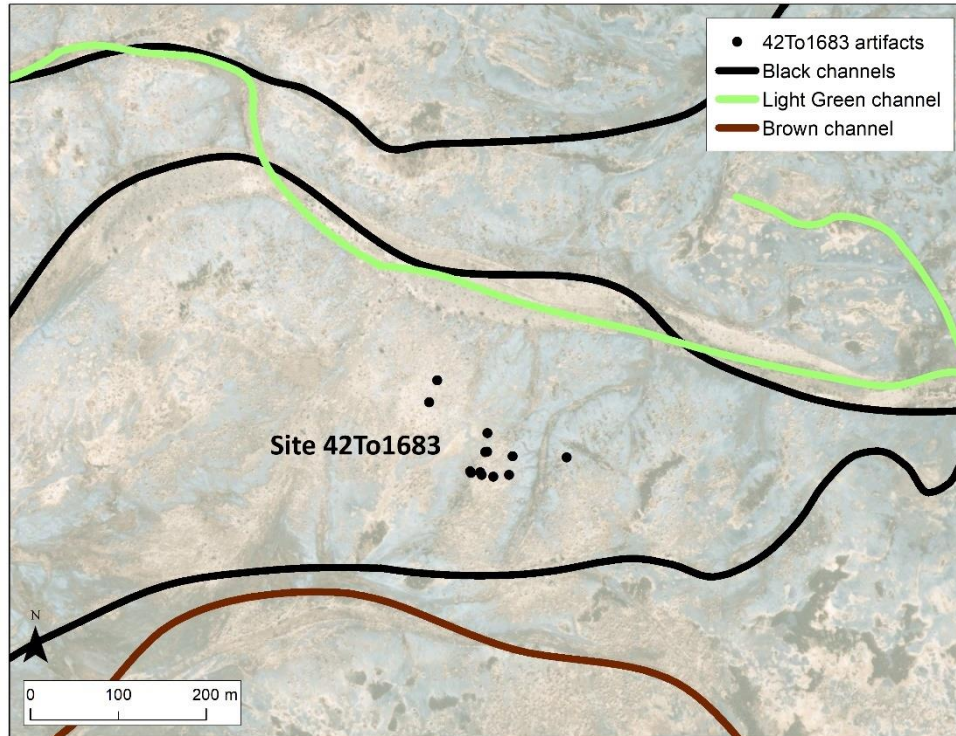
Figure A-3: Site 42TO1683 amidst Black, Light Green, and Brown channels

- 42TO1683 also has two flake samples (Table A-12) that have placeholder coordinates (99, 99). These two artifacts were set to the Mean Center UTM coordinates (■, ■) for the site cluster and UsesCentroid was set to "Y".

Table A-12: 42TO1683 artifacts missing coordinates

SampleID	TYPE$	TECH$	UTME	UTMN
42TO1683.13	INT FLAKE	FLAKE	99	99
42TO1683.14	INT FLAKE	FLAKE	99	99

42TO1684 [Black D, 19 artifacts]

- Sample 42TO1684.5 has a transposed UTME (■ should be ■) when compared to the cluster of 42TO1684 artifacts. The UTME coordinate was fixed.

42TO1686 [Black, 75 artifacts]

- See the notes in 42TO1668.

- Two artifacts have UTM issues:

    o 42TO1686.1 is missing UTMN. Reviewing samples 2, 3, and 4 for this site, they

    occur progressively and within 110 m of each other. This artifact fits well within the

    site cluster with a UTMN of ■.

    o 42TO1686.61 is missing a digit in UMTN and was changed from ■ to ■).

42TO1688 [Black, 63 artifacts]

- Artifact 42TO1668.26 has an incorrect UTMN and appears to have both a transposed

    decimal and two digits transposed. The UTMN was changed from ■ to ■. This change fits

    well with the other artifacts surrounding this sample number.

- Artifact 42TO1688.55 has an incorrect UTMN with a transposed decimal point and was

    changed from ■ to ■. This change provides a good fit with the surrounding artifacts (54 and

    56).

42TO1858 [Black, 2 artifacts]

- This site consists of only two samples with the exact same coordinates. No changes were

    made.

42TO1859 [Black, 6 artifacts]

- Artifact 42TO1859.6 has an incorrect UTMN; it is missing a digit in either the tens or

    hundreds position. It was corrected from ■to ■, which places it within the site cluster.

- Artifact 42TO1859.3 occurs twice (see Table A-6, above). After viewing the spatial distribution in ArcMap, the copy with UTMN of ■ was determined as the duplicate. This record was deleted, as noted above.

42TO1860 [Black, 17 artifacts]

- Seven artifacts from this site do not have coordinates (Table A-13). Six are flakes, but one is a graver (13). These seven artifacts were set to the Mean Center UTM coordinates (■, ■) and UsesCentroid was set to "Y".

Table A-13: 42TO1860 artifacts missing coordinates.

SampleID	TYPE$	TECH$	UTME	UTMN
42TO1860.8	INT FLAKE	FLAKE	99	99
42TO1860.9	INT FLAKE	FLAKE	99	99
42TO1860.10	INT FLAKE	FLAKE	99	99
42TO1860.11	INT FLAKE	FLAKE	99	99
42TO1860.12	INT FLAKE	FLAKE	99	99
42TO1860.13	GRAVER	UNIFACE	99	99
42TO1860.14	INT FLAKE	FLAKE	99	99

42TO1862 [Black, 20 artifacts]

- Artifact 42TO1862.6 has an incorrect UTMN; it is missing a digit. Changing the value from ■ to ■ appears to place it correctly in the site cluster.

42TO1872 [Black, 53 artifacts]

- Artifact 42TO1872.50 has an incorrect UTMN; it is missing a digit. The value was changed from ■ to ■, in accord with other artifacts in the site cluster.

- Artifacts 65 – 71 share identical UTM coordinates (rounded, unlike other UTM coordinates which have values to two decimal places). In addition, they are offset from the main 42TO1872 cluster and lie within the 42TO1874 cluster. This makes their placement

confusing but lacking sufficient information to correct any problems that might exist, they
remain unchanged.

- Spatially, site 42TO1872 blends into sites 42TO1874 and 42TO1875 – and should potentially
  be considered all one "site" (Figure A-4).
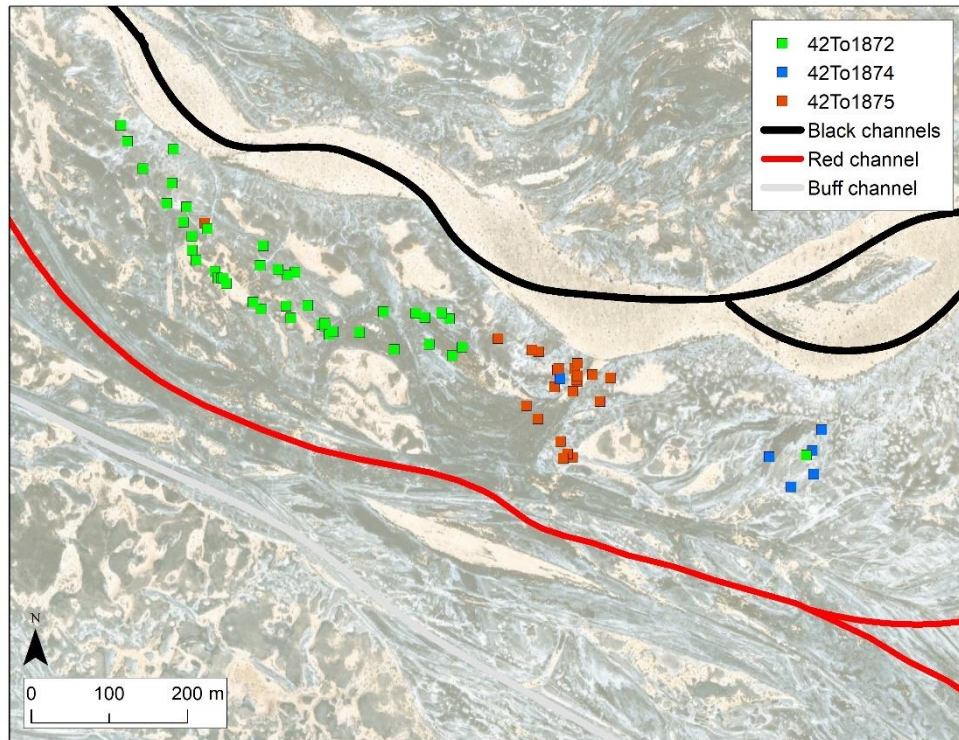
Figure A-4: Sites 42TO1872, 1874, and 1875 between Black and Red channels

42TO1873 [Black / Brown?, 31 artifacts]

- Artifact 42TO1873.2 has an incorrect UTME; two digits were mistyped. The UTME was
  changed from ■ to ■, in accord with other artifacts in the site cluster.

- This site cluster is within the Black 250 m buffer (described below); however, it does cross
  the Brown channel (Figure A-5). The scatter seems to follow a minor channel parallel to the
  Black channel, but this interpretation may be in doubt. Without further data, I have left this
  site assigned to Black per the monograph's authors.
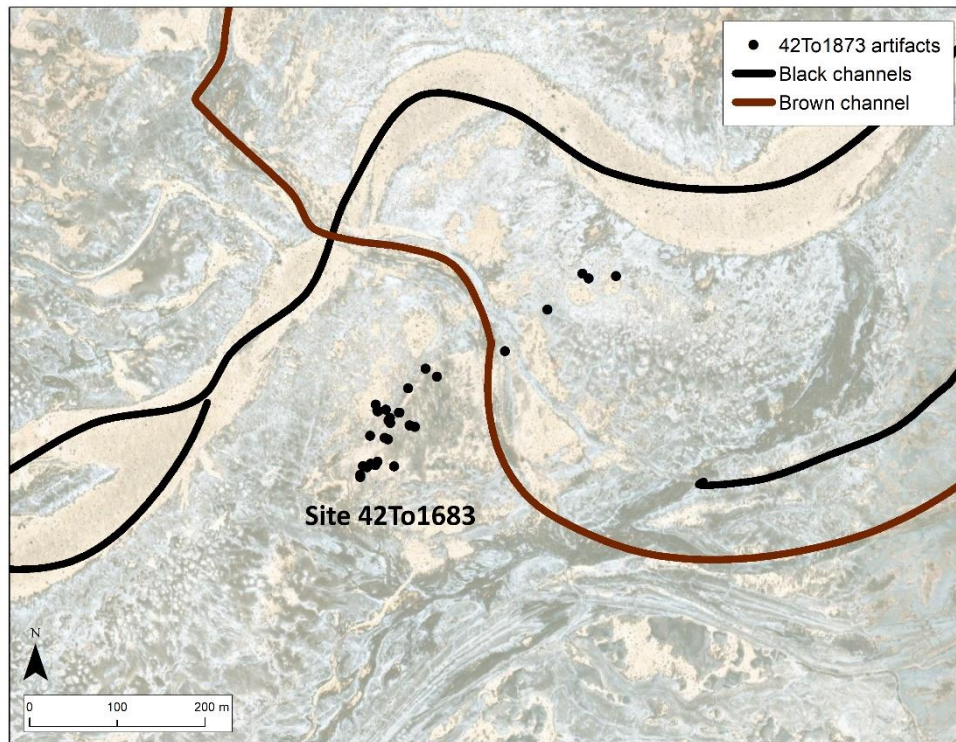
Figure A-5: Site 42TO1873 artifacts in context with the Black and Brown channels

42TO1874 [Black, 6 artifacts]

- Artifact 42TO1874.6 appears to be out of place. It is about 280 m from the rest of the site cluster and fully within the 42TO1875 cluster. There is not enough information to warrant moving it.

42TO1875 [Black, 26 artifacts]

- Artifact 42TO1875.19 has an incorrect UTMN; it is missing a digit. Changing it from ■ to ■ places it correctly in the site cluster.

- Artifacts 42TO1875.24, 25, and 26 appear to be out of place, about 400 m from the nearest edge of the 42TO1875 cluster and fully within the 42TO1872 cluster (Figure A-4, above). Each of these artifacts shares identical UTM coordinates (rounded, no decimal, unlike most

of the other UTM coordinates). There is not enough data to warrant moving them within the cluster.

42TO1877 [moved to Brown, 5 artifacts]

- In the monograph, this site is associated with the Black channel, but this is problematic. Figure A-6 shows a direct association with the undated Brown channel. None of these samples were XRF tested. The association of this site was updated to the Brown channel (moving 5 artifacts from the Black channel to the Brown channel).
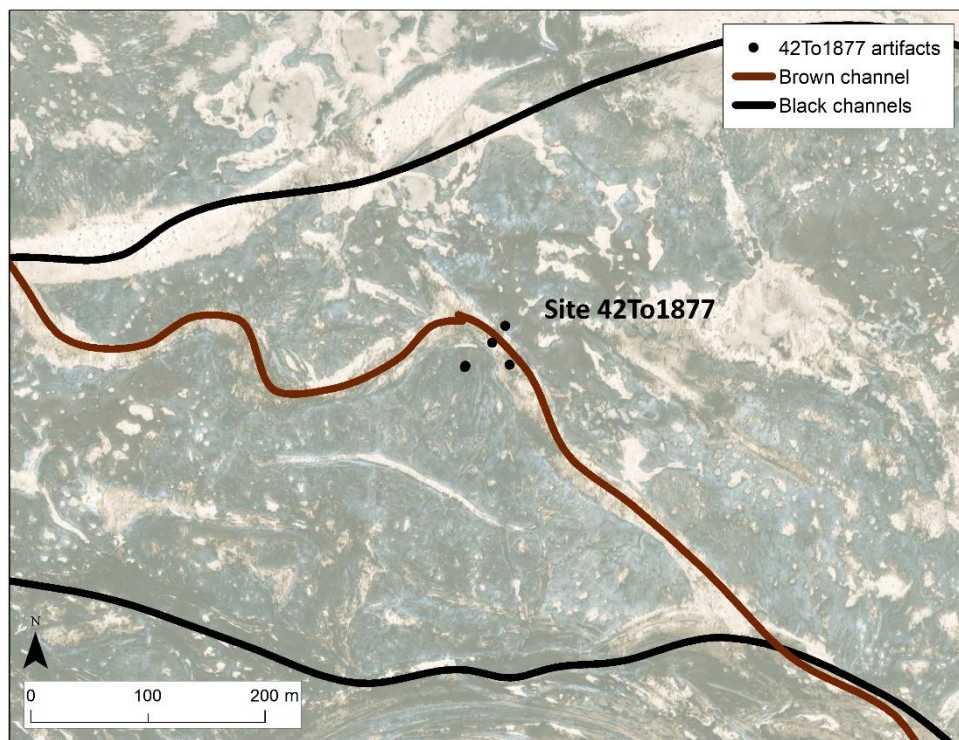
Figure A-6: Site 42TO1877 in context with the Brown channel.

42TO1878 [Black, 14 artifacts]

- Artifact 42TO1878.13 has an incorrect UTME; two digits were mistyped. Changing the UTME from ■ to ■ places the artifact correctly in the site cluster.

42TO1891 [Black, 3 artifacts]

- This site does not appear in the monograph's Table 4.2 (listing Black channel sites) but is found in the "*ORB Final General File.xls*" spreadsheet. It is clearly situated on the Black channel.
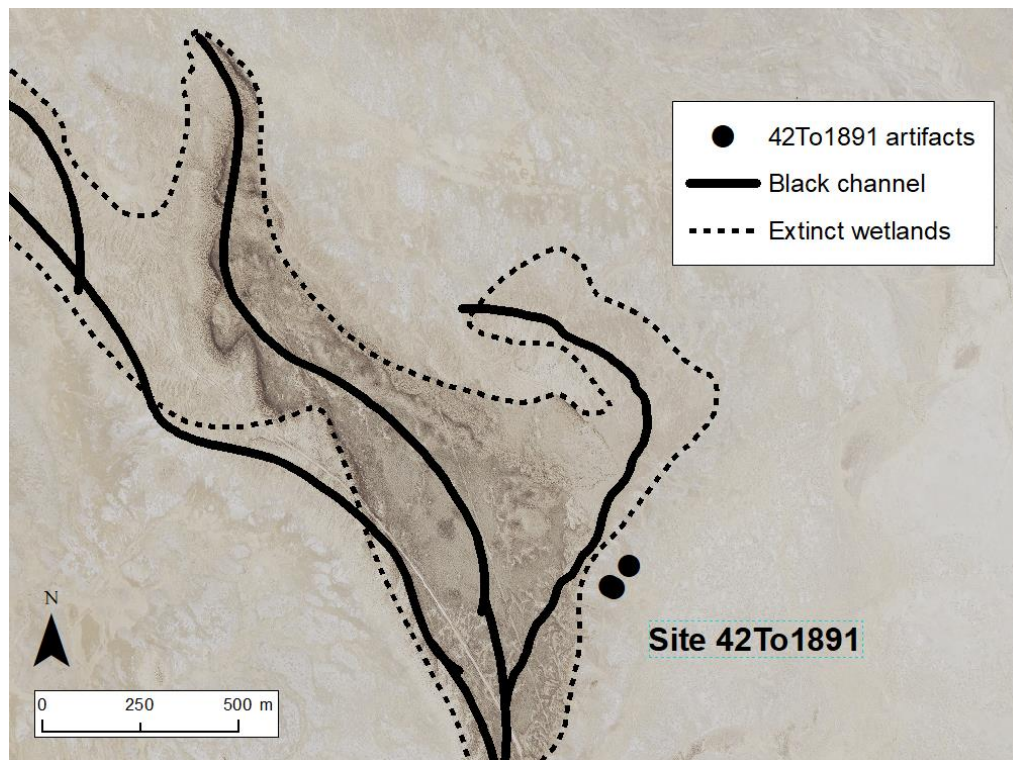
Figure A-7: Site 42TO1891 in context with the Black channel.

42TO1921 [Black, 9 artifacts]

- This site was moved from the Limestone channel to the Black channel during the Limestone channel review (see details in section A.5.5, below).

A.5.3 Yellow Channel (12 sites, 131 artifacts)

The following Yellow channel sites were geolocated and visually reviewed using ArcMap, and all artifact data appear correct and have the appropriate channel association (Table A-14):

Table A-14: Yellow channel sites without changes.

Site	Channel	# of Artifacts
42TO2951	Yellow	8
42TO2953	Yellow	4
42TO2954	Yellow	2
42TO3219	Yellow	42
42TO3220	Yellow	4
42TO3223	Yellow	11
42TO3224	Yellow	17
42TO3225	Yellow	9
42TO3521	Yellow	2
Total		**99**

The following Yellow channel sites required corrections or warranted further comment:

42TO2950 [Yellow, 0 artifacts]

- This site is listed in the monograph's Table 4.4, but no artifacts are assigned to this site in the "*ORB Final General File.xls*" spreadsheet. This site is not included in site totals.

42TO2952 [Yellow, 5 artifacts -- 3 moved to Pink, leaving 2 at Yellow]

- This site is situated at a position on the Yellow channel that is crosscut by the undated Pink channel (Figure A-8). Three of the artifacts (42TO2952.2, 13, and 14) appear to lie on the cut itself, suggesting a better association with the Pink channel. The channel assignments (ChannelID=17) for these three artifacts were updated directly in the database.
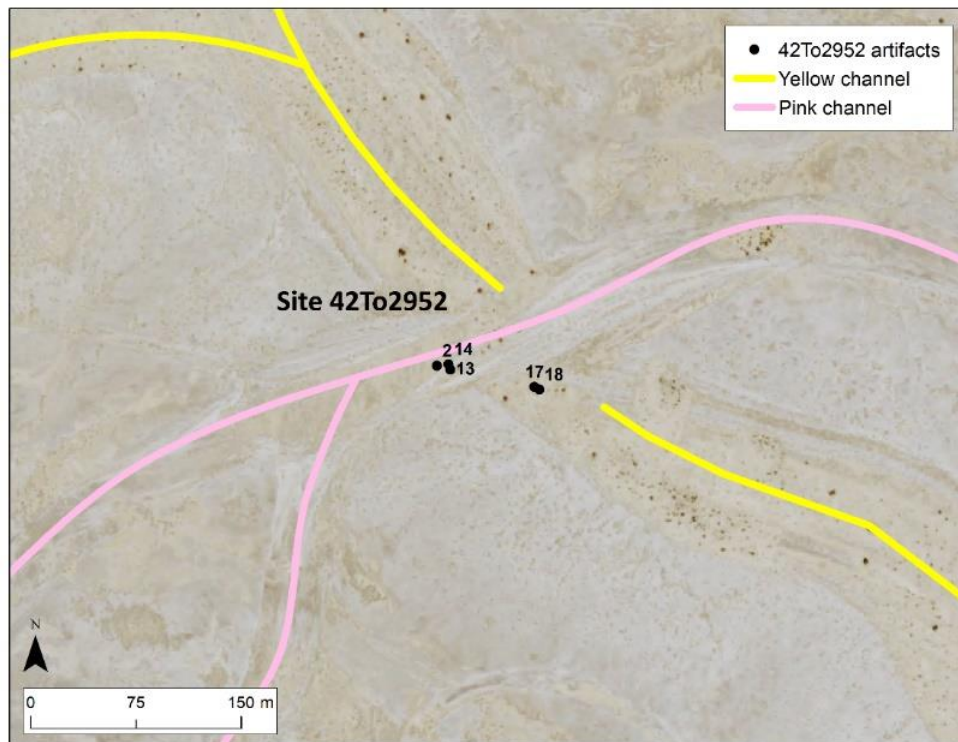
Figure A-8: Site 42TO2952 in context with the Yellow and Pink channels.

42TO3221 [Yellow, 5 artifacts]

- This site is listed in the monograph's Table 4.4 and assigned to the Yellow channel, but the younger Lime channel is intertwined with these artifacts Figure A-9. However, there is not enough evidence to change the monograph's association with the Yellow channel.
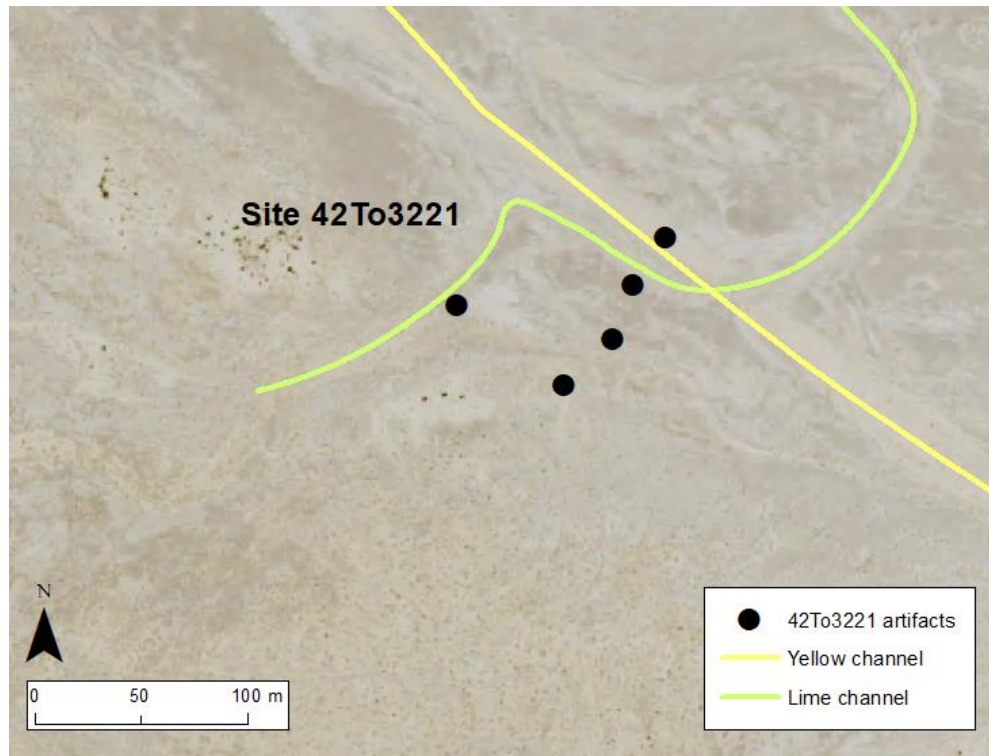
Figure A-9: Site 42TO3221 in context with the Yellow and Lime channels.

42TO3222 [Yellow, 22 artifacts – moved to Lime]

- The Lime channel (ChannelID=11) appears to be a better association for this site than the

    Yellow channel (Figure A-10). This site was moved to the Lime channel as a result.
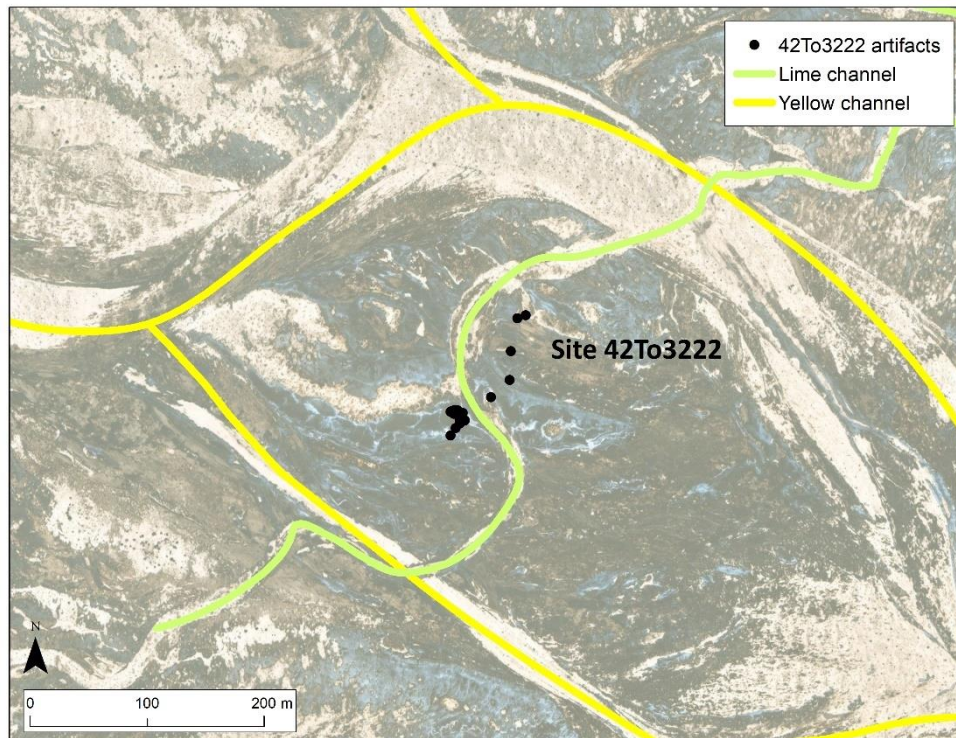
Figure A-10: Site 42TO3222 in context with the Lime channel.

42TO3226 [Yellow, 25 artifacts]

- Artifact 44To3226.27 has an incorrect site ID (44To vs 42TO), which was corrected. This

    artifact also has placeholder coordinates (99, 99). The coordinates were set to the Mean

    Center UTM coordinates (■, ■) and UsesCentroid was set to "Y".

A.5.4 Green Channel (7 sites, 110 artifacts)

The following Green channel sites were geolocated and visually reviewed using ArcMap,

and all artifact data appear correct and have the appropriate channel association (Table A-15):

Table A-15: Green channel sites without changes.

Site	Channel	# of Artifacts
42TO2551	Green	24
42TO2552	Green	6
42TO2553	Green	5
42TO2556	Green	26
Total		**61**

The following Green channel sites required corrections or warranted further comment:

42TO2557 [Green, 2 artifacts]

- The assignment of this site to the Green channel seems problematic (Figure A-11). The two artifacts are slightly closer to the much older Gold channel (99 m vs. 133 m), but there is not enough data to overturn the monograph's association with the Green channel.
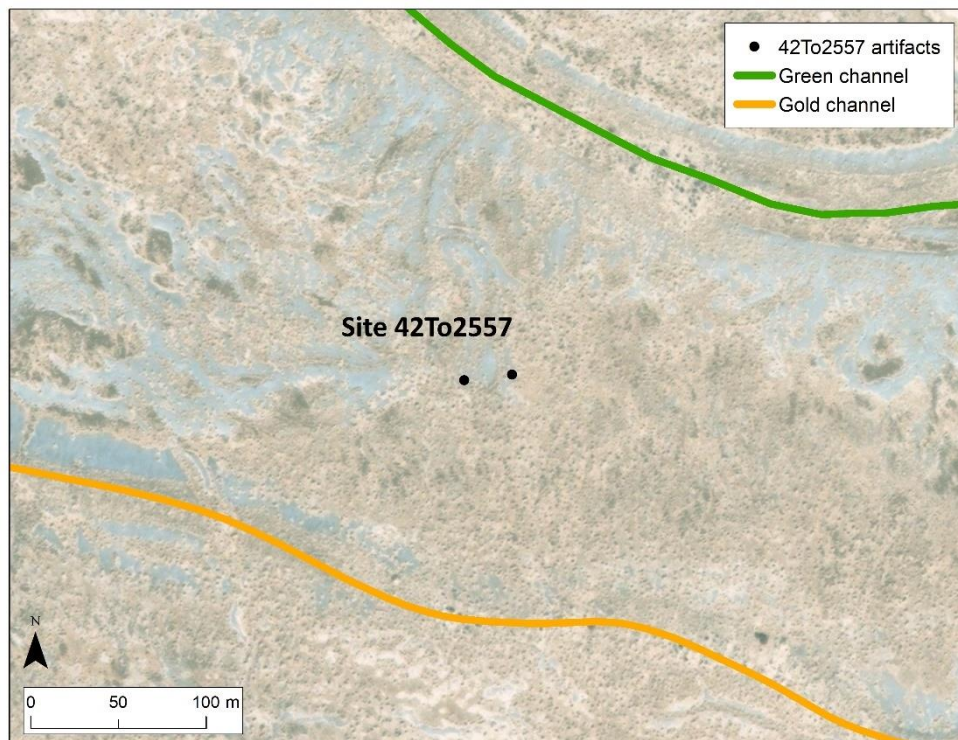
Figure A-11: Site 42TO2557 in context between the Green and Gold channels.

42TO2558 [Green, 7 artifacts]

- Like 42TO2557, this site is situated between the Green and Gold channels and is very close

  to both (87 m vs. 107 m, respectively). I have followed the monograph assignment and left it

  associated with the Green channel.

- Artifact 42TO2558.1 has placeholder coordinates (99, 99). The coordinates were set to the

  Mean Center UTM coordinates (■, ■) and UsesCentroid was set to "Y".

42TO2559 [Green, 40 artifacts]

- Artifact 42TO2559.63 has placeholder coordinates (99, 99). The coordinates were set to the

  Mean Center UTM coordinates (■, ■) and UsesCentroid was set to "Y".

A.5.5 Limestone Channel (1 site, 6 artifacts)

The following Limestone channel site was geolocated and visually reviewed using

ArcMap, and all artifact data appear correct and have the appropriate channel association (Table

A-16):

Table A-16: Limestone channel sites without changes.

Site	Channel	# of Artifacts
42TO1922	Limestone	6
Total		**6**

The following Limestone channel sites required corrections or warranted further comment:

42TO1921 [Limestone, 9 artifacts – moved to the Black channel]

- The assignment of this site to the Limestone channel seems problematic (Figure A-12). It is situated directly on a Black channel region and more than 130 m from the Limestone channel. This site was assigned to the Black channel (ChannelID = 4).
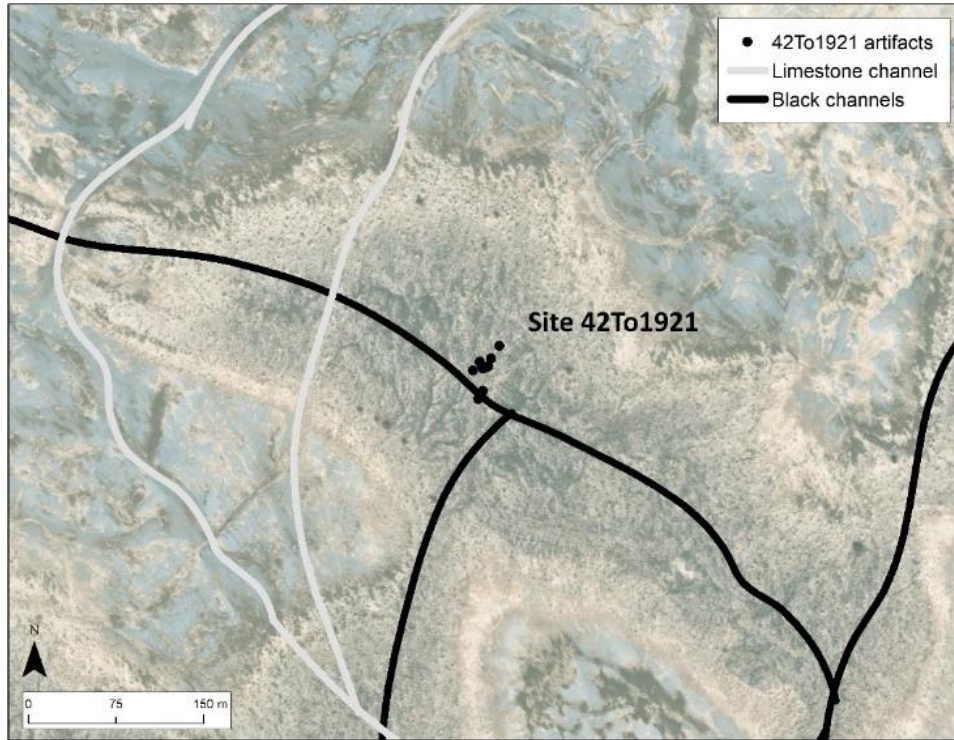
Figure A-12: Site 42TO1921 in context with the Black and White channels.

A.5.6 Red Channel (3 sites, 6 artifacts)

The following Red channel sites were geolocated and visually reviewed using ArcMap, and all artifact data appear correct and have the appropriate channel association (Table A-17):

Table A-17: Red channel sites without changes.

Site	Channel	# of Artifacts
04DM01	Red	1
04DM02	Red	2
04DM03	Red	3
Total		**6**

A.5.7 Blue A Channel (2 sites, 2 artifacts)

The following Blue A channel sites were geolocated and visually reviewed using ArcMap, and all artifact data appear correct and have the appropriate channel association (Table A-18):

Table A-18: Blue A channel sites without changes.

Site	Channel	# of Artifacts
42TO3227	Blue A	1
42TO3232	Blue A	1
Total		**2**

A.5.8 Light Blue (23 sites, 359 artifacts)

The following Light Blue channel sites were geolocated and visually reviewed using ArcMap, and all artifact data appear correct and have the appropriate channel association (Table A-19):

Table A-19: Light Blue channel sites without changes.

Site	Channel	# of Artifacts
42TO1161	Light Blue	10
42TO1168	Light Blue	1
42TO1352	Light Blue	10
42TO1357	Light Blue	5
42TO1383	Light Blue	21
42TO1671	Light Blue	10
42TO1674	Light Blue	3
42TO1675	Light Blue	3
42TO1677	Light Blue	14
42TO1678	Light Blue	12
42TO1679	Light Blue	10
42TO2767	Light Blue	26
Total		**125**

The following Light Blue sites required corrections or warranted further comment:

42TO1000 [Light Blue, 37 artifacts]

- Artifact 42TO1000.20 has an incorrect UTMN; it is missing a digit. The UTMN was changed from ■ to ■, in accord with other site artifacts.

- Artifacts 42TO1000.26 and 38 have placeholder coordinates (99, 99). The coordinates were set to the Mean Center UTM coordinates (■, ■) and UsesCentroid was set to "Y".

42TO1153 [Light Blue, 27 artifacts]

- Artifacts 42TO1153.14 and 38 have placeholder coordinates (99, 99). The coordinates were set to the Mean Center UTM coordinates (■, ■) and UsesCentroid was set to "Y".

42TO1157 [Light Blue, 8 artifacts]

- Artifact 42TO1157.2 has an incorrect UTMN; it is missing a digit. The UTMN was changed from ■ to ■, to place it approximately in line with the artifacts catalogued before and after it.

42TO1163 [Light Blue, 14 artifacts]

- Artifact 42TO1163.13 is missing UTMN. The artifacts numbered before and after it do not appear to occur in sequential order, so a sequential UTMN cannot be inferred. The UTMN coordinate was set to the Mean Center UTMN coordinate (■) for the cluster and UsesCentroid was set to "Y".

42TO1165 [Light Blue, 3 artifacts, all deleted]

- This is site is problematic as it consists of only three artifacts, and none have UTM coordinates. As a result, there is no way of inferring where this site appropriately resides. These artifacts were deleted from the Artifact table.

42TO1166 [Light Blue, 4 artifacts]

- This site consists of four artifacts, of which only two possess UTM coordinates. The other two have been set to the midpoint between the two known artifacts (■, ■).

42TO1169 [Light Blue, 5 artifacts, all deleted]

- This is site is problematic as it consists of five artifacts, none of which have UTM coordinates. As a result, there is no way of inferring where this site appropriately resides. These artifacts were deleted from the Artifact table.

42TO1171 [Light Blue, 3 artifacts]

- Artifact 42TO1171.2 is missing UTM coordinates. It has been set to the midpoint between the two known artifacts (■, ■).

42TO1172 [Light Blue, 20 artifacts]

- Artifact 42TO1172.9 has an incorrect UTMN; it is missing a digit. The UTMN was changed from ■ to ■, in accord with other site artifacts.

42TO1173 [Light Blue, 22 artifacts, all deleted]

- This is site is problematic as it consists of 22 artifacts, none of which have UTM coordinates. As a result, there is no way of inferring where this site appropriately resides. These artifacts were deleted from the Artifact table.

- This site also does not appear in Table 4.8 of the monograph (sites associated with the Light Blue channel).

42TO1182 [Light Blue, 29 artifacts]

- This is site is problematic as it consists of 29 artifacts only 8 of which have UTM coordinates. The artifacts missing coordinates include diagnostic projectile points (both WST and Archaic). The missing UTM coordinates were set to the Mean Center UTMN coordinate (■, ■) for the cluster of eight and UsesCentroid was set to "Y".

42TO1358 [Light Blue, 87 artifacts]

- Artifact 42TO1358.43 has placeholder coordinates (99, 99). The coordinates were set to the Mean Center UTM coordinates (■, ■) and UsesCentroid was set to "Y".

42TO1676 [Light Blue, 4 artifacts]

- All artifact data appear correct, but this site does not appear in Table 4.8 of the monograph. It is clearly associated with the Light Blue channel and has been treated as such here.

42TO2766 [Light Blue, 1 artifact]

- The single artifact at this site was moved to the Light Blue channel (see notes in section A.5.12, below).

A.5.9 Lime Channel (4 sites, 155 artifacts)

The following Lime channel sites were geolocated and visually reviewed using ArcMap, and all artifact data appear correct and have the appropriate channel association (Table A-20):

Table A-20: Lime channel sites without changes.

Site	Channel	# of Artifacts
42TO3522	Lime	12
Total		**12**

42TO3222 [Lime, 22 artifacts]

- This site was moved from the Yellow channel to the Lime channel (see notes in section A.5.3, above).

42TO3520 [Lime, 120 artifacts]

- Artifact 42TO3520.121 has placeholder coordinates (99, 99). The coordinates were set to the Mean Center UTM coordinates for the cluster (■,■) and UsesCentroid was set to "Y".

08DM30 [Lime, 1 artifact]

- The single artifact at this site was associated with the Lime channel (see notes in section A.5.12, below).

A.5.10 Lavender Channel (11 sites, 114 artifacts)

The following Lavender channel sites were geolocated and visually reviewed using ArcMap, and all artifact data appear correct and have the appropriate channel association (Table A-21):

Table A-21: Lavender channel sites without changes.

Site	Channel	# of Artifacts
42TO2943	Lavender	2
42TO2944	Lavender	1
42TO2945	Lavender	14
42TO2946	Lavender	4
42TO2947	Lavender	9
42TO2948	Lavender	6
42TO2949	Lavender	10
42TO3236	Lavender	1
42TO3237	Lavender	42
42TO3238	Lavender	12
42TO3239	Lavender	13
Total		**114**

42TO2955 [Lavender, 4 artifacts – moved Coral channel]

- This site does not appear in Table 4.7 of the monograph, but is in the "*site_channel_list.xls*"
  spreadsheet, associated with the Lavender channel (Figure A-13). It is closer to the Coral
  channel (312 m vs. 482 m) and I have changed the association to the Coral channel
  (ChannelID = 15).
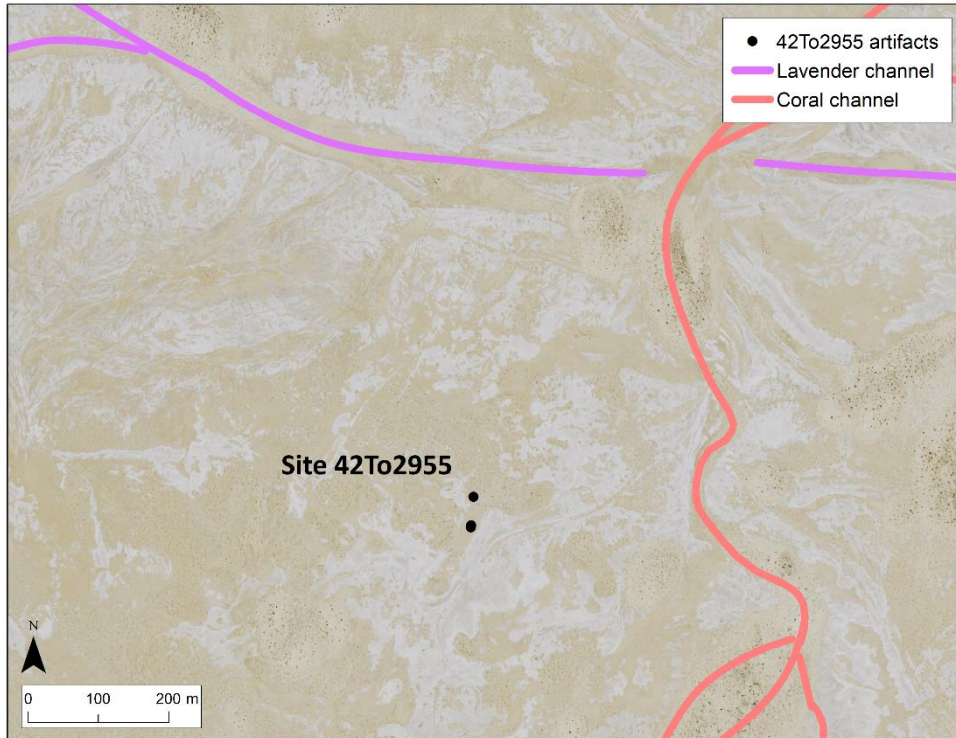
Figure A-13: Site 42TO2955 in context to the Coral and Lavender channels.

A.5.11 Blue B Channel (8 sites, 165 artifacts)

The following Blue B channel sites were geolocated and visually reviewed using ArcMap, and all artifact data appear correct and have the appropriate channel association (Table A-22):

Table A-22: Blue B channel sites without changes.

Site	Channel	# of Artifacts
42TO2555	Blue B	13
42TO3228	Blue B	13
42TO3229	Blue B	12
42TO3231	Blue B	5
42TO3233	Blue B	22
42TO3234	Blue B	28
42TO3235	Blue B	50
Total		**143**

42TO2554 [Blue B, 22 artifacts]

- Artifact 42TO2554.23 has placeholder coordinates (99, 99). The coordinates were set to the Mean Center UTM coordinates for the cluster (■, ■) and UsesCentroid was set to "Y".

A.5.12 Artifacts / Sites without Dated Channel Assignments

There are 138 site-artifacts that are not associated with a dated channel in the original dataset. Some of these sites are not associated with any channel at all. Artifacts that could not be associated with a site or channel were removed from the Artifact table.

07DM01.1

This is single artifact (biface), essentially an isolate, that is located more than 400 m from any channel (surrounded by Red, Lavender, and Yellow channels). It cannot be directly assigned to any channel and was removed from the Artifact table.

08DM30.1

This Cougar Mountain point, an isolate, is located less than 100 m from the Lime channel and was assigned to this channel (see notes in section A.5.9, above).

42TO0385.3

This Lake Mohave point, an isolate, is located on the far east edge of the ORB delta and is not in association with any dated channels. It was removed from the Artifact table.

42TO0394.2

This square stem, an isolate, is located far south of the ORB delta and is not in association with any dated channels. It was removed.

42TO0962.2

This square stem, an isolate, is located far east of the ORB delta and is not in association with any dated channels. It was removed.

42TO1152 [4 artifacts]

None of the artifacts associated with site 42TO1152 have coordinates. They were removed.

42TO1177 [2 artifacts]

These artifacts are in the "unexposed section" of the ORB (monograph, p. 38) and are not in association with any dated channels. They were removed.

42TO1178 [4 artifacts]

These artifacts are in the "unexposed section" of the ORB (monograph, p. 38) and are not in association with any dated channels. They were removed.

42TO1195 [3 artifacts]

These artifacts are in the "unexposed section" of the ORB (monograph, p. 38) and are not in association with any dated channels. They were removed.

42TO1359 [8 artifacts]

These artifacts are in the dunes area of the ORB (monograph, p. 38) and are not in association with any dated channels. One of the site-artifacts (42TO1359.2) has no UTM coordinates. They were all removed.

42TO1367 [2 artifacts]

These artifacts are in the dunes area of the ORB (monograph, p. 38) and are not in association with any dated channels. They were removed.

42TO1372.1

This single artifact has no UTM coordinates. It was removed.

42TO1689 [Brown, 8 artifacts]

This site is associated with the undated Brown channel.

42TO1871.1

This single artifact has no UTM coordinates. It was removed.

42TO1877 [Brown, 5 artifacts]

This site was previously moved from the Black channel to the undated Brown channel (see notes in section A.5.2, above).

42TO1977.1

This artifact, an isolate, is directly associated with the undated Brown channel. It was assigned accordingly.

42TO2766.4

This artifact, an isolate, is directly associated with the Light Blue channel (see section A.5.8). It was assigned accordingly.

42TO2952 [Pink, 3 artifacts]

Three of the five artifacts from this site were associated with the undated Pink channel (see notes in section A.5.3, above).

42TO2955 [Coral, 4 artifacts]

This site was previously moved from the Lavender channel to the undated Coral channel (see notes in section A.5.10, above).

42TO2957 [4 artifacts]

These four artifacts are in good association with the undated Seafoam channel. They were assigned accordingly.

42TO3140 [13 artifacts]

This site is associated with the Buff channel, though an argument could be made for association with the Royal channel. Regardless, neither channel has been dated.

42TO3230 [66 artifacts]

This site is on the far west side of the ORB delta, more than 4km from the nearest mapped channel. It has been removed from the dataset.

42TO1353 [2 artifacts]

These artifacts are in the dunes area (monograph, p. 38) of the ORB and are not in association with any dated channels. They were removed.

42TO1354 [13 artifacts]

These artifacts are in the dunes area of the ORB (monograph, p. 38) and are not in association with any dated channels. They were removed.

Summary: Starting with 138 artifacts, 110 were deleted due to lack of association with an ORB channel or for being out of the research region. Two isolates (08DM30.1 and 42TO2766.4) were associated with dated channels. Site 42TO1877 (5 artifacts) was moved from the Black channel to the Brown channel. Three artifacts from site 42TO2952 were associated with the Pink channel. Site 42TO2955 (4 artifacts) was moved to the Coral channel. In the end, 38 site-artifacts remain, associated with an undated ORB delta channel (Brown, Buff, or Seafoam).

A.5.13 Site-Artifact Cleaning Summary

Following cleaning and review, out of 1973 site-artifacts, 1790 were geolocated and well associated with a dated ORB channel (Table A-23).

Table A-23: Channel assignments following review.
Asterisk indicates that the channel is undated.

Channel Association	Artifacts
Gold	45
Black	697
Yellow	131
Limestone	110
Green	6
Blue A	2
Red	6
Blue B	165
Lime	155
Lavender	114
Light Blue	359
Brown *	14
Pink *	3
Coral *	4
Seafoam *	4
Buff *	13
Deleted/out of scope	145
Total	**1973**

A.6 ORB Isolates

The "*ORB Final General File.xls*" spreadsheet contains 315 isolates (artifacts not directly associated with ORB delta "sites") with a site designation (Site$) of either "DPGIF" or "ISO". As these isolates "stand alone", there is no other context or reference point (such as the site cluster) to help correctly situate these points or make associations with ORB channels other than their given coordinates. These isolates were inspected individually and adjudicated in a binary fashion (associated/not associated with a dated channel).

There is inconsistency in the source spreadsheets in how isolate sample numbers (Site$ and FS$) are formatted. These were standardized to the Site$.FS$ (or SampleID) format (e.g., DPGIF.123), strictly for the organizational purposes of this project.

A.6.1 Initial Cleaning of Isolate Data

The Isolates data was cleaned using the same process described in section A.4.1. The SampleID (Site$ + FS$) in bold indicates the isolate that was retained following review of each duplicate pair (Table A-24). The resolutions are described below the table.

Table A-24: Duplicate Isolates from "ORB Final General File.xls" spreadsheet.

SITE$	FS$	UTME	UTMN	PMAT$	WT	ABRASION$	CLASS$	TYPE$	TECH$
DPGIF	**196**	■	■	OBS	5.04	MEDIUM	IND BIFACE	IND BIFACE	BIFACE
DPGIF	196B	■	■	OBS	4.99	HEAVY	CORT FLAKE	CORT FLAKE	FLAKE
DPGIF	735B	■	■	FGV	5.68	HEAVY	BF BEAK A	SCRAPER	BIFACE
DPGIF	**735**	■	■	FGV	5.68	MEDIUM	LAKE MOHAVE	LAKE MOHAVE	PP

Duplicate resolutions:

DPGIF.196: This appears to be a misnumbering; the samples have different coordinates, weights, and classifications. The biface appears in the *"ORB Bifaces Final 2011.xls"* spreadsheet. I changed the field sample number for the cortex flake to 196B. Neither sample was XRF tested.

DPGIF.735: This appears to be a duplicate; the samples have the same UTM as well as the same weights. It is not duplicated in the *"Final ORB Projectile Points.xls"* spreadsheet where it is classified as a Lake Mohave point. I cannot make a duplication determination from the data. I changed the field sample number for the scraper to 735B. Neither sample was XRF tested.

No records were deleted during this cleaning step for Isolates.

A.6.2 Checking Coordinates

By importing the isolates into ArcMap and plotting them visually it is obvious that several have incorrect coordinates. The first step in associating isolates with channels is correcting these coordinates, where possible. As isolates are not members of a "site", or necessarily collected

sequentially (for example, during a linear survey transect), isolates without coordinates are

essentially meaningless. These isolates were removed from the dataset.

The following isolates were problematic (Table A-25):

Table A-25: Isolates with problematic coordinates.

Sample ID	UTME	UTMN	Notes
ISO-2.2	99	99	This sample has invalid UTM coordinates. This is not enough information to place this sample, but it is likely to occur somewhere between ISO-1.1 and ISO-3.3. It does appear this sample was XRF tested (ISOLATE.02 matches the description), but without coordinates, this sample cannot be associated with a channel. This sample was deleted from the dataset.
DPGIF.194	■	blank	This isolate is missing UTMN. This sample was not XRF tested. This sample was deleted from the dataset.
DPGIF.200	■ ■	■	There is a typographical error in UTME. Samples DPGIF.199 and 201 occur about 100 m away if this is corrected to ■. This has been updated in the database. This sample was not XRF tested.
DPGIF.207	■	■ ■	UTMN has a typographical error; it is missing a digit. Based on the values for DPGIF.206 and 208, the correct value is likely ■. The UTMN was updated to add a zero to the end. This approximates the location and associates the isolate with the Light Blue channel. This sample was not XRF tested.
DPGIF.329	■	■	UTMN has a typographical error; it is missing a digit. The coordinates for sample DPGIF.328 are more than 15 km from sample 327, and sample 330 is missing coordinates (below), so it is impossible to infer where this sample belongs (but probably on the Seafoam channel based on the similarity of UTME with sample 328). This sample was not XRF tested (a chert crescent). This sample was deleted from the dataset.
DPGIF.330	99	99	This sample has invalid UTM coordinates. It is an Archaic Rosegate that was XRF tested. This sample was deleted from the dataset.
DPGIF.454	■	■ ■	There appears to be a typographical error in UTMN; it has a transposed decimal. Samples DPGIF.453 and 455 occur about 600 m away if this is corrected to ■. Each of these three samples appears to be in association with the Black channel. The UTMN was revised to ■. This sample was not XRF tested.
DPGIF.503	99	99	This sample has no UTM coordinates. This sample was

Sample ID	UTME	UTMN	Notes
			not XRF tested. This sample was deleted from the dataset.
DPGIF.507	■	■ ■	There appears to be a typographical error in UTMN. Comparing with samples DPGIF.506 and 508, it is clear the UTMN is missing a "5" after the 44_. This was corrected to ■. This sample was not XRF tested.
DPGIF.515	■	■ ■	There appears to be a typographical error in UTMN. Comparing with the UTME values for samples DPGIF.514 and 516 (which are less than 100 m apart), sample 515 appears to fall in between them. Changing the UTMN to ■ places the artifact between the two. The UTMN was updated. This sample was not XRF tested.
DPGIF.728	■	■ ■	There appears to be a typographical error in UTMN. Compared with the UTME values for samples DPGIF.727 and 730 (there is no 729), which are less than 100 m apart, sample 728 appears to fall in between them. Changing the UTMN to ■ places the artifact between the two. The UTMN was updated. This sample was not XRF tested, but the cluster of nearby artifacts appears to fall in association with the Black channel.
DPGIF.796	99	99	Missing UTM coordinates. This sample was not XRF tested. This sample was deleted from the dataset.
DPGIF.1553.1	99	99	Missing UTM coordinates. This sample was not XRF tested. This sample was deleted from the dataset.
DPGIF.1561	99	99	Missing UTM coordinates. This sample was XRF tested but cannot be associated with a channel without coordinates. This sample was deleted from the dataset.
DPGIF.1562	99	99	Missing UTM coordinates. This sample was XRF tested but cannot be associated with a channel without coordinates. This sample was deleted from the dataset.
DPGIF.1651.1	99	99	Missing UTM coordinates. This sample was not XRF tested. This sample was deleted from the dataset.

There were 315 isolates at the beginning of this process. Ten artifacts were deleted, leaving 305 records in the Isolate table.

A.6.3 Rules for Associating Isolates with Channels

The next step in the process was associating the individual isolates with an ORB channel, if possible. For the artifacts in the Artifact table, this process was completed by the original ORB

investigators. Review of these associations was accomplished using aerial imagery, ArcMap, and the georeferenced locations of the established site clusters as references.

To process the isolates, I created a methodology based on the following rules:

1. Any isolate 500 m or more from a channel is excluded from the dataset (these are "out of scope").

2. Any isolate within 250 m of a channel (a 250 m buffer) with no overlap with other channel buffers is assigned to that channel.

3. The remaining isolates (> 250 m, but < 500 m distance) are visually inspected and associated with the closest channel.

A.6.4 Methods

All channel shapefiles (provided by Page, see section A.2, item 5) were projected to WGS_1984_UTM_Zone12N (Figure A-14) using ArcMap. There are 24 channels, but the Blue channel is split into two segments, Blue A and Blue B, with different ages (see Table A-1and Table A-2).
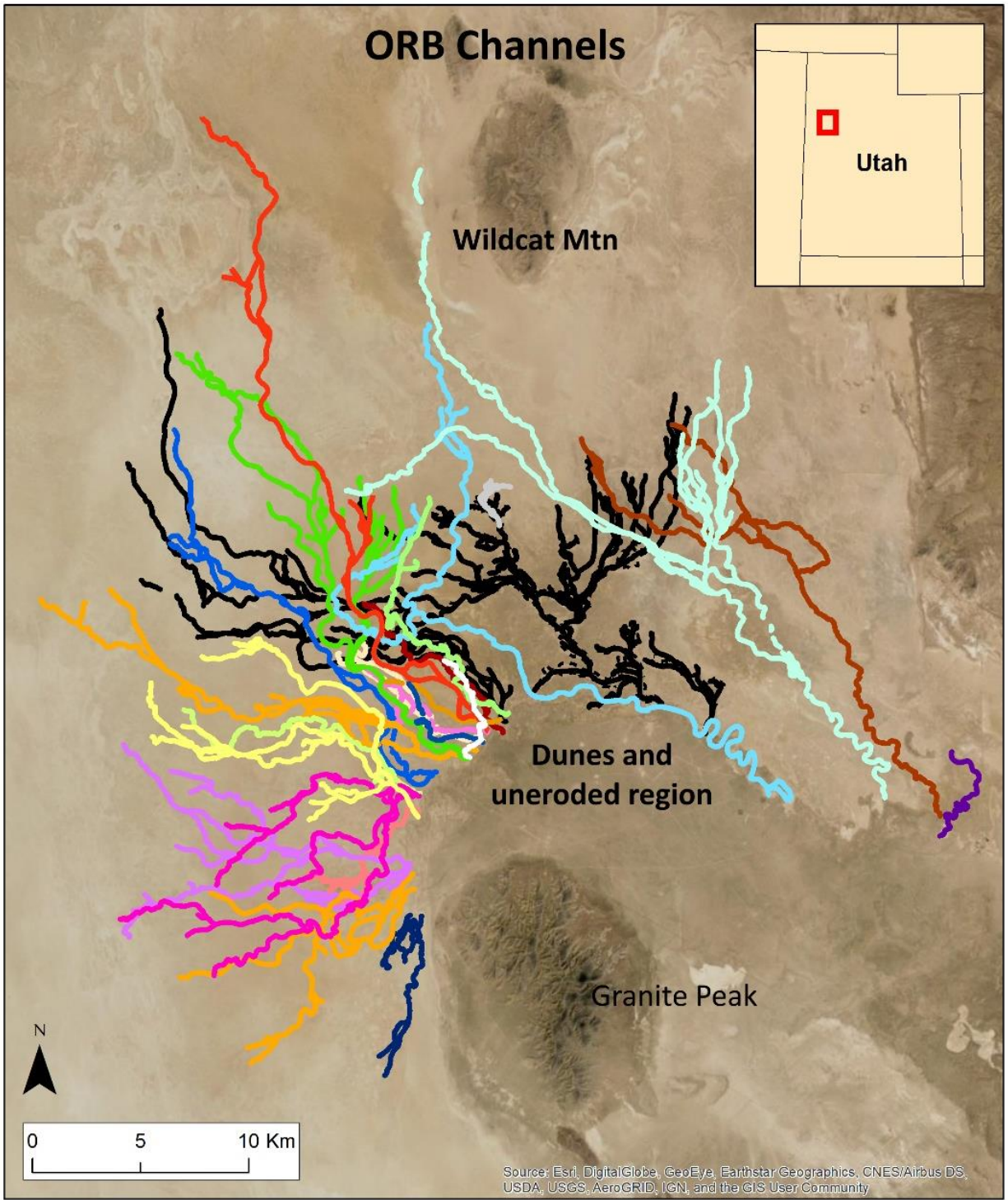
Figure A-14: Identified channels of the Old River Bed delta (see Table A-1 for color legend). Channel data by David Page (personal comm., August 22, 2018).

The 305 cleaned isolates were similarly projected onto this map (Figure A-15). It is clear

the isolates are quite spread out, with several far south or east of the channels.
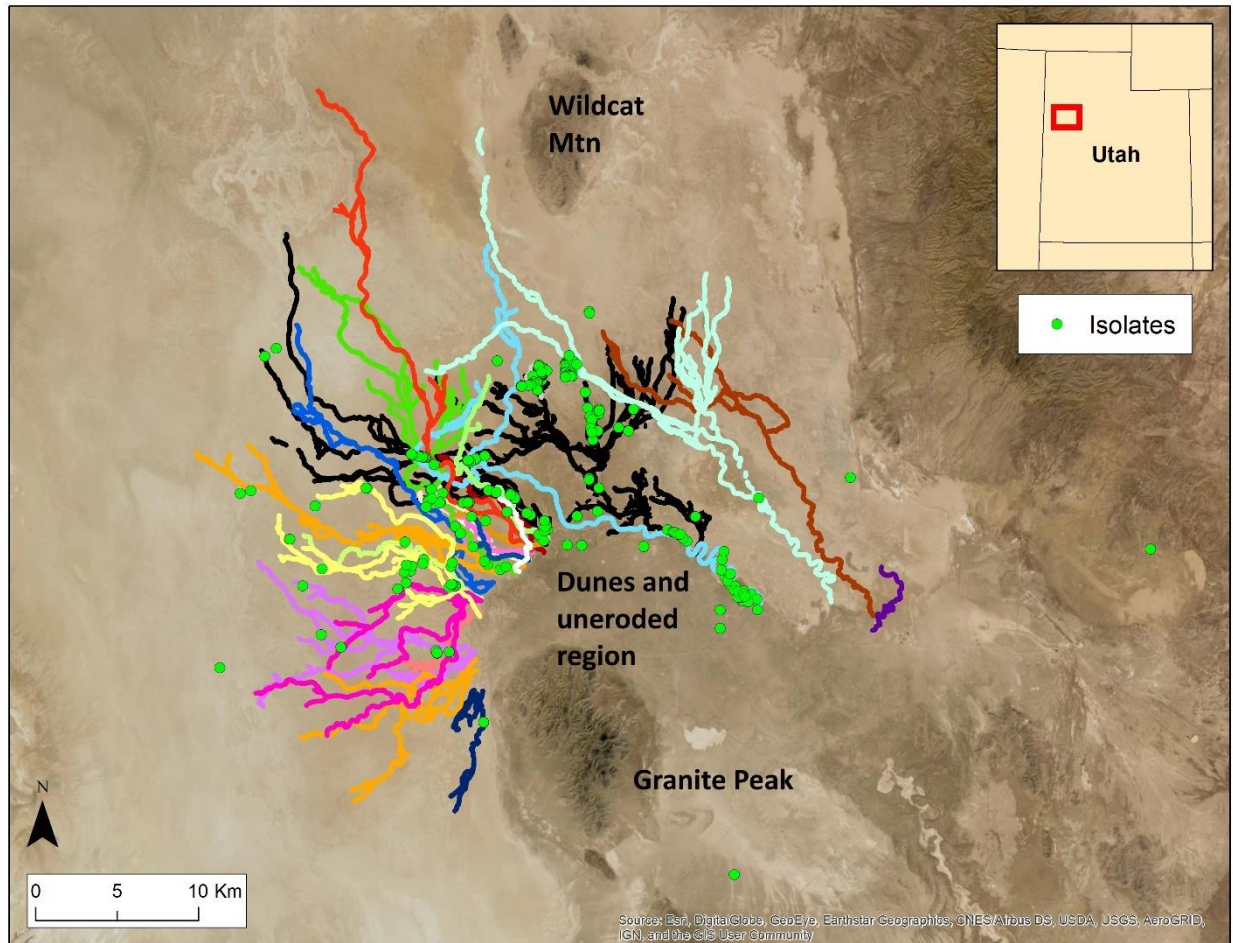
Figure A-15: Isolates in the Old River Bed delta (green dots).
Channel data by David Page (personal comm., August 22, 2018).

Step 1: Elimination of out-of-scope isolates (500 m or more from any channel, *n*=24)

The close association of artifacts with dated/ordered ORB channels is key to my model. Since artifacts more than 500 m from a channel cannot be linked to a channel (see step 2, below), they will be eliminated from this analysis.

a. Using the ArcMap Merge tool, all channels were merged into one shapefile.

b. Using the Buffer tool, a 500 m buffer was created around all the channels.

c. Using the ArcMap Clip and Erase tools, all isolates outside of the 500 m buffer were removed (*n*=24) and the remaining isolates preserved (*n*=281).

Step 2: Assigning isolates to channels using 250 m buffers (*n=176*)

As part of the initial assignment of isolates to channels, I selected a 250-meter buffer (on each side of the channel). Isolates within this buffer are assigned to that channel. While this is a seemingly arbitrary range, it provides good concordance with the scale of the research region and with the assignment of sites to channels in the monograph.

To support this buffer size, I calculated the distances of all site-artifacts to the nearest channel. The results of this are displayed in Figure A-16. The mean distance is 91 m with a maximum distance of 354 m. A buffer of 250 m captures 97% of all site-artifacts, providing a good tool for assigning isolates to channels.
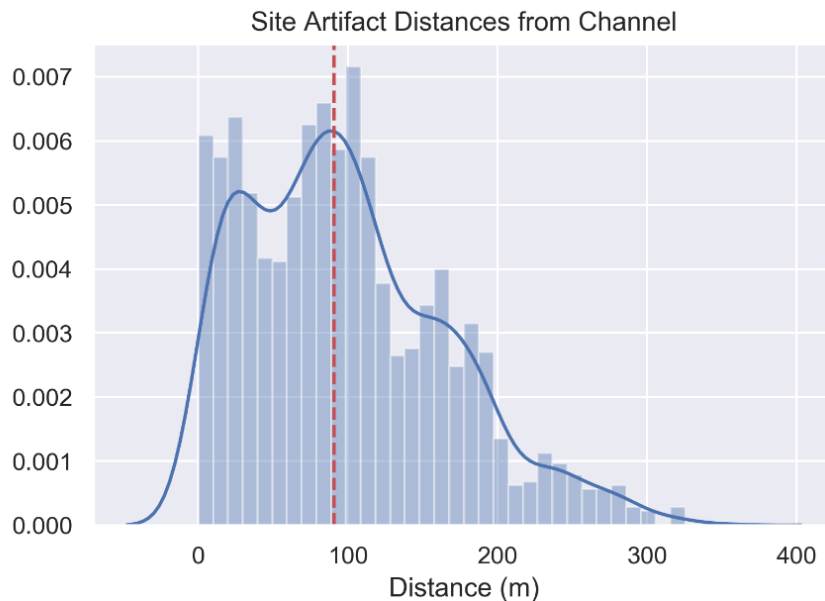
Figure A-16: Distribution of artifact distances from channels (mean = 91 m, red line).

Figure A-17 provides an example of the 250 m buffer on the Black channel. Site-artifacts associated with the Black channel fit neatly within this buffer. Similarly Isolate 379 will be assigned to the Black channel while Isolate 378 needs further analysis (see below).
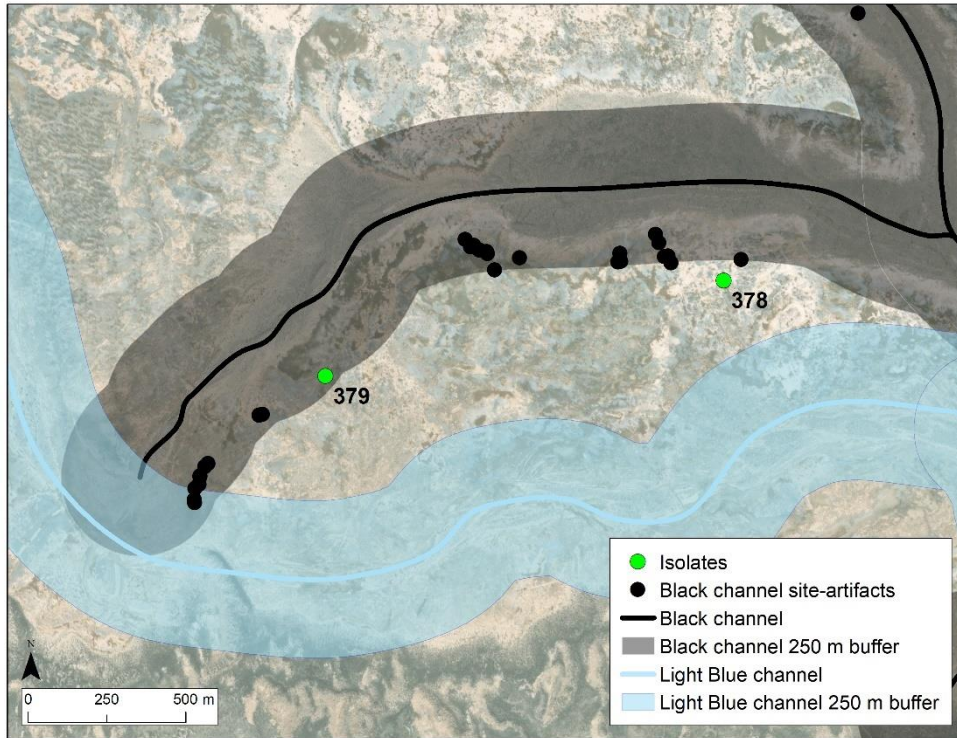
Figure A-17: Example of site-artifacts and isolates relative to the 250 m buffer for the Black channel.

a. Using the ArcMap Buffer tool, 250-meter buffers were created for each channel.

Important note: The black channel (Figure A-18) is the largest surveyed ORB channel. At 253 km mapped, it is more than twice the length of the next largest surveyed ORB channel and includes wide surrounding regions which would have hosted extensive wetlands, now extinct. These extinct wetland areas have been surveyed and are highlighted by the *"black_outline_UTM12.shp"* shapefile, provided by Page (see item 5 in section A.2). For the Black channel, a 250 m buffer was added around the surveyed wetlands area (dotted line in Figure A-18), and isolates captured in this buffer extension were assigned to the Black channel. Many isolates fall within this additional buffer area (Isolate 378, in the example above, is such a case). Only the Black channel has surveyed wetlands data at this time.
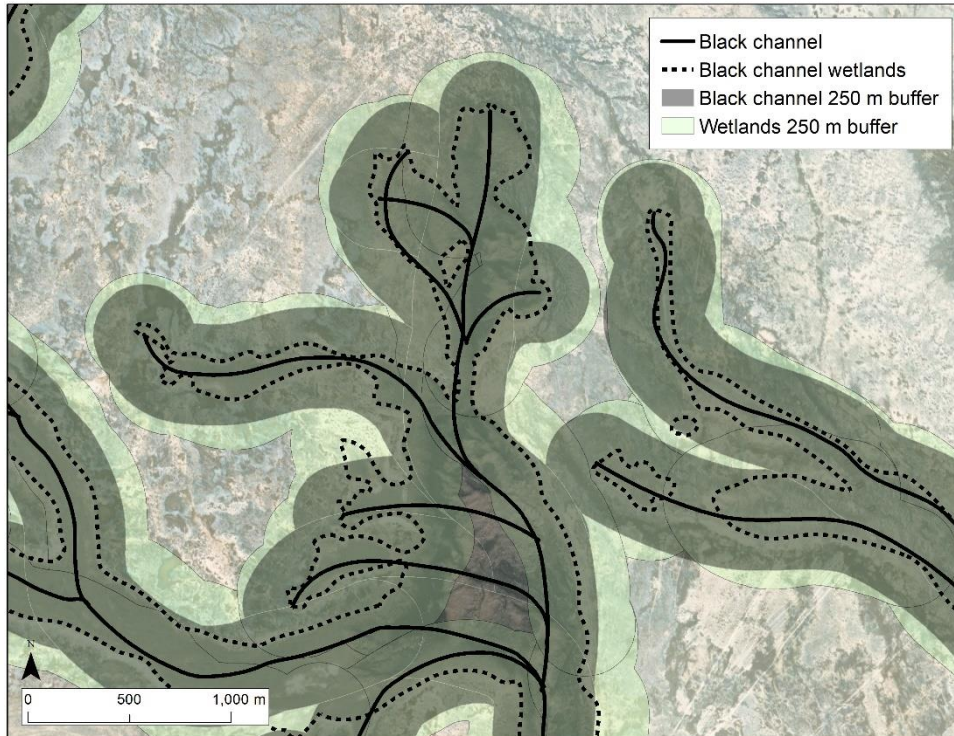
Figure A-18: A portion of the Black channel showing wide, former wetland regions and extended buffer.

b. For each channel, any intersecting or overlapping channel buffers were erased using the ArcMap Erase tool. Isolates within this overlap region required further visual review. For several intertwined channels this required multiple erasures to eliminate all overlapping channels.

Figure A-19 provides a simplified example, showing an intersection of the Black and Light Blue channels and the overlap of their buffers. In this case, Isolates 521-524 and 527-529 will remain associated with the Black channel, while Isolates 525 and 526 are "in contention" and require individual review to determine whether an assignment can be made (see below). Similarly, Isolate 520 falls outside both buffers (but inside the 500 m buffer) and requires individual evaluation.
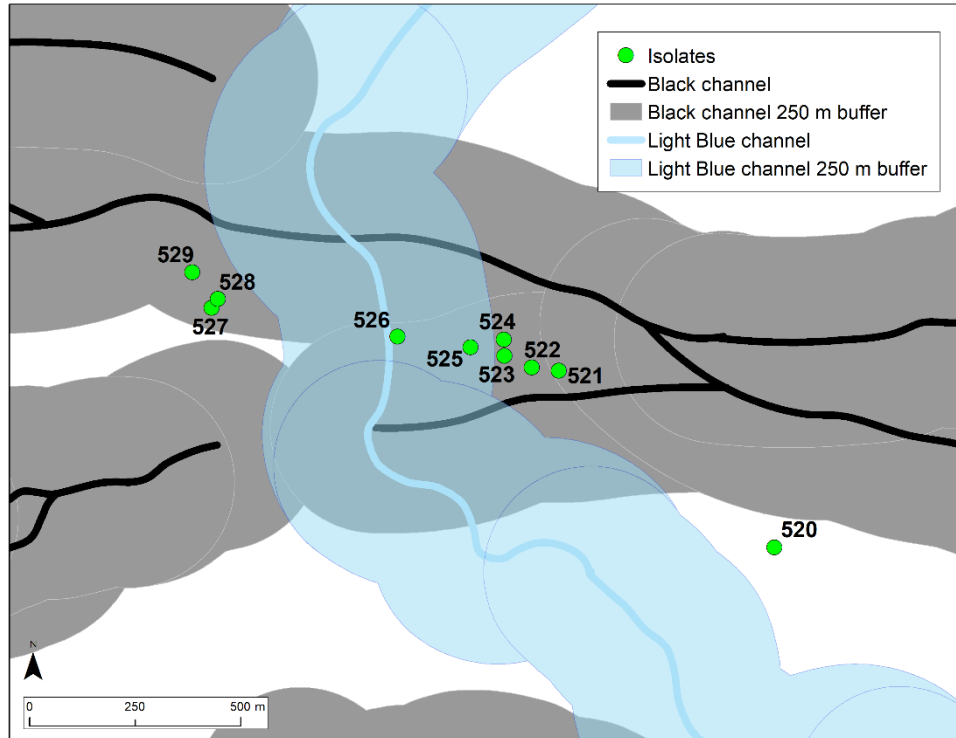
Figure A-19: Example of channel intersection and isolate assignment.

c. Once all intersections/overlaps were eliminated, isolates within the remaining buffer
    zone for each channel were clipped and moved to shapefiles associated with the
    channel. The resulting segregation is reported in Table A-26 (*n*=176).

Table A-26: Isolates assigned using 250 m buffer method.

Channel	Associated isolates (within 250 m buffer)
Black	76
Light Blue	35
Limestone	23
Seafoam	21
Yellow	4
Green	3
Lavender	3
Navy	3
Blue B	2
Coral	2
Pink	2
Gold	1
Mango	1
Total	**176**

Step 3: Processing the isolate exceptions (*n=105*)

Following Step 2, the remaining isolates (*n=105*) fall into two categories: (a) isolates falling between 250 and 500 m distance from any channel (*n=11*), or (b) isolates falling within a region of overlap between two or more channels (*n=94*). Each of these 105 isolates was inspected individually using aerial imagery in ArcMap (Esri, 2021a) and Google Earth (*Google Earth Pro*, 2020) and the associations are enumerated in Table A-27. Thirteen of the isolates fell into areas where visual inspection could not adequately associate the artifact with a specific channel (Indeterminates).

Table A-27: Isolates associated with channel by visual inspection.

Channel	Associated isolates
Black	53
Green	11
Yellow	9
Light Blue	6
Gold	3
Lime	3
Red	2
Brown	2
Blue	2
Coral	1
Indeterminate	13
Total	**105**

Problematic areas: Despite the structured process outlined here, there are a few areas that are problematic.

Example: At one of the northern lobes of the Black channel, there is an intersection/overlap with the Limestone channel, shown in Figure A-20. The green dots represent isolates while the black dots represent site artifacts (i.e., artifacts assigned to Black channel sites in the monograph). The gray and beige regions represent the 250 m buffers for the Black and Limestone channels, respectively. The Black channel is the older channel and hosted extensive wetlands, the outline of which is shown by the dashed line. By the rules listed above, isolates in the beige region would be assigned to the Limestone channel. Similarly, any isolates only in the Black region would be assigned to the Black channel. Isolates in the overlap areas (Black and Limestone buffer overlaps) would be analyzed individually and assigned to a channel, if possible, based on proximity to the channel. In this case, the density and location of these isolates manifest more as a "site" than as isolates. It is unknown to me why they were not treated as a site, but it seems clear to me that this site would most likely reside in association with the much larger Black channel wetlands than the later, smaller Limestone channel (as judged with

aerial imagery). With this mindset, the isolates within the Black/Limestone overlap region were assigned to Black.
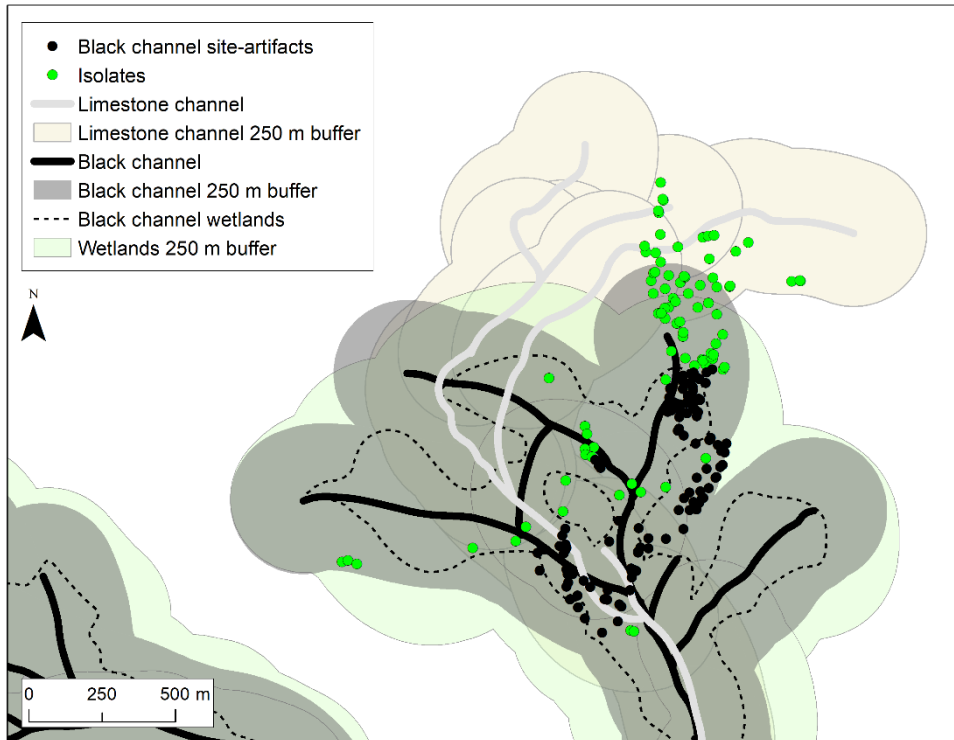
Figure A-20: Problematic isolate association example.

A.6.5 Isolates Summary

Following these processes, most of the isolates catalogued in the ORB have been associated with a channel (Table A-28). At this step in the cleaning process, the isolates were segregated in a separate database table (Isolate). This table is largely identical to the Artifact table, but it includes a ChannelID column for linkage to the relevant channel (site-artifacts find linkage through the SitesChannels relationship). This table was populated with the 305 isolates, and each was assigned a ChannelID (or zero for Indeterminate and Out of Scope).

Table A-28: Isolate channel assignments.

Channel	Isolates out of scope (>=500 m)	Associated isolates (within 250 m buffer)	Manually assigned isolates	Totals
Black	-	76	53	129
Gold	-	1	3	4
Limestone	-	23	-	23
Green	-	3	11	14
Yellow	-	4	9	13
Red	-	-	2	2
Light Blue	-	35	6	41
Lime	-	-	3	3
Blue B	-	2	2	4
Lavender	-	3	-	3
Navy	-	3	-	3
Seafoam	-	21	-	21
Brown	-	-	2	2
Pink	-	2	-	2
Mango	-	1	-	1
Coral	-	2	1	3
Indeterminate	-	-	13	13
Out of scope	24	-	-	24
Totals	**24**	**176**	**105**	**305**

Following cleaning and review, out of 315 samples, 236 are geolocated and well associated with a dated ORB channel.

A.7 ORB XRF Samples

A third source of potentially useful artifacts for this dataset is provided by the list of ORB XRF samples that appears in the Supplemental material for Chapter 6 of the monograph – "*Results of XRF and pXRF Analysis*" by David Page (2015a). Many of the XRF results in this table correspond with samples already discussed and incorporated into the database, but some samples appear exclusively in this spreadsheet.

David Page was kind enough to provide me with an Excel spreadsheet copy of this table – "*Dugway Table 7_XRF_pXRF trace element concentration estimates for 2007 obsidian and FGV artifacts from DPG and UTTR.xls*". Artifact coordinates were not included with this data. This spreadsheet was cleaned for relevant data and then imported into the Access database.

A.7.1 Matching Artifact Types

In the XRF spreadsheet, the Artifact Types do not exactly match those used by Beck & Jones for the lithic analysis in the same monograph. To incorporate these artifacts into the database, I mapped Page's XRF artifact types to Beck & Jones' artifact types (Table A-29). I added one definition (for Desert Side-notched / DESERT SN) to Beck's list, following Beck and Jones's style, to accommodate a type only found in Page's XRF list.

Table A-29: Type definition mapping.

XRF Artifact Type used by Page	Mapped to Beck and Jones's lithic types	
	TYPE$	**TECH$**
AR - CTW (Cottonwood)	COTTONWOOD	PP
AR - DSN (Desert Side-notched)	DESERT SN	PP
AR - ELKO	ELKO	PP
AR - GC	GATECLIFF	PP
AR - HUM	HUMBOLDT	PP
AR – Rosegate	ROSEGATE	PP
AR – RSN	ROCKER	PP
AR – SSN (Small side-notched)	SMALL SN	PP
Biface	AM BIFACE	BIFACE
Chisel	CHISEL	BIFACE
Core	AM CORE	CORE
Crescent	CRESCENT	BIFACE
Drill	DRILL	BIFACE
EH – BVCN	BVCN	PP
EH – GBS [Early Holocene – Great Basin Stemmed]	EXP STEM	PP
EH – Pinto	PINTO	PP
Graver	GRAVER	BIFACE
Knife	KNIFE	BIFACE
LSN/NSN (Large Side-notched, Northern Side-notched	NSN	PP
Modified Flake	INT FLAKE	FLAKE
Rosegate	ROSEGATE	PP
RSN (Rocker Side-notched)	ROCKER SN	PP
Scraper	SCRAPER	BIFACE
Uniface	AM UNIFACE	UNIFACE
Utilized Flake	INT FLAKE	FLAKE
WST	WST STEM	PP
WST – CM	COUGAR MT	PP
WST – CM/Haskett	CM/H STEM	PP
WST – GBCB-UF (Great Basin Concave Base – Unfluted)	GBCB-UF	PP
WST – Haskett	HASKETT	PP
WST – LM	LAKE MOHAVE	PP
WST – Parman	PARMAN	PP
WST – SL	SILVER LAKE	PP

A.7.2 Initial Cleaning of XRF Data

A review of the XRF data revealed several duplicates (Table A-30). In this table, some limited XRF data is included to highlight comparisons. The SampleID (Site$ + FS$) in bold indicates the artifact that was retained following review of each duplicate pair. The resolutions are described below the table.

Table A-30: X-ray fluorescence (XRF) sample potential duplicates.

SampleID	Artifact Type	Ti	Mn	Fe	Zn	Ga	Rb	Sr	Y	Zr	Material	Geochemical Type
42TO1684.15	EH - GBS	nm	nm	nm	49	20	440	9	45	134	OBS	Topaz Mountain
42TO1684.15	EH - GBS	1146	455	0.8	31	19	460	11	49	148	OBS	Topaz Mountain
42TO1924.141	Scraper	3470	654	4.4	93	24	110	361	31	245	FGV	Flat Hills D
42TO1924.141	Uniface	3470	654	4.4	93	24	110	361	31	245	FGV	Flat Hills D
42TO3834.14A	Modified flake	< LOD	415.7	6526.7	< LOD	NM	212.8	< LOD	188.1	130.4	OBS	Topaz Mountain
42TO3834.14B	Biface	3931.08	1893.3	41213.1	40	NM	52.1	288.2	205.1	237.3	FGV	Flat Hills D
42TO3834.2A	Core	< LOD	507.9	7562.2	< LOD	NM	247.3	2.8	191.1	131.5	OBS	Topaz Mountain
42TO3834.2B	Modified flake	3160.39	1456.5	39713.2	45.9	NM	50.4	275.9	206.7	241.9	FGV	Flat Hills D
42TO3834.6A	Biface	1045.94	1132.5	10904.6	< LOD	NM	218.2	5.4	196.8	134.8	OBS	Topaz Mountain
42TO3834.6B	Biface	3350.37	1085.9	39829.1	33.1	NM	51.4	269.1	186.1	232.2	FGV	Flat Hills D
42TO3834.7A	Biface	3285.37	1073.4	40677	36	NM	49.9	279.7	190.2	230.3	FGV	Flat Hills D
42TO3834.7B	EH - GBS	4387.29	2534.5	48317	44.5	NM	44.8	273.7	196.5	220	FGV	Flat Hills D
42TO3834.8A	EH - Pinto	3572.78	992.1	40561.1	49.6	NM	51.9	287.6	188	235.2	FGV	Flat Hills D
42TO3834.8B	EH - GBS	3661.66	927.5	41334.8	33.9	NM	52.2	281.7	203.2	240	FGV	Flat Hills D
42TO3858.1A	EH - Pinto	< LOD	395.1	7148.4	< LOD	NM	126.4	7.9	307.6	91.1	OBS	Black Rock Area
42TO3858.1B	EH - GBS	4213.23	519.8	31432.6	44.6	NM	45.4	490.4	94.5	269.3	FGV	Flat Hills A

Duplicate resolutions:

42TO1684.15: This is a clear duplicate; the samples have the same type, material, and geochemical result. This artifact was sampled at two different XRF labs or machines, which explains the individual element variations. The first instance was deleted.

42TO1924.141: This is a clear duplicate. It is described as a Scraper and Uniface, but with the same XRF trace elements and geochemical type resolution. This artifact is described as an "amorphous uniface" in Beck's "*ORB Final General File.xls*" so I kept the uniface instance and deleted the scraper instance.

42TO3834 and 42TO3858: The remaining duplicates are associated with sites 42TO3834 and 42TO3858. Neither of these sites appear in the *"ORB Final General File.xls"*, *"Final ORB*

337

Projectile Points.xls" or *"site_channel_list.xls"* spreadsheets so both sites lack coordinate information and association with ORB channels. There is enough variation between each pair that I cannot determine which is correct, or even if they are actual duplicates. I added "A" and "B" suffixes to the field sample numbers to keep the SampleIDs unique.

There were 2007 artifacts at the beginning of this cleaning stage. Two duplicates were deleted, leaving 2005 samples. The duplicates were not preserved in the database, as they serve no useful purpose. The cleaned XRF samples were imported into the XRF table in Access.

A.7.3 Associating XRF Samples with Site Coordinates

The XRF data is missing explicit site identifiers, so the SiteID was parsed from the SampleID using the following SQL:

UPDATE XRF SET XRF.SiteID = Trim(Left([SampleId],InStr([SampleId],".")-1));

All sample IDs were also edited programmatically and manually to removed unnecessary leading zeros (for example, 42TO1000.01 changed to 42TO1000.1). This ensures consistency across tables for future cross-referencing.

Excluding the sites already processed, there are 315 additional, identifiable sites associated with the XRF artifacts. Using the State of Utah's Department of Cultural & Community Engagement's SEGO system, I was able to locate the site datum coordinates (UTM) for 314 of these sites. These are listed in the "XRF Sites" table in the database. Some XRF artifacts are not identifiable to site, having names such as Isolate.02 or Green.1.01, and were excluded from further analyses.

The 314 site points were projected onto a map with the channels and channel buffers (Figure A-21).
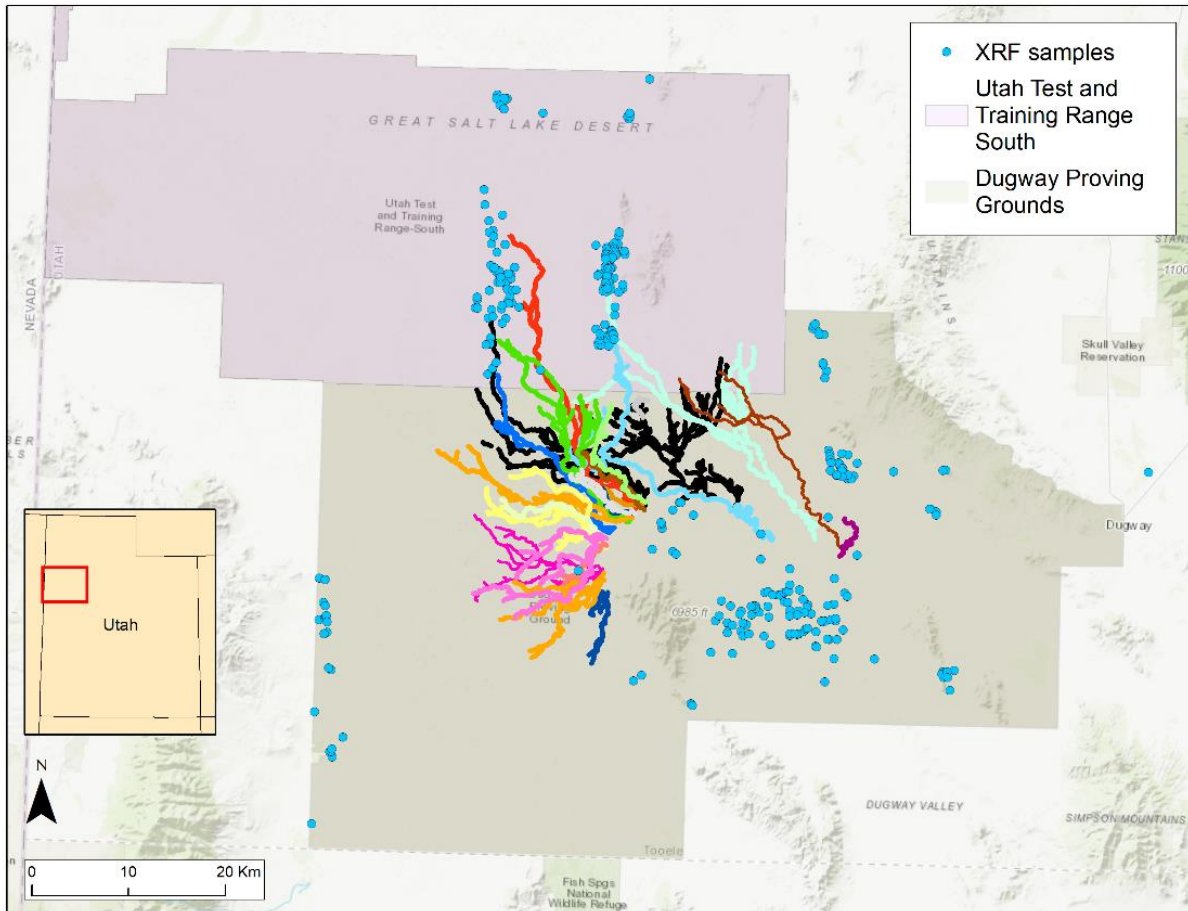
Figure A-21: Site locations for all X-ray fluorescence (XRF) samples in relation to Old River Bed (ORB) channels (see Table A-1 for channel color legend). Channel data by David Page (personal comm., August 22, 2018).

As can be seen in Figure A-21, the XRF test artifacts (blue dots) cover a wide range of areas throughout (and even one outside, far east) the Dugway military zone (light beige region). There are several isolates that appear in association with the distal ends of several channels, specifically the Black, Light Blue, Red, and Seafoam channels. It is important to reiterate that all these artifacts are also using the site centroid coordinates as recorded on the site report in the SEGO system. I do not have individual coordinates for these XRF artifacts.

These points were visually inspected, and the following sites fall within the 250-meter channel buffers and appear to be well associated with the following channels (Table A-31):

Table A-31: X-ray fluorescence (XRF) sample channel assignments.

Site ID	Channel	# of XRF-Tested Artifacts
42TO1053	Black	1
42TO1054	Black	6
42TO1033	Red	1
42TO5135	Red	1
42TO0921	Light Blue	3
42TO1170	Light Blue	1
42TO2724	Light Blue	1
42TO2726	Light Blue	12
42TO2727	Light Blue	2
42TO2728	Light Blue	1
42TO2729	Light Blue	1
42TO0909	Seafoam	40
42TO0924	Seafoam	21
42TO2592	Seafoam	1
42TO2597	Seafoam	1
42TO2607	Seafoam	5
42TO2611	Seafoam	4
42TO2612	Seafoam	1
42TO2616	Seafoam	1
42TO2730	Seafoam	1
42TO2733	Seafoam	2
42TO2833	Seafoam	3
42TO2845	Seafoam	1
42TO2846	Seafoam	4
Total		**115**

The Seafoam channel is included in Table A-31, even though it is an undated channel, as there are a significant number of artifacts associated with this channel. There are also a great number of sites at the distal end of the Seafoam channel, at Wildcat Mountain.

Following cleaning and review, out of these 115 samples, 30 are geolocated and well associated with a dated ORB channel (Black, Red, or Light Blue) (Table A-32).

A.8 Union of Site-Artifacts, Isolates, and XRF Samples

The site-artifacts, isolates, and additional ORB artifacts with XRF tests for were joined into a single, simplified table (CleanArtifact) in the Access database (*n*=2211). This table includes the

SampleID, UTM coordinates, ChannelID, and artifact Type (following Beck's naming convention).

The artifacts associated with dated channels (Table A-32) will provide the temporal framework for my subsequent analysis (*n*=2056):

Table A-32: Summary of Old River Bed Channel-Associated Artifact Cleaning Process.

Channel Association	Site-artifacts	Isolates	XRF	Totals
Gold	45	4	0	49
Black	697	129	7	833
Yellow	131	13	0	144
Green	6	14	0	20
Limestone	110	23	0	133
Red	6	2	2	10
Blue A	2	0	0	2
Light Blue	359	41	21	421
Lime	155	3	0	158
Lavender	114	3	0	117
Blue B	165	4	0	169
Total	**1790**	**236**	**30**	**2056**

A.9 Filtering out Non-Paleoindian Artifacts

The final step in processing the 2056 cleaned and joined ORB samples involves distilling out those artifacts that are associated with the earliest peoples in the Great Basin, collectively referred to as Paleoindian, from those that are typically associated with occupations that occurred after the terminal date of the youngest dated ORB channel. In this case, the Light Blue channel, with a terminal date around 8800 ^{14}C yr BP (10,130 – 9,670 cal BP) sets the latest cut-off date for inclusion in this dataset (Madsen et al., 2015). As will be discussed below, this correlates with the end of the Paleoindian period, and the transition into the Archaic period, which occurs roughly around 8500 ^{14}C yr BP (9500 cal BP) (Haynes, 2007; Madsen, 2007).

Beck & Jones (2015) originally classified the ORB artifacts described here to Type. These classifications, along with a few types from Page (discussed in section A.7.1, above) are carried forward into this dataset. The classifications are grouped into roughly five subgroups (Tables 5.9 and 5.10 in the monograph) and each is considered here for inclusion or exclusion from the final working dataset. To facilitate this filtering process, I added an attribute field named "IsPaleo" to the CleanArtifact table. Artifact types were set to either "Y" (Yes) if they fall within the Paleoindian period, "N" if not, and "I" if Indeterminate. "Indeterminate" is reserved for utility items, such as scrapers and chisels, which are found widely throughout Paleoindian and Archaic temporal periods. The handling of these items is discussed below.

A.9.1 Type Filtering

Each of the type classes, below, is considered for inclusion:

Great Basin Concave Base: Unfluted GBCB lanceolate points (GBCB-UF) remain enigmatic within Great Basin archaeology with regard to cultural affiliation and timing; however, they are well associated with the Paleoindian period and are generally found in association with WST types (Beck & Jones, 2009, 2015; Clewlow, 1968; Layton, 1970; Pendleton, 1979). In the ORB, the majority of GBCB artifacts occur in association with the youngest channels. For these artifacts, I set the "IsPaleo" field to "Y" ($n=8$) in the CleanArtifact table.

Western Stemmed Tradition: This subgroup includes several widely accepted WST types, including Cougar Mountain, Crescents, Haskett, Lake Mohave, Parman, and Silver Lake, as well as artifacts Beck and Jones (2015) classified as having characteristics of WST technology ("WST blade", "WST bl/mid", "WST mid", "WST stem", and "CM/H stem"). For these artifacts, I set the "IsPaleo" field to "Y" ($n=464$) in the CleanArtifact table.

Table A-33: Types included in the Western Stemmed Tradition subgroup.

Type	Totals
Cougar Mtn/Haskett Stem	9
Cougar Mountain	15
Crescent	24
Haskett	11
Lake Mohave	32
Parman	18
Silver Lake	99
WST Blade/Midsection	2
WST Blade	118
WST Midsection	2
WST Stem	134
Totals	**464**

Early Holocene: Beck & Jones (2015) assign several types temporally to the Early Holocene and these are addressed here on an individual basis:

Butte Valley Corner-Notched (BVCN): These points were first defined by Beck & Jones (2009) at the Sunshine Locality. However, in their ORB report the authors concede that these points, with expanding stems and convex bases, might be better described as "corner-*removed*" rather than as "corner-*notched*" (2015, p. 139) and that they fit the same criteria as the "North Creek Stemmed" points defined by Janetski et al. (2012) at North Creek Shelter in Utah. In the site report for North Creek Shelter, Janetski et al. report that eight of nine North Creek Stemmed points were recovered within Level II (2012, Table 2), below an AMS radiocarbon date of 9510 ± 80 ^{14}C yr BP (11,140 – 10,560 cal BP). This places the type, regardless of naming convention, firmly in the Paleoindian period and appropriate for inclusion within this final analysis. For these Butte Valley Corner-notched (aka North Creek Stemmed) artifacts, I set the "IsPaleo" field to "Y" (*n=15*) in the CleanArtifact table.

Dugway Stubbies are a recent WST type definition specific to the ORB region (Beck & Jones, 2015; Duke, 2011; Rosencrance, 2019; Schmitt et al., 2007; Smith et al., 2020) and may be a particular manifestation of toolstone conservation and reuse. Stubbies are a small (< 30 mm), short-stemmed form with an "abbreviated blade segment" (Jones, Beck, & Kessler, 2003, p. 23, as cited in Beck & Jones 2015, p. 138) that is likely the result of breakage and resharpening, perhaps recycled from other WST forms (Beck & Jones, 2015; Schmitt et al., 2007). They are abundant within the ORB, including in association with the oldest dated channels in the system (Table A-34). Duke observes that Stubbies exhibit "an extreme association with obsidian" (2011, pp. 192–193) and Beck & Jones (2015) similarly record obsidian proportions in excess of 85% in comparison to FGV. Their abundance and ubiquity across a wide range of dated ORB channels demonstrates that they will provide valuable evidence of Paleoindian activity across this temporal study. For these artifacts, I set the "IsPaleo" field to "Y" (*n*=158) in the CleanArtifact table.

Table A-34: Dugway Stubby abundances according to Old River Bed delta channel.

Channel	Channel Age (^{14}C yr BP) †	# of Dugway Stubbies
Gold	~11,300-10,500	1
Black	~11,000-10,300	80
Limestone	~10,500-10,000	1
Yellow	~10,300-10,100	9
Green	~10,300-9,800	25
Blue B	~10,000-9,500	21
Lime	~9,800->9,200	2
Lavender	~9,100-9,000	10
Light Blue	~9,800-8,800	9
Total		**158**

† Madsen et al., 2015

Contracting, Expanding, and Square Stems: A large number of broken stems have been recovered in the ORB and these occur across many channels (Table A-35). While Beck & Jones

do not use the type in their analysis, they remark that Duke's "Bonneville" type "appears to

subsume our Square, Expanding, and Contracting Stem categories" (2015, p. 151). The

Bonneville type was defined by Duke to describe stemmed points that "possess long blades

relative to their stem" (2011, p. 174), similar to Silver Lake points. Like the Dugway Stubby, the

Bonneville type is a recent WST type definition specific to the ORB region (Beck & Jones,

2015; Duke, 2011; Rosencrance, 2019; Schmitt et al., 2007; Smith et al., 2020). Of particular

importance is that Duke assigns Bonneville stemmed points to the Paleoindian period. It is

interesting to note that Duke also states that "stems for Stubby vary widely from contracting to

expanding to square" (2011, p. 174), so that this group of stems could be remnants of either

Stubby or Bonneville types. For these artifacts, I set the "IsPaleo" field to "Y" (*n*=88) in the

CleanArtifact table.

Table A-35: Stem types recovered in the Old River Bed delta.

Channel	Contracting stem	Expanding stem	Square stem	Totals
Gold	6	2	1	9
Black	-	8	13	21
Limestone	-	-	1	1
Yellow	-	5	5	10
Green	-	8	3	11
Blue B	-	7	7	14
Lime	-	2	1	3
Lavender	-	6	4	10
Light Blue	-	9	-	9
Totals	**6**	**47**	**35**	**88**

Pinto: The Pinto projectile point is a problematic type in both chronological and stylistic

terms, leading to a persisting long- versus short-chronology debate (Layton, 1970; Schroth,

1994; Warren, 1980). Recently, Duke (2011) and Hamilton (2012) have forwarded compelling

arguments that Pinto points should be considered a component of the Paleoindian toolkit. Both

have argued that a regional variant of the Pinto type originated earlier in the ORB than at the type site in the Mojave Desert and that the Pinto and Great Basin Stemmed (GBS) points found in the ORB "appear to be a part of the same technological tradition" (Hamilton, 2012, p. 89; contra Janetski et al., 2012, p. 153). I find the evidence compelling and, for this reason, for these artifacts, I set "IsPaleo" to "Y" (*n=28*) in the CleanArtifact table.

Cody Knives are not assigned a temporal period by Beck & Jones (2015) but are a component of the Cody Cultural Complex, described in the Horner type site monograph (Frison & Todd, 1987; Gibbon & Ames, 1998). The complex is temporally associated with the very late Paleoindian period and the beginning of the Archaic, with their earliest date falling between 10,060 and 9,875 cal BP. While these dates push the limiting edge for inclusion in my dataset, for these artifacts, I set "IsPaleo" to "Y" (*n=6*).

Archaic: The Light Blue channel terminal date also signifies the waning of the ORB wetlands, which became uninhabitable by 8500 ^{14}C BP with the onset of the dry, middle Holocene (Beck & Jones, 2015). Not coincidentally, this also marks the beginning of the Early Archaic period, which is characterized by two key attributes as people adapted to this new, more arid, environment: the widespread appearance of ground stone, for the processing of hard seeds, and the appearance of corner-notched points as hunting shifted to small game (Haynes, 2007; Madsen, 2007; Rhode & Louderback, 2007, 2015).

By definition, Archaic point types should be younger than the latest ORB channel date ranges, and Beck & Jones state that they consider their presence in the sample set to be "intrusive" (2015, p. 147), likely the result of visits to the region after the demise of the ORB wetlands. As such, they can be excluded from further consideration in this analysis. These types include Elko, Gatecliff, Humboldt, Northern Side-notched, Rocker Side-notched, Rosegate, and

Small Side-notched types (*n*=38). Each of these well-established Archaic types occur in low numbers in the ORB (Beck & Jones, 2015; Thomas, 1981), as shown in Table A-36. Parsimoniously, I also included the single groundstone artifact in the Archaic dataset as seed processing is typically regarded as an Archaic technology (though see Janetski et al., 2012 and Louderback, 2014 for early groundstone at North Creek Shelter). For these Archaic artifacts that are explicitly "not Paleoindian", the "IsPaleo" flag was set to "N" (*n*=39).

Table A-36: Archaic types excluded
from this analysis.

Type	Totals
Elko/Rocker Side-notched	2
Elko	15
Gatecliff	1
Ground stone	1
Humboldt	6
Notch	1
Northern Side-notched	1
Rocker Side-notched	5
Rosegate	4
Small Side-notched	3
Totals	**39**

Indeterminate types: Following the classification of these well-established cultural types (*n*=806), many artifacts (*n*=1250) remain that are neither temporal nor cultural markers, but rather general utility tools that appear across multiple periods and occupations (Table A-37).

Table A-37: General utility types.

Type	Totals
ABLADE	12
AM BIFACE	53
AM CORE	2
AM UNIFACE	26
BF CHIS/SCRP	1
BF SCRP/GR	5
BLADE FLAKE	3
CHISEL	3
CHUNK	9
COMBO TOOL	32
CORE	17
CORT FLAKE	25
DRILL	17
GRAVER	34
HAMMERSTONE	2
IND BIFACE	228
IND UNIFACE	8
INT FLAKE	257
KNIFE	1
MANUPORT	1
PT BF/GRAVER	1
PT BIFACE	115
SCRAPER	223
SPLIT COBBLE	1
SPLIT PEBBLE	2
UF C/C S/G	1
UNCL PP	164
UNIQUE BF	5
UNKNOWN PP	1
WORKED PEBBL	1
Totals	**1250**

I reviewed these tools on a site-by-site basis. If Paleoindian artifacts also occur at the site ($n>=1$), then any associated utility tools were also considered "Paleoindian". If no Paleoindian artifacts were present at the site, the utility tools for that site were considered "not Paleoindian". For Paleoindian sites, the utility tools were flagged as "YY" in the "IsPaleo" field. Similarly,

"not Paleoindian" utility tools were marked as "NN" in the "IsPaleo" field. The results are captured in Table A-38, below.

Table A-38: Utility artifacts in association with Paleoindian artifacts.

TYPE	Totals
ABLADE	11
AM BIFACE	41
AM CORE	1
AM UNIFACE	22
BF CHIS/SCRP	1
BF SCRP/GR	5
BLADE FLAKE	3
CHISEL	3
CHUNK	9
COMBO TOOL	30
CORE	15
CORT FLAKE	21
DRILL	13
GRAVER	32
HAMMERSTONE	1
IND BIFACE	199
IND UNIFACE	8
INT FLAKE	242
KNIFE	1
MANUPORT	1
PT BF/GRAVER	1
PT BIFACE	89
SCRAPER	191
SPLIT COBBLE	1
SPLIT PEBBLE	2
UF C/C S/G	1
UNCL PP	130
UNIQUE BF	3
UNKNOWN PP	1
WORKED PEBBL	1
Totals	**1079**

Forty artifacts were associated with sites (*n*=18) where no Paleoindian artifacts were present. The sites with no Paleoindian artifacts, as defined here by type, are listed in Table A-39.

Table A-39: Sites with no Paleoindian evidence.

SiteID	Channel	# of Artifacts
42TO1384	Black	1
42TO1385	Black	1
42TO1667	Black	1
42TO1670	Black	3
42TO1680	Black	5
42TO1891	Black	3
04DM01	Red	1
42TO3227	Blue A	1
42TO3232	Blue A	1
42TO3521	Yellow	2
42TO5135	Red	1
42TO1168	Light Blue	1
42TO1170	Light Blue	1
42TO1171	Light Blue	3
42TO1352	Light Blue	8
42TO1675	Light Blue	3
42TO1676	Light Blue	3
42TO2766	Light Blue	1
Total		**40**

For isolates, with no surrounding site association, this process eliminates any non-Paleo artifacts, for a total of 131 artifacts marked as "NN".

A.9.2 Filtering Summary

A total of 1079 utility artifacts were found in association with Paleoindian artifacts (Table A-40). Artifacts with no such association (*n*=171) were filtered out. The result of this process is 1846 Paleoindian artifacts associated with a dated channel.

Table A-40: Paleoindian artifacts.

Types	Totals
Western Stemmed Tradition	464
Dugway Stubby	158
Cont, Exp, Sq Stem	88
Great Basin Concave Base - Unfluted	8
Butte Valley Corner-notched	15
Pinto	28
Cody Knife	6
Utility tools	1079
Totals	**1846**

A.10 Summary: XRF-tested Paleoindian Artifacts

Cross-referencing the CleanArtifact samples with the XRF data table provides the final working dataset of 442 Paleoindian artifacts with geochemical sources across ORB dated channels. The results are provided in Table A-41.

Table A-41: Paleoindian artifacts with X-ray fluorescence (XRF) results.

Types	Totals
Western Stemmed Tradition	167
Dugway Stubby	85
Cont, Exp, Sq Stem	43
Great Basin Concave Base - Unfluted	3
Butte Valley Corner-notched	5
Pinto	11
Cody Knife	1
Utility tools	127
Totals	**442**

The geochemical sources within this cleaned and filtered dataset reveal the intensity with which each toolstone source was used within the ORB (Table A-42). These sources and quantities will be used in my Discoverability analyses (Chapter 5).

Table A-42: Old River Bed delta Paleoindian toolstone sources.

Sources	Totals
Badlands A	18
Bear Gulch	1
Black Rock Area	10
Browns Bench	41
Browns Bench Area	5
Cedar Mountain B	8
Currie Hills	3
Deep Creek A	10
Ferguson Wash	1
Flat Hills A, C, D, E	182
Kane Springs Wash Caldera	1
Malad	4
Modena	1
Owyhee	2
Paradise Valley	3
Pumice Hole Mine	1
Topaz Mountain	130
Wildhorse Canyon	9
Unknown 1	1
Unknown FGV	6
Unknown OBS	5
Totals	**442**

A.11 Repository Access

The location data for the archaeological sites and artifacts referenced in this appendix have been removed from the public copy of this work, for legal site protection reasons. For access to the unredacted edition of this appendix and the supporting Microsoft Access database, please contact the Utah State Historic Preservation Office, Salt Lake City, Utah.

Appendix B: Survey Data

This appendix catalogues the observations and sample data of natural obsidian from field

work at five primary source locations and the surveys of their secondary extents (see Chapter 3).

B.1 Black Rock Area

Table B-1: Black Rock Area (BRA) sample data. Bolded samples
were X-ray fluorescence (XRF) tested and confirmed as "Black Rock Area" obsidian.

BRA SampleID	UTM Zone (WGS84)	Easting	Northing
TSTS*	12	359475	4297008
201	12	359592	4295721
202	12	359100	4294693
TSTS	12	359507	4293681
203	12	359505	4293674
204	12	359574	4293666
205	12	359714	4292899
206	12	360269	4292002
207	**12**	**360341**	**4292007**
208	12	360356	4292045
209	12	360368	4292049
210	12	360349	4292016
211	12	358639	4289147
212	**12**	**359161**	**4289044**
213	12	357094	4288323
214	12	357176	4288265
ONC**	12	359599	4297904
215	12	359407	4298240
TSTS	12	359429	4298255
216	12	359463	4298281
217	12	359494	4298303
TSTS	12	359519	4298321
218	12	359544	4298320
219	12	359584	4298360
220	12	359624	4298381
221	12	359878	4298577
222	**12**	**360040**	**4298624**
TSTS	12	360244	4298775
223	12	360409	4298837
224	12	359830	4299251
225	12	359843	4299268
226	12	358180	4300202
227	12	358073	4301472

BRA SampleID	UTM Zone (WGS84)	Easting	Northing
TSTS	12	357872	4303327
228	12	357930	4303360
229	12	357943	4303374
230	12	358015	4303449
TSTS	12	358164	4303604
231	12	358241	4303686
232	**12**	**358286**	**4303756**
233	12	358356	4303941
TSTS	12	356373	4297585
TSTS	12	351352	4299192
234	**12**	**355456**	**4294763**
235	**12**	**351364**	**4299234**
236	12	355783	4293714
237	12	356610	4288804
238	12	356639	4288726
239	12	356662	4288728
240	12	356841	4288925
241	**12**	**356800**	**4288871**
242	12	356597	4288846
TSTS	12	355681	4288538
243	12	355677	4288545
244	12	355673	4288556
245	12	354754	4288625
246	12	354763	4288536
247	12	354910	4287890
ONC	12	354855	4287952
ONC	12	354848	4287989
ONC	12	354820	4287991
ONC	12	354796	4288082
ONC	12	354775	4288125
ONC	12	354798	4288172
ONC	12	354825	4288190
ONC	12	354986	4288136
ONC	12	354948	4288088
ONC	12	354932	4288058
ONC	12	354909	4288038
248	**12**	**354923**	**4288140**
ONC	12	354933	4288205
ONC	12	354921	4288305
ONC	12	354862	4288402
249	12	354821	4288466
250	12	355522	4290567
251	12	355562	4291664

BRA SampleID	UTM Zone (WGS84)	Easting	Northing
252	12	355022	4292509
TSTS	12	354994	4292509
253	12	355052	4296014
254	12	354359	4295873
TSTS	12	354320	4295879
TSTS	12	351153	4299229
255	12	350906	4299497
ONC	12	350909	4299497
TSTS	12	350925	4299493
256	12	350931	4299490
257	12	350935	4299486
258	12	342647	4286593
259	12	342598	4286477
260	12	342572	4286424
261	**12**	**342549**	**4286331**
262	12	342518	4286216
263	12	342234	4287374
264	12	344070	4287854
265	12	343964	4288377
266	12	345802	4287740
267	12	345769	4287840
268	**12**	**345768**	**4287807**
TSTS	12	345747	4288020
269	12	345750	4288020
270	12	346090	4287580
271	12	346104	4287578
272	12	344336	4289022
273	12	344667	4289659
TSTS	12	345218	4290577
TSTS	12	345269	4290559
274	12	344353	4291605
275	12	344485	4291608
276	12	344797	4291430
277	12	345504	4291219
ONC	12	345464	4292491
278	**12**	**345642**	**4292382**
ONC	12	345587	4293568
279	12	346460	4293586
ONC	12	346566	4294179
280	12	346934	4294517
281	12	347058	4294694
ONC	12	346977	4294711
ONC	12	347322	4295265

BRA SampleID	UTM Zone (WGS84)	Easting	Northing
282	12	347363	4295254
283	12	347665	4295151
284	12	347610	4295166
285	12	347986	4295367
286	12	349187	4295928
287	12	349243	4295884
288	**12**	**349758**	**4295798**
289	12	350068	4295942
ONC	12	348267	4297173
290	12	347882	4297187
291	12	346117	4298564
292	12	346414	4300006
TSTS	12	346445	4300137
293	12	346438	4300143
294	12	346779	4301143
295	12	346749	4301169
296	**12**	**347766**	**4302085**
297	12	343379	4300106
TSTS	12	345279	4300358
298	12	345275	4300275
299	12	341964	4287363
300	12	341861	4287421
ONC	12	342089	4287403
ONC	12	342023	4287385
ONC	12	341968	4287505
ONC	12	341944	4287533
ONC	12	341917	4287564
ONC	12	341113	4287647
301	12	341136	4287562
ONC	12	341138	4287577
ONC	12	341117	4287645
ONC	12	340412	4288050
302	12	340237	4287991
ONC	12	340047	4288583
ONC	12	340036	4288573
303	12	339690	4288851
304	**12**	**339284**	**4289973**
305	12	339261	4289974
306	12	338861	4290965
307	12	339053	4291056
ONC	12	338252	4291776
308	12	338193	4291670
309	12	338237	4291715

BRA SampleID	UTM Zone (WGS84)	Easting	Northing
ONC	12	337494	4292096
310	12	337564	4291696
ONC	12	336534	4292912
311	12	336362	4292386
ONC	12	335501	4291338
312	12	339635	4299891
TSTS	12	339659	4299933
313	**12**	**341164**	**4302001**
TSTS	12	341277	4302318
TSTS	12	341036	4301623
314	12	340833	4301024
315	12	339372	4299879
316	12	337647	4297587
317	12	336262	4296844
318	12	336061	4297029
319	12	335955	4297496
320	**12**	**335615**	**4297888**
TSTS	12	335368	4298191
321	12	332991	4295925
322	12	331762	4292997
323	**12**	**331703**	**4292997**
ONC	12	331142	4283846
324	12	340386	4284533
326	12	337399	4283379
327	**12**	**335887**	**4282306**
328	12	332517	4282768
329	**12**	**331122**	**4283199**
330	12	328696	4287213
331	12	327210	4286527
332	12	327258	4286497
334	12	327292	4281871
335	**12**	**330276**	**4286845**
TSTS	12	330850	4287122
336	12	330850	4287329
337	12	331086	4287966
338	12	330556	4286618
TSTS	12	332013	4286021
339	12	332296	4286064
TSTS	12	334608	4287756
340	**12**	**334608**	**4287756**
TSTS	12	334697	4287975
341	12	334815	4288267
342	12	335030	4288926

BRA SampleID	UTM Zone (WGS84)	Easting	Northing
343	12	334965	4289650
344	12	335662	4290591
345	12	335684	4291640
346	12	334233	4293061
347	12	337243	4292414
348	**12**	**336843**	**4291798**
349	12	336523	4291239
ONC	12	336589	4291198
350	12	335718	4290000
ONC	12	336259	4290853
ONC	12	335863	4290274
351	12	338185	4285513
352	**12**	**338720**	**4285886**
353	12	355759	4298358
354	12	355638	4298216
355	12	355585	4298199
356	**12**	**355345**	**4298938**
357	12	352187	4290154
358	12	347388	4289456
359	**12**	**347853**	**4289361**
360A	**12**	**350972**	**4290811**
360B	**12**	**350972**	**4290811**
361	12	353112	4289656
TSTS	12	354795	4291597
810*	**12**	**332881**	**4275139**
811*	**12**	**330266**	**4275195**
816*	**12**	**326514**	**4267999**
820*	**12**	**326119**	**4260240**

* TSTS = "too small to sample", typically < 2mm in diameter

** ONC = "observed not collected", typically near another collected sample

*** Originally collected during nearby Mineral Mtns survey, XRF tested as BRA

B.2 Ferguson Wash

*Table B-2: Ferguson Wash (FW) sample data. Bolded samples were X-ray fluorescence (XRF)
tested and confirmed as "Ferguson Wash" obsidian.*

FW SampleID	UTM Zone (WGS84)	Easting	Northing
TSTS*	11	752031	4477503
1	11	752037	4477501
2	11	751553	4476526
3	11	751580	4476567
4	**11**	**751797**	**4476886**
5	11	752064	4477028
6	11	752217	4477319
ONC**	11	752222	4477343
7	11	752278	4477523
8	**11**	**752417**	**4477699**
ONC	11	752420	4477745
9	11	752309	4477633
10	11	752315	4477588
11	11	752298	4477309
12	11	752298	4476508
13	**11**	**751114**	**4475904**
ONC	11	750995	4475939
ONC	11	750936	4475935
14	11	750911	4475971
ONC	11	750847	4476002
ONC	11	750739	4476072
15	**11**	**750729**	**4476077**
ONC	11	750663	4476098
ONC	11	750575	4476175
ONC	11	750524	4476226
ONC	11	750489	4476250
ONC	11	750369	4476276
ONC	11	750297	4476301
ONC	11	750208	4476400
ONC	11	750155	4476463
ONC	11	750072	4476534
ONC	11	750084	4476600
ONC	11	750169	4476770
ONC	11	750156	4476852
ONC	11	750287	4476876
16	**11**	**750287**	**4476877**
ONC	11	750268	4476878
17	**11**	**750204**	**4476939**
18	**11**	**750179**	**4476968**

FW SampleID	UTM Zone (WGS84)	Easting	Northing
ONC	11	750163	4476975
ONC	11	750118	4477051
19	11	750086	4477116
ONC	11	750050	4477145
ONC	11	750043	4477190
ONC	11	750006	4477258
ONC	11	750067	4477300
ONC	11	750106	4477351
ONC	11	750083	4477431
ONC	11	750136	4477514
ONC	11	750142	4477556
20	**11**	**750134**	**4477585**
ONC	11	750064	4477509
ONC	11	750054	4477400
ONC	11	749999	4477176
ONC	11	750051	4477067
ONC	11	750064	4477046
ONC	11	750066	4477011
ONC	11	750096	4476984
ONC	11	750197	4476791
ONC	11	750186	4476695
ONC	11	750158	4476650
ONC	11	750096	4476570
ONC	11	750116	4476518
ONC	11	750170	4476479
ONC	11	750348	4476340
ONC	11	750402	4476305
ONC	11	750458	4476294
ONC	11	750525	4476289
ONC	11	750589	4476288
ONC	11	750640	4476293
ONC	11	750731	4476289
ONC	11	750777	4476304
ONC	11	750862	4476302
ONC	11	750955	4476312
ONC	11	751007	4476347
21	**11**	**751075**	**4476348**
ONC	11	751127	4476333
ONC	11	751170	4476209
ONC	11	751201	4476174
ONC	11	751233	4476152
ONC	11	751270	4476129
ONC	11	751310	4476143

FW SampleID	UTM Zone (WGS84)	Easting	Northing
ONC	11	751351	4476181
ONC	11	751398	4476238
22	11	751418	4476326
ONC	11	752308	4476363
ONC	11	752361	4476383
23	11	752555	4476384
ONC	11	752594	4476377
ONC	11	752310	4476224
ONC	11	752324	4476181
24	**11**	**752364**	**4476040**
ONC	11	753787	4477588
25	**11**	**753788**	**4477590**
26	11	753643	4477705
27	11	753634	4478039
ONC	11	753688	4478058
ONC	11	753698	4478070
28	11	753379	4478523
ONC	11	753398	4478536
ONC	11	753475	4478608
ONC	11	753153	4478994
29	**11**	**753191**	**4479001**
ONC	11	753910	4476917
TSTS	11	751350	4476019
30	11	751362	4476016
TSTS	11	753436	4476214
ONC	11	753249	4476812
31	11	753445	4476718
ONC	11	753644	4476815
32	**11**	**753839**	**4476883**
33	11	753082	4478713
34	11	753094	4478711
ONC	11	753082	4478750
35	11	753105	4478777
ONC	11	753138	4478937
36	11	752847	4478176
37	11	752811	4478208

* TSTS = "too small to sample", typically < 2mm in diameter

** ONC = "observed not collected", typically near another collected sample

B.3 Mineral Mountains

Table B-3: Mineral Mountains (MM) sample data. Bolded samples were X-ray fluorescence (XRF) tested and confirmed as "Wildhorse Canyon" obsidian.

MM SampleID	UTM Zone (WGS84)	Easting	Northing
800	12	342473	4261116
ONC**	12	342381	4260544
801	**12**	**342455**	**4260425**
802	12	342536	4260549
803	12	342218	4261372
804	12	341617	4262067
805	**12**	**340677**	**4262227**
806	12	339713	4262426
807	**12**	**338855**	**4262685**
808	**12**	**340712**	**4258246**
809	12	340175	4257420
813A	**12**	**326881**	**4273539**
813B	**12**	**326881**	**4273539**
814	**12**	**326814**	**4272812**
815	**12**	**326632**	**4271140**
TSTS*	12	326531	4269499
817	**12**	**326409**	**4266146**
818	**12**	**326379**	**4264039**
819	**12**	**326323**	**4261755**
TSTS	12	325587	4259399
821	12	326343	4259031
ONC	12	332719	4257722
822	**12**	**332708**	**4257149**
823	12	332624	4256325
824	12	332642	4256463
ONC	12	332076	4256374
ONC	12	332248	4256509
ONC	12	341445	4260689
ONC	12	341529	4260516
827	12	341777	4259973
828	12	342052	4259958
ONC	12	341724	4259804
829	**12**	**341538**	**4259976**
830	12	341406	4260149
ONC	12	340997	4260848
831	12	340758	4261027
832	12	339875	4261363
833	12	339203	4257288
ONC	12	339357	4257035

MM SampleID	UTM Zone (WGS84)	Easting	Northing
ONC	12	339588	4256860
834	12	340726	4257560
835	**12**	**341171**	**4257099**
ONC	12	340811	4256924
836	12	340824	4256907
837	12	340797	4256631
838	12	340652	4256638
839	**12**	**339941**	**4256427**
840	12	339160	4256323
841	12	338716	4256592
842	12	338468	4256945
843	12	337839	4256516
848	**12**	**338485**	**4260887**
849	**12**	**325358**	**4256371**
850	**12**	**325269**	**4255479**
851	12	334522	4260002
ONC	12	334508	4259919
853	12	334861	4260076
ONC	12	334838	4260108
854	12	334822	4260130
ONC	12	334785	4260176
855	12	334777	4260199
856	12	335772	4260020
857	**12**	**335569**	**4259735**
858	**12**	**333381**	**4266441**
859	12	333879	4264680
860	12	334055	4264667
861	12	334784	4263481
862	**12**	**335196**	**4264363**
863	12	334611	4268552
864	**12**	**332859**	**4271842**

* TSTS = "too small to sample", typically < 2mm in diameter

** ONC = "observed not collected", typically near another collected sample

B.4 Panaca Summit / Modena

Table B-4: Panaca Summit/Modena (PS/M) sample data. Bolded samples were X-ray fluorescence (XRF) tested and confirmed as "Modena" obsidian.

PS/M SampleID	UTM Zone (WGS84)	Easting	Northing
TSTS*	11	761571	4188174
401	**11**	**761562**	**4188187**
402	12	238882	4186231
ONC**	12	238810	4185817
403	12	238955	4185684
404	12	237289	4185882
405	12	236625	4186078
406	11	763653	4186492
407	11	762914	4186556
408	11	762322	4187170
409	11	761124	4189217
TSTS	11	760196	4190910
410	11	760084	4190897
411	11	760030	4191800
412	**11**	**758224**	**4192890**
TSTS	11	757404	4193748
413	11	757382	4193740
414	**11**	**756840**	**4194313**
415	11	756555	4194838
416	11	761543	4179648
417	**11**	**761517**	**4179640**
418	11	763567	4181558
419	12	236487	4182973
420	12	236526	4182942
421	12	257968	4183479
422	12	259679	4186528
423	12	261279	4186314
424	12	261224	4184691
425	12	261161	4182602
426	**12**	**261117**	**4180887**
427	11	757475	4180627
428	11	757132	4181282
429	11	757129	4181305
430	11	756779	4182448
ONC	11	756671	4182733
431	11	756485	4182703
432	11	755949	4183606
433	**11**	**755481**	**4184630**
434	11	758218	4180551

PS/M SampleID	UTM Zone (WGS84)	Easting	Northing
435	11	758341	4180310
436	**11**	**758579**	**4179663**
437	12	241292	4185194
438	12	241460	4185398
439	**12**	**242574**	**4185462**
440	12	244089	4185163
441	12	245375	4183255
442	12	245289	4182653
443	**12**	**244958**	**4181036**
444	12	246968	4180776
445	12	248212	4180583
446	12	251471	4181943
447	**12**	**251402**	**4180365**
448	**12**	**262910**	**4186448**
449	**12**	**255005**	**4190866**
ONC	11	756458	4193519
450	11	756180	4193596
ONC	11	756095	4193212
ONC	11	755948	4193031
ONC	11	755854	4192826
451	**11**	**755717**	**4192826**
452	11	755742	4192873
453	11	755834	4193133
454	12	242319	4188278
455	12	242065	4189118
456	**12**	**241683**	**4190314**
457	12	248454	4189267
458	12	245036	4186987
460	12	242544	4189600
461	**12**	**238909**	**4185866**
100	**12**	**266170**	**4187978**
101	12	266254	4189560
102	11	740019	4198138
103	**11**	**740694**	**4197861**
ONC	11	749541	4188030
472	**11**	**750074**	**4187943**
473	**11**	**752083**	**4188889**
ONC	11	750020	4187935
474	11	749567	4188037
475	11	749007	4188824
476	11	748828	4189826
477	11	748173	4190895
478	11	747938	4191632

PS/M SampleID	UTM Zone (WGS84)	Easting	Northing
ONC	11	747789	4192458
479	11	746856	4193358
480	11	747332	4192267
481	11	746629	4192174
ONC	11	746097	4192441
482	11	747824	4192493
ONC	11	745714	4192582
483	**11**	**744191**	**4192726**
ONC	11	742644	4193245
484	11	741169	4193686
485	11	746759	4192018
486	11	748927	4189273
ONC	11	749749	4187923
ONC	11	747162	4192294
487	11	739622	4191865
488	**11**	**738629**	**4191722**
489	**11**	**736746**	**4192648**
TSTS	11	736856	4193670
490	11	737505	4194678
491	11	737549	4196165
492	11	747337	4191887
493	11	746047	4192157
494	**11**	**746531**	**4197550**
495	11	745831	4197764
496	11	746637	4197824
497	11	746037	4196618
ONC	11	746040	4196621
498	11	745703	4196659
ONC	11	745806	4195950
499	11	745440	4195793
500	11	745114	4195343
ONC	11	744995	4195266
501	**11**	**744496**	**4195246**
502	11	743998	4195270
503	**11**	**743614**	**4195614**
504	11	747164	4197689
505	11	736655	4192708
506	**11**	**736524**	**4197825**
507	11	736216	4197772
508	11	747398	4197354
509	**11**	**749385**	**4195383**
510	**11**	**749527**	**4194188**
ONC	11	747794	4192476

PS/M SampleID	UTM Zone (WGS84)	Easting	Northing
511	11	747992	4192591

* TSTS = "too small to sample", typically < 2mm in diameter

** ONC = "observed not collected", typically near another collected sample

B.5 Topaz Mountain

Table B-5: Topaz Mountain (TM) sample data. Bolded samples were X-ray fluorescence (XRF) tested and confirmed as "Topaz Mountain" obsidian.

TM SampleID	UTM Zone (WGS84)	Easting	Northing
601	12	327302	4410578
ONC**	12	327579	4410521
ONC	12	327693	4410520
ONC	12	327829	4410510
602	12	328031	4410485
603	**12**	**327417**	**4413687**
ONC	12	327653	4413747
TSTS*	12	328009	4413650
604	12	328002	4413742
ONC	12	327998	4413977
ONC	12	327962	4414021
ONC	12	327761	4414243
605	**12**	**327450**	**4405777**
606	12	327494	4403660
ONC	12	327318	4400284
607	12	327277	4400273
608	**12**	**327280**	**4397797**
ONC	12	327682	4397954
ONC	12	327794	4398003
609	12	327868	4397950
ONC	12	327741	4397769
ONC	12	322616	4399209
610	**12**	**323018**	**4400007**
611	12	322544	4399522
ONC	12	327200	4409345
612	12	327199	4409326
613	12	323172	4404963
ONC	12	322584	4404005
ONC	12	322294	4404207
614	12	322575	4403995
615	12	321505	4403213
ONC	12	321257	4403190
ONC	12	320900	4402993
616	12	320827	4402787
ONC	12	320792	4402760
ONC	12	320733	4402593
ONC	12	320772	4402421
ONC	12	320739	4402326
ONC	12	320656	4402314

TM SampleID	UTM Zone (WGS84)	Easting	Northing
617	12	320615	4402320
ONC	12	320708	4402053
618	**12**	**319718**	**4401542**
619	12	319741	4401504
620	12	319783	4401463
621	12	319783	4401463
ONC	12	320558	4402609
622	12	325759	4397872
623	**12**	**325741**	**4397964**
ONC	12	322401	4398959
624	12	322420	4398985
625	12	321406	4398449
626	12	320784	4398352
ONC	12	320507	4398497
627	12	315132	4396034
ONC	12	316135	4396254
628	**12**	**316730**	**4396455**
629	12	317428	4397183
630	12	314579	4390847
631	12	312158	4389896
632	12	309276	4388517
633	12	305006	4390211
634	**12**	**302737**	**4390037**
635	12	299717	4389475
ONC	12	300901	4388967
ONC	12	313559	4403092
636	12	313653	4403702
637	12	314624	4403682
638	12	314102	4402624
639	12	314154	4402579
640	12	313627	4402934
ONC	12	313560	4403009
ONC	12	313495	4403323
ONC	12	315589	4403103
641	12	315565	4403121
ONC	12	315417	4402939
642	12	315384	4402868
ONC	12	315331	4402859
643	12	315018	4402628
644	12	314892	4402548
ONC	12	314786	4402478
645	12	314754	4402463
646	12	314740	4402473

TM SampleID	UTM Zone (WGS84)	Easting	Northing
ONC	12	314510	4402530
647	**12**	**303269**	**4409570**
648	12	297303	4394063
649	12	297412	4394446
650	12	297575	4394870
651	**12**	**297298**	**4394060**
652	12	296172	4390889
653	**12**	**295973**	**4390188**
654	12	309895	4389768
655	12	309085	4390862
656	12	308379	4391752
657	12	307936	4392375
658	12	307479	4392966
659	12	306906	4393619
660	12	306537	4394240
661	12	305912	4394604
662	12	305311	4395087
663	12	302775	4396959
664	**12**	**302440**	**4397153**
665	12	307371	4396254
666	12	311006	4388295
667	**12**	**316105**	**4393954**
668	12	315824	4391920
669	12	315585	4394540
670	12	313482	4397722
671	**12**	**313051**	**4396715**
672	**12**	**314051**	**4398808**
673	12	314162	4400065
674	12	314878	4401014
675	12	314109	4401907
676	12	313965	4402254
677	12	313528	4403246
678	12	311801	4404501
679	12	312103	4404535
680	12	312486	4404723
ONC	12	311504	4404642
681	**12**	**311159**	**4404935**
682	12	311095	4404891
683	12	311856	4409623
684	**12**	**311949**	**4409661**
685	**12**	**311935**	**4409623**
686	**12**	**311845**	**4409618**
687	12	326386	4408619

TM SampleID	UTM Zone (WGS84)	Easting	Northing
688	**12**	**323854**	**4408226**
689	12	323753	4406710
690	12	323655	4406745
691	12	327941	4408996
ONC	12	311990	4409892
692	12	312127	4409509
693	12	312272	4409437
694	12	312319	4409438
695	12	312316	4409440
TSTS	12	312803	4410979
TSTS	12	313065	4412390
696	12	312860	4413454
697	12	312899	4414743
698	12	312115	4415953
700	12	311103	4417478
701	12	311325	4408835
702	12	309994	4414454
703	12	310204	4413079
704	12	310205	4411779
705	12	309528	4410779
ONC	12	309570	4410776
TSTS	12	310096	4410779
706	12	310747	4408771
708	12	311687	4409046
709	12	297757	4397998

* TSTS = "too small to sample", typically < 2mm in diameter

** ONC = "observed not collected", typically near another collected sample

B.6 Pilot Project Observations

Table B-6: Hunt obsidian observations during 2019 pilot survey.

Source	UTM Zone (WGS84)	Easting	Northing
Black Rock Area	12	340655	4289739
Black Rock Area	12	340564	4289688
Black Rock Area	12	340026	4289274
Black Rock Area	12	339138	4290689
Black Rock Area	12	339621	4290143
Black Rock Area	12	340668	4288861
Black Rock Area	12	336363	4290854
Black Rock Area	12	338831	4285990
Black Rock Area	12	338733	4286014
Black Rock Area	12	339200	4285775
Black Rock Area	12	339160	4285658
Black Rock Area	12	342108	4288192
Black Rock Area	12	341703	4289645
Black Rock Area	12	342108	4288192
Black Rock Area	12	341952	4288100
Black Rock Area	12	341878	4288049
Black Rock Area	12	341855	4288029
Ferguson Wash	11	750290	4476864
Ferguson Wash	11	750136	4476710
Ferguson Wash	11	750116	4476521
Ferguson Wash	11	750286	4476877
Ferguson Wash	11	750302	4476844
Ferguson Wash	11	750267	4477079
Ferguson Wash	11	750266	4477077
Ferguson Wash	11	750289	4476857
Ferguson Wash	11	750346	4477032
Ferguson Wash	11	750341	4477025
Ferguson Wash	11	750335	4477017
Ferguson Wash	11	750220	4476985
Ferguson Wash	11	750083	4476529
Ferguson Wash	11	750161	4476463
Ferguson Wash	11	750274	4476331
Ferguson Wash	11	750316	4476297
Ferguson Wash	11	750388	4476268
Ferguson Wash	11	750488	4476253
Ferguson Wash	11	750543	4476228
Ferguson Wash	11	750606	4476210
Ferguson Wash	11	750746	4476357
Ferguson Wash	11	750802	4476143
Ferguson Wash	11	750909	4476149

Source	UTM Zone (WGS84)	Easting	Northing
Ferguson Wash	11	751028	4476188
Ferguson Wash	11	751180	4476147
Ferguson Wash	11	751282	4476131
Ferguson Wash	11	751461	4476394
Ferguson Wash	11	751580	4476588
Ferguson Wash	11	751730	4476553
Ferguson Wash	11	751776	4476787
Ferguson Wash	11	751812	4476634
Ferguson Wash	11	751836	4476899
Ferguson Wash	11	751882	4476942
Ferguson Wash	11	752008	4477189
Ferguson Wash	11	752051	4476989
Ferguson Wash	11	752558	4476436
Mineral Mountains	12	338768	4256812
Mineral Mountains	12	338744	4256821
Mineral Mountains	12	338796	4256744
Mineral Mountains	12	338818	4256667
Mineral Mountains	12	338863	4256651
Mineral Mountains	12	338817	4256671
Mineral Mountains	12	338890	4256649
Mineral Mountains	12	338896	4256695
Mineral Mountains	12	338911	4256687
Mineral Mountains	12	338911	4256713
Mineral Mountains	12	338938	4256807
Mineral Mountains	12	338782	4256824
Mineral Mountains	12	338702	4256813
Mineral Mountains	12	338614	4256813
Mineral Mountains	12	338557	4256798
Mineral Mountains	12	340497	4262031
Mineral Mountains	12	340944	4261320
Mineral Mountains	12	340786	4261212
Mineral Mountains	12	340746	4261167
Mineral Mountains	12	340202	4261531
Panaca Summit / Modena	11	759510	4189500
Panaca Summit / Modena	11	757259	4190628
Panaca Summit / Modena	11	757261	4190646
Panaca Summit / Modena	11	757263	4190643
Panaca Summit / Modena	11	757278	4190615
Panaca Summit / Modena	11	757263	4190643
Panaca Summit / Modena	11	757276	4190615
Panaca Summit / Modena	11	757273	4190570
Panaca Summit / Modena	11	757280	4190551
Panaca Summit / Modena	11	757478	4190465

Source	UTM Zone (WGS84)	Easting	Northing
Panaca Summit / Modena	11	757520	4190436
Panaca Summit / Modena	11	759439	4189617
Panaca Summit / Modena	11	759510	4189499
Panaca Summit / Modena	11	762194	4186864
Topaz Mountain	12	322748	4400578
Topaz Mountain	12	322670	4400643
Topaz Mountain	12	322729	4403197
Topaz Mountain	12	322590	4402429
Topaz Mountain	12	327541	4406520
Topaz Mountain	12	322528	4402448
Topaz Mountain	12	316811	4400873
Topaz Mountain	12	316731	4400831
Topaz Mountain	12	314299	4395808
Topaz Mountain	12	314296	4395146

B.7 Currie Hills 2021 Observations

Table B-7: Hunt 2021 Currie Hills observations.

Source	UTM Zone (WGS84)	Easting	Northing
Currie Hills	11	694000	4459139
Currie Hills	11	694311	4465092
Currie Hills	11	694303	4465014

Appendix C: X-ray Fluorescence Samples

This appendix lists the field samples that were XRF-confirmed for each of the five survey regions (see Chapter 3 and Appendices E and F).

C.1 Black Rock Area

Table C-1: Black Rock Area XRF-confirmed samples (n=32).

BRA SampleID	UTM Zone (WGS84)	Easting	Northing	NWROSL catalog ID
207	12	360341	4292007	BO-20-86 #1
212	12	359161	4289044	BO-20-86 #2
222	12	360040	4298624	BO-20-86 #3
232	12	358286	4303756	BO-20-86 #4
234	12	355456	4294763	BO-20-86 #5
235	12	351364	4299234	BO-20-86 #6
241	12	356800	4288871	BO-20-86 #7
248	12	354923	4288140	BO-20-86 #8
261	12	342549	4286331	BO-20-86 #9
268	12	345768	4287807	BO-20-86 #10
278	12	345642	4292382	BO-20-86 #11
288	12	349758	4295798	BO-20-86 #12
296	12	347766	4302085	BO-20-86 #13
304	12	339284	4289973	BO-20-86 #14
313	12	341164	4302001	BO-20-86 #15
320	12	335615	4297888	BO-20-86 #16
323	12	331703	4292997	BO-20-86 #17
327	12	335887	4282306	BO-20-86 #19
329	12	331122	4283199	BO-20-86 #20
331	12	327210	4286527	BO-20-86 #21
335	12	330276	4286845	BO-20-86 #23
340	12	334608	4287756	BO-20-86 #24
348	12	336843	4291798	BO-20-86 #25
352	12	338720	4285886	BO-20-86 #26
356	12	355345	4298938	BO-20-86 #27
359	12	347853	4289361	BO-20-86 #28
360A	12	350972	4290811	BO-20-86 #29
360B	12	350972	4290811	BO-20-86 #30
810	12	332881	4275139	BO-20-86 #48
811	12	330266	4275195	BO-20-86 #49
816	12	326514	4267999	BO-20-86 #51
820	12	326119	4260240	BO-20-86 #52

C.2 Ferguson Wash

Table C-2: Ferguson Wash XRF-confirmed samples (n=13).

FW Sample ID	UTM Zone (WGS84)	Easting	Northing	NWROSL catalog ID
4	11	751797	4476886	BO-21-64 #31
8	11	752417	4477699	BO-21-64 #32
13	11	751114	4475904	BO-21-64 #33
15	11	750729	4476077	BO-21-64 #34
16	11	750287	4476877	BO-21-64 #35
17	11	750204	4476939	BO-21-64 #36
18	11	750179	4476968	BO-21-64 #37
20	11	750134	4477585	BO-21-64 #38
21	11	751075	4476348	BO-21-64 #39
24	11	752364	4476040	BO-21-64 #40
25	11	753788	4477590	BO-21-64 #41
29	11	753191	4479001	BO-21-64 #42
32	11	753839	4476883	BO-21-64 #43

C.3 Mineral Mountains

Table C-3: Mineral Mountains XRF-confirmed samples (n=22).

MM SampleID	UTM Zone (WGS84)	Easting	Northing	NWROSL catalog ID
801	12	342455	4260425	BO-20-86 #44
805	12	340677	4262227	BO-20-86 #45
807	12	338855	4262685	BO-20-86 #46
808	12	340712	4258246	BO-20-86 #47
813A	12	326881	4273539	BO-20-86 #105
813B	12	326881	4273539	BO-20-86 #106
814	12	326814	4272812	BO-20-86 #107
815	12	326632	4271140	BO-20-86 #108
817	12	326409	4266146	BO-20-86 #109
818	12	326379	4264039	BO-20-86 #110
819	12	326323	4261755	BO-20-86 #111
822	12	332708	4257149	BO-20-86 #112
829	12	341538	4259976	BO-20-86 #54
835	12	341171	4257099	BO-20-86 #55
839	12	339941	4256427	BO-20-86 #56
848	12	338485	4260887	BO-20-86 #59
849	12	325358	4256371	BO-20-86 #60
850	12	325269	4255479	BO-20-86 #114
857	12	335569	4259735	BO-20-86 #61
858	12	333381	4266441	BO-20-86 #62
862	12	335196	4264363	BO-20-86 #63
864	12	332859	4271842	BO-20-86 #64

C.4 Panaca Summit / Modena

Table C-4: Panaca Summit/Modena XRF-confirmed samples (n=28).

PS/M SampleID	UTM Zone (WGS84)	Easting	Northing	NWROSL catalog ID
100	12	266170	4187978	BO-20-86 #65
103	11	740694	4197861	BO-20-86 #66
401	11	761562	4188187	BO-20-86 #67
412	11	758224	4192890	BO-20-86 #68
414	11	756840	4194313	BO-20-86 #69
417	11	761517	4179640	BO-20-86 #70
426	12	261117	4180887	BO-20-86 #71
433	11	755481	4184630	BO-20-86 #72
436	11	758579	4179663	BO-20-86 #73
439	12	242574	4185462	BO-20-86 #74
443	12	244958	4181036	BO-20-86 #75
447	12	251402	4180365	BO-20-86 #76
448	12	262910	4186448	BO-20-86 #77
449	12	255005	4190866	BO-20-86 #78
451	11	755717	4192826	BO-20-86 #79
456	12	241683	4190314	BO-20-86 #80
461	12	238909	4185866	BO-20-86 #82
472	11	750074	4187943	BO-21-64 #1
473	11	752083	4188889	BO-21-64 #2
483	11	744191	4192726	BO-21-64 #3
488	11	738629	4191722	BO-21-64 #4
489	11	736746	4192648	BO-21-64 #5
494	11	746531	4197550	BO-21-64 #6
501	11	744496	4195246	BO-21-64 #7
503	11	743614	4195614	BO-21-64 #8
506	11	736524	4197825	BO-21-64 #9
509	11	749385	4195383	BO-21-64 #10
510	11	749527	4194188	BO-21-64 #11

C.5 Topaz Mountain

Table C-5: Topaz Mountain XRF-confirmed samples (n=22).

TM SampleID	UTM Zone (WGS84)	Easting	Northing	NWROSL catalog ID
603	12	327417	4413687	BO-20-86 #83
605	12	327450	4405777	BO-20-86 #84
608	12	327280	4397797	BO-20-86 #85
610	12	323018	4400007	BO-20-86 #86
618	12	319718	4401542	BO-20-86 #87
623	12	325741	4397964	BO-20-86 #88
628	12	316730	4396455	BO-20-86 #89
634	12	302737	4390037	BO-20-86 #90
647	12	303269	4409570	BO-20-86 #91
651	12	297298	4394060	BO-20-86 #92
653	12	295973	4390188	BO-20-86 #93
664	12	302440	4397153	BO-20-86 #94
665	12	307371	4396254	BO-20-86 #95
666	12	311006	4388295	BO-20-86 #96
667	12	316105	4393954	BO-20-86 #97
671	12	313051	4396715	BO-20-86 #98
672	12	314051	4398808	BO-20-86 #99
681	12	311159	4404935	BO-20-86 #100
684	12	311949	4409661	BO-20-86 #101
685	12	311935	4409623	BO-20-86 #102
686	12	311845	4409618	BO-20-86 #103
688	12	323854	4408226	BO-20-86 #104

Appendix D: Supporting Sample Data

This appendix catalogues natural obsidian and FGV sample data by various authors for the

sources utilized in the ORB delta.

Table D-1: Hull (1994) X-ray fluorescence (XRF) sample township-range locations and their conversion to latitude and longitude coordinates (WGS84)

Source	ID	Township and Range	Centroid † Latitude	Centroid Longitude
Black Rock Area	BR-1	NWNWSW 13 24S 9W UT	38.7232218	-112.8219975
Black Rock Area	BR-2	NWSWNW 12 24S 9W UT	38.7418582	-112.8214867
Black Rock Area	BR-3	NENWSW 36 23S 9W UT	38.7677413	-112.8203949
Black Rock Area	BR-4	SWSESW 35 23S 9W UT	38.7641468	-112.834278
Black Rock Area	BR-5	NWNWSE 26 23S 9W UT	38.7822631	-112.8296661
Black Rock Area	BR-6	SENWSE 26 23S 9W UT	38.7822631	-112.8296661
Black Rock Area	BR-7	SWNESW 24 23S 9W UT	38.7967276	-112.8157881
Negro Mag Wash [Bailey Ridge, Mineral Mtns]	NM-1	NWNWSE 1 27S 9W UT	38.4898364	-112.8130553
Negro Mag Wash [Bailey Ridge, Mineral Mtns]	NM-2	SWSESE 1 27S 9W UT	38.4862149	-112.8084321
Negro Mag Wash [Bailey Ridge, Mineral Mtns]	NM-3	SWSESE 1 27S 9W UT	38.4862149	-112.8084321
Negro Mag Wash [Bailey Ridge, Mineral Mtns]	NM-4	SENENE 12 27S 9W UT	38.48259	-112.8084117
Negro Mag Wash [Bailey Ridge, Mineral Mtns]	NM-5	NENESE 2 27S 9W UT	38.4898206	-112.8268561
Negro Mag Wash [Bailey Ridge, Mineral Mtns]	NM-6	NWSWSE 2 27S 9W UT	38.4861896	-112.8314395
Negro Mag Wash [Bailey Ridge, Mineral Mtns]	NM-7	SENWSE 2 27S 9W UT	38.489813	-112.8314517
Negro Mag Wash [Bailey Ridge, Mineral Mtns]	NM-8	SESESE 2 27S 9W UT	38.4861975	-112.8268437
Wild Horse Canyon [Mineral Mtns]	WH-1	SENWSE 22 27S 9W UT	38.4463265	-112.8497395
Wild Horse Canyon [Mineral Mtns]	WH-2	SWNWSE 23 27S 9W UT	38.4463139	-112.8313305
Wild Horse Canyon [Mineral Mtns]	WH-3	SWNWNW 24 27S 9W UT	38.4535663	-112.8221501
Wild Horse Canyon [Mineral Mtns]	WH-4	SENENW 24 27S 9W UT	38.4535742	-112.8175472
Wild Horse Canyon [Mineral Mtns]	WH-5	SWNENW 24 27S 9W UT	38.4535742	-112.8175472
Wild Horse Canyon [Mineral Mtns]	WH-6	NWNWSW 24 27S 9W UT	38.4463178	-112.8221334
Wild Horse Canyon [Mineral Mtns]	WH-7	NWNWSW 24 27S 9W UT	38.4463178	-112.8221334

Source	ID	Township and Range	Centroid † Latitude	Centroid Longitude
Wild Horse Canyon [Mineral Mtns]	WH-8	NESESE 23 27S 9W UT	38.4426903	-112.8267253
Wild Horse Canyon [Mineral Mtns]	WH-9	SWSWNW 23 27S 9W UT	38.4499361	-112.8405294
Wild Horse Canyon [Mineral Mtns]	WH-10	NENWSW 23 27S 9W UT	38.4463128	-112.8405252
Wild Horse Canyon [Mineral Mtns]	WH-11	NENWSW 23 27S 9W UT	38.4463128	-112.8405252
Wild Horse Canyon [Mineral Mtns]	WH-12	NESESW 23 27S 9W UT	38.4426898	-112.8359225
Wild Horse Canyon [Mineral Mtns]	WH-13	NWSENE 22 27S 9W UT	38.4499407	-112.8451332
Wild Horse Canyon [Mineral Mtns]	WH-14	SWNESE 22 27S 9W UT	38.4463173	-112.8451292
Modena	M-01	NESESE 1 34S 19W UT	37.8693114	-113.9167252
Modena	M-02	SWSENE 20 1S 71E NV	37.8479157	-114.0647501
Modena	M-03	SESESE 36 34S 20W UT	37.7966774	-114.0260685
Modena *	M-04	SESESE 35 1S 70E NV	37.810913	-114.118534
Modena **	M-05	NESENE 2 2S 70E NV	37.805302	-114.118605
Modena *	M-06	SESENE 2 2S 70E NV	37.803654	-114.118646
Modena	M-07	NWNWSE 32 1S 71E NV	37.8153024	-114.0693187
Modena *	M-08	NWNWNE 5 2S 71E NV	37.808813	-114.070304
Modena ***	M-09	NWSESE 36 1S 70E NV	37.812513	-114.102208
Modena *	M-10	NESWNE 36 1S 70E NV	37.81983	-114.105074
Topaz Mtn	T-1	SESESW 22 12S 11W UT	39.7573398	-113.0732351
Topaz Mtn	T-2	NWNWNW 33 12S 11W UT	39.7391769	-113.0969001
Topaz Mtn	T-3	NWSENW 28 12S 11W UT	39.7500723	-113.0921471
Topaz Mtn	T-4	SENENE 19 12S 11W UT	39.7681815	-113.1203614
Topaz Mtn	T-5	NWSWSW 22 12S 11W UT	39.7573428	-113.0779613
Topaz Mtn	T-6	SESWSE 27 12S 11W UT	39.7428071	-113.0686701
Topaz Mtn *	T-7	SESWNE 24 13S 12W UT	39.676654	-113.142123
Topaz Mtn *	T-8	NENWNW 1 13S 12W UT	39.725644	-113.151578
Topaz Mtn	T-9	NESWNW 36 12S 12W UT	39.7355532	-113.152728
Topaz Mtn *	T-10	NESWNE 14 13S 12W UT	39.692492	-113.160865

Table D-1 Notes:

† Township and range locations were converted to centroid latitudes and longitudes using Earth Point (Clark 2021)

* Quarter/Quarter does not exist for this section, visually located quarter/quarter/quarter centroid using Google Earth (2020) and the Earthpoint PLSS overlay.

** There appears to be a typographical error in Hull (1994) Table 7-2 for this location. Township "2S1" was corrected to 2S. Quarter/Quarter does not exist for this section; I visually located quarter/quarter/quarter centroid using Google Earth and the Earthpoint PLSS overlay.

*** There appears to be a typographical error in Hull (1994) Table 7-2 for this location. Township 15S is more than 100 km from the PS/M location. This township corrected to 1S. Quarter/Quarter does not exist for this section; I visually located quarter/quarter/quarter centroid using Google Earth and the Earthpoint PLSS overlay.

Table D-2: Sample data provided by Craig Skinner, personal comm., May 13, 2021, see also www.sourcecatalog.com and www.deschutesmeridian.com.

Geochemical Source	NWROSL #	UTM Zone (WGS84)	Easting/Lat	Northing/Long
Badlands A/Wildcat Mountain FGV	SO-65-1058	12	244952	4449974
Badlands A/Wildcat Mountain FGV	SO-65-1060	12	303328	4478808
Badlands A/Wildcat Mountain FGV	SO-65-1392	11	753205	4449458
Badlands A/Wildcat Mountain FGV	SO-65-1393	11	753372	4449005
Badlands A/Wildcat Mountain FGV	SO-65-1394	11	742606	4463279
Badlands A/Wildcat Mountain FGV	SO-65-1395	11	748234	4453084
Badlands A/Wildcat Mountain FGV	SO-65-1396	11	748153	4453084
Badlands A/Wildcat Mountain FGV	SO-65-1397	11	748507	4448934
Badlands A/Wildcat Mountain FGV	SO-65-1398	11	751519	4448934
Badlands A/Wildcat Mountain FGV	SO-65-1400	11	747450	4443046
Badlands A/Wildcat Mountain FGV	SO-65-1401	11	742451	4439893
Badlands A/Wildcat Mountain FGV	SO-65-1403	11	741948	4439385
Badlands A/Wildcat Mountain FGV	SO-65-1404	11	749244	4441846
Badlands A/Wildcat Mountain FGV	SO-65-1405	11	753049	4451173
Badlands A/Wildcat Mountain FGV	SO-65-1406	11	751834	4451541
Badlands A/Wildcat Mountain FGV	SO-65-1407	11	752108	4451452
Badlands A/Wildcat Mountain FGV	SO-65-1421	12	250918	4466353
Badlands A/Wildcat Mountain FGV	SO-65-1422	12	251052	4466458
Badlands A/Wildcat Mountain FGV	SO-65-1423	12	250940	4466345
Badlands A/Wildcat Mountain FGV	SO-65-1456	11	738165	4451555
Badlands A/Wildcat Mountain FGV	SO-65-1461	11	738392	4449635
Badlands A/Wildcat Mountain FGV	SO-65-1462	11	738903	4445531
Badlands A/Wildcat Mountain FGV	SO-65-1463	11	742542	4446136
Badlands A/Wildcat Mountain FGV	SO-65-1464	11	747859	4446631
Badlands A/Wildcat Mountain FGV	SO-65-1472	12	302054	4478767
Badlands A/Wildcat Mountain FGV	SO-65-1473	12	302715	4478888
Badlands A/Wildcat Mountain FGV	SO-65-1778	11	629198	4424291
Bear Gulch	SO-65-342	NA	-112.01	44.46
Bear Gulch	SO-65-343	NA	-111.98	44.46
Bear Gulch	SO-65-345	NA	-111.98	44.45
Bear Gulch	SO-65-346	NA	-111.96	44.44
Bear Gulch	SO-65-347	NA	-111.94	44.42
Bear Gulch	SO-65-352	NA	-112.01	44.46
Bear Gulch	SO-65-353	NA	-111.98	44.45
Black Rock Area	SO-65-1592	NA	38.74	-112.65
Black Rock Area	SO-65-1352	NA	38.75	-112.7
Black Rock Area	SO-65-1353	NA	38.75	-112.78

Geochemical Source	NWROSL #	UTM Zone (WGS84)	Easting/Lat	Northing/Long
Black Rock Area	SO-65-1354, SO-65-1355	NA	38.77	-112.82
Black Rock Area	SO-65-1606	NA	38.78	-112.82
Black Rock Area	SO-65-1607	NA	38.79	-112.82
Black Rock Area	SO-65-1603	NA	38.72	-112.83
Black Rock Area	SO-65-1604	NA	38.73	-112.83
Black Rock Area	SO-65-1605	NA	38.74	-112.84
Black Rock Area	SO-65-1356	NA	38.76	-112.84
Browns Bench	SO-65-1224	11	729800	4666375
Browns Bench	SO-65-1300	11	738309	4676137
Browns Bench	SO-65-1301	11	737676	4674464
Browns Bench	SO-65-1302	11	737019	4673806
Browns Bench	SO-65-1303	11	714117	4681395
Browns Bench	SO-65-1304	11	714184	4676886
Browns Bench	SO-65-1305	11	725606	4681240
Browns Bench	SO-65-1306	11	691175	4645282
Browns Bench	SO-65-1307	11	684035	4646333
Browns Bench	SO-65-1308	11	684882	4647606
Browns Bench	SO-65-1311	11	718879	4697018
Browns Bench	SO-65-1555	11	731955	4683065
Browns Bench	SO-65-1557	11	551695	4781340
Browns Bench	SO-65-1572	11	552335	4782040
Browns Bench	SO-65-1573	11	556200	4776660
Browns Bench	SO-65-1583	11	682592	4780682
Browns Bench	SO-65-1597	11	745958	4649756
Browns Bench	SO-65-1610	11	683853	4781495
Browns Bench	SO-65-1611	11	683853	4781495
Browns Bench	SO-65-1634	11	537134	4772431
Browns Bench	SO-65-1654	11	741105	4660041
Browns Bench	SO-65-1655	11	739568	4661621
Browns Bench	SO-65-1656	11	747932	4677836
Browns Bench	SO-65-1657	11	746146	4681158
Browns Bench	SO-65-1658	11	746153	4682749
Browns Bench	SO-65-1744	11	583942	4759722
Browns Bench	SO-65-1745	11	587042	4754324
Browns Bench	SO-65-1746	11	605814	4755078
Browns Bench	SO-65-1747	11	629076	4765556
Browns Bench	SO-65-1756	11	586240	4755513
Browns Bench	SO-65-1757	11	671345	4723759
Browns Bench	SO-65-1758	11	671345	4723759

Geochemical Source	NWROSL #	UTM Zone (WGS84)	Easting/Lat	Northing/Long
Browns Bench	SO-65-1764	11	561582	4766323
Browns Bench	SO-65-1765	11	559131	5766358
Browns Bench	SO-65-1767	11	601456	4757271
Browns Bench	SO-65-1770	12	263365	4661070
Browns Bench	SO-65-1832	11	598904	4759102
Browns Bench	SO-65-1833	11	597936	4759524
Browns Bench	SO-65-1834	11	605374	4753701
Browns Bench	SO-65-1835	11	649866	4752094
Browns Bench	SO-65-1836	11	598099	4756295
Browns Bench	SO-65-1837	11	588744	4760306
Browns Bench	SO-65-1838	11	660720	4674777
Browns Bench	SO-65-1888	11	740575	4800803
Browns Bench	SO-65-1892	12	263365	4661070
Browns Bench Area	SO-65-1747	11	629076	4765556
Browns Bench Area	SO-65-1758	11	671345	4723759
Browns Bench Area	SO-65-1764	11	561582	4766323
Browns Bench Area	SO-65-1767	11	601456	4757271
Browns Bench/Butte Valley Group A	SO-65-1573	11	556200	4776660
Browns Bench/Butte Valley Group A	SO-65-1583	11	682592	4780682
Browns Bench/Butte Valley Group A	SO-65-1597	11	745958	4649756
Browns Bench/Butte Valley Group A	SO-65-1610	11	683853	4781495
Browns Bench/Butte Valley Group A	SO-65-1611	11	683853	4781495
Browns Bench/Butte Valley Group A	SO-65-1636	11	754192	4679257
Browns Bench/Butte Valley Group A	SO-65-1758	11	671345	4723759
Cedar Mountains B FGV	SO-65-1057	12	333100	4460300
Currie Hills FGV	BO-18-81	11	703961	4449355
Deep Creek A FGV	SO-65-1058	12	244952	4449974
Deep Creek A FGV	SO-65-1392	11	753205	4449458
Deep Creek A FGV	SO-65-1393	11	753372	4449005
Deep Creek A FGV	SO-65-1394	11	742606	4463279
Deep Creek A FGV	SO-65-1395	11	748234	4453084
Deep Creek A FGV	SO-65-1397	11	748507	4448934
Deep Creek A FGV	SO-65-1405	11	753049	4451173
Deep Creek A FGV	SO-65-1406	11	751834	4451541
Deep Creek A FGV	SO-65-1407	11	752108	4451452
Deep Creek A FGV	SO-65-1456	11	738256	4451574
Deep Creek A FGV	SO-65-1457	11	738165	4451555
Deep Creek A FGV	SO-65-1458	11	738177	4451485
Deep Creek A FGV	SO-65-1459	11	738179	4451480

Geochemical Source	NWROSL #	UTM Zone (WGS84)	Easting/Lat	Northing/Long
Deep Creek A FGV	SO-65-1460	11	738179	4451480
Deep Creek A FGV	SO-65-1464	11	747859	4446631
Ferguson Wash	SO-65-886	NA	40.4	-114.01
Ferguson Wash	SO-65-893, SO-65-894, SO-65-895, SO-65-1435, SO-65-1593	NA	40.4	-114.01
Ferguson Wash	SO-65-896	NA	40.39	-114.05
Ferguson Wash	SO-65-1436	NA	40.41	-114.05
Kane Springs Wash Caldera Variety 1	SO-65-1085	11	688460	4121647
Kane Springs Wash Caldera Variety 1	SO-65-1086	11	683478	4096390
Kane Springs Wash Caldera Variety 1	SO-65-1129	11	689120	4122894
Kane Springs Wash Caldera Variety 1	SO-65-1130	11	691265	4122894
Kane Springs Wash Caldera Variety 1	SO-65-1151	11	697927	4126450
Kane Springs Wash Caldera Variety 1	SO-65-1153	11	695734	4128981
Kane Springs Wash Caldera Variety 1	SO-65-1154	11	698950	4117483
Kane Springs Wash Caldera Variety 1	SO-65-1155	11	699886	4118146
Kane Springs Wash Caldera Variety 1	SO-65-1156	11	700335	4126455
Kane Springs Wash Caldera Variety 1	SO-65-1157	11	702949	4125428
Kane Springs Wash Caldera Variety 1	SO-65-1158	11	709033	4125674
Kane Springs Wash Caldera Variety 1	SO-65-1159	11	710409	4120123
Kane Springs Wash Caldera Variety 1	SO-65-1160	11	714079	4121192
Kane Springs Wash Caldera Variety 1	SO-65-1161	11	714627	4120631
Kane Springs Wash Caldera Variety 1	SO-65-1212	11	708256	4126353
Kane Springs Wash Caldera Variety 1	SO-65-1213	11	708671	4125397
Kane Springs Wash Caldera Variety 1	SO-65-1214	11	708256	4126353
Kane Springs Wash Caldera Variety 1	SO-65-1225	11	706580	4123430
Kane Springs Wash Caldera Variety 2	SO-65-924	11	707995	4128520
Kane Springs Wash Caldera Variety 2	SO-65-1122	11	689120	4122894
Kane Springs Wash Caldera Variety 2	SO-65-1123	11	706582	4124352
Kane Springs Wash Caldera Variety 2	SO-65-1158	11	709033	4125674
Kane Springs Wash Caldera Variety 2	SO-65-1161	11	714627	4120631
Kane Springs Wash Caldera Variety 2	SO-65-1211	11	708761	4125734
Kane Springs Wash Caldera Variety 2	SO-65-1215	11	708671	4125397
Malad	SO-65-62	NA	-112.38	42.42
Mineral Mountains	SO-65-1599	NA	38.48	-112.81
Mineral Mountains	SO-65-1598	NA	38.47	-112.82
Mineral Mountains	SO-65-1062, SO-65-1063	NA	38.49	-112.83

Geochemical Source	NWROSL #	UTM Zone (WGS84)	Easting/Lat	Northing/Long
Mineral Mountains	SO-65-1601	NA	38.44	-112.82
Mineral Mountains	SO-65-1349, SO-65-1350, SO-65-1351	NA	38.46	-112.83
Mineral Mountains	SO-65-1600	NA	38.45	-112.85
Mineral Mountains	SO-65-1377, SO-65-1378	NA	38.44	-112.86
Mineral Mountains	SO-65-1361	NA	38.47	-112.9
Owyhee	SO-65-184	11	468739	4834203
Owyhee	SO-65-933	11	531680	4743380
Owyhee	SO-65-967	11	534018	4747532
Owyhee	SO-65-968	11	534772	4747628
Owyhee	SO-65-969	11	537109	4749954
Owyhee	SO-65-970	11	539623	4753707
Owyhee	SO-65-971	11	539885	4753888
Owyhee	SO-65-972	11	539322	4753789
Owyhee	SO-65-973	11	537109	4749954
Owyhee	SO-65-974	11	536606	4757617
Owyhee	SO-65-975	11	533157	4764722
Owyhee	SO-65-976	11	539824	4749402
Owyhee	SO-65-977	11	535533	4747199
Owyhee	SO-65-978	11	534233	4743760
Owyhee	SO-65-979	11	533006	4747313
Owyhee	SO-65-980	11	532004	4747343
Owyhee	SO-65-981	11	535312	4742203
Owyhee	SO-65-982	11	542795	4758502
Owyhee	SO-65-983	11	538820	4754380
Owyhee	SO-65-984	11	535533	4747199
Owyhee	SO-65-985	11	534018	4747532
Owyhee	SO-65-996	11	546460	4758620
Owyhee	SO-65-997	11	555320	4759155
Owyhee	SO-65-998	11	559555	7765770
Owyhee	SO-65-999	11	545635	4770600
Owyhee	SO-65-1003	11	552164	4769325
Owyhee	SO-65-1004	11	540747	4748305
Owyhee	SO-65-1007	11	539522	4777675
Owyhee	SO-65-1008	11	536636	4760240
Owyhee	SO-65-1015	11	539340	4776030
Owyhee	SO-65-1016	11	538370	4774020
Owyhee	SO-65-1017	11	537355	4772440

Geochemical Source	NWROSL #	UTM Zone (WGS84)	Easting/Lat	Northing/Long
Owyhee	SO-65-1066	11	557463	4773361
Owyhee	SO-65-1067	11	557109	4756265
Owyhee	SO-65-1068	11	558134	4753104
Owyhee	SO-65-1102	11	460937	4839035
Owyhee	SO-65-1109	11	463151	4833380
Owyhee	SO-65-1453	11	511810	4763265
Owyhee	SO-65-1475	11	509770	4763990
Owyhee	SO-65-1477	11	507893	4764560
Owyhee	SO-65-1479	11	508330	4759680
Owyhee	SO-65-1480	11	518770	4745650
Owyhee	SO-65-1503	11	474150	4831450
Owyhee	SO-65-1504	11	474140	4835300
Owyhee	SO-65-1557	11	551695	4781340
Owyhee	SO-65-1572	11	552335	4782040
Owyhee	SO-65-1573	11	556200	4776660
Owyhee	SO-65-1633	11	535511	4773060
Owyhee	SO-65-1634	11	537134	4772431
Owyhee	SO-65-1635	11	538220	4776265
Owyhee	SO-65-1708	11	500290	4789600
Owyhee	SO-65-1766	11	549311	4767942
Owyhee	SO-65-1862	11	485675	4829861
Panaca Summit/Modena	SO-65-1121	NA	37.73	-114.03
Panaca Summit/Modena	SO-65-802	NA	37.82	-114.04
Panaca Summit/Modena	SO-65-1366	NA	37.81	-114.06
Panaca Summit/Modena	SO-65-1367	NA	37.81	-114.07
Panaca Summit/Modena	SO-65-801	NA	37.83	-114.08
Panaca Summit/Modena	SO-65-1364, SO-65-1365	NA	37.82	-114.08
Panaca Summit/Modena	SO-65-1369, SO-65-1589	NA	37.83	-114.09
Panaca Summit/Modena	SO-65-1738	NA	37.9	-114.27
Paradise Valley	SO-65-260	10	455050	4606645
Paradise Valley	SO-65-1222	11	463243	4612710
Paradise Valley	SO-65-1659	10	458072	4620791
Pumice Hole Mine	SO-65-1350	12	340344	4258295
Pumice Hole Mine	SO-65-1351	12	340528	4258207
Pumice Hole Mine	SO-65-1376	12	337966	4256545
Topaz Mountain	SO-65-810, SO-65-1596	NA	39.74	-113.13
Topaz Mountain	SO-65-811	NA	39.73	-113.13

Geochemical Source	NWROSL #	UTM Zone (WGS84)	Easting/Lat	Northing/Long
Topaz Mountain	SO-65-812	NA	39.76	-113.07
Topaz Mountain	SO-65-813	NA	39.75	-113.09
Topaz Mountain	SO-65-814	NA	39.76	-113.06
Topaz Mountain	SO-65-1430	NA	39.74	-113.07
Topaz Mountain	SO-65-1427, SO-65-1428, SO-65-1429	NA	39.77	-113.07
Topaz Mountain	SO-65-1432	NA	39.71	-113.16
Topaz Mountain	SO-65-1433	NA	39.74	-113.16
Topaz Mountain	SO-65-1431	NA	39.69	-113.17
Topaz Mountain	SO-65-1434	NA	39.81	-113.2

Table D-3: Panaca Summit/Modena natural obsidian samples by Talbot et al. (2015).

Natural nodule sample	Easting (NAD27Z11)	Northing (NAD27Z11)
JA-1	759831	4186737
JA-2	759896	4186710
JA-3	759687	4185230
JA-4	759791	4180982
JA-5	759771	4182339
JA-6	759701	4182073
JB-5	757586	4190451
JB-6	757339	4190441
KR-2	756466	4193492
KR-3	759574	4190680
KR-4	759095	4190598
LJ-1	759196	4191736
LJ-10	758010	4190859
LJ-14	757105	4190457
LJ-16	755988	4191422
LJ-2	759127	4191583
LJ-3	759127	4191583
LJ-4	757245	4193496
LJ-7	755857	4191261
MR-1	757998	4185663
MR-10	760212	4189658
MR-11	761200	4188420
MR-12	761783	4187300
MR-13	761937	4186192
MR-14	760789	4184959
MR-15	760723	4183960
MR-2	758056	4184285
MR-3	758030	4183609
MR-4	758660	4193095
MR-5	758675	4192244
MR-6	758086	4180124
MR-7	758022	4180757
MR-8	758034	4182237
MR-9	758048	4183071
RT-13	754080	4185885
RT-14	761465	4186802
RT-15	758266	4186217
RT-16	757797	4186491
RT-17	757864	4186709
RT-18	757644	4187131
RT-19	757278	4187595
RT-21	755920	4187798
RT-22	756321	4187554

Natural nodule sample	Easting (NAD27Z11)	Northing (NAD27Z11)
RT-23	756656	4187064
RT-24	757257	4186835
RT-25	758005	4186306
RT-26	760393	4187273
RT-27	757525	4193491
RT-28	758085	4192840
RT-29	760150	4191500
RT-3	759224	4186746
RT-5	756500	4185760
RT-6	755800	4185650
RT-7	754760	4186060
SF-1	756041	4185161
SF-2	755914	4185277
SF-3	755914	4185277
SF-4	759423	4191781
SF-5	756064	4183421
SU-12	755585	4190362
SU-4	758626	4189883
SU-9	758200	4191400
M2	242893	4186241
M3	242893	4186241
M4	242748	4185255

Table D-4: Sample data provided by Richard Holmer (personal comm., July 24, 2019).

Chemical Type	Obsidian source	NAD83 Latitude	NAD83 Longitude
Bear Gulch	Bear Gulch	44.47782	-111.99007
Bear Gulch	Bear Gulch Camas Creek	44.49806	-111.93884
Bear Gulch	Bear Gulch east	44.45367	-111.97319
Bear Gulch	Bear Gulch lower	44.44906	-111.97404
Brown's Bench	Blue Hill Road Cut	42.05301	-113.93385
Brown's Bench	Coal Banks 1	42.06944	-113.98102
Brown's Bench	Coal Banks 2	42.06808	-113.98144
Brown's Bench	Coal Banks 3	42.05438	-113.9785
Brown's Bench	Coal Banks 4	42.05491	-113.97877
Brown's Bench	Coal Banks 5	42.05485	-113.97768
Brown's Bench	House Creek 1	42.10297	-115.02393
Brown's Bench	House Creek 2	42.09665	-115.02002
Brown's Bench	House Creek 3	42.08971	-115.01756
Brown's Bench	House Creek 4	42.07918	-115.01694
Brown's Bench	Ibex Hollow 1	42.13719	-114.07437
Brown's Bench	Ibex Hollow 2	42.13027	-114.0713
Brown's Bench	Ibex Hollow 3	42.13546	-114.07487
Brown's Bench	Old Man 1	42.06061	-114.87823
Brown's Bench	Old Man 2	42.06014	-114.88472
Brown's Bench	Old Man 3	42.06018	-114.88334
Brown's Bench	Young Man 1	42.06764	-114.86072
Brown's Bench	Young Man 2	42.06941	-114.86059
Malad	Malad	42.46599	-112.39963
Owyhee	Browns Creek	42.95533	-116.4981
Owyhee	Castle Creek	42.89381	-116.55782
Owyhee	Meadow Creek	42.84706	-116.61188
Owyhee	Oreana	43.02389	-116.39416

Table D-5: Page (2008) fine-grained volcanic (FGV) samples.

Source	Catalog #	Latitude	Longitude
Badlands A	UR-06	40.19336	-114.08491
Badlands A	UR-08	40.15502	-114.04703
Badlands A	UR-10	40.10324	-114.09698
Badlands A	UR-11	40.07632	-114.15676
Badlands A	UR-13	40.0719	-114.16284
Badlands A	UR-14	40.09192	-114.07645
Badlands A	UR-31	40.31247	-113.93115
Badlands A	UR-33	40.31346	-113.92961
Badlands A	UR-102	40.18265	-114.2016
Badlands A	UR-108	40.12888	-114.19664
Badlands A	UR-110	40.13248	-114.15336
Badlands A	UR-111	40.13248	-114.15336
Badlands A	UR-113	40.13538	-114.09076
Badlands B	UR-12	40.07549	-114.16927
Cedar Mountain A	1296-4	40.29945	-112.92899
Cedar Mountain A	1296-6	40.29924	-112.92902
Cedar Mountain A	1296-7	40.29854	-112.92859
Cedar Mountain A	1296-13	40.30933	-112.92129
Cedar Mountain A	UR-20	40.31025	-112.94454
Cedar Mountain B	1336-1	40.2804	-112.94367
Cedar Mountain B	1336-2	40.28449	-112.94239
Cedar Mountain B	1336-3	40.27900	-112.94159
Cedar Mountain B	1336-4	40.28441	-112.9399
Cedar Mountain B	1336-5	40.28254	-112.94195
Cedar Mountain B	1296-2	40.30372	-112.92837
Cedar Mountain B	1296-8	40.29675	-112.9285
Cedar Mountain B	1296-9	40.29571	-112.92913
Cedar Mountain B	1296-10	40.29369	-112.92957
Cedar Mountain B	1296-11	40.2869	-112.93807
Cedar Mountain B	1296-17	40.30205	-112.92801
Cedar Mountain B	1296-19	40.30203	-112.92965
Cedar Mountain B	1296-20	40.3009	-112.93194
Cedar Mountain B	1296-21	40.2804	-112.94367
Cedar Mountain C	1296-3	40.30415	-112.92791
Cedar Mountain D	1296-5	40.29948	-112.92927
Cedar Mountain D	1296-12	40.3095	-112.9215
Cedar Mountain D	UR-19	40.30584	-112.9645
Cedar Mountain E	1296-18	40.30203	-112.92899
Cedar Mountain F	1296-15	40.30548	-112.92524

Source	Catalog #	Latitude	Longitude
Cedar Mountain G	1296-16	40.30462	-112.92571
Cedar Mountain H	1296-14	40.30917	-112.92205
Cedar Mountain I	1296-1	40.29343	-112.93133
Deep Creek A	UR-01	40.15923	-114.02706
Deep Creek A	UR-02	40.15902	-114.02817
Deep Creek A	UR-04	40.28672	-114.14614
Deep Creek A	UR-05	40.19334	-114.08396
Deep Creek A	UR-07	40.19202	-114.0808
Deep Creek A	UR-15	40.1747	-114.02821
Deep Creek A	UR-17	40.17787	-114.03913
Deep Creek A	UR-100	40.18264	-114.2016
Deep Creek A	UR-101	40.18264	-114.2016
Deep Creek A	UR-103	40.18249	-114.20267
Deep Creek A	UR-104	40.18186	-114.20255
Deep Creek A	UR-105	40.18186	-114.20255
Deep Creek A	UR-106	40.18181	-114.20253
Deep Creek A	UR-107	40.16515	-114.20072
Deep Creek A	UR-112	40.13538	-114.09084
Deep Creek C	UR-16	40.17838	-114.04232
Deep Creek D	UR-09	40.14694	-114.06275
Deep Creek E	UR-32	40.31241	-113.93088
Flat Hills A	1335-2	40.1957	-112.74256
Flat Hills A	1335-3	40.19571	-112.74258
Flat Hills A	1335-4	40.19545	-112.74275
Flat Hills A	1335-6	40.1996	-112.75451
Flat Hills A	1335-7	40.20161	-112.75409
Flat Hills A	1335-8	40.19963	-112.75303
Flat Hills A	UR-21	40.19887	-112.75827
Flat Hills A	UR-22	40.20139	-112.75872
Flat Hills A	UR-25	40.20043	-112.7559
Flat Hills A	UR-26	40.20187	-112.75731
Flat Hills A	UR-28	40.20186	-112.7573
Flat Hills A	UR-29	40.20246	-112.75399
Flat Hills B	1335-1	40.18869	-112.75368
Flat Hills B	UR-23	40.20136	-112.7588
Flat Hills C	1335-5	40.16954	-112.73823
Flat Hills C	UR-120	40.16625	-112.75558
Flat Hills C	UR-121	40.16623	-112.75561
Flat Hills C	UR-122	40.16624	-112.75562
Flat Hills C	UR-123	40.16694	-112.7554

Source	Catalog #	Latitude	Longitude
Flat Hills C	UR-124	40.16914	-112.75156
Flat Hills C	UR-125	40.1752	-112.74947
Flat Hills D	UR-24	40.20051	-112.75597
Flat Hills D	UR-30	40.18906	-112.75919
Flat Hills D	UR-35	40.19292	-112.75557
Flat Hills E	UR-27	40.2018	-112.75725
Flat Hills E	UR-36	40.19354	-112.76013

Table D-6: Page & Bacon (2016) Browns Bench, Browns Bench Area, and Butte Valley Group A obsidian samples.

Source	ID	UTM Zone	Easting	Northing
Browns Bench	CD-1	11	658515	4662154
Browns Bench	BBS-1	11	678187	4664142
Browns Bench	TC-1	11	672670	4659900
Browns Bench	TC-2	11	672958	4660159
Browns Bench	DP-1	11	633997	4651115
Browns Bench	GC-1	11	645574	4637300
Browns Bench	THC-1	11	648477	4656984
Browns Bench	CD-2	11	663420	4664072
Browns Bench	CCR-1	11	673639	4674321
Browns Bench	CD-3	11	663156	4664099
Browns Bench	JP-1	11	691141	4644342
Browns Bench	MHS-1	11	637586	4652133
Browns Bench	MHS-2	11	636875	4652566
Browns Bench	CCR-2	11	673604	4674413
Browns Bench	DP-2	11	633420	4651212
Browns Bench	CD-4	11	663642	4663874
Browns Bench	MMB-1	11	714306	4681542
Browns Bench	PM-1	11	719076	4669542
Browns Bench	PM-2	11	716650	4678822
Browns Bench	HG-2	11	715828	4677346
Browns Bench	HG-3	11	716311	4678432
Browns Bench	HG-4	11	711605	4678530
Browns Bench	MMB-2	11	714081	4681315
Browns Bench	MMB-3	11	714233	4681293
Browns Bench	TB-1	11	718108	4666844
Browns Bench	MMB-4	11	712890	4680860
Browns Bench	PM-4	11	719839	4669185
Browns Bench	SS-2	11	737975	4675394
Browns Bench	SS-1	11	738620	4676068
Browns Bench	H-1	11	704690	4688517
Browns Bench	BH-6	11	749524	4666214
Browns Bench	BH-1	11	750564	4659977
Browns Bench	IP-2	11	747563	4656452
Browns Bench	BBR-1	11	678330	4649443
Browns Bench	NS-1	11	745382	4648268
Browns Bench	BH-2	11	749994	4661147
Browns Bench	NS-2	11	747323	4650214
Browns Bench	BH-3	11	749376	4662078

Source	ID	UTM Zone	Easting	Northing
Browns Bench	MMB-5	11	707795	4691462
Browns Bench	BH-5	11	748070	4663604
Browns Bench	IP-1	11	747728	4655238
Browns Bench	BCR-3	11	717046	4654230
Browns Bench	TB-8	11	722569	4654039
Browns Bench	TB-3	11	719179	4659974
Browns Bench	TB-7	11	722136	4659962
Browns Bench	GM-2	11	711651	4651685
Browns Bench	TB-2	11	718494	4659996
Browns Bench	TB-5	11	720860	4659537
Browns Bench	GM-1	11	708988	4650467
Browns Bench	BCR-2	11	716923	4657966
Browns Bench	TB-6	11	721377	4659939
Browns Bench	TB-4	11	719324	4659293
Browns Bench	MB-1	11	729810	4666864
Browns Bench	BCR-1	11	709887	4662124
Browns Bench	BR-3	11	657540	4624991
Browns Bench	MGH-2	11	700819	4655716
Browns Bench	MGH-3	11	703205	4655515
Browns Bench	MGH-1	11	700810	4655603
Browns Bench Area	CD-1	11	658515	4662154
Browns Bench Area	TC-1	11	672670	4659900
Browns Bench Area	DP-1	11	633997	4651115
Browns Bench Area	GC-1	11	645574	4637300
Browns Bench Area	THC-1	11	648477	4656984
Browns Bench Area	MHS-1	11	637586	4652133
Browns Bench Area	MHS-2	11	636875	4652566
Browns Bench Area	DP-2	11	633420	4651212
Browns Bench Area	GR-1	11	659578	4621571
Browns Bench Area	BR-1	11	661276	4624563
Browns Bench Area	BR-2	11	660270	4625600
Browns Bench Area	BR-3	11	657540	4624991
Butte Valley Group A	BBN-1	11	675611	4673165
Butte Valley Group A	CCR-1	11	673639	4674321
Butte Valley Group A	CCR-2	11	673604	4674413
Butte Valley Group A	PM-1	11	719076	4669542
Butte Valley Group A	HG-1	11	713669	4675993
Butte Valley Group A	PM-30	11	717883	4667938
Butte Valley Group A	TB-1	11	718108	4666844
Butte Valley Group A	MMB-4	11	712890	4680860

Source	ID	UTM Zone	Easting	Northing
Butte Valley Group A	PM-4	11	719839	4669185
Butte Valley Group A	SS-2	11	737975	4675394
Butte Valley Group A	SS-1	11	738620	4676068
Butte Valley Group A	BH-6	11	749524	4666214
Butte Valley Group A	NS-2	11	747323	4650214
Butte Valley Group A	BH-4	11	748556	4662008
Butte Valley Group A	BH-3	11	749376	4662078
Butte Valley Group A	TB-8	11	722569	4654039
Butte Valley Group A	TB-3	11	719179	4659974
Butte Valley Group A	TB-2	11	718494	4659996
Butte Valley Group A	TB-5	11	720860	4659537
Butte Valley Group A	BCR-2	11	716923	4657966
Butte Valley Group A	TB-6	11	721377	4659939
Butte Valley Group A	TB-4	11	719324	4659293
Butte Valley Group A	BCR-1	11	709887	4662124
Butte Valley Group A	SS-3	11	737431	4674197
Butte Valley Group A	TP-2	11	734022	4671173
Butte Valley Group A	MGH-3	11	703205	4655515
Butte Valley Group A	TP-3	11	734560	4671448
Butte Valley Group A	TP-1	11	732921	4671074

Appendix E: X-ray fluorescence (XRF) Lab Results 2020

X-Ray Fluorescence Analysis of Geologic Obsidian Samples from Alluvial and Colluvial Contexts in Western Utah and Eastern Nevada

Alex J. Nyers
Northwest Research Obsidian Studies Laboratory

One hundred and fourteen geologic samples collected from alluvial and colluvial contexts in western Utah as well as eastern Nevada were submitted for energy dispersive X-ray fluorescence trace element provenance analysis. The samples were prepared and analyzed at the Northwest Research Obsidian Studies Laboratory under the accession number 2020-86.

Analytical Methods

X-Ray Fluorescence Analysis. Nondestructive trace element analysis of the samples was completed using a Thermo NORAN QuanX-EC energy dispersive X-ray fluorescence (EDXRF) spectrometer. The analyzer uses an X-ray tube excitation source and a solid-state detector to provide spectroscopic analysis of elements ranging from sodium to uranium (atomic numbers 11 to 92) and in concentrations ranging from a few parts per million to 100 percent. The system is equipped with a Peltier-cooled Si(Li) detector and an air-cooled X-ray tube with a rhodium target and a 76 micron Be window. The tube is driven by a 50 kV 2mA high voltage power supply, providing a voltage range of 4 to 50 kV. During operation, the tube current is automatically adjusted to an optimal 50% dead time, a variable that is significantly influenced by the varying physical sizes of the different analyzed samples. Small specimens are mounted in 32 mm-diameter sample cups with mylar windows on a 20-position sample tray while larger samples are fastened directly to the surface of the tray.

For the elements that are reported in Table A-1, we analyzed the collection with a 3.5 mm as well as an 8.8 mm beam collimator installed with tube voltage and count times adjusted for optimum results. Instrument control and data analysis are performed using WinTrace software (version 7) running under the Windows 7 operating system.

The diagnostic trace element values used to characterize the samples are compared directly to those for known obsidian and fine-grained volcanic (FGV) sources reported in the literature and with unpublished trace element data collected through analysis of geologic source samples (Northwest Research 2020a). Artifacts are correlated to a parent obsidian, FGV, or basalt source (or geochemical source group) if diagnostic trace element values fall within about two standard deviations of the analytical uncertainty of the known upper and lower limits of chemical variability recorded for the source. Occasionally, visual attributes are used to corroborate the source assignments although sources are never assigned solely on the basis of megascopic characteristics.

Results of Analysis

X-Ray Fluorescence Analysis. The obsidian samples analyzed by X-ray fluorescence methods were collected from five sampling locations. These sampling locations were tailored to understand the geologic extent of the following obsidian sources: Black Rock Area, Ferguson Wash, Mineral Mountains, Modena, and Topaz Mountain. XRF analysis resulted in six distinct obsidian sources identified within the submitted samples. One of these, dubbed here as "Ferguson Wash B", represents a newly identified sub-source of Ferguson Wash which is distinguished by elevated strontium (Sr) and yttrium (Y) levels relative to the well-characterized Ferguson Wash source. Four of the 114 analyzed samples could not be correlated to any obsidian within the NWROSL database.

1
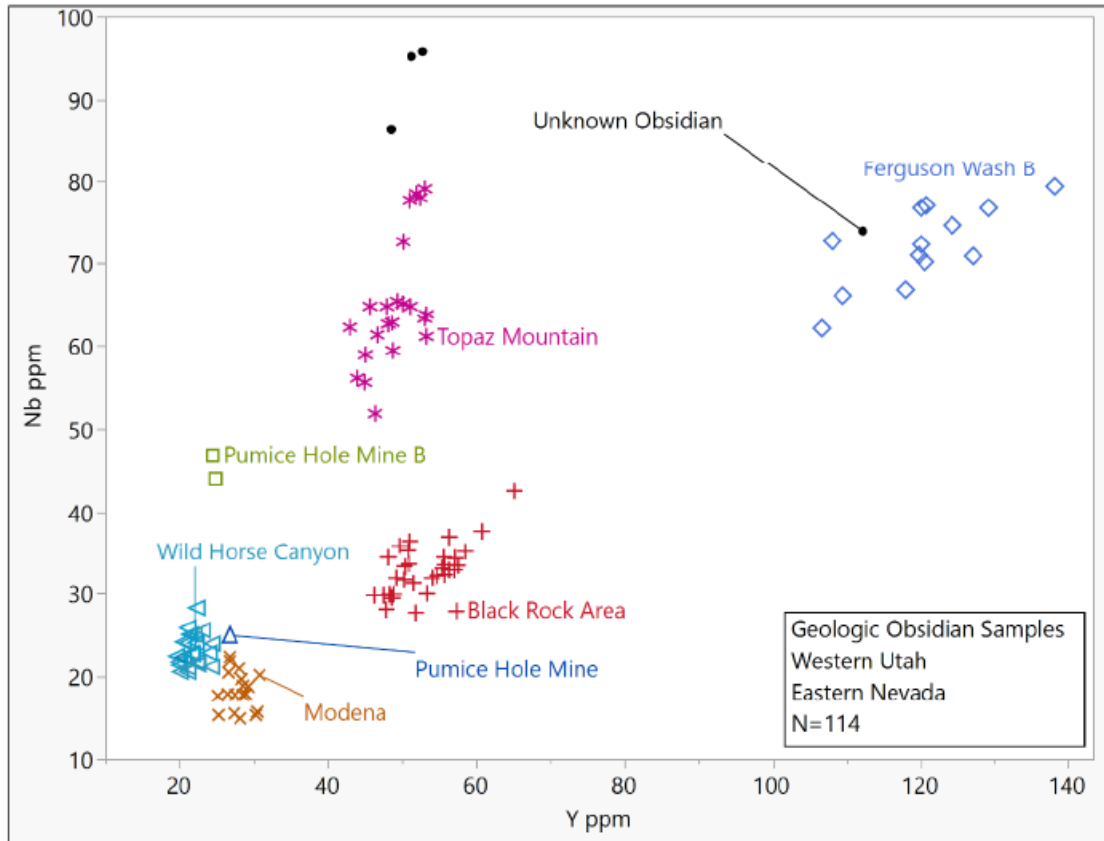
Figure 3 - Scatterplot of yttrium (Y) plotted versus niobium (Nb) for analyzed samples.

Information concerning the location, geologic setting, and prehistoric use of obsidian sources identified in the current investigation may be found at www.sourcecatalog.com (Northwest Research 2020b).

References Cited

Northwest Research Obsidian Studies Laboratory

  2020a   Northwest Research Obsidian Studies Laboratory World Wide Web Site (www.obsidianlab.com).

  2020b   Northwest Research U. S. Obsidian Source Catalog (www.sourcecatalog.com).

Appendix

Results of X-Ray Fluorescence Analysis

Table A-1. Results of XRF Studies: Geologic Obsidian Samples from Western Utah and Eastern Nevada

Site	Specimen No.	Catalog No.	Trace Element Concentrations						Geochemical Source
			Rb	Sr	Y	Zr	Nb	Ba	
BRA	1	207	265	26	58	111	34	0	Black Rock Area
			± 4	2	2	3	3	21	
BRA	2	212	227	18	51	98	35	0	Black Rock Area
			± 4	2	2	3	3	46	
BRA	3	222	360	24	56	110	35	0	Black Rock Area
			± 6	2	2	3	3	32	
BRA	4	232	266	31	50	115	32	0	Black Rock Area
			± 4	2	2	3	3	35	
BRA	5	234	288	22	57	106	33	0	Black Rock Area
			± 4	2	2	3	3	24	
BRA	6	235	251	19	52	102	31	0	Black Rock Area
			± 4	2	2	3	3	42	
BRA	7	241	271	27	57	108	28	0	Black Rock Area
			± 4	2	2	3	3	21	
BRA	8	248	263	22	56	106	32	0	Black Rock Area
			± 4	2	2	3	3	21	
BRA	9	261	232	25	49	114	32	0	Black Rock Area
			± 4	2	2	3	2	45	
BRA	10	268	285	22	48	99	35	0	Black Rock Area
			± 5	2	2	3	3	30	
BRA	11	278	280	22	54	100	32	0	Black Rock Area
			± 5	2	3	3	3	20	
BRA	12	288	333	26	56	120	33	0	Black Rock Area
			± 5	2	2	3	3	22	
BRA	13	296	375	25	61	118	38	0	Black Rock Area
			± 5	2	2	3	3	21	
BRA	14	304	200	17	51	105	37	0	Black Rock Area
			± 4	2	2	3	3	38	
BRA	15	313	135	29	56	110	34	0	Black Rock Area
			± 2	2	2	3	3	38	
BRA	16	320	377	21	65	113	43	0	Black Rock Area
			± 6	2	3	3	3	20	
BRA	17	323	238	18	59	106	35	0	Black Rock Area
			± 4	2	2	3	3	24	
BRA	18	325	343	32	53	283	96	0	Unknown Obsidian
			± 5	2	2	4	3	26	
BRA	19	327	219	20	55	106	33	0	Black Rock Area
			± 4	2	2	3	3	28	
BRA	20	329	214	31	52	106	28	0	Black Rock Area
			± 3	2	2	3	3	46	

All trace element values reported in parts per million; ± = analytical uncertainty estimate (in ppm).

NA = Not available; ND = Not detected; NM = Not measured; * = Small sample; FGV = Fine-grained volcanic specimen.

A - 1

Northwest Research Obsidian Studies Laboratory

Table A-1. Results of XRF Studies: Geologic Obsidian Samples from Western Utah and Eastern Nevada

Site	Specimen No.	Catalog No.	Trace Element Concentrations						Geochemical Source
			Rb	Sr	Y	Zr	Nb	Ba	
BRA	21	331	291	21	56	104	37	0	Black Rock Area
			± 5	2	2	3	3	36	
BRA	22	333	247	28	49	261	86	0	Unknown Obsidian
			± 4	2	2	4	3	48	
BRA	23	335	247	18	50	99	33	6	Black Rock Area
			± 4	2	2	3	3	49	
BRA	24	340	298	25	57	115	34	0	Black Rock Area
			± 4	2	2	3	3	44	
BRA	25	348	281	20	49	100	30	0	Black Rock Area
			± 5	2	2	3	3	34	
BRA	26	352	182	18	51	98	34	6	Black Rock Area
			± 3	2	2	3	3	43	
BRA	27	356	316	24	48	102	30	0	Black Rock Area
			± 5	2	2	3	3	36	
BRA	28	359	160	21	46	103	30	6	Black Rock Area?
			± 3	2	2	3	3	42	
BRA	29	360A	237	24	48	94	28	0	Black Rock Area
			± 4	2	2	3	3	38	
BRA	30	360B	180	19	48	93	30	0	Black Rock Area?
			± 4	2	2	3	3	22	
FW	31	004	489	22	120	178	71	0	Ferguson Wash B
			± 6	2	3	3	3	38	
FW	32	008	420	22	127	157	71	6	Ferguson Wash B
			± 5	2	3	3	3	37	
FW	33	013	495	25	129	167	77	6	Ferguson Wash B
			± 6	2	3	3	3	27	
FW	34	015	514	25	120	178	77	0	Ferguson Wash B
			± 6	2	3	4	3	41	
FW	35	016	335	19	108	152	73	0	Ferguson Wash B
			± 4	2	3	4	3	45	
FW	36	017	491	27	121	168	77	0	Ferguson Wash B
			± 6	2	3	4	3	40	
FW	37	018	465	25	124	164	75	0	Ferguson Wash B
			± 5	2	3	3	3	38	
FW	38	020	384	22	110	146	66	6	Ferguson Wash B
			± 5	2	3	3	3	44	
FW	39	021	413	21	120	148	72	0	Ferguson Wash B
			± 5	2	3	3	3	23	
FW	40	024	486	27	121	164	70	0	Ferguson Wash B
			± 6	2	3	3	3	44	

All trace element values reported in parts per million; ± = analytical uncertainty estimate (in ppm).

NA = Not available; ND = Not detected; NM = Not measured; * = Small sample; FGV = Fine-grained volcanic specimen.

A - 2

Northwest Research Obsidian Studies Laboratory
Table A-1. Results of XRF Studies: Geologic Obsidian Samples from Western Utah and Eastern Nevada

Site	Specimen No.	Catalog No.	Trace Element Concentrations						Geochemical Source
			Rb	Sr	Y	Zr	Nb	Ba	
FW	41	025	486	27	138	174	79	0	Ferguson Wash B
			± 5	2	3	3	3	35	
FW	42	029	384	27	118	150	67	0	Ferguson Wash B
			± 5	2	3	3	3	37	
FW	43	032	356	22	107	144	62	0	Ferguson Wash B
			± 4	2	3	3	3	21	
MM	44	801	191	46	22	113	22	98	Wild Horse Canyon
			± 4	2	2	3	2	38	
MM	45	805	192	51	23	117	22	111	Wild Horse Canyon
			± 4	3	2	3	2	38	
MM	46	807	192	50	24	122	21	161	Wild Horse Canyon
			± 4	3	2	3	2	38	
MM	47	808	142	49	21	132	22	150	Wild Horse Canyon
			± 3	3	2	3	3	41	
MM	48	810	316	24	50	106	36	0	Black Rock Area
			± 5	2	2	3	3	33	
MM	49	811	254	27	55	128	32	0	Black Rock Area
			± 4	2	2	3	3	37	
MM	50	812	368	33	51	284	95	0	Unknown Obsidian
			± 5	2	2	4	3	35	
MM	51	816	289	20	53	102	30	0	Black Rock Area
			± 5	2	2	3	3	44	
MM	52	820	251	24	49	112	30	87	Black Rock Area
			± 4	2	2	3	3	35	
MM	53	825	213	14	25	110	48	0	Pumice Hole Mine B
			± 3	2	2	3	3	40	
MM	54	829	146	48	23	111	26	135	Wild Horse Canyon
			± 3	2	2	3	2	39	
MM	55	835	172	48	21	110	21	172	Wild Horse Canyon
			± 4	2	2	3	2	40	
MM	56	839	227	53	25	122	24	126	Wild Horse Canyon
			± 4	3	2	3	3	37	
MM	57	845	208	15	24	104	47	0	Pumice Hole Mine B
			± 3	2	2	3	3	35	
MM	58	847	181	76	27	130	22	307	Modena
			± 4	3	2	3	2	37	
MM	59	848	207	45	21	118	24	126	Wild Horse Canyon
			± 4	3	2	3	3	33	
MM	60	849	193	49	22	115	25	181	Wild Horse Canyon
			± 4	3	2	3	3	32	

All trace element values reported in parts per million; ± = analytical uncertainty estimate (in ppm).

NA = Not available; ND = Not detected; NM = Not measured; * = Small sample; FGV = Fine-grained volcanic specimen.

Table A-1. Results of XRF Studies: Geologic Obsidian Samples from Western Utah and Eastern Nevada

Site	Specimen No.	Catalog No.	Trace Element Concentrations						Geochemical Source
			Rb	Sr	Y	Zr	Nb	Ba	
MM	61	857	180	44	20	111	22	158	Wild Horse Canyon
			± 4	2	2	3	2	40	
MM	62	858	191	52	21	112	21	125	Wild Horse Canyon
			± 4	3	2	3	2	36	
MM	63	862	162	47	20	109	21	0	Wild Horse Canyon
			± 3	2	2	3	2	40	
MM	64	864	144	41	22	105	23	132	Wild Horse Canyon
			± 3	2	2	3	2	41	
MOD	65	100	229	106	31	128	20	461	Modena
			± 5	3	2	3	2	40	
MOD	66	103	141	84	29	119	18	347	Modena
			± 3	3	2	3	2	41	
MOD	67	401	193	86	31	134	16	383	Modena
			± 4	3	2	3	2	41	
MOD	68	412	166	86	27	133	18	353	Modena
			± 3	3	2	3	2	46	
MOD	69	414	167	83	30	128	15	406	Modena
			± 3	3	2	3	2	45	
MOD	70	417	158	85	27	114	16	371	Modena
			± 3	3	2	3	2	55	
MOD	71	426	199	97	28	125	15	413	Modena
			± 4	3	2	3	2	37	
MOD	72	433	189	91	28	123	20	374	Modena
			± 4	3	2	3	3	42	
MOD	73	436	89	80	28	115	21	389	Modena?
			± 2	3	2	3	3	45	
MOD	74	439	164	81	25	122	15	415	Modena
			± 3	3	2	3	2	42	
MOD	75	443	239	103	29	146	19	425	Modena
			± 4	3	2	3	2	46	
MOD	76	447	248	95	27	130	22	404	Modena
			± 5	3	2	3	2	37	
MOD	77	448	190	91	29	120	18	398	Modena
			± 4	3	2	3	2	41	
MOD	78	449	155	93	29	134	19	304	Modena?
			± 3	3	2	3	2	50	
MOD	79	451	122	76	25	123	18	426	Modena?
			± 3	3	2	3	3	42	
MOD	80	456	207	88	27	112	21	376	Modena
			± 4	3	2	3	2	67	

All trace element values reported in parts per million; ± = analytical uncertainty estimate (in ppm).

NA = Not available; ND = Not detected; NM = Not measured; * = Small sample; FGV = Fine-grained volcanic specimen.

Northwest Research Obsidian Studies Laboratory
Table A-1. Results of XRF Studies: Geologic Obsidian Samples from Western Utah and Eastern Nevada

Site	Specimen No.	Catalog No.	Trace Element Concentrations						Geochemical Source
			Rb	Sr	Y	Zr	Nb	Ba	
MOD	81	459	211	16	112	217	74	0	Unknown Obsidian
			± 3	2	3	3	3	33	
MOD	82	461	196	87	28	128	18	328	Modena
			± 4	3	2	3	2	41	
TM	83	603	444	19	53	130	64	0	Topaz Mountain
			± 6	2	2	3	3	45	
TM	84	605	460	26	48	137	65	0	Topaz Mountain
			± 5	2	3	3	3	36	
TM	85	608	514	31	50	145	73	0	Topaz Mountain
			± 6	3	3	3	3	20	
TM	86	610	368	23	49	146	63	0	Topaz Mountain?
			± 5	2	3	3	3	42	
TM	87	618	434	21	53	123	78	0	Topaz Mountain
			± 5	2	3	3	3	34	
TM	88	623	446	37	49	156	65	0	Topaz Mountain
			± 5	2	3	3	3	36	
TM	89	628	396	25	50	154	65	0	Topaz Mountain
			± 5	2	3	3	3	34	
TM	90	634	449	27	53	149	61	0	Topaz Mountain
			± 5	2	2	3	3	37	
TM	91	647	414	28	51	128	78	0	Topaz Mountain
			± 4	2	3	3	3	82	
TM	92	651	398	25	43	127	62	0	Topaz Mountain
			± 4	2	2	3	3	36	
TM	93	653	354	24	45	127	56	0	Topaz Mountain
			± 5	2	2	3	3	31	
TM	94	664	345	23	45	144	59	0	Topaz Mountain
			± 4	2	2	3	3	37	
TM	95	665	529	29	52	129	78	0	Topaz Mountain
			± 5	2	3	3	3	22	
TM	96	666	285	28	48	151	63	0	Topaz Mountain?
			± 3	2	2	3	3	45	
TM	97	667	359	22	49	140	59	0	Topaz Mountain
			± 4	2	2	3	3	41	
TM	98	671	434	20	46	144	65	0	Topaz Mountain
			± 6	2	2	3	3	35	
TM	99	672	549	23	53	129	79	0	Topaz Mountain
			± 6	2	3	3	3	34	
TM	100	681	368	25	44	126	56	0	Topaz Mountain
			± 5	2	2	3	3	49	

All trace element values reported in parts per million; ± = analytical uncertainty estimate (in ppm).

NA = Not available; ND = Not detected; NM = Not measured; * = Small sample; FGV = Fine-grained volcanic specimen.

A - 5

Northwest Research Obsidian Studies Laboratory

Table A-1. Results of XRF Studies: Geologic Obsidian Samples from Western Utah and Eastern Nevada

Site	Specimen No.	Catalog No.	Trace Element Concentrations						Geochemical Source
			Rb	Sr	Y	Zr	Nb	Ba	
TM	101	684	294	29	46	144	52	0	Topaz Mountain?
			± 4	2	2	3	3	37	
TM	102	685	464	21	47	146	61	0	Topaz Mountain
			± 6	2	2	3	3	34	
TM	103	686	530	26	51	147	65	0	Topaz Mountain
			± 6	2	3	3	3	33	
TM	104	688	322	28	53	152	63	0	Topaz Mountain
			± 3	2	3	3	3	31	
MM	105	813A	169	44	20	103	21	138	Wild Horse Canyon
			± 3	2	2	2	2	41	
MM	106	813B	196	51	21	110	26	112	Wild Horse Canyon
			± 3	2	2	2	2	39	
MM	107	814	188	48	22	104	23	120	Wild Horse Canyon
			± 3	2	2	2	2	52	
MM	108	815	196	56	24	112	23	157	Wild Horse Canyon
			± 3	2	2	2	2	37	
MM	109	817	193	48	22	114	28	152	Wild Horse Canyon
			± 4	2	2	2	2	38	
MM	110	818	219	53	22	116	25	130	Wild Horse Canyon
			± 4	2	2	2	2	40	
MM	111	819	200	50	20	109	23	115	Wild Horse Canyon
			± 3	2	2	2	2	39	
MM	112	822	194	49	21	108	24	185	Wild Horse Canyon
			± 3	2	2	2	2	40	
MM	113	826	170	73	27	135	25	338	Pumice Hole Mine
			± 4	3	2	3	2	39	
MM	114	850	202	52	22	111	24	195	Wild Horse Canyon
			± 3	2	2	2	2	44	
NA	RGM-1	RGM-1	148	111	30	219	12	806	RGM-1 Reference Standard
			± 4	3	2	4	2	27	

All trace element values reported in parts per million; ± = analytical uncertainty estimate (in ppm).

NA = Not available; ND = Not detected; NM = Not measured; * = Small sample; FGV = Fine-grained volcanic specimen.

A - 6

Appendix F: X-ray fluorescence (XRF) Lab Results 2021

Results of X-Ray Fluorescence Analysis
2021 – 64

Geologic Specimens

Ferguson Wash Area, Tooele County, Utah (N=13)

Modena Area, Lincoln County, Nevada (N=11)

Topaz Mountain Area, Juab County, Utah (N=1)

Alex J. Nyers

November 2021

Northwest Research Obsidian Studies Laboratory

Table 1. Summary of results of trace element analysis of the project specimens.

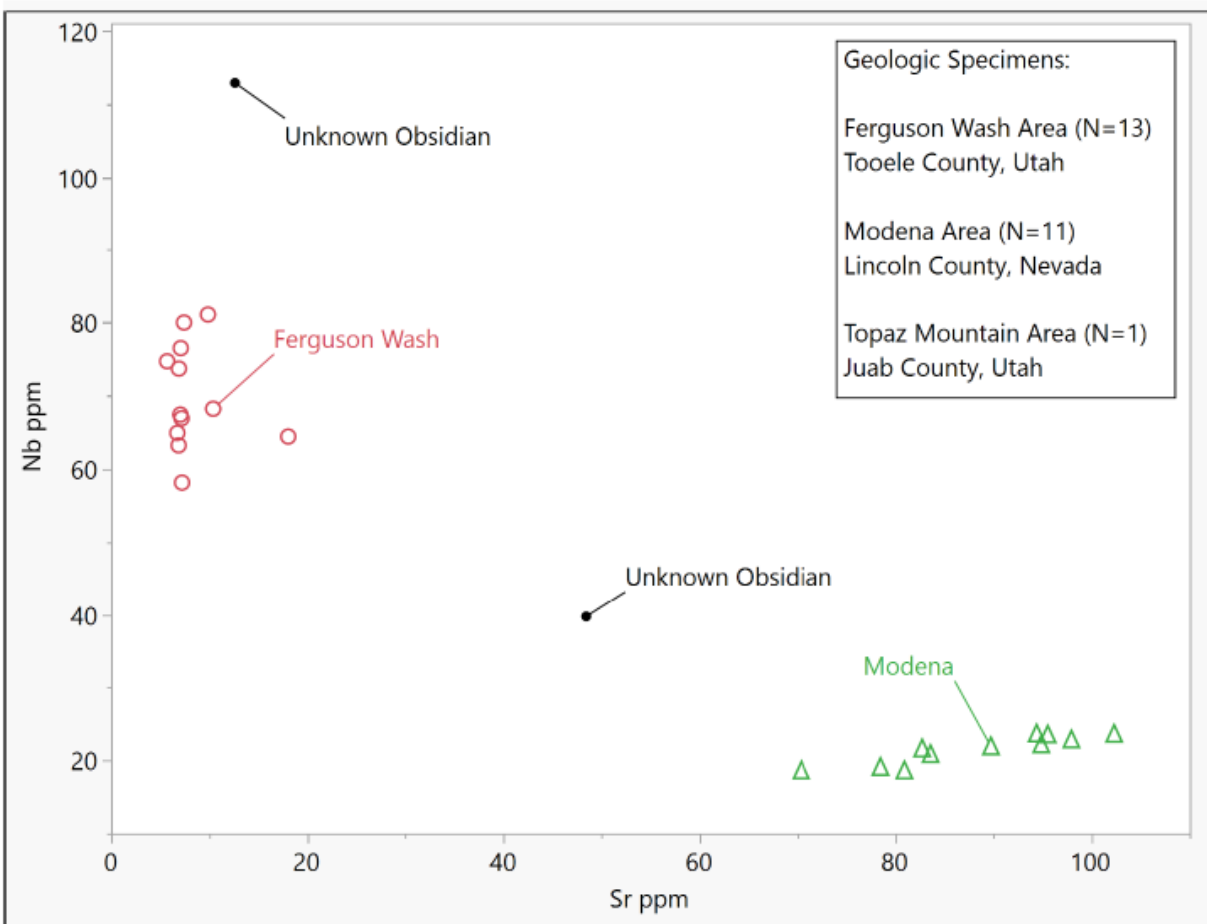| GEOCHEMICAL SOURCE | GEOLOGIC SAMPLES ANALYZED | | | TOTAL |
	FERGUSON WASH AREA	MODENA AREA	TOPAZ MOUNTAIN AREA	
Modena	-	11	-	11
Ferguson Wash	12	-	-	12
Unknown Obsidian	1	-	1	2
TOTAL	13	11	1	25

Figure 1 - Scatterplot of strontium (Sr) plotted versus niobium (Nb) for analyzed obsidian artifacts.

Northwest Research Obsidian Studies Laboratory

Table A-1. Results of XRF Studies: Geologic Specimens, Lincoln County, Nevada, Juab County, Utah, and Tooele County, Utah

Site	Specimen No.	Catalog No.	Trace Element Concentrations								Geochemical Source
			Rb	Sr	Y	Zr	Nb	Ba	Ti	Fe	
Modena Area	1	472	193 ± 0.4	78 0.3	25 0.4	132 0.4	19 0.4	491 5	1264 4	9882 10	Modena
Modena Area	2	473	270 ± 0.7	102 0.5	37 0.7	157 0.7	24 0.7	440 3.9	694 3	2454 6	Modena
Modena Area	3	483	223 ± 0.6	90 0.4	29 0.5	145 0.6	22 0.6	382 4.5	1054 4	5258 7	Modena
Modena Area	4	488	238 ± 0.6	96 0.4	31 0.5	156 0.6	24 0.6	379 4.9	1366 4	8987 9	Modena
Modena Area	5	489	216 ± 0.7	83 0.5	29 0.6	135 0.7	22 0.7	481 4.3	927 4	5412 7	Modena
Modena Area	6	494	212 ± 0.6	84 0.4	27 0.5	139 0.6	21 0.6	303 3.9	771 3	2854 6	Modena
Modena Area	7	501	239 ± 0.6	95 0.5	30 0.6	149 0.6	22 0.6	310 3.9	709 3	2363 5	Modena
Modena Area	8	503	243 ± 0.6	98 0.4	32 0.6	157 0.6	23 0.6	347 3.9	617 3	3376 6	Modena
Modena Area	9	506	209 ± 0.5	81 0.3	29 0.4	135 0.5	19 0.5	521 4.2	652 4	4276 7	Modena
Modena Area	10	509	186 ± 1.1	70 0.7	26 0.9	128 1	19 1	352 9.7	647 10	3282 13	Modena
Modena Area	11	510	237 ± 0.7	94 0.5	32 0.6	152 0.7	24 0.7	290 3.7	655 3	2883 6	Modena
Topaz Mountain Area	12	699	194 ± 1.1	50 0.6	33 0.9	181 1.1	41 1	269 11	1083 11	6024 16	Unknown Obsidian
Ferguson Wash Area	31	4	454 ± 1.1	7 0.2	108 0.9	165 0.9	58 0.9	53 3.9	443 3	8635 9	Ferguson Wash
Ferguson Wash Area	32	8	546 ± 1.4	10 0.4	126 1.2	164 1.1	68 1.2	56 3.3	317 2	4954 7	Ferguson Wash
Ferguson Wash Area	33	13	639 ± 1.6	10 0.4	144 1.4	190 1.3	81 1.4	46 3.5	376 3	5754 8	Ferguson Wash
Ferguson Wash Area	34	15	531 ± 1.2	7 0.3	122 1	157 0.9	65 1	79 4.6	758 3	9826 10	Ferguson Wash
Ferguson Wash Area	35	16	613 ± 1.5	7 0.3	137 1.3	164 1.1	74 1.2	22 3.5	420 3	5425 7	Ferguson Wash
Ferguson Wash Area	36	17	671 ± 1.6	7 0.3	143 1.3	195 1.2	77 1.3	49 3.8	521 3	5816 8	Ferguson Wash
Ferguson Wash Area	37	18	556 ± 1.3	7 0.3	125 1.1	163 1	67 1.1	32 3.8	486 3	6420 8	Ferguson Wash
Ferguson Wash Area	38	20	577 ± 1.4	7 0.3	126 1.1	170 1	67 1.1	52 4.1	591 3	6590 8	Ferguson Wash

Trace element values reported in parts per million except where specifically designated; ± = analytical uncertainty estimate (in ppm).
NA = Not available; ND = Not detected; NM = Not measured; * = Small sample; FGV = Fine-grained volcanic specimen.

A - 1

413

Table A-1. Results of XRF Studies: Geologic Specimens, Lincoln County, Nevada,
Juab County, Utah, and Tooele County, Utah

Site	Specimen No.	Catalog No.	Rb	Sr	Y	Zr	Nb	Ba	Ti	Fe	Geochemical Source
			Trace Element Concentrations								
Ferguson Wash Area	39	21	611 ±1.6	6 0.4	141 1.4	170 1.2	75 1.4	ND ND	361 2	4421 7	Ferguson Wash
Ferguson Wash Area	40	24	870 ± 2	13 0.5	202 1.7	273 1.5	113 1.7	146 4.4	594 3	8762 9	Unknown Obsidian
Ferguson Wash Area	41	25	650 ±1.4	7 0.3	144 1.1	191 1	80 1.1	72 4.1	469 3	10474 10	Ferguson Wash
Ferguson Wash Area	42	29	519 ±1.3	18 0.4	120 1.1	153 1	64 1.1	105 4.2	653 3	6286 8	Ferguson Wash
Ferguson Wash Area	43	32	531 ±1.3	7 0.3	117 1.1	157 1	63 1.1	36 3.8	467 3	6912 8	Ferguson Wash
NA	RGM-1	RGM-1	155 ±0.4	109 0.4	24 0.4	231 0.5	10 0.4	809 6	1573 5	13035 12	RGM-1 Reference Standard

Trace element values reported in parts per million except where specifically designated; ± = analytical uncertainty estimate (in ppm).
NA = Not available; ND = Not detected; NM = Not measured; * = Small sample; FGV = Fine-grained volcanic specimen.

A - 2